What lies beneath: investigating the distribution and dynamics of landslides in lakes, and fjords of New Zealand

Ryan Martin Dick

Thesis submitted for the degree of

Doctor of Philosophy



School of Geography, Politics & Sociology

Newcastle University

March 2021

Abstract

Subaerial and subaqueous landslides are a significant hazard in intramountainous lake and fjord landscapes across the globe. Landslides into, and within, the lakes and fjords can generate tsunamis that present a risk to shoreline communities and infrastructure. Understanding the landslide and associated hazard cascade (e.g. landslide tsunamis) is reliant on both identification of deposits to assess their magnitude-frequency relationship, and detailed analysis of the deposits, which can provide information on the landslide's emplacement dynamics. This thesis aims to better understand the distribution and dynamics of landslides within lakes and fjords in the seismically active, high-mountain landscape of the South Island, New Zealand, to improve the understanding of the hazard. Despite the similar physiographic setting to many global counterparts (e.g. Norway, European Alps, western Canada, Patagonia), there have only been a few studies to quantify the hazard from landslides into and within lakes and fjords of New Zealand, compared to the subaerial landslide hazard. Previous research suggests that the lakes and fjords of New Zealand may provide a well-preserved archive of previously unknown landslide deposits.

A new literature-based inventory of lakes and fjords with known landslides is presented within this thesis. In total, 15 lakes and 5 fjords were identified as having documented landslide events. The lakes and fjords contain a variety of landslide types; including subaerial originating *(n=7),* deltaic landslides *(n=4),* and mass-transport deposits, assumed to have originated from the subaqueous slopes *(n=7).* Previous bathymetric data investigations in Lake Tekapo and Milford Sound/Piopiotahi reveal deposits from multiple sources. Earthquakes are the main trigger, with 9 cases related to known earthquakes. Earthquakes are assumed to be the trigger in 5 further lakes and fjords. In Milford Sound/Piopiotahi, morphological and morphometric analysis, and numerical modelling by DAN3D of previously identified deposits from high-resolution bathymetric data indicate that the landslides exhibit a variety of morphologies, morphometries, and generally low apparent mobility. Factors such as transitioning from air to water, abrupt slope angle changes from the steep fjord walls to flat basin wall, and lack of lateral confinement resulting in freely spreading deposits appear to contribute to the apparent low mobility. Furthermore, the best fit numerical simulations required high basal friction angles, and/or low turbulence parameters to retard the landslide runout The modelling results also found a Voellmy rheology to be effective in simulating the subaqueous portion of landslide runout, as varying the velocity-dependent turbulence coefficient parameter could represent the resistance to flow

by the water, in contrast to the frictional rheology where resistance is governed only by basal friction angle.

In Lake Wānaka, newly collected bathymetric and sub-bottom data reveal comparatively few deposits on the lakebed (*n=17*), in contrast to the large number of subaerial deposits mapped and identified within the terrestrial catchment in this thesis (*n=202*). Limited subsurface penetration precludes identifying more deposits within the lake infill. Sub-bottom data do reveal that some of the visible deposits within the lake are draped by lake sediments, obscuring their true thicknesses. Therefore, burial of deposits may be obscuring the total number of deposits within the lake basin. The research presented within this thesis builds a proposed conceptual model for landslide distributions in New Zealand lakes and fjords. Landslides may occur more frequently in areas of frequent and strong seismicity. In contrast, regions with low frequency seismicity will likely trigger fewer landslides into, and within the subaqueous basins less often. Variations in sedimentation rates within the lakes and fjords control how long deposits will be visible on the basin floors for. Furthermore, the newly identified deposits, and quantitative insights into the landslide emplacement dynamics provide information that can be taken forward to assess tsunami hazard, which may present the greatest risk to shoreline communities and infrastructure around New Zealand lakes and fjords.

Dedication

Dedicated to my mum

(1957-2016)

At least you didn't have to listen to my peenging these last few years, and at least you don't have to read this one!

Acknowledgements

First and foremost I would like to thank my supervisors: Stuart Dunning, Andy Henderson, Nick Rosser, Richard Bates, and Dave Tappin. Stu, I just have to say a huge thanks, mostly for putting up with me these last few years, especially when this PhD was at times, a metaphorical, and literal car crash. I don't think anyone could have envisaged the logistical nightmares and excessive levels of faff that we've endured just to get off the ground. I'm sure you didn't think you were signing up to be learning about New Zealand Maritime Law and international shipping consignment regulations, chasing down DHL over missing kit and carnets, and being up near midnight trying to cancel a boat purchase. All of that to just even try and look for some nice lake rock avalanche deposits! But thanks also for the encouragement, letting me crack on, but keeping me on track when I invariably went off on many tangents. You also never did get some nice New Zealand fieldwork with me. Next time! (But we're not buying a boat)

Rich, thank you for the opportunities to get some insight and experience into doing a marine survey. And thank you for all your help with the data processing. Nick, thanks for all your help, support, detailed insight, and for taking the time to provide such detailed feedback and guidance. Dave, thank you for always taking the time to sit with me and have a good chat and discussion when I was down visiting the BGS. Andy, thanks for all your support and great insight into the practicalities of working and conducting fieldwork in lake systems. Also, thank you all for your encouragement, and for putting up with my rather sporadic correspondences.

Over to the other side of the world, this project would not have happened without the help of so many kind and generous New Zealanders that I will forever be eternally grateful for. I hope I can repay the favour to you all someday. Firstly, to Heather Purdie, Nick Key, and Justin Harrison at the University of Canterbury. Heather, thank you for taking the plunge to work with us, and helping to organise the boat and multibeam usage for the fieldwork. I never thought I would have even been able to acquire multibeam data during the PhD, so I am eternally grateful for that. Nick and Justin, thank you for all your help during the bathymetric survey on the lake. Your patience, friendliness, and level-headedness when things went wrong/kit didn't arrive from the UK/mounting parts went missing(?!) helped keep me from spiralling. Also, thanks for getting us safely ashore when the lake suddenly got choppy on our final day of surveying!

I also want to extend a sincere thanks to Graeme, Heather, and James Halliday, Chris Barker, Fraser Wilson, and James Stewart. Graeme, thank you for all your help and support over the last few years. Thank you for sharing your knowledge of Lake Wānaka, and the local area. Your

knowledge is so impressive. I learned a lot that was helpful in doing some of the analysis (or at least I hope I did). Also, thank you to both you and Heather for the wonderful hospitality, volunteering your time and boat to collect the sub-bottom data. Similarly, thanks to Chris, Fraser, James S and James H for all your help, volunteering your time and boats for me to complete the sub-bottom survey.

I'd also like to thank Scott McDougall for allowing me to use his model DAN3D, and for his help and advice with getting to grips with the modelling in the initial stages, and Phil Barnes for providing the 3 m MBES dataset for Milford Sound/Piopiotahi and allowing me to work on it. Also, thanks to Joshu Mountjoy for your continued interest and advice in this work.

Thanks to Prof. Andy Russell and Dr. Simon Cook for agreeing and taking the time to examine my thesis. Your recommendations that have greatly improved the quality of the thesis.

Thank you to the Iapetus Natural Environment Research Council Doctoral Training Partnership, and my CASE Partner, the British Geological Survey University Funding Initiative PhD studentship, for the financial support, without which, this thesis would not have been possible.

I'd also like to thank all the current and former staff in the School of Geography at Newcastle that I've had the pleasure of knowing over these last few years. Thank you for your support, insight, and encouragement over these last few years, and for putting up with the logistical headaches I invariably put you through. Hopefully no future student tries to buy a boat abroad, tries to do some international shipping of field equipment, or crashes and writes off the department vehicle anytime soon.

I'd like to thank my PGR colleagues: Arminel, Izzy, Jack, that dodgy character Will, Caroline, Lou, James B, James L, Alex, Dísa and Birgir. Thanks for your friendship, support, coffee breaks, continual supply of cakes and biscuits, fun times in and out (mostly out) the office. I hope you have enjoyed the many, many, MANY, trials, and tribulations that was my PhD (the sun was low in the sky, the morning dew glistened). I look forward to catching up with you at some point soon, ideally not on zoom, or at a social distance. Also, thanks to the countless others that I've not named here (otherwise my acknowledgements would be longer than the actual thesis!). But if you're reading this, then you know who you are!

Two final thanks. To begin, I want to give a special shout out and thanks to the OG 67 Rothbury Crew: Devin Harrison, Emily Hill, and Jake Collins-May. Devin, the Geordie geophysics guru,

thank you for all your help with my never-ending list of geophysics/GIS-related questions. You helped make me feel less out of my depth. Emily, the Matlab genius amongst other things. Thank you for helping to solve my ever-growing coding-related questions. Sorry to tell you though that my scripts are still not very computationally efficient. Jake, the man with the facts, thanks for all your help with solving my never-ending issues, whether GIS or life! Also thank you for some dutty and sussy new vocabulary! But seriously, thank you all for your support and encouragement, and helping to keep picking me up and keeping me going when everything was imploding, and I was at my lowest. Whether it was just being a sounding board for me to have a rant, helping me take some much-needed mental breaks with some nice cycle rides through Northumberland, or making me laugh with good and terrible puns or ridiculous memes. I don't think you realise how much it helped, but it definitely did so thank you! Also, thanks for not holding it against me when I put us and the Hilux in a ditch on the side of the road in Northumberland.

Finally, thank you to my family. It wasn't the easiest of times to be moving away given the circumstances but thank you for your continued support and encouragement. Also thanks for putting up with my ever-increasingly sporadic visits home, not least brought about by the many national lockdowns. I'm sure you'll be bored of the site of me soon enough!

“Ever tried. Ever failed. No matter. Try again. Fail again. Fail better”

- Samuel Beckett

Table of Contents

Abstract i

Dedication iii

Acknowledgements iv

Table of Contents viii

List of Figures xiii

List of Tables xxiv

List of Abbreviations xxv

Chapter 1. Introduction 1

1.1. Landslide hazards 3

1.2. Distribution of landslides in lakes and fjords 4

1.3. New Zealand 6

1.4. Rationale 9

1.5. Thesis aims and objectives 10

1.6. Thesis structure 11

Chapter 2. Literature Review: Current understanding of landslide deposits in lake and fjord environments 13

2.1. Landslide terminology 13

2.2. Controlling and triggering factors on subaerial and subaqueous landslide occurrence in lakes and fjords 16

2.2.1. Preconditioning and preparatory factors 16

2.2.2. Triggering factors 19

2.2.2.1. Earthquakes 19

2.3. Censoring processes of deposits 23

2.3.1. Subaerial censoring processes 24

2.3.2. Subaqueous censoring processes 25

2.4. Investigation of subaqueous landslide deposits 27

2.4.1. Methods of investigation 27
2.4.2. Geomorphology of subaqueous landslide deposits 29
2.5. Landslide flow dynamics and runout mechanisms 38
2.5.1. Factors controlling landslide mobility and runout 39
2.6. Conclusion 42
Chapter 3. Overview to the study area: South Island, New Zealand; and current understanding into the distribution of subaerial and subaqueous landslides 44
3.1. Introduction 44
3.2. Tectonic setting 44
3.3. Glacial setting 47
3.4. Physiographic setting 51
3.5. Spatial and temporal distribution of subaerial landslides across New Zealand 51
3.6. New Zealand subaqueous landslides: current understanding on distribution and controls 54
3.6.1. Subaqueous landslides in lakes and fjords 58
3.6.1.1. Distribution 59
3.6.1.2. Triggering mechanisms 66
3.7. Conclusion 70
Chapter 4. Morphology and dynamics of subaerial to subaqueous rock slope failures in Milford Sound/Piopiotahi, New Zealand. 72
4.1. Introduction 72
4.2. Study area 74
4.3. Methods 78
4.3.1. Datasets 78
4.3.2. Mapping and morphometric characteristics 78
4.3.2.1. Morphometric error estimations 79
4.3.3. Numerical Runout Modelling 82
4.3.3.1. DAN3D 86

4.3.3.2. Rheological Equations 87
4.3.3.3. DAN3D Input Data 89
4.4. Results 91
4.4.1. STS landslide deposit geomorphology 91
4.4.2. Morphometric characteristics 96
4.4.3. Runout modelling 102
4.4.3.1. Description of modelled rock avalanches 102
4.4.3.2. Calibrated parameters and rheologies of modelled rock avalanches 105
4.4.3.3. Transferability of model parameters 112
4.5. Discussion 116
4.5.1. Deposit geometry, morphology, and implications for flow dynamics 116
4.5.1.1. Substrate influence 117
4.5.2. The apparent mobility of the rock avalanches 118
4.5.3. Model capabilities and calibrated parameters 121
4.6. Conclusion 125
Chapter 5. Insights into the distribution and controls of subaerial and subaqueous landslides in the Lake Wānaka catchment, New Zealand 127
5.1. Introduction 127
5.2. Study area 129
5.2.1. Glacial setting 131
5.2.2. Seismic setting 131
5.2.3. Landslide setting 132
5.3. Methods 133
5.3.1. Subaerial landslide distribution and topographic position 133
5.3.2. Subaqueous landslide distribution 135
5.3.3. Landslide size-frequency distribution 140
5.4. Results 142

5.4.1. Subaerial landslide distribution 142
5.4.2. Lake geomorphology 147
5.4.3. Subaqueous landslides 149
5.4.4. Fan deltas and deltaic failures 155
5.4.5. The sedimentary infill of Lake Wānaka 158
5.4.6. Landslide size-frequency distribution 161
5.5. Discussion 162
5.5.1. Distribution of subaerial and subaqueous landslides 162
5.5.2. Potential triggering mechanisms 169
5.5.2.1. Rainfall 169
5.5.2.2. Permafrost degradation 170
5.5.2.3. Earthquakes 170
5.5.2.4. Paraglacial processes 174
5.6. Conclusion 177
Chapter 6. Discussion 180
6.1. Do lakes and fjords in New Zealand contain an archive of landslide deposits that help to resolve the landslide magnitude-frequency relationship? 180
6.1.1. Burial of deposits by sedimentation 185
6.2. What are the controls on landslide distribution within lakes and fjords in New Zealand? 190
6.2.1. Conceptual model of landslide distribution in New Zealand lake and fjords 192
6.2.1.1. Fjords 192
6.2.1.2. Intramountainous Lakes 195
6.2.1.3. Piedmont Lakes 198
6.3. What is the dynamic behaviour of landslides in a lake or fjord environment? 201
6.4. Geohazard implications 204
6.4.1. Landslide tsunami hazard and risk assessments 204
6.4.2. Future landslides in the subaqueous environments 210

6.5. Limitations and future research directions 212
Chapter 7. Conclusions 216
Appendix A. Morphology of Milford Sound/Piopiotahi STS rock avalanche deposits 221
Appendix B. DAN3D best fit model parameters from cases in literature 276
Appendix C. Unprocessed sub-bottom profiles from Lake Wānaka 281
References 287

List of Figures

Figure 1.1. Box and whisker plot illustrating landslide event size (deposit volume) and preservation of geomorphic evidence in the landscape. Data taken from global distributions. The lack of smaller, older deposits indicate that larger landslides have a longer associated residence time in a landscape than those of a smaller size. Figure source: Korup and Clague (2009). 2

Figure 1.2. Distribution of known landslide deposits in lakes globally. Note the term "mass-transport deposit (MTD)" is more or less equivalent to landslide deposit (Praet *et al.*, 2017). Figure source: Sammartini *et al.,* (2019). 6

Figure 1.3. Flow chart of likely geomorphic consequences from a future Alpine Fault earthquake, with steps in bold relating to the focus of this thesis. I – immediate consequence: occurring seconds to a few days after the event; P – prolonged consequences: lasting weeks and even years after; and L – long-term: lasting years to decades after the event. Figure sourced and modified from Robinson and Davies (2013). 9

Figure 2.1. Examples of landslide deposits, based on Sammartini *et al.,* (2019) classification, found in lake and fjord basins. A – Lateral slope failures along subaqueous slope. Source: Strupler *et al.*, (2019); B – subaqueous margin collapse with source scar identifiable in western edge, and deposit across the basin. Figure source https://cmgds.marine.usgs.gov/data/pacmaps/lt-shd.html; C – deposits from deltaic failures. Source: Hilbe and Anselmetti (2014); D – STS rockfall deposits on the lake basin from subaerial steep slope (inset). Source: Hilbe *et al.,* (2011); E- STS rock avalanche in Taan Fiord. Deposit extent mapped by green line. Source: Haeussler *et al*., (2018). 15

Figure 2.2. Effects and processes from an earthquake that may be detected, and/or leave an imprint, within a lake (and possibly fjord). Most records relate to landslide processes (indicated in red). Figure source: Moernaut (2020). 23

Figure 2.3. Schematic of methods used to identify subaqueous landslides including MBES and SSS surveys (A), and SBP surveys (B). Figure source and copyright Alexandre Normandeau licensed under a Creative Commons Attribution 4.0 International License. Figures available at https://sites.google.com/view/normandeau/outreach/methods-in-marine-geoscience 29

Figure 2.4. Cutaway schematic of common morphological features identified in subaqueous landslide deposits. Figure source: Mountjoy and Micallef (2018). 30

Figure 2.5. Bilogarithmic plot showing the H/L ratio (height fall of the landslide, H, and the horizontal runout, L) of subaerial and subaqueous landslide deposits against their volume. Debris flows are indicated by grey squares, subaerial rock avalanches are the empty diamonds, subaqueous rock avalanches are black circles and Outrunner blocks are denoted by black triangles. The segments (with the length indicating their uncertainty in the volume) are the debris flow lobes of the Storegga Slide. Figure sourced from De Blasio *et al*., (2006), and sources of data used in the figure are listed therein. 31

Figure 2.6. MBES data, and schematics of morphological features of subaqueous landslide deposits. BSS – Basal Shear Surface; KI – Kinematic Indicator. Figure sources: A – Livanos *et al.,* (2013); B and D - adapted from Dufresne and Davies (2009); C – Masson *et al.,* (2006); E – Hughes *et al.,* (2020); F – Bull *et al.,* (2009); G – Sammartini *et al.,* (2019); H – Moernaut and De Batist (Moernaut and De Batist, 2011). 33

Figure 2.7. SBP characteristics of blocky surface (A), characterised as hyperbolae facies in 3.5 kHz (top line of panel A), and chaotic facies in airgun profile (lower line of panel A). SBP data of frontally confined thrusts (B) in landslide deposits. Panel A source: Deplus et al., (2001). Panel B source: Moernaut and De Batist (Moernaut and De Batist, 2011). 34

Figure 2.8. Bathymetric (A), SBP characteristics (C), and schematic (B) of deformed basin plain sediment deposits. Classification refers to the classification of Van Daele *et al.,* (2013). Panel A source: Lastras *et al.,* (2016), Panel B and C source: Van Daele *et al.,* (2013). 37

Figure 3.1. Tectonic setting of New Zealand within the Australian and Pacific Plate boundaries. HSZ- Hikurangi Subduction Zone, PSZ – Puysegur Subduction Zone, AF- Alpine Fault. Plate motion rates from Wallace *et al.,* (2007, 2012). Plate boundary vectors from https://github.com/fraxen/tectonicplates, courtesy of Hugo Ahlenius, Nordpil, and Peter Bird, available under Creative Commons License 1.0. Offshore bathymetry data is sourced from NIWA and licensed under the NIWA Open Data Licence v1.0. Data is available at: https://niwa.co.nz/our-science/oceans/bathymetry. 46

Figure 3.2. Overview maps of New Zealand South Island including the distribution of active faults (a); modelled Last Glacial Maximum (LGM) ice thickness (b); total suspended sediment yield (c); and 30-year average mean annual precipitation (rainfall) (d). Topographic data and lake polygons are from LINZ Data service (https://data.linz.govt.nz/). Active Faults shapefiles are from GNS Active Fault Database (https://data.gns.cri.nz/af/), based on Langridge *et al.,* (2016). LGM model from James *et al.,* (2019) Suspended sediment yield model is based on the work of Hicks *et al.,* (2003, 2011), and GIS layer is available from the National Institute of Water and Atmospheric Science (NIWA) (https://niwa.co.nz/freshwater/management-tools/sediment-tools/suspended-sediment-yield-estimator). 1981-2010 mean annual rainfall model data is provided by, and copyright of NIWA. 49

Figure 3.3. Modelled MM shaking intensities across the South Island, New Zealand, from a $M_w = 8.0$ Alpine Fault earthquake with (a) Northern Hypocentre, (b) Central Hypocentre, (c) Southern Hypocentre, and (d) maximum shaking intensities. Figure sourced from Bradley *et al*., (2017). 50

Figure 3.4. Bainbridge (2017) inventory of identified subaerial RSF (rock avalanche) deposits across the South Island. Dataset from Bainbridge (pers. comm.). 53

Figure 3.5. Notable subaqueous landslide deposits offshore the North Island, including the Matakaoa Debris Flow and Debris Avalanche deposits that comprise the Matakaoa Submarine Instability Complex (panel B); the Ruatoria Debris

Avalanche deposit (panel D); and the Tuaheni Landslide and Poverty Debris Avalanche (panel E). Location of the Matakaoa deposits shown in panel A, locations of deposits in panels D and E are shown in Figure 3.5. Figure A-C source from Joanne *et al.,* (2013), Figure D and E from Pouderoux *et al.,* (2012). 56

Figure 3.6. Distribution of subaqueous landslides in the eastern offshore New Zealand. The distribution shows a higher density of deposits in the active Hikurangi Margin region compared to the passive margin, offshore south-east South Island. TLC – Tuaheni Landslide Complex. Figure source: Watson *et al.,* (2020). 57

Figure 3.7. Compilation of currently known distribution of lakes and fjords with known landslide deposits across New Zealand's South Island. 1:50k lake shapefiles and DEM (of which hillshade was derived from) available at https://data.linz.govt.nz/. 60

Figure 3.8. Compilation of currently known distribution of landslide deposits/events in lakes of New Zealand's North Island. 1:50k lake shapefiles and DEM (of which hillshade was derived from) available at https://data.linz.govt.nz/..... 61

Figure 3.9. Inventory of lakes and fjords with known landslide deposits classified based on known type of landslide deposit within the lake at present. In (**A**): lateral slope collapses, deltaic collapses, and MTDs are all evident. In (**N**), STS landslide deposits and a deltaic collapse deposit are evident. **A** – Lake Tekapo, **B** – Lake Pukaki, **C** – Lake Ōhau, **D** – Grey-Maud Glaciers proglacial lake, **E** – Volta Glacier proglacial lake, **F** – Lake Ellery, **G** – Lake Paringa, **H** – Lake Mapourika, **I** – Lake Wakatipu, **J** – Lake Te Anau, **K** – Lake Hauroko, **L** – Lake Taupo, **M** – Lake Tutira, **N** – Milford Sound/Piopiotahi, **O** – Taiporoporo/Charles Sound, **P** – Doubtful Sound/Patea, **Q** – Lake Rotoiti, **R** – Te Houhou/ George Sound, **S** – Rakituma/ Preservation Inlet, **T** – Lake Kaniere..... 62

Figure 3.10. MBES (A) and SBP (B) data of Lake Tekapo showing landslide deposits on the surface, and within the stratigraphic sequence. (C) – SBP data from Lake Ōhau showing a series of stacked landslide deposits within the stratigraphic sequence (denoted by MWD - Mass wasting deposits). Figure A and B sourced from Mountjoy *et al*., (2019), Figure C sourced from Fitzsimons and Howarth (2018). 69

Figure 4.1. Overleaf. (A) Overview of the Milford Sound/Piopiotahi catchment in the Fiordland region (see inset map for location in New Zealand). Offshore bathymetry data is sourced from NIWA and licensed under the NIWA Open Data Licence v1.0. Data are available at: https://niwa.co.nz/our-science/oceans/bathymetry; (B) Geological map of Milford Sound/Piopiotahi with bathymetric digital elevation model, with place names mentioned in text. Geological information and layers from New Zealand QMAP (Turnbull *et al.*, 2010; Rattenbury and Isaac, 2012); (C) Map of the subaerial and subaqueous deposits identified by Dykstra (2012). DF deposits are submarine density flow, SM deposits are subaerial source with submarine deposit. Figure source: Dykstra (2012). 76

Figure 4.2. Schematic of landslide morphometric parameters recorded. Top panel modified from Strom *et al.,* (2019). DoT= direction of travel. 80

Figure 4.3. Geomorphological map of Milford Sound/Piopiotahi fjord bottom (A). The ID of the rock avalanche deposits are illustrated in Panel B. 92

Figure 4.4. Overleaf. Morphological features, predominately diagnostic features (transverse ridges, aligned blocks, concentric ring features, blocky surface carapace) of the rock avalanche deposits, clockwise from top left: (A) RA4 and RA5; (B) RA7-RA10; (C) RA11 and RA12; (D) RA13 and RA14 (E) RA15 (F) RA2 and RA16; and (G) RA1 and RA6. Detailed view of each deposit, including source areas, is available in Appendix A 96

Figure 4.5. (A) Morphology of deposit RA3; (B) polar histogram showing orientation of the blocks' long axes against average flow direction (024°N); (C) scatter plot of block area (in m^2) against distance from source. R^2 value from least squares linear regression. 96

Figure 4.6. Relationships of the rock avalanche deposit L_d/W_d ratio to (a) depositional path slope; (b) overall mobility (H/L_{max}); (c) average travel path slope; and (d) overall runout (L_{max}). Plot (e) is the overall rock avalanche mobility against the average travel path slope. Adjusted R^2 value and line of best fit from least-squares linear regressions..... 101

Figure 4.7. Interpolated spatial deposit thicknesses of rock avalanche cases derived from recreation of a pre-event DEM..... 104

Figure 4.8. Extents and thicknesses of runout modelling results using the best fit rheological parameters in Table 4.7. 108

Figure 4.9. Longitudinal profiles of the deposit thickness through the observed (solid line) and the modelled deposits (dashed line) for the five simulated events. The vertical grey line demarcates the boundary between the subaerial (left hand side of the line) and subaqueous (right hand side of the line) environment. 109

Figure 4.10. Centreline transects of the maximum cell velocity (m s^{-1}) through the modelled deposits (orange line) for the five simulated events. The vertical line demarcates the boundary between the subaerial (left hand side of the line) and subaqueous (right hand side of line) environment. The solid blue line is a graphical representation on the water level..... 110

Figure 4.11. Runout and depositional extents from the best fit parameters of each case applied to the other respective cases 113

Figure 4.12. Plot of apparent mobility (H/L_{max}) (a) and maximum runout (b) vs. volume of volcanic and non-volcanic rock avalanche events from literature, with the addition of the Milford Sound/Piopiotahi rock avalanches. Note that the non-rock avalanche submarine landslides are excluded here. 120

Figure 4.13. Comparison of the best fit parameters from Milford Sound/Piopiotahi rock avalanches against those in literature based on (A) landslide type; and (B) runout path material. Data from Aaron and McDougall (2019) and references

therein; Sosio, Crosta, and Hungr (2012), Mazzanti and Bozzano (2009; 2011), and Schleier *et al.* (2017). Individual parameters for each case, and associated references, can be found in Appendix B.....124

Figure 5.1. Location of Lake Wānaka and its catchment. Inset map shows location of the main figure in New Zealand's South Island. Extent of Figure 5.2 also indicated by blue box. Identified active faults are sourced from Institute of Geological and Nuclear Sciences (GNS Science) Active Faults Database (Langridge *et al.*, 2016) (https://data.gns.cri.nz/af/). The inferred inactive faults are sourced from the 1:250,000 QMAP (Heron, 2014). The location of earthquakes ≥M5 from 1840 to present are shown and sourced from the GeoNet Earthquake Catalogue. Glacier extents are from the Randolph Glacier Inventory 6.0 (2017). Lake polygons and the topographic data are sourced from LINZ data service (https://data.linz.govt.nz/).....130

Figure 5.2. Overview of PDBS and SBP (chirp) data collected in this study. Frame indicators relate to subsequent figures and letters correspond to named panels in the respective figures. Bathymetric data denoted by coloured bathymetric hillshade model and chirp profiles by black lines. River shapefiles are sourced from LINZ data service (https://data.linz.govt.nz/).....139

Figure 5.3. Frequency distribution of surface slope angles normalised by total area of the hillslopes and RSF deposits and grouped by deposit area.....144

Figure 5.4. Location of subaerial landslides with respect to their distance to ridge crests and streams with relative density of data points underlying plot (a); and the relative frequency distribution of the computed data values (b).....145

Figure 5.5. (a) the distribution of RSF deposits in the catchment, represented as centroid points, scaled proportionally by deposit area (m^2); (b) the deposit distribution (by centroid point) against mean annual rainfall (rainfall contours shown by black lines (in mm yr^{-1})); (c) the deposit distribution (by centroid point) against the Euclidean distance (in km) to the main faults (active and inferred inactive (black lines)) within the region; and (d) Euclidean distance to the active faults (red lines) within the region. See Figure 5.1 for fault names. Mean annual rainfall model data provided by and copyright of the National Institute for Water and Atmospheric Science (NIWA, pers. comm.).....146

Figure 5.6. Overleaf. Bathymetric expressions of sublacustrine channels at Matukituki delta (A); near the Makarora River delta (B); and along the lakebed not associated with a river delta (C). Profile of subaerial river deltaic region and subaqueous channel thalweg (D). Note the full extent of the subaerial profile is not visible in Panel A. All Panels are orientated north. Aerial imagery and topographic data available from LINZ data service (https://data.linz.govt.nz/).....147

Figure 5.7. Bathymetric morphologies and sub-bottom profiles of STS landslide deposits at the southern end of the Peninsula (A-C), and near the Matukituki Delta (D-F). Panels A and D are orientated North. In vertically exaggerated 3D perspective panels (B, E), the backscatter data are overlain. See Figure 5.2 for location. Unprocessed versions of these and following SBP presented within the chapter are available in Appendix B.....152

Figure 5.8. Bathymetric morphologies and sub-bottom profiles of wholly subaqueous deposits (A-C) and scars with no associated deposit (D-F). Perspective view in Panel B has backscatter data overlain on the deposit. See Figure 5.2 for location. 153

Figure 5.9. Bathymetric morphology of a subaqueous RSF deposit (A, B), and subaerial to subaqueous RSF deposits (C, D), both with conical morphologies. Also shown is sub-bottom profile collected over one STS deposit (E). See Figure 5.2 for location. 154

Figure 5.10. A-C - Examples of deltaic collapse deposits and scars on subaqueous fan delta slopes within the lake. D – Topographic profile over subaqueous fans with deposit, illustrating the break in slope at deposit boundaries. Locations of profiles are indicated in Panel A. Locations of Panels A-C are indicated on Figure 5.2. 156

Figure 5.11. Sub-bottom profiles showing typical horizontal, laterally continuous facies interpreted as natural sediment infill in the lake (A) and the maximum subsurface depth achieved of 115 m below the bed, with bedrock trace of Mou Tapu island (B). See Figure 5.2 and Figure 5.6 for line locations of A and B respectively. 160

Figure 5.12. The cumulative and non-cumulative distribution of the subaerial (A, C) and combined subaerial-subaqueous (B, D) deposits in this study. A power law is fitted to both the cumulative and non-cumulative distributions, whilst a lognormal fit is only fitted to the cumulative distributions. The exponents and cutoff points are detailed in Table 5.2. The data in the non-cumulative distributions are logarithmically binned, therefore the areas cannot be plotted by deposit type. 161

Figure 5.13. A-D: Modelled isoseismals of past Alpine Fault earthquakes. Star superimposed is location of Lake Wānaka in relation to the isoseismals; E – Robinson et al., (2016) modelled coseismic landslide hazard across Queenstown Lake District from a M_w 8.0 Alpine Fault earthquake scenario; F – modelled isoseismals of potentially active faults producing $M_w \geq 7$ earthquakes with Wanaka Fault highlighted. Figures A-D sourced and modified from Howarth et al., (2014); Figure E provided from Tom Robinson (pers. comm.); Figure F sourced and modified from Howarth et al., (2016). Note, Howarth et al., (2014) favour scenario B over C for the ~1570 AD earthquake. 173

Figure 5.14. Distribution of subaerial RSF deposits compared to modelled LGM ice extents and thicknesses LGM ice model from James et al., (2019). Black line delineates the catchment boundary from the lake outlet. 176

Figure 6.1. Size-frequency distribution of subaqueous and subaerial Milford Sound/Piopiotahi landslide deposits. Panel A figure from Taig and McSaveney (2015), based on original findings from Dykstra (2012). Panel B recalculated with the STS RSF A_L results from *Chapter 4* within this thesis. Panel B only focusses on the RSF (rock avalanche) deposits in Milford Sound/Piopiotahi,

therefore excluding talus cones and deltaic collapse deposits. Subaerial RSF deposit surface areas from Dykstra (2012). 183

Figure 6.2. Airgun profile data and subsequent seismic interpretation. Profile location indicated in top panel. Middle panel is the seismic interpretation of the airgun profile (bottom panel). Note thick, discontinuous, parallel-bedded unit (lacustrine, light brown) overlying poorly reflective, chaotic diamicton fill (till and landslide debris, red). Figure source: Dykstra (2012) 184

Figure 6.3. Overleaf. Conceptual model of landslide occurrence in fjords since the LGM to present day. Relative earthquake magnitude is denoted by size of the symbol. The '?' are where such information are currently unknown but suggested within the model. (1) illustrates that no sediment is draping the steep lateral slopes; (2) – marine transgression during eustatic sea level rise; (3) – precipitation variations depending on site, with comparatively lower precipitation to the fjords in the south; (4) – the vertical arrow represents fluctuations in palaeolake level and then sea level with marine transgression; (5) – limited apparent post-event sedimentation covering the deposits, so surface morphology is still visible. Curved black lines adjacent to subaerial and subaqueous slopes symbolise shaking intensity. More lines represent stronger shaking intensities. The figures have been designed to be consistent with Moernaut (2020) model (Figure 2.2). 193

Figure 6.4. Overleaf. Conceptual model of landslide occurrence in intramountainous lakes since the LGM to present day. Relative earthquake magnitude is denoted by size of the symbol. The '?' are where such information are currently unknown but suggested within the model. (1) illustrates that no sediment is draping the steep lateral slopes; (2) – precipitation variations depending on site, with comparatively lower precipitation east of the Southern Alps Main Divide; (3) – the vertical arrow represents fluctuations in lake level since LGM; (4) – high sedimentation (dark grey) rapidly burying STS RSF deposit. The figures have been designed to be consistent with Moernaut (2020) model (Figure 2.2). 196

Figure 6.5. Overleaf. Conceptual model of landslide occurrence in piedmont lakes since the LGM to present day. Relative earthquake magnitude is denoted by size of the symbol. The '?' are where such information are currently unknown but suggested within the model. (1) illustrates the beginning of sediment draping lateral slopes; (2) – precipitation variations depending on site, with comparatively lower precipitation east of the Main Divide; (3) – the vertical arrow represents fluctuations in lake level since LGM; (4) – sedimentation (light grey) burying the subaqueous delta collapse deposit (dark grey). Curved black lines adjacent to subaerial and subaqueous slopes symbolise shaking intensity. More lines represent stronger shaking intensities. The figures have been designed to be consistent with Moernaut (2020) model (Figure 2.2). 201

Figure 6.6. Probable tsunami wave heights on Lake Tekapo from a landslide at Boundary Stream (a); deltaic collapse of the Cass River Delta (b); and both landslides occurring concurrently (c). Township highlighted on (a) for context. Figure modified from Mountjoy et al., (2019). 205

Figure 6.7. Coseismic landslide susceptibility from an M_w 8.0 Alpine Fault earthquake for A) Lake Coleridge and Lake Kaniere; B) Lake Sumner; C) Lake Paringa; D) Lake McKerrow and Milford Sound/Piopiotahi; and E) Lake Te Anau, Lake Wakatipu, Lake Wānaka, and Lake Hāwea. Figure modified from Robinson (2014). 211

Figure A.1. RA1 subaqueous deposit and source scar area. Imagery available under Creative Commons 4.0. Copyright is owned by The Southland Consortium (Southland District Council, Gore District Council, Environment Southland, and Department of Conservation). 221

Figure A.2. Morphology of RA1 deposit, showing the radial fan shape, and lack of features beyond the blocky carapace. 222

Figure A.3. 3D perspective view of RA1 subaqueous deposit with 1.5x vertical exaggeration. 223

Figure A.4. RA2 subaerial and subaqueous deposit and source scar area. Imagery available under Creative Commons 4.0. Copyright is owned by The Southland Consortium (Southland District Council, Gore District Council, Environment Southland, and Department of Conservation). 224

Figure A.5. Detailed, uninterpreted morphology of RA2 subaqueous deposit. 225

Figure A.6. Interpreted morphology of RA2 subaqueous deposit. 226

Figure A.7. 3D perspective view of RA2 subaqueous deposit with 1.5x vertical exaggeration. 227

Figure A.8. 3D perspective view of RA3 subaqueous deposit with 1.5x vertical exaggeration. 227

Figure A.9. RA3 subaqueous deposit and source scar area. Imagery available under Creative Commons 4.0. Copyright is owned by The Southland Consortium (Southland District Council, Gore District Council, Environment Southland, and Department of Conservation). 228

Figure A.10. Detailed, uninterpreted morphology of RA3 subaqueous deposit. 229

Figure A.11. Interpreted morphology of RA3 subaqueous deposit 230

Figure A.12. RA4 subaerial and subaqueous deposit and source scar area. Imagery available under Creative Commons 4.0. Copyright is owned by The Southland Consortium (Southland District Council, Gore District Council, Environment Southland, and Department of Conservation). 231

Figure A.13. Detailed, uninterpreted morphology of RA4 subaqueous deposit. 232

Figure A.14. Interpreted morphology of RA4 subaqueous deposit. 233

Figure A.15. 3D perspective view of RA4 subaqueous deposit with 1.5x vertical exaggeration. 234

Figure A.16 3D perspective view of RA5 subaqueous deposit with 1.5x vertical exaggeration.....234

Figure A.17. RA5 subaqueous deposit and source scar area. Imagery available under Creative Commons 4.0. Copyright is owned by The Southland Consortium (Southland District Council, Gore District Council, Environment Southland, and Department of Conservation).....235

Figure A.18. Detailed, uninterpreted morphology of RA5 subaqueous deposit. 236

Figure A.19. Interpreted morphology of RA5 subaqueous deposit.....237

Figure A.20. RA6 subaqueous deposit. No source scar area mapped as it could not be confidently identified. Imagery available under Creative Commons 4.0. Copyright is owned by The Southland Consortium (Southland District Council, Gore District Council, Environment Southland, and Department of Conservation). 238

Figure A.21. Morphology of RA6 deposit, showing the radial fan shape, and lack of features beyond the blocky carapace, possibly due to overprinting by fan development. 239

Figure A.22. 3D perspective view of RA6 subaqueous deposit with 1.5x vertical exaggeration.....240

Figure A.23. RA7 subaqueous deposit and source scar area. Imagery available under Creative Commons 4.0. Copyright is owned by The Southland Consortium (Southland District Council, Gore District Council, Environment Southland, and Department of Conservation).....241

Figure A.24. Detailed, uninterpreted morphology of RA7 subaqueous deposit. 242

Figure A.25. 3D perspective view of RA7 subaqueous deposit with 1.5x vertical exaggeration.....243

Figure A.26. Interpreted morphology of RA7 subaqueous deposit.....244

Figure A.27. RA8 subaqueous deposit and source scar area. Imagery available under Creative Commons 4.0. Copyright is owned by The Southland Consortium (Southland District Council, Gore District Council, Environment Southland, and Department of Conservation).....245

Figure A.28. Detailed, uninterpreted morphology of RA8 subaqueous deposit. 246

Figure A.29. Interpreted morphology of RA8 subaqueous deposit.....247

Figure A.30. 3D perspective view of RA8 subaqueous deposit with 1.5x vertical exaggeration.....248

Figure A.31. 3D perspective view of RA9 subaqueous deposit (in red) with 1.5x vertical exaggeration.....248

Figure A.32. Detailed, uninterpreted morphology of RA9 subaqueous source and deposit. 249

Figure A.33. Interpreted morphology of RA9 subaqueous deposit. 250

Figure A.34. RA10 subaqueous deposit and source scar area. Imagery available under Creative Commons 4.0. Copyright is owned by The Southland Consortium (Southland District Council, Gore District Council, Environment Southland, and Department of Conservation). 251

Figure A.35. Detailed, uninterpreted morphology of RA10 subaqueous deposit. 252

Figure A.36. Interpreted morphology of RA10 subaqueous deposit. 253

Figure A.37. 3D perspective view of RA10 subaqueous deposit with 1.5x vertical exaggeration. 254

Figure A.38. 3D perspective view of RA11 subaqueous deposit with 1.5x vertical exaggeration. 254

Figure A.39. RA11 subaqueous deposit and source scar area. Imagery available under Creative Commons 4.0. Copyright is owned by The Southland Consortium (Southland District Council, Gore District Council, Environment Southland, and Department of Conservation). 255

Figure A.40. Detailed, uninterpreted morphology of RA11 subaqueous deposit. 256

Figure A.41. Interpreted morphology of RA11 subaqueous deposit. 257

Figure A.42. RA12 subaerial and subaqueous deposit and source scar area. Imagery available under Creative Commons 4.0. Copyright is owned by The Southland Consortium (Southland District Council, Gore District Council, Environment Southland, and Department of Conservation). 258

Figure A.43. Detailed, uninterpreted morphology of RA12 subaqueous deposit. 259

Figure A.44. Interpreted morphology of RA12 subaqueous deposit. 260

Figure A.45. 3D perspective view of RA12 subaqueous deposit with 1.5x vertical exaggeration. 261

Figure A.46. 3D perspective view of RA13 subaqueous deposit with 1.5x vertical exaggeration. 261

Figure A.47. RA13 subaerial and subaqueous deposit and source scar area. Imagery available under Creative Commons 4.0. Copyright is owned by The Southland Consortium (Southland District Council, Gore District Council, Environment Southland, and Department of Conservation). 262

Figure A.48. Detailed, uninterpreted morphology of RA13 subaqueous deposit. 263

Figure A.49. Interpreted morphology of RA13 subaqueous deposit. 264

Figure A.50. RA14 subaerial and subaqueous deposit and source scar area. Imagery available under Creative Commons 4.0. Copyright is owned by The Southland Consortium (Southland District Council, Gore District Council, Environment Southland, and Department of Conservation). 265

Figure A.51. Detailed, uninterpreted morphology of RA14 subaqueous deposit. 266

Figure A.52. Interpreted morphology of RA14 subaqueous deposit..... 267

Figure A.53. 3D perspective view of RA14 subaqueous deposit with 1.5x vertical exaggeration..... 268

Figure A.54. RA15 subaqueous deposit and source scar area. Imagery available under Creative Commons 4.0. Copyright is owned by The Southland Consortium (Southland District Council, Gore District Council, Environment Southland, and Department of Conservation)..... 269

Figure A.55. Detailed, uninterpreted morphology of RA15 subaqueous deposit. 270

Figure A.56. 3D perspective view of RA15 subaqueous deposit with 1.5x vertical exaggeration..... 270

Figure A.57. Interpreted morphology of RA15 subaqueous deposit..... 271

Figure A.58. RA16 subaqueous deposit and source scar area. Imagery available under Creative Commons 4.0. Copyright is owned by The Southland Consortium (Southland District Council, Gore District Council, Environment Southland, and Department of Conservation)..... 272

Figure A.59. Detailed, uninterpreted morphology of RA16 subaqueous deposit. 273

Figure A.60. Interpreted morphology of RA16 subaqueous deposit..... 274

Figure A.61. 3D perspective view of RA16 subaqueous deposit with 1.5x vertical exaggeration..... 275

Figure C.1. Unprocessed SBP line of Figure 5.8C..... 281

Figure C.2 Unprocessed SBP line of Figure 5.7C..... 282

Figure C.3. Unprocessed SBP line of Figure 5.7F 282

Figure C.4. Unprocessed SBP line of Figure 5.8F 283

Figure C.5. Unprocessed SBP line of Figure 5.9E..... 284

Figure C.6. Unprocessed SBP line of Figure 5.11A..... 285

Figure C.7. Unprocessed SBP line of Figure 5.11B..... 286

List of Tables

Table 3.1. Number and type of lake across the North and South Island, New Zealand. Source: Lowe and Green (1992) 48

Table 3.2. Summary of lakes and fjords across New Zealand with known landslide deposits within them, their triggering mechanism (where known), and methods of detection. 63

Table 4.1. Summary of morphometric parameters collected in this study 81

Table 4.2. Summary of commonly used dynamic landslide runout models 84

Table 4.3. Morphometric attributes of Milford Sound/Piopiotahi STS rock avalanche deposits and associated error 98

Table 4.4. Morphometric attributes of Milford Sound/Piopiotahi STS rock avalanche runout characteristics, and associated error 100

Table 4.5. Summary statistics from the rock avalanche morphometric data 101

Table 4.6. Volume difference between source and deposit of modelled cases and estimated volume error 102

Table 4.7. Best fit rheologies (frictional (F), Voellmy (V)) and corresponding parameters for each modelled rock avalanche 105

Table 4.8. Results of best fit simulations compared to observed data and associated morphometric error (where available). Percentage variation in modelled columns are in relation to observed data is in brackets. 111

Table 4.9. Results from the calibrated best fit parameters to the other respective cases 114

Table 5.1. Summary of identified scars with no associated deposit in bathymetry, and estimated areas and volumes 157

Table 5.2. The power-law and log normal exponents, cutoff values, mLS for the subaerial and combined subaerial-subaqueous deposits in this study 162

Table 6.1. Catchment areas, sedimentation rates, and suspended sediment yields (SSYs) from lakes and fjords in New Zealand from literature. 188

Table 6.2. Comparisons of velocity data derived from the runout modelling in *Chapter 4*, with initial analytical estimates from Dykstra (2012). 204

Table B.0.1. Summary of DAN3D case parameters. FID 1-44 taken from Aaron and McDougall (2019), and references therein; 45-51 from Sosio *et al.* (2012a,b), 52-56 from this study; 57 from Mazzanti and Bozzano (2009); 58 from Schleier *et al.,* (2017); and 59 from Mazzanti and Bozzano (2011). 276

List of Abbreviations

2D	2 dimensions
3D	3 dimensions
AEQ	Assumed earthquake
ALOS	Advanced Land Observing Satellite
API	Aerial Photo Interpretation
ASTER	Advanced Spaceborne Thermal Emission and Reflection Radiometer
AUV	Autonomous Underwater Vehicle
BPI	Bathymetric Position Index
BTM	Bathymetric Terrain Model
CDF	Cumulative Density Function
DAE	Depth averaged equations
DEM	Digital Elevation Model
DoT	Direction of Travel
DSGSD	Deep-Seated Gravitational Slope Deformation
DSM	Digital Surface Model
EQ	Earthquake
EQTL	Earthquake-triggered landslide
FAD	Frequency Area Distribution
FDD	Frequency Density Distribution
GIS	Geographical Information System
HRDP	High-resolution, deep penetrating
IHO	International Hydrographic Organisation
IMU	Internal Motion Unit
JAXA	Japan Aerospace Exploration Agency
KS	Kolmogorov-Smirnov
LIA	Little Ice Age
LGIT	Late Glacial-Interglacial Transition
LGM	Last Glacial Maximum
LINZ	Land Information New Zealand
MBES	Multibeam Bathymetric Echosounder
MM	Modified Mercalli
MPM	Multi-Phase Model
MTD	Mass-Transport Deposit

NIWA National Institute of Water and Atmospheric Science
NOC Non-oscillatory Central
NSE Navier Stokes Equation
NZNLD New Zealand National Landslide Database
OSL Optically Stimulated Luminescence
PDBS Phase Differencing Bathymetric Sonar
PDF Probability Density Function
PGA Peak Ground Acceleration
PPK Post-Processed Kinematic
QMAP Quarter-million MAP
RMSE Root Mean Square Error
RQ Research Question
RSF Rock Slope Failure
RTK Real-Time Kinematic
S Storm
SBP Sub-bottom Profile
SPH Smoothed Particle Hydrodynamics
SPM Single Phase Model
SSS SideScan Sonar
SSY Suspended Sediment Yield
STS Subaerial to Subaqueous
SVP Sound Velocity Profile
U Unknown
VDA Volcanic Debris Avalanche
VHR Very High Resolution

Chapter 1. Introduction

Landslides are a common geomorphic process that have been observed in perhaps every mountainous landscapes across the globe (Korup *et al.*, 2007, 2010). They can be highly effective agents of erosion that limit the overall relief of a landscape, particularly in tectonically active mountain belts where uplift and denudation are in long-term equilibrium (Korup *et al.*, 2007). Deposits from landslides are also important agents that contribute to the flux of sediment (Korup, 2012) and organic carbon (Hilton *et al.*, 2008) to the seas and oceans. Landslides are also a major geohazard in these landscapes (section 1.1). Understanding landslide distribution, hazard, and their role as landscape processes is contingent on establishing databases and records of events that capture timing, associated triggering factors, and magnitude and frequency of these events (Malamud *et al.*, 2004; Van Den Eeckhaut and Hervás, 2012; Tebbens, 2020). Complete landslide inventories can be attained if focussed on landslides triggered by an external event, such as earthquakes (Malamud *et al.*, 2004). However, inventories that incorporate historical and pre-historical landslides are often incomplete (Van Den Eeckhaut and Hervás, 2012; Pánek, 2019). This is because processes can (rapidly) censor deposits, resulting in a comparatively short residence time (10^3 – 10^6 years) in the terrestrial landscape (Figure 1.1 (Clague, 2015)). Such censoring processes include erosion and reworking of deposits through fluvial (Barth, 2014; Bainbridge, 2017), and glacial (Hewitt, 2009b; Reznichenko *et al.*, 2011; Dunning *et al.*, 2015) systems, or obscured by vegetation (Chevalier *et al.*, 2009), or within water bodies (Blikra *et al.*, 2006; Dykstra, 2012; Böhme *et al.*, 2015). The effect of these processes on the preservation of deposits makes establishing long-term magnitude-frequency relationships of landslides challenging, particularly pre-historical events (Korup and Clague, 2009; McColl, 2020). Pre-historical events and activity may reflect major geological triggering events (e.g. earthquakes), or major climatic shifts.

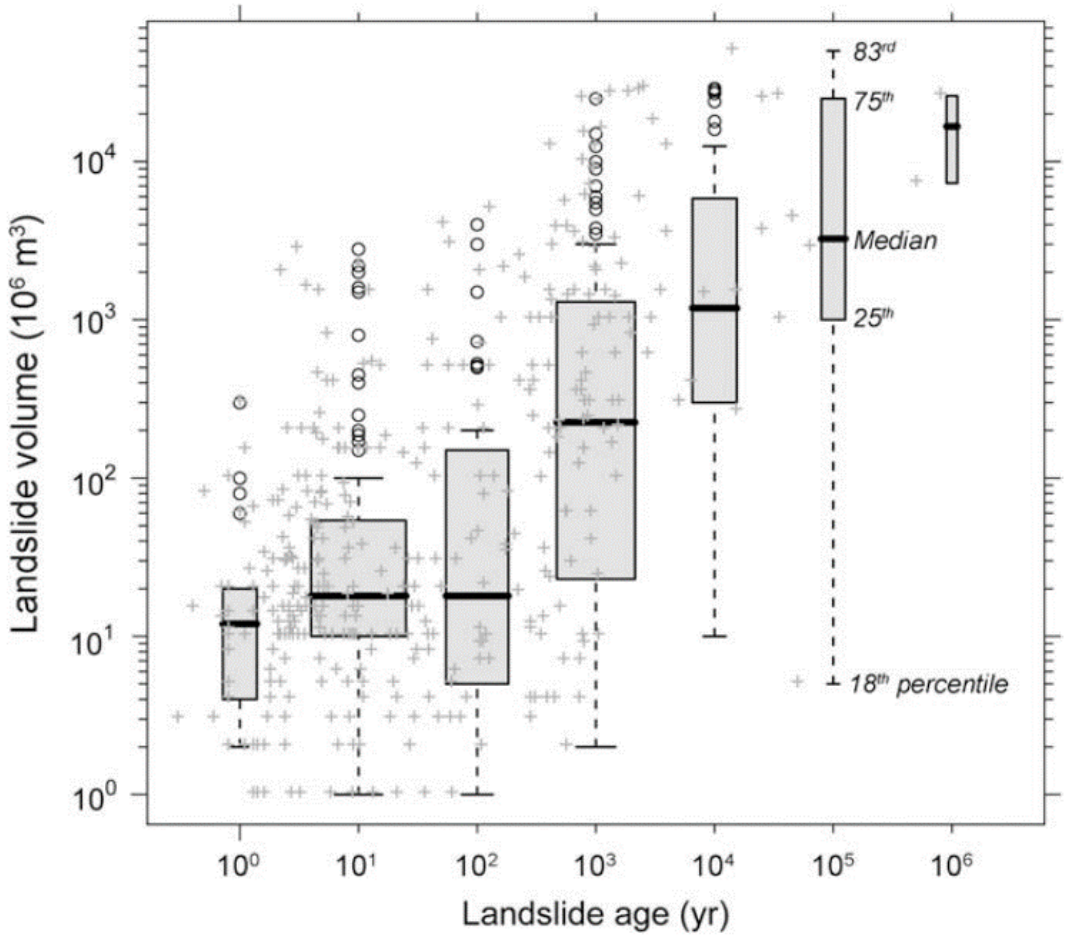

Figure 1.1. Box and whisker plot illustrating landslide event size (deposit volume) and preservation of geomorphic evidence in the landscape. Data taken from global distributions. The lack of smaller, older deposits indicate that larger landslides have a longer associated residence time in a landscape than those of a smaller size. Figure source: Korup and Clague (2009).

Landslides also occur within subaqueous environments across the globe (Hampton *et al.*, 1996). Subaqueous environments can contain excellent archives of landslide events, and associated deposits, in the geological record. However, compared to their subaerial equivalents, subaqueous landslides are less well understood (Talling *et al.*, 2014). The expansion and advancement in the use of modern hydroacoustic survey techniques such as multibeam echosounder systems (MBES) has allowed acquisition of high-resolution bathymetric terrain models (BTMs) of subaqueous environments (Tappin, 2010; Hughes Clarke, 2018). These datasets have aided in the identification of previously unknown landslide deposits on basin floors. Similarly, with seismic reflection/sub-bottom profile (SBP) surveys, and subaqueous coring campaigns, deposits buried by sediment can be identified (Crutchley and Kopp, 2018), and their absolute ages can be established. These datasets have allowed a greater insight into the characteristics of subaqueous landslides (Mountjoy and Micallef, 2018). The datasets also

allow the spatial and temporal distributions to be reconstructed beyond the historical record (Blikra *et al.*, 2006; Böhme *et al.*, 2015).

Lakes and fjords can offer excellent environments to study past events owing to typically shallower water depths than the oceans and some seas. The shallower water depths allow for potentially higher horizontal resolution data from higher frequency MBES systems (Sammartini *et al.*, 2019). Similarly, the use of Very High Frequency (VHF) SBP systems (e.g. pinger, chirp) in the shallower lakes and fjords can result in decimetre vertical resolution (Sammartini *et al.*, 2019). Higher spatial resolution data can therefore address an apparent limitation of landslide size relative to the dataset resolution in marine settings (Clare *et al.*, 2018). Additionally, the comparatively smaller size of a lake and fjord basins means landslides can be investigated on a basin-wide scale (Sammartini *et al.*, 2019). Preconditioning and triggering factors and processes of landslides studied in the deep oceans (Hampton *et al.*, 1996; Locat and Lee, 2002) are comparable to those in lakes (Strasser *et al.*, 2007, 2013; Moernaut *et al.*, 2014) and fjords (L'Heureux *et al.*, 2013; Bellwald *et al.*, 2016; Lastras *et al.*, 2016). Therefore, lakes and fjords can be natural laboratories that have significant advantages for investigating landslides that can aid investigations of landslides in oceanic environments (Sammartini *et al.*, 2019).

1.1. Landslide hazards

Landslides have long been recognised as a geohazard, both in the subaerial (Froude and Petley, 2018) and subaqueous (Masson *et al.*, 2006) environments. Over 55,000 fatalities from landslides have been documented between 2004-2016 (Froude and Petley, 2018). Importantly, these fatalities are from landslides not triggered by earthquakes. Earthquakes can cause large numbers of coseismic failures (Keefer, 1984), which in turn, can result in large numbers of fatalities. Notable examples include over 25,000 fatalities because of the 1970 Huascarán landslide in Peru. The landslide was triggered by the M_w 7.8 earthquake (Evans, Bishop, *et al.*, 2009). Also, the 2005 M_w 7.6 Kashmir earthquake resulted in nearly 100,000 fatalities, but over 26,000 of those were the direct results of coseismic landslides, including the Hattian Bala rock avalanche, which accounted for 1000 fatalities alone (Dunning *et al.*, 2007). Landslides in the subaerial environment can also severely impact critical infrastructure, such as road networks (Meyer *et al.*, 2015; Robinson, 2018). Subaerial landslides can dam river valleys, leading to a landslide-dammed lake forming upstream (Costa and Schuster, 1988; Korup, 2002; Fan *et al.*, 2020). Catastrophic breaches or overtopping of the dam can result in potentially catastrophic outburst floods that threaten communities and infrastructure downstream (Korup and Tweed,

2007). Subaqueous landslides within water bodies also present significant hazards. Shoreline infrastructure such as docks can be destroyed if a subaqueous landslide occurs on the slope on which the infrastructure is built (e.g. Lee *et al.,* 2006; Parsons *et al.,* 2014). Runout of subaqueous landslides can damage or break subaqueous telecommunication cables which are of critical importance for carrying global data and communication (Pope *et al.*, 2017).

Landslides into, and within, water bodies can also generate potentially large and destructive tsunamis that pose a hazard to coastal communities and infrastructure (Bornhold and Thomson, 2012). Over 250 documented landslide-tsunamis have occurred since the 14th Century (Roberts *et al.*, 2014). Landslide-tsunamis can produce exceptionally high runups, particularly from subaerial to subaqueous (STS) landslides. Ten of the 14 highest recorded tsunami runups have been generated by non-volcanic STS landslides into natural water bodies (Higman *et al.*, 2018). The most notable example is the 524 m high runup from the 1958 Lituya Bay landslide-tsunami (Miller, 1960). Recent events include: the 2015 Taan Fiord landslide-tsunami that generated a wave with a maximum runup of 193 m (Dufresne *et al.*, 2018; Haeussler *et al.*, 2018), and the 2017 Karrat Fjord landslide-tsunami that impacted the village of Nuugaatsiaq, Greenland, leaving four people missing, presumed dead (Gauthier *et al.*, 2018).

Subaqueous landslide-generated tsunamis typically produce smaller wave heights, but can still be highly destructive to shorelines (Bornhold and Thomson, 2012). In enclosed water bodies such as lakes/reservoirs, the tsunami wave can overtop the lake outlet, resulting in an outburst flood downstream (Korup and Tweed, 2007). The 1963 Vajont disaster may be considered an example of this. The Monte Toc landslide into the reservoir generated a large tsunami wave that overtopped the dam, flooding the towns in the valley below, resulting in 2000 fatalities (Ghirotti, 2012). Therefore, the cascade from the initial landslide can often be more severe and far-reaching than the landslides themselves. Additionally, the recent examples mentioned above occurred with no discernible external trigger (e.g. an earthquake or extreme precipitation) but occurred in actively deglaciating fjords. Therefore, such events may become more frequent with climate changes (Grämiger *et al.*, 2017). Due to the hazard landslides present, understanding their runout and emplacement behaviour is of critical importance

1.2. Distribution of landslides in lakes and fjords

Across the globe, investigations into subaqueous landslides have traditionally focussed on the open marine environment (coastal waters, seas, oceans), possibly due to research foci on the largest deposits, which may present the largest tsunamigenic risk to coastal populations and

infrastructure (Lintern *et al.*, 2019). Similarly, lakes and fjords may lack large populations or critical infrastructure to justify an extensive hazard assessment (Lintern *et al.*, 2019). However, growing settlements, development, infrastructure, populations, and tourism along the shorelines of lakes and fjords creates greater exposure, and therefore the potential for more disastrous landslide and associated tsunami events (Harbitz *et al.*, 2014).

Studies within lake basins have identified landslide deposits in over 170 lakes globally (Figure 1.2 (Sammartini et al., 2019; and references therein)). The deposits identified include recent, historic, and palaeo events. Deposits have been identified in all types of lakes, including, but not exclusively to, glacial, tectonic, volcanic crater, and dammed (Sammartini et al., 2019; and references therein), with glacial lakes are the dominant lake type where landslides have been identified globally. Investigations and subsequent databases of landslide deposits within lakes have predominately focussed on European (Schnellmann *et al.*, 2002; Monecke *et al.*, 2004; Strasser *et al.*, 2007; Hilbe *et al.*, 2011; Kremer *et al.*, 2015; Hansen *et al.*, 2016), North American lakes (Gardner *et al.*, 2000; Normandeau *et al.*, 2013; Roberts *et al.*, 2013; Lajeunesse *et al.*, 2017; Poiré *et al.*, 2018; Hughes *et al.*, 2020), and more recently, South American (Chilean) (Moernaut *et al.*, 2007, 2009, 2019; Van Daele *et al.*, 2015) lakes. However, there are regions that are underrepresented, including Africa, Asia (including the contemporary glaciated regions of the Himalayas), and Australia and New Zealand (Figure 1.2).

Similarly to lakes, landslide deposits have also been identified in fjords globally. Locations include, but not exclusively, Greenland (Pedersen *et al.*, 2002; Dahl-Jensen *et al.*, 2004; Gauthier *et al.*, 2018), Norway (Blikra *et al.*, 2006; Longva *et al.*, 2009; L'Heureux *et al.*, 2013; Böhme *et al.*, 2015; Bellwald *et al.*, 2016, 2019; Schleier *et al.*, 2017), Chile (Lastras *et al.*, 2013; Van Daele *et al.*, 2013), Canada (Prior *et al.*, 1982; Bornhold *et al.*, 2007; Conway and Barrie, 2015; Shaw *et al.*, 2017; Stacey *et al.*, 2020), Alaska (Miller, 1960; Lee *et al.*, 2006; Parsons *et al.*, 2014; Dufresne *et al.*, 2018; Haeussler *et al.*, 2018), Scotland (Stoker *et al.*, 2010; Carter *et al.*, 2020), and New Zealand (Pickrill, 1987; Hancox *et al.*, 2003; Power *et al.*, 2005; Dykstra, 2012). A similar geographical bias to the lakes is also observed in fjord-led landslides investigations. In the abovementioned list, locations such as Greenland and New Zealand have had observable landslide events but lack the pre- and/or post-hydroacoustic data.

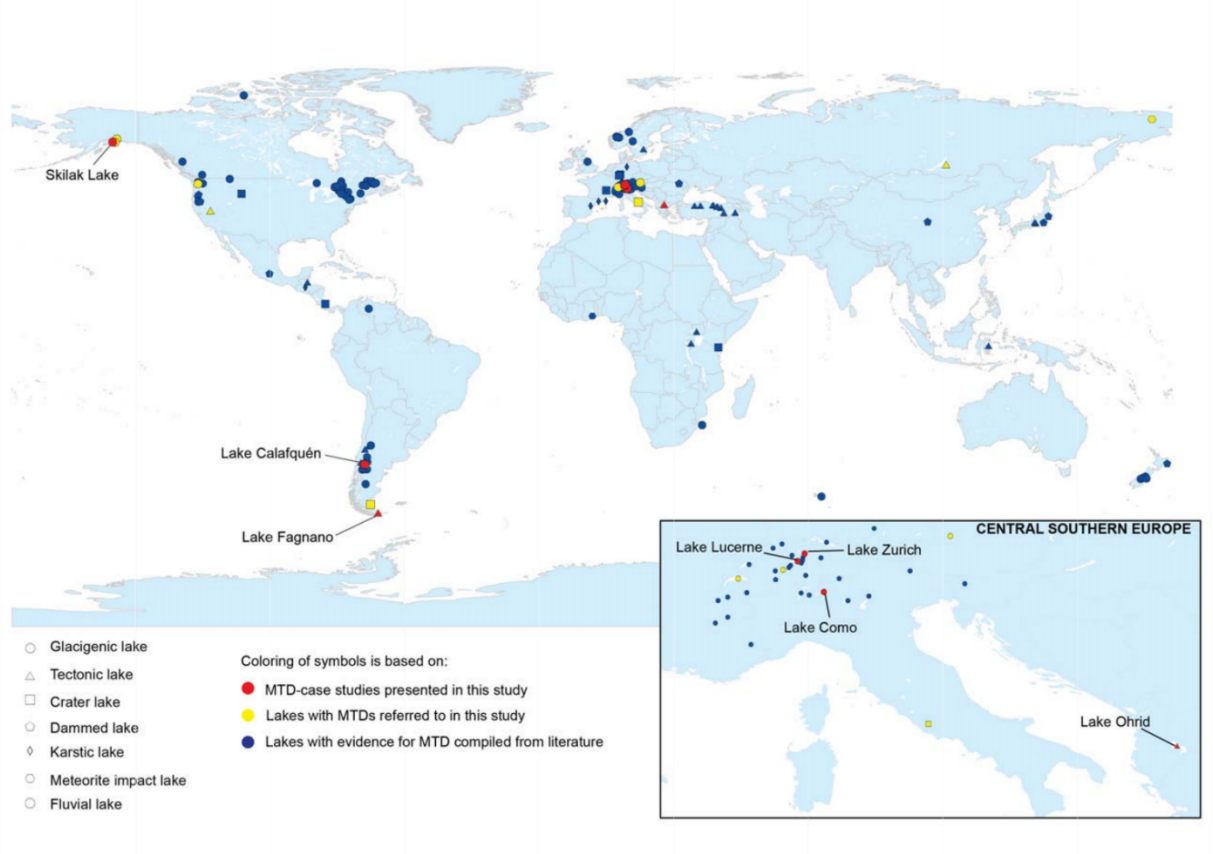

Figure 1.2. Distribution of known landslide deposits in lakes globally. Note the term "mass-transport deposit (MTD)" is more or less equivalent to landslide deposit (Praet *et al.*, 2017). Figure source: Sammartini *et al.,* (2019).

1.3. New Zealand

New Zealand is a location that has several large fjords and lakes, many bordered by steep slopes and mountains that have been carved out and modified by repeated glaciations (Lowe and Green, 1987; Barrell, 2011). New Zealand is located along an active tectonic margin, at the boundary between the Australian and Pacific plates (Norris and Cooper, 2001; Robinson and Davies, 2013). The hazard of landslides within, and into, lakes and fjords has been highlighted across the South Island of New Zealand (e.g. Hancox, 2012; Clark *et al.*, 2015; Mackey, 2015), but is largely unquantified. Despite being located along an active tectonic boundary, and having been extensively glaciated throughout the Pleistocene, few investigations and landslide hazard assessments have been conducted on New Zealand's lakes (Dykstra, 2012; Clark *et al.*, 2015; Mountjoy *et al.*, 2019). Only in a few studies has some hydroacoustic data (MBES and SBP) been collected to assess the landslide hazard (Dykstra, 2012; Clark *et al.*, 2015; Mountjoy *et al.*, 2019). New Zealand may be considered under-represented in lake and fjord subaqueous landslide investigations. This is despite many of the lakes and fjords being similar in origin and morphology (i.e. glacial) to many global counterparts. Furthermore, the lakes and fjords are

situated within the actively tectonic landscape of New Zealand. New Zealand therefore presents the opportunity to expand the knowledge on the spatial and temporal distribution of landslides in fjord and easier to access lakes. Collection of high-resolution datasets in the lakes and fjords would also allow intra-basin comparisons. Such information is especially pertinent given the heightened probability of a future Alpine Fault earthquake in the 50 years (Cochran *et al.*, 2017; Howarth *et al.*, 2021). Furthermore, such a catalogue would contribute to the global database of landslides and associated deposits, allowing for a more robust understanding of where is more susceptible to landslides (Clare *et al.*, 2018).

Subaerial landslides are a common geomorphic process in the mountains across New Zealand, where high rates of tectonic uplift and seismicity (Tippett and Kamp, 1995; Langridge *et al.*, 2016), coupled with glacially-steepened relief, and subsequent paraglacial processes, have triggered and/or primed slopes for failure (McColl, 2012). Across the Southern Alps in the South Island, large (>10^6 m^3), catastrophic landslide (rock slope failure (RSF)) deposits have been identified (Whitehouse, 1983; Korup, 2005b; Hancox and Perrin, 2009; Bainbridge, 2017). However, the subaerial record is posited as being spatially, and temporally incomplete, as various censoring processes have either masked or removed deposits from the subaerial landscape. Bainbridge (2017) posited that catastrophic RSFs may have runout and deposited into the many lakes and fjords, therefore censored from the record.. Furthermore, the historical record in New Zealand is temporally short, constrained to only the last c. 180 years (Howarth *et al.*, 2018). Integration of *Mātauranga Māori* (Māori Environmental Knowledge, culture, values and world view (King and Goff, 2010; Wilkinson *et al.*, 2020)) into geomorphic studies may provide a longer temporal record of geomorphic impacts and events through *pūrākau* (Māori oral histories (King *et al.*, 2007, 2018; King and Goff, 2010)). This is still largely underutilised (Wilkinson *et al.*, 2020), and risks misrepresentation (King *et al.*, 2018).

Analysis of existing high-resolution MBES and SBP data from Milford Sound/Piopiotahi revealed previously unknown, subaerial to subaqueous (STS) postglacial landslide deposits located across the fjord bottom and buried in the subsurface (Dykstra, 2012). Furthermore, recent MBES and SBP data collected in Lake Tekapo revealed entirely subaqueous landslide deposits covering 25% of the lake floor (Mountjoy *et al.*, 2019). Deposits were also identified buried within the sedimentary infill (Upton and Osterberg, 2007; Mountjoy *et al.*, 2019). Therefore, subaqueous landslides can also occur in the lakes, and may also be capable of generating locally hazardous tsunamis (Mountjoy *et al.*, 2019). This suggests that the other fjords and alpine lakes of the South Island that are bound by steep, mountainous topography,

may also hold an archive of previously unknown STS, and/or subaqueous landslides deposits. However, few other investigations have been conducted within many of the other lakes and fjords across the South Island. Therefore, the distribution of landslides in these subaqueous environments remains largely unknown. A more comprehensive overview to New Zealand is given within *Chapter 3*.

The importance of identifying further landslide deposits within lakes and fjords in New Zealand is driven by the potential for future failures, particularly because of a future earthquake along the Alpine Fault. The Alpine Fault has a geologically short recurrence interval (c.300 years), and the last known rupture was in 1717 AD (Sutherland *et al.*, 2007; Berryman, Cochran, *et al.*, 2012; Howarth *et al.*, 2018). The Alpine Fault has now exceeded the mean recurrence seismic cycle (Howarth *et al.*, 2018; Orchiston *et al.*, 2018). There is a 75% probability that a future earthquake on the fault will occur within the next 50 years (Howarth *et al.*, 2021), significantly higher than previous estimates of 29% (Cochran *et al.*, 2017). A future earthquake on the Alpine Fault could be M_w 8.0+. This could trigger geohazard cascades across the whole of the South Island (Figure 1.3). The hazard cascade may include STS, and subaqueous landslides, into and/or within, lakes and fjords (Robinson and Davies, 2013). Such landslides could generate potentially large lake and fjord tsunamis, which are a significant hazard to ever-expanding shoreline communities and infrastructure. Consequently, there is a need to understand the potential lake and fjord landslide, and associated tsunami hazard for disaster risk management and emergency response planning (Orchiston *et al.*, 2018).

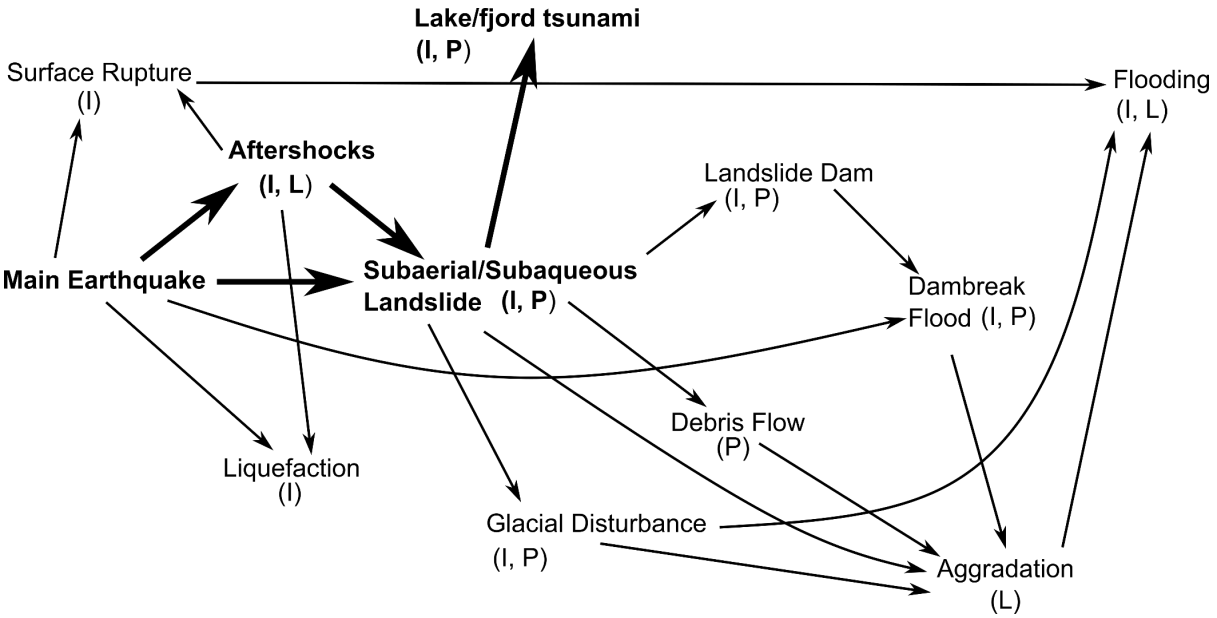

Figure 1.3. Flow chart of likely geomorphic consequences from a future Alpine Fault earthquake, with steps in bold relating to the focus of this thesis. I – immediate consequence: occurring seconds to a few days after the event; P – prolonged consequences: lasting weeks and even years after; and L – long-term: lasting years to decades after the event. Figure sourced and modified from Robinson and Davies (2013).

1.4. Rationale

To summarise the above, landslides are a major hazard into and within inland water bodies, presenting a significant risk to communities, settlements, and critical infrastructure along the shorelines from landslide-generated tsunamis. Identifying deposits in these water bodies through hydroacoustic surveys can provide insight into their spatial and temporal distribution. This information can aid in establishing a magnitude-frequency relationship of past failures, which is critical in the hazard and risk assessment of both landslide and associated hazards. Furthermore, the depositional characteristics of the landslides are important in understanding their behaviour, which can be important in understanding secondary hazards, such as landslide-tsunamis.

In New Zealand, the temporally short historical record, and limited hydroacoustic investigations in the lakes and fjords, mean that the landslide distribution, and therefore both the landslide and associated hazard (landslide-tsunami), is largely unknown. However, initial studies have shown lakes and fjords contain archives of deposits (Dykstra, 2012; Clark *et al.*, 2015; Mountjoy *et al.*, 2019). Therefore, it is not unlikely to suggest that many of the other basins could also contain deposits. Such data could aid in resolving spatial and temporal gaps in the landslide distribution. Furthermore, the well-preserved nature of deposits in the subaqueous environment may provide some insight into their emplacement dynamics which could aid in predicting future

landslide runout and tsunamis. Such information is critical with the likelihood of an Alpine Fault earthquake in the near future. The question remains however about whether the other lakes and fjords across New Zealand, particularly the South Island, contain a similar, well-preserved archive of deposits, either on the basin floor, or buried within the sedimentary infill. This thesis therefore focusses on investigating landslide deposits within the lakes and fjords of New Zealand.

1.5. Thesis aims and objectives

The overarching aim of this thesis is to better understand the distribution and dynamics of landslides within lakes and fjords in New Zealand, to improve the understanding of the hazard. Investigating the landslide distribution in lakes and fjords is to establish whether subaqueous environments contain an archive of deposits that could be otherwise lost in a subaerial environment. This, in conjunction with investigating the dynamic behaviour of the landslides, is to better understand both the landslide and associated hazards. To achieve the aim, a series of research questions (RQs) with associated objectives have been outlined:

> RQ1. Do lakes and fjords in New Zealand contain an archive of landslide deposits that help to resolve the landslide magnitude-frequency relationship?
>
> RQ2. What are the controls on the landslide distribution within lakes and fjords in New Zealand?
>
> RQ3. What is the dynamic behaviour of landslides in a lake or fjord environment?

To address the research questions and overall thesis aims, the following objectives were outlined:

1. To establish an inventory of known occurrences where landslides into, and within, lakes and fjords have been documented in New Zealand, to understand potential controls and triggers.
2. To characterise the morphology and morphometry of well-preserved, previously identified subaerial originating landslide deposits in a New Zealand fjord from literature, to gain insight into their emplacement dynamics.
3. To numerically model the runout of landslide deposits in subaqueous environments to investigate whether the modelling can also provide information on the landslide emplacement dynamics.

4. To collect high-resolution bathymetric data of a lake to generate a high-resolution bathymetric terrain model (BTM) to assist identification of landslide deposits on the lakebed.
5. To collect sub-bottom profiler data to detect any potential landslide deposits buried within the sedimentary infill.

1.6. Thesis structure

The thesis is structured as follows: *Chapter 2* provides a literature review surrounding the current understanding of landslide deposits within lakes and fjords. This includes the types of deposits, controlling and trigger factors, censoring processes, and their geomorphology and seismic architecture derived from hydroacoustic methods. Much of the New Zealand specific literature surrounding subaerial and subaqueous landslides has been purposely excluded from this review as it forms much of the background to *Chapter 3*.

Chapter 3 gives an overview of New Zealand as a study location. Site-specific literature surrounding the two study locations: Milford Sound/Piopiotahi, and Lake Wānaka, are contained within their respective chapters (*Chapter 4* and *Chapter 5*, respectively). *Chapter 3* also presents a new inventory of all the lakes and fjords in New Zealand with known landslide and associated deposits within their basins (prior to the research undertaken in *Chapter 5*). The chapter summarises deposit type(s), identification method(s), and triggering mechanism(s), where known. This information helps to address objective 1, and RQs 1 and 2.

The primary results chapters (*Chapter 4* and *Chapter 5*) are presented in a self-contained style with respective introductions, brief reviews into the relevant literature, methodologies, presentation of results, and discussions. As a result there may be repetition of background literature referred to in the literature review (*Chapter 2*), and study area (*Chapter 3*).

The first results chapter (*Chapter 4)* presents morphological and morphometric analysis on previously identified, well-preserved subaerial to subaqueous (STS) rock slope failure (rock avalanche) deposits in Milford Sound/Piopiotahi, New Zealand. Such information is pertinent to understanding the emplacement dynamics of landslides. Additionally, numerical runout modelling is conducted on five of the deposits using DAN3D. The modelling further enhances the understanding of the runout, and emplacement dynamics of subaerial originating rock avalanches into subaqueous environments. This research addresses objectives 2 and 3, which help to answer RQ3.

Chapter 5 presents the results of the subaqueous and subaerial distribution of landslide deposits within Lake Wānaka and its surrounding catchment. This includes the first ever collected high-resolution bathymetric sonar and sub-bottom profile data collected from the lake to identify landslide deposits on the lakebed, and within the sedimentary infill. Analysis of the subaerial and subaqueous deposits provides some insight into possible controls of landsliding within the catchment. This information also helps to address objectives 4 and 5, which further aid with answering RQs 1 and 2.

Chapter 6 synthesises the key findings from the results, presenting a summary of findings and how the research addresses the three research questions and overall thesis aim. The chapter also provides conceptual models on the distribution of landslides within New Zealand lakes and fjords, the hazard implications of the research within this thesis, and highlights scope for future work. Finally, *Chapter 7* presents how the research objectives outlined in section 1.5 were met, and the main conclusions from the research conducted within this thesis.

Chapter 2. Literature Review: Current understanding of landslide deposits in lake and fjord environments

The overarching aim of this thesis is to better understand the distribution and dynamics of landslides within lakes and fjords in New Zealand, to improve the understanding of the hazard. This chapter provides an overview of the existing literature on the broader research on landslides in lakes and fjords that underlies the work in the thesis. This chapter explores landslide triggering and controlling factors that limit or facilitate landslide occurrence, processes that may censor deposits, methods of investigating subaqueous landslides and associated, deposit geomorphology, and flow processes. Overall, this chapter positions the research within this thesis in its broader context.

2.1. Landslide terminology

Landslides occur in subaerial (Varnes, 1958), subaqueous (Locat and Lee, 2002), and even extra-terrestrial (Crosta *et al.*, 2018) environments. As a result, several classification schemes exist for subaerial (Varnes, 1958; Cruden and Varnes, 1996; Hungr *et al.*, 2014) and subaqueous (Hampton *et al.*, 1996; Mulder and Cochonant, 1996; Locat and Lee, 2002; Masson *et al.*, 2006; Talling *et al.*, 2014) landslides, including a lake-specific classification system (Sammartini *et al.*, 2019). Reconciling and resolving the similarities and differences between the terminologies applied to similar landslide failures, and/or deposits, in these respective environments is beyond the scope of this thesis. This thesis primarily discusses landslide deposits in subaqueous environments. The focus of the subaqueous environments is on deposits within lakes and fjords, which originated as either subaerial or subaqueous failures. The term "landslide" is used in this thesis in a generic sense when referring to non-specific failures, or deposits in both the subaerial and subaqueous environment. In this thesis, the following classifications are adopted.

With reference to those in subaerial environments, this thesis focusses on landslides resulting from rock slope failures (RSFs), inclusive of both catastrophic (i.e. rockslides and rock avalanches), and deep-seated gravitational slope deformations (DSGSDs). A "rock avalanche (RA)" in this thesis is defined as a large volume (typically $>10^6$ m^3), extremely rapid (>5 m s^{-1} (Cruden and Varnes, 1996)) long-runout landslide, that exhibits a flow-like motion (Hungr *et al.*, 2014). In subaqueous literature, the term "rock avalanche" and "debris avalanche" are often used interchangeably (Locat and Lee, 2002; Canals *et al.*, 2004; Mountjoy and Micallef, 2018). In this thesis, rock avalanche (RA) is used for such deposits, except when referencing specific

named landslides from literature. (for example, the Ruatoria Debris Avalanche (Collot *et al.*, 2001)). A "rockslide" is defined here as an extremely rapid failure of rock mass that has not fully transformed into a fragmented, flow-like landslide (cf. Hungr *et al*., 2014). Rockslides can originate as a translational slide along a bedding plane or can be a rotational failure. A DSGSD is used here to define bedrock failures that exhibit sackung-type morphological characteristics such as double ridges, uphill-facing scarps, and counterscarps, and possible toe bulging (Agliardi *et al.*, 2001; Pánek and Klimeš, 2016). DSGSD is used instead of slow creeping landslides as DSGSD does not infer or imply rates of movement (Korup, 2005d), though typical rates of movement may be mm yr^{-1} (Agliardi *et al.*, 2001).

From a global review of landslide deposits identified in lake basins, Sammartini *et al.,* (2019) classified deposits into four main categories (Figure 2.1). The classification is based upon the source region, mode of failure initiation, transport mechanism and resultant deposit, where possible. The categories include:

1. **Lateral slope landslides -** landslides that occur on non-deltaic slopes and involve failure of the hemipelagic/lacustrine sediment drape on the subaqueous slopes. Failures usually form as rotational or translational slides along a weak failure plane (Schnellmann *et al.*, 2002; Strupler *et al.*, 2017; Sammartini *et al.*, 2019).
2. **Margin collapse landslides –** landslides that are typically larger in extent than lateral slope failures. They can be complex multistage failures, deep seated, mobilising subaqueous bedrock as well as sediments. Margin collapses appear analogous to subaerial catastrophic RSFs and can evolve into subaqueous rock avalanches (Gardner *et al.*, 2000). Margin collapses can also be slow-moving failures however (Conway and Barrie, 2018).
3. **Deltaic collapse landslides –** landslides on subaqueous delta fan slopes that are independent from gravitational sediment transport mechanisms on the delta from the river such as turbidity currents or hyperpycnal discharges. Failures can be triggered externally (Kremer *et al.*, 2015; Praet *et al.*, 2017) or can occur spontaneously (Girardclos *et al.*, 2007; Hilbe and Anselmetti, 2014), and they can exhibit a variety of deposit morphologies.
4. **Subaerial rockfalls –** landslides that refer to near vertical-vertical fall of blocks/rocks from steep cliffs. They can originate in both the subaerial or subaqueous environment, with subaerial origins common in intramountainous environments with steep subaerial rock slopes above (Schnellmann *et al.*, 2006; Bozzano *et al.*, 2009; Hilbe *et al.*, 2011)

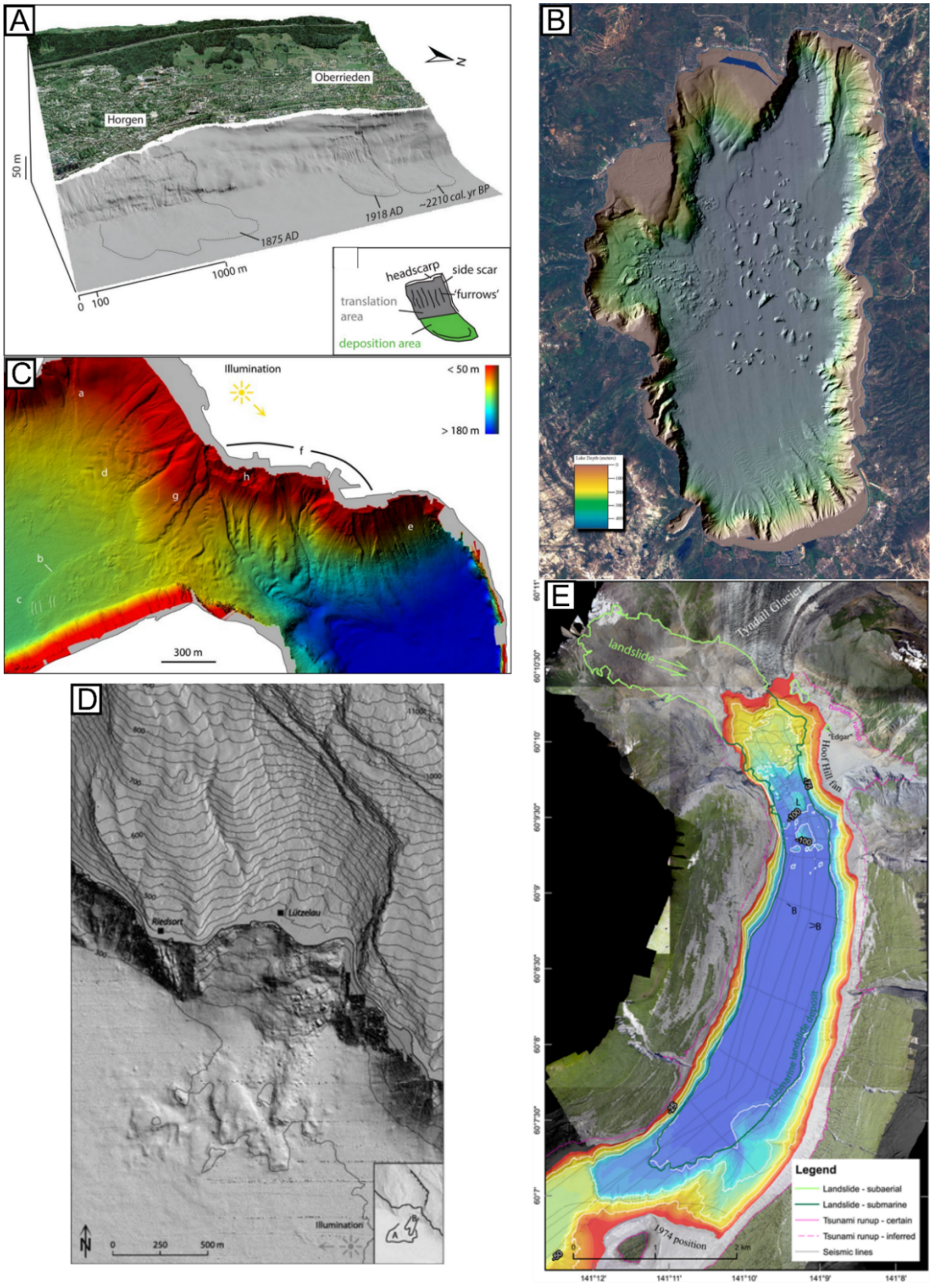

Figure 2.1. Examples of landslide deposits, based on Sammartini *et al.,* (2019) classification, found in lake and fjord basins. A – Lateral slope failures along subaqueous slope. Source: Strupler *et al.*, (2019); B – subaqueous margin collapse with source scar identifiable in western edge, and deposit across the basin. Figure source https://cmgds.marine.usgs.gov/data/pacmaps/lt-shd.html; C – deposits from deltaic failures. Source: Hilbe and Anselmetti (2014); D – STS rockfall deposits on the lake basin from subaerial steep slope (inset). Source: Hilbe *et al.,* (2011); E- STS rock avalanche in Taan Fiord. Deposit extent mapped by green line. Source: Haeussler *et al*., (2018).

For continuity, deposits discussed in lakes and fjords in this thesis will aim to follow the proposed classification of Sammartini *et al.* (2019). However, "subaerial rockfalls" refers to a very specific mode of failure and deposit that is perhaps not entirely representative of all subaerial-sourced deposits found in lakes and fjords. Deposits relating to other subaerial-originating catastrophic RSFs, such as rockslides and rock avalanches, have been identified globally in fjords (Blikra *et al.*, 2006; Longva *et al.*, 2009; Dufresne *et al.*, 2018) (Figure 2.1E) and lakes (Roberts *et al.*, 2013; Hughes *et al.*, 2020). Therefore, in this thesis, landslides that are sourced from the subaerial environment but runout and deposit in the subaqueous environment are referred to as "subaerial to subaqueous (STS) landslides". This follows the proposed terminology of Haeussler *et al.,* (2018). Further classification of the landslide is adopted where information on the failure and resultant deposit morphology allows e.g. STS rock avalanche, rockslide, and rockfall.

In subaqueous landslide studies, deposits are often classified as "Mass-transport deposits (MTDs)". MTDs are often ascribed to deposits resulting from gravity-induced failure, usually identified within core analysis and/or sub-bottom data (Frey-Martínez *et al.*, 2006; Bull *et al.*, 2009; Moscardelli and Wood, 2016). The mode of failure is often undefined, and the MTDs can have little to no bathymetric expression to derive surface morphological features and adopt a landslide classification. MTD is more or less equivalent to "landslide deposit" (Praet *et al.*, 2017). In this thesis, MTD is only used when referring to examples in literature that use such terminology. The term "landslide deposit" is used instead.

2.2. Controlling and triggering factors on subaerial and subaqueous landslide occurrence in lakes and fjords

2.2.1. Preconditioning and preparatory factors

The stability of a subaerial and subaqueous slope is ultimately controlled by the rock mass properties (Evans *et al.*, 2006; Hewitt *et al.*, 2008). The properties include the rock mass strength and deformability, which can control the critical threshold angle a slope can sustain before it fails (McColl, 2015). The lithology and rock structure (bedding planes, foliations, jointing, and faults) can also control the inherent strength of the rock mass, and the geometry a slope can maintain, as it resists the stresses acting upon it (McColl, 2012). These are fixed properties of the slope, but stability can change due to preparatory and triggering factors.

Geological characteristics of subaqueous slope material may precondition slopes for failure through creation of weak layers. Weak layers may result from variations in sediment

composition (Locat *et al.*, 2016). The weak layers can act as glide planes on which landslides can fail along. Within some glacigenic lakes (Strasser *et al.*, 2007; Strupler *et al.*, 2017) and fjords (Bøe *et al.*, 2000), this has been identified in glacial depositional layers stratigraphy. In Lake Lucerne for example, a weak layer, and subsequent failure plane, developed at the lithological boundaries between over-consolidated glaciolacustrine deposits (that exhibit elevated pore pressures as a result), and slightly unconsolidated, low-strength, Late Glacial clays (Strasser *et al.*, 2007). Similar lithostratigraphic position of the weak layer has been identified in Lake Zürich (Strupler *et al.*, 2017), and Lake Wörthersee (Daxer *et al.*, 2020).

In mountainous environments, processes such as glacial and fluvial erosion, coupled with tectonic uplift, are often associated with preparing slopes for failure by steepening slopes in subaerial environments (Korup *et al.*, 2007; Clarke and Burbank, 2010). Often these slopes are characterised as being 'oversteepened'. Oversteepened in this context often refers to slopes above a critical threshold angle (Clarke and Burbank, 2010). Oversteepened slopes in subaerial environments may be considered as having 'excess topography' (Blöthe *et al.*, 2015). However, this may be misleading, as it would imply that any slope that has been eroded and steepened by these processes are inherently unstable (Augustinus, 1995) and not every slope that had been subjected to these processes had failed (Bovis, 1982). Stress release and redistribution of the rock mass can begin to destabilise a slope through formation of stress-induced fracture propagation and sheet jointing and exfoliation joints, leading to long-term weakening of the rock mass strength (McColl, 2012, 2015; Grämiger *et al.*, 2017).

Oversteepening is also a preparatory factor for subaqueous landslides (Strasser *et al.*, 2011; Praet *et al.*, 2017). For subaqueous slopes, the slope angles affect the thickness and volume of sediment cover the slope can hold before failure. Studies in lakes globally have identified that subaqueous landslides and associated deposits occur within a range of threshold slope angles, typically between 5-20° (Strasser *et al.*, 2011; Praet *et al.*, 2017; Moernaut *et al.*, 2019). The lower the slope angle, the greater volume of sediment it can accumulate before failure, and therefore generate the largest landslides. Slopes steeper than 20° cannot accumulate a large sediment drape to generate noticeable landslides and associated deposits (Hilbe and Anselmetti, 2014; Praet *et al.*, 2017). The steep slopes are likely to have small-scale, frequent spontaneous failures that may not leave discernible deposits. The steep slopes of fjords and some intramountainous lakes may mean that sediment cover may be too thin for lateral slopes failures to occur (Strasser *et al.*, 2020). Sedimentation rates will also affect oversteepening of slopes. Higher or rapid sedimentation results in faster sediment loading of slopes. This oversteepening

will affect the overburden weight of material, decreasing slope stability (Clare *et al.*, 2016; Praet *et al.*, 2017). Rapid sedimentation may also inhibit normal consolidation of the sediments, leading to the development of excess pore pressures (overpressure) (Sultan *et al.*, 2004; Flemings *et al.*, 2008). The excess pressures may reduce shear strengths, and eventually lead to failure (Dugan and Sheahan, 2012; Wiemer *et al.*, 2015).

Glacial debuttressing is seen as both a preparatory and a trigger factor for slope failure (McColl, 2012). Glaciers may buttress slopes, or rather, change the stress field in the rock masses (Grämiger *et al.*, 2017). Repeated glacial loading and unloading will alter the stress fields in the rock mass over time. As a trigger, it would imply that rock slopes would fail immediately after deglaciation, which may be true if a rock mass is already weakened and ready to fail (McColl, 2012; Grämiger *et al.*, 2017). However, its efficacy as a trigger has been questioned as it is frequently observed that there are lag times between deglaciation and slope failure (Prager *et al.*, 2008; Ballantyne *et al.*, 2014; Pánek *et al.*, 2018). Ice is less dense than rock and behaves in a ductile manner, and therefore cannot provide lateral support to buttress adjacent rock slopes (McColl *et al.*, 2010). Therefore, slopes may begin to collapse before ice retreat (McColl and Davies, 2013) but glacier retreat could hasten that collapse. In contemporary glacial fjord regions, gradual slope deformation (Dai *et al.*, 2020), and/or full catastrophic failures (Dufresne *et al.*, 2018; Gauthier *et al.*, 2018) have been observed in the past few decades in association with down-wasting and terminus retreat of fjord glaciers. Therefore, if hillslope movement and landslide activity is a paraglacial response to ice retreat then such processes may have occurred in currently ice-free fjords and glacigenic lakes that were occupied by ice during the Last Glacial Maximum (LGM).

Climate warming is being increasingly considered as a preparatory factor for failures due to the degradation of permafrost (the trigger factor) in rock slopes. The removal of the permafrost in rock masses, which acts as a binding agent for the rock mass discontinuities, can destabilise the slope through increased porewater pressure in joints that are not free draining, and raises the permafrost level, reducing rock strength below this level (McColl, 2012). Whilst climate warming (and associated permafrost degradation) is suggested as a mechanism for RSFs in the European Alps (Haeberli *et al.*, 2017), there is currently insufficient evidence to support a similar relationship in New Zealand's Southern Alps (Allen and Huggel, 2013). Some landslides here have been found to occur in the lower boundaries of the permafrost. It is difficult to elucidate permafrost degradation as a factor from other processes including seismicity, strain accumulation, weathering and tectonic uplift (Allen *et al.*, 2011; McSaveney *et al.*, 2015).

2.2.2. Triggering factors

Triggering factors are traditionally external forces that are often instantaneous. In subaerial environments, triggering factors include earthquakes (Keefer, 1984), heavy precipitation (Dortch *et al.*, 2009), and permafrost degradation, discussed previously. Precipitation (rainfall) can be considered both a preparatory and triggering factor for subaerial RSFs through the development of increased porewater pressures within the bedrock (Dortch *et al.*, 2009; McColl, 2012). Intense rainfall events and monsoons can cause flooding events, with high flows undercutting the toes of slopes, further destabilising the slope (Dortch *et al.*, 2009).

Triggering factors for subaqueous landslides include loading and impact of subaerial RSFs (Kremer *et al.*, 2015; Daxer *et al.*, 2018), and human activities such as anthropogenic loading of subaqueous slopes (Dan *et al.*, 2007). Water level fluctuations, whether it is sea or lake levels, can trigger subaqueous landslides. This can occur through a reduction in the overburden pressure during lowstands, as well as increasing terrestrial sediment input to slopes (Anselmetti *et al.*, 2009; Urlaub *et al.*, 2013). Drops in water level have also been considered to precondition or trigger subaerial slope failures adjacent to water bodies. Drawdowns in water level cause changes in seepage and groundwater levels which may trigger slope failures (Pánek *et al.*, 2018). However, one of the most significant triggers for landslides across subaerial and subaqueous settings is earthquakes.

2.2.2.1. Earthquakes

Earthquakes have long been identified as a triggering mechanism for subaerial (Keefer, 1984, 2002; Meunier *et al.*, 2007, 2008; Parker *et al.*, 2015) and subaqueous (Locat and Lee, 2002; Masson *et al.*, 2006; Strasser *et al.*, 2006; Mountjoy *et al.*, 2018) landslides. Earthquakes are a particularly common triggering mechanisms for large subaerial catastrophic RSFs along plate boundaries where terrain is uplifting and subject to seismic activity (e.g. the Himalayas, Andes, Southern Alps (Keefer, 1984; Malamud *et al.*, 2004; Meunier *et al.*, 2007)). Subaerial hillslopes subjected to earthquake shaking can experience enhanced horizontal and vertical peak ground acceleration (PGA) (Keefer, 2000; Meunier *et al.*, 2007). The shaking and PGA induce instantaneous shear stresses that can overcome the rock mass strength. Earthquakes can also result in increased porewater pressure and propagation of fractures through the rock mass, leading to formation of a failure surface on the hillslope (McColl, 2015). The spatial distribution of earthquake-triggered landslides (EQTLs) generally indicate that the number of landslides reduces with increasing distance from the earthquake epicentre. This relates to the attenuation of shaking intensity and PGA (Keefer, 2002; Meunier *et al.*, 2007; McColl, 2015). EQTLs are

not solely governed by the proximity to the epicentre, however. Their subaerial distribution correlates with topographic conditions, with landslides often originating on ridge crests and upper flanks of slopes through topographic amplification (Meunier *et al.*, 2008; Korup *et al.*, 2010; McColl, 2015). The effect of seismic waves entering hillslope edifices partially reflect the waves back into the rock mass, converging along slope convexities, causing enhanced ground motion. The seismic amplification in hillslopes may result in a cluster of earthquake-triggered landslides along ridge crests or upper portions of hillslopes (Meunier *et al.*, 2008; Wang *et al.*, 2020).

Assigning earthquakes, or indeed other triggering mechanisms, is more difficult for subaqueous failures as direct observation and monitoring is often more limited (Mountjoy *et al.*, 2020). The presence of coeval subaqueous deposits (i.e. deposits that occur at the same time/located at the same stratigraphic position at different locations) across a lake basin (Upton and Osterberg, 2007; Praet *et al.*, 2017; Mountjoy *et al.*, 2019) or fjord (Lastras *et al.*, 2013; Bellwald *et al.*, 2016) is often indicative of a seismic trigger (Schnellmann *et al.*, 2002; Moernaut *et al.*, 2007; Upton and Osterberg, 2007; Strasser *et al.*, 2013; Van Daele *et al.*, 2015; Praet *et al.*, 2017). Studies across multiple lake or fjord basins allow greater confidence in assigning a seismic trigger if the ages of failures are synchronous between basins (Moernaut *et al.*, 2007; Van Daele *et al.*, 2015; Howarth *et al.*, 2016; Praet *et al.*, 2017; Bellwald *et al.*, 2019). Where deposits are dated, temporal correlation with independent ages of past fault ruptures from historical or independently dated palaeo records provides support to seismic triggering (Schnellmann *et al.*, 2002, 2006; Strasser *et al.*, 2006, 2013; Moernaut *et al.*, 2007; Howarth *et al.*, 2014, 2016; Kremer *et al.*, 2015, 2017; Praet *et al.*, 2017). However, low sedimentation rates in subaqueous basins can under-record past earthquakes if there is insufficient sediment build-up on lateral slopes between seismic intervals for failures to occur (Moernaut *et al.*, 2009).

Coseismic triggering of subaerial and subaqueous landslides is often linked to earthquake magnitude, PGA, and shaking intensities, referred to in this thesis under the Modified Mercalli intensity scale (MM) (Keefer, 1984, 2002; Jibson, 1996; Meunier *et al.*, 2007). However, earthquake magnitude is perhaps not a useful proxy for understanding which earthquake magnitudes will trigger subaerial and subaqueous landslides. Earthquakes with a minimum magnitude of $M_w \sim 4.0$ have been documented as triggering rockfalls and rockslides, and rock avalanches have been triggered at a minimum magnitude of $M_w \sim 6.0$ (Keefer, 1984). Earthquakes as low as M_w 3.0 have been identified as triggering landslides in subaqueous

environments (Pope *et al.*, 2017), whilst $M_w > 8$ have recorded few (Tappin *et al.*, 2007; Völker *et al.*, 2011; Sumner *et al.*, 2013; Pope *et al.*, 2017).

Glacial cycles are known to influence regional seismicity, with relationships between enhanced seismicity during the late-Glacial/early Holocene, and an apparent increased landsliding activity during this period (Muir-Wood, 2000; Bøe *et al.*, 2003; McColl, 2012; Ballantyne *et al.*, 2014; Bellwald *et al.*, 2016). It is suggested that unloading of ice masses will either generate, or increase seismic activity (McColl, 2012). Due to a long response time of stress changes (Muir-Wood, 2000) there is a lag in enhanced post-glacial seismicity from deglaciation, which may explain, in part, a lag in higher rate of post-glacial landslide activity (McColl, 2012; Ballantyne *et al.*, 2014). This may aid in explaining spatial distributions of subaerial and subaqueous landslide deposits in tectonically aseismic, but formerly glaciated regions (Bøe *et al.*, 2003; Blikra *et al.*, 2005, 2006; Longva *et al.*, 2009; Ballantyne *et al.*, 2014; Bellwald *et al.*, 2016, 2019).

Where a seismic trigger is known or inferred, relative delineation between moderate and strong earthquakes can be interpreted from deposits in the lakes and fjords. MM ≥ 6 shaking intensities have been found sufficient to generate subaqueous landsliding in lakes (Monecke *et al.*, 2004; Howarth *et al.*, 2014; Moernaut *et al.*, 2014; Van Daele *et al.*, 2015). Subaqueous slopes are more sensitive to ground shaking than terrestrial hillslopes due to factors such as water saturation, buoyancy, and reduced friction of sediments (Tripsanas *et al.*, 2008; Orpin *et al.*, 2010). Therefore, lower shaking intensities are typically required for triggering subaqueous landslides. Deltas are considered more susceptible to failure than sediment-covered lateral slopes (Strasser *et al.*, 2013; Van Daele *et al.*, 2015) through potential over-steepening, and elevated pore pressures as a result of high fluvial input of coarse clastic sediments (Sammartini *et al.*, 2019). Therefore, deltaic failures could provide useful proxies of past earthquake shaking in a basin (Van Daele *et al.*, 2015). However, this may only apply where earthquake recurrence is more frequent than the time needed for deltas to become unstable and result in a gravitational collapse induced by continuous sediment loading (Van Daele *et al.*, 2015). MM ≥ 9 shaking typically generates significant landsliding and catastrophic RSF events in the subaerial environment (Hancox *et al.*, 2002; Howarth *et al.*, 2014). Therefore, the source of the deposits in these basins, whether from subaerial or subaqueous source, can provide proxies to delineate relative magnitude and intensity of palaeoearthquakes. This may be appropriate for fjords, and lakes in intramountainous settings (Figure 2.2). However, for lakes in piedmont settings where

steep subaerial slopes are absent, the earthquake magnitude and intensity may be more difficult to decipher.

Large earthquakes may also act as a preparatory factor. In subaerial environments, brittle material hillslopes that do not fail in the initial earthquake event are subject to stresses during the quake. The stresses are assumed to structurally weaken slopes sufficiently through increased micro fracturing and joint dilation, resulting in an elevated susceptibility of landslides from post-seismic precipitation or future seismic events (Parker *et al.*, 2015; Brain *et al.*, 2017). However, this cannot entirely explain observations in all environments of post-seismic landslides (Brain *et al.*, 2017). Some studied locations show that whilst a higher normalized post-seismic landslide rate was observed after the earthquake, hillslopes return to pre-seismic landslide rates over sub-decadal and decadal timescales, depending on the magnitude of the initial earthquake event (Marc *et al.*, 2015). Similarly, for ductile hillslopes, lower ground shaking intensities prior to the main shock may cause progressive densification and frictional strengthening of hillslope sediment. These processes may reduce the susceptibility of coseismic landsliding and to precipitation events (Brain *et al.*, 2017), indicating that the pattern of seismicity exhibits a significant control on the number of EQTLs. Therefore focussing solely on the main earthquake may not provide an accurate estimate of landslide risk during coseismic intervals (Hovius *et al.*, 2011).

Subaqueous slopes, particularly deltaic systems, may be more susceptible to failures from rapid sediment loading from heightened sediment flux in the terrestrial catchments (Howarth *et al.*, 2012, 2014). Deltaic failures may occur decades after the initial quake as an indirect impact of the earthquake (Howarth *et al.*, 2012; Van Daele *et al.*, 2015). Earthquakes may also generate weak layers in slopes by reducing the strength and/or increase pore pressures of certain layers (Locat *et al.*, 2016). Conversely, earthquakes may also strengthen subaqueous material where the initial shaking did not trigger a failure through processes such as densification (Sawyer and Devore, 2015; ten Brink *et al.*, 2016).

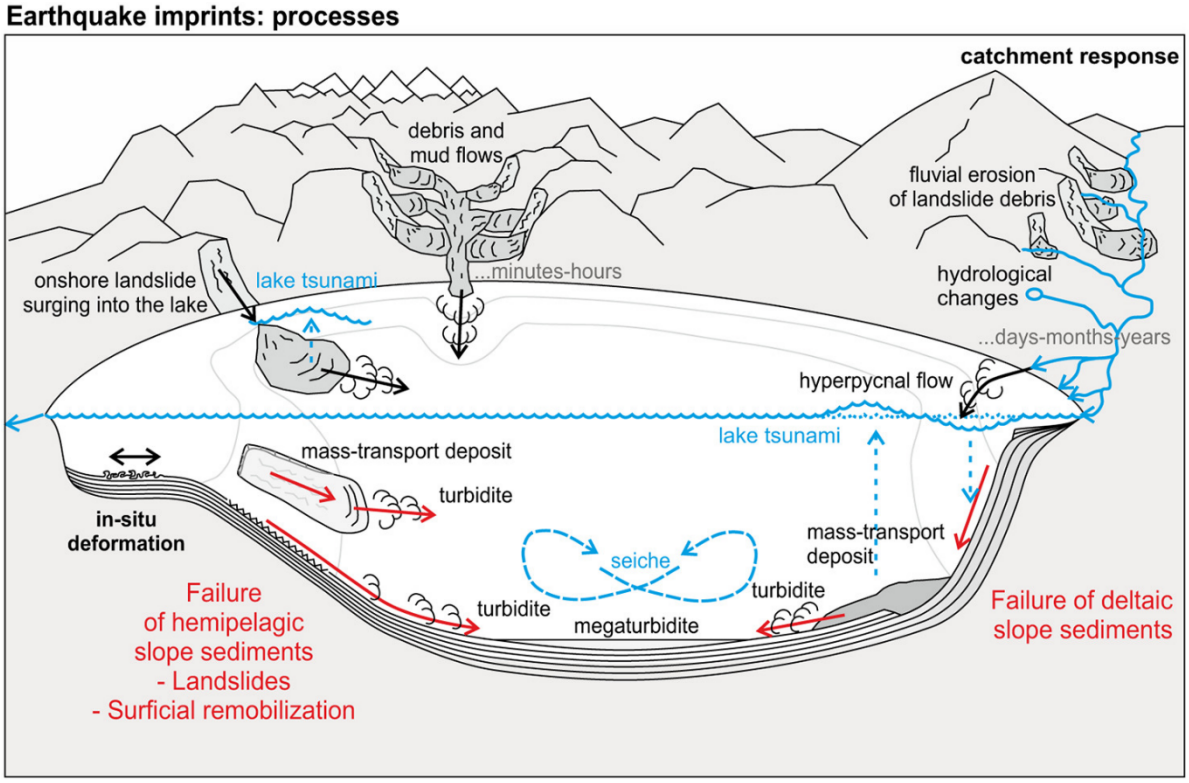

Figure 2.2. Effects and processes from an earthquake that may be detected, and/or leave an imprint, within a lake (and possibly fjord). Most records relate to landslide processes (indicated in red). Figure source: Moernaut (2020).

Large, catastrophic RSFs in subaerial environments can occur without any discernible trigger (McSaveney, 2002; Blikra *et al.*, 2006; Massey *et al.*, 2013). These events could be associated with progressive weakening of a rock mass over time, until the inherent rock strength is lowered and overcome by gravitational induced stress (Glade and Crozier, 2005). Additionally there may be some other unidentified external factor that was involved in generating failure (McColl, 2012). Some subaqueous failures appear to have occurred without an external trigger (Glimsdal *et al.*, 2016). Deltas have been documented to fail through the impact and loading of aseismically triggered RSFs (Kremer *et al.*, 2015). Deltas can also fail spontaneously, without external triggers, through continued gradual sediment loading (Girardclos *et al.*, 2007), preconditioned by aforementioned processes. This observation is significant for quantitative hazard and risk assessments in mountainous regions.

2.3. Censoring processes of deposits

Identification and mapping of deposits in both subaerial and subaqueous environments is critical for landslide hazard assessments, and understanding potential controls on occurrence (Mountjoy and Micallef, 2018). This requires extensive knowledge of the spatial and temporal distribution of landslide deposits in order to assess the magnitude-frequency relationship

through time, particularly beyond the observed written timescale (Korup and Clague, 2009; Clare *et al.*, 2018; McColl, 2020). Deposits however, are susceptible to censoring processes that impact the preservation potential of deposits (Smith *et al.*, 2007; Weidinger *et al.*, 2014; Clare *et al.*, 2018). This can result in a spatial and temporal bias towards identified deposits that are younger in age (Hewitt *et al.*, 2008). Landslide hazard assessments therefore need to account for the preservation bias in hazard assessments in a region (Clare *et al.*, 2018; McColl, 2020).

2.3.1. Subaerial censoring processes

Deposits in subaerial environments are subject to several censoring processes such as fluvial dissection and erosion, glacial sequestration, transportation, and/or modification; vegetation regrowth; or occlusion in water bodies. Fluvial erosion of deposits can occur rapidly, particularly in an active fluvial system (Chevalier *et al.*, 2009) and regions where precipitation is high (Barnard *et al.*, 2001; Korup, 2005a). In mountain valley systems, the deposit may block a valley creating a dam. Catastrophic failure of the dam will remove large quantities of the deposit in a short space of time (Korup and Tweed, 2007; Hewitt *et al.*, 2011). Deposits therefore may only remain recognisable for decades to a few centuries (Chevalier *et al.*, 2009). Deposits may also be obscured by vegetation growth over deposits and source areas (Korup, 2005a; Chevalier *et al.*, 2009). In glaciated environments, landslides that deposit in the accumulation area may undergo rapid (weeks to months) sequestration and advection into the glacier system (Uhlmann *et al.*, 2013; Dunning *et al.*, 2015). Supraglacial deposition in the lower reaches of a glacier may be transported far from the source area (Hewitt, 2009b, 2009a; Shugar and Clague, 2011). Deposits in the proglacial region can be eroded or heavily modified by ice overriding deposit material by possible subsequent glacial advances (Cook, Porter, *et al.*, 2013; Bichler *et al.*, 2016; Ballantyne, 2018). The deposits may then be initially misidentified as other morphological features, such as glacial features. Thorough analysis of such features can aid in deciphering between glacial or landslide origin (McColl and Davies, 2011; McColl *et al.*, 2019).

Lakes and fjords may censor records of past STS landslides through subaqueous occlusion of the deposit. Landslides within, and into lakes and fjords are rarely observed directly, often only detected by secondary methods such as seismic detection (Ekström and Stark, 2013), or from the resultant tsunami they can produce (Miller, 1960; Blikra *et al.*, 2005; Gauthier *et al.*, 2018). However, in particularly remote and high-mountain environments, events may go undetected. Subaerial geomorphological evidence, such as onshore deposit material (Dufresne *et al.*, 2018), or source scars (Carter, 2015), may provide indication of past STS landslides at

intramountainous lakes and fjords. However, attempting to reconstruct past subaerial landslides from scars alone is limiting as it is uncertain whether the scar resulted from a single, or multiple events. Single scars can be the source of multiple large RSF landslides (Hermanns *et al.*, 2006; Lee *et al.*, 2009; Schleier *et al.*, 2017) and subsequent failures may remove the scars of previous failures. Similarly, the geometry of scars can result in misidentification and misclassification as other morphological features of geometric similarity (e.g. cirques (Turnbull and Davies, 2006)). Onshore deposit evidence is rarer in fjords and intramountainous lakes where terrestrial accommodation space is limited (Korup and Dunning, 2015). However, deposit material of a STS RSF has been documented onshore in the post-survey investigation of the 2015 Taan Fiord rock avalanche (Dufresne *et al.*, 2018). In this case, the rock avalanche flowed down the fjord wall and into the water where it was able to runout across the fjord bottom. Part of the rock avalanche had sufficient momentum to runup the opposite side of the fjord wall, exiting the water, and flow over a subaerial fan, depositing hummocks onshore. To date, this is the only known documented example, and the onshore deposit is susceptible to the subaerial censoring processes mentioned previously. In the absence of observations and historical documentation, deposits in lakes and fjords can be identified through modern hydroacoustic techniques including multibeam echosounder (MBES) and other bathymetric sonar systems, sidescan sonar (SSS), and sub-bottom profile (SBP) surveys (section 2.4).

2.3.2. Subaqueous censoring processes

Subaqueous environments are also prone to censoring processes that can affect the preservation potential of deposits. Collection of MBES datasets provide a snapshot in time of deposits within the respective subaqueous environments. However, repeat MBES surveys over a short time period (≤ 5 years) have shown subaqueous deposits have been rapidly reworked and reduced in size (Smith *et al.*, 2007), or all evidence has been completely removed (Clare *et al.*, 2016). Therefore, deposits identified in bathymetric datasets may not reflect the true number of landslides to have affected a subaqueous environment. The preservation of deposits has been found particularly susceptible in areas of rapid sedimentations such as fan deltas (Clare *et al.*, 2018), or canyon systems. Canyons can undergo regular, episodic flushing by turbidity currents (Azpiroz-Zabala *et al.*, 2017), or by external perturbations such as earthquakes (Mountjoy *et al.*, 2018). This can rework recent deposits in a short period of time (Smith *et al.*, 2007), and may potentially erode all traces of older deposits over time (Mountjoy and Micallef, 2018). Similar flushing processes have been identified in subaqueous channels in fjords (Heijnen *et*

al., 2020). Therefore, landslide deposits in lake and fjords may be susceptible to reworking if basins contain channels and deposits are in close proximity.

Deposits in lakes and fjords may be temporally censored. Within glacially carved fjords and lakes, deposits are more likely largely temporally censored to post-LGM, or postglacial, period. Any older deposits are likely to have been eroded through subsequent climate-related glacial advances, as mentioned above. Similarly, supraglacial deposition of subaerial RSF deposit debris can result in glacial advances not associated with climatic changes (Reznichenko *et al.*, 2011). The advance may override, and potentially erode, deposits in the subaqueous environment that occurred in close proximity to the glacier terminus (Dufresne *et al.*, 2018). Lateral slopes in the basins may be devoid of sediments during glacial maximum, with sediment accumulation only occurring during ice margin retreat (Strasser *et al.*, 2007). As previously mentioned, subaerial-originating RSFs that occur during down-wasting and retreat of a lake- or fjord-terminating glacier may be deposited supraglacially and be transported away (Hewitt, 2009b) leaving a scar with no associated deposit in the lake or fjord (Carter, 2015).

Post-landslide sedimentation may bury deposits in lakes and fjords. This may result rapidly through remobilisation of hemipelagic sediment during the landslide, resulting in landslide-triggered megaturbidites (Haeussler *et al.*, 2018). Such megaturbidites may onlap onto the landslide deposit, resulting in rapid burial, or obscuration of surface morphological features (Dufresne *et al.*, 2018). Deposits may also become rapidly buried in environments with high sedimentation rates. Burial of deposits obscures detection from MBES and SSS systems. However, burial of deposits can be highly effective at preserving the deposits, and identification of deposits can be addressed with utilising 2D and 3D SBP surveys in the subaqueous environments (Schnellmann *et al.*, 2006; Gee *et al.*, 2007; Bellwald *et al.*, 2019). However, older deposits may be subject to post-depositional modification under burial by lithification and compaction that can alter the original the landslide deposit morphology (Clare *et al.*, 2018). Comparisons of seismic characteristics between recent and ancient landslides therefore need to recognise that landslide deposits of similar emplacement dynamics may not have similar seismic facies. Conversely, low sedimentation rates may limit preservation of individual events. As in subaerial environments, repeated failures from the same source area may result in deposit amalgamation (Tanyaş *et al.*, 2019; Carter *et al.*, 2020), or erosion and entrainment of older deposit material into the most recent deposit.

Deposits in subaqueous environments may also be censored through a scaling/detection bias based on the size of the deposit relative to available surveying methods (Clare *et al.*, 2018; Watson *et al.*, 2020). Dataset resolution can affect demarcation of landslide boundaries in the subaqueous environment. Identifying small blocks or small flow structures from the landslide will be difficult to detect in lower spatial resolution bathymetric data (Masson *et al.*, 2002; Clare *et al.*, 2018). However, advancements and improvements in bathymetric sonar systems and implementation of autonomous underwater vehicles (AUVs) in recent decades has addressed this in part, allowing for data collection at a higher spatial resolution. Additionally, this is more likely an issue in the deep oceans. Fjords and lakes typically have shallower water depths, allowing for high spatial resolution data to be collected from higher frequency, boat-mounted MBES systems (Sammartini *et al.*, 2019).

2.4. Investigation of subaqueous landslide deposits

2.4.1. Methods of investigation

Compared to subaerial deposits, which can be more easily observed and their sedimentology studied more readily, direct observation and investigation of landslides in the subaqueous environment is more difficult (Piper *et al.*, 2012). Identification and investigation of subaqueous deposits traditionally relies on utilising hydroacoustic survey techniques such as MBES, SSS, and 2D and 3D SBP surveys (Figure 2.3). Additionally, cores may be taken from deposits to investigate sedimentology (Tripsanas *et al.*, 2008). Technological improvements in the hydroacoustic methods have improved in recent decades, allowing complete mapping, imaging and identification of deposits, both recent, and those in the geological record (Mountjoy and Micallef, 2018). MBES surveys can provide high-resolution, 3D bathymetric terrain models (BTMs) of the bed, whether lake, fjord, sea, or ocean (Tappin, 2010; Hughes Clarke, 2018). The horizontal and vertical resolution is often a function of the frequency of the system, and water depth (Tappin, 2010; Hughes Clarke, 2018). Shaded relief maps derived from MBES BTMs allow identification of deposits which may exhibit a positive bathymetric expression compared to the surrounding unaffected bed. Additionally, surface features may be identifiable and characterised on the MBES BTM (Mountjoy and Micallef, 2018). The surface roughness and morphology can allow for qualitative estimates on the relative age of the deposit based upon deposit "freshness", i.e. whether surface deposit features have been obscured or covered by post-event sediment drape (Blikra *et al.*, 2006). However, such estimates are highly subjective, and deposits in environments with low sedimentation rates may appear unobscured for several thousands of years. Recently, Strupler *et al.,* (2017) developed a method of

quantitatively estimating relative ages of past landslides (between 150-5000 years) by deriving the standard deviation of the bathymetric position index (BPI) of translational areas. A linear relationship was derived between BPI and previously independently dated landslide deposits (Strasser *et al.*, 2013). Whilst such methods appear promising, more work is needed to see whether it can be broadly applied to other lakes, particularly where known ages and/or sedimentation rates are unknown.

Backscatter intensity from SSS is an important tool that can aid in identifying deposits, particularly those that exhibit little to no visible bathymetric expression in a subaqueous environment. Backscatter from SSS is indicator of the reflectivity of the acoustic sonar signal by a material (Tappin, 2010; Klaucke, 2018). High backscatter values often indicate coarse sediments, or a hard substrate rock material, as the material does not absorb a lot of the sonar signal, thereby reflecting most of it back the receiver (Tappin, 2010; Klaucke, 2018; Strasser *et al.*, 2020). Conversely, typical hemipelagic sediments such as clays and silt are efficient at absorbing a lot of the signal, thereby producing low backscatter values (Tappin, 2010; Hilbe *et al.*, 2011). Backscatter data can be particularly useful where blocks are smaller than the spatial resolution of the MBES BTM. This data can aid in identifying any fine-grained sediment runouts from large landsliding events (Masson *et al.*, 2002; Coombs *et al.*, 2007; Watt, Talling, Vardy, Masson, *et al.*, 2012). Speckled backscatter, with areas of high backscatter interspersed by low backscatter areas results from blocks of avalanche material standing above hemipelagic sediments (Gee *et al.*, 2001; Watts and Masson, 2001). Backscatter levels can also be a qualitative estimation of relative ages of deposits since reflectivity is also related to the degree of sediment cover (Masson *et al.*, 2002).

Both MBES and SSS data only resolve the bed of the subaqueous environment, thus only resolving the surficial morphology of a landslide deposit. SBPs are required in order to understand the internal architecture of deposits (Watt *et al.*, 2014). Deposits within SBPs are often characterised as an acoustically chaotic-to-transparent facies, typically with a wedge-shaped geometry (Schnellmann *et al.*, 2002; Strasser *et al.*, 2006; Moernaut and De Batist, 2011; Daxer *et al.*, 2020). 3D data, or a dense grid of 2D SBP data, can resolve thicknesses of deposits that may be partially buried and cannot be fully resolved in MBES data. Various SBP methods include very high resolution (VHR) systems such as chirp, pinger, and boomer (Canals *et al.*, 2004; Mountjoy and Micallef, 2018). VHR systems typically use frequencies from several hundreds of Hz to a few kHz. Such systems can resolve subsurface information of tens up to c.100 m (dependent on bottom sediments), with theoretical vertical resolutions of tens of

centimetres to ≤ 3 m (Canals *et al.*, 2004; Sammartini *et al.*, 2019). High-resolution, deep penetrating (HRDP) systems include airgun and sparker systems. HRDP systems typically use frequencies of up to a few hundred Hz, penetrate hundreds of metres up to about 1 km, but vertical resolution can be tens of metres (Canals *et al.*, 2004). SBP data can also aid identifying deposits buried within the stratigraphic sequence.

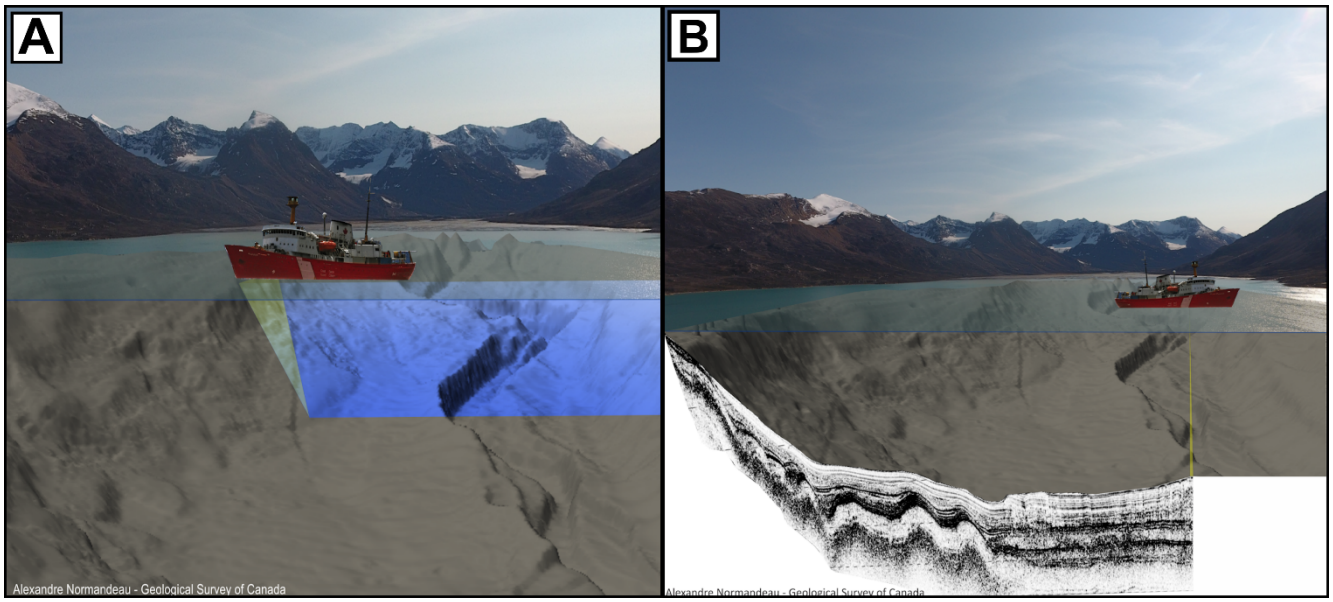

Figure 2.3. Schematic of methods used to identify subaqueous landslides including MBES and SSS surveys (A), and SBP surveys (B). Figure source and copyright Alexandre Normandeau licensed under a Creative Commons Attribution 4.0 International License. Figures available at https://sites.google.com/view/normandeau/outreach/methods-in-marine-geoscience

2.4.2. Geomorphology of subaqueous landslide deposits

The proliferation of landslide studies in both subaerial and subaqueous environments has aided in the identification of deposits through a detailed, comprehensive suite of diagnostic criteria. Landslide deposits can exhibit common geomorphological features, irrespective of deposit classification (Figure 2.4) (Bull *et al.*, 2009; Mountjoy and Micallef, 2018). Identifying and describing the features provides a first-order understanding of the dynamic behaviour of a landslide during emplacement as morphological features can be used as kinematic indicators (Bull *et al.*, 2009; Mountjoy and Micallef, 2018). Following classification of Bull *et al.,* (2009), a kinematic indicator is a feature that provides information related to the dynamics and behaviour of the landslide's motion during its emplacement.

Geomorphological analysis of subaqueous deposits ideally needs to utilise a combination of complimentary datasets, such as MBES or SSS, with SBP. Similar surficial features may have been formed by different processes (Hilbe and Anselmetti, 2014). Therefore, any interpretations based solely on surface morphology may misidentify and misinterpret the emplacement

dynamics of the deposit (Watt *et al.*, 2014). This highlights the need to reconcile the seismic geomorphology with surficial morphological analysis, where possible. Geomorphic analysis has traditionally involved qualitative subjective interpretations (Micallef, 2011). Qualitative interpretations have value, but are affected by the knowledge and experience of the analyst (Micallef, 2011). Interpretations may not be robust or reproducible between users. Geomorphometric analysis of deposits can provide quantitative measurements of deposits and associated features, reducing subjectivity (Micallef, 2011; Moscardelli and Wood, 2016). Morphometric parameters such as volume, drop height (H) and runout length (L) provide an empirical statistical index of a landslide's relative mobility (H/L or *fahrböschung* angle (= $\tan^{-1}\left(\frac{H}{L}\right)$) (Figure 2.5)) (Legros, 2002). The way in which such morphometrics are measured has varied between studies, therefore lacking consistency (Clare *et al.*, 2018). Recently, the implementation of a standardised approach has addressed the lack of consistency. This allows cross comparisons of deposits in different regions (Clare *et al.*, 2018). A combination of qualitative interpretations, and quantitative morphometric analysis, can provide robust analysis of deposits (Mountjoy and Micallef, 2018). Many of the most common deposit features are summarised in Figure 2.4. However, other surficial or seismic features, not evident in Figure 2.4, also provide key kinematic information of the landslide deposit. The features include the alignment of surface blocks, and perpendicular-to-flow pressure ridges.

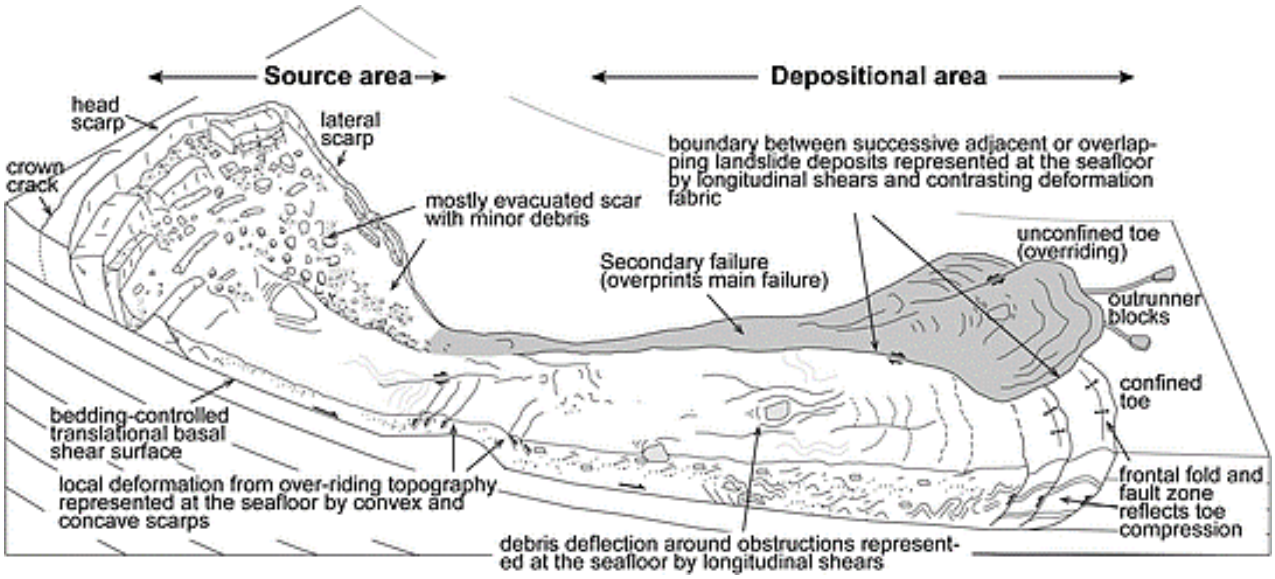

Figure 2.4. Cutaway schematic of common morphological features identified in subaqueous landslide deposits. Figure source: Mountjoy and Micallef (2018).

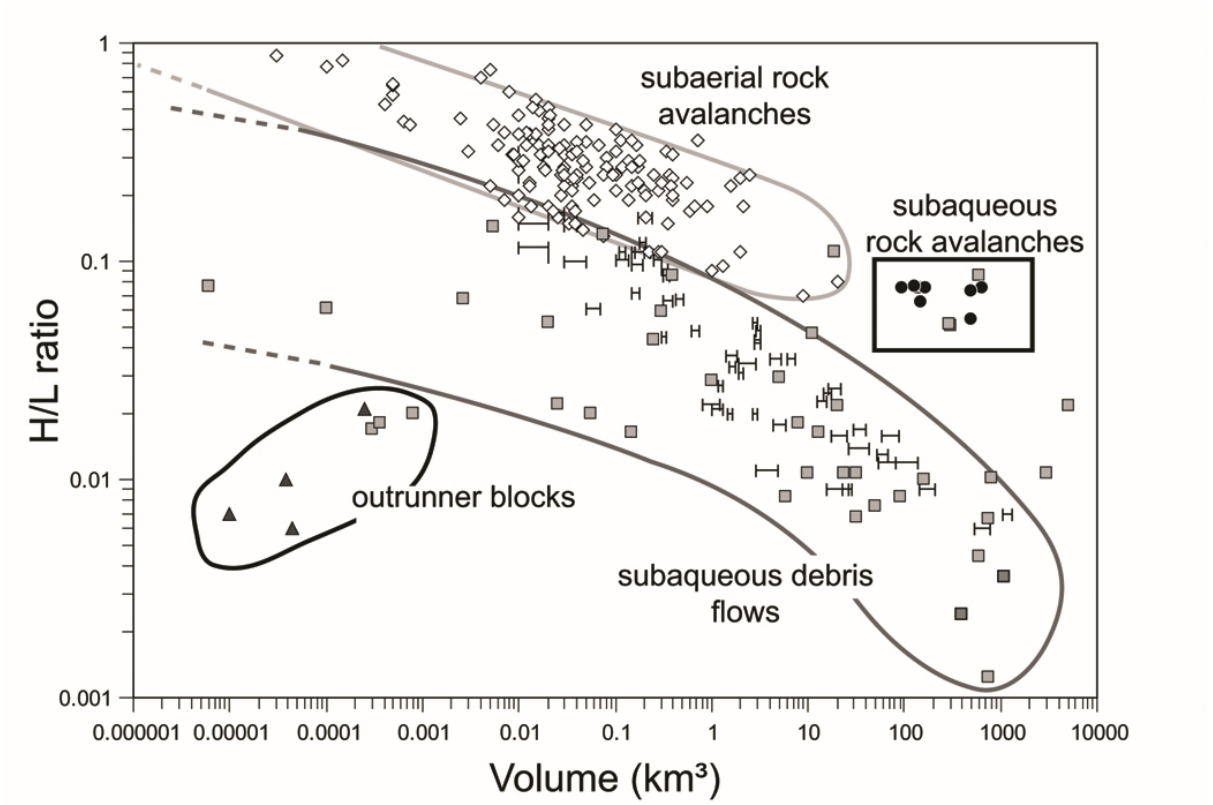

Figure 2.5. Bilogarithmic plot showing the H/L ratio (height fall of the landslide, H, and the horizontal runout, L) of subaerial and subaqueous landslide deposits against their volume. Debris flows are indicated by grey squares, subaerial rock avalanches are the empty diamonds, subaqueous rock avalanches are black circles and Outrunner blocks are denoted by black triangles. The segments (with the length indicating their uncertainty in the volume) are the debris flow lobes of the Storegga Slide. Figure sourced from De Blasio *et al*., (2006), and sources of data used in the figure are listed therein.

Blocks (or hummocks) are often detected on the surface of landslide deposits in MBES and SSS data, particularly those originating from STS, and subaqueous RSFs. The orientation of blocks provide insight into emplacement velocities (Dufresne and Davies, 2009). The blocks can exhibit elongation and orientation with the direction of flow (Figure 2.6 A, B) (Deplus *et al.*, 2001; Masson *et al.*, 2002; Watt, Talling, Vardy, Heller, *et al.*, 2012). Aligned blocks can indicate that the velocity in the direction of flow is greater than or equal to the perpendicular-to-flow velocities (Dufresne and Davies, 2009). In some deposits, subaqueous blocks have been identified as aligned perpendicular to the main flow direction (Dufresne *et al.*, 2018). However, Dufresne *et al.,* (2018) postulate that rapid sedimentation in the fjord as a result of a megaturbidite triggered by the landslide impacting the fjord bottom sediments obscures the interpretation of the blocks in the bathymetric dataset. The most distal blocks identified exhibit parallel alignment with the flow direction. Blocks may also be randomly distributed in a deposit and exhibit no alignment to the main flow direction. This occurs where velocities perpendicular

to flow are greater than the main flow direction (Figure 2.6 C, D) (Dufresne and Davies, 2009). Scattered blocks may be associated with free radial spreading and fan-shaped deposits (Masson *et al.*, 2002). The radial spreading can increase deposit surface area, lower the thickness, and contribute to a reduction or loss of excess pore pressures (Masson *et al.*, 2002; Watt *et al.*, 2014). The typical seismic characteristic of angular, blocky surface is a facies of diffraction hyperbolae (Figure 2.7 A) (Masson *et al.*, 2002; Bohannon and Gardner, 2004). Similar facies have been exhibited in both terrestrial geophysical surveys of subaerial RSFs (Dunning *et al.*, 2015). Typically, no subsequent facies or reflectors can be resolved beneath the hyperbolae in VHR systems as acoustic energy is blocked (Longva *et al.*, 2009). HRDP systems that penetrate through the deposit often note an acoustically chaotic facies (Deplus *et al.*, 2001).

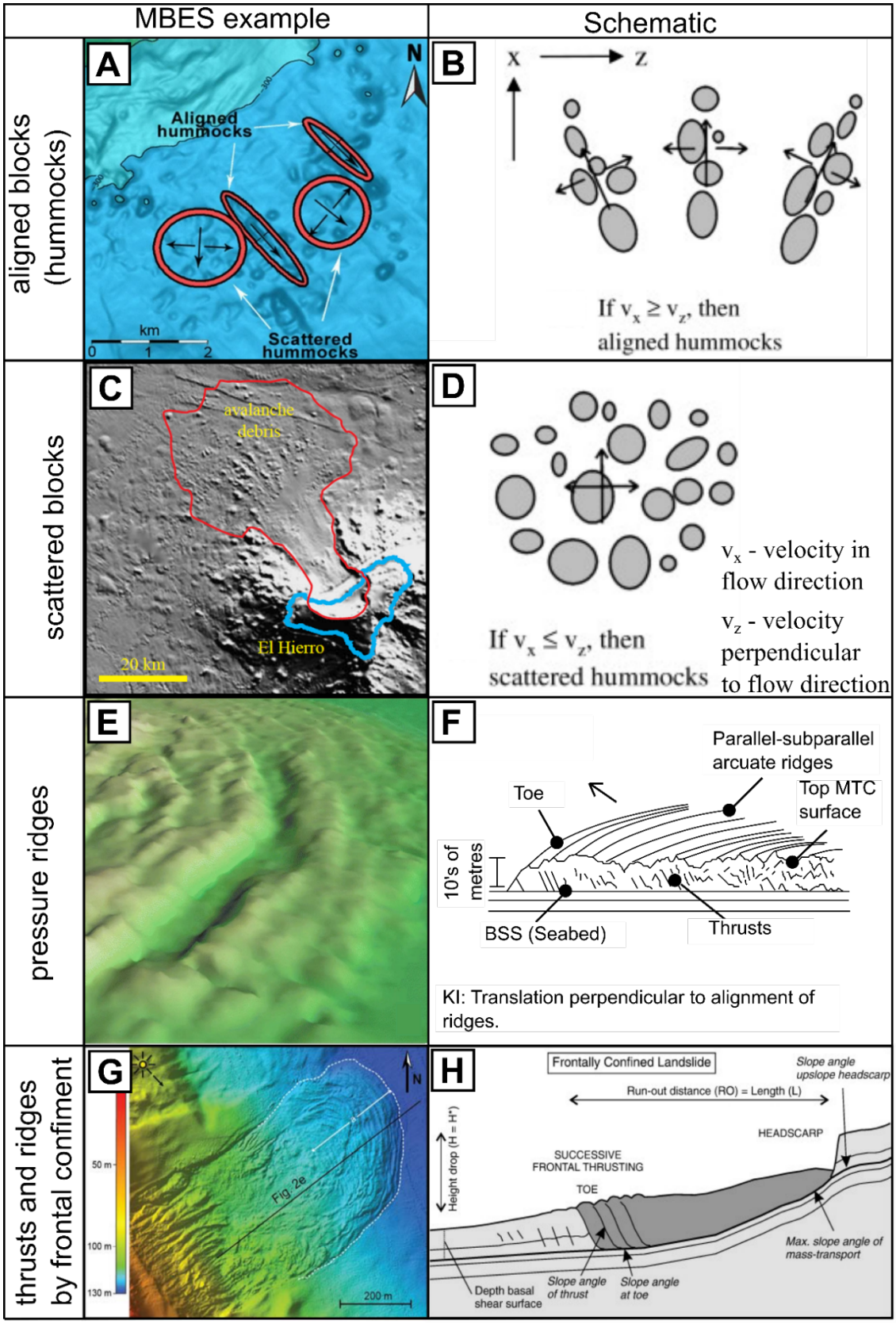

Figure 2.6. MBES data, and schematics of morphological features of subaqueous landslide deposits. BSS – Basal Shear Surface; KI – Kinematic Indicator. Figure sources: A – Livanos *et al.,* (2013); B and D - adapted from Dufresne and Davies (2009); C – Masson *et al.,* (2006); E – Hughes *et al.,* (2020); F – Bull *et al.,* (2009); G – Sammartini *et al.,* (2019); H – Moernaut and De Batist (Moernaut and De Batist, 2011).

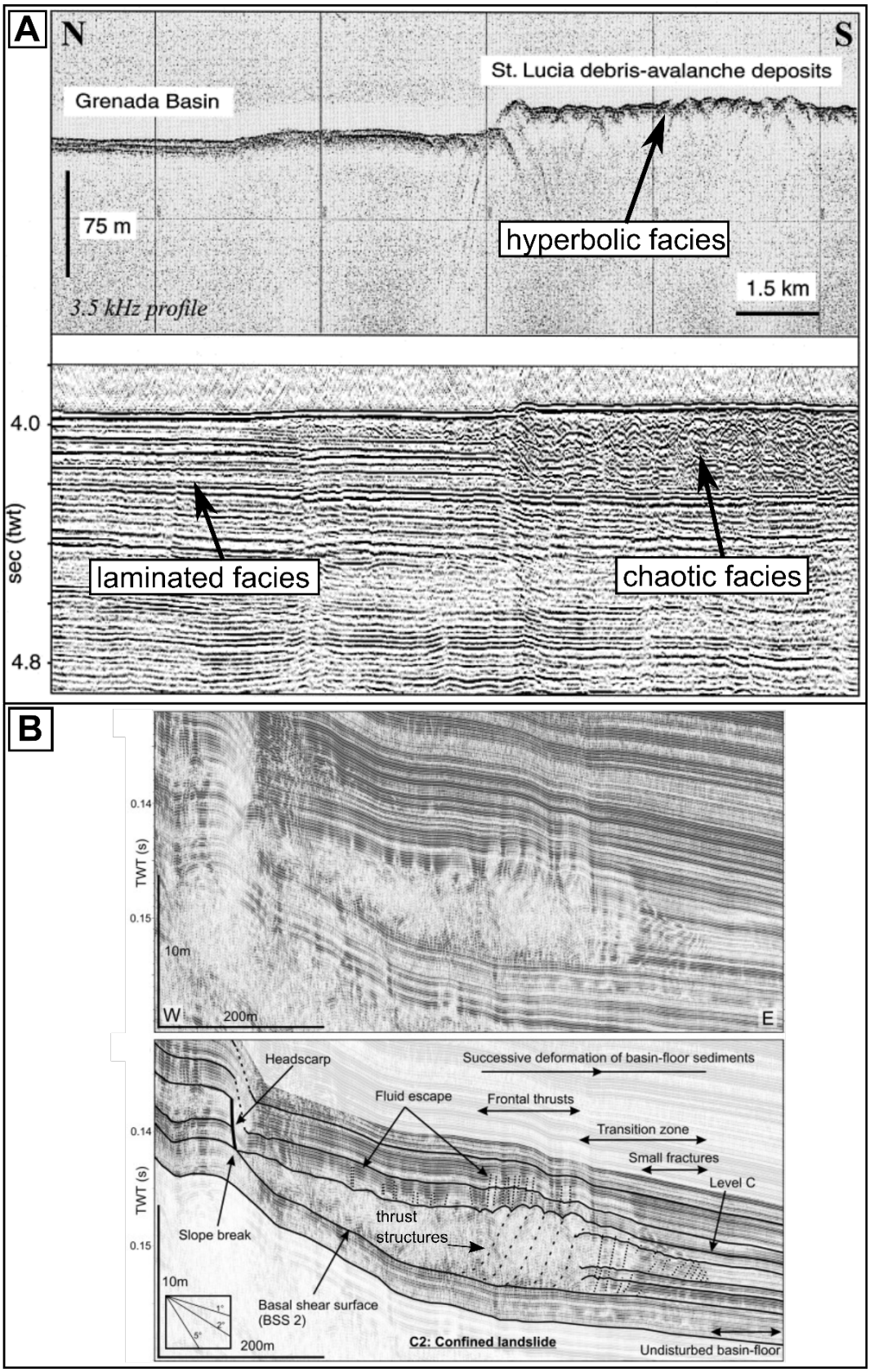

Figure 2.7. SBP characteristics of blocky surface (A), characterised as hyperbolae facies in 3.5 kHz (top line of panel A), and chaotic facies in airgun profile (lower line of panel A). SBP data of frontally confined thrusts (B) in landslide deposits. Panel A source: Deplus et al., (2001). Panel B source: Moernaut and De Batist (Moernaut and De Batist, 2011).

Pressure ridges may also be an identifiable feature at the toe of deposits (Figure 2.6 E, F). Pressure ridges are compressional, linear to arcuate parallel ridges up to several metres high. Such features are identifiable primarily on MBES datasets, but may also be detected in SBP data (Bull *et al.*, 2009). The ridges are useful as a kinematic indicator as they are typically orientated perpendicular to the flow direction, therefore providing directional information of deposit runout (Frey-Martínez *et al.*, 2006; Bull *et al.*, 2009; Dufresne and Davies, 2009). The features typically a result of deceleration of the landslide moving front (Bull *et al.*, 2009; Dufresne and Davies, 2009). The deceleration of the landslide might result due to a change in the underlying, or surrounding medium (Dufresne and Davies, 2009). Examples include propagation and flow from a subaerial environment into a water body (Siebert, 2002); runout over soft, deformable substrates (Shea and van Wyk de Vries, 2008; Shea *et al.*, 2008); or abrupt changes in topographic gradient (Strom, 2006). However, similar compressional ridges have been identified on deposit surfaces that are related to frontal confinement of the deposit buttressed within undisturbed substrate (Figure 2.6 G, H) (Frey-Martínez *et al.*, 2006; Moernaut and De Batist, 2011). The buttressing may cause compression and thrusts within the deposit, creating either single or a series of raised frontal bulges (Frey-Martínez *et al.*, 2006). On bathymetric data, deciphering between pressure ridges or bulges created by frontal confinement is difficult. Thrust features may be identifiable within the deposit facies on SBP data (Figure 2.7 B). Tracing the deposit facies can indicate whether a deposit has been able to ramp up from the basal shear surface (Frey-Martínez *et al.*, 2006; Bull *et al.*, 2009; Moernaut and De Batist, 2011).

Whilst not explicitly a feature of a landslide deposit, deformation of the hemipelagic/lacustrine sediments, and/or irregularities in the acoustic lamination can point to evidence of landslide impacts (Schnellmann *et al.*, 2005; Mazzanti and De Blasio, 2010; Van Daele *et al.*, 2013). Propagation and loading of the landslide deposit in the subaqueous environment can cause deformation of typically soft, saturated, basin-plain sediments on the basin floor (Schnellmann *et al.*, 2005; Van Daele *et al.*, 2013). The deformed basin sediments contrast from the regular, horizontal, laterally continuous stratified facies typically associated with background hemipelagic sedimentation (Gee *et al.*, 2001; Masson *et al.*, 2002; Longva *et al.*, 2009). The deformation of basin plain sediments may create singular, or successive, topographic concentric rings exhibit positive bathymetric expression (Figure 2.8) (Blikra *et al.*, 2006; Mazzanti and De Blasio, 2010; Hilbe *et al.*, 2011). The features are similar in bathymetric expression to compressional pressure ridges identified within landslide deposits (Figure 2.6, Figure 2.7).

However, such features are formed of the basin sediments and not landslide deposit material. Other features of landslide impact and deformation that have been identified include overdeepened depression in the proximal regions (Van Daele *et al.*, 2013; Daxer *et al.*, 2020). Many landslide deposits, particularly those originating as STS RSFs, are characterised as conical wedge of blocky deposits in the proximal region, with seismic characteristics of chaotic facies and hummocky upper surface (Blikra *et al.*, 2006; Bornhold *et al.*, 2007; Bozzano *et al.*, 2009; Longva *et al.*, 2009). The deformation of basin sediments is often evident in the distal regions.

The degree of deformation has been found dependant on drop height, basin slope angle, and whether the impact occurs from subaerial and subaqueous originating landslides (Schnellmann *et al.*, 2005; Van Daele *et al.*, 2013; Daxer *et al.*, 2020). Larger drop heights and steeper slope angles facilitate higher impact velocities of a landslide, allowing a higher energy transfer into the basin sediments (Van Daele *et al.*, 2013). The most pronounced basin-plain deformations (Type 3 and 4 (Van Daele *et al.*, 2013)) occur primarily from impact of STS deposits onto the basin floor (Van Daele *et al.*, 2013; Daxer *et al.*, 2020). This may be a result of a greater density of the landslide material (typically bedrock), as well as larger drop height, and potentially greater velocity ascertained in the subaerial environment before subaqueous propagation (Schnellmann *et al.*, 2005; Van Daele *et al.*, 2013; Daxer *et al.*, 2020). However, deformed basin sediments are not identifiable in every basin where deposits are evident. Whether this is due to burial of such features, dynamics of the landslide during emplacement, or geotechnical properties of the basin sediment is unknown.

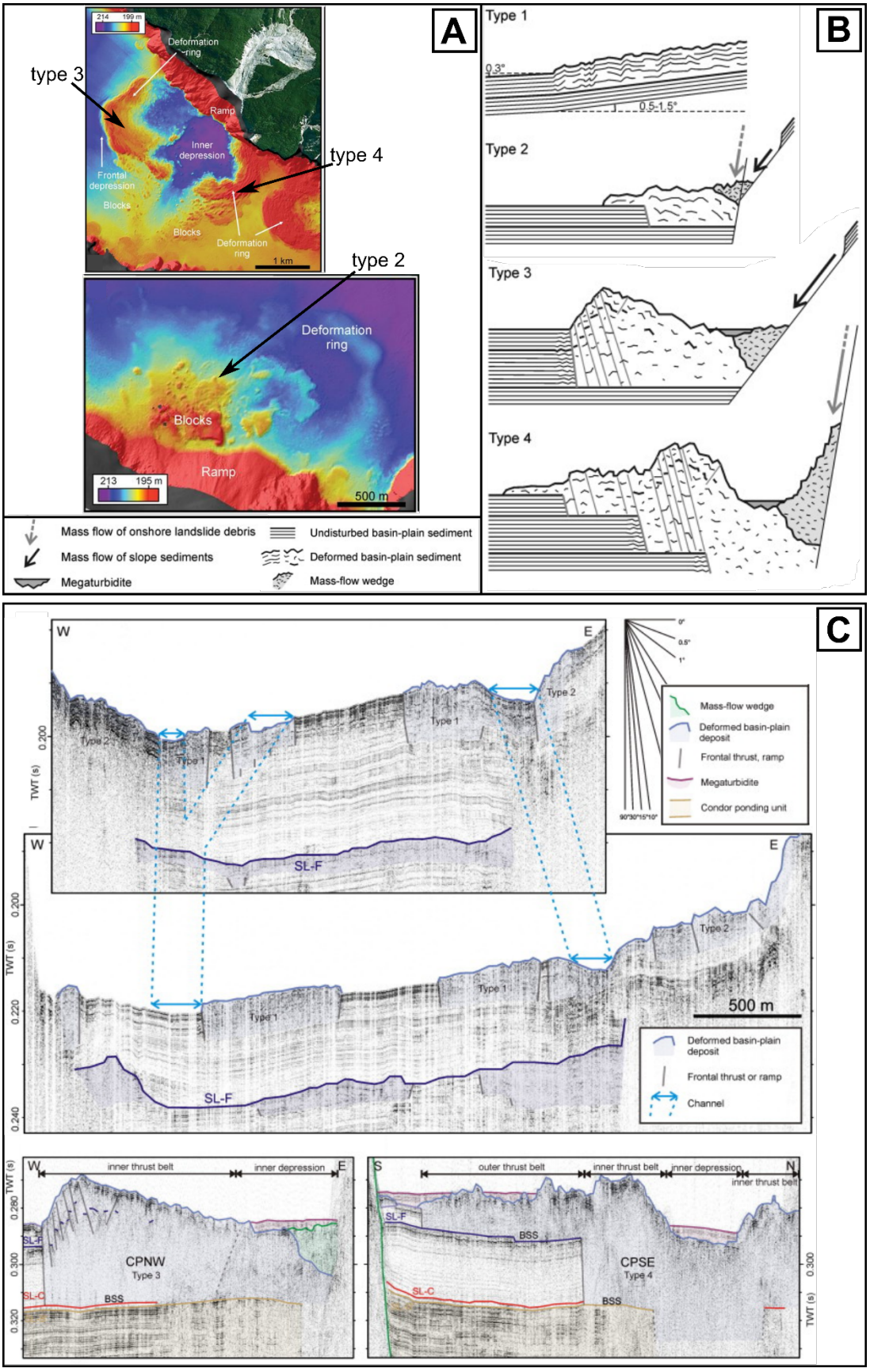

Figure 2.8. Bathymetric (A), SBP characteristics (C), and schematic (B) of deformed basin plain sediment deposits. Classification refers to the classification of Van Daele *et al.,* (2013). Panel A source: Lastras *et al.,* (2016), Panel B and C source: Van Daele *et al.,* (2013).

2.5. Landslide flow dynamics and runout mechanisms

The flow behaviour of subaerial and subaqueous landslides is complex as landslides occur across a continuum where different materials are involved in the failure and runout. Much of this is beyond the scope of this thesis. This section instead provides background to mobility of landslides, particularly granular flows (e.g. rock avalanches) as these landslides are within the scope of the work later within the thesis (*Chapter 4*). Background to cohesive wet mixture flows (e.g. debris flows) is also given as these landslides appear common in subaqueous environments, and rock avalanches can transform into debris flows in subaerial (Iverson, 1997) and subaqueous (Masson *et al.*, 2002) environments. This section also provides some of the theories controlling landslide mobility and runout. Mobility of landslides, particularly flow-like landslides such as rock avalanches and debris flows, is often quantified by their apparent coefficient of friction (H/L, H/L_{max}), or their *Fahrböschung* angle ($tan^{-1}\left(\frac{H}{Lmax}\right)$), as mentioned above (section 2.4.2). This metric has been applied to flow-like landslides in subaerial, subaqueous, and extra-terrestrial environments (Legros, 2002).

Rock avalanches are rapid, flow-like landslides, and their flow behaviour is analogous to granular flow rheology, governed by Coulomb friction laws (Legros, 2002; Davies and McSaveney, 2009). In the Coulomb frictional law, motion in a purely dry granular flow is resisted by a frictional force. The frictional force should be approximate to the internal friction angle between the grains of fragmented rock (~35˚-40˚) (Legros, 2002). Therefore, Coulomb friction laws would indicate that in a dry granular flow (independent of landslide volume), the H/L value should be ~0.6 (tan^{-1} (30˚)) (Legros, 2002). However, a common characteristic of rock avalanches in the natural environment is they exhibit exceptional mobility (H/L<0.6) (Davies and McSaveney, 1999, 2012; Legros, 2002; Aaron and McDougall, 2019). Therefore, the assumption rock avalanches follow Coulomb friction laws appears incorrect, rock avalanches are not purely dry granular flows, or that some other factor(s) are reducing frictional forces in the flowing mass.

Subaqueous landslides along slopes often involve failure of cohesive, saturated sediments, except in the instances of margin collapses that can often involve failure and mobilisation of bedrock material (p.14). Subaqueous landslides that behave as slides (such as those initiated on lateral slopes) initiate along a basal shear surface/weak layer, which runs parallel to the slope, and slide along this plane, or as a rotational slide. The slide may deform and transform into a debris flow landslide as a result of Coulomb friction failure within the mass, liquefaction by

high pore fluid pressures, and transformation of sliding energy into internal energy within the landslide mass (Iverson, 1997; Piper *et al.*, 2012). In subaerial and subaqueous environments, debris flow landslides exhibit high mobility and behave as a non-Newtonian Bingham flow rheology (Piper *et al.*, 2012). However, landslides that runout into, or within, subaqueous environments are rarely observed. Therefore the dynamic behaviour of these events are poorly known (Piper *et al.*, 2012; De Blasio, 2013). Information relating to their dynamics has come from analysis of their internal seismic architecture (Bull *et al.*, 2009), internal sedimentology retrieved by cores (Tripsanas *et al.*, 2008), comparison of their morphologies to subaerial equivalents (Mulder and Cochonant, 1996; Locat and Lee, 2002), and physical (Mohrig *et al.*, 1998) and/or numerical modelling. The identification of self-similar deposits and resultant morphologies in both subaerial and subaqueous environments suggests that similar mechanisms and processes control the flow behaviour and runout in both air and water (Davies and McSaveney, 2012; Piper *et al.*, 2012).

2.5.1. Factors controlling landslide mobility and runout

Increased runout and mobility of subaerial and subaqueous landslides has often been linked to increasing deposit volume (Scheidegger, 1973). However, significant scatter exists in the data of H/L vs. volume (Figure 2.5), suggesting volume alone cannot account for the mobility of landslides (Davies and McSaveney, 2012; Aaron and McDougall, 2019). The role of topography leading to geomorphic confinement is also important in the mobility of landslides (Nicoletti and Sorriso-Valvo, 1991; Corominas, 1996; Strom *et al.*, 2019). However topography alone cannot explain the variations in runout. Other mechanisms must therefore contribute to the runout behaviour and mobility of landslides. Mechanisms involve either a reduction in basal and/or internal friction of the landslide mass that cause subaerial and subaqueous landslides to run out further than expected (Imre *et al.*, 2010). Subaqueous landslides in general are highly mobile, and in some cases an order of magnitude greater than subaerial landslides (Figure 2.5) (De Blasio *et al.*, 2006), yet subaqueous landslides have diminished effective gravity in water due to buoyancy effects, and water provides a much greater turbulent drag resistance than in air which reduces the overall landslide velocity (De Blasio *et al.*, 2006; De Blasio, 2011; Davies and McSaveney, 2012).

Many theories are suggested for the mobility of long runout landslides and have hypothesised mechanisms intrinsic to the flowing landslide. Such theories include air lubrication (Shreve, 1968), mechanical fluidisation (Davies, 1982), acoustic fluidisation (Melosh, 1979; Collins and Melosh, 2003), dynamic fragmentation (Davies *et al.*, 1999; Davies and McSaveney, 2009;

Bowman *et al.*, 2012), frictional heating and melting (Goren and Aharonov, 2007; Lucas *et al.*, 2014; Hu *et al.*, 2019), and the presence of interstitial fluid that reduces grain to grain friction, partially reducing the granular stress within the flow (Crosta *et al.*, 2009). The identification of similar deposits in the subaqueous water saturated environment means air lubrication is not such a universal mechanism. Whilst some deposits may contain interstitial fluids in the subaqueous environment with the material being water-saturated, and the presence of ice in some rock slope failures in the subaerial environment, long runout landslides have occurred in arid (Strom *et al.*, 2019) and extra-terrestrial (Crosta *et al.*, 2018) environments.

Dynamic fragmentation processes appear to explain the mobility of flow-like RSFs landslides (rock avalanches) in both subaerial and subaqueous environments (Davies and McSaveney, 2009, 2012). Dynamic fragmentation can simultaneously aid in explaining the sedimentology and grain size distribution of some rock avalanche deposits (Dufresne and Dunning, 2017). In dynamic fragmentation, the rock masses disintegrate along failure planes, and pre-existing joints, behaving similar to a granular flow (Davies and McSaveney, 2009). The process of fragmentation of grains creates new surfaces on which new failures can occur. Each grain fragmentation and radiates and redistributes energy in the flow, creating high effective stress in the flow, whilst simultaneously support the overburden material, and a basal isotropic dispersive pressure, leading to a reduced frictional resistance to shear at the base of the flow (Davies and McSaveney, 2009; Bowman *et al.*, 2012; Rait *et al.*, 2012).

In the subaqueous environment, the presence of jigsaw clasts have been found in cores from subaqueous RA deposits (Tripsanas *et al.*, 2008). Large (10^2 – 10^3 m in diameter), angular, individual blocks identified in the deposit morphology of subaqueous RAs represent intact fragments of the failed slopes and are generally larger in subaqueous RADs compared to subaerial ones (Watt *et al.*, 2014). This suggests that whilst dynamic fragmentation of flow-like RSFs, such as rock avalanches, may be evident in the subaqueous environment, its effect is somewhat minimised compared to the terrestrial environment. This is possibly an indication of a reduction or dampening of the internal fragmentation of the deposit material in the subaqueous setting (Mazzanti and De Blasio, 2013; Watt *et al.*, 2014). Crushing and internal disintegration of the deposit is likely to have been reduced due to presence of a drag force in the subaqueous environment, which is affected by the rock avalanche velocity and travel path roughness (Mazzanti and De Blasio, 2013). Both these parameters are lower in the subaqueous environment due to a lower density contrast between the rock avalanche material and the surrounding water which reduces the energy of internal collisions (Mazzanti and De Blasio,

2013; Watt *et al.*, 2014). The reduced fragmentation leads to a lower percentage of fine matrix material, making the deposit more permeable than subaqueous debris flows. The higher permeability reduces the efficacy of the hydroplaning effect that has been observed in experiments of subaqueous debris flows (De Blasio *et al.*, 2006), and increases the basal friction coefficient (Mazzanti and De Blasio, 2013).

The interaction of the substrate and path material (Hungr and Evans, 2004; Sassa and Wang, 2005; Dufresne *et al.*, 2009; Voight *et al.*, 2012; Aaron and McDougall, 2019) can affect basal friction. Basal lubrication by rapid undrained loading over water saturated sediments (Legros, 2002; Hungr and Evans, 2004; Sassa and Wang, 2005) can reduce basal friction of the moving mass whilst also entraining water saturated material, that lowers internal friction (Hungr and Evans, 2004). This could alter the rheology of a granular flow into a debris flow (Iverson, 1997; McArdell *et al.*, 2007). This would suggest that landslides in subaqueous environments would entrain water saturated material and evolve its rheology into a non-Newtonian debris flow-like landslide, irrespective of the whether the initial landslide began as a wet granular flow-like landslide (e.g. subaqueous rock avalanche). However, the identification of rock avalanches in the subaqueous environment suggests that this does not always happen (Legros, 2002). Therefore, basal lubrication may not be a universal mechanism for long runout landslide mobility. In the subaqueous environments, additional mechanisms such as basal substrate emergence or confinement, as mentioned previously (Figure 2.8) (Frey-Martínez *et al.*, 2006; Moernaut and De Batist, 2011; Van Daele *et al.*, 2013), and hydroplaning (Mohrig *et al.*, 1998) are believed to contribute to mobility and flow dynamics.

Hydroplaning has been suggested as a mechanism that facilitates the exceptionally long runouts of subaqueous landslides, particularly cohesive material landslides such as debris flows (Figure 2.5) (Mohrig *et al.*, 1998; De Blasio *et al.*, 2004, 2006). Hydroplaning occurs when a cohesive mass exceeds a critical velocity that prevents the ambient fluid being displaced fast enough (Mohrig *et al.*, 1998; Elverhøi *et al.*, 2002; De Blasio *et al.*, 2004, 2006). Therefore, the head of the moving deposit is lifted, allowing water to intrude below the mass, acting as a lubricant and reducing basal friction (Elverhøi *et al.*, 2002; De Blasio, 2013). Elevated pore pressures of fine-grained material within deposits allows the development of elevated internal pore pressures, and reduces permeability of the landslide deposit (Iverson, 1997; Masson *et al.*, 2002; Watt *et al.*, 2014) The higher pore pressures help reduce frictional resistance. This enhances mobility by facilitating hydroplaning, which can further enhance the mobility of the landslide (De Blasio *et al.*, 2004; De Blasio, 2013; Mazzanti and De Blasio, 2013). Hydroplaning results

in reduced basal shear resistance and can flow until the deposit reaches a critical velocity and begins to slow down and stop (De Blasio, 2013).

Hydroplaning may be able to account for the high mobility of subaqueous cohesive-like debris flows (Mohrig *et al.*, 1998; De Blasio *et al.*, 2004). For subaqueous granular landslides (e.g. rock avalanches) however, their resultant mobility follows a similar linear trend as the entirely subaerial deposits (Figure 2.5), suggesting that hydroplaning is not a prominent process in their mobility. The porous nature of granular flows can result in percolation of water, preventing water intruding below the landslide mass (De Blasio, 2013; Mazzanti and De Blasio, 2013). STS landslides such as rock avalanches provide additional complications as they propagate from one medium (i.e. air) to another (water) and therefore percolation by water will occur during landslide runout. However, hydroplaning has not been directly observed in subaqueous environments, only during physical modelling, so the real-world applicability remains uncertain.

2.6. Conclusion

The literature review has highlighted that landslide deposits of varying types and morphologies are prevalent within lakes and fjords across the globe. Whilst censoring processes in the subaqueous environment can affect their preservation potential, deposits in lakes and fjords may be better preserved than deposits in the subaerial environment. Therefore, lakes and fjords can present an archive of previously unknown landslide deposits, identifiable through the collection of high-resolution hydroacoustic and sub-bottom survey data. The understanding of subaqueous landslides has greatly advanced due to technological advances, allowing for the collection of high resolution hydroacoustic (MBES and SBP) data. However, in regions of the globe where such datasets are limited, the landslide (and associated) hazard remain largely unquantified. For landslide hazard assessments, and magnitude-frequency of past events, establishing an inventory of subaqueous deposits is necessary. Collection and analysis of multiple lake and/or fjord datasets can allow inter-basin comparisons. These comparisons could aid in understanding possible regional triggering mechanisms, such as earthquakes, if landslides occurred concurrently in different basins.

Furthermore, landslides into, and within lakes and fjords are rarely observed. This means understanding landslide runout and emplacement dynamics is contingent on identification and analysis of deposits in MBES and SBP datasets. Analysis of the deposit morphology can provide insight into the emplacement dynamics of the landslide. However, interpretations can

be subjective so there is a need to integrate with standardised morphometric analyses. Numerically modelling past landslides can also aid in understanding their complex behaviour during runout where direct monitoring and observations are lacking. Whilst numerical models can also provide some insight to the assumed rheology of a landslide, the efficacy of the rheologies chosen usually requires well-constrained events for back analysis, coupled with in-situ field investigations of the sediment properties. In subaqueous environments, such information is largely lacking. Deposits identified in either bathymetric or seismic reflection data represent an end-member product of a dynamic and evolving landslide runout process. In modelling subaqueous landslides, the results can provide time step information on landslide frontal geometry, flow thicknesses, and velocity. These parameters are necessary to understand the emplacement dynamics of the landslide. The parameters can be used as inputs to estimate possible past landslide-generated tsunamis that may have occurred in such environments. Runout modelling of STS RSFs, however, has received comparatively less attention than entirely subaerial and entirely subaqueous events due to the additional need for bathymetric data, and complexities of integrating the subaerial and subaqueous components of motion and transition between mediums (air to water). This thesis aims to address these gaps, with a focus on New Zealand, where the landslide hazard in the lakes and fjords is largely unknown, and unquantified (*Chapter 3*).

Chapter 3. Overview to the study area: South Island, New Zealand; and current understanding into the distribution of subaerial and subaqueous landslides

3.1. Introduction

New Zealand is an island archipelago located in the south-western margin of the Pacific Ocean. New Zealand provides a natural laboratory to investigate subaqueous landslide deposits in lacustrine and fjord environments. This is due to its physiographic and tectonic setting, Pleistocene glacial history, high number of lakes and fjords, extensive knowledge on the spatial distribution of subaerial deposits, and rapidly expanding knowledge of offshore subaqueous deposit distributions. This chapter provides a broad overview to these background processes across New Zealand, but with a particular focus on Te Waipounamu/South Island. Specific background literature reviews relating to the two study areas, Milford Sound/Piopiotahi and Lake Wānaka, are contained within their respective chapters (*Chapter 4* and *Chapter 5*).

This chapter also presents the current knowledge on the distribution of subaqueous landslide deposits in lakes and fjords across New Zealand, which is largely unknown, and unquantified. To date, no inventory has compiled or analysed the distribution of landslide deposits across the lakes and fjords of New Zealand. Therefore in this chapter, a new literature-based inventory of all known lakes and fjords containing subaqueous landslide deposits is also presented. This inventory details the physiographic setting of the lakes and fjords, the type of known landslide and associate deposit(s), identification method(s), and triggering mechanism, where known. Such information is important for understanding the control mechanisms of landslides in New Zealand, which have implications for the landslide and associate geohazards.

3.2. Tectonic setting

New Zealand is a seismically active country owing to its geographic position along the boundary of the Australian and Pacific plates. Rates of movement along the plates vary between 48-39 mm yr^{-1} (Norris and Cooper, 2001; Wallace *et al.*, 2007). The plate boundary is marked by two offshore subduction zones, and a central onshore fault boundary. The west dipping Hikurangi Subduction Zone in the offshore eastern margin of the North Island marks the northern margin of the boundary (Figure 3.1). The east-dipping Puysegur Subduction Zone south-west of the South Island, marks the southern margin (Norris and Cooper, 2001; Robinson and Davies, 2013). The Alpine Fault marks the onshore boundary between the two plates in the

South Island (Norris and Cooper, 2001, 2007; Wallace *et al.*, 2007). The Alpine Fault is a transform structure that connects the opposite dipping Hikurangi and Puysegur Subduction Zones (Norris and Cooper, 2001, 2007; Howarth *et al.*, 2018). The fault is an active dextral strike-slip fault with a c.600 km long onshore expression (Norris and Cooper, 2001; Robinson and Davies, 2013). The fault is segmented which accommodates varying rates of horizontal and vertical slip rates (Figure 3.2A) (Howarth *et al.*, 2018). The most recent long-term estimates of strike-slip rate across the central section over c.270 kyr are 29.6 (+2.5/-4.5) mm yr^{-1} (Barth *et al.*, 2014). The slip rates are slightly higher than 23 ± 2 mm yr^{-1} proposed by Sutherland *et al*., (2006), but are comparably similar to the average strike slip rate (~28 mm yr^{-1}) estimated by Norris and Cooper (2001). Assuming a 29.6 (+2.5/-4.5) mm yr^{-1} in the central section, the fault accommodates 81% of plate motion (Barth *et al.*, 2014). Slip rates decrease rapidly north of the central section, but increase propagating southward to the offshore segment (Norris and Cooper, 2001; Barnes, 2009; Barth *et al.*, 2014; Howarth *et al.*, 2018). Uplift/dip-slip rates also vary along the fault, with ~ 0 mm yr^{-1} at the south-western end, whilst in the central section of the fault, values range from 7.8 ± 1 mm yr^{-1} - > 12 mm yr^{-1} (Norris and Cooper, 2001). New Zealand is in long-term tectonic dynamic equilibrium and therefore rates of uplift are matched by denudation rates (Adams, 1980).

Palaeoseismic studies indicate that the Alpine Fault is capable of producing large (M_w>7) or great (M_w>8) earthquakes (Sutherland *et al.*, 2007). Twenty seven ruptures along the fault have been identified and dated over the last 8000 years (Berryman, Cochran, *et al.*, 2012; Berryman, Cooper, *et al.*, 2012; Howarth *et al.*, 2012, 2014, 2016, 2018; Cochran *et al.*, 2017). The dates show quasi-periodic ruptures every 250-330 years (Berryman, Cochran, *et al.*, 2012; Berryman, Cooper, *et al.*, 2012). Recent studies calculate the mean recurrence intervals of 291 ± 23 years (1 standard error (SE)) (Cochran *et al.*, 2017), 263 ± 63 years (1SE) (Howarth *et al.*, 2018), and 249± 63 years (1SE) (Howarth *et al.*, 2021). The last earthquake along the fault occurred in 1717 AD (De Pascale and Langridge, 2012). Therefore, the time since the last rupture has exceeded the mean recurrence interval (Cochran *et al.*, 2017; Howarth *et al.*, 2018). There is an estimated 75% probability that an earthquake will occur along the fault in the next 50 years (Howarth *et al.*, 2021), significantly higher than previous estimates of 27% (Biasi *et al.*, 2015) and 29% (Cochran *et al.*, 2017). Due to the fault's geologically short and regular recurrence period, and potential to generate M_w>8 earthquakes, the Alpine Fault represents the greatest seismic hazard to New Zealand's South Island (Sutherland *et al.*, 2007; Berryman, Cochran, *et al.*, 2012; Stirling *et al.*, 2012; Orchiston *et al.*, 2018).

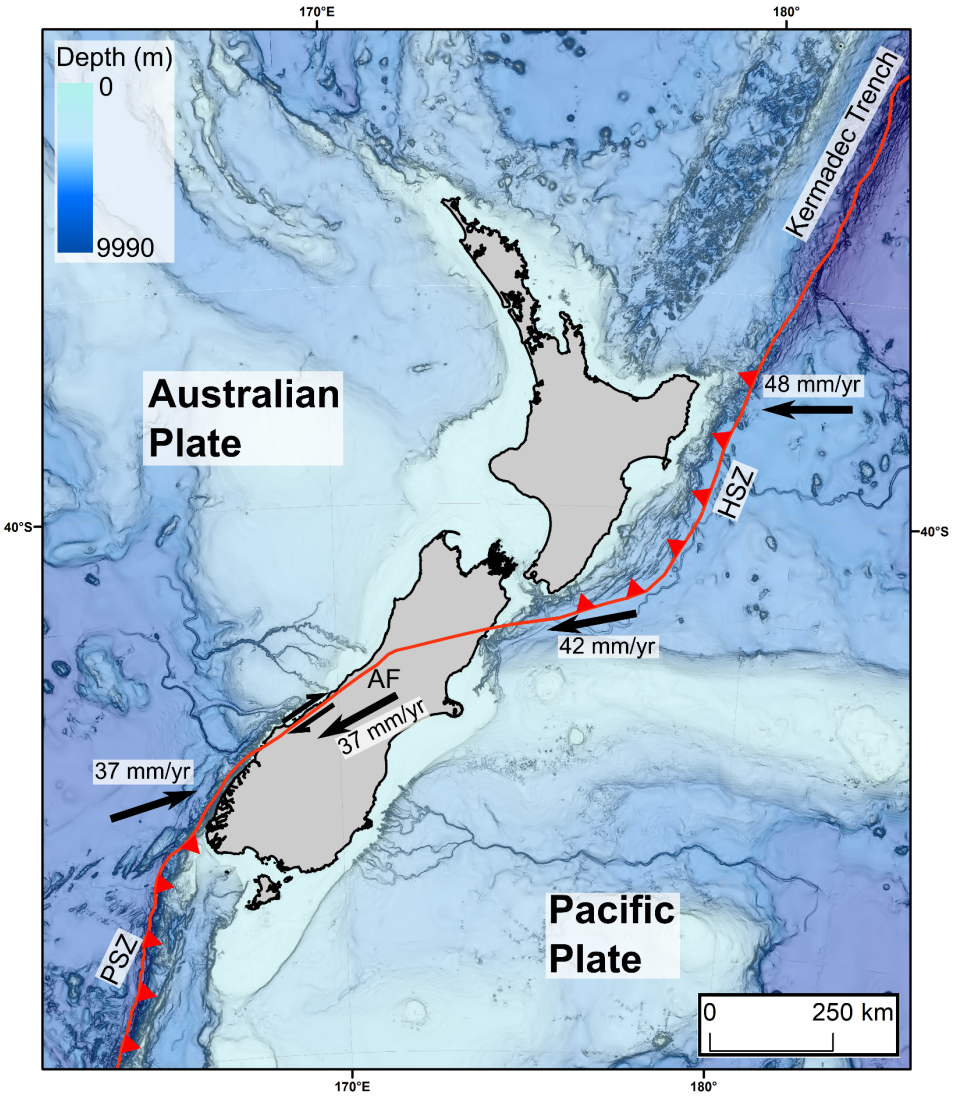

Figure 3.1. Tectonic setting of New Zealand within the Australian and Pacific Plate boundaries. HSZ- Hikurangi Subduction Zone, PSZ – Puysegur Subduction Zone, AF- Alpine Fault. Plate motion rates from Wallace *et al.,* (2007, 2012). Plate boundary vectors from https://github.com/fraxen/tectonicplates, courtesy of Hugo Ahlenius, Nordpil, and Peter Bird, available under Creative Commons License 1.0. Offshore bathymetry data is sourced from NIWA and licensed under the NIWA Open Data Licence v1.0. Data is available at: https://niwa.co.nz/our-science/oceans/bathymetry.

Modelling of a M_w 8.0 earthquake on the fault is estimated to trigger 30,000 - 70,000 subaerial coseismic landslides, predominately across the Southern Alps (Robinson *et al.*, 2016). The earthquake and coseismic landslide models assume a south-western hypocentre for the earthquake, north-east trending rupture directivity, and the resultant MM are based on this scenario. The exact hypocentre location and rupture directivity will affect the overall MM (Bradley *et al.*, 2017), and subsequent number of coseismic landslides. However, the model scenario does not consider coseismically generated subaqueous landslides. Predicted shaking intensities of a future M_w 8.0 Alpine Fault rupture indicates shaking intensities of MM 5-6 around most of the lakes and fjords in the South Island, dependant on the earthquake hypocentre

(Figure 3.3) (Bradley *et al.*, 2017). Therefore, shaking intensities may be sufficient to generate subaqueous failures (Howarth *et al.*, 2014).

Beyond the Alpine Fault, there are > 600 active faults that have been traced across the South Island (Litchfield *et al.*, 2014; Langridge *et al.*, 2016) (Figure 3.1). Potentially many other active faults exist that are capable of producing large (M_w>7) earthquakes (Cox *et al.*, 2012; Langridge *et al.*, 2016; Barrell, 2019). Currently, the faults have not been traced as they may extend under water bodies, where the subaqueous expression is not identifiable without hydroacoustic or seismic reflection data (Langridge *et al.*, 2016). The faults may also have long recurrence intervals as a result of low long term displacement rates (Litchfield *et al.*, 2014) which lack geomorphic expression due to rapid rates of erosion, particularly in the Central Southern Alps (Cox *et al.*, 2012).

3.3. Glacial setting

New Zealand is only one of three mid-latitude Southern Hemisphere regions (along with Patagonia and Tasmania) that has experienced extensive and repeated Pleistocene glaciations (Fitzharris *et al.*, 2007; Shulmeister *et al.*, 2019; Sutherland, Carrivick, Shulmeister, *et al.*, 2019). Currently, New Zealand has >3000 glaciers, most of which are in the Southern Alps, that cover approximately 1200 km^2 (Chinn, 2001). Annual ice volume estimates since the 1970s indicate these glaciers are rapidly losing ice (Chinn *et al.*, 2012, 2014; Salinger *et al.*, 2019; Carrivick *et al.*, 2020). Estimated ice volume in 2018 was 37.3 km^3 (Salinger *et al.*, 2019), whilst modelling by Carrivick *et al.,* (2020) estimate 2019 ice volumes between 33.7 km^3 and 50.5 km^3. Both estimated volumes indicate ice loss from the calculated volumes of 54.5 km^3 in 1976 and 46.1 km^3 by 2008 (Chinn *et al.*, 2012). Ice volume loss since the Little Ice Age (LIA) extents is estimated to equate to 41% to 62% volume lost (Carrivick *et al.*, 2020). Estimates of LGM ice volume from modelled reconstructions range between 6,400 km^3 (Golledge *et al.*, 2012) to 6,800 km^3 (James *et al.*, 2019), indicating New Zealand has lost >99% of its glacial ice since the LGM (26.5-19ka (Clark *et al.*, 2009)). Reconstructions of LGM ice extents were attempted by Golledge *et al.* (2012), who applied a climate model using inferred mapped limits of Barrell (2011). The model suggested an 'icefield' style of glaciation during the LGM. However, discrepancies exist between the modelled and mapped ice limits in some valleys. Recent modelling of LGM ice extents using a glacial geomorphological approach as constraints suggests an extensive valley-constrained style of glaciation, with several exposed ridgelines and nunataks, and a localised ice cap-style glaciation over the Fiordland region, because of lower relief (Figure 3.2B) (James *et al.*, 2019). This regional model correlates to individual

catchment glacier reconstructions (Putnam *et al.*, 2013) that also suggest a valley-constrained style of glaciation during the LGM.

The repeated glacial cycles throughout the Pleistocene carved out the fjords in Fiordland, and several of the present-day lake basins. Approximately 38% of New Zealand's lakes (60% of the South Island's lakes) are glacial in origin (Table 3.1) (Lowe and Green, 1987; Hamilton *et al.*, 2012). Several of the largest lakes occupy intra-mountainous settings, with surrounding steep hillslopes (including, but not limited to, Lake Wakatipu, Wānaka, Hāwea, Hauroko, Sumner, Rotoiti, and Rotoroa (Gage, 1975; Lowe and Green, 1987; Sutherland, Carrivick, Shulmeister, *et al.*, 2019)). Some lakes extend beyond the confines of the valley and into a more piedmont setting, such as the lakes of the Mackenzie basin (Lakes Tekapo, Pukaki, and Ōhau), and Lakes Brunner, Te Anau, and Manapouri (Sutherland, Carrivick, Shulmeister, *et al.*, 2019).

Table 3.1. Number and type of lake across the North and South Island, New Zealand. Source: Lowe and Green (1992)

Type	**North Island**		**South Island**		**Total**	
	Number	% of total	Number	% of total	Number	% of total
Glacial	0	0	289	60	289	38
Volcanic	30	10	0	0	30	4
Dune	106	35	13	3	119	15
Riverine	67	22	54	11	121	16
Landslide	18	6	22	5	40	5
Barrier-bar	14	5	18	4	32	4
Tectonic	6	2	0	0	6	1
Solution	1	<1	0	0	1	<1
Peat	0	0	0	0	0	0
Artificial	34	11	31	7	65	8
Undetermined	23	8	49	10	72	9
Totals	299		476		775	

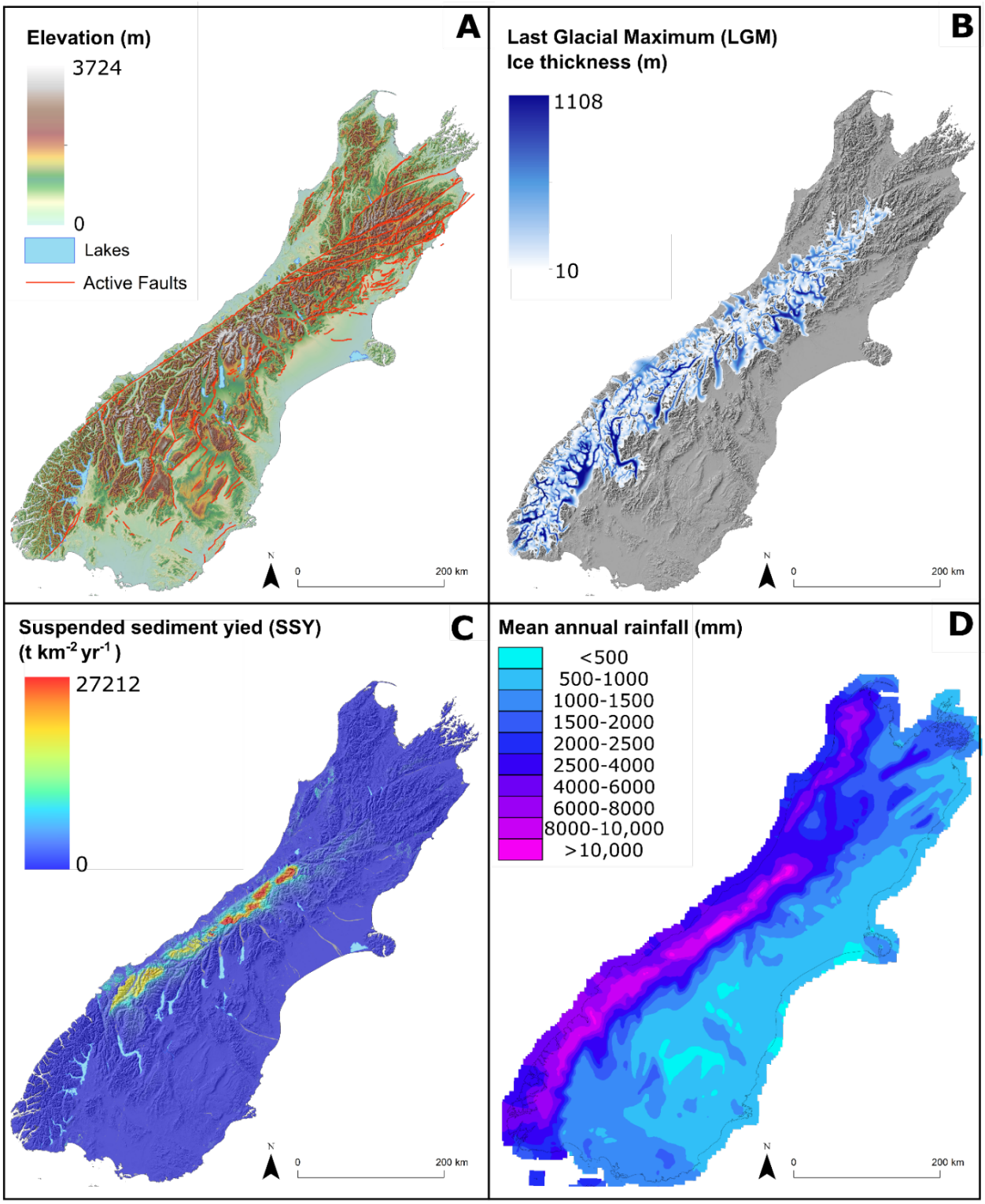

Figure 3.2. Overview maps of New Zealand South Island including the distribution of active faults (a); modelled Last Glacial Maximum (LGM) ice thickness (b); total suspended sediment yield (c); and 30-year average mean annual precipitation (rainfall) (d). Topographic data and lake polygons are from LINZ Data service (https://data.linz.govt.nz/). Active Faults shapefiles are from GNS Active Fault Database (https://data.gns.cri.nz/af/), based on Langridge *et al.,* (2016). LGM model from James *et al.,* (2019) Suspended sediment yield model is based on the work of Hicks *et al.,* (2003, 2011), and GIS layer is available from the National Institute of Water and Atmospheric Science (NIWA) (https://niwa.co.nz/freshwater/management-tools/sediment-tools/suspended-sediment-yield-estimator). 1981-2010 mean annual rainfall model data is provided by, and copyright of NIWA.

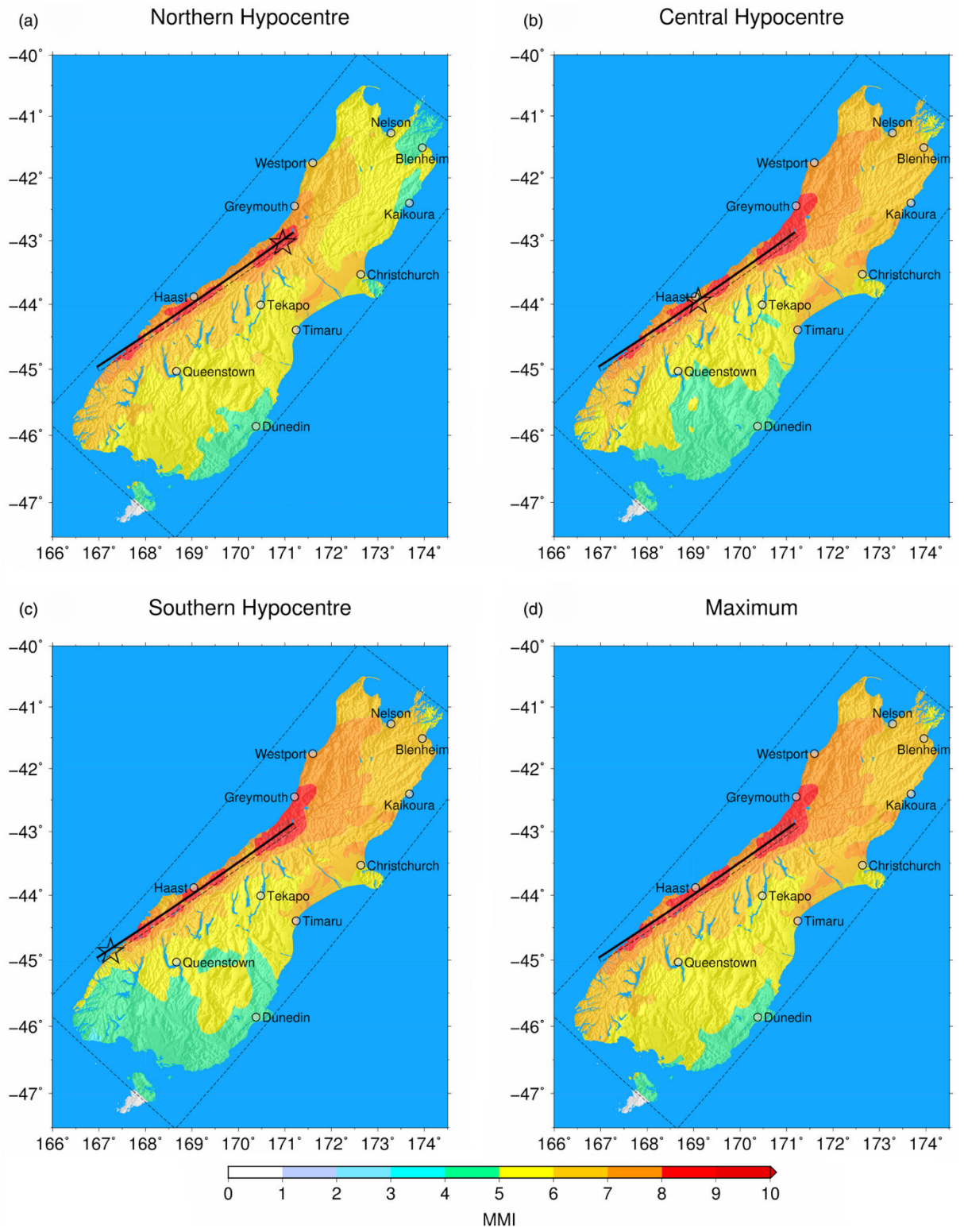

Figure 3.3. Modelled MM shaking intensities across the South Island, New Zealand, from a $M_w = 8.0$ Alpine Fault earthquake with (a) Northern Hypocentre, (b) Central Hypocentre, (c) Southern Hypocentre, and (d) maximum shaking intensities. Figure sourced from Bradley *et al*., (2017).

3.4. Physiographic setting

New Zealand's geographic position exposes it to dominantly westerly maritime air masses from the Tasman Sea. The orographic effects of the Southern Alps result in high mean annual precipitation (>11, 000 mm a^{-1}) across the Southern Alps, particularly in westward facing catchments of the Western Southern Alps (Hicks *et al.*, 1996) (Figure 3.1D). Short-term, decadal suspended sediment yield (SSY) measurements across the South Island are high, particularly west of the Southern Alps Main Divide, as a result of rapid uplift and orographic-induced high precipitation (Figure 3.1C) (Hicks *et al.*, 2011; Robinson *et al.*, 2016). The lakes of the South Island are highly effective sediment traps, with assumed 100% sediment trapping efficiency (Hicks *et al.*, 2011). The presence of lakes along a fluvial systems has resulted in lower fluvial-transported sedimentation to the continental shelves (Carter and Carter, 1990; Hicks *et al.*, 2011). As a result, many of the lakes in the Southern Alps have assumed thick sediment packages, accumulated since formation of the basins. Available seismic reflection survey data from the Mackenzie lakes reveal postglacial sediment thicknesses of at least 150 m in Lake Ōhau, (Clark *et al.*, 2015; Krause, 2016; Levy *et al.*, 2018), and up to 300 m thick in Lake Tekapo (Mountjoy *et al.*, 2019). In Lake Pukaki, postglacial sediment thickness of 150 m thick have been identified in the southern end of the lake (Carter and Carter, 1990; Yetton and McCahon, 2008). Towards the delta head at the northern end of the lake, sediment thickness has been detected as being over 300 m thick (Clark *et al.*, 2015), though this may include some of river valley material drowned post-dam construction. Sediment thicknesses have also been reported in Milford Sound/Piopiotahi, at over 300 m thick in Stirling Basin, as seismic reflection data fails to detect the acoustic basement (possible bedrock surface) (Dykstra, 2012). Further fjords contain up to 16 m, and 15 – 25 m of postglacial hemipelagic sediments in Te Awaroa/Long Sound, Rakituma/Preservation Inlet, and Te Awa -o- Tū/Thompson Sound Kaikiekie/Bradshaw Sound, respectively (Pickrill, 1993). In those fjords, the acoustic basement is also undetected.

3.5. Spatial and temporal distribution of subaerial landslides across New Zealand

Due to the physiographic and tectonic setting, and Pleistocene glacial history steepening hillslopes, landslides and associated deposits are prevalent across both the North and South Island (Rosser *et al.*, 2017). Beyond isolated case examples across New Zealand (Smith *et al.*, 2006; Lee *et al.*, 2009; Cox, McSaveney, *et al.*, 2015), studies and databases of deposit distributions have traditionally focussed on either coseismically-generated landslides (Hancox *et al.*, 2003; Fry *et al.*, 2010; Parker *et al.*, 2015; Massey *et al.*, 2020), or regional studies

(Whitehouse, 1983; Whitehouse and Griffiths, 1983; Hovius *et al.*, 1997; Korup, 2005a, 2006a; Hancox and Perrin, 2009; Allen *et al.*, 2011).

Most recently, Bainbridge (2017) analysed the spatial and temporal distribution of catastrophic RSF (rock avalanche) deposits (*n=268*) across the whole of the South Island (Figure 3.3). The study identified rock avalanche deposits across the whole of the South Island, indicating that such events can occur irrespective of geology. However, the database identified that rock avalanche occurrence is most dominant in sedimentary rocks (*n=178*). The occurrence of rock avalanches in New Zealand has been found to occur above a critical threshold slope angle of 32°, irrespective of region, geology and lithology (Clarke and Burbank, 2010; Allen *et al.*, 2011; Bainbridge, 2017). This appears to be the critical threshold angle for New Zealand rock avalanche occurrence.

Only 101 of the deposits have a known trigger, with earthquake the most common (98 of the 101 known) (Bainbridge, 2017). Of the unknown triggered deposits, Bainbridge (2017) has suggested that rainfall is unlikely to be the main trigger for the unknown events. Rainfall has only triggered 2 of the known deposits, and deposits appear in areas with comparatively low annual rainfalls (cf. Figure 3.3 and Figure 3.1D). Due to estimated high, long term PGA values (Stirling *et al.*, 2012) and close proximity of deposits to known active faults, Bainbridge (2017) suggests that many more deposits are coseismic but timing of past ruptures, and/or deposit ages, are lacking. High shear strain accumulation between seismic cycles in New Zealand (Haines and Wallace, 2020) may explain the occurrence of known aseismic rock avalanches in the Central Southern Alps (McSaveney *et al.*, 2015). Bainbridge (2017) suggests this may also explain the apparent absence of aseismic rock avalanches in Fiordland, and the southern region of the Southern Alps, where accumulated shear strain is low.

Many of the most recent (post-1950 AD) rock avalanches have been documented in the Aoraki/Mt. Cook region of the Southern Alps (McSaveney, 2002; Allen *et al.*, 2011; Cox, McSaveney, *et al.*, 2015; Dunning *et al.*, 2015; Cody *et al.*, 2020). Processes such as paraglacial adjustment (Cody *et al.*, 2020), climatic changes resulting in possible permafrost degradation (Allen *et al.*, 2011; Allen and Huggel, 2013), and/or deformation from increased shear strain rates (McSaveney *et al.*, 2015), have all been suggested as likely triggering and/or preparatory factors. It is possible a combination of such processes has contributed to the failures. The uncertainty in assigning one (or more) trigger is most likely due to an incomplete inventory of deposits (Allen *et al.*, 2011). Such deposits have been identified as rapidly sequestered into

glaciers (Dunning *et al.*, 2015). Establishing a better inventory with new remote sensing detection methods (Smith *et al.*, 2020) will allow better understanding of such preparatory and triggering factors (Coe, 2020). Such information could then aid as a contemporary analogue for processes that may have occurred during LGM ice retreat in formerly glaciated regions in New Zealand.

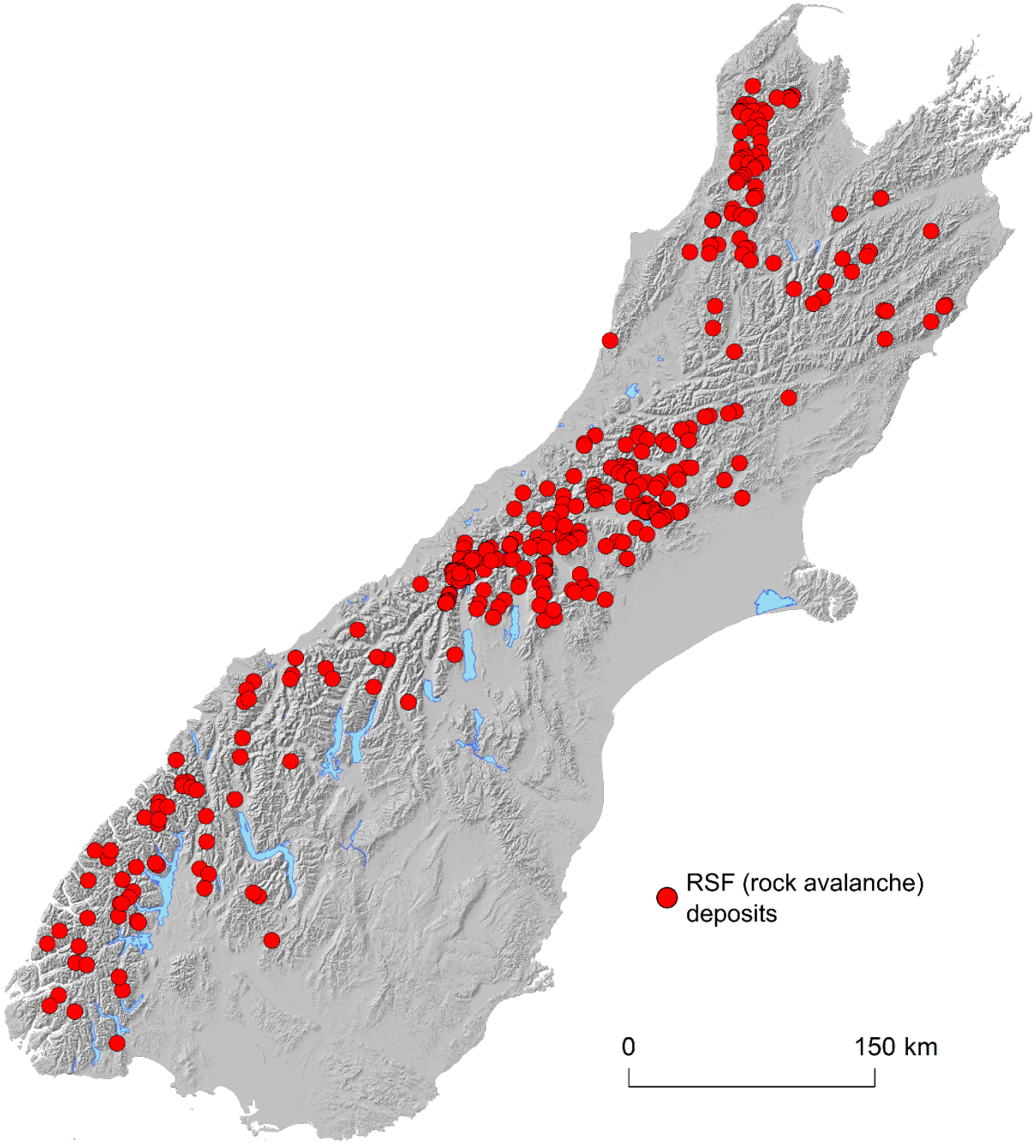

Figure 3.4. Bainbridge (2017) inventory of identified subaerial RSF (rock avalanche) deposits across the South Island. Dataset from Bainbridge (pers. comm.).

The temporal record of the database appears to show an apparent increase in the frequency of rock avalanches, but Bainbridge (2017) suggests that is unlikely to be the case. Only 66% of the deposits in the database have absolute ages, with a temporal bias from observed and EQTLs from earthquake events within the historical record. Only two deposits have pre-Holocene ages (Hancox and Perrin, 2009; McColl, 2020). High rates of geomorphic erosion and change occur across New Zealand for it to maintain its long-term dynamic equilibrium. Therefore, many older deposits have likely been censored due to fluvial and/or glacial processes, or deposits may be subaqueously occluded in the lakes and fjords across the South Island (Chevalier *et al.*, 2009; Dykstra, 2012; Dunning *et al.*, 2015). With the exception of Lake Coleridge (Lee *et al.*, 2009), deposits are largely absent around many of the South Island lakes. However, the identification of rock avalanche deposits in the bottom of Milford Sound/Piopiotahi (Dykstra, 2012) suggests that deposits could be censored in subaqueous environments. The water bodies may therefore hold an archive of deposits. Whilst the focus on rock avalanche deposits knowingly excludes other catastrophic and non-catastrophic RSF, the findings may provide a useful analogue to compare other catastrophic RSF, such as rockslides, deposit distributions.

3.6. New Zealand subaqueous landslides: current understanding on distribution and controls

Compared to the subaerial environment, much less is known about the spatial and temporal distribution of subaqueous landslides in and around New Zealand. However, subaqueous landslides and associated deposits have been identified in New Zealand's offshore marine environment. Some examples include three large subaqueous failures that comprise the Matakaoa Submarine Instability Complex, offshore East Cape, north-eastern coast of the North Island. The complex is comprised of the 1400 ± 360 km^3, largely buried, Raukumara Slump, estimated age between upper Miocene and lower Pleistocene (Lamarche *et al.*, 2008), the 430 ± 100 km^3 Matakaoa Debris Avalanche (600±150 ka) (Lamarche *et al.*, 2008; Joanne *et al.*, 2010), and the Matakaoa Debris Flow 1250 ± 250 km^3 (38-100 ka) (Figure 3.4B) (Carter, 2001; Joanne *et al.*, 2013). Other very large (>1 km^3) landslides have been identified along the Hikurangi subduction margin, and in the Hikurangi Trough, offshore eastern margin of the North Island, including the 3150 ±63 km^3 Ruatoria Debris Avalanche (Collot *et al.*, 2001; Pouderoux *et al.*, 2012) (Figure 3.4D), the Tuaheni Landslide Complex (Pouderoux *et al.*, 2012) (Figure 3.4E), and the Poverty Debris Avalanche (Pedley *et al.*, 2010) (Figure 3.4E).

Studies on these subaqueous landslide studies have focussed on their respective individual case example, allowing for an understanding in the preconditioning and triggering factors for the

individual landslides (Watson *et al.*, 2020). This has restricted understanding of the broader controls on landsliding in such environments. However, the availability of recently collected higher spatial resolution multibeam bathymetric data over a more expansive area in the continental offshore environment has allowed more regional-scale mapping of subaqueous landslides. This has allowed investigation into broader spatial distribution, magnitude of deposits, and controls. Watson *et al.,* (2020) collated the pre-existing database of subaqueous landslides in these offshore regions with newly identified landslides from mapping on the recently collected multibeam bathymetric data. This produced an inventory of 2215 subaqueous landslides (Figure 3.5). The distribution of the landslides showed higher concentrations in the active margin and clustering along canyon walls. Canyon development appears to precondition the walls for slope failure, whilst on the active margin, tectonic uplift and oversteepening, as well as proximity to active fault systems appears to control the occurrence of landslides there (Watson *et al.*, 2020).

However, 99% of the landslide scar features mapped had no associated deposit. Watson *et al.,* (2020) acknowledged some deposits may still exist, but are censored by burial through post-event sedimentation, or flushed through canyon systems. A seismic reflection survey could address the burial of deposits, and therefore provide a greater insight into the magnitude-frequency distribution of such deposits in the region. Also, the actual number of landslide deposits may be greater but limited in size relative to dataset resolution. The spatial resolution of the data (25 m) limited detection of any deposit smaller than 100 m in length (4 pixels) (Watson *et al.*, 2020). This could be resolved with collecting higher resolution data with MBES systems mounted on AUVs.

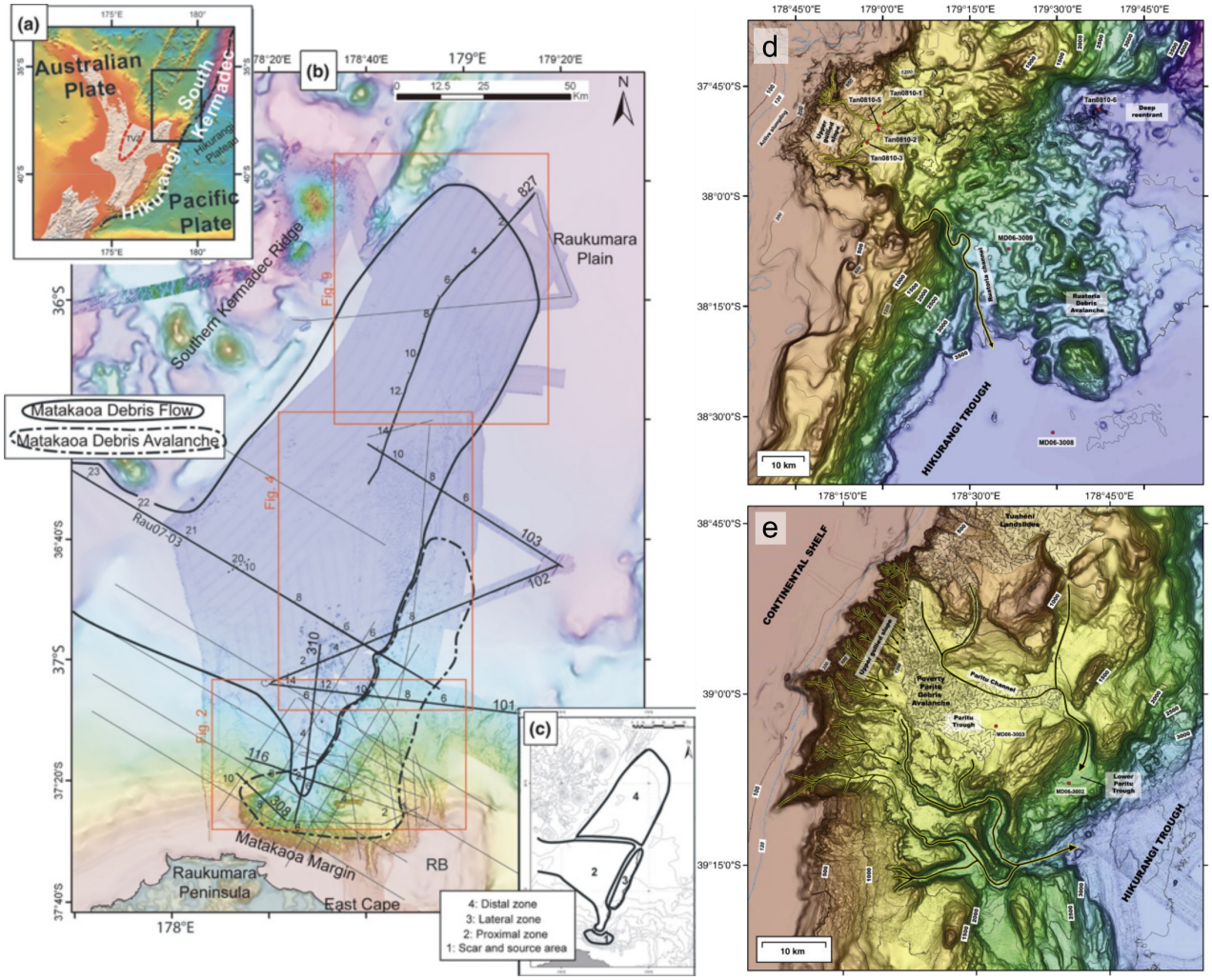

Figure 3.5. Notable subaqueous landslide deposits offshore the North Island, including the Matakaoa Debris Flow and Debris Avalanche deposits that comprise the Matakaoa Submarine Instability Complex (panel B); the Ruatoria Debris Avalanche deposit (panel D); and the Tuaheni Landslide and Poverty Debris Avalanche (panel E). Location of the Matakaoa deposits shown in panel A, locations of deposits in panels D and E are shown in Figure 3.5. Figure A-C source from Joanne *et al.,* (2013), Figure D and E from Pouderoux *et al.,* (2012).

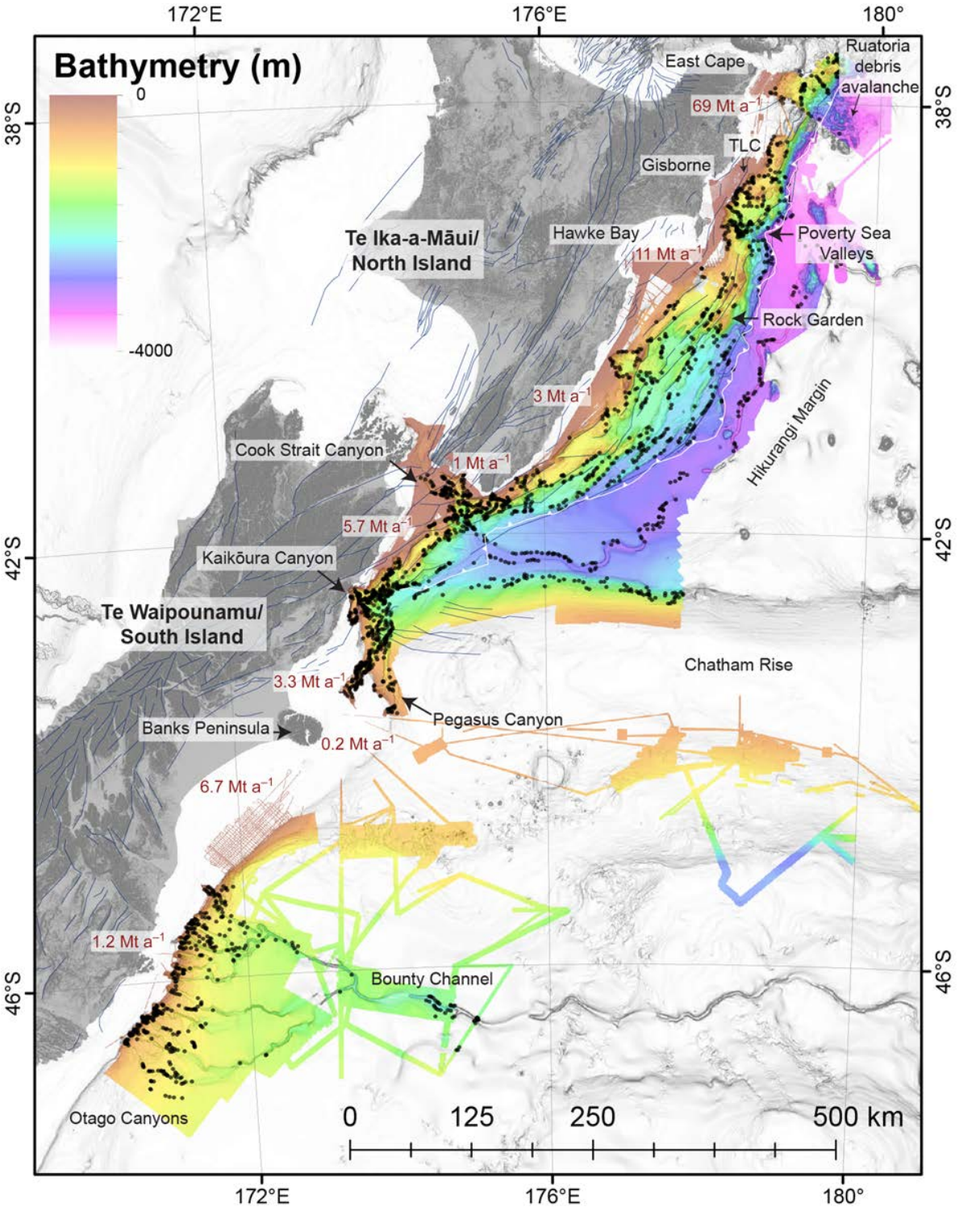

Figure 3.6. Distribution of subaqueous landslides in the eastern offshore New Zealand. The distribution shows a higher density of deposits in the active Hikurangi Margin region compared to the passive margin, offshore south-east South Island. TLC – Tuaheni Landslide Complex. Figure source: Watson *et al.,* (2020).

3.6.1. Subaqueous landslides in lakes and fjords

New Zealand has >770 lakes of at least 500 m in length (Table 3.1) (Lowe and Green, 1987), and 15 fjords that are located in Fiordland region, south-west South Island (Sounds and Inlets). Unlike the subaerial and offshore submarine environment, knowledge on the spatial and temporal distribution of landslide deposits within New Zealand's lakes and fjords is comparatively even more limited. This is largely due to the lack of both MBES and SBP data within the lakes. Currently, Lake Tekapo is the only lake that has complete MBES data available (Mountjoy *et al.*, 2019). Therefore, recorded cases of where landslides have occurred in lake and fjords are largely restricted to eyewitness accounts. However, contemporary historical records for New Zealand are temporally short, only extending to the last c.180 years (Howarth *et al.*, 2018). The remote nature of some of the lakes and fjords may mean observations of landslides have gone unrecorded. Furthermore, many documented cases are largely limited to single lake or fjord examples in New Zealand. To date, no inventory has compiled or analysed the known distribution of landslide deposits across all the lakes and fjords of New Zealand. The first spatial inventory of landslide and associated deposits in lakes and fjords across New Zealand is therefore presented here. The inventory covers both the North and South Island.

An inventory of lakes and fjords where landslides have been observed occurring, or where deposits have been identified within, were collated from published articles, technical reports, and theses (Figure 3.7, 3.8, 3.9; Table 3.2). In many cases, morphometric data on the landslide deposits are lacking (for example, total number of deposits, volumes, and runout distances). Rather, this inventory serves to highlight the lakes and fjords where known landslides or deposits have been reported, landslide type, triggering mechanism (where known), and any information pertaining to the detection or identification of landslides and/or landslide deposits. It is possible that this compilation may not be complete as some descriptions of landslides occurring may have been missed, possibly due to variations in terminology used.

Categorising of the landslide type follows the proposed classification method of Sammartini *et al.,* (2019) but with the amended "STS landslides" classification (section 2.1). Furthermore, in categorising the deposits within the lakes and fjords, MTD is used only where such terms are used in the source material be in accordance with the terminology used within the source material. In those articles, MTDs are often described within cores (e.g. Howarth *et al.*, 2012, 2014), or from SBP data (e.g. Upton and Osterberg, 2007). Lakes and fjords that contain multiple different landslide types, for example Lake Tekapo that contains lateral slope and

deltaic collapse landslide deposits (Mountjoy et al., 2019), are categorised as "multiple". The lake types (for example glacial and volcanic) have previously been categorised in independent studies (Lowe and Green, 1992). Furthermore, all the fjords are categorised as "glacial".

3.6.1.1. Distribution

From analysis of the literature across New Zealand, landslides and/or associated deposits have been documented or have occurred within 15 lakes, and 5 fjords. Evidence is found predominately across the South Island with 18 cases reported here (Figure 3.7). In the North Island, only two lakes have reported landslide occurrences (Figure 3.8). This compilation shows that landslide events have occurred in various types of lakes (Table 3.2), including volcanic lakes (*n=1*), and landslide-dammed lakes (*n=1*), but predominantly in glacial lakes (*n=13* (excluding the 5 fjords which are also of glacial origin, otherwise *n=18* in total) (McSaveney, 2002; Hancox et al., 2003; Dykstra, 2012)). Identification of landslides predominantly in glacial lakes is similar to the global pattern (Sammartini *et al.*, 2019). However, whether this plays some factor in landslide occurrence is uncertain here. This is simply due to contemporary and relict glacial lakes being the most common lakes in New Zealand, particularly in the South Island where 60% lakes are glacial in origin (Table 3.1), whilst all the fjords are of glacial origin. Furthermore, these findings may also be biased by investigation foci and methodological approaches in the cited studies.

The lakes and fjords have various landslide types identified within their basins, including STS landslides (*n=7*), deltaic collapses (*n=4*), and undefined MTDs (*n=7*) (Figure 3.9). In Lake Tekapo and Milford Sound/Piopiotahi, multiple different deposits have been identified. Lake Tekapo contains both lateral slope and deltaic failures (Mountjoy *et al.*, 2019), whilst Milford Sound/Piopiotahi has STS RSFs and deltaic failures (Dykstra, 2012; Taig and McSaveney, 2015). With the current data, it is unknown whether many of the other lakes and fjords also contain multiple deposits. Furthermore, many of the MTDs identified have been attributed as deposits from either lateral slope or deltaic failures (Howarth *et al.*, 2012, 2014, 2016; Krause, 2016), but with the current information, failure modes of these MTDs cannot be elucidated.

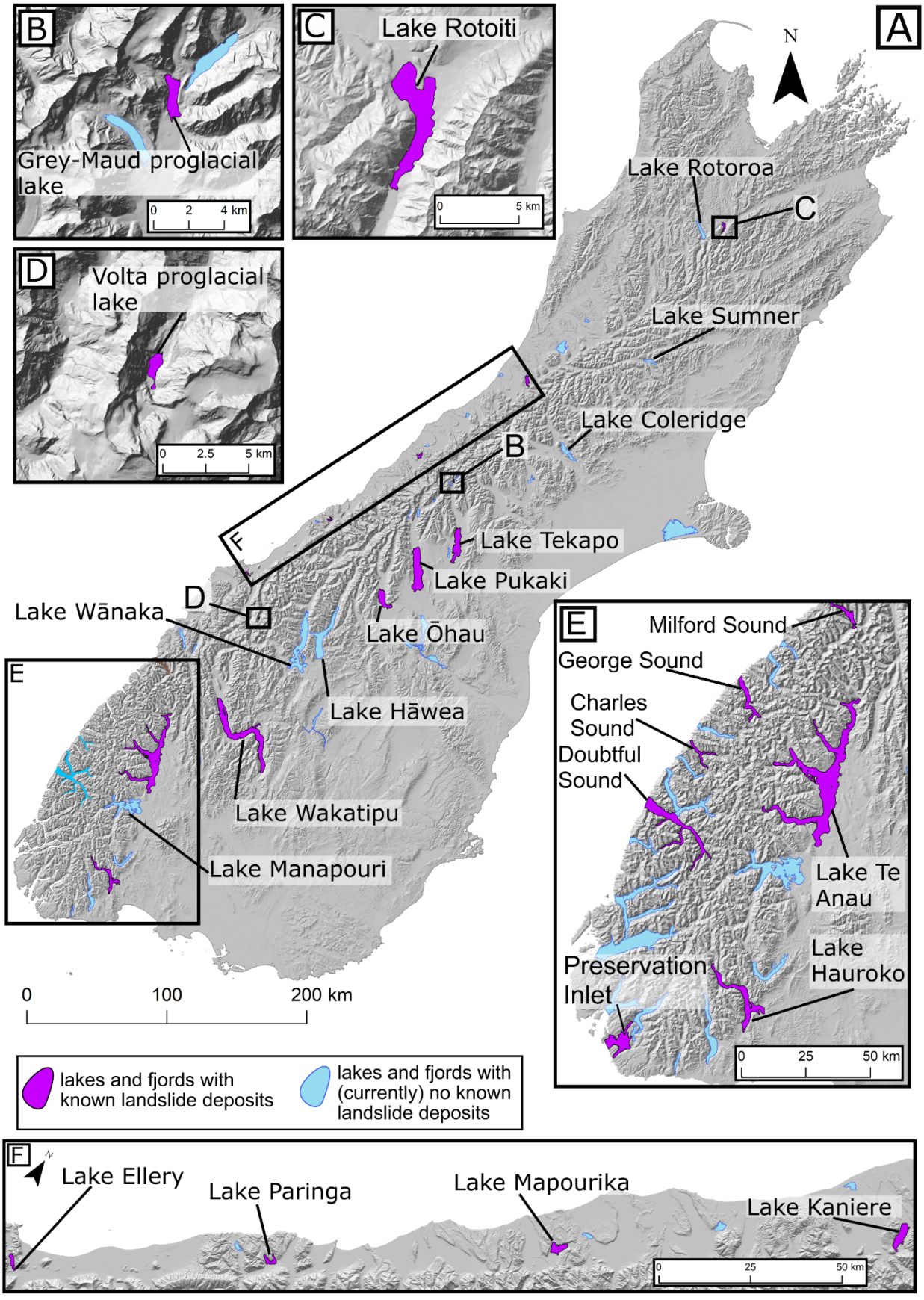

Figure 3.7. Compilation of currently known distribution of lakes and fjords with known landslide deposits across New Zealand's South Island. 1:50k lake shapefiles and DEM (of which hillshade was derived from) available at https://data.linz.govt.nz/.

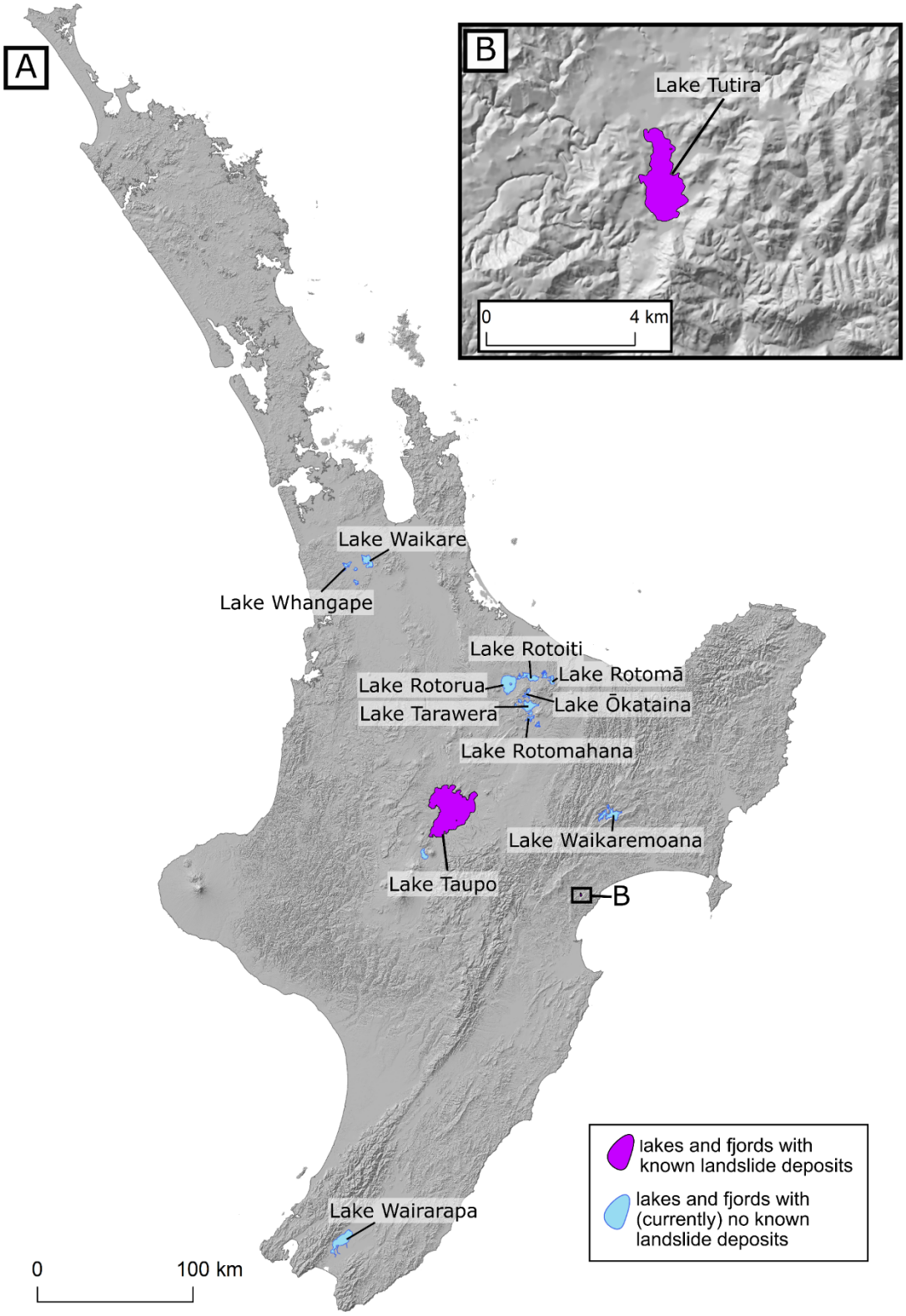

Figure 3.8. Compilation of currently known distribution of landslide deposits/events in lakes of New Zealand's North Island. 1:50k lake shapefiles and DEM (of which hillshade was derived from) available at https://data.linz.govt.nz/.

Figure 3.9. Inventory of lakes and fjords with known landslide deposits classified based on known type of landslide deposit within the lake at present. In (**A**): lateral slope collapses, deltaic collapses, and MTDs are all evident. In (**N**), STS landslide deposits and a deltaic collapse deposit are evident. **A** – Lake Tekapo, **B** – Lake Pukaki, **C** – Lake Ōhau, **D** – Grey-Maud Glaciers proglacial lake, **E** – Volta Glacier proglacial lake, **F** – Lake Ellery, **G** – Lake Paringa, **H** – Lake Mapourika, **I** – Lake Wakatipu, **J** – Lake Te Anau, **K** – Lake Hauroko, **L** – Lake Taupo, **M** – Lake Tutira, **N** – Milford Sound/Piopiotahi, **O** – Taiporoporo/Charles Sound, **P** – Doubtful Sound/Patea, **Q** – Lake Rotoiti, **R** – Te Houhou/ George Sound, **S** – Rakituma/ Preservation Inlet, **T** – Lake Kaniere.

Table 3.2. Summary of lakes and fjords across New Zealand with known landslide deposits within them, their triggering mechanism (where known), and methods of detection.

ID[1]	Lake/Fjord Name	Lake/fjord type	Triggering mechanism	Detection method	Reference
A	Lake Tekapo	G	AEQ	MBES+ SBP	(Upton and Osterberg, 2007; Mountjoy *et al.*, 2019)
B	Lake Pukaki	G	U	SBP	(Clark *et al.*, 2015)
C	Lake Ōhau	G	AEQ+U	SBP+ Core analysis	(Krause, 2016; Fitzsimons and Howarth, 2018)
D	Grey-Maud Glaciers proglacial lake	G	U	Observational[2]	(McSaveney, 2002)
E	Volta Glacier proglacial lake	G	U	Observational[2]	(Korup, 2005c; Rattenbury *et al.*, 2010)
F	Lake Ellery	G	EQ	Core analysis	(Howarth *et al.*, 2016)
G	Lake Paringa	G	EQ	Core analysis	(Howarth *et al.*, 2014)
H	Lake Mapourika	G	EQ	Core analysis	(Howarth *et al.*, 2012)
I	Lake Wakatipu	G	EQ	Observational[2]	(Brodie and Irwin, 1970)
J	Lake Te Anau	G	EQ	Observational[2]	(Forsyth *et al.*, 2006)
K	Lake Hauroko	G	U	Observational[2]	(Bainbridge, 2017)
L	Lake Taupo	V	U	Observational[2]	(Downes *et al.*, 2017)
M	Lake Tutira	LS	EQ+S	Core analysis	(Orpin *et al.*, 2010)
N	Milford Sound/Piopiotahi	G	AEQ	MBES+SBP	(Dykstra, 2012)
O	Taiporoporo/Charles Sound	G	EQ	Observational[2]	(Hancox *et al.*, 2003)
P	Doubtful Sound/Patea	G	U	Observational[2]	(Downes *et al.*, 2005)
Q	Lake Rotoiti	G	EQ	Observational[2]	(Hancox *et al.*, 2002)
R	Te Houhou/George Sound	G	AEQ or S	SBP	(Pickrill, 1987)
S	Rakituma/Preservation Inlet	G	AEQ or S	SBP	(Pickrill, 1987)
T	Lake Kaniere	G	EQ	Core analysis	(Howarth *et al.*, 2021)

[1]ID corresponds to Figure 3.9, [2]observational includes eyewitness accounts of the landslide or tsunami, post-event reconnaissance shortly after the event, or identifying source scar. G – glacial, V-volcanic, LS-landslide-dammed; AEQ – assumed earthquake, U – unknown, EQ – earthquake, S – storm, MBES – multibeam echosounder survey, SBP – sub-bottom profile.

Observations of landslides and/or associated tsunamis occurring are the most common detection method (*n=8*) in the inventory (Table 3.2). Like the observed occurrence of subaerial rock avalanches and associated deposits (section 3.5), many of the most recent non-seismic landslides have occurred in contemporary ice-contact proglacial lakes in the South Island. The events involved STS landslides into proglacial lakes. At the Grey-Maud proglacial lake in the Aoraki/Mt. Cook region (Figure 3.7B, Figure 3.9D), two separate rock avalanches (combined volume ~11 x 10^6 m^3) occurred, with no apparent trigger, from Mt. Fletcher in May and September 1992 (McSaveney, 2002). Both rock avalanches ran out over Maud Glacier and some of the deposits propagated into the proglacial lake, generating localised tsunamis. The first tsunami left ice blocks stranded 20 m above the lake, whilst the second left ice blocks and blackened snow up to 7 m above the lake (McSaveney, 2002). Both tsunamis caused subsequent outburst floods from the lake outlet, down the Godley River, and into Lake Tekapo. At the Volta Glacier proglacial lake, in the Mt. Aspiring National Park (Figure 3.7C, Figure 3.9E), a catastrophic subaerial RSF occurred in 1978 that run out into the lake. Impact into the lake generated a localised tsunami, resulting in an outburst flood down the Waiatoto River (Korup, 2005c). A similar event occurred again in November 1991 when a 0.5 x 10^6 m^3 volume landslide runout into the lake, generating a tsunami approximately 15 m high that then flowed out of the lake. The volume of water released was c. 6 x 10^6 m^3, causing another outburst flood down the Waiatoto River (Rattenbury *et al.*, 2010). Lake Taupo in the North Island (Figure 3.8A, Figure 3.9L) also has several historical examples. A subaerial landslide from the Hipaua cliffs runout into the lake in 1910, and possibly also in 1846 and 1895 (Downes *et al.*, 2017). The 1910 landslide also generated a 3 m high tsunami that swept across the lake.

However, many of these reported cases are single, isolated events and are largely limited to observations or post-event reconnaissance. This largely hampers the temporal record, and relative magnitude-frequency. Core extractions, and/or the expansion of modern marine geophysical data within the lakes, however, has identified previously unknown distribution of landslide deposits in such environments. Deposits have been identified within 6 lake cores (Table 3.2). The cores provide the only evidence of landslides/MTDs in 5 of these lakes as no landslides have been observed here and hydroacoustic data are available. In Lakes Mapourika, Paringa, Kaniere and Ellery (Figure 3.7F, Figure 3.9F, G, H, T), various stacked MTDs have been detected in cores from all four lakes (Howarth *et al.*, 2014, 2016, 2021). The MTDs are either turbidites generated by deltaic and/or non-deltaic subaqueous landslides, or hyperpycnites generated by increased post-seismic sediment fluxes from terrestrial catchments

(Howarth *et al.*, 2014, 2016). The deposits are intercalated between natural lake sedimentation layers, indicating repeated failures occurring through time. Analysis of the sedimentary record from cores from Lake Tutira identified several thick, brown MTDs (also termed 'homogenites' in Oprin *et al.,* (2010)). These MTD layers are attributed to subaqueous failures within the lake, possibly triggered from earthquakes (Orpin *et al.*, 2010). Thinner, grey MTDs are also identified that are attributed to storm events, but exact triggers and emplacement remains uncertain.

Two-dimensional (2D) SBP data from Lakes Pukaki (Clark *et al.*, 2015), Ōhau (Krause, 2016; Fitzsimons and Howarth, 2018), and Tekapo (Upton and Osterberg, 2007; Mountjoy *et al.*, 2019) have identified MTDs within the stratigraphic sequence (Figure 3.10). In some locations the MTDs are stacked within the succession, indicating a location that is repeatedly susceptible to landsliding. The identification of deposits within the stratigraphic sequence provides insight into the relative temporal frequency since the lake basin formed. In New Zealand, this most likely relates to the deglacial and postglacial period when the basins were no longer occupied by ice. Wide grid spacing during the SBP surveys have limited establishing the spatial distribution of the MTDs. The recent collection of MBES data by Mountjoy *et al.,* (2019) for Lake Tekapo has complemented initial SBP studies (Figure 3.10A). The MBES data revealed multiple landslide deposits from lateral slope and deltaic failures collectively covering 25% of the lakebed (Mountjoy *et al.*, 2019). The data has aided in establishing a relative magnitude-frequency relationship of coeval failures occurring approximately every 3000 years, but discrete events possibly <500 years (Mountjoy *et al.*, 2019). The data has also aided in constraining failure volumes for tsunami modelling of past events for probabilistic hazard assessments of potential future landslide-tsunami events (Mountjoy *et al.*, 2019).

The remote nature of the fjords mean observations are more limited. Initial identifications of landslide occurrences in the fjords were from post reconnaissance of coseismic failures (Hancox *et al.*, 2003) and in some cases, resultant tsunamis. For example, in 1987, an STS landslide occurred in Deep Cove of Doubtful Sound/Patea that was not triggered by any seismic event. The landslide impacted the fjord, also generating a localised tsunami (Downes *et al.*, 2005). However, there is a greater availability of MBES and SBP data in the fjords compared to the lakes. Every fjord has, at minimum, a single long-profile SBP data (Stanton and Pickard, 1981). MBES data has been collected and analysed in Milford Sound/Piopiotahi (Dykstra, 2012), and Te Awa -o- Tū/Thompson Sound and Kaikiekie/Bradshaw Sound (Barnes *et al.*, 2016). Since 2014, MBES data have also been available from Land Information New Zealand (LINZ) for

Taiari/Chalky Inlet, Moana-whenua-pōuri/Edwardson Sound, Te Korowhakaunu/Cunaris Sound, Rakituma/Preservation Inlet, and Te Awaroa/Long Sound. Partial MBES datasets are also available for Tamatea/Dusky Sound and Te Pauitaha/Breaksea Sound. The SBP profiles in Te Houhou/George Sound (Figure 3.9R), and Doubtful Sound/Patea (Figure 3.9P) have identified facies relating to deltaic slumps (Pickrill, 1987). However, of the available MBES, only Milford Sound/Piopiotahi has known STS deposits on the fjord bottom (Dykstra, 2012). Barnes *et al.,* (2016) report subaerial landslide scars within Kaikiekie/Bradshaw Sound, but no associated subaqueous deposit, only subaqueous fans. The fans, however, may be in part, emplaced on top of landslide deposits.

3.6.1.2. Triggering mechanisms

From the lakes where landslides have been observed or identified, earthquakes appear to be the most common trigger (Table 3.2). Earthquakes are the known trigger of landslides in 9 lakes and fjords, whilst earthquakes are assumed as the trigger for a further 5. An earthquake in the summer of 1937-1938 triggered a deltaic collapse of the Rees-Dart delta in Lake Wakatipu (Figure 3.9I) (Brodie and Irwin, 1970). The M_L 6.1 1988 earthquake also generated a deltaic failure in Narrows Creek of Lake Te Anau (Figure 3.9J) (Forsyth *et al.*, 2006). No tsunami was reported during the Lake Wakatipu deltaic collapse, but a 1 m high wave was generated in Lake Te Anau. The M_w 7.8 1929 Murchison earthquake also triggered landslides on the hillslopes around Lake Rotoiti (Figure 3.9Q), 55 km east of the epicentre, that were reported to have slipped into the lake (Hancox *et al.*, 2002). The earthquake may have also triggered subaqueous landslides at Lakes Rotoroa and Brunner (Moana). Waves were reported on both lakes but were considered seiches rather than tsunamis as no subaerial landslides were documented around the lake (Yetton and McCahon, 2008). However, one or several subaqueous landslides, whether lateral slope failure(s) and/or delta collapse(s), cannot be ruled out as no hydroacoustic data exist (Yetton and McCahon, 2008) and therefore not included in the inventory.

A seismic origin from the Alpine Fault is attributed as the trigger of the MTD event layers in Lakes Mapourika, Paringa, Kaniere and Ellery (Figure 3.7F, Figure 3.9F, G, H, and T). This is due to synchronous ages of the deposits between basins, despite a 150 km distance separating the lakes, and correlation of the deposit ages with independently dated ages of Alpine Fault ruptures (Howarth *et al.*, 2014, 2016, 2021). Comparison between lakes gives greater confidence in a seismic origin from the Alpine Fault compared to a more localised, non-seismic trigger (e.g. storms) that cannot be ruled out when investigating a single basin (Howarth *et al.*, 2016). This also excludes other seismic sources as modelled shaking intensities on other

localised faults cannot trigger sufficient shaking to affect all three lakes simultaneously (Howarth *et al.*, 2016). The MTDs also provide an estimate of relative shaking intensities from the earthquakes. Shaking intensities MM>6 are needed to generate the subaqueous landslide turbidites, whilst MM>8 is needed to generate significant landsliding in the subaerial catchments that results in hyperpycnites in the lake (Howarth *et al.*, 2014, 2016). The heightened sediment flux (and resultant hyperpycnites layers) continue to occur for ~50 years post-earthquake (Howarth *et al.*, 2012, 2014). Geochemical signatures of these layers also correspond to geochemical signatures on the higher elevations of the catchment terrestrial hillslopes (Wang *et al.*, 2020). This further strengthens a seismic origin by amplification of seismic waves to the upper hillslopes during earthquakes.

Earthquakes have also been suggested as a trigger of some subaqueous landslide deposits and MTDs identified in Lake Tekapo (Figure 3.9A, Figure 3.10A, B) (Upton and Osterberg, 2007), and MTDs identified in Lake Ōhau (Figure 3.9C, Figure 3.10C) (Fitzsimons and Howarth, 2018). Many deposits identified in sub-bottom and the bathymetric data across the Lake Tekapo basin are coeval in nature (Mountjoy *et al.*, 2019) but establishing the absolute ages of the deposits is still needed. Preliminary dating of the most recent MTD from a core from Lake Ōhau yields an age of ~1717 AD (Fitzsimons and Howarth, 2018) which corresponds to the last major rupture along the Alpine Fault (Howarth *et al.*, 2018).

Where landslides have been documented in the fjords, earthquakes also appear to be the inferred trigger. The M_w 7.2 2003 Fiordland earthquake generated over 400 landslides, including a 200,000 m^3 STS rockslide that ran out into the Gold Arm of Taiporoporo/Charles Sound (Figure 3.9R). The landslide triggered a tsunami that removed vegetation 4-5 m above the water level 800 m away (Hancox *et al.*, 2003; Power *et al.*, 2005). Earthquakes along the Fiordland Subduction Zone have also been considered the likely trigger for deltaic slumps recorded in SBP profile from Te Houhou/George Sound (Figure 3.9R), and Rakituma/Preservation Inlet (Figure 3.9S) (Pickrill, 1987). However, deltas can fail through other processes such as gradual loading (Girardclos *et al.*, 2007) or impacting subaerial landslide (Kremer *et al.*, 2015). Storm wave loading is also considered as a possible trigger (Pickrill, 1987), especially as the fjords are directly in the path of prevailing westerly weather systems. In the Milford Sound/Piopiotahi catchment, several large (>10^6 m^3) STS RSFs have been identified on the fjord bottom (Figure 3.9N), as well as in the terrestrial catchment (Dykstra, 2012). Some of the subaerial deposits in the catchment have absolute dates synchronous to known rupture dates of the Alpine Fault. No dates are available for the subaqueous deposits, but due to close proximity to the Alpine Fault,

and correlated ages of some of the subaerial events to known ruptures, it is assumed that the subaqueous deposits are also coseismically-generated (Dykstra, 2012).

However, landslides and/or deposits across 7 of the lakes and fjords have no known trigger (Table 3.2). In the cases of Lake Taupo, Doubtful Sound/Patea, Grey-Maud and Volta lakes, STS landslides were observed occurring with no apparent external triggering mechanism. Given that landslides have occurred into both contemporary (Grey-Maud and Volta lakes), and relict (Doubtful Sound/Patea) glacial lakes, and a volcanic lake (Lake Taupo), it may mean that there is a currently unknown triggering mechanism. Another factor may be that the hillslopes have weakened over time, exceeded its critical threshold of stability, and failed without any apparent trigger (Glade and Crozier, 2005). A lack of age constraints of deposits identified within the lakes and fjords is another issue limiting identification of a triggering mechanism. The MTDs in SBP data from Lakes Pukaki and Ōhau are undated (with exception to the most recent MTD in Lake Ōhau (Fitzsimons and Howarth, 2018)). Therefore connecting their ages to possible external triggers such as earthquakes remains challenging without cores. In the fjords, the limited SBP data currently precludes identifying coeval deposits which may indicate earthquake(s) as a triggering mechanism.

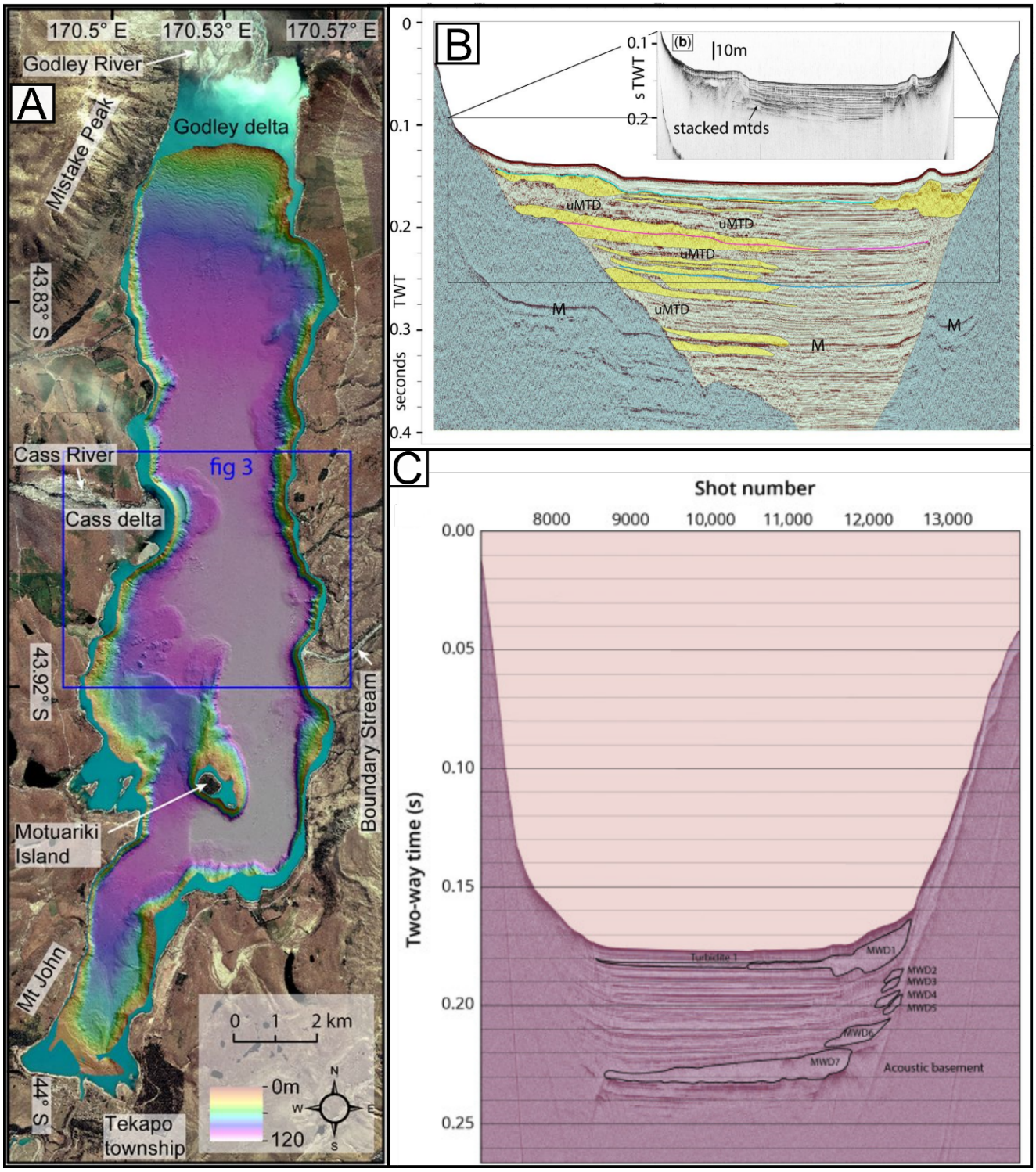

Figure 3.10. MBES (A) and SBP (B) data of Lake Tekapo showing landslide deposits on the surface, and within the stratigraphic sequence. (C) – SBP data from Lake Ōhau showing a series of stacked landslide deposits within the stratigraphic sequence (denoted by MWD - Mass wasting deposits). Figure A and B sourced from Mountjoy *et al*., (2019), Figure C sourced from Fitzsimons and Howarth (2018).

3.7. Conclusion

New Zealand is a highly dynamic landscape with tectonic, glacial, physiographic processes all acting across the South Island. Landsliding is a common geomorphic process in both subaerial and subaqueous environments as a result. Spatial distributions of subaerial landslides are well-documented across New Zealand through regional investigations and coseismic occurrence. Geomorphic processes erode and censor the spatial and temporal distribution of landslides, whilst runout into water bodies occludes the deposits from the record. Advancements and expansion of MBES and SBP surveys and data in the subaqueous environment has expanded the distribution of deposits. However the traditional focus of such surveys has been on isolated, exceptionally large deposits in the offshore marine region. Only recently have more region wide studies been conducted in the offshore marine regions. This has identified wider controls on the occurrence of landslides in such environments. For the distribution of landslides in lakes and fjords however, this has been poorly known.

A new comprehensive and up-to-date inventory has been presented here, highlighting the known distribution of landslides within lakes and fjords in New Zealand (*n=20*). The inventory has highlighted: (1) the type(s) of deposits within these settings; (2) the identification method; and (3) the triggering mechanism(s), where known. Analysis of the inventory has shown that many different types of landslides in the various lakes and fjords have occurred including STS landslides (*n=7*), deltaic collapses (*n=4*), and undefined MTDs (*n=7*). Milford Sound/Piopiotahi and Lake Tekapo contain multiple different deposit types. From the known landslide occurrences, earthquakes are the primary trigger (*n=9*), or inferred trigger (*n=5*), with storms the trigger in possibly 2 cases. However, there is currently no known trigger or control for 7 of the lakes and fjords. Many of these identified cases are single, isolated events that preclude understanding any controls on the occurrence. Additionally, some are temporally restricted to the historical and observational record, which in New Zealand is comparatively short (c.180 years).

The inventory has also highlighted that there are significant gaps in the knowledge of the spatial and temporal distribution. Despite the large number of lakes and fjords, the number containing known landslide deposits is comparatively small. It is possible that this inventory may not be complete as some descriptions of landslides occurring in the literature may have been missed. The comparatively few lakes and fjords with deposits does not necessarily mean the deposits are not present on their basin floors or buried within their stratigraphy. Rather there has been either no observations of such events in the temporally short historical record, and/or no

hydroacoustic investigations. Expansion of MBES, SBP, and sediment core data are needed from the other large lakes in the South Island to identify if landslide deposits are prevalent across many more of the lake and fjord basins.

Chapter 4. Morphology and dynamics of subaerial to subaqueous rock slope failures in Milford Sound/Piopiotahi, New Zealand.

4.1. Introduction

Catastrophic rock slope failures (RSFs), such as rockslides and rock avalanches, are among the most hazardous landslide events in mountainous regions (Korup *et al.*, 2007; Korup and Dunning, 2015). Additionally, these events can trigger a geohazard cascade that could have secondary impacts beyond the initial footprint of the landslide event. Secondary hazards can include the damming of river valleys, subsequent breach, and resultant outburst flood (Korup, 2002; Korup and Tweed, 2007). Where catastrophic RSFs and other landslides runout and impact water bodies, tsunamis (also referred to as 'displacement waves' (Hermanns *et al.*, 2013)) can be generated (Pedersen *et al.*, 2002; Higman *et al.*, 2018). Tsunamis generated by subaerial to subaqueous (STS) RSFs can produce exceptionally high runups, with 10 of the 14 highest recorded tsunami runups coming from non-volcanic STS RSFs into natural water bodies (Higman *et al.*, 2018). STS rock avalanches in particular have the potential to generate large and particularly hazardous tsunami waves as these RSFs are typically long runout landslides of fragmented rock, characterised by large volumes (typically $>10^6$ m^3), high velocities (≥ 5 m s^{-1}), and exceptional mobility (Hungr *et al.*, 2014).

Due to the hazard catastrophic STS landslides present, understanding how such events are both triggered and emplaced is of critical importance (Watt, Talling, Vardy, Heller, *et al.*, 2012; Watt, Talling, Vardy, Masson, *et al.*, 2012; Crutchley *et al.*, 2013). However, they are rarely directly observed (Piper *et al.*, 2012). Therefore, understanding of the runout behaviour and emplacement dynamics relies on detailed analysis of the deposit (Bull *et al.*, 2009; Crutchley *et al.*, 2013) and numerical modelling (Giachetti *et al.*, 2011; Schleier *et al.*, 2017). The acquisition and analysis of high-resolution hydroacoustic datasets, including multibeam bathymetric echosounder (MBES) and sub-bottom profile (SBP) data, have improved the understanding of STS RSF landslides in recent decades (Dufresne *et al.*, 2018; Haeussler *et al.*, 2018; Mountjoy and Micallef, 2018). Morphological and morphometric analysis of deposits within these datasets can provide insights into the landslide emplacement dynamics (Bull *et al.*, 2009; Micallef, 2011; Crutchley *et al.*, 2013). These datasets have also identified previously unknown deposits in many locations (Blikra *et al.*, 2006; Dykstra, 2012).

Numerical modelling has also been used to understand the runout and behaviour of various different landslides, particularly in cases where direct observations are lacking (Pitman *et al.*, 2003; McDougall and Hungr, 2004; Kelfoun and Druitt, 2005; Kelfoun *et al.*, 2010; Sosio, Crosta and Hungr, 2012; Sosio, Crosta, Chen, *et al.*, 2012; Mergili *et al.*, 2017). Runout modelling of STS RSFs, however, has received comparatively less attention than entirely subaerial events due to the additional need for bathymetric data, and complexities of integrating the subaerial and subaqueous components of motion. Some modelling studies have therefore focussed only on constraining the subaerial portion of runout (Benjamin *et al.*, 2018), or where available, the resultant tsunami generated (Fritz *et al.*, 2009; George *et al.*, 2017; Paris *et al.*, 2019). In these models, the subaqueous portion of runout, and subsequent depositional extents of the landslide material remain uncalibrated unless there are MBES data to constrain extents (George *et al.*, 2017). Where MBES data exist, numerical simulations of the full subaerial-subaqueous runout provides additional information on the landslide frontal geometry, flow thicknesses, and velocity at the point of impact with the water (Schleier *et al.*, 2017). These parameters are necessary to understand the emplacement dynamics of the landslide. Furthermore, these parameters can also be coupled to numerical tsunami models to provide initial estimations on wave generation (Yavari-Ramshe and Ataie-Ashtiani, 2016).

Catastrophic RSFs are a common process across the mountainous reaches of New Zealand's South Island (Korup, 2005a; Bainbridge, 2017). High rates of tectonic uplift and denudation, frequent seismicity (Tippett and Kamp, 1995; Langridge *et al.*, 2016), coupled with glacially-(over)steepened relief have triggered, and/or primed slopes for failure (McColl, 2012). Recent catastrophic RSFs into lakes (McSaveney, 2002) and fjords (Hancox *et al.*, 2003), and subsequent generated tsunamis, indicate that such events may have occurred in the recent past. These landslide and associated landslide-tsunami events have been identified as a potential hazard to the many inland water bodies within New Zealand (Hancox, 2012; Clark *et al.*, 2015; Mackey, 2015). However, due to the lack of hydroacoustic data from the lakes and fjords, the STS landslide distribution is, compared to the subaerial distribution, poorly known.

However, in Milford Sound/Piopiotahi, several (previously unknown) STS landslide deposits have been identified across the fjord bottom (Dykstra, 2012). Although the deposits have previously been mapped, there has been no work on their dynamics and kinematics. The deposits pre-date the observed historical record so information regarding their emplacement is lacking. However, the deposits are closely spaced, and are clearly visible in the MBES dataset

(Dykstra, 2012). This presents a unique opportunity to investigate and model a suite of deposits that are sourced from hillslopes of relatively uniform geology, and experience similar external tectonic (e.g. earthquakes), para- and post-glacial, and physiographic processes (e.g. rainfall).

In this study, the STS deposits in Milford Sound/Piopiotahi are investigated through detailed morphological and morphometric analysis. The analysis characterises the morphology and geometry of the deposits to gain insight into the landslide emplacement dynamics. Furthermore, this study also applies a single-phase landslide model (DAN3D) to 5 of the deposits that are representative of all STS morphologies and geometries identified within Milford Sound/Piopiotahi. Each back analysed case is calibrated against the morphometric characteristics of the deposits, which provides further insight into their respective flow behaviours and emplacement dynamics. The back analysis provides an envelope of parameters that may then be used for predictive runout forecasting of any possible future events into Milford Sound/Piopiotahi. Additionally, the landslide modelling results can be taken forward in any future numerical tsunami model in the fjord, as tsunami inundation presents a significant hazard to populations and infrastructure at Milford Sound Village (Taig and McSaveney, 2015).

4.2. Study area

Milford Sound/Piopiotahi is a single arm fjord, located in the northern section of the Fiordland National Park region of New Zealand's South Island (Figure 4.1). It is one of New Zealand's top tourist attractions, with > 650,000 visitors to Fiordland in 2017 (>1700 people per day) (Venture Southland, 2017). Milford Sound/Piopiotahi is approximately 15 km long, and lies in a glaciated valley with the terminal moraine complex located offshore, on the continental shelf (Barnes, 2009; Dykstra, 2012). The fjord has a relict cross-valley parabolic geometry, steep (>70˚) bedrock slopes that extend to over 1000 m above sea level (m.a.s.l.) and extend down to the flat fjord bottom. The fjord basin is mainly flat and deep, and divided into three sections. Entrance and Dale Basin are marked by shallow water depths (up to 130 m deep). Stirling Basin is deeper (maximum water depth 291 m) and extends towards the Cleddau Delta at the head of the fjord at Milford Sound Village. During the Last Glacial Maximum (LGM) (26.5-19 ka (Clark *et al.*, 2009)) the fjord was glaciated and sea levels were 120 m lower (Pickrill *et al.*, 1992; Dykstra, 2012; Dlabola *et al.*, 2015). The fjord was ice-free by c.17 ka, when the glacier had retreated to the present-day head of the fjord at Milford Sound Village (Dykstra, 2012). During deglaciation, the fjord area was a proglacial lacustrine environment, with the palaeolake impoundment by an outer moraine sill (Dykstra, 2012). Marine transgression in Milford Sound/Piopiotahi occurred between 15 and 8ka (Pickrill *et al.*, 1992; Dlabola *et al.*, 2015),

during the Late Glacial Interglacial Transition (LGIT) (17-11 ka (Shulmeister *et al.*, 2019)), and continued until ~ 6 ka. Since ~6 ka, sea levels have remained relatively similar to the present day (Dykstra, 2012; Dlabola *et al.*, 2015).

Post-LGM sedimentation in the fjord was investigated by Dykstra (2012) using two long-valley seismic reflection profiles collected by NIWA. Dykstra (2012) identified horizontal, parallel-bedded facies (interpreted as lacustrine sediments) up to 100 m thick, overlying a chaotic depositional facies (interpreted as possible glacial till or landslide debris). The bedrock horizon was not apparent in the data in Entrance and Dale Basin, but strong reflectors indicate that it may be 250-300 m below the basin floor. In Stirling Basin, the parallel-bedded facies are similar in thickness to the Entrance and Dale Basin, and the chaotic facies appears to extend down to 300 m below the basin floor. In Stirling Basin, no bedrock horizons were visible on the data, so total sediment thickness may be even greater. Sedimentation rates in Stirling Basin have been calculated from a 4 m core retrieved in 1983, providing a rate of between 222 - 313 cm kyr^{-1} over the last 1340 years (Knudson *et al.*, 2011).

The geology of the fjord and its catchment is a composite of Mesozoic plutonic rock units, including Pembroke Granulite, Milford Orthogneiss, and Harrison Gneiss. The Harrison Gneiss units are composed of dioritic, gabbroic and granitic orthogneiss, with lesser ultramafics and migmatites (Turnbull *et al.*, 2010). Milford Sound/Piopiotahi is bounded to the west by several smaller disjointed faults, and the southern section of the Alpine Fault. The Alpine Fault is an active, oblique strike slip fault that marks the transpressional boundary between the Australian and Pacific tectonic plates. Palaeoseismic investigations indicate that large ($M_w \geq 7$) or great ($M_w \geq 8$) earthquakes have been generated along the Alpine Fault. Ruptures on the southern fault section have a mean recurrence interval of <300 years (Cochran *et al.*, 2017; Howarth *et al.*, 2018). The last rupture was in 1717 AD. There is a 75% likelihood of a future earthquake occurring on this southern section over the next 50 years (Howarth *et al.*, 2021).

In the Milford Sound/Piopiotahi catchment and the fjord bottom, Dykstra (2012) identified and mapped 33 landslide deposits. Eleven are in subaerial valleys that were interpreted as rock avalanche deposits. Twenty-six subaqueous landslide deposits were identified on the fjord bottom, 22 of which were interpreted as STS rock avalanche deposits, and 4 as wholly subaqueous deltaic failures. The landslides pre-date the short (~180 year) historical written record. Absolute and relative ages of 6 of the subaerial rock avalanche deposits are known. Radiocarbon dating of the Bowen rock avalanche provides an age of 8.8 ± 0.1 ka (Dykstra,

2012). The other dated deposits include Tutoko – 4.05 ± 0.06 ka; Ada – 0.91 ± 0.03 ka; and Lower Cleddau – 4.65 ± 0.1 ka (Dykstra, 2012). The 625x10^6 m^3 Lake Adelaide rock avalanche deposit has also been dated, providing an age 6.144 ± 0.143 ka (Hancox *et al.*, 2013). Furthermore, relative dating by Schmidt Hammer analysis of the Upper Cleddau rock avalanche suggest that it may have occurred at a similar time to the Bowen rock avalanche (Dykstra, 2012). Of the dated deposits, Dykstra (2012) correlates their ages to a known rupture age of the Alpine Fault (Berryman, Cochran, *et al.*, 2012), suggesting that these rock avalanches were triggered coseismically.

However, the absolute ages and triggering mechanism(s) of the STS deposits are unknown. Dykstra (2012), based on the reconstructed deglacial chronology of the area, gives a conservative maximum age constraint of the subaqueous deposits as ~17 ka. It is possible that anything older may have been either eroded by the glacier during phases of advance or deposited and transported away supraglacially as the ice thinned during advances and retreats. The close proximity of the fjord to the Alpine Fault, and the correlation of some of the dated subaerial rock avalanches to past Alpine Fault ruptures, Dykstra (2012) proposed that the STS deposits are most likely of coseismic origin. The predicted shaking intensities from Alpine Fault ruptures are likely to be sufficient to generate many subaerial landslides across the Southern Alps and northern Fiordland, including Milford Sound/Piopiotahi (Robinson *et al.*, 2016). In addition to the STS and subaqueous landslides identified, talus-like debris cones along the base of the fjord slopes were also identified across the fjord bottom. Dykstra (2012) attributed these to ongoing rockfall and debris flow activity.

Figure 4.1. Overleaf. (A) Overview of the Milford Sound/Piopiotahi catchment in the Fiordland region (see inset map for location in New Zealand). Offshore bathymetry data is sourced from NIWA and licensed under the NIWA Open Data Licence v1.0. Data are available at: https://niwa.co.nz/our-science/oceans/bathymetry; (B) Geological map of Milford Sound/Piopiotahi with bathymetric digital elevation model, with place names mentioned in text. Geological information and layers from New Zealand QMAP (Turnbull *et al.*, 2010; Rattenbury and Isaac, 2012); (C) Map of the subaerial and subaqueous deposits identified by Dykstra (2012). DF deposits are submarine density flow, SM deposits are subaerial source with submarine deposit. Figure source: Dykstra (2012).

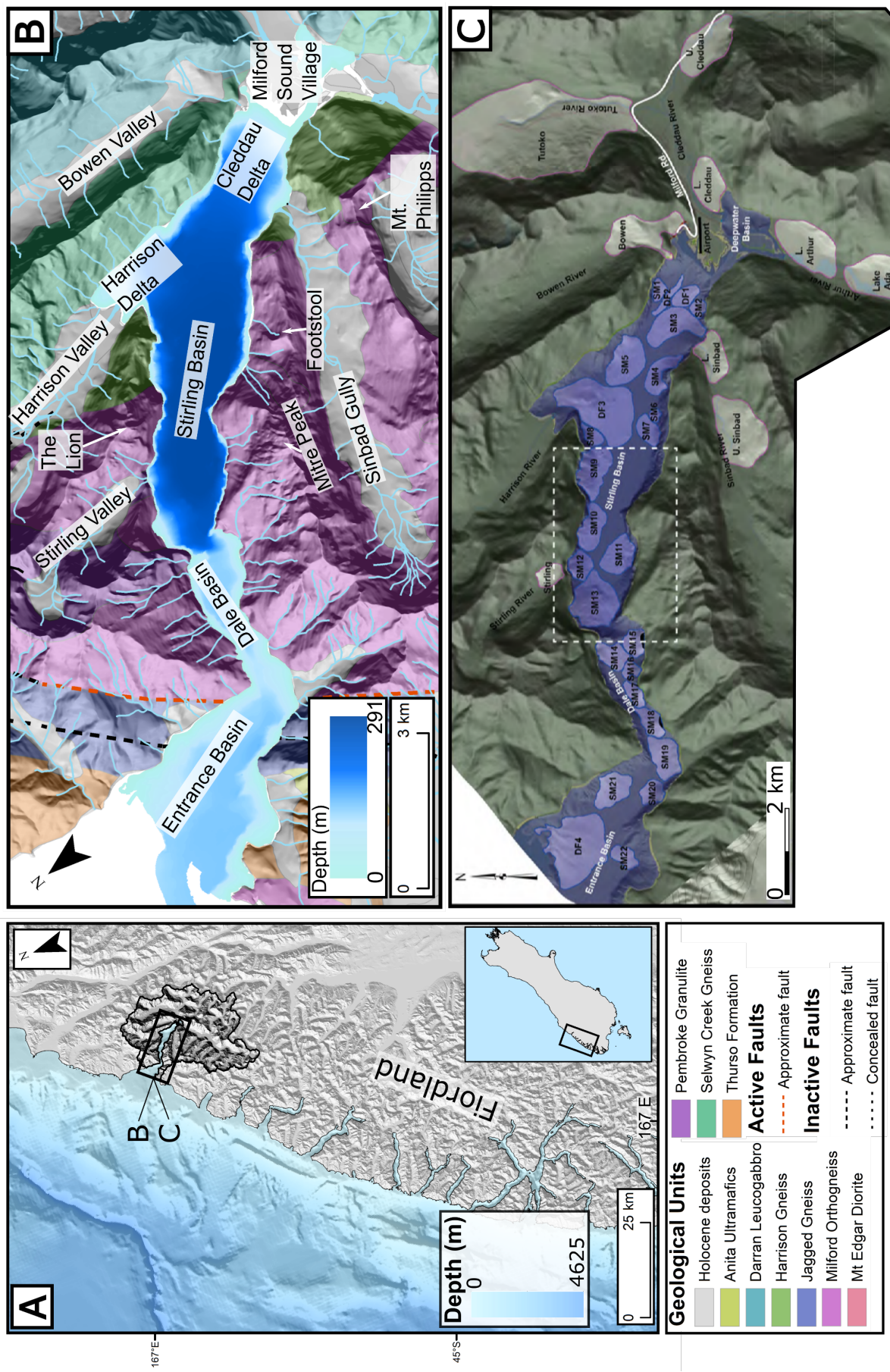
A
B
C
Fiordland
167 E
25 km
Depth (m)
0
4625
167°E
45°S
Geological Units
Holocene deposits
Anita Ultramafics
Darran Leucogabbro
Harrison Gneiss
Jagged Gneiss
Milford Orthogneiss
Mt Edgar Diorite
Pembroke Granulite
Selwyn Creek Gneiss
Thurso Formation
Active Faults
Approximate fault
Inactive Faults
Approximate fault
Concealed fault
Milford Sound Village
Bowen Valley
Cleddau Delta
Harrison Delta
Harrison Valley
Stirling Basin
Footstool
Mt. Philipps
The Lion
Mitre Peak
Sinbad Gully
Stirling Valley
Dale Basin
Entrance Basin
Depth (m)
291
0
3 km
Tutoko River
Tutoko
Milford Road
Cleddau River
U. Cleddau
L. Cleddau
Bowen
Airport
Deepwater Basin
L. Arthur
Arthur River
Lake Ada
Bowen River
L. Sinbad
U. Sinbad
Sinbad River
Harrison River
Stirling River
Stirling
Dale Basin
Entrance Basin
DF1
DF2
DF3
DF4
SM1
SM2
SM3
SM4
SM5
SM6
SM7
SM8
SM9
SM10
SM11
SM12
SM13
SM14
SM15
SM17
SM18
SM19
SM20
SM21
SM22
2 km
0

4.3. Methods

4.3.1. Datasets

Mapping and analysis of the Milford Sound/Piopiotahi STS deposits were based on two MBES bathymetric terrain models (BTMs): a 3 x 3 m BTM with a horizontal accuracy ± 3 m and vertical error 1±2% depth (IHO Standards Zone of Confidence A2), provided by NIWA; and a 5 x 5 m BTM with a horizontal accuracy ± 5.8 m, and vertical error 0.5±1% depth (IHO Standards Zone of Confidence A1), provided by Land Information New Zealand (LINZ). The terrestrial digital elevation model (DEM) used for deriving landslide morphometric parameters and for numerical modelling (section 4.3.3) was the 15 m NZSoSDEM v1.0 terrestrial DEM (maximum absolute error (MAE) 53.2 m, root mean square error (RMSE) ± 7.1 m), created by ANUDEM interpolation applied to NZTopo50 20 m map contours by the National School of Surveying, University of Otago (Columbus *et al.*, 2011), and available at https://koordinates.com/. The 0.75 m aerial orthophotos over Milford Sound/Piopiotahi, collected during 2005-2011, were also used to compliment DEM analyses. The aerial imagery is available at LINZ Data Service (https://data.linz.govt.nz/) under the Creative Commons Attribution 4.0 International license.

4.3.2. Mapping and morphometric characteristics

The deposits were mapped at a scale of 1:3,000 on vertically exaggerated, multi-direction shaded relief maps generated from the MBES BTMs using ESRI ArcMap v.10.5. The deposits were identified first by using the approximate extents of Dykstra (2012). Surface morphological features were mapped on the deposits that may be used to infer flow and emplacement dynamics. These features included longitudinal ridges, concentric rings at distal margins, hummocks/blocks, and perpendicular-to-flow ridges, where possible. Where perpendicular-to-flow ridges were not directly visible on the BTM, the method of Crutchley et al. (2013) was applied to identify possible transverse ridges. The method calculates the standard deviation of the local slope angles of each deposit from their respective mean slope angle. The minimum sized feature identifiable in the MBES data is 9 m in length and width (3 x 3 pixels at 3 m resolution). Large blocks on the fjord floor were digitised manually, surface areas were calculated, and bounding boxes were computed to calculate the orientation, length and width of the blocks (Shugar and Clague, 2011; Yoshida *et al.*, 2012; Yoshida, 2014). Block alignment was calculated following the method of Yoshida (2014), where the block angle was the angle between the block's main axis, and main direction of landslide flow. Each block's alignment relative to their individual flow angle (representative of a freely spreading landslide) was also

calculated. Individual flow angles of the blocks were derived by calculating the azimuth of straight lines between centroid points of the blocks and the highest source point. Linear distance from the highest source point to the centroid point was also calculated. The metrics were all recorded to understand block size and orientation against inferred flow direction, and distance from source. Additionally, features related to deformation of the fjord bottom sediments by impacting landslides were also mapped, where visible. Such features include concentric ridges and rings and frontally raised rims. These features have been noted in fjords and lakes impacted by rock avalanches and other landslide events (Schnellmann *et al.*, 2005; Blikra *et al.*, 2006; Hilbe *et al.*, 2011; Van Daele *et al.*, 2013). The landslide source areas were identified for the corresponding deposits through (1) mapping data presented in Dykstra (2012); who identified deposits from field and aerial reconnaissance and historic aerial imagery; and (2) analysis of aerial imagery and the 8 m DEM, identifying niches/cavities in the hillslopes.

A set of several commonly measured morphometric parameters of the deposits were also recorded (Figure 4.2, Table 4.1) (Moscardelli and Wood, 2016; Clare *et al.*, 2018). Deposit volume estimates for the modelled STS landslides ($n=5$) ($V_L{}^1$) were calculated from creation of pre-event bathymetric BTMs (section 4.3.3.3). The volumes of the mapped deposits where no pre-event bathymetry was reconstructed were estimated using a volume-area scaling empirical relationship of the form $V_L^2 = \varepsilon A_L^b$, (Guzzetti *et al.*, 2009; Larsen *et al.*, 2010). The surface areas (A_L) and volumes ($V_L{}^2$) of the mapped deposits in the Milford Sound/Piopiotahi catchment (in m^2 and m^3 respectively) from Dykstra (2012) were used to derive exponents ε and b. The calculated A_L and volumes $V_L{}^1$ for the modelled subaqueous deposits ($n=5$) were supplemented in the analysis. The volume-area scaling relationship was fit with a least trimmed squares linear fit ($R^2 = 0.9$) yielding exponents of $\varepsilon = 0.043$ and $b = 1.43$ (Guzzetti *et al.*, 2009).

4.3.2.1. Morphometric error estimations

The primary error related to the mapping of the deposits was manual digitiser error. Quantification of the digitisation error was computed through repeated manual digitisation of the deposits over 6 concurrent days and computing variations in the surface areas (Korup, 2005a). The maximum relative error computed was +13/-7%. Therefore a maximum error of ±13% was applied to all the deposit planimetric (A_{plan}), and surface areas (A_L). Obscuration or burial of parts of the deposit by post-event sediment drape may also introduce error (cf. Haeussler et al., 2018), but with the available data, these cannot be assessed and/or quantified. Lower and upper bounds for the estimated deposit volumes derived by volume-area scaling ($V_L{}^2$) were then derived using the corresponding estimates for (A_L). The errors related to many

of parameters measured are primarily due to the spatial data resolution (Clare *et al.*, 2018). The maximum horizontal error for the NIWA bathymetric BTM is 3 m. Deposit lengths (L_d), and widths (W_d) are measured between 2 points, the overall error for these measurements is ±6 m. The error related to runout (L_{max}) was estimated by combining the terrestrial DEM and bathymetric BTM horizontal errors, giving an overall horizontal error of ±56 m. The error estimations for the drop height (H) and maximum drop height (H_{max}) were calculated by combining the RMSE of the NZSoSDEM (±7.1 m), and the maximum vertical error from NIWA BTM (1±2% depth). The maximum vertical error was taken from the greatest depth (290 m.b.s.l.). Therefore the maximum error from the bathymetric BTM is 1±5.8 m. Both errors combined and averaged gives an overall error of ±13 m. Upper and lower bounds for the estimated apparent friction coefficient (H/L_{max}) were derived by using the corresponding estimates for the drop height (H) and total runout (L_{max}).

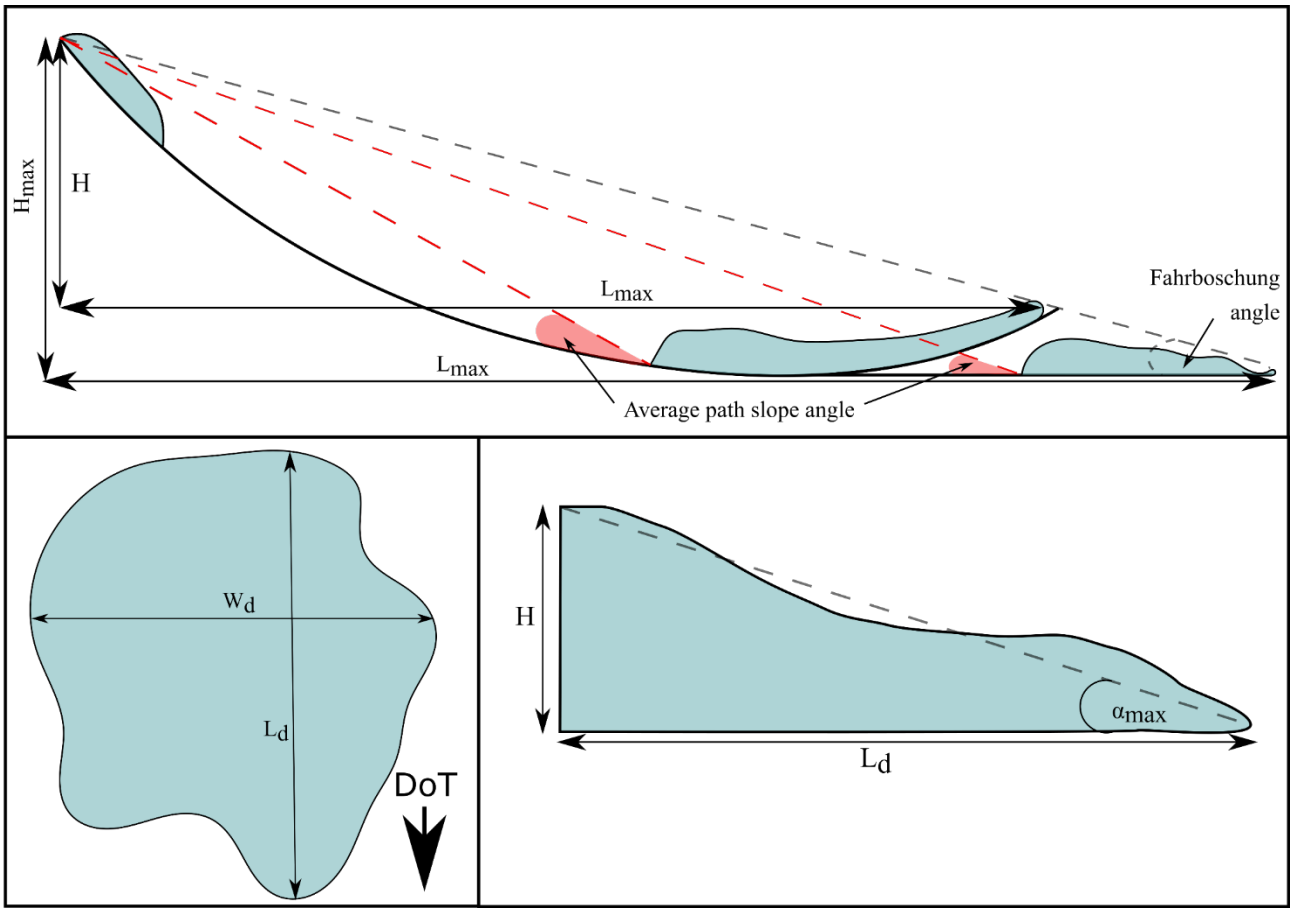

Figure 4.2. Schematic of landslide morphometric parameters recorded. Top panel modified from Strom *et al.,* (2019). DoT= direction of travel.

Table 4.1. Summary of morphometric parameters collected in this study

Parameter		**Description**
Maximum drop height	H_{max}	Elevation difference between crown of the source headscarp and lowermost point of the deposit (in metres).
Drop height	H	Elevation difference between crown of the source headscarp and the most distal point of the deposit (in metres).
Total runout	L_{max}	The Euclidean distance generated along a centreline between crown of the source headscarp and the most distal point of the deposit (in metres).
Average slope angle (°)	-	The average gradient and corresponding angle between the highest point in the source area to the highest point of the STS landslide deposit.
Depositional path slope angle (°)	-	The average gradient from a profile from unaffected fjord bottom adjacent to the deposits.
Deposit length	L_d	The Euclidean distance generated along a centreline between the highest point and the most distal point of the deposit (in metres).
Maximum deposit width	W_d	The maximum width perpendicular to the deposit length minimum bounding rectangles (in metres).
Planimetric area	A_{plan}	The 2D planimetric area of the mapped landslide deposit (in m^2).
Surface area	A_L	The area of the mapped landslide deposit over the bathymetric surface of the deposit (in m^2).
Maximum regional slope (°)	α_{max}	The inverse tangent of the vertical difference of the deposit over its length as in Pinet *et al*. (2015) and Deering *et al.* (2018).
Apparent friction coefficient	H/L_{max}	Ratio of the drop height to overall runout length.
Fahrböschung (°)	F	Calculated as the inverse tangent of the ratio of the drop height to overall runout length ($\tan^{-1}(H/L_{max})$).
Volume	V_L^1	Calculate as the volumetric difference from pre and post DEMs using Cut Fill analysis (in m^3).
	V_L^2	Calculated using volume-area scaling empirical relationship $V_L=\varepsilon A_L^b$ (in m^3).

4.3.3. Numerical Runout Modelling

There are many numerical landslide runout models that have been developed in the last two decades (Table 4.2 (McDougall, 2017)). The more advanced models now integrate 3D topographic data, meaning that landslide runout and deposition can be simulated over complex terrain, allowing spatial analysis of the model results. Some numerical models base the input parameter values on measured physical properties of landslide materials derived from field or laboratory analysis (Iverson and George, 2014). These models represent a move towards a more mechanistic-based runout analysis (McDougall, 2017). However, smaller-scale laboratory analyses that derive material parameters may be invalid when applied to full-scale landslide events (McDougall and Hungr, 2004). Similarly, replication of field-scale physical properties in the laboratory can be challenging (McDougall, 2017). Furthermore, the material properties of STS deposits are rarely constrained with the exception of a few studied deposits where cores have been extracted (Tripsanas *et al.*, 2008). However, for large STS RSF deposits, core extraction can be difficult due to the blocky, coarse nature of the deposits (Expedition Scientists, 2012; Le Friant *et al.*, 2015).

Most numerical runout models however, use a calibration-based approach (McDougall *et al.*, 2012; McDougall, 2017). In a calibration-based approach, the basal rheological parameters are systematically adjusted through trial-and-error or statistical back-analysis of full-scale observed landslide events (McDougall *et al.*, 2012; McDougall, 2017). Successful calibration is achieved when the simulated landslide is able to match, or is in close agreement with, observed external geometrical properties of the case-studied landslide (Hungr, 1995; McDougall and Hungr, 2004; McDougall *et al.*, 2012). The properties include runout distance, depositional areal distribution, deposit material thicknesses, velocities, and emplacement durations (McDougall *et al.*, 2012). The assessment of the model output is typically in that order of priority due to decreasing availability and/or reliability of observed data (McDougall *et al.*, 2012). Calibration-based approaches use relatively simple rheological models that provide apparent calibrated parameters, rather than capturing actual micromechanical material properties (McDougall and Hungr, 2004). Therefore, calibration-based models can be seen as semi-empirical models (McDougall, 2017). However, such models can simulate the bulk behaviours of the landslides which is often the main aim in in runout analysis and forecasting (McDougall, 2017). A criticism of models that use empirical calibration however, is that tuning of parameters has questionable physical significance (Iverson, 2003). This criticism can be valid when modelling single case examples, as the calibration can show model adaptability rather than accuracy

(Iverson, 2003; McDougall *et al.*, 2012). Therefore for prediction and forecasting purposes, calibration should seek consistent patterns of rheology type and ranges of parameter values that reproduce the behaviour of groups of similar events (McDougall, 2017; Benjamin *et al.*, 2018).

Several of the most used models are summarised in Table 4.2. Most of the models share several similarities. These similarities include: adopting the Savage and Hutter (1989) depth-averaged equations (DAEs) (McDougall, 2017); being single-phase models (SPMs); adopting either a Eulerian or Lagrangian reference frame; and use a calibration-based approach (McDougall, 2017). Eight of the numerical models in Table 4.2 (excluding D-Claw, MassMov2D, r.avaflow, and VolcFlow) were assessed against case landslide runout studies in a benchmark workshop (Hungr *et al.*, 2007). Some model comparisons showed that, despite different reference frames (i.e. Eulerian or Lagrangian), using the same basal rheologies and similar input parameters produced similar model results (Hungr *et al.*, 2007). However, Eulerian frames encounter difficulties modelling long runout landslides with large amounts of deformation as Eulerian frames use a fixed special mesh (Yavari-Ramshe and Ataie-Ashtiani, 2016). In such landslide cases, a Lagrangian frame, particularly meshless, is better suited as a Lagrangian frame is commonly attached and moves with the landslides, therefore avoiding excessive distortion (Crosta *et al.*, 2006; Mckinnon, 2010; Yavari-Ramshe and Ataie-Ashtiani, 2016).

With the exception of the TOCHNOG model, motion in the DAE models in Table 4.2 is governed primarily by depth-integrated Saint-Venant equations of shallow, unsteady flow (Savage and Hutter, 1989; McDougall and Hungr, 2004; McDougall, 2006). The SPMs treat the landslide material as a homogenous “equivalent fluid” (Hungr, 1995). An equivalent fluid is a hypothetical material, controlled by a simple internal rheology, which replaces the complex and heterogeneous nature of the landslide material. The equivalent fluid allows for simulation of the bulk external behaviour of the flowing landslide body (Hungr, 1995; McDougall and Hungr, 2004). The data available for validating model outputs in this study are from the morphometric and geometric parameters constrained from the deposits within the MBES data (section 4.3.2). Therefore a numerical model utilising a calibration-based approach represents the most appropriate application to simulate the landslide runout.

Table 4.2. Summary of commonly used dynamic landslide runout models

Model	Model Dim.[1]	Gov. Eqn.	Rheologies	Reference frame	Variation of Rheology	Entrainment rate	Phase	Reference
				Continuum Integrated				
3dDMM	3D	DAE	Frictional, Voellmy,	Eulerian	yes	Defined	SPM	(Kwan and Sun, 2007)
DAN	2D	DAE	Frictional, Voellmy, Bingham, Newtonian, Plastic	Lagrangian meshless	yes	Defined	SPM	(Hungr, 1995)
DAN3D	3D	DAE	Frictional, Voellmy, Bingham, Newtonian, Plastic	Lagrangian meshless	yes	Defined	SPM	(McDougall and Hungr, 2004)
D-CLAW	3D	DAE	Coulomb	Godunov	no	No entrainment rate is used	MPM	(George and Iverson, 2014; Iverson and George, 2014)
FLATModel	3D	DAE	Bingham, Voellmy, Herschel-Bulkley	Eulerian	no	Process based	SPM	(Medina *et al.*, 2008)
MADFLOW	3D	DAE	Frictional, Voellmy, Bingham	Lagrangian mesh	no	Defined	SPM	(Chen and Lee, 2003)
MassMov2D	3D	DAE	Frictional, Voellmy, Bingham, Coulomb	Eulerian	yes	Defined	SPM	(Beguería, Van Asch, *et al.*, 2009)
r.avaflow	3D	DAE	Savage-Hutter Model	NOC	no	No entrainment rate is used	MPM	(Mergili *et al.*, 2017)

Table 4.2. continued

Model	Model Dim.[1]	Gov. Eqn	Rheologies	Reference frame	Variation of Rheology	Entrainment rate	Phase	Reference
				Continuum Integrated				
RAMMS	3D	DAE	Voellmy, random kinetic energy	Eulerian	yes	Process based and defined	SPM	(Christen *et al.*, 2010)
RASH3D	3D	DAE	Frictional, Voellmy, Pouliquen	Eulerian	no	No entrainment rate is used	SPM	(Pirulli, 2005)
TITAN2D	3D	DAE	Frictional	Lagrangian meshless	no	No entrainment rate is used	SPM	(Pitman *et al.*, 2003)
VolcFlow	3D	DAE	Frictional, Voellmy, Plastic	Eulerian	no	No entrainment rate is used	SPM[2]	(Kelfoun and Druitt, 2005) (Kelfoun, 2011)
				Continuum Differential				
TOCHNOG	3D	NSE	Frictional (elastoplastic model)	Differential (adaptive mesh)	yes	Process based	SPM	(Crosta *et al.*, 2003)

Model Dim – Model Dimensions; Gov. Eqn – Governing Equations; DAE – Depth-Averaged Equations; NSE – Navier Stokes Equations; NOC- Non-Oscillatory Central; SPM – Single Phase Model; MPM – Multi-Phase Model

[1] dimension refers to the topography in which the models simulate landslide runout over, whether a 2D path or 3D surface (McDougall *et al.,* 2012); [2] VolcFlow has both a one and two fluid version. The two fluid models both landslide and surrounding water, but both are treated as independent unlike in other MPMs

4.3.3.1. DAN3D

In this study, a subset of the STS landslides were modelled using the numerical code DAN3D (McDougall and Hungr, 2004; McDougall, 2006). DAN3D is a depth-averaged, quasi-3D, SPM extension of the 2D DAN model developed by Oldrich Hungr (Hungr, 1995). DAN3D is, therefore, capable of simulating landslides of varying types over complex topography. The model adopts a meshless Lagrangian numerical method adapted from Smoothed Particle Hydrodynamics (SPH) to solve the depth-integrated Saint-Venant equations of shallow, unsteady flow (McDougall and Hungr, 2004; McDougall, 2006). DAN3D was used in this study as it is one of the models from Table 4.2 that adopts a calibration-based approach. DAN3D also allows for user-defined, variable basal rheologies along landslide travel paths. Rheological changes are important when considering changes in either the runout path material (e.g. bedrock, snow/ice, saturated and unsaturated substrates (Aaron and McDougall, 2019)), or possibly the surrounding medium (e.g. air to water) (Mazzanti and Bozzano, 2009, 2011). DAN3D also allows estimations of entrainment and has greater choice of basal rheologies available compared with many of the available models. Recent extensions of DAN3D have incorporated an initial coherent sliding stage of the landslide before it spreads, improving simulations, with little or no alteration of basal rheological parameters (Aaron and Hungr, 2016b). Additionally, objective calibration methods have been developed exclusively for DAN3D (Aaron *et al.*, 2019).

DAN3D has been successfully used to back analyse a wide range of rapid landslides, including debris flows (Schraml *et al.*, 2015; Gao *et al.*, 2017), debris avalanches (Dahl *et al.*, 2013), volcanic debris avalanches (VDAs) (Sosio, Crosta and Hungr, 2012), and rock avalanches (Delaney and Evans, 2015; Nagelisen *et al.*, 2015; Aaron and Hungr, 2016a). DAN3D is also one of the few models in Table 4.2 that has been used, and/or adapted, to simulate the runout of STS rock avalanches. The STS rock avalanche examples include contemporary (Si *et al.*, 2018), historical (Mazzanti and Bozzano, 2011), and palaeo events (Mazzanti and Bozzano, 2009; Schleier *et al.*, 2017). Whilst VolcFlow has been used to simulate the full runout of STS VDAs (Giachetti *et al.*, 2011; Kelfoun, 2011), the model does not allow for changes in rheology along the runout path. An iteration of the D-Claw model has been used to simulate an STS landslide and tsunami (George *et al.*, 2017). However, the modelled landslide runout has not yet been compared against available MBES and seismic reflection data of the deposit (cf. Haeussler *et al.*, 2018). Similarly, D-Claw requires material properties for calibration, which are unknown for the deposits in the fjord.

4.3.3.2. Rheological Equations

DAN3D considers a fixed internal rheology for the moving mass, which is governed by an internal friction angle, ϕ_i. This internal rheology is assumed to be frictional and separate from the basal rheology that is applied at the slide plane (McDougall, 2006). The internal friction angle is assumed to be different to the basal friction angle, allowing for both basal resistance and the internal strength to be accounted for (Savage and Hutter, 1989; McDougall and Hungr, 2004; Aaron and Hungr, 2016a). This accounts for non-hydrostatic, anisotropic internal stresses and pressures that can develop in a moving mass (Hungr and McDougall, 2009). These internal properties are represented through the passive and active earth pressure coefficients:

$$k_{x(min/max)} = 2\left(\frac{1\pm\sqrt{1-\cos^2\phi_i(1+k_{zx}^2)}}{\cos^2\phi_i}\right)-1 \qquad [4.1]$$

where $k_{x(min/max)}$ is the earth pressure coefficient, and k_{zx} is the ratio of basal shear stress to total normal stress (Hungr and McDougall, 2009). The minimum values occur when flowing mass is stretching (active) and maximum values correspond to the compression (passive) of the flowing mass (Hungr and McDougall, 2009).

The resistance to landslide motion is factored by the basal shear stress, τ_{zx} (Hungr and McDougall, 2009). In equivalent fluid models, τ_{zx} is governed by the basal rheology chosen for the landslide. A number of basal rheologies have been invoked in simulating landslide propagation including frictional (Sosio *et al.*, 2008; Grämiger *et al.*, 2016), Voellmy (Sosio, Crosta, Chen, *et al.*, 2012), plastic (Kelfoun and Druitt, 2005; Manzella *et al.*, 2016; Benjamin *et al.*, 2018), and Bingham (Hungr and Evans, 1996; Kelfoun, 2011). These rheologies are available for selection in DAN3D. The basal rheologies are independent of the internal rheology and may be different to one another. In this study, the frictional and Voellmy rheologies were used for the runout simulations. Frictional and Voellmy rheologies appear the most representative for granular flows (McDougall, 2006; Giachetti *et al.*, 2011). Additionally, such rheologies are the most widely used rheologies in published simulations (Yavari-Ramshe and Ataie-Ashtiani, 2016). This has the added advantage that a broad rheological envelope of key parameter values are available for differing landslide types (Sosio *et al.,* 2008) and substrates (Aaron and McDougall, 2019). Although successfully used, the plastic rheological model generally exhibits deposition along almost the full extent of the propagation area (Sosio, Crosta and Hungr, 2012; Benjamin *et al.*, 2018). In contrast, here each prototype case exhibits a clear deposit at the base of the slope only i.e. full evacuation occurred (Figure 4.3).

The frictional rheology assumes that τ_{zx} is dependent only on the effective bed-normal stress, σ_z. This equation is expressed in DAN3D as:

$$\tau_{zx} = -\sigma_z(1 - r_u)\tan\phi \quad [4.2]$$

where ϕ is the dynamic basal friction angle, and r_u is the pore-pressure ratio. The pore pressure ratio is derived as the basal pore fluid pressure u, normalised by the bed-normal stress σ_z, such that $r_u = u/\sigma_z$. If r_u is constant, then the frictional rheology in Equation 4.2 can be alternatively expressed by only one independent variable, the bulk basal friction angle, ϕ_b, where:

$$\phi_b = \arctan(1 - r_u)\tan\phi \quad [4.3]$$

which can be simplified as:

$$\tau_{zx} = -\sigma_z \tan\phi_b \quad [4.4]$$

Therefore, resistance to motion in a frictional rheology is effectively controlled by the basal friction angle. Estimating the pore pressure in a moving landslide is difficult, as it is coupled to changes in the total normal stress in the material (Hungr and McDougall, 2009). Assuming a constant r_u implies that partial drainage occurs during the landslide flow, or a combination of purely undrained and liquefied material, and coarser, undrained material (Hungr and McDougall, 2009; Aaron and Hungr, 2016a). Frictional rheological models often produce forward-tapering deposits, and relatively high, sometimes overestimated, peak velocities (McDougall, 2006, 2017).

The Voellmy rheology introduces a velocity-dependent component, combining frictional and turbulence behaviour:

$$\tau_{zx} = -\left(\sigma_z\mu + \frac{\rho g v_x^2}{\xi}\right) \quad [4.5]$$

where μ is the friction coefficient. The friction component of the Voellmy rheology assumes τ_{zx} is dependent on σ_z, as in Equation 4.2 (μ is analogous to tan ϕ). The Voellmy rheology introduces the turbulence parameter, ξ: a term that empirically accounts for all factors of velocity-dependent flow resistance along a landslide path (McDougall and Hungr, 2004; Sosio, Crosta and Hungr, 2012). It is expressed as the square of the velocity,v, the density of the material, ρ, and the gravitational acceleration, g (Hungr and McDougall, 2009). Using a Voellmy rheology often produces a more uniform thickness distribution of deposit material, and, lower peak velocities due to the influence of the turbulence parameter (McDougall, 2017).

4.3.3.3. DAN3D Input Data

Five of the STS deposits were selected for runout modelling that fit a set of criteria. The criteria include: (i) clearly defined deposit extents to reduce model validation uncertainty; (ii) a clearly defined source area that is discernible as the only likely source for the associated deposit, to mitigate as much uncertainty in all the modelled results; (iii) morphology and geometry of the deposits were representative of those in the fjord; and (iv) encompass the range of deposit volumes. This eliminated several deposits, whose boundaries are contiguous and so may be overlapping. The criteria also excluded deposits whose extents and morphologies are likely to have been heavily affected by post-event sediment drape and/or fan build-up.

DAN3D requires an elevation grid file as an input that includes a pre-failure path topography, isolated source depths, and an erosion map grid. Each grid file was made using DEMs. The bathymetric BTM was resampled by bilinear interpolation to the same spatial resolution as the terrestrial DEM (15 m). Both models were merged to create a continuous subaerial-subaqueous fjord DEM, representing the post-event topography. No pre-failure topography, or direct measurements of deposit thickness are available for any of the deposits in the fjord bottom. To reconstruct the pre-failure topography in all cases, a similar approach to Paris et al., (2011), Conway and Balme (2014), and Nagelisen et al., (2015) was used. Modification of the available terrain data was done by manually adjusting the deposit and source area contours of each modelled case. The deposits were erased from the original DEM and the topographic contours from adjacent, unaffected subaqueous fjord walls and basin floor were extended across the deposit area. The pre-event bathymetry contours were then interpolated using the 'Topo to Raster' (ANUDEM algorithm) method on the adjacent bathymetric and modified contours in ArcMap 10.5. The pre-failure topography over the deposit areas were mosaicked back into the original bathymetric BTM. Rock unit weights were derived from the New Zealand Petlab database values (Tenzer *et al.*, 2011; Strong *et al.*, 2016), based on the geological information obtained from the 1:250,000 Geological Map of New Zealand (QMAP) for the source areas (Turnbull *et al.*, 2010).

The volumes for each modelled case were derived from the deposit. This accounted for any bulking of landslide material through its motion and propagation due to processes such as fragmentation (Aaron and Hungr, 2016a; Benjamin *et al.*, 2018) or entrainment. DAN3D cannot simulate the bulking process by fragmentation. Entrainment of material in either the subaerial or subaqueous environment was not considered in the runout modelling along the runout path. This process may have occurred, but there are no data available to quantify entrainment.

Therefore the contours of each source area were adjusted until the source and deposit volumes matched. This assumes the sliding material bulks instantly at the point of failure and that the landslide involves only a single release of material (Aaron and Hungr, 2016a). The volumes of each modelled case were calculated using Cut Fill in ArcGIS ArcMap by subtracting the reconstructed pre-failure topography from the post-event bathymetric BTM. The volumes were compared against the likely source volume by extending the contours over their extent and interpolating a plausible pre-event surface. Isolated source depths were extracted by subtracting the filled source area grid from the post-failure path grid. Uncertainty and error in the derived deposit volumes was quantified by calculating the RMSE of the interpolated DEMs, relative to the original DEM. The RMSE value derived (±0.6 m) was multiplied by the deposit surface area. This yielded lower and upper volume bounds on both the deposits, and source areas.

Calibration of the modelled events was done using a trial-and-error procedure. The basal rheological parameters were manually adjusted until the simulated landslide matched, or was in close agreement with, some of the calculated morphometric parameters. The properties include runout distance (L_{max}), planimetric and surface areas (A_{plan} and A_L), and then derived values for apparent friction coefficients (H/L_{max}) and respective fahrböschung angles. Velocities are typically constrained by super elevation measurements (e.g. Evans *et al.,* 1994), seismic records (e.g. Pedersen *et al*., 2002), or video evidence (e.g. Sosio *et al.*, 2008; Hancox and Thomson 2013; Dunning *et al.*, 2015). The lack of historical and observable data for the deposits in the fjord makes constraining event duration, velocity profiles and emplacement times difficult. Velocities were therefore assessed by comparison with known velocity ranges from published literature (c. 30 – >100 m s^{-1}) (Dufresne *et al.*, 2016). Deposit thickness distribution was also assessed but due to the lack of available seismic reflection data, thicknesses were derived by subtracting the interpolated pre-failure topography from the original post-failure DEM. Whilst there is uncertainty with the interpolated pre-event topography, the relative RMSE of those DEMs (± 0.6 m) have negligible effect on the overall derived thicknesses. The best fit calibrated parameters of each modelled landslide were then run on the other respective cases. This was done as a means to assess the transferability of the parameters, which can be useful for predictive modelling of future events (Benjamin *et al.*, 2018). A total of 346 models were run across the 5 cases. The models were run until the deposit fully came to rest or, were run until velocities were low (≤ 2 m s^{-1}). In those instances, there was only small internal movements of the model material that did not cause forward

propagation of the leading deposit edge. Therefore did not affect the overall runout length of the deposit. In those cases, the models were stopped manually (cf. Delaney and Evans 2014).

4.4. Results

4.4.1. STS landslide deposit geomorphology

From re-mapping on the fjord bathymetry, the number of previously identified STS landslide deposits is revised upwards to 35 from the 26 initially identified by Dykstra (2012) (cf. Figure 4.3 and Figure 4.1). Some of the previously identified deposits by Dykstra (2012) are considered and mapped here as more representative of subaqueous fan deltas found in fjords, with linear and concave profiles and smooth surficial morphology (Gales *et al.*, 2019). Many are situated at the mouth of terrestrial fluvial systems within subaerial valleys (Figure 4.3). There is also evidence of crescentic bedform features within channels coming off the Cleddau Delta, and within the deltaic system in Entrance Basin. These bedform features are likely sediment dunes that represent cyclic steps and their associated deposits from supercritical turbidity flows, causing repeated hydraulic jumps down the channel (Hage *et al.*, 2018; Heijnen *et al.*, 2020). Debris talus cones are also identifiable along the base of the fjord walls, and align to where the aerial imagery shows shallow, regolith failures have occurred on the subaerial fjord walls; and a large, prominent deltaic collapse from the Harrison River delta in the fjord. These were previously identified by Dykstra (2012) and are not discussed in further analysis.

The STS landslides identifiable on the BTM exhibit a clear topographic expression on the fjord bottom. The deposits can be categorised into two groups. The first group are small-scale, smooth surfaced, conical features with limited runout. These deposits are mapped and categorised as scree cones, most likely because of subaerial rockfalls and/or regolith failures from the fjord wall. Some, but not all, of these deposits were initially mapped by Dykstra (2012) and are not discussed further.

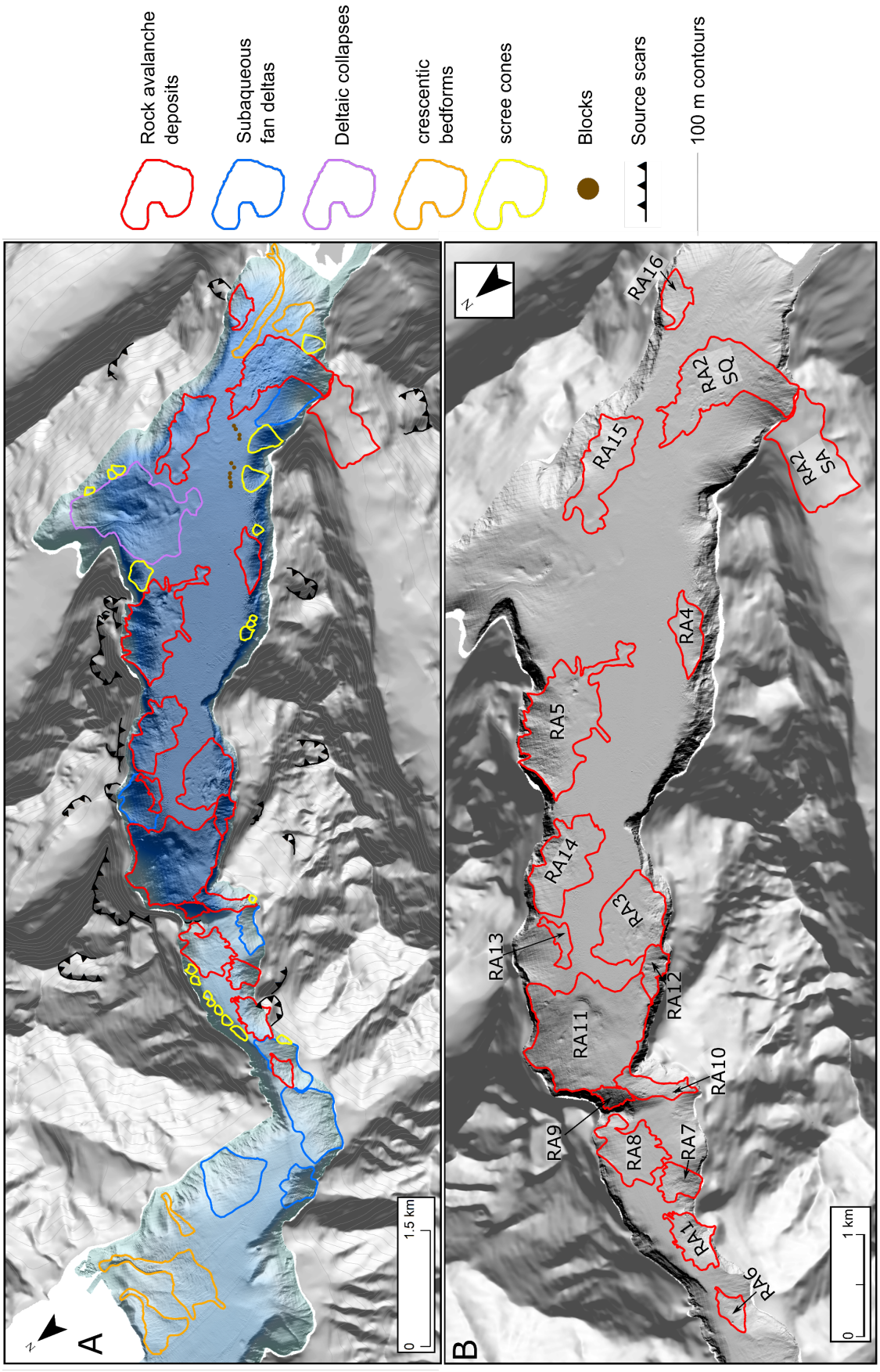

Figure 4.3. Geomorphological map of Milford Sound/Piopiotahi fjord bottom (A). The ID of the rock avalanche deposits are illustrated in Panel B.

The other category of deposits consists of 16 large-scale deposits from catastrophic RSFs (Figure 4.3B). Most of the deposits exhibit a blocky boulder carapace, though this is more pronounced on some deposits, with some showing a smoother surficial morphology. The full extents of deposits RA6 and RA13 appear masked by fan overprinting (Figure 4.4D, G). Only a small area (c.76 000 m^2 and c.65 750 m^2) of the boulder carapace is identified at the distal ends of the fan for RA6 and RA13 respectively. From the morphology, the deposits are inferred as likely rock avalanche deposits (Figure 4.3B). The deposit geometries can be categorised as two types and appear to be either: (1) those with a cone-shaped morphology, that are likely proximally thick, and thinning with distance from the source (RAs 1,4-9,11-16); and (2) irregular, where the apparent thickness is variable, and appears to be independent from distance from the source (RAs 2, 3, 10). RA9 is the sole subaqueous source, caused by a partial collapse of the bedrock sill that marks the boundary between Dale and Stirling Basin. The deposit RA2 appears to be likely part of the same event that emplaced the subaerial deposit in the lower reaches as Sinbad Gully identified by Dykstra (2012). There does not appear to be an obvious separate subaerial source scar that would have deposited RA2 in that location. Similarly, there is no identifiable subaqueous source scar that would indicate a margin collapse. Furthermore, the morphology of RA2 is also inconsistent with a deltaic collapse when compared to the deposit at Harrison Delta, and elsewhere (e.g. Prior *et al.*, 1982; Hilbe & Anselmetti, 2014). Therefore, the morphometric analysis (4.3.2) and numerical modelling back analysis (4.3.3) assumes that these deposits originated from a single event. Many of the source areas have previously been demarcated and identified by Dykstra (2012) as planar failures along steep rock faces. Many extend towards the ridge crests, whilst some involve the whole valley side, extending to sea level e.g. RA 5 and 11.

Several morphological features are identified on the deposit surfaces (Figure 4.4, Appendix A). On 7 of the deposits, probable perpendicular to flow ridges were detected (Figure 4.4A-D, F). The ridges are discontinuous across the width of the deposits. Beyond the extent of the bulk of the RA4 deposit, 7 isolated blocks are visible, ranging in area from 144 – 1610 m^2. It is unknown whether these blocks are related to the emplacement of RA4 as the area between the mapped deposit extent and the blocks is largely flat with no positive bathymetric expression. Therefore, the blocks are mapped as independent of RA4, and the morphometric analysis and model calibration is conducted using the bulk deposit. Some aligned blocks are visible on the surface of the subaqueous portion of RA2 (Figure 4.4F). Beyond the mapped extent of RA2 are several blocks that appear to form a sinuous line, heading down from the RA2 deposit into Stirling

Basin. With the present data availability, it cannot be ascertained if the blocks are part of the RA2 event. The blocks are mapped but are also treated as independent from the mapped extent of RA2 for the morphometric analysis and calibration of the modelling. Twenty-five blocks scattered across the fjord bottom in the middle and distal reaches of the RA3 deposit were also mapped. The blocks range in length, width, and area, with the largest block 220 m long, c. 117 m wide, with a surface area of 17 156 m^2 (Figure 4.5A, C). There are several blocks (*n=18*) in the western half of the deposit. Most of the blocks here are aligned perpendicular to the main flow direction (024° N) ((Figure 4.5B) and show a weak trend of decreasing area with distance from the source (Figure 4.5C). There is evidence of a small, raised (1 m high) smooth-surfaced concentric-shaped ring at the eastern distal end of the deposit on the fjord bottom (Figure 4.4A), and a prominent elongated ridge/frontal lobate feature extends southwards from the bulk of the deposit which demarcates the most distal reach of RA5 deposit.

.

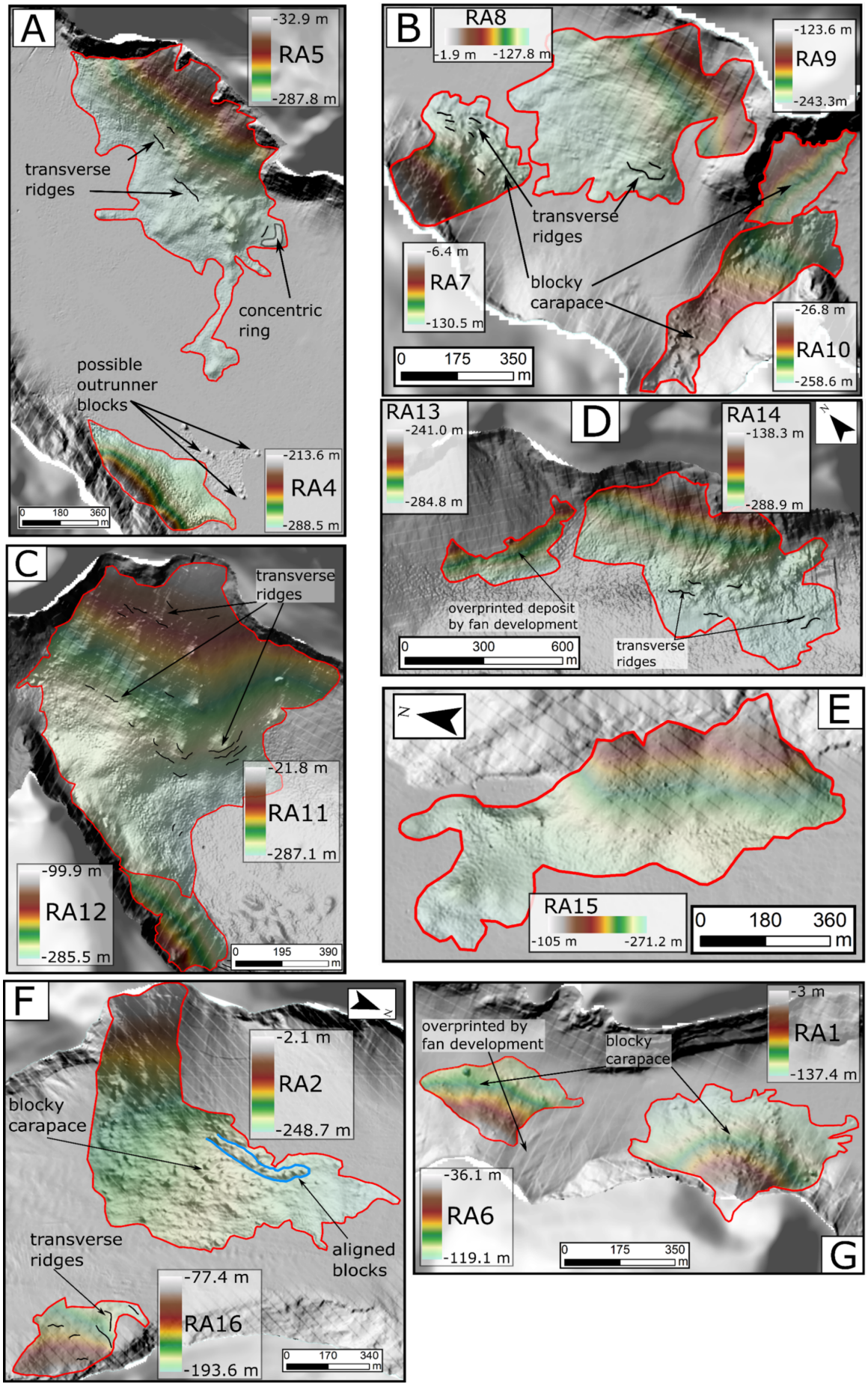
A
-32.9 m
RA5
-287.8 m
transverse ridges
concentric ring
possible outrunner blocks
-213.6 m
RA4
-288.5 m
0 180 360 m
B
RA8
-1.9 m -127.8 m
-123.6 m
RA9
-243.3m
transverse ridges
blocky carapace
-6.4 m
RA7
-130.5 m
-26.8 m
RA10
-258.6 m
0 175 350 m
C
transverse ridges
-21.8 m
RA11
-287.1 m
-99.9 m
RA12
-285.5 m
0 195 390 m
D
RA13
-241.0 m
-284.8 m
RA14
-138.3 m
-288.9 m
N
overprinted deposit by fan development
transverse ridges
0 300 600 m
E
N
RA15
-105 m -271.2 m
0 180 360 m
F
N
-2.1 m
RA2
-248.7 m
blocky carapace
transverse ridges
aligned blocks
-77.4 m
RA16
-193.6 m
0 170 340 m
G
overprinted by fan development
blocky carapace
-3 m
RA1
-137.4 m
-36.1 m
RA6
-119.1 m
0 175 350 m

Figure 4.4. Overleaf. Morphological features, predominately diagnostic features (transverse ridges, aligned blocks, concentric ring features, blocky surface carapace) of the rock avalanche deposits, clockwise from top left: (A) RA4 and RA5; (B) RA7-RA10; (C) RA11 and RA12; (D) RA13 and RA14 (E) RA15 (F) RA2 and RA16; and (G) RA1 and RA6. Detailed view of each deposit, including source areas, is available in Appendix A.

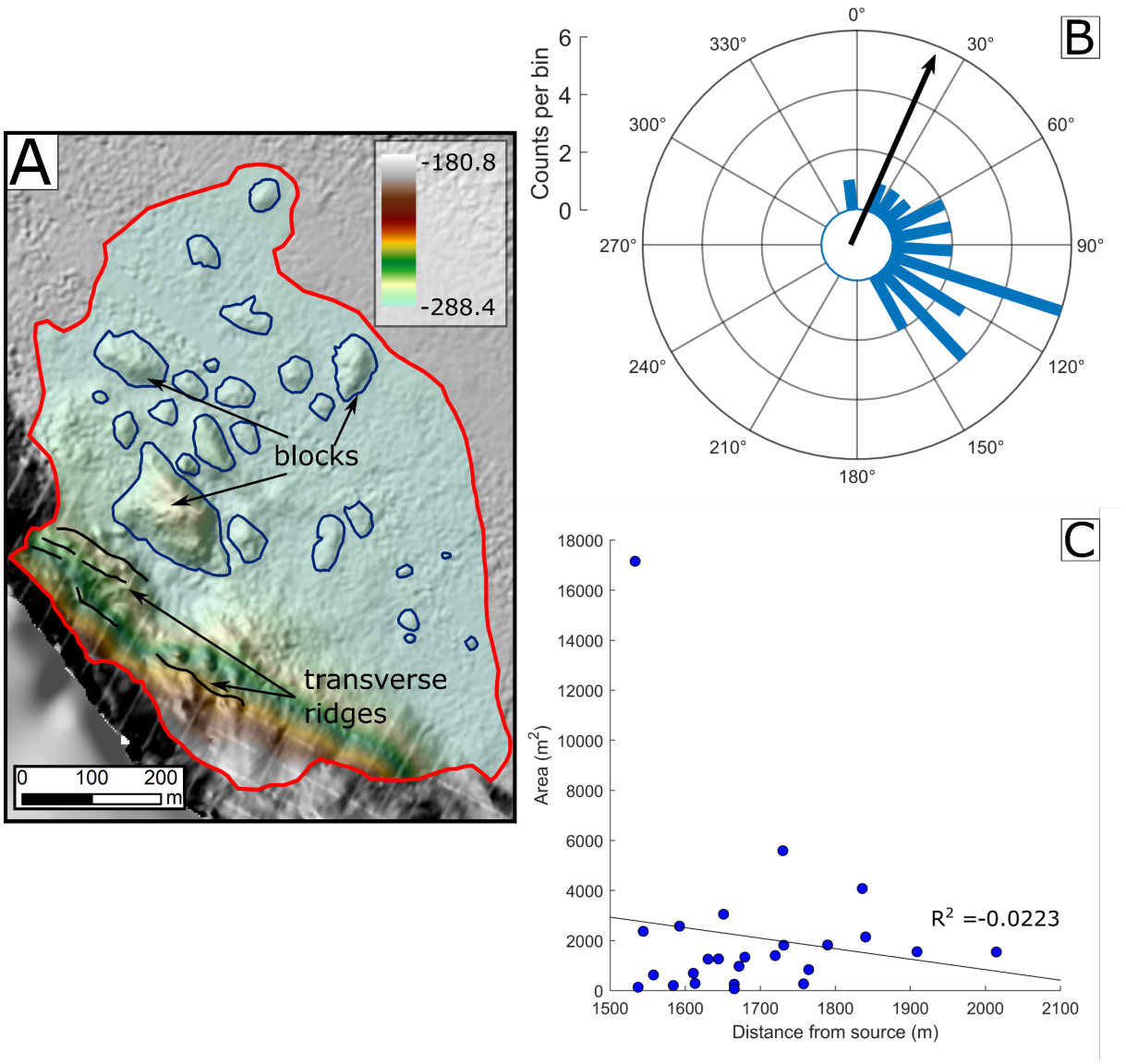

Figure 4.5. (A) Morphology of deposit RA3; (B) polar histogram showing orientation of the blocks' long axes against average flow direction (024°N); (C) scatter plot of block area (in m^2) against distance from source. R^2 value from least squares linear regression.

4.4.2. Morphometric characteristics

The morphometric data of the rock avalanche deposits, and full events, are presented in Table 4.3 and Table 4.4 respectively. Additionally, summary statistics are presented in Table 4.5. The morphometric data illustrates that the rock avalanches vary significantly in maximum runouts (L_{max}) from 314 m to > 3400 m. RA1 has the shortest runout of all the STS rock avalanches. Only RA9, which is the only fully subaqueous event that involved the partial collapse of the

bedrock sill, has a smaller height drop and shorter runout. However, as it is a rock avalanche event that overlaps with the deposits of RA10 and RA11, the exact runout is uncertain. The H/L_{max} data of the rock avalanche deposits range from 0.46 (RA2 when considering the subaerial and subaqueous component as a single event) to 0.89 (RA14). Their corresponding fahrböschung angles are also the lowest and highest respectively. The source area of RA6 could not be ascertained with any level of confidence, therefore much of the morphometric data on the landslide event are missing. The rock avalanches descended steep path slopes with a mean angle of 52.2˚, and with 10 of the 16 deposits having originated from slopes >50˚on average. Twelve of the 16 rock avalanches deposit onto a largely flat fjord bottom floor (mean slope 3.3°). The depositional slope for RA2 and RA16 is slightly steeper at 4.2° and 5° respectively, as they are deposited at the shallowing end of the fjord near the Cleddau Delta. RA10 has the steepest slope of all deposits at 15.8°, as the deposit spans a slope that separates Dale and Entrance Basin. The volume-area scaling relationship derived gave a range of volumes for the subaqueous deposits between $2.9x10^5$ (RA9) to $1.7x10^7$ m^3 (RA11). However, the scaling relationship appears to overestimate volumes of 'type 2' deposits. The volumes of RA2 (based on combined subaerial and subaqueous areas) and RA3 are over by 150% and 100% respectively, compared to their volumes calculated from the numerical modelling analysis (Table 4.6). Comparison of volume-area scaling on the subaerial and subaqueous deposit of RA2 indicates that the large area (0.67 km^2) and the relatively thin subaqueous deposit causes the error in the scaled deposit (Table 4.3). The scaling relationship for the subaerial portion of the deposit underestimates its calculated volume by <10%, which is within the 13% error range derived from the error calculated on the pre-post DEM analysis (Table 4.6). However, the volume of the subaqueous deposit is overestimated by >75% compared to the volume calculated in the model file set up. Similarly, the deposit area and morphology of RA3 is characterised by several large hummocks/blocks that extend up from the fjord floor, creating an irregular thickness over the deposit area. The deposit geometries in terms of L_d/W_d ratio show a mean ratio of 1.13, and median ratio of 0.97 for the deposits (Table 4.5). 9 of the deposits have ratios <1, indicating that they are wider than their respective lengths.

Table 4.3. Morphometric attributes of Milford Sound/Piopiotahi STS rock avalanche deposits and associated error

ID	A_{plan} (m^2)	error (m^2)	A_L (m^2)	error (m^2)	V_L[1] (m^3)	V_L[1] Error (m^3)	V_L[2] (m^3)	V_L[2] upper bound (m^3)	V_L[2] lower bound (m^3)
1	1.65×10^5	$\pm 2.15 \times 10^4$	1.91×10^5	$\pm 2.48 \times 10^4$	3.14×10^6	$\pm 1.1 \times 10^5$	1.48×10^6	1.76×10^6	1.21×10^6
2 (SA)	5.08×10^5	$\pm 6.60 \times 10^4$	5.51×10^5	$\pm 7.17 \times 10^4$	6.05×10^6	$\pm 7.9 \times 10^5$	6.71×10^6	7.99×10^6	5.50×10^6
2 (SQ)	6.55×10^5	$\pm 8.52 \times 10^4$	6.71×10^5	$\pm 8.72 \times 10^4$	2.11×10^6	$\pm 2.7 \times 10^5$	8.88×10^6	1.06×10^7	7.28×10^6
(SA+SQ)	1.16×10^6	$\pm 1.51 \times 10^5$	1.22×10^6	$\pm 1.59 \times 10^5$	[1]8.12×10^6	[1]$\pm 7.3 \times 10^5$	[1]2.09×10^7	2.49×10^7	1.71×10^7
3	4.30×10^5	$\pm 5.59 \times 10^4$	4.42×10^5	$\pm 5.75 \times 10^4$	2.40×10^6	$\pm 2.7 \times 10^5$	4.90×10^6	5.84×10^6	4.02×10^6
4	1.60×10^5	$\pm 2.08 \times 10^4$	1.68×10^5	$\pm 2.18 \times 10^4$	1.65×10^6	$\pm 1 \times 10^5$	1.23×10^6	1.46×10^6	1.01×10^6
5	7.06×10^5	$\pm 9.17 \times 10^4$	7.51×10^5	$\pm 9.77 \times 10^4$	1.35×10^7	$\pm 4.5 \times 10^5$	1.04×10^7	1.24×10^7	8.56×10^6
6[1]	7.28×10^4	$\pm 9.46 \times 10^3$	7.62×10^4	$\pm 9.90 \times 10^3$	-	-	4.00×10^5	4.76×10^5	3.28×10^5
7	1.09×10^5	$\pm 1.42 \times 10^4$	1.17×10^5	$\pm 1.52 \times 10^4$	-	-	7.35×10^5	8.75×10^5	6.03×10^5
8	2.90×10^5	$\pm 3.77 \times 10^4$	2.97×10^5	$\pm 3.86 \times 10^4$	-	-	2.78×10^6	3.31×10^6	2.28×10^6
9	5.26×10^4	$\pm 6.84 \times 10^3$	6.14×10^4	$\pm 7.98 \times 10^3$	-	-	2.94×10^5	3.50×10^5	2.41×10^5
10	1.21×10^5	$\pm 1.58 \times 10^4$	1.30×10^5	$\pm 1.69 \times 10^4$	-	-	8.59×10^5	1.02×10^6	7.04×10^5
11	1.01×10^6	$\pm 1.32 \times 10^5$	1.06×10^6	$\pm 1.38 \times 10^5$	-	-	1.70×10^7	2.02×10^7	1.39×10^7
12	9.19×10^4	$\pm 1.19 \times 10^4$	1.07×10^5	$\pm 1.40 \times 10^4$	-	-	6.53×10^5	7.77×10^5	5.35×10^5
13[1]	6.58×10^4	$\pm 8.55 \times 10^3$	6.67×10^4	$\pm 8.67 \times 10^3$	-	-	3.31×10^6	3.94×10^5	2.71×10^5
14	4.06×10^5	$\pm 5.28 \times 10^4$	4.25×10^5	$\pm 5.52 \times 10^4$	-	-	4.63×10^6	5.51×10^6	3.79×10^6
15	3.85×10^5	$\pm 5.01 \times 10^4$	4.05×10^5	$\pm 5.26 \times 10^4$	-	-	4.32×10^6	5.14×10^6	3.54×10^6
16	1.06×10^5	$\pm 1.37 \times 10^4$	1.12×10^5	$\pm 1.46 \times 10^4$	-	-	6.94×10^5	8.26×10^5	5.69×10^5

Table continued overleaf

ID	Width (W_d) (m)	Error (m)	Length (L_d) (m)	Error (m)	L_d/ W_d	H (m)	α_{max} (°)
1	719	±6	648	±6	0.9	234	19.9
2 (SA)	660	-	1273	-	0.5	246	10.9
2 (SQ)	689	±6	1826	±6	2.0	244	7.6
(SA+SQ)	-	-	-	-	-	-	-
3	723	±6	997	±6	1.4	107	6.1
4	868	±6	446	±6	0.5	70	8.9
5	1691	±6	1740	±6	1.0	252	8.2
6[2]	430	±6	416	±6	1.0	83	11.4
7	375	±6	499	±6	1.3	125	14.1
8	561	±6	897	±6	1.6	121	7.7
9	438	±6	264	±6	0.6	121	24.6
10	297	±6	873	±6	2.9	233	14.9
11	1164	±6	1554	±6	1.3	261	9.5
12	570	±6	333	±6	0.6	193	30.1
13[2]	559	±6	372	±6	0.7	44	6.8
14	1079	±6	1017	±6	0.9	152	8.5
15	1237	±6	1321	±6	1.1	166	7.2
16	588	±6	496	±6	0.8	106	12

SA – subaerial; SQ – subaqueous; A_{plan} – planimetric area; A_L – surface area; V_L[1] Volume derived from Cut Fill on pre- and post-DEM for numerical modelling analysis; V_L[1] error as reported in Table 4.6; V_L[2] volume derived from the calculated scaling relationship $V_L=0.043A_L^{1.43}$; L_d – deposit length; W_d – deposit width; α_{max} – maximum regional slope; [1] Volumes and error derived from combined SA-SQ area; [2] Measurements made only on visible deposit in bathymetry.

Table 4.4. Morphometric attributes of Milford Sound/Piopiotahi STS rock avalanche runout characteristics, and associated error

ID	H_{max} (m)	error (m)	H (m)	error (m)	L_{max} (m)	error (m)	L_{max} Error (%)	H/L_{max} (-)	H/L_{max} Upper bound (-)	H/L_{max} Lower bound (-)	F (˚)	F Upper bound (˚)	F Lower bound (˚)	Average path slope (˚)	Depositional slope(˚)
1	467	±13	462	±13	797	±56	7	0.58	0.56	0.61	30.1	29.1	31.2	64.9	1.3
2 (SA)	-	-	-	-	-	-		-						58.1	4.4
2 (SQ)	-	-	-	-	-	-		-						9.4[1]	4.2
(SA+SQ)	1618	±13	1618	±13	3495	±56	2	0.46	0.46	0.47	24.8	24.7	25.0	39.8[2]	-
3	1950	±13	1948	±13	2247	±56	2	0.87	0.85	0.88	40.9	40.4	41.4	56.4	1.1
4	992	±13	984	±13	1418	±56	4	0.69	0.68	0.71	34.8	34.1	35.5	48.8	3
5	1092	±13	1088	±13	2234	±56	3	0.49	0.48	0.49	26.0	25.7	26.3	58.6	1.1
6[3]	-	-	-	-	-	-		-						-	1.6
7	542	±13	542	±13	890	±56	6	0.61	0.59	0.63	31.4	30.4	32.4	49.2	2.1
8	1557	±13	1553	±13	2406	±56	2	0.65	0.64	0.66	32.8	32.5	33.2	41.6	2
9	227	±13	227	±13	315	±56	18	0.72	0.65	0.83	35.8	33.0	39.6	63.8	-[4]
10	983	±13	983	±13	1800	±56	3	0.55	0.54	0.56	28.6	28.2	29.1	37.1	15.8
11	1399	±13	1392	±13	2139	±56	3	0.65	0.64	0.66	33.1	32.6	33.5	62.4	1.4
12	844	±13	737	±13	891	±56	6	0.83	0.79	0.87	39.6	38.4	40.9	61.3	2.9
13[5]	693	±13	692	±13	878	±56	6	0.79	0.75	0.83	38.2	37.0	39.5	62.4	3.2
14	1106	±13	1106	±13	1249	±56	4	0.89	0.86	0.92	41.5	40.6	42.5	71.9	1.8
15	1323	±13	1323	±13	2191	±56	3	0.60	0.59	0.61	31.1	30.7	31.5	48	2.3
16	680	±13	663	±13	904	±56	6	0.73	0.70	0.77	36.3	35.2	37.5	54.3	5

[1] measured from the highest point in the deposit to the lowest, rather than from the source area; [2] measured from source to top of subaqueous deposit; [3] source area could not be identified so morphometric measurements could not be conducted with any degree of confidence; [4] deposit onlaps with another deposit where no unaffected fjord bottom is available to estimate; [5] morphometric measurements made based on the extent visible in the bathymetric data.

Table 4.5. Summary statistics from the rock avalanche morphometric data

		Mean	Median	Min	Max	Q1	Q3
Deposit	A_{plan} (m^2)	3.26 x10^5	2.64 x10^5	5.26 x10^4	1.01 x10^6	1.09 x10^5	4.30 x10^5
	A_L (m^2)	3.45 x10^5	2.95 x10^5	6.14 x10^4	1.06 x10^6	1.17 x10^5	4.42 x10^5
	V_L (m^3)	4.23 x10^6	2.75 x10^6	2.94 x10^5	1.70 x10^7	7.97 x10^5	4.47 x10^6
	(W_d) (m)	591	562	297	1164	430	689
	(L_d) (m)	901	873	264	1826	496	1273
	L_d/W_d	1.1	1.0	0.5	2.9	0.7	1.3
	H (m)	173	166	70	261	121	236
	α_{max} (˚)	12.9	10.9	6.1	30	8.2	14.9
Rock avalanche	L_{max} (m)	1590	1418	315	3495	890	2213
	H/L_{max} (-)	0.67	0.65	0.46	0.89	0.59	0.76
	F (˚)	31.6	33.0	24.8	41.5	29.7	36.8
	Path slope (˚)	52.2	56.4	9.4	71.9	48.0	62.4
	Depositional slope (˚)	3.3	2.2	1.1	15.8	1.6	3.5

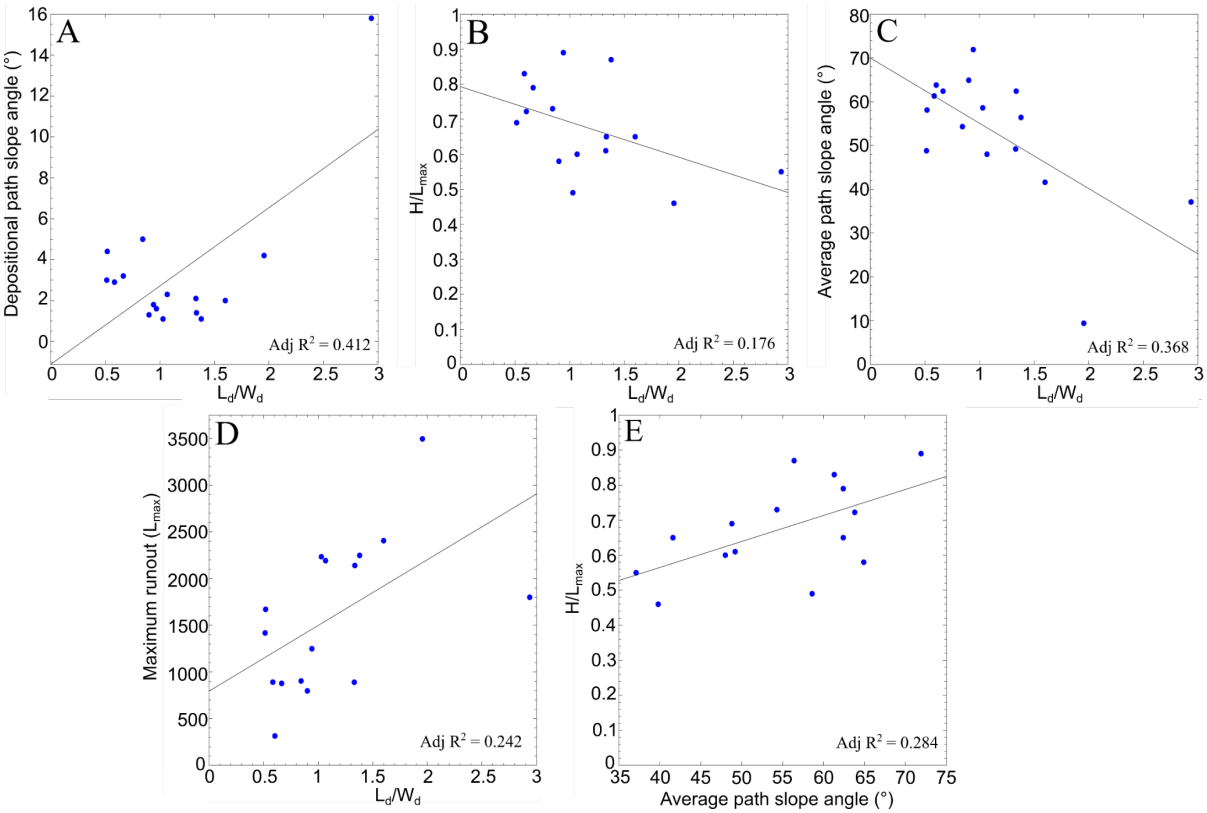

Figure 4.6. Relationships of the rock avalanche deposit L_d/W_d ratio to (a) depositional path slope; (b) overall mobility (H/L_{max}); (c) average travel path slope; and (d) overall runout (L_{max}). Plot (e) is the overall rock avalanche mobility against the average travel path slope. Adjusted R^2 value and line of best fit from least-squares linear regressions.

4.4.3. Runout modelling

4.4.3.1. Description of modelled rock avalanches

The deposits selected for numerical modelling were RAs 1-5. Based on the available data, each case was modelled as a single failure. The source areas for these deposits are ones where there is the most confidence in the correct identification of the source. This aids to mitigate uncertainty throughout the runout modelling. However, as all deposits pre-date the observed period, there is still a degree of uncertainty in accurately attributing the correct source. Therefore the runout modelled results still have some degree of uncertainty. In all cases, the source volume was less than the deposit (3 – 25%) (Table 4.6), but, with the exception of RA4 (~3%), are within the invoked 7-26% range that could possibly be attributed to volume growth by fragmentation during motion or entrainment (Hungr, 1981; Hungr and Evans, 2004).

Table 4.6. Volume difference between source and deposit of modelled cases and estimated volume error

Modelled event	Modelled deposit volume (x10^6 m^3)	Calculated source volume (x10^6 m^3)	% difference (source/deposit)	Deposit volume error (m^3)	Deposit volume error (%)
RA1	3.1	3	7.1	± 1.1 x10^5	± 3.7
RA2	8.1	7	13.9	± 7.3 x10^5	± 9
RA3	2.4	2.1	11.7	± 2.7 x10^5	± 11
RA4	1.7	1.6	3.2	± 1 x10^5	± 6.1
RA5	13.5	10.1	24.9	± 4.5 x10^5	± 3.3

RA1 is the largest volume rock avalanche deposit in Dale Basin (3.1 M m^3). It can be categorised as a 'type 1' deposit, with a proximally thick, conical shaped deposit geometry, with a blocky surface carapace. The source area is a prominent hollow on the fjord wall and extends from c. 350 m.a.s.l. down to sea level, with a small fraction of the deposit remaining at the base of the source area. RA1 is the only event modelled that occurs in Dale Basin, where water depths are shallower than those in Stirling Basin (maximum depth c. 140 m compared to 290 m respectively). The deposit spreads laterally and reaches a maximum water depth of 137 m below sea level (m.b.s.l). No flow features are visible on the surface of the deposit (Figure 4.7).

RA2 is sourced on the north-eastern face of Mount Philipps, with the crown of the source scarp at c. 1370 m.a.s.l. It can be categorised as a 'type 2' deposit: an irregular deposit, where the apparent thickness is variable, and appears to be independent from distance from the source.

The creation of the pre-event DEM estimates the total volume of the rock avalanche to be 8.1 M m^3, and that c. 6 M m^3 of the rock avalanche deposited in Sinbad Gully, and c. 2.1 M m^3 propagated into the fjord, where it deflected downslope towards the deeper part of Stirling Basin. The distal end of the deposit reaches a maximum water depth of c. 249 m.b.s.l. Owing to dense vegetation cover over the deposit in the aerial imagery, the DEM resolution (15 m), and its generation by the ANUDEM interpolation applied to NZTopo50 map 20 m contours, it is not possible to detect any features on the subaerial deposit. The subaqueous surficial morphology changes in the distal regions from largely blocky to a comparatively smoother with only a few blocks visible on the DEM. It is likely that the subaerial RA2 deposit in the Sinbad Gully blocked the valley, as the deposit is evident either side of the present-day river channel. Therefore, it is assumed that some of the deposit has since been dissected and transported by the Sinbad River. The river cut channel was infilled in the post-event DEM before removing the deposit to ensure as accurate a volume as possible (Figure 4.7).

RA3 is sourced on the northern face of Mitre Peak, just below its summit at c. 1660 m.a.s.l. The deposit extends across the Stirling Basin and reaches a maximum depth of 288 m.b.s.l. The deposit volume is calculated at c. 2.4 M m^3. In its proximal reaches, the deposit consists of a blocky, conical geometry with some perpendicular-to-flow ridges at the base of the slope. In the middle and distal reaches, the deposit is comprised of an angular-sub angular block field across the fjord bottom (Figure 4.5).

RA4 is the smallest rock avalanche modelled, with a total calculated volume of c. 1.65 M m^3. The source area of RA4 is located on the north-eastern face below Footstool Peak, at a maximum scarp elevation of c.705 m.a.s.l, and descends to a maximum depth of 288.5 m.b.s.l. The deposit has a largely smooth surface morphology compared to the other modelled rock avalanches and consists of a thick proximal deposit mass at the base of the slope, which thins distally. Calibration of the model is against the bulk of the deposit and does not include blocks beyond the bulk of the deposit (Figure 4.7).

RA5 is the largest volume event modelled of the five, and the second largest event in the fjord with a calculated volume of c. 13.5 M m^3. Only RA11 has an estimated larger volume from the scaling relationship (Table 4.3). The source area is located on the south-east face of The Lion summit peak, with the crown of the scarp at c. 800 m and the failure involving most of the fjord wall. The deposit geometry is predominantly a large cone at the base of the slope. Towards the south-western distal end, the deposit surface appears much smoother than the conical area and

creates a snout raised 6 m above the fjord bottom. The front thins moving northwards until it cannot be distinguished at the base of the cone (Figure 4.7).

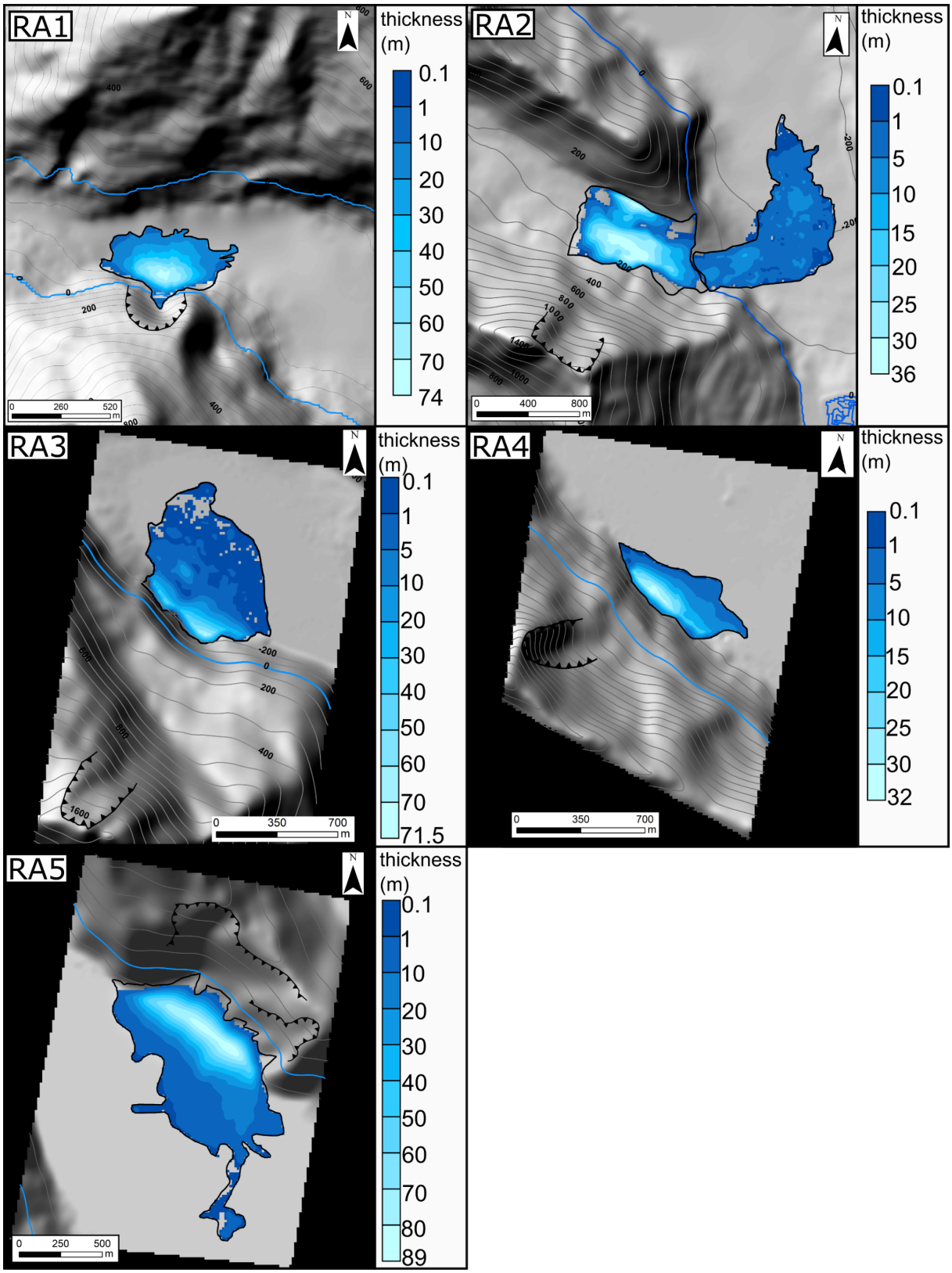

Figure 4.7. Interpolated spatial deposit thicknesses of rock avalanche cases derived from recreation of a pre-event DEM

4.4.3.2. Calibrated parameters and rheologies of modelled rock avalanches

In each modelled case, simulations were run using a single basal rheology and adjusted using the trial-and-error calibration procedure. Both frictional and Voellmy rheologies were tried. However, a single rheology was unable to successfully reproduce the bulk behaviour in all modelled cases. In the back analysis of all modelled cases, a best fit was achieved with a two rheology approach (Figure 4.8, Table 4.7, and Table 4.8). The change in rheology was enforced at the present-day sea level, to simulate the change from the subaerial to subaqueous environment. Sea levels may have been lower when the rock avalanches occurred, based on the reconstructed relative sea level curve of Dlabola *et al.* (2015). However, the sea level remains difficult to ascertain due to the unknown ages of each rock avalanche deposit, and the palaeolake levels prior to transgression. Therefore, various sea levels were not tested. In all the best fit modelled cases, a Voellmy rheology was employed in the subaqueous component of the rock avalanche runout. A Voellmy rheology was also used in the subaerial component of all modelled rock avalanches, except RA4, which had a frictional rheology for the subaerial component of runout (Table 4.7). The models all varied in emplacement duration, ranging from 79s for RA1 to 1300s for RA2 (Table 4.8).

Table 4.7. Best fit rheologies (frictional (F), Voellmy (V)) and corresponding parameters for each modelled rock avalanche

Rheological parameters										
			Subaerial				Subaqueous			
	Unit Weight (kN/m^3)	Internal Friction Angle (˚)	ϕ_b (F)	r_u (F)	μ (V)	ξ (V)	ϕ_b (F)	r_u (F)	μ (V)	ξ (V)
RA1	25.79	35	-	-	0.57	500	-	-	0.57	50
RA2	27.00	35	-	-	0.25	300	-	-	0.1	100
RA3	25.79	35	-	-	0.1	500	-	-	0.1	100
RA4	25.79	35	28	0	-	-	-	-	0.25	100
RA5	26.48	35	-	-	0.1	500	-	-	0.32	100

In all the best fit modelled cases, the simulations all result in an over- and under-estimation of the depositional surface area (A_L) of +8/-12% respectively (Table 4.8). However, these values are within the maximum error bounds on the mapped deposit uncertainty (±13%). The simulation of RA3 replicates A_L to within 0.4% of the mapped deposit. However, the model mismatches the mapped extent of the deposit, predicting more lateral propagation and deposition along the fjord, and less across the fjord bottom, than observed (Figure 4.8). This

mismatch in the model propagation results in an underestimation of deposit length by 37.5%, and maximum runout of 15.1% (Table 4.9) and an overestimation of the H/L_{max} ratio and fahrböschung angle as a result. However, in all but RA5, the runout is within 20% of the observed. The modelled output for RA5 replicates the lateral spreading and deposition along the fjord, though overestimates the deposit width by 34%. The best fit results underestimate the runout of RA5 by 34.2%, largely as the model fails to simulate the southward extending lobate feature identifiable in the mapped deposit (Figure 4.8). The deposit length is therefore underestimated by 20.8% as a result, which then results in an overestimation of the H/L_{max} by 59.5% (Table 4.8). The maximum runout of RA2 is also underestimated by 11.4%, despite the snout of the model going beyond the furthest extent of the mapped deposit. The model does manage to achieve >3 km runout of the deposit, however. The runout is taken from the calculated centreline, and the model does not flow as far to the east on the fjord bottom as the mapped deposit before deflecting northwards. The deposit exits Sinbad Gully further north than the observed. This may explain the discrepancy in the measured runout. The H/L_{max} value and corresponding fahrböschung angle are higher than observed because of the shorter runout.

Apart from RA3, the longitudinal profiles of deposit thicknesses of the modelled outputs are similar in shape to the observed (Figure 4.9). Furthermore, the modelled results for RA1 replicates some material remaining in the source area, as was mapped in the observed (Figure 4.8). Additionally, the model reproduces the proximally thick geometry of the deposit, with the thickest area of deposition at the base of the slope, gradually thinning across the fjord bottom. In the RA3 simulation however, the simulation also fails to replicate the blocky morphology of the observed deposit in the distal reaches, instead creating a gradually thinning deposit with distance from the source (Figure 4.8, Figure 4.9). The simulation of RA2 gives a reasonable distribution of mass in both the subaerial and subaqueous portions of the runout (Figure 4.8). However, the simulation gives a slightly more even distribution of the subaqueous deposit mass compared to the more irregular distribution in the observed (Figure 4.9). Analysis of the volumetric distribution of the deposit in Sinbad Gully and the fjord from the modelled simulation estimates a smaller volume of material remains in Sinbad Gully than derived from the DEM analysis (c.5.45 M m^3 compared to c.6 M m^3). Subsequently more material propagated into the fjord compared to the calculated (c.2.67 M m^3 compared to c.2.1 M m^3). In all best fit simulation cases, the model underestimates the maximum thickness (Table 4.8). Similarly, the average thickness is also underestimated in all cases except RA4, where the model overestimates the average thickness by 14.9%. The longitudinal profile of the modelled

RA4 deposit show that the distal extent of the model material thins more gradually than in the observed, which falls off sharply, which may explain the overestimation of average thickness (Figure 4.9). However, due to the uncertainty in the palaeotopography, the modelling results can be considered as providing a reasonable first-order estimation.

The modelled data also provides insight into the velocities of the rock avalanches. In the RA1 simulation, the maximum and average velocity achieved are 39.6 m s^{-1} and 19.3 m s^{-1}, which are the lowest values of all simulated events (Table 4.8). Despite the reduction in the turbulence parameter into the subaqueous environment, the velocity increases slightly as the rock avalanche moves downslope before gradually decelerating as it moves across the fjord bottom (Figure 4.10). In the simulation of RA2 however, the velocity drops off initially abruptly when the deposit enters the water, before gradually decelerating as it moves along the subaqueous path (Figure 4.10). The RA2 rock avalanche accelerates as it flows down the subaerial slope from Mt. Philipps, achieving a maximum velocity of 94.94 m s^{-1}, before it begins to decelerate as the material reaches the valley floor of Sinbad Gully, prior to runout into the fjord. The velocities attained in the RA3 simulation are the highest of all the simulated events, with a maximum velocity of 142.27 m s^{-1} and an average of 39.12 m s^{-1} (Table 4.8). Similar to RA2, the modelled velocities show a drop off in the velocity initially as the rock avalanche flows into the water (Figure 4.10). In the RA5 simulation, the velocity profile shows a sharp drop in the maximum cellular velocity as the landslide material initially flows subaqueously. The landslide begins to accelerate gradually until the material reaches the flat fjord bottom, where it begins to decelerate as it comes to rest on the fjord bottom (Figure 4.10). In the RA4, simulation, the model shows a phase of deceleration in the subaerial environment, before the landslide accelerates up until reaching the water, where deceleration generally occurs once the rock avalanche enters the water. There are small phases of acceleration as it propagates over the fjord bottom before decelerating rapidly and finally coming to rest (Figure 4.10). The model achieves a maximum velocity of 71.9 m s^{-1} and an average of 33.3 m s^{-1} (Table 4.8).

Furthermore, the model simulations of RA2 supports the hypothesis that both the subaerial and subaqueous deposit originated from a single rock avalanche collapse. The rock avalanche does not flow out from the Sinbad Gully delta in the exact location as the observed deposit. This may be due to the approximate nature of the reconstructed pre-event terrestrial and bathymetric DEMs. The model does simulate the deposit deflecting downslope towards the deepest area of Stirling Basin (Figure 4.8). Analysis of the volumetric distribution of the deposit in Sinbad Gully and the fjord from the simulation estimates a smaller volume of

material remains in Sinbad Gully than derived from the DEM analysis (c. 5.45 M m^3 compared to c. 6 M m^3) and that more material propagated into the fjord compared to the calculated (c. 2.67 M m^3 compared to c. 2.1 M m^3).

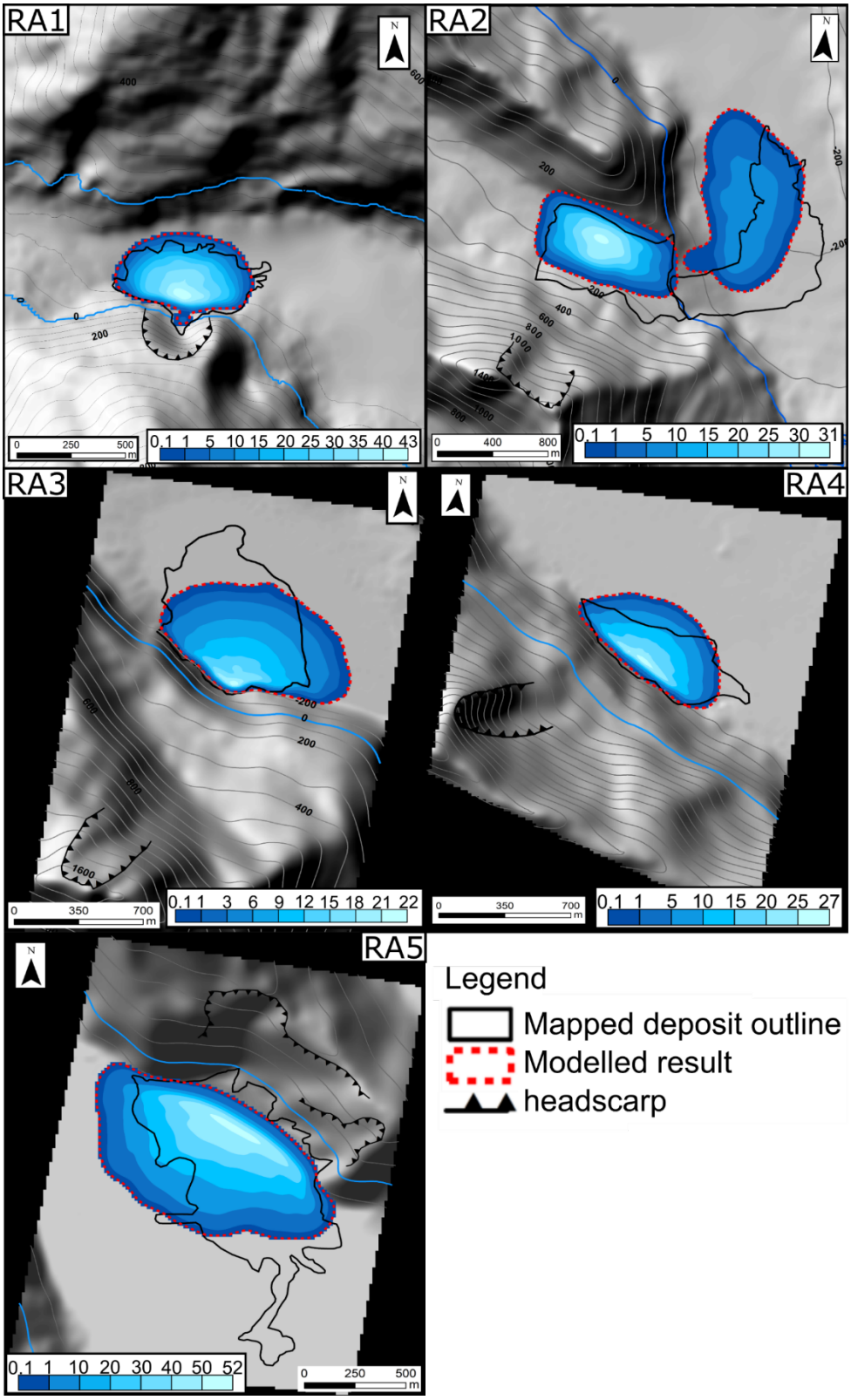

Figure 4.8. Extents and thicknesses of runout modelling results using the best fit rheological parameters in Table 4.7.

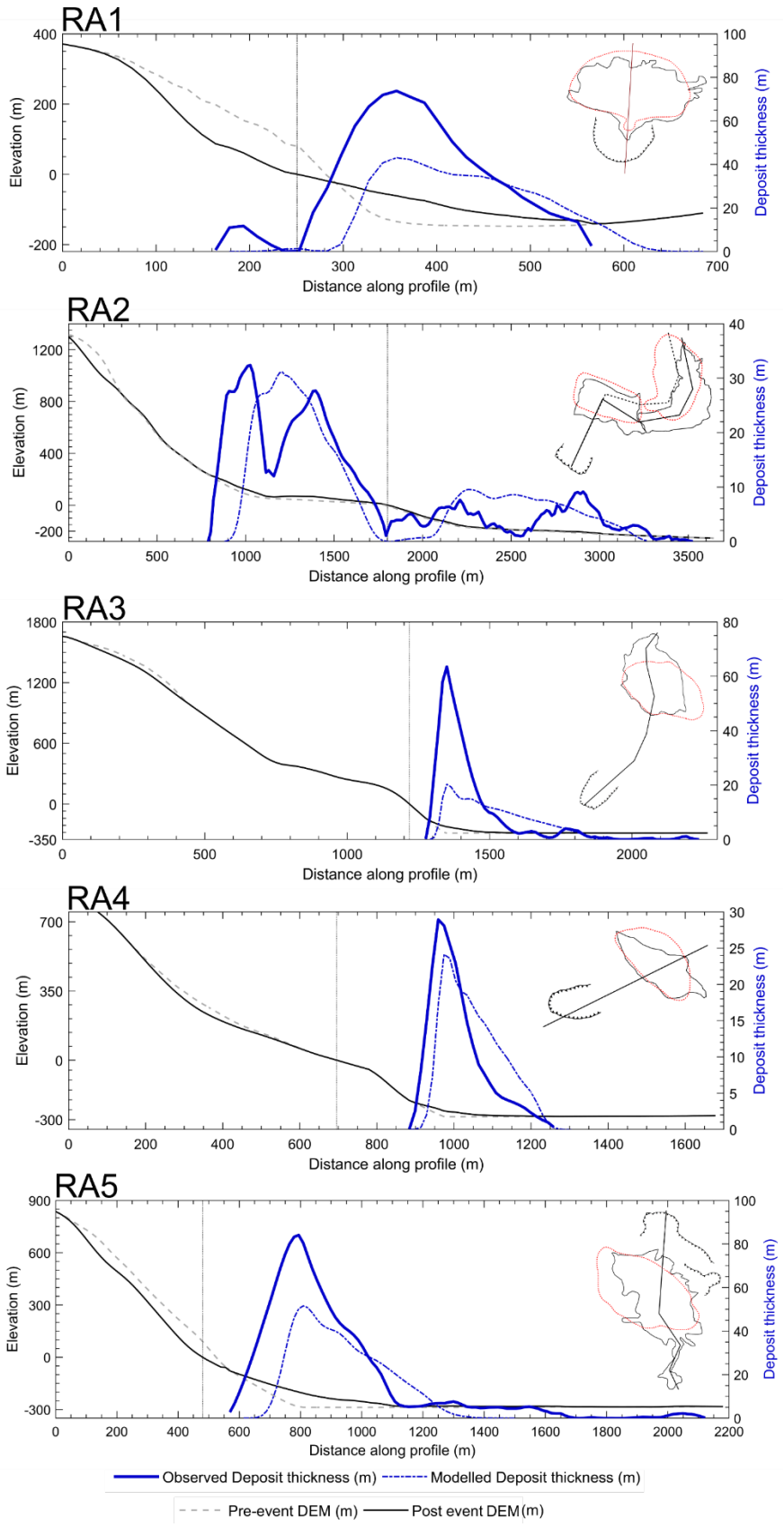

Figure 4.9. Longitudinal profiles of the deposit thickness through the observed (solid line) and the modelled deposits (dashed line) for the five simulated events. The vertical grey line demarcates the boundary between the subaerial (left hand side of the line) and subaqueous (right hand side of the line) environment.

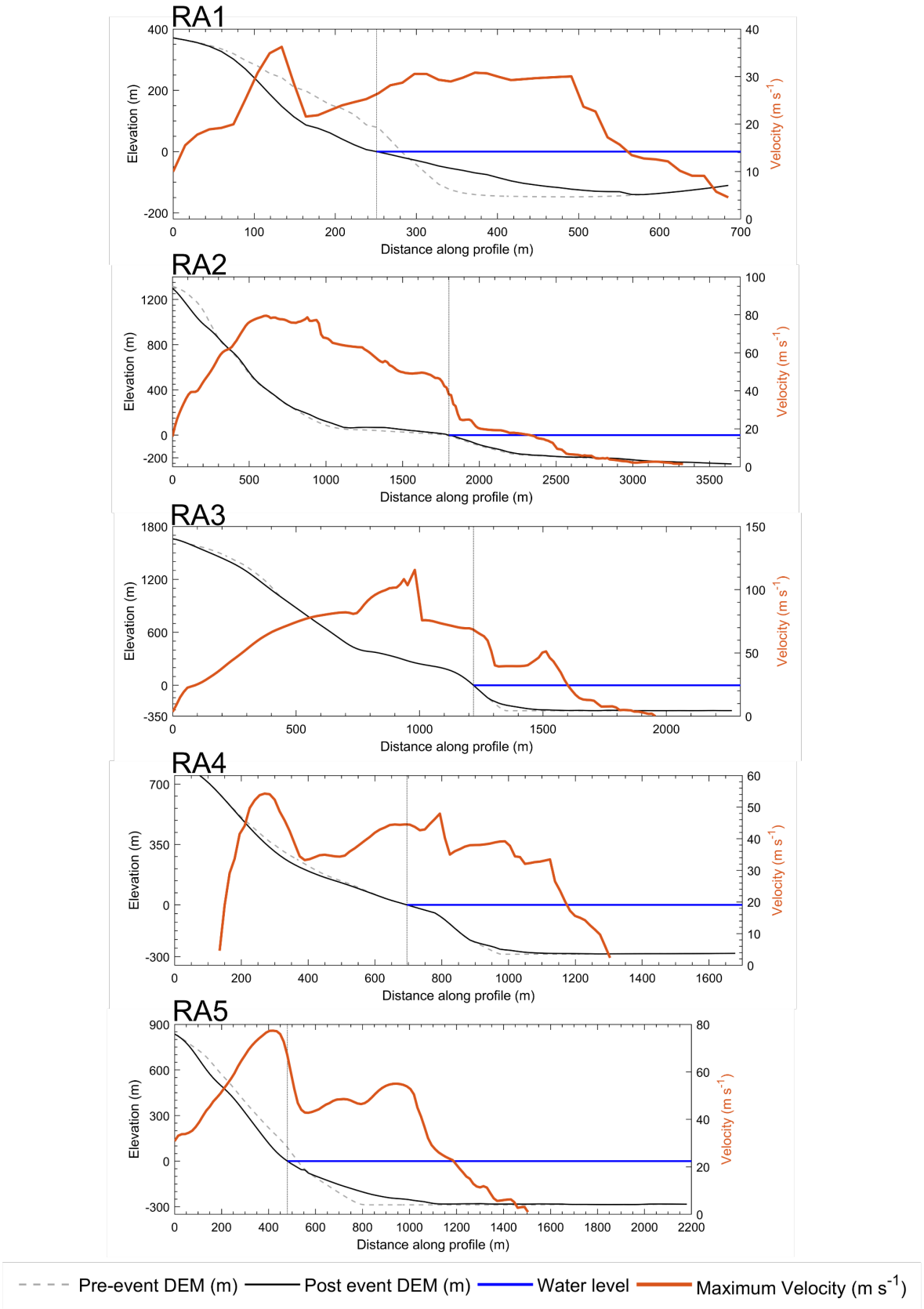

Figure 4.10. Centreline transects of the maximum cell velocity (m s^{-1}) through the modelled deposits (orange line) for the five simulated events. The vertical line demarcates the boundary between the subaerial (left hand side of the line) and subaqueous (right hand side of line) environment. The solid blue line is a graphical representation on the water level.

Table 4.8. Results of best fit simulations compared to observed data and associated morphometric error (where available). Percentage variation in modelled columns are in relation to observed data is in brackets.

Measurable parameters	RA1		RA2		RA3		RA4		RA5	
	Observed	**Modelled**	**Observed**	**Modelled**	**Observed**	**Modelled**	**Observed**	**Modelled**	**Observed**	**Modelled**
Maximum flow velocity ($m\ s^{-1}$)	-	39.6	-	94.9	-	142.3	-	71.9	-	88.9
Average flow velocity ($m\ s^{-1}$)	-	19.3	-	32	-	39.1	-	33.3	-	35.3
Duration of emplacement (s)	-	79[1]	-	400 (1300)[1,2]	-	480[1]	-	244[1]	-	582
Planimetric area (A_{plan}) (m^2)	1.65×10^5 (±13%)	1.79×10^5 (+8.1%)	[3]1.16×10^6 (±13%)	[3]1.26×10^6 (+8.1%)	4.30×10^5 (±13%)	4.13×10^5 (-4%)	2.29×10^5 (±13%)	2.01×10^5 (-12.4%)	7.06×10^5 (±13%)	7.26×10^5 (+2.9%)
Surface area (A_L) (m^2)	1.91×10^5 (±13%)	1.85×10^5 (-3%)	[3]1.22×10^6 (±13%)	[3]1.30×10^6 (+6.3%)	4.42×10^5 (±13%)	4.44×10^5 (+0.4%)	2.37×10^5 (±13%)	2.11×10^5 (-11%)	7.51×10^5 (±13%)	7.35×10^5 (-2.1%)
Apparent coefficient of friction (H/L_{max})	0.58	0.76 (+31.4%)	0.46	0.53 (+14.3%)	0.88	1.00 (+16.3%)	0.61	0.78 (+27.1%)	0.49	0.75 (+53.8%)
Fahrböschung angle (˚)	30.1	37.3 (+24%)	24.8	27.9 (+12.2%)	40.9	45.2 (+10.6%)	31.5	37.9 (+20.3%)	26	36.8 (+41.9%)
Deposit Length (L_d)	647.7 (±6)	417 (-35.6%)	3099[3] (±6)	2561[3] (-17.3%)	997 (±6)	623 (-37.5%)	446 (±6)	462 (+3.5%)	1740 (±6)	715 (-58.9%)
Deposit Width (W_d)	719 (±6)	634 (-11.8%)	660[4] (±6) 689[5] (±6)	529[4] (-19.8%) 773[5] (+12.2%)	722 (±6)	596 (-17.5%)	868 (±6)	737 (-15.2%)	1029 (±6)	1378 (+33.9%)
Maximum runout (L_{max}) (m)	797 (±56)	659 (-17.4%)	3495 (±56)	3099 (-11.4%)	2247 (±56)	1907 (-15.1%)	1418 (±56)	1203 (-15.1%)	2234 (±56)	1470 (-34.2%)
Maximum deposit thickness (m)	74 (±0.6)	4 (-41.8%)	36 (±0.6)	31 (-14.2%)	72 (±0.6)	22 (-69.1%)	32.05 (±0.6)	26.80 (-16.4%)	89 (±0.6)	52 (-41.9%)
Average deposit thickness (m)	27	15 (-44.8%)	8	6 (-18.7%)	6	5 (-11.5%)	7	8 (+14.9%)	20	17 (-16.7%)
		<25%				25-50%			>50%	

[1]Model stopped manually as only small internal movements are occurring and not affecting the overall runout or outline; [2]Bulk of material had deposited in both subaerial and subaqueous environments (non-bracket time), but material continued to slowly transfer from subaerial to subaqueous deposit. Brackets denote the time when model was stopped; [3]Combined area of subaerial and subaqueous deposit of RA2; [4] subaerial value; [5]subaqueous value

4.4.3.3. Transferability of model parameters

Each modelled case was simulated with the best fit parameters of the respective other cases. This was done to identify if there is an overall governing set of parameters that could provide reasonable simulations of all the rock avalanches, which could aid in predictive runout forecasting of future events in Milford Sound/Piopiotahi. However, the best fit parameters of each respective rock avalanche did not provide reasonable simulations of the other cases. The high basal friction (μ) and low turbulence (ξ) values attained with the RA1 parameters (Table 4.8) resulted in very short runouts in the simulations of RA2-5 (Figure 4.11, Table 4.9). In some instances, subaerial deposition in the source area (RA2), or along the runout path (RA3, RA4) occurred. Furthermore, no subaqueous runout and deposition occurs when the RA1 parameters are applied to RA2. The high basal friction and low turbulence values from the RA5 best fit parameters also resulted in comparatively short runouts, and smaller depositional areas in the other cases. Only in the RA1 did the simulation exceed the observed and best fit runouts and depositional areas.

The best fit parameters of RA2 also fail to achieve successful simulations of the other four case studies (Figure 4.11, Table 4.9). The modelled deposit produces overly thin deposits, and in RA1, RA4, and RA5 simulations, exceed mapped runout and depositional areas. In all cases apart from the best fit results here, the depositional area is the largest of all calibrated cases (Table 4.9). A similar finding from the RA3 parameters where the modelled runouts and depositional extents exceed the mapped outlines, also producing thinner deposits than derived from the observed data, and best fit case. The RA3 parameters do, however, produce similar depositional areas to the extents from applying RA2 parameters in the RA1, 4, and 5 simulations. This is likely as the subaqueous rheological parameters in both cases are the same. However, the RA3 μ and ξ parameter values are different in the subaerial environment than RA2, with a lower basal friction and higher turbulence parameters. These parameters increase rock avalanche velocity from the RA2 source area, possibly attributing to the little subaerial deposition in the RA2 simulation. The calibrated parameters of RA4 here fail to achieve successful simulations in the other cases (Figure 4.11, Table 4.9). The high friction in the subaerial portion of runout results in some deposition in the source of RA2 only. Despite the difference in the rheologies and respective parameter values between RA5, the modelled results produce similar depositional areas and runouts in RA1-RA3.

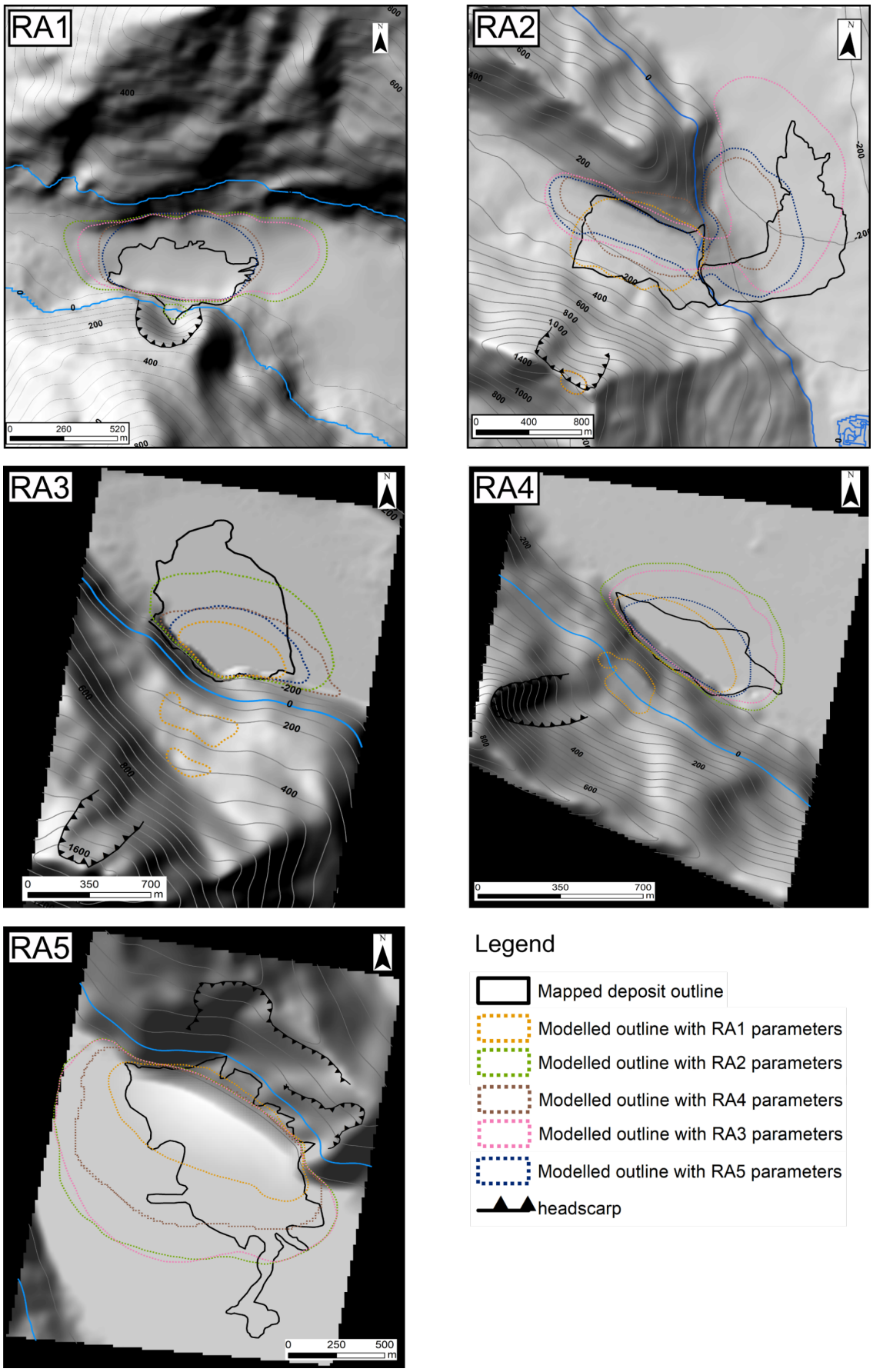

Figure 4.11. Runout and depositional extents from the best fit parameters of each case applied to the other respective cases

Table 4.9. Results from the calibrated best fit parameters to the other respective cases

	Max flow velocity ($m\ s^{-1}$)	Average flow velocity ($m\ s^{-1}$)	Duration of emplacement (s)	A_{plan} (m^2)	A_L (m^2)	H/L_{max} (-)	F (°)	L_{max} (m)	Max deposit thickness (m)	Average deposit thickness (m)
RA1 observed	-	-	-	1.65×10^5	1.91×10^5	0.58	30.1	797	74	27
best fit	40	19	79	1.79×10^5	1.85×10^5	0.76	37.3	659	43	15
RA2 parameter	251	30	1000	4.83×10^5	4.55×10^5	0.43	23.1	1168	17	6
RA3 parameters	82	23	526	4.08×10^5	4.09×10^5	0.42	22.6	1209	17	7
RA4 parameters	62	25	230	2.87×10^5	2.87×10^5	0.59	30.3	779	24	10
RA5 parameters	67	28	161	1.95×10^5	2.01×10^5	0.60	30.8	738	37	10
RA2 observed	-	-	-	1.16×10^6	1.22×10^6	0.46	24.8	3495	36	8
best fit	95	32	1300	1.26×10^6	1.30×10^6	0.53	27.9	3099	31	6
RA1 parameters	74	43	195	5.27×10^5	5.03×10^5	0.84	39.9	1671	45	15
RA3 parameters	127	38	1000	1.67×10^6	1.67×10^6	0.49	26.1	3329	14	5
RA4 parameters	112	61	310	8.77×10^5	8.32×10^5	0.67	33.7	2387	46	9
RA5 parameters	127	48	1405	9.88×10^5	9.83×10^5	0.63	32.1	2582	30	8
RA3 observed	-	-	-	4.30×10^5	4.42×10^5	0.87	40.9	2247	72	6
best fit	142	39	480	4.13×10^5	4.44×10^5	1.01	45.2	1907	22	5
RA1 parameters	72	35	1000	1.86×10^5	1.98×10^5	1.36	53.7	1405	56	8
RA2 parameters	107	29	1000	4.24×10^5	4.55×10^5	0.98	44.5	1946	14	5
RA4 parameters	130	71	756	2.49×10^5	2.53×10^5	1.14	48.7	1683	26	8
RA5 parameters	152	47	561	1.95×10^5	2.01×10^5	1.12	48.2	1710	37	10
RA4 observed	-	-	-	2.29×10^5	2.37×10^5	0.61	31.5	1418	32	7
best fit	72	33	244	2.01×10^5	2.11×10^5	0.78	37.9	1203	27	8
RA1 parameters	43	22	1000	1.84×10^5	1.68×10^5	0.89	41.7	1034	37	8
RA2 parameters	60	25	1000	3.78×10^5	3.56×10^5	0.73	36.1	1265	17	4
RA3 parameters	74	29	482	3.05×10^5	3.06×10^5	0.73	36	1266	17	5
RA5 parameters	66	33	475	1.62×10^5	1.66×10^5	0.81	39.2	1130	29	9

Table 4.9 continued

	Max flow velocity ($m\ s^{-1}$)	**Average flow velocity ($m\ s^{-1}$)**	**Duration of emplacement (s)**	**A_{plan} (m^2)**	**A_L (m^2)**	**H/L_{max} (-)**	**F (°)**	**L_{max} (m)**	**Max deposit thickness (m)**	**Average deposit thickness (m)**
RA5 observed	-	-	-	7.06×10^5	7.51×10^5	0.49	26.0	2234	89	20
best fit	89	35	582	7.26×10^5	7.35×10^5	0.75	36.8	1470	52	17
RA1 parameters	68	27	190	4.86×10^5	5.04×10^5	0.86	40.8	1275	74	24
RA2 parameters	113	32	1000	1.29×10^6	1.28×10^6	0.60	30.9	1840	25	10
RA3 parameters	127	34	434	1.27×10^6	1.27×10^6	0.59	30.5	1872	24	10
RA4 parameters	95	38	1000	9.06×10^5	8.80×10^5	0.69	34.6	1597	43	14

4.5. Discussion

4.5.1. Deposit geometry, morphology, and implications for flow dynamics

The rock avalanche deposits within Milford Sound/Piopiotahi are characterised by notably variable morphologies and geometries, despite originating in relatively uniform geologies within the fjord. All but three of the deposits (RA2, 3 and 10), exhibit quasi-conical geometries, with greater thickness in the proximal reaches, but thinning distally. Geometrically similar deposits have been identified for STS rock avalanches in fjords elsewhere (Blikra *et al.*, 2006; Bornhold *et al.*, 2007; Longva *et al.*, 2009). These conical geometries were noted in other subaerial deposits by Strom (2006), who observed that they occurred where moving rock masses struck the foot of slopes at or near right angles. The path slope angles of the rock avalanches in Milford Sound/Piopiotahi reach >70°, and the deposits accumulate on mean slopes of 3.3°. Such an abrupt change in the slope angles of the deposits travel paths create obstructions to flow, resulting in energy absorption from the flowing mass (Whittall *et al.*, 2017), the compaction of the deposits' fronts (Strom, 2006) and reduction in their overall length.

The more elongated deposits observed here are located where runout was over shallower slope gradients (Figure 4.6). The average slope angles for RA2 and RA10 are the shallowest angles (< 40°) of all RAs, whilst the deposits are the most elongated of those identified (Table 4.4, Table 4.5). Similarly, steeper subaqueous depositional slopes may have resulted in the rock avalanches maintaining their acceleration and momentum, thereby increasing their overall runout (Figure 4.6D), further elongating the deposits (Figure 4.6A). The presence of aligned blocks on the distal lateral margin of subaqueous deposit RA2, indicates that velocities in the direction of flow were greater than the perpendicular flow velocities in these distal regions (Dufresne and Davies, 2009).

The rock avalanches, during their runout, flow over the bedrock down the fjord walls, in both their subaerial and subaqueous portions. This may result in the avalanches experiencing higher basal friction compared to over a saturated substrate such as snow, ice, or saturated valley fill sediments (Whittall *et al.*, 2017; Aaron and McDougall, 2019). During the subaqueous runout, interaction of the rock avalanches with the water, causes some landslide momentum transfer to the water (Mohammed and Fritz, 2012; Mulligan and Take, 2017). In addition, the increased drag forces result from the increase in the surrounding medium density (due to moving through water compared to air) (Bregoli *et al.*, 2017). These factors result in greater resistance to landslide motion, prior to deposition. Reductions in rock avalanche velocity upon entering the

water is seen in the numerical back analysis of RA2-5 (Figure 4.10), that is considered representative of these processes. Additionally, ridges perpendicular to the inferred-flow directions are identified on the surfaces of 7 deposits (RA3, RA5, RA7, RA8, RA11, RA14 and RA16). These features are interpreted as compressional, transverse ridges resulting from deceleration of the flowing mass. They form either by a change in the surrounding (i.e. water), or underlying (hard bedrock to soft, deformable fjord bottom sediments) medium, or a combination of both. These increase the frictional resistance, or absorb the flow energy (Dufresne and Davies, 2009), and have been identified on STS VDAs elsewhere (Siebert, 2002; Crutchley *et al.*, 2013). The discontinuous nature of the ridges may result from spatial variations across the deposit in its emplacement velocities (Crutchley *et al.*, 2013). Apart from the transverse ridges, and the aligned blocks in RA2, most of deposits lack other surface features (Figure 4.5). The absence of many identifiable flow structures, such as longitudinal ridges, flowbands, and aligned blocks (Dufresne and Davies, 2009) may be because of current low resolution, relative to the deposit feature size, of the dataset (Clare *et al.*, 2018), or because of possible overprinting by a post-event sediment drape which obscures the original morphology (Haeussler *et al.*, 2018). The lack of surface features may also indicate that energy is expended and dissipated by collisions between clasts (Masson *et al.*, 2002).

The geometry of 9 of the rock avalanche deposits on the fjord bottom, specifically in terms of L_d/W_d, is less than 1. Therefore, the lateral spreading of the rock avalanche is (slightly) more dominant than its forward motion. Lateral spreading increases the deposit surface area to volume ratio which, proportionally, increases the surface area in contact with the water, and, overall, the drag/friction of the rock avalanche. The lateral spreading may also increase the transverse velocities perpendicular to the main flow (Dufresne and Davies, 2009), resulting in a reduction in the deposit thickness (Masson *et al.*, 2002). If there are resistant blocks in the fluidised matrix, which increase solid interaction with the ground, this reduction in thickness may also increase the basal friction (Kelfoun, 2011). The scattered distribution of the blocks in deposit RA3 suggests that here, the lateral spreading and, therefore, velocities perpendicular to main flow direction on the fjord bottom, were greater than those in the main flow direction (Dufresne and Davies, 2009).

4.5.1.1. Substrate influence

The interaction and impact of the rock avalanches down the steep bedrock slope onto fjord bottom sediments that are likely soft, saturated, deformable, and comparatively low basal shear strength relative to the impacting rock avalanche (Van Daele *et al.*, 2013) can also facilitate the

lateral spreading of deposit material in all directions (Strom, 2006). The saturated material can be entrained into the rock avalanche, which may reduce basal friction through rapid undrained loading (Hungr and Evans, 2004; Sassa and Wang, 2005; Voight *et al.*, 2012) or transforming it into more mobile debris flow-like landslides (Masson *et al.*, 2002; Dufresne and Davies, 2009). The blocky surficial morphology of the deposits suggest that this was unlikely to have occurred during emplacement of most of the deposits. The surficial morphology of the southward-extending lobe in RA5 is smoother compared to the rest of the deposit, which has a clear blocky morphology. This lobate feature may represent a longitudinal ridge. Alternatively, the feature may be a debris flow deposit because of partial rheological transformation of the rock avalanche material.

The substrate can be an impediment to the rock avalanche motion. Runout over a deformable fjord bottom substrate, which is likely saturated, can cause sediment deformation and bulldozing at the leading front of the rock avalanche. This will impede its advance and cause basal confinement of the deposit within deep basal shear surfaces (Frey-Martínez *et al.*, 2006; Moernaut and De Batist, 2011; Van Daele *et al.*, 2013). These features and processes have been identified in lakes and fjords impacted by rock avalanches and other landslides events elsewhere (Schnellmann *et al.*, 2005; Blikra *et al.*, 2006; Hilbe *et al.*, 2011; Van Daele *et al.*, 2013). This suggests that this may be a common feature of landslide impacts on basins. In the bathymetric data, evidence of basal confinement of the rock avalanche deposit is only evident on RA5 where a 1 m high concentric ridge feature on its eastern lateral limit (Figure 4.5A). Furthermore, a smooth surfaced snout in front of the main blocky conical deposit is visible. However, the lack of any similar features elsewhere on the fjord bottom suggests initially that basal confinement is not likely a factor in the limited runout and mobility of all the rock avalanches here. However it is possible that such features did occur and have been buried by post-event sedimentation, especially as rock avalanche material has been identified in the long-valley seismic profile that are not visible in the bathymetric data (Dykstra, 2012). A further, more extensive coverage of the seismic reflection data in the fjord would test this hypothesis, as well as any possible deformation and basal interaction of the rock avalanche with the fjord bottom sediments.

4.5.2. The apparent mobility of the rock avalanches

Comparison of some of the morphometric data gathered from the rock avalanches (volume (m^3), L_{max}, and H/L_{max}) allows comparison of the apparent empirical mobility of the Milford Sound/Piopiotahi rock avalanches against similar data of VDAs and non-volcanic rock avalanche events from different environments (e.g. subaerial, glacial, wholly subaqueous)

(Figure 4.12). In general, the empirical comparison indicates that the rock avalanches in Milford Sound/Piopiotahi are, on average, towards the lower end of apparent mobility, though not too dissimilar to other non-volcanic STS rock avalanches (Figure 4.12). This apparent relatively low mobility is coupled with the results from the numerical runout modelling associated in most cases with high basal friction angles (for frictional rheology) and coefficients (for Voellmy rheology), and/or low turbulence parameters are needed in all five simulations to reproduce reasonable simulations of the observed runout, giving support that many of these events were of comparatively low mobility. Whilst this comparison utilises H/L_{max} as an index of mobility, this index is often criticised as being physically meaningless (Corominas, 1996; Legros, 2002; Davies and McSaveney, 2012; Johnson *et al.*, 2016; Strom *et al.*, 2019). Nonetheless, H/L_{max} continues to be used as an index.

Volume may have some effect on the overall runout and mobility of rock avalanches. The deposits here range in volume from 10^5 – 10^7 m^3, some of which are comparatively small volumes for rock avalanches (Figure 4.12). The volumes derived here are also based on an assumption that each deposit is from a single failure. It is possible that the rock avalanche deposits are composite events, which would indicate a greater number of (smaller) deposits, and perhaps even smaller volumes per failure than those calculated, but this cannot be discerned solely from the bathymetric data. However, probability distribution analysis of the subaerial and subaqueous deposit volumes derived by Dykstra (2012), were analysed by Taig and McSaveney (2015) who found that all deposits greater than 10^6 m^3 fit within the same population of volumes. Therefore it is reasonable to assume each deposit as a single failure event.

The uncertainty with deposit volumes due to the interpolation methods and volume-area scaling has been assessed (Table 4.3, Table 4.6). However, the uncertainty in deposits may also be the result of partial deposit burial as Dykstra (2012) identified areas of buried deposit material in a seismic profile down the fjord. Whether these represent older deposits or buried distal extents of the visible deposits remains unknown. Similarly, the visible extents of RA6 and RA13 are likely obscured by post-event sediments. Therefore the spatial extents and volumes of some of the deposits may be underestimated. However, the volume of the rock avalanches may only partially explain the mobility (Nicoletti and Sorriso-Valvo, 1991; Legros, 2002; Aaron and McDougall, 2019). There is scatter in the H/L_{max} and runout between rock avalanche deposits of similar volumes, both in Milford Sound/Piopiotahi, and globally (Figure 4.12), that also

appears to be irrespective of rock avalanche type (glacial, subaerial, STS). Therefore, other extrinsic properties may also be affecting the mobility of the rock avalanches.

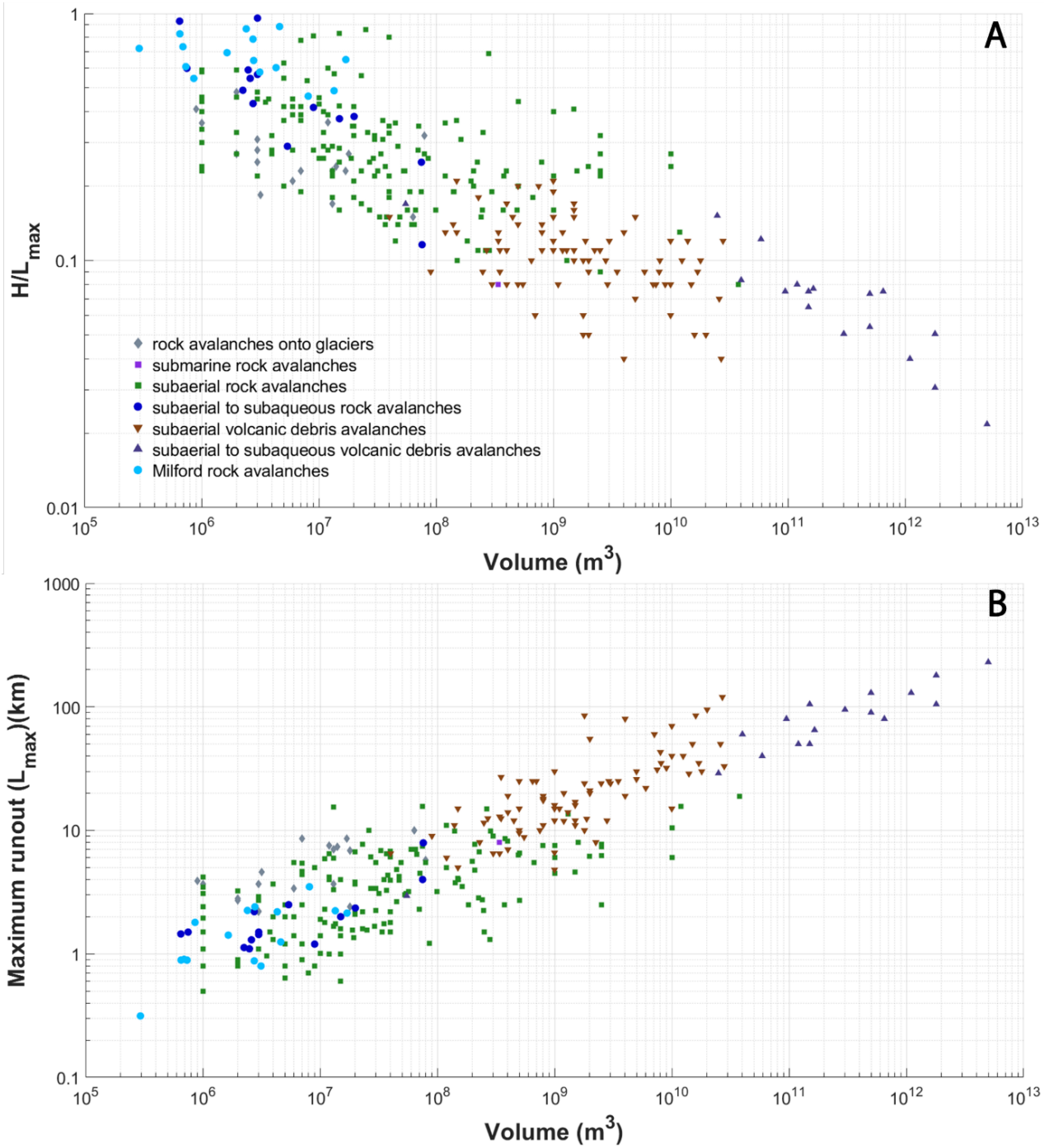

Figure 4.12. Plot of apparent mobility (H/L_{max}) (a) and maximum runout (b) vs. volume of volcanic and non-volcanic rock avalanche events from literature, with the addition of the Milford Sound/Piopiotahi rock avalanches. Note that the non-rock avalanche submarine landslides are excluded here.

Geomorphic frontal confinement of rock avalanche deposits against opposite slopes has long been identified in the subaerial environment as a factor in controlling rock avalanche mobility (Nicoletti and Sorriso-Valvo, 1991; Strom *et al.*, 2019). The Milford Sound/Piopiotahi rock

avalanches all exist in a valley setting, where geomorphic confinement could perhaps restrict runout. However, RA11, the largest of the deposits, is the only rock avalanche that visibly extends to the opposite fjord wall. Therefore the H/L_{max} value calculated for RA11 is likely to be a maximum as it may be restricted by topographic frontal confinement, which has been documented in subaerial to subaqueous deposits in fjord settings elsewhere (Blikra *et al.*, 2002). The numerical back analysis of RA2 suggests that frontal confinement may also have played a role in the runout of this rock avalanche. The model simulates landslide impact with the opposite valley wall in the subaerial component of runout in Sinbad Gully, with partition and downslope deflection of the deposit from the valley into the fjord (Figure 4.8). However, RA2 has the lowest H/L_{max} value, longest deposit length (L_d) and runout (L_{max}), and the calibrated basal friction coefficient for RA2 is the lowest of all 5 in the subaqueous portion. The other rock avalanches in the fjord do not appear to extend across to the opposite side of the fjord, but geomorphic frontal confinement may still be a minor factor in their mobility as the H values of the most distal point of all but three of the rock avalanches (exceptions are RA7, 9, and 15) are higher than the calculated H_{max} values.

The lack of immediate lateral and frontal confinement of many of the deposits can allow the deposits to spread laterally, reducing forward runout. The morphometry of the valley slope may have some effect on the overall runout too. Whittall *et al.,* (2017) show for their database that landslide events with the steepest slope angle typically show the lowest H/L_{max} values. They attribute these abrupt path angle changes to partially explaining runout mobility. A similar trend is evident here, where the most mobile deposits are elongated (Figure 4.7B) and appeared to have occurred on overall shallower slope angles (Figure 4.7E).

4.5.3. Model capabilities and calibrated parameters

The uncertainties in the reconstruction of the pre-event basal topography, source areas, mode of detachment and emplacement (single events or multistage failures), post-depositional modification of deposits, and the assumed volumes are the main limiting factors in the runout modelling (Sosio, Crosta and Hungr, 2012; Schleier *et al.*, 2017). Additional uncertainties arise from the complexity of the palaeoenvironmental conditions when the rock avalanches occurred. In the back-analysed cases presented here, all these uncertainties apply as no events have been directly observed, and only have a maximum age bound. Post-glacial relative sea level changes are constrained well (Dlabola *et al.*, 2015), but the timings of each respective STS rock avalanche are unknown so their occurrence in relation to changing sea levels are uncertain. Furthermore, the lack of age constraints meant that palaeoclimatic factors such as ice within the

source mass could not be assessed. Ice may have been present, which could reduce the bulk friction of the rock avalanche material through melting and lubrication (Schneider *et al.*, 2011; Sosio, Crosta, Chen, *et al.*, 2012). However, the best fit subaerial parameters for all the modelled cases here are consistent with dry granular flows over bedrock (Figure 4.13).

In all the modelled cases, a single basal rheology, irrespective of frictional or Voellmy, was unable to replicate the deposit observations. A single rheology provides an average basal friction over the whole runout path. Therefore a single rheology is very hard to capture the transition from subaerial (air) to subaqueous (water), and the change from steep fjord walls to relatively flat fjord bottom, all of which have effects on the flow and emplacement dynamics discussed above. A reasonable runout simulation of the case examples was achieved by employing a change in the basal rheology at present-day sea level (Figure 4.8, Table 4.8). This change in rheology could possibly be representative of simulating the phase change from subaerial to subaqueous runout environments.

The use of the Voellmy rheology is shown to be important for simulating subaqueous runout as all 5 cases use Voellmy in the subaqueous portion of runout irrespective of their subaerial rheology. The effectiveness of Voellmy rheology is likely a result of the additional turbulent parameter ξ which contributes to providing flow resistance beyond just basal frictional resistance. The turbulence parameter limits the velocity of the rock avalanche motion in a manner equivalent to water increasing drag and buoyancy during subaqueous runout. The calibrated turbulence values in the subaqueous portion are comparatively low (ξ range between 50 – 100 m s^{-2}) which reduces the overall landslide velocity. Other models utilise a non-hydrostatic pressure coefficient component on entering the water to simulate this interaction and increased resistance to motion of the landslide body with water (Tinti *et al.*, 2006; Kelfoun *et al.*, 2010; Si *et al.*, 2018). DAN3D has not been designed for simulating STS landslides, so currently does not have this component implicitly included. It is therefore important to note that the calibrated results here may not be transferable to other dynamic models. However, the Voellmy rheology has been adopted elsewhere to simulate the subaqueous propagation and runout of STS rock avalanches using DAN3D (Mazzanti and Bozzano, 2009, 2011; Schleier *et al.*, 2017; Si *et al.*, 2018). Additionally, the calibrated parameters from this study are generally within the ranges derived by subaerial and STS rock avalanches (Figure 4.13) (Sosio *et al.*, 2008; Mazzanti and Bozzano, 2009, 2011; Aaron and McDougall, 2019).

The respective calibrated parameters of each modelled case were not transferable to the other respective cases here. This is despite the relatively uniform geology and runout path topography. The lack of transferability may be due to the variations in deposit geometries and morphologies of the cases modelled. A single set of parameters may therefore be hard to replicate the bulk behaviour of the deposits compared to if they were all morphologically similar (e.g. Benjamin *et al.* 2018). The calibrated parameters are, however, consistent in that they occupy a relatively narrow range of turbulence parameters, particularly in the subaqueous components of runout. These parameters may be broadly applicable to potential runout forecasting from future rock avalanches into the fjord and may be useful if future instabilities are identified on the fjord walls. Application of the modelled parameters to other STS rock avalanches in fjords elsewhere, or the other mapped events in Milford Sound, might give a more robust indication of how suitable these calibrated parameters are (Figure 4.13).

Whilst best fits were achieved with the aforementioned parameters for each case, the trial-and-error methodology adopted has several limitations. These include that subjective interpretation means different parameter combinations might be found by different users for the same example (Aaron *et al.*, 2019). Attempts to reduce subjectivity have been made by comparing the results against quantitative, morphometric data (Table 4.8). Nevertheless, there is still some degree of subjectivity in the comparisons. Additionally, trial-and-error calibrations mean the entire parameter space is not explored. Therefore it cannot be guaranteed that the best fit parameters have been determined, and the approach does not acknowledge parameter non-uniqueness (Aaron *et al.*, 2019). The new calibration methods developed for DAN3D allow for efficient means of addressing these limitations using analysis that results in objective, systematic and repeatable results (Aaron *et al.*, 2019).

However, the effectiveness of these new methods in addressing the limitations, particularly parameter non-uniqueness, is contingent on available data, such as velocity or accurate deposit thickness data, for constraint (Aaron and Hungr, 2016a; Aaron *et al.*, 2019). The availability of the bathymetric dataset here provides only measurable depositional area data of the rock avalanche deposits, which is subject to uncertainty due to burial and obscuration of extents. There is limited other data available to constrain the result parameters, which would limit assessment of parameter uniqueness in each simulated case. As no velocity constraints exist for the given rock avalanches, further data on individual deposit thicknesses and thickness distribution from systematic seismic reflection studies would give further information for calibration constraint.

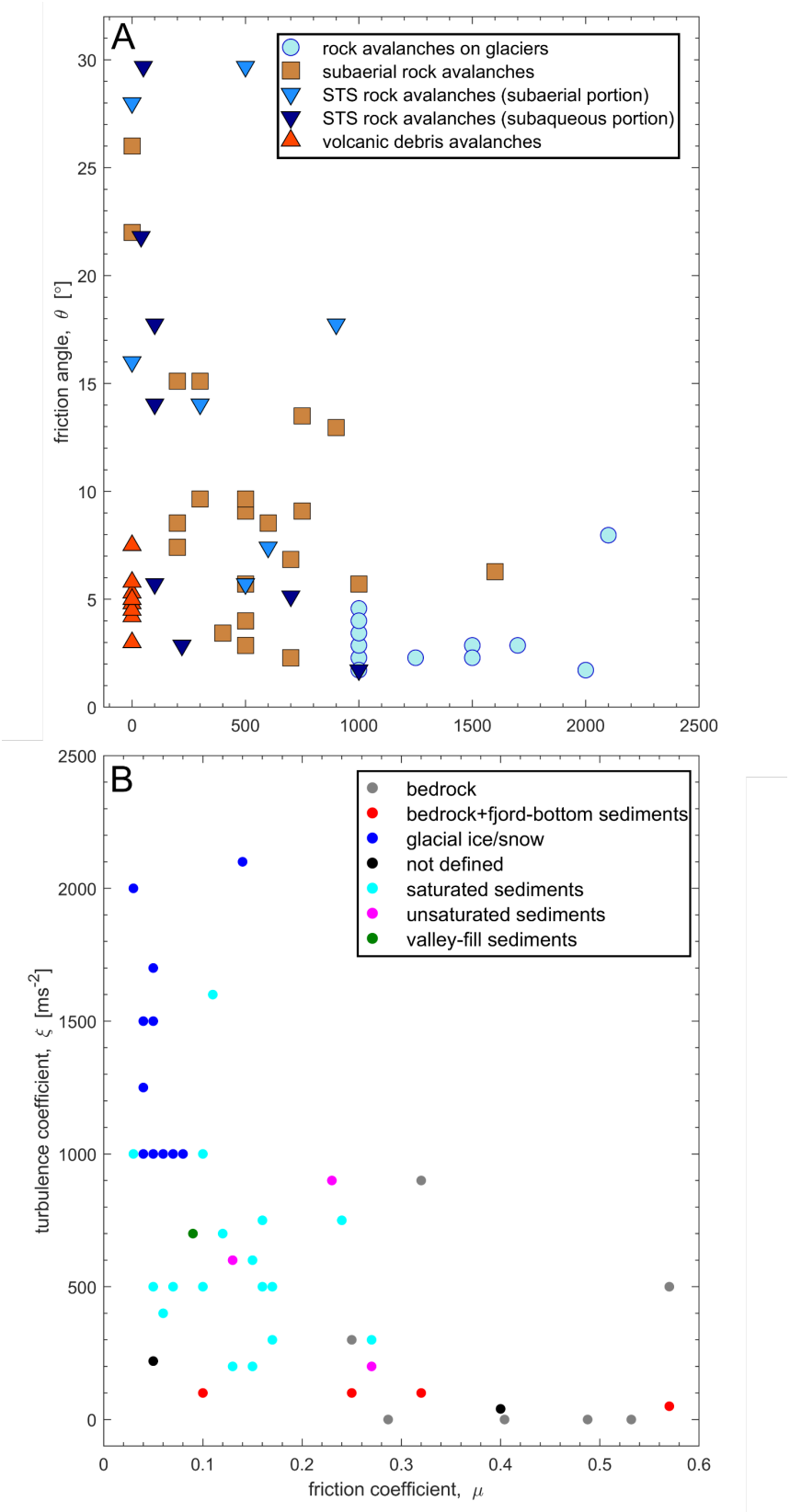

Figure 4.13. Comparison of the best fit parameters from Milford Sound/Piopiotahi rock avalanches against those in literature based on (A) landslide type; and (B) runout path material. Data from Aaron and McDougall (2019) and references therein; Sosio, Crosta, and Hungr (2012), Mazzanti and Bozzano (2009; 2011), and Schleier *et al.* (2017). Individual parameters for each case, and associated references, can be found in Appendix B.

The results here suggest a Voellmy rheology is suitable for modelling STS rock avalanches, and attempts have been made to evaluate the results in terms of flow behaviour with extrinsic factors. However, the use of a Voellmy rheology often lacks any physical explanation or verification (Schneider *et al.*, 2010; Fischer *et al.*, 2012; Pudasaini and Krautblatter, 2014). The developments of two- and multi-phase flow models may aid in addressing some of the complex behaviour of STS rock avalanches. These new models can actively consider changes related to physical factors such as lubrication, fluidisation, dilatancy, and variations in fractions of fluids and friction coefficients (Pudasaini, 2012, 2014; Pudasaini and Mergili, 2019). The factors may be more physically representative of the behaviour of a dry, granular rock avalanche incorporating water, and possible erodible basin sediments during runout in the subaqueous environment.

However, such models require validation against well-constrained prototypes, which may be unsuitable for the deposits in Milford Sound/Piopiotahi given the lack of observation data, uncertainty in deposit thicknesses, and possible effects of post-event sedimentation in burying deposits. Nevertheless, the model results provided good agreement with the mapping interpretations and available morphometric data from the deposits such as mapped extents and runout. Such parameters are often of importance in predictive forecast modelling (McDougall *et al.*, 2012). Furthermore, the consistency in all modelled cases employing a Voellmy rheology reduces the criticism of model adaptability for calibration-based models (Iverson, 2003; McDougall *et al.*, 2012). The consistency in rheologies and calibrated parameters derived here are also in agreement with other studies. Therefore, the parameters established here could provide first-order predictions in forecasting the runout of potential future failures into Milford Sound/Piopiotahi if sites of instability are identified. Furthermore, the modelling results here could be coupled with numerical tsunami models to estimate initial wave heights with landslide impact, as tsunami inundation may be a more significant hazard to the shoreline infrastructures at Milford Sound Village.

4.6. Conclusion

The analysis of the morphology and morphometry of 16 rock avalanche deposits on the fjord bottom of Milford Sound/Piopiotahi, coupled with numerical runout back analysis of a subset of 5 of these rock avalanche events using DAN3D, provides an improved understanding of their emplacement dynamics and mobility. This study found that the lack of topographic confinement, together with runout down the steeper subaerial fjord walls onto the flatter fjord bottom dissipated energy at the front of the rock avalanche. This results in proximally thick,

more lobate deposits that spread both laterally as well as forward. Conversely, rock avalanches that runout over a shallower gradient subaerial path onto steeper fjord bottom appear to form more elongated deposits. Additionally, rock avalanches moving from a subaerial to subaqueous environment exhibit deceleration as momentum is transferred to the water body, which also causes a drag on the flowing landslide mass. These factors control the overall runout length and the mobility of the deposits, which are towards the low end of traditional metrics used to assess apparent rock avalanche mobility (H/L_{max}). However, such values are not too dissimilar to other studied STS rock avalanches globally, suggesting that similar factors may have occurred in those cases. Interaction of the rock avalanches with fjord-bottom sediments may also contribute to their overall runout and mobility through basal deformation and confinement. The evidence is too limited to investigate this fully. Further work based on a more extensive seismic reflection survey of the fjord bottom would provide greater insight into the basal interaction of the impacting rock avalanche with fjord-bottom sediments, by providing greater spatial coverage of the buried rock avalanche deposits which are not visible in the bathymetry.

The runout modelling using DAN3D produced reasonable simulations of STS rock avalanche runouts using two rheologies along the travel path, with a change at the water level, and using parameters within the range of those already published, can plausibly simulate these events, irrespective of the presence of the rock avalanche interaction with water. The Voellmy rheology appears to be the most effective rheology in simulating STS events here. The two adjustable parameters of basal friction coefficient and turbulence in the Voellmy rheology give more control in replicating runout, particularly underwater where Voellmy is employed in all 5 best fit case examples. The turbulence coefficient likely represents resistance to flow in the same way that the water would resist the flowing of the rock avalanche through increased drag and momentum transfer to the water on impact. These modelled results are crucial for hazard planning of future rock avalanche events, and potential tsunami generation of both past and future events in Milford Sound/Piopiotahi.

Chapter 5. Insights into the distribution and controls of subaerial and subaqueous landslides in the Lake Wānaka catchment, New Zealand

5.1. Introduction

Landslides represent a common geomorphic process in hillslope evolution within mountainous landscapes (Montgomery, 2001; Korup, 2008). This is especially relevant in tectonically active regions where high rates of uplift and seismicity can generate abundant landslides (Jibson *et al.*, 2006; Massey *et al.*, 2020). Similarly, in contemporary and previously glaciated mountain regions, glacial and paraglacial processes may have prepared slopes to fail (McColl, 2012; Ballantyne *et al.*, 2014; Pánek, 2019). Landslides also represent a major hazard in these environments (Froude and Petley, 2018). Assessment of the landslide hazard and potential controls requires an extensive spatial and temporal inventory of past events (Pánek, 2019; McColl, 2020). However, few landslide inventories can be considered complete. Landslides and their deposits in tectonically active and humid environments are subject to rapid censoring that alter the true magnitude-frequency distribution (Bainbridge, 2017; McColl, 2020). Such censoring includes reworking or removal of deposits by rivers and glaciers (Barth, 2014; Dunning *et al.*, 2015; Harrison *et al.*, 2015). Additionally, deposits may be obscured by vegetation (Chevalier *et al.*, 2009), or by water bodies such as lakes and fjords (Schnellmann *et al.*, 2002; Blikra *et al.*, 2006; Dufresne *et al.*, 2018).

However with subaqueous investigations, water bodies have the potential to archive and preserve landslide deposits. This can include wholly subaqueous deposits, or subaerial to subaqueous (STS) landslide deposits. The use of modern hydroacoustic (multibeam echosounder (MBES)) surveys of water bodies have been able to identify archives of deposits that are remarkably well preserved on the basin floor (Blikra *et al.*, 2006; Longva *et al.*, 2009; Hilbe *et al.*, 2011; Mountjoy *et al.*, 2019; Sammartini *et al.*, 2019). Additionally, sub-bottom investigations of the basin stratigraphy have identified deposits intercalated within the stratigraphic sequence that extend the temporal history of past landslides that is often not available on land (Schnellmann *et al.*, 2002; Upton and Osterberg, 2007). Therefore, water bodies might hold a high-resolution archive of the magnitude and frequency of past landslides beyond the historical record and so such censoring can be overcome. Identification of deposits in water bodies is also of significance as they may provide insight into the potential of subaerial and subaqueous landslides for generating secondary hazard (tsunamis (Higman *et al.*, 2018)).

In the South Island of New Zealand, rapid geomorphic change occurs due to high rates of tectonic uplift and erosion (Adams, 1980; Korup, 2008), high annual precipitation and sediment yields (Hicks *et al.*, 1996), and glacial erosion by successive glacial cycles throughout the Pleistocene (Shulmeister *et al.*, 2019). Such factors impact the preservation of past landslide deposits, thereby limiting their duration in the sedimentary archive, or altering their distribution (Korup and Clague, 2009; Clague, 2015; Bainbridge, 2017). Additionally, of the deposits that have been identified in the subaerial landscape, information relating to the timing and trigger of many failures and associated deposits is also unknown due to a temporally-short observation record (c. 180 years (Howarth *et al.*, 2018)), and limited absolute dating of such deposits (Bainbridge, 2017; McColl, 2020).

Subaqueous deposition of landslides sourced from terrestrial hillslopes around lakes has been postulated to explain the apparent absence of deposits around many of the water bodies across the South Island (Bainbridge, 2017). Studies commissioned by local authorities have highlighted the hazard from landslides within, or into, lakes in New Zealand (Hancox, 2012; Clark *et al.*, 2015; Mackey, 2015). The landslides may occur independently, or as a cascading geomorphic consequence from external seismic triggers (Robinson and Davies, 2013; Orchiston *et al.*, 2018). However, only within Lake Tekapo is the landslide hazard quantified through the collection of high resolution hydroacoustic MBES and sub-bottom profile (SBP) data (Mountjoy *et al.*, 2019). Acquisition of such datasets within other lakes therefore has the potential to allow quantification of the landslide and associated hazards in the lakes of New Zealand. This is especially pertinent given the probability of a future Alpine Fault earthquake occurring within the next 50 years is 75% (Howarth *et al.*, 2021), significantly greater than previous estimates of 29% (Cochran *et al.*, 2017), which is an event that is likely to trigger a large number of slope failures (Robinson *et al.*, 2016).

This study aims to expand current knowledge by identifying and examining the distribution of subaqueous and subaerial landslides in Lake Wānaka and its surrounding catchment. Lake Wānaka is an intramountainous lake located at the southern end of the Southern Alps of New Zealand. Lake Wānaka was selected as a case study because of its popularity for tourism and shoreline residential infrastructure. There is a large gap in the distribution of large volume ($>10^6$ m^3) catastrophic rock slope failure (RSF) (for example, rockslide and rock avalanche) deposits in this region compared to other locations within the Southern Alps (Bainbridge, 2017). Unlike the Mackenzie Lakes (Tekapo, Pukaki, and Ōhau), no MBES or SBP data exist for Lake Wānaka. Therefore, this study presents the first high-resolution bathymetric and sub-bottom

profile data from the lake. This will quantify both the subaerial and subaqueous landslide distribution, allowing a test of whether deposits in the subaqueous environment can help to complete the landslide record. This will aid with quantification of the landslide hazard in and around the lake basin.

5.2. Study area

Lake Wānaka (277 m.a.s.l., 192 km^2 surface area (Irwin, 1980)) and the surrounding catchment (2578 km^2 surface area) is located in the upper Clutha Valley of the Otago region, at the south-eastern base of the Southern Alps (Figure 5.1). The Wanaka township is located along the southern shores of the lake, with an estimated population of 8900. The lake is a popular tourist destination, particularly in the summer, resulting in heightened numbers during the main tourist window. The NNE-SSW-orientated lake occupies a long, narrow, ice-scoured overdeepened bedrock depression. The lake has a maximum length of 45.5 km, maximum width of 11.6 km, and a maximum local depth of 311 m (Irwin and Ridgeway, 1976; Irwin, 1980). The catchment drainage area (2578 km^2) is largely mountainous, encompassing elevations from 271 to 2685 m.a.s.l. Mean annual rainfall varies significantly across the catchment. The 30 year mean annual rainfall is <600 mm a^{-1} at the southern end of the lake (Macara, 2015). At Makarora, north of the head of the lake, annual rainfall is >2400 mm a^{-1} (Macara, 2015). The primary geology in the catchment is rather uniform, consisting of pelitic and psammitic schistose rocks of the Rakaia Terrane (Turnbull, 2000). The lake is fed by two primary inflow rivers: the Makarora River at the northern end and the Matukituki River towards the south-west. Several smaller rivers and streams from tributary valleys also feed into the lake. Unlike several South Island lakes (including, but not limited to, Lakes Coleridge, Hāwea, Manapouri, Pukaki, Tekapo, and Ōhau), Lake Wānaka has not been artificially dammed for hydroelectric power. Therefore, past, and present lake levels reflect the natural evolution of the lake basin.

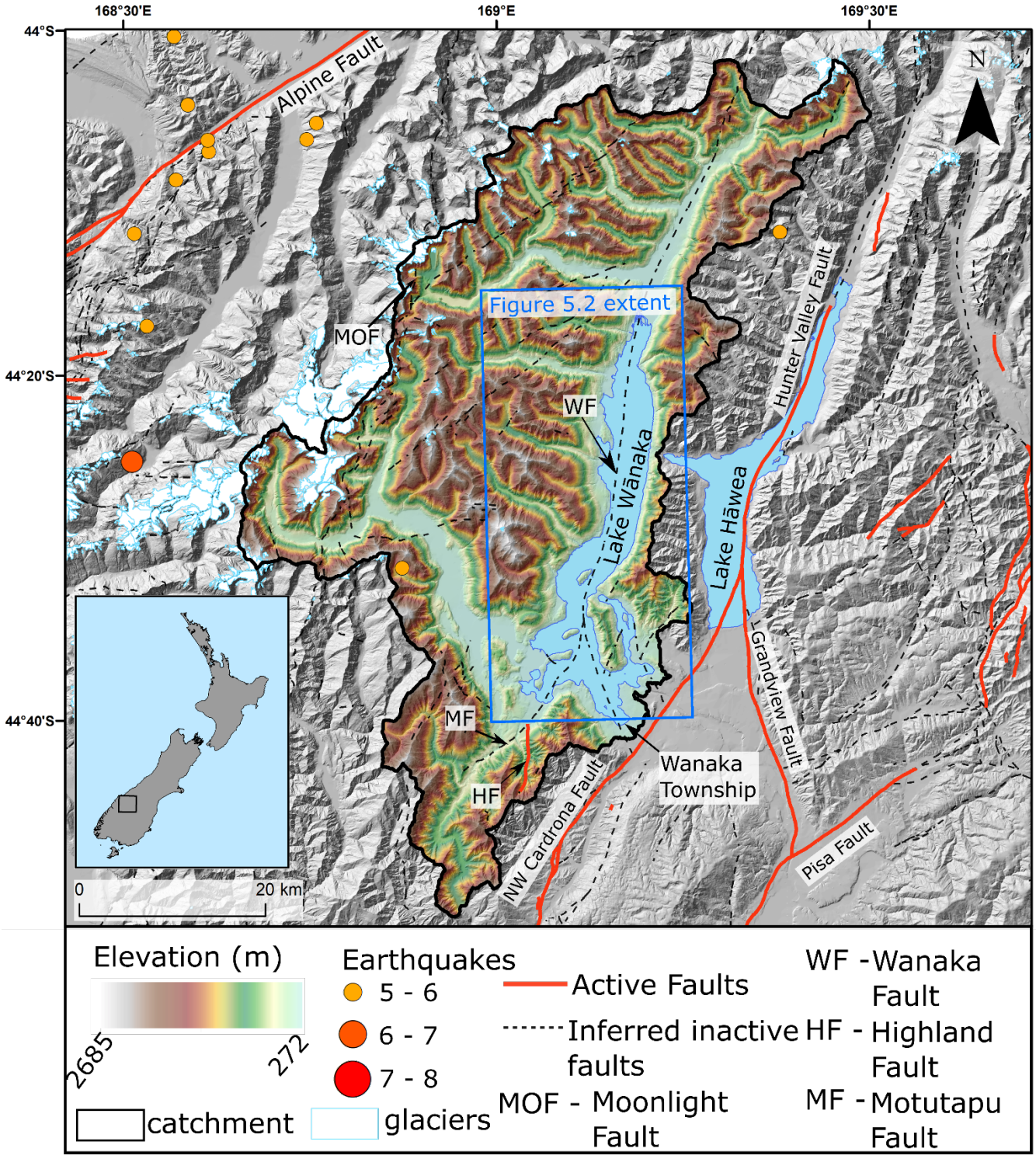

Figure 5.1. Location of Lake Wānaka and its catchment. Inset map shows location of the main figure in New Zealand's South Island. Extent of Figure 5.2 also indicated by blue box. Identified active faults are sourced from Institute of Geological and Nuclear Sciences (GNS Science) Active Faults Database (Langridge *et al.*, 2016) (https://data.gns.cri.nz/af/). The inferred inactive faults are sourced from the 1:250,000 QMAP (Heron, 2014). The location of earthquakes ≥M5 from 1840 to present are shown and sourced from the GeoNet Earthquake Catalogue. Glacier extents are from the Randolph Glacier Inventory 6.0 (2017). Lake polygons and the topographic data are sourced from LINZ data service (https://data.linz.govt.nz/).

5.2.1. Glacial setting

The catchment is a largely relict glacial landscape. At present, only small valley and cirque glaciers remain in the catchment, approximately 30 km from the lake (Figure 5.1). The lake is glacial in origin, created through repeated glacial cycles. The lake is partially blocked by a moraine and a large outwash fan at its southern end (Gage, 1975; Sutherland, Carrivick, Shulmeister, *et al.*, 2019). During the Last Glacial Maximum (LGM) (26.5-19 ka) (Clark *et al.*, 2009), modelled ice reconstructions indicate the lake basin and adjoining valleys were extensively glaciated (Barrell, 2011; Golledge *et al.*, 2012; James *et al.*, 2019). Palaeo-shorelines indicate prominent highstands after the LGM (Sutherland, Carrivick, Shulmeister, *et al.*, 2019). The highest of such shorelines has been mapped to 320 m.a.s.l., 43 m above the present-day lake level. Other prominent shorelines are mapped at 318 m, 311 m, and 309 m (Sutherland, Carrivick, Shulmeister, *et al.*, 2019). Formation of the present lake may have begun after the local New Zealand LGM (LLGM) advance (35-28 ka BP) (Alloway *et al.*, 2007; Barrell, 2011; Putnam *et al.*, 2013). Optically Stimulated luminescence (OSL) dating of sedimentary exposures around the southern shores of the lake constrains the timing of the ice margin position to 32.1 ± 0.57 ka BP (Evans, 2015). Additional dates at 29 ± 0.5 ka BP suggest the ice had retreated into the present day lake basin (Evans, 2015). No younger dates are available around the shoreline at present. It is currently unknown whether deglaciation and lake formation occurred either continuously from 29 ± 0.5 ka BP, or whether there were periods of stillstand and readvance to correlate with the timing of the late and peak global LGM (Shulmeister *et al.*, 2019). Periods of stillstand or readvance have been recorded at other lakes in the Southern Alps at ~21 ka and 18-17 ka (Sutherland, Carrivick, Shulmeister, *et al.*, 2019 and references therein). Absolute dates from many other South Island lakes in the eastern Southern Alps (Hāwea, Wakatipu, Ōhau, Pukaki, Heron, and Coleridge) all indicate a relatively synchronous formation chronology at 19-17 ka BP (Sutherland, Carrivick, Shulmeister, *et al.*, 2019). Therefore, a conservative maximum age of 18 ka for the present-day lake basin is adopted.

5.2.2. Seismic setting

Few earthquakes of M_w >5 have been recorded in the Central Otago region (Figure 5.1) (Warren-Smith *et al.*, 2017). A M_w 5.8 earthquake occurred about 30 km northwest of the Wanaka township in the Matukituki valley on the 4th May 2015, the largest earthquake recorded in the region since GeoNet records began (Cox, Barrell, *et al.*, 2015; Warren-Smith *et al.*, 2017). The lake sits c.50 km from the Alpine Fault, a c.600 km transpressional strike slip fault that

ruptures approximately every 291 ± 23 years (Cochran *et al.*, 2017), and capable of generating M_w 8.0+ earthquakes (Sutherland *et al.*, 2007). Several, more localised faults have been mapped in closer proximity to the lake (Cox *et al.*, 2012; Litchfield *et al.*, 2014; Langridge *et al.*, 2016; Barrell, 2019). The faults identified in Central Otago generally have low long-term displacement rates (Litchfield *et al.*, 2014), resulting in long recurrence intervals. South of the Wanaka township is the NW Cardrona Fault which is the most active fault in the region with a calculated rupture interval of c. 5500 years (Barrell, 2019). Other nearby active faults include the Hunter Valley Fault that extends through Lake Hāwea, and the Highland Fault that extends through the Glendhu Bay area. Other faults have been mapped within the catchment, including through Lake Wānaka by Turnbull (2000), but fault activity is unknown. These other faults include: the Motatapu Fault that extends north-east from the Glendhu Bay under the lake towards The Peninsula; and the Wanaka Fault (Makarora Fault in Litchfield *et al.*, (2014)), which extends the length of lake and under the Makarora River floodplain.

5.2.3. Landslide setting

Large, slow-moving landslides are common across the schist hillslopes in the Central Otago region (Whitehouse, 1983; Turnbull, 2000). Flexural toppling, and block flexural toppling failures have also been identified along the eastern slopes of Lake Wānaka, towards the head of the lake (Halliday, 2010). The toppling occurs on anti-dip slopes where the dip exceeds ~45° (Halliday, 2010). Catastrophic RSFs also occur but appear sparser compared to other regions in the Southern Alps. Only a few former rockslides and associated dams have been identified or documented in both the Wānaka catchment, and neighbouring catchments (Korup, 2011; Massey *et al.*, 2013). In 2007, an 11 million m^3 rockslide occurred in the North branch of the Young River valley, blocking the river, and formed a landslide-dammed lake, which still remains at present (Massey *et al.*, 2013). There is an apparent absence of rock avalanche deposits within the catchment (Bainbridge, 2017). Adjacent catchments contain several large RSF deposits, including the 140 x 10^6 m^3 Polnoon Burn rockslide (Korup, 2011), and the 690 x 10^6 m^3 Lochnagar rockslide dam in the Shotover River catchment (Korup, 2011; Sweeney *et al.*, 2013), and the Hillocks rock avalanche in the nearby Lake Wakatipu catchment (McColl and Davies, 2011; McColl *et al.*, 2019). The 2015 M_w 5.8 earthquake triggered 37 landslides in an area of 800 km^2 surveyed through two aerial reconnaissance flights. Twenty seven of the landslides were reactivations of older events, and cumulatively produced a total landslide volume of only 30,000 m^3 (Cox, Barrell, *et al.*, 2015). However, the flight paths were restricted to the south and west of the epicentre. Regions to the north and east were not investigated but

could have potentially contained other coseismically generated landslides. Debris flows are also common in many of the tributary catchments. Significant debris flow events in Waterfall Creek in 1983, and again in 1994, destroyed a bridge both times, removing both bridges into the lake (McSaveney, 1995).

5.3. Methods

5.3.1. Subaerial landslide distribution and topographic position

To identify the landslides and compile an inventory of deposits within the subaerial catchment, a methodology similar to Korup (2005a) was adopted, using the following datasets:

1. Aerial photo interpretation (API) of 0.3 m resolution aerial imagery collected during 2017-2019, and 0.75 m imagery collected during 2004-2011, over the catchment region. Both imagery datasets were sourced from the LINZ Data Service (https://data.linz.govt.nz/layer/51910-otago-075m-rural-aerial-photos-2004-2011/, https://data.linz.govt.nz/layer/104460-otago-03m-rural-aerial-photos-2017-2019/), and licenced by Otago Regional Council (for 0.3 m imagery), and Terralink International Limited and Otago Regional Council (for 0.75 m imagery), for re-use under the Creative Commons Attribution 4.0 (CC BY 4.0) International licence.
2. Analysis of digital elevation/surface models (DEMs/DSMs) including:
    i. The Landcare Research 25 m DEM for New Zealand (https://lris.scinfo.org.nz/layer/48127-nzdem-south-island-25-metre/)
    ii. The 2012 8 m NZ DEM v2.1, created by Geographx. The dataset was sourced from LINZ Data Service (https://data.linz.govt.nz/layer/51768-nz-8m-digital-elevation-model-2012/), licenced for reuse under the CC BY 4.0.
    iii. the 15 m NZSoSDEM v1.0 (Columbus *et al.*, 2011), licenced under Creative Commons Attribution-Share Alike 3.0, and available at https://koordinates.com/.
    iv. The 30 m Japan Aerospace Exploration Agency (JAXA) Advanced Land Observing Satellite (ALOS) World 3D (AW3D30) DSM v2.1. available at https://www.eorc.jaxa.jp/ALOS/en/aw3d30/index.htm.
    v. The Advanced Spaceborne Thermal Emission and Reflection Radiometer (ASTER) 30 m Global DEM (GDEM) v2.
3. Review of scientific literature, including theses and published reports, where available.
4. Landslide databases including:
    i. The rock avalanche database from Bainbridge (2017).

ii. The 1:250 000 QMAP (Turnbull, 2000; Rattenbury *et al.*, 2010; Rattenbury and Isaac, 2012; Heron, 2014). Web Map Service layers for GIS are available for download from GNS Science (https://www.gns.cri.nz/Home/Our-Science/Land-and-Marine-Geoscience/Regional-Geology/Geological-Maps/1-250-000-Geological-Map-of-New-Zealand-QMAP). The data is licenced under the CC BY 4.0 licence, © GNS Science 2016.

iii. The New Zealand National Landslide Database (NZNLD) (http://data.gns.cri.nz/landslides/) (Rosser *et al.*, 2017).

Manual mapping of deposits was conducted in ArcGIS ArcMap v.10.6 at a 1:3,000 scale on the 0.3 m imagery. The 0.75 m imagery was used to aid where shadows obscured areas on the 0.3 m imagery. Where clearly defined, both the headscarp and deposit were mapped. In some cases, the scar was not clearly identifiable so only the deposit was mapped. Mapping focussed only on RSFs. Diagnostic landform assemblages that aided mapping included exposed rock surfaces in scars, asymmetric valley profiles, bulging toes, headwater piracy (Korup 2005b), surficial flow structures (Dufresne and Davies, 2009), and other surface morphological features e.g. sackung (Pánek and Klimeš, 2016). River planform disruption was also quantified through knickpoint extraction. Knickpoints were extracted along river profiles within the catchment using 'knickpointfinder' in Topotoolbox (Schwanghart and Scherler, 2014, 2017). Knickpoints are useful diagnostic features that can be the result of bedrock landslide-river disruption in mountainous catchments (Korup, 2006b). Knickpoints were extracted on the AW3D30 DSM and ASTER GDEM. Knickpoints were then displayed against the digital QMAP (Heron, 2014) and modelled LGM ice extents (James *et al.*, 2019). This allowed for delineating knickpoints because of likely landslide-river disruption, and those caused by glacial erosion and truncation, and/or geological controls such as faults, folds, and lithological contacts.

Surface areas (A_L) were calculated for each mapped deposit. Digitisation error tests were computed through repeated manual digitisation of a 10% subset of the total number deposits over 5 concurrent days, and computing variations in the surface areas. The maximum relative error for (A_L) was +17.6/-17.5 %. Estimated volumes (V_L) were derived using a previously published volume-area scaling relationship from New Zealand. Only the 2007 Young River RSF has a reported deposit area and volume from pre- and post- terrain analysis (Massey *et al.*, 2013). Some previously reported deposits within the catchment only report volumes, and no available polygon shapefiles to derive deposit areas (Korup, 2011). There is insufficient independently calculated deposit volumes and area data to derive a catchment-specific volume-

area scaling relationship. The volume-area scaling used is the New Zealand bedrock relationship from Larsen *et al.,* (2010), that fits the form $V_L = \varepsilon A_L^{\ b}$:

$$V_L = 10^{-1.60} A_L^{\ 1.49} \quad [5.1]$$

Larsen *et al.,* (2010) report ε in its base log10 form, so Equation 5.1 calculates volume by taking the inverse log 10^{ε}.

The topographic position of the mapped landslides were also investigated following the methodology of Meunier *et al.,* (2008). The positions of the landslides were plotted relative to ridge crests and streams. Ridges and streams were extracted automatically on the AW3D30 DSM using Topotoolbox (Schwanghart and Scherler, 2014). A stream network was extracted on areas above a calculated hillslope-channel slope area threshold (Montgomery, 2001). In the catchment, this was computed at 1.9 km^2. A ridge network was extracted from drainage divides from the computed stream network (Scherler and Schwanghart, 2020). Flow distances from the nearest ridge (d_{top}) and to the nearest stream (d_{st}) were then computed along a flow path. The flow distances were normalised by the total length of the slope using:

$$\left|d_{st}, d_{top}\right| = \frac{d_{st}, d_{top}}{d_{st}+d_{top}} \quad [5.2]$$

$|d_{st}|$ ranges between 0 and 1, where 0 is for cells located in river channel and 1 is for a ridge cell, and $|d_{top}|$ is the inverse. The position is reported from the highest and lowest point in individual landslides, where $|d_{top}|$ and $|d_{st}|$ are used as dimensionless coordinates (x, y). The areas of the respective landslide are displayed by means of circles with varying diameters. The centroids of the landslides were also used to estimate the non-weighted spatial density of deposits within a moving kernel window with a 2 km radius.

5.3.2. Subaqueous landslide distribution

To identify any deposits within Lake Wānaka, a bathymetric and sub-bottom survey was conducted. An initial bathymetric raster was created to aid the survey by digitising the bathymetric contours of Irwin and Ridgeway (1976). The surface area of the lakebed from this raster was 204.9 km^2. High-resolution bathymetric data was collected over 6 days in November 2018 on board the University of Canterbury's research vessel *R.V. Muritai*. These data were collected using a 117 kHz Bathyswath-1 interferometric phase-differencing bathymetric sonar (PDBS) system. Pitch and roll were accounted for with a Ship Motion Control Internal Motion Unit (IMU) (Type IMU-108). Position was recorded using Trimble R8 GNSS GPS in real-time kinematic (RTK) where possible. A second unit recorded position for post-processed kinematic

(PPK) position, where necessary. Specific areas were targeted during the survey based on probable locations for subaqueous landslide deposits (Sammartini *et al.*, 2019). Targeted areas focussed primarily on surveying: (i) the subaqueous lateral slopes around the lake perimeter, (ii) the Matukituki and Makarora deltas, and (iii) areas directly below slopes where probable geomorphic evidence of past subaerial landsliding were present. Sound velocity profiles (SVPs) were taken daily during the bathymetric data acquisition using a Valeport™ miniSVP in the locations surveyed to correct for velocity changes in the water column. Corruption of one of the SVP files occurred from the area south of the Peninsula, meaning it was unusable for the processing. Data in this region were corrected using the next closest SVP. The PDBS data were recorded, filtered, and velocity corrected using Bathyswath Swath Processor. Post-processing was done in Bathyswath Grid Processor. Processing steps involved roll calibrations of the survey data, manual point cloud editing and deletion, and automatic despiking, smoothing, and interpolation. The data were gridded at 2 m in QT Modeller®, generating a bathymetric terrain model (BTM). The model was imported into ArcGIS ArcMap v10.6.1 for interpretation and mapping. Slope and multidirectional hillshade rasters (3x vertical exaggeration) were derived from the BTM to aid interpretations. The Bathyswath-1 PDBS system also recorded backscatter amplitude data of the lakebed. The backscatter data were rasterised to create a 2D side-scan sonar dataset. A lost component of the PDBS mount on one survey day resulted in half a days' surveying being lost whilst a replacement part was constructed. Poor weather and rough lake conditions on the final surveying day meant the bathymetric survey return pass on the northwestern side of the lake had to be abandoned (Figure 5.2).

A sub-bottom profiling survey was conducted using a SyQwest Bathy2010PC and StrataboxHD 3510 dual 3.5 kHz transducer chirp system. The sub-bottom survey was done separately after the bathymetric survey. Due to a combination of poor weather/lake conditions, boat availability, and instrument mount damage, only 4 and a half days of surveying could be completed (Figure 5.2). Positional information for each ping during the sub-bottom survey was obtained using a GlobalSat® GPS system receiver (<±2.5 m 2D root mean square horizontal error (RMSE)). Targeted survey lines were collected over areas of previously acquired multibeam data. Other targeted areas were located across the lake from where no bathymetric sonar data had been collected, but where geomorphic evidence indicated that subaerial landsliding had occurred (i.e. identified probable landslide scars). The sub-bottom profile (SBP) data files were imported and processed in SonarWiz 7 software. Processing steps involved digitising the lakebed reflector. An Automatic Gain Control with 30% window size and 11% intensity was then applied to the

data, starting from the digitised lakebed reflector. These gain values were applied to all the data files. No SVPs were taken during the duration of the sub-bottom profile survey. Therefore, the two-way travel time-to-depth conversion is based on a constant p-wave velocity of 1450 m s^{-1} for both the water column and sediment sequence. The assumed velocity was based on the typical velocity at depth in the previously collected SVPs. All references to sub-bottom thicknesses and depths are based on this time to depth conversion.

Morphometric parameters of the landslides were calculated following the approach of Clare *et al.,* (2018), and are reported in detail in *Chapter 4*. The volume of deposits originating from the subaerial environment, and where SBP data were unavailable, or were unable to detect the base of the deposits, are calculated using the volume-area scaling outlined in 5.3.1. Volumes of deposits where the base is detected in SBP are calculated using the following volume-area scaling relationship for subaqueous landslide deposits from Clare *et al.,* (2018):

$$V_L = A_L \times \frac{2}{3}\ maximum\ deposit\ thickness \qquad [5.3]$$

No cores were taken during the field campaign. Therefore, interpretations and analysis of the lake morphology and sedimentology were done from the bathymetric sonar and SBP data where available.

A first-order estimation of the current annual sedimentation rate into Lake Wānaka was calculated following the approach of Robinson *et al.,* (2016). This approach calculates catchment denudation rates using the annual suspended sediment yield (SSY, measured in t km^{-2} yr^{-1}) model (Hicks *et al.*, 2011; NIWA, 2020). It is assumed lakes have a 100% sediment trapping efficiency (Hicks *et al.*, 2003, 2011). Therefore, denudation rate in the catchment is directly proportional to an annual sedimentation rate in Lake Wānaka. Over the defined catchment, the total denudation rate in the catchment was calculated by:

$$Denudation\ rate = \left(\frac{2SSY}{\rho}\right)/(total\ catchment\ area - depositional\ area) \qquad [5.4]$$

where ρ is the density of the suspended sediment in t m^{-3}. The value of ρ is set to 2.5 t m^{-3} as it corresponds to the density of schist (Robinson *et al.*, 2016), the primary rock type in the catchment. The factor of 2 corresponds to an estimation that suspended sediment in rivers in New Zealand may only be ~50% of the total sediment capacity of the river (Davies and McSaveney, 2006; Robinson *et al.*, 2016). Unlike SSY, the information related to other transport mechanisms, particularly bedload transport, in New Zealand rivers is poorly known (Hicks *et al.*, 2011). This limits additional yield estimations within the rivers by such processes.

Some estimates of bedload yields are available for gravel-braided rivers crossing the Central Canterbury Plains such as the Waimakiriri, Ashburton, Waitaki, and Rakaia Rivers. Their bedload sediment yields equate to ~13% the SSY (Carson and Griffiths, 1989; Hicks *et al.*, 2011). However, there is likely significant variations between rivers either side of the Main Divide and draining different geological regions (Carson and Griffiths, 1989; Hicks *et al.*, 2011). Therefore, the factor of 2 in Equation 5.4 theoretically and conservatively accounts for all other sediment yield capacities within the rivers, including bedload. The depositional area (in km^2) is the area of most recent Quaternary units in each catchment, derived from the 1:250,000 digital QMAP (Rattenbury and Isaac, 2012; Heron, 2014). The catchment denudation rate also factored in trapping of sediment in both modern proglacial lakes, and the 2007 RSF-dammed lake on the North Young River.

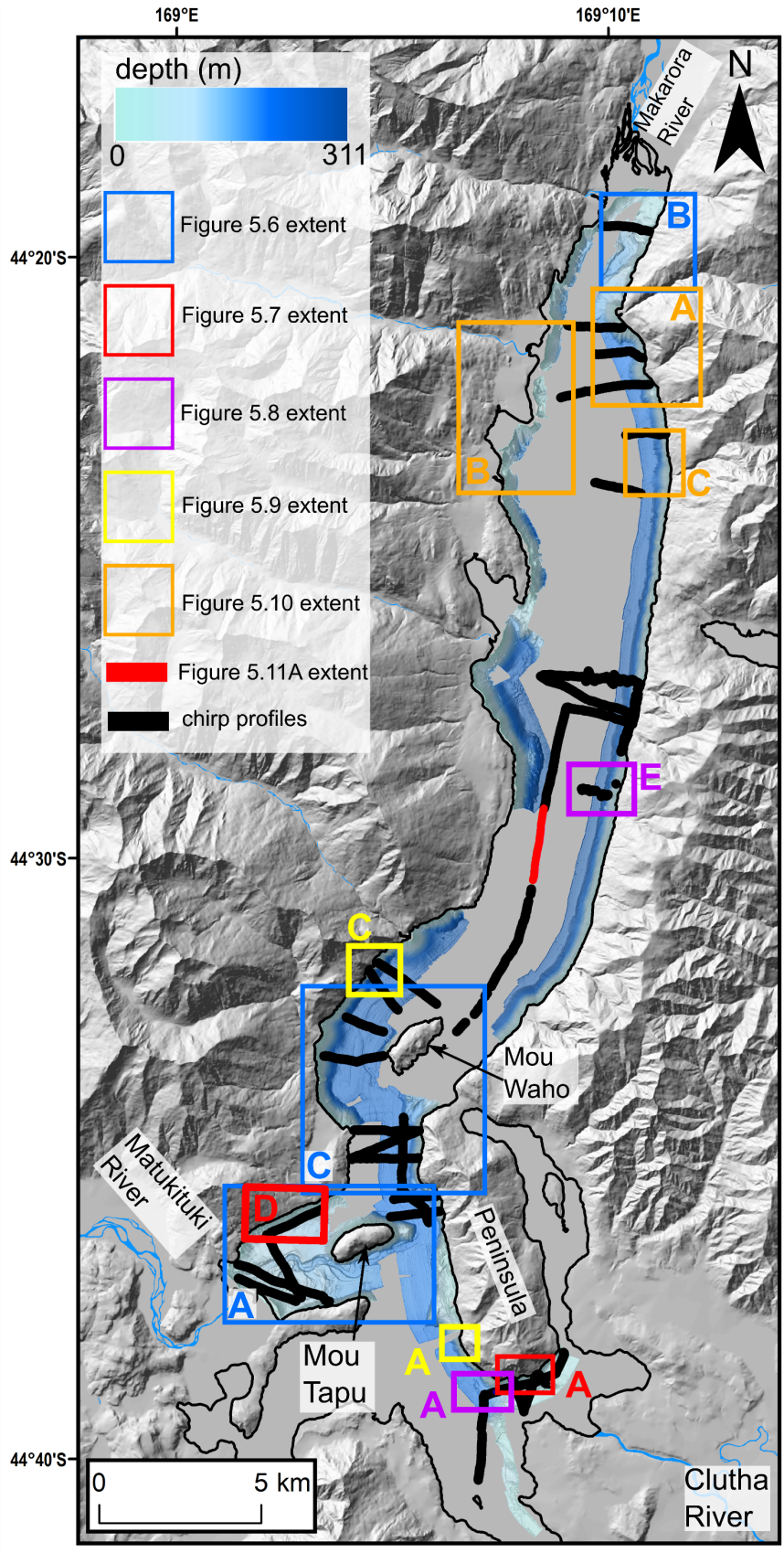

Figure 5.2. Overview of PDBS and SBP (chirp) data collected in this study. Frame indicators relate to subsequent figures and letters correspond to named panels in the respective figures. Bathymetric data denoted by coloured bathymetric hillshade model and chirp profiles by black lines. River shapefiles are sourced from LINZ data service (https://data.linz.govt.nz/).

5.3.3. Landslide size-frequency distribution

The frequency distribution of the subaerial and subaqueous landslides in the catchment of Lake Wānaka was assessed. The relationship between volume (and/or area), and frequency of moderate to large landslides in distributions tends to be well described by a power law function (Tanyaş *et al.*, 2018, 2019; Tebbens, 2020). Several methods to characterise landslide frequency distributions have been adopted. These methods include probability density function (PDF), cumulative (CDF), and non-cumulative frequency-area distribution (FAD), and frequency density distributions (FDD) (Tebbens, 2020). Methods have been applied to extend the power law distribution across the whole dataset using a double-Pareto (Stark and Hovius, 2001), or inverse gamma distribution (Malamud *et al.*, 2004). Lognormal distributions have also been applied to landslide databases (Dunning *et al.*, 2007).

For smaller landslides within an inventory, the relative frequencies can often depart or diverge from this power law function that is fit to the largest landslides. Where this divergence first happens in the curve is defined as the cutoff point and is visible in cumulative and non-cumulative FADs (Stark and Hovius, 2001). The distribution curve fit to the landslide inventory in non-cumulative FADs can change slope from a positive gradient which is often fit to the smaller landslides, to a negative slope which is fit to the medium and larger landslides (Tanyaş *et al.*, 2019; Tebbens, 2020). The peak point at which the slope changes sign and the frequency density value begins to decrease is referred to the rollover point (Malamud *et al.*, 2004; Tanyaş *et al.*, 2018; Tebbens, 2020).

In this study, the power law distribution of the landslides was analysed. The analysis was first done on the deposits mapped solely in the subaerial environment. This was then replicated to incorporate deposits identified in the lake, creating a combined subaerial-subaqueous distribution. This approach applies a power law function to the cumulative distribution of landslides, $p(X)$, for areas above the cutoff value following the equation:

$$p(X) = cX^{-\beta} \quad [5.5]$$

Where X is the landslide area (in log bins), c is the normalisation constant, and β is the power law function scaling exponent (Tanyaş *et al.*, 2018). The surface areas (in m^2) of each mapped landslide deposit were used as input rather than volumes due to uncertainties with accurate volume estimation by the volume-area scaling relationship. Furthermore, areas vs. landslide magnitude have been shown to exhibit power law scaling as well (Stark and Hovius, 2001).

First, the cumulative frequency-area continuous distribution (CDF) (Equation 5.6) of all mapped landslide deposits identified in the Wanaka catchment was analysed. This follows the methodology of Clauset *et al.,* (2009), applied using R (R Core Team, 2019).

$$P(X \leq x) = 1 - \left(\frac{x}{x_{min}}\right)^{-\beta+1} \quad [5.6]$$

The cutoff (x_{min}) and β values were defined following the method of Clauset *et al.,* (2009) which adopts a reproducible numerical approach. This allows objective estimation of landslide event magnitude (Equation 5.7), removing the uncertainty of visual comparison (Malamud *et al.*, 2004). The exponent parameter α is derived using a Maximum Likelihood Estimator (MLE) method, which for the continuous power law is:

$$\hat{\alpha} \simeq 1 + n\left[\sum_{i=1}^{n} ln\frac{x_i}{x_{min}}\right]^{-1} \quad [5.7]$$

Where x_i is the observed data values and $x_i \geq x_{min}$ (Gillespie, 2015) and conditions on particular value of x_{min}. The x_{min} value was derived using a Kolmogorov-Smirnov (KS) goodness-of-fit statistical approach (Clauset *et al.*, 2009; Gillespie, 2015) which calculates the maximum distance between the data and model fit of CDF:

$$D = \max_{x \geq x_{min}} \left|S_{(x)} - P_{(x)}\right| \quad [5.8]$$

Where $S_{(x)}$ is the CDF of the data, and $P_{(x)}$ is of the model (for $x \geq x_{min}$). The x_{min} value returned is where x_{min} minimises D. The derived α can be erroneously large when x_{min} estimates are so large that the number of observed $x \geq x_{min}$ data is small. Therefore, the search of x_{min} was truncated to avoid generating erroneously large values, minimising the finite-size bias. The uncertainties in the estimated parameters x_{min} and α were calculated following the Clauset *et al.,* (2009) method using a non-parametric bootstrap algorithm. The validity of the power-law distribution to the data was also tested using a goodness-of-fit test KS statistic in a bootstrapping algorithm to generate a p-value. A p-value $\simeq$ 0 and < 0.1 may indicate that the power-law distribution is not a good fit for the dataset, whilst a p-value $\simeq$ 1 indicates that the data is a good fit to the power-law distribution (Clauset *et al.*, 2009; Tanyaş *et al.*, 2018). For comparison, the lognormal cumulative distribution of the data was also calculated.

A non-cumulative FAD curve was also generated, as cumulative distributions often do not show the rollover (Tanyaş *et al.*, 2018). The FAD and landslide event magnitude (*mLS*) was derived following the methodology and MATLAB script of Tanyaş *et al.,* (2018). In the FAD curve, the deposits were sorted in automatically generated logarithmic bins. Tanyaş *et al.,* (2018) also

follow the method of Clauset *et al.,* (2009) to derive the x_{min} and β parameter values. Therefore, the values and uncertainties derived for the CDF plot were used as input. The generated value for *mLS* and its uncertainty provides an objective and reproducible method to generate the landslide event magnitude. This reduces uncertainties compared to subjective visually based methods. The precursory approach to derive x_{min} and β follows the method of Clauset *et al.,* (2009). Therefore, the results derived in generating the power law for the CDF are used as inputs, as well as the uncertainty values derived by the bootstrap algorithm.

5.4. Results

5.4.1. Subaerial landslide distribution

Within the catchment, 202 subaerial RSF deposits were identified. Of the deposits identified, *n=201* were newly mapped within this study. Many of the mapped deposits overlap pre-existing hillslopes with identified deposits, including 3 previously identified palaeo rockslides from Korup (2011). However, these original shapefiles were not available and therefore were mapped independently here. Additionally, in this study the deposits are mapped as polygons rather than point files. Similar non-descript point files are the only data available in the NZNLD (Rosser *et al.*, 2017). Many of the hillslopes with deposits are only identified on the geological map (QMAP). However, those deposits are non-specific on landslide type, not delineating bedrock and regolith failures. Also, the QMAP data often shows entire valley hillslopes as a single landslide, rather than individual events. Therefore it is unknown the exact number of previously identified landslide deposits there are in comparison to the inventory presented here. Furthermore, the landslides in QMAP are mapped at 1:250,000 scale. In contrast here the deposits are mapped at 1:3,000 scale, using DEMs of various resolution (8 – 30 m), and high-resolution aerial imagery (<1 m scale). Therefore the subaerial inventory here represents the highest resolution inventory available across the catchment. The only deposit not mapped in this study was the Young River RSF (Massey *et al.*, 2013) which was already in the Bainbridge (2017) database as a polygon shapefile.

Deposit A_L and volumes range between 2.43×10^4 to 4.61×10^6 m^2 and 8.55×10^5 to 2.13×10^8 m^3 respectively. The volume-area scaling overestimates the volume of the Young River RSF by around 4% of the 11 M m^3 volume derived from pre- and post-failure DEM analysis (McSaveney and Massey, 2013). There is an over- and under-estimation by 111% and 71% respectively, of two other independently derived volumes of rockslides identified by Korup (2011). However the polygons and therefore areas of the rockslides calculated by Korup (2011) were unknown and therefore cannot be compared to the areas derived from mapping in this

study. Similarly, the method used to derive volumetric estimates by Korup (2011) is unknown. The cumulative area affected by subaerial RSF deposits in the catchment is 118.2 km^2, equating to 4.6% of the total catchment area. The deposits identified are primarily translational or rotational rockslides (Hungr *et al.*, 2014), or deep-seated gravitational slope deformation (DSGSD) landslides (Agliardi *et al.*, 2001; Pánek and Klimeš, 2016). Collectively, the RSF deposits exhibit a lower modal slope angle (27°) to the modal hillslope angle within the catchment (33°) (Figure 5.3). The smallest area RSF deposits (10^4 -≤ 10^5 m^2) exhibit the highest modal slope angle (30°). In contrast, the largest deposits (>10^6 m^2) exhibit the most subdued slope angles (26°), possibly indicating more hillslope angle lowering by the largest landslides.

The relative topographic position of RSF deposits shows a higher apparent density towards streams (Figure 5.4). Of the mapped deposits, 145 (~72%) extend to the lowest 25% of hillslopes ($|d_{st}| \leq 0.25$), whilst over 50% are almost directly connected to streams ($|d_{st}| \leq 0.1$) (Figure 5.4B). The largest deposits (by area) extend to the upper 25% of hillslopes ($|d_{top}| \leq 0.25$), and/or are clustered towards the ridge crests ($|d_{top}| \leq 0.1$). Fifty-four (26.7%) of the mapped deposits extend from the upper quarter of the slope to the lower quarter of the slope, with some deposits clustered towards the origin of the plot (Figure 5.4A). This indicates RSF that involved whole slope failures. There is a small cluster of 12 (6%) smaller deposits (by area) towards the toe of the slopes ($|d_{top}| \geq 0.75$ $|d_{st}| \leq 0.25$) and a less dense cluster of slightly larger deposits up towards the ridge crests ($|d_{top}| \leq 0.25 |d_{st}| \geq 0.75$).

The spatial density of the mapped deposits shows areas of apparent higher densities towards the southern end of the catchment, and in the central region, within the western tributary valleys to Lake Wānaka (Figure 5.5). The density of deposits in the southern region is within the driest region of the catchment (<1000 mm a^{-1}), and the density of deposits in the central region of the catchment is within the mid-range of 2000 – 4000 mm a^{-1} deposits (Figure 5.5B). The regions with the highest estimated mean annual rainfall show a comparatively low apparent density of deposits (Figure 5.5B). The areas of highest apparent density of events are within 10 km of the main fault structures near the catchment (Figure 5.5C). However, when considering only the known active faults, the central cluster of deposits are up to 40 km from the nearest active fault (Figure 5.5D).

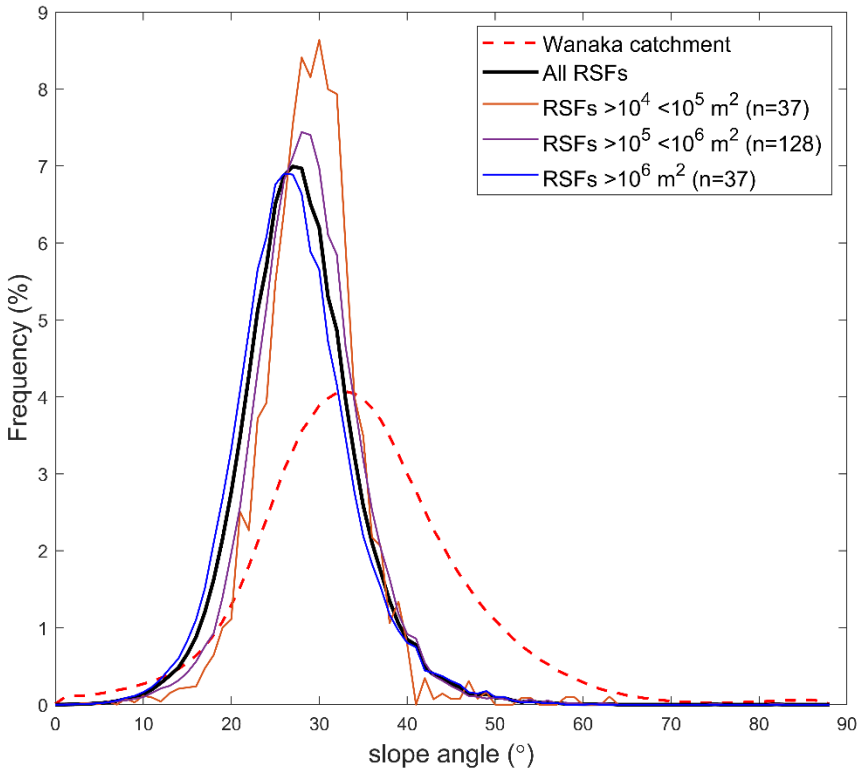

Figure 5.3. Frequency distribution of surface slope angles normalised by total area of the hillslopes and RSF deposits and grouped by deposit area.

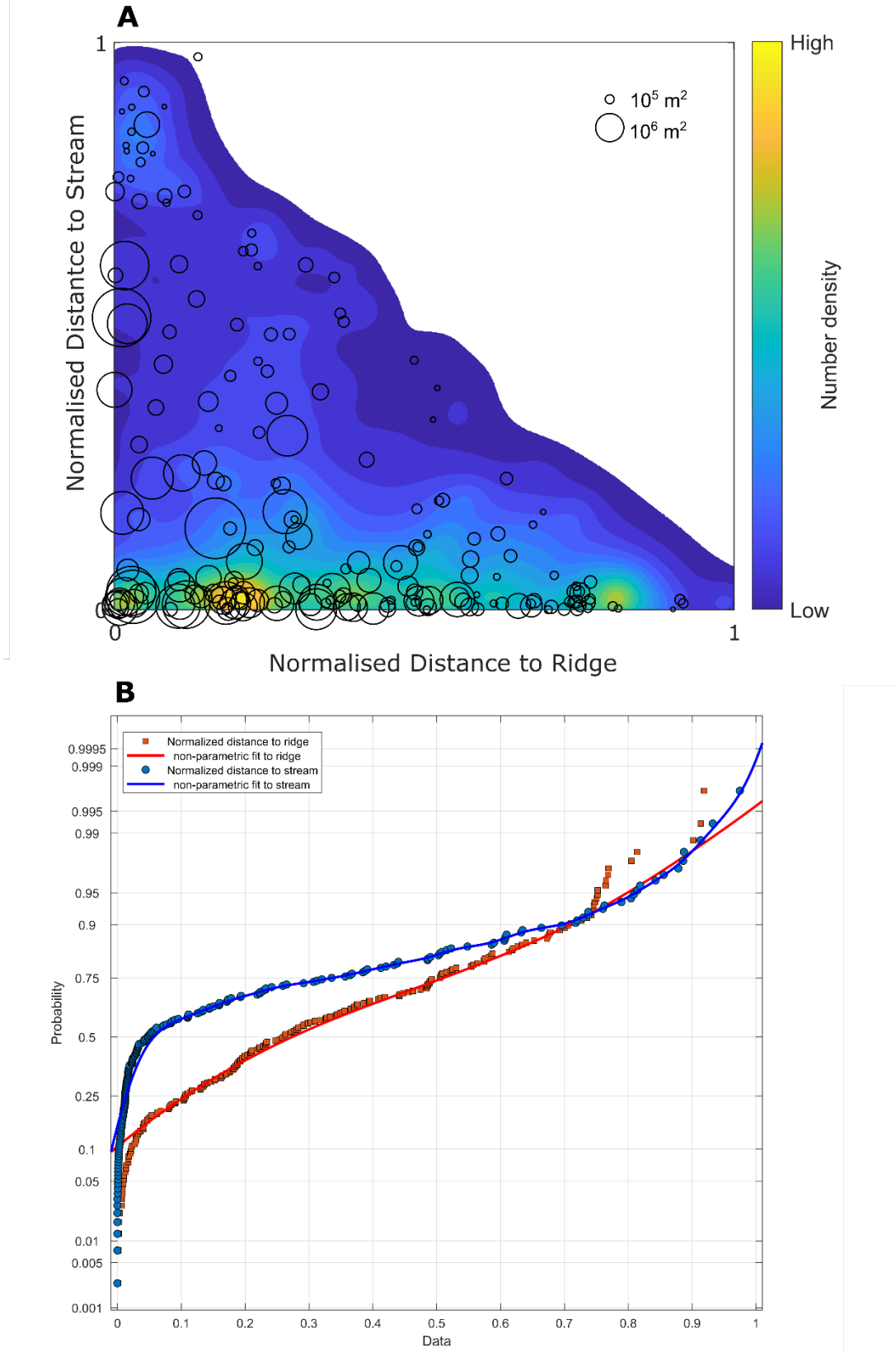

Figure 5.4. Location of subaerial landslides with respect to their distance to ridge crests and streams with relative density of data points underlying plot (a); and the relative frequency distribution of the computed data values (b).

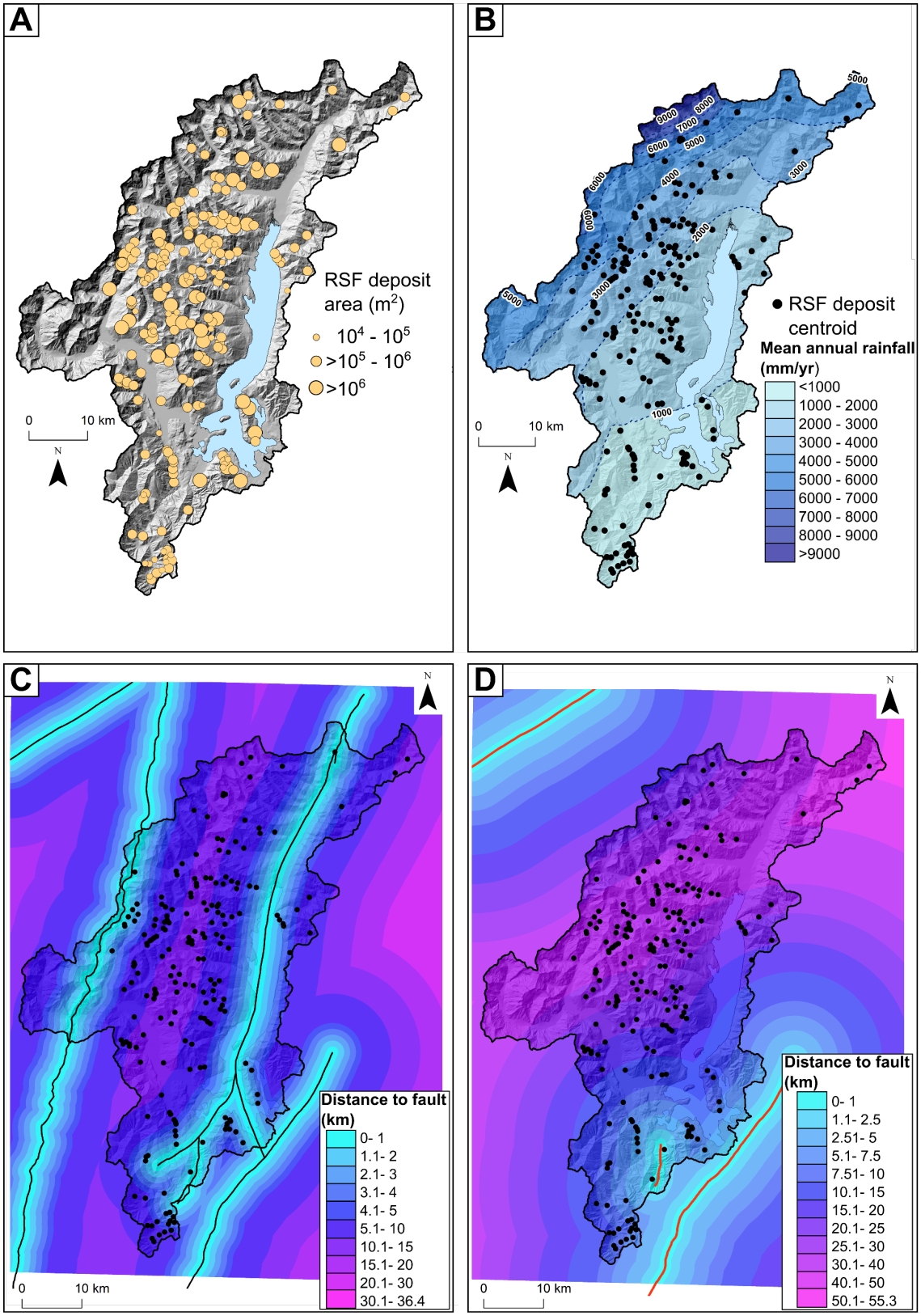

Figure 5.5. (a) the distribution of RSF deposits in the catchment, represented as centroid points, scaled proportionally by deposit area (m^2); (b) the deposit distribution (by centroid point) against mean annual rainfall (rainfall contours shown by black lines (in mm yr^{-1})); (c) the deposit distribution (by centroid point) against the Euclidean distance (in km) to the main faults (active and inferred inactive (black lines)) within the region; and (d) Euclidean distance to the active faults (red lines) within the region. See Figure 5.1 for fault names. Mean annual rainfall model data provided by and copyright of the National Institute for Water and Atmospheric Science (NIWA, pers. comm.).

5.4.2. Lake geomorphology

A total of 77.5 km^2 of new, high-resolution bathymetric data was collected during the survey. This equates to 37.5% of the total lakebed mapped, compared to the surface area from the initial bathymetric raster digitised from contours (204.9 km^2). The new BTM data reveals previously unknown details of the subaqueous geomorphology of Lake Wānaka. The lake morphology is typical of an intra-mountainous glaciogenic lake. The lateral slopes of the lake basin are steep (>20° to near vertical subaqueous cliffs), whilst the lakebed is relatively flat (<4°). The lake appears to lack any glacial morphological features on the bed.

Three distinct sublacustrine channel sections are identifiable in the BTM (Figure 5.6) (Irwin, 1980). Beyond the modern delta front of the Matukituki River, a distinct network of sublacustrine channels is identifiable. The most northerly channel is connected to the mouth of the main inflow from the Matukituki River, whilst the middle and southern channels identified are more associated with gravel bars and dry river channels on aerial imagery, indicating that these sublacustrine channels may only become active during high flow events on the Matukituki River. The Matukituki channel is approximately 200 m wide at its maximum, and the channel is approximately 35 m deep. The channel depths rapidly decrease with distance from the modern delta front. Channel depths decrease from 25-35 m on the tributary and main channel near the delta front, to c.5 m south of the island of Mou Tapu, before becoming unconfined east of the island. In the proximal reaches, crescentic bedform features within the channel are visible, as is slumping of the channel walls. Part of a sublacustrine channel is also detected towards the Makarora Delta (Figure 5.6B) but is not fully captured in the available BTM. The channel is similar in geometry to the Matukituki channel, with high banks of c. 65 m, and widths of c. 300 m. Another channel is detected along the deep lake bottom (Figure 5.6C). This channel is narrower than the other two, with a maximum width of 80 m, but typically between 50 – 70 m. The channel is also shallower than the other two, with channel wall heights ranging between 5 and 10 m. It is also discontinuous across the bed, with no bathymetric expression in some locations.

Figure 5.6. Overleaf. Bathymetric expressions of sublacustrine channels at Matukituki delta (A); near the Makarora River delta (B); and along the lakebed not associated with a river delta (C). Profile of subaerial river deltaic region and subaqueous channel thalweg (D). Note the full extent of the subaerial profile is not visible in Panel A. All Panels are orientated north. Aerial imagery and topographic data available from LINZ data service (https://data.linz.govt.nz/).

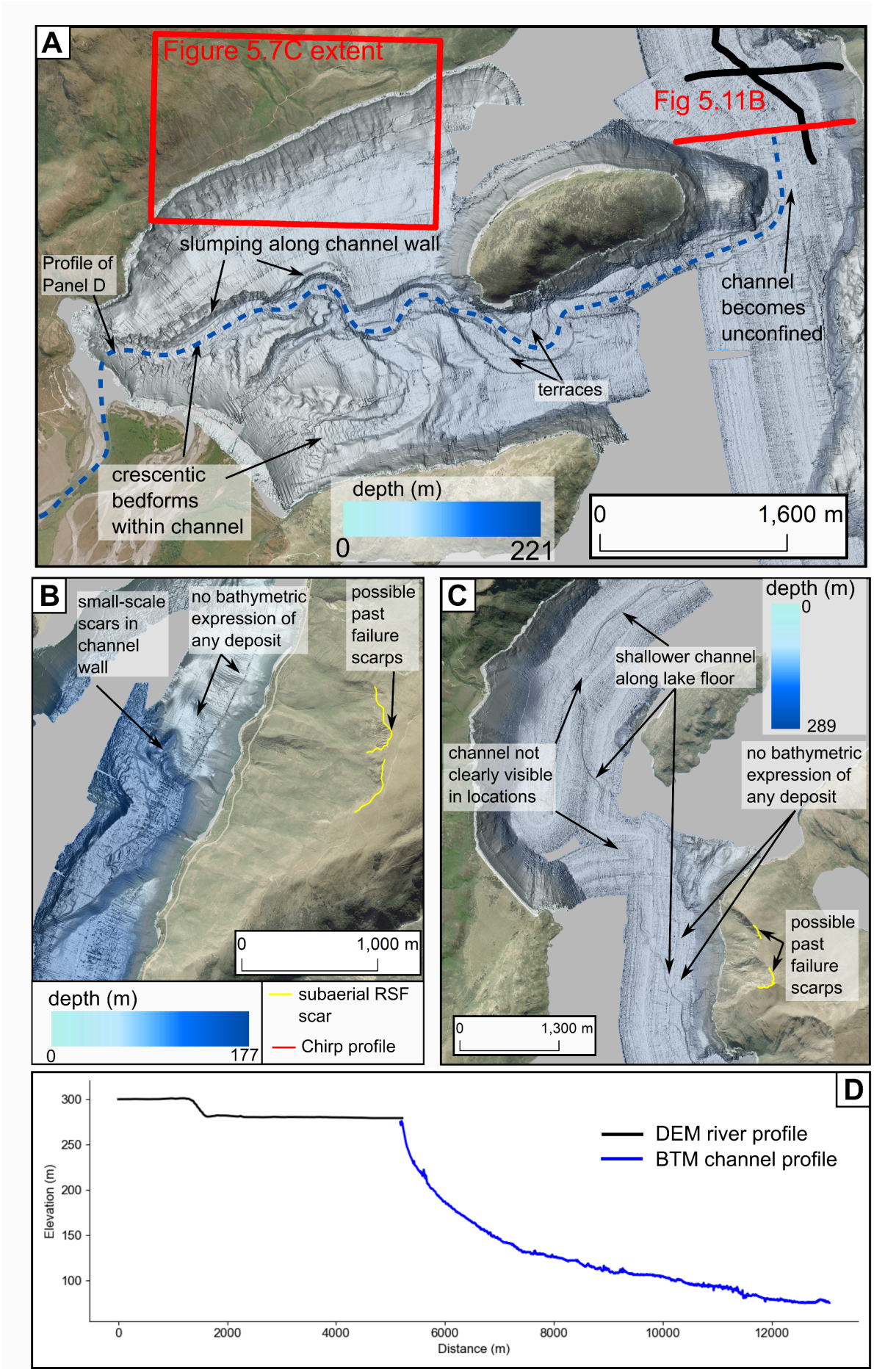
A
Figure 5.7C extent
Fig 5.11B
slumping along channel wall
Profile of Panel D
channel becomes unconfined
terraces
crescentic bedforms within channel
depth (m)
0
221
0
1,600 m
B
small-scale scars in channel wall
no bathymetric expression of any deposit
possible past failure scarps
0
1,000 m
depth (m)
0
177
subaerial RSF scar
Chirp profile
C
depth (m)
0
289
shallower channel along lake floor
channel not clearly visible in locations
no bathymetric expression of any deposit
possible past failure scarps
0
1,300 m
D
DEM river profile
BTM channel profile
Elevation (m)
300
250
200
150
100
0
2000
4000
6000
8000
10000
12000
Distance (m)

5.4.3. Subaqueous landslides

Landslides and their associated deposits are the primary morphological feature identified in the BTM. The deposits identified are the result of non-deltaic and deltaic failures. Deltaic failures are discussed in 5.4.4. From the non-deltaic failures, deposits can be categorised as resulting from either subaerial to subaqueous (STS) failures (n=6); and wholly subaqueous failures (n=2 + 2 scars). The non-deltaic deposits range in area between 4.01×10^4 to 5.66×10^5 m^2. A common characteristic in all the deposits identified is that they exhibit similar backscatter values to adjacent, unaffected lakebeds, indicating either failure of the lake sediments, or that the deposits are covered in post-depositional drape of lake sediments. The deposits are therefore identified in the BTM as they exhibit a positive bathymetric expression compared to the surrounding unaffected lakebed.

Three STS deposits are identified close together at the southern end of The Peninsula (Figure 5.7A). Two of the deposits appear to have originated from the subaerial environment as prominent scars are identifiable on the subaerial hillslope immediately above and are deposited entirely underwater. Surficial features are absent, however. Subsurface information is poorly constrained in available SBP data. One profile appears to show some hyperbolic reflectors with acoustic blanking below where the data cross the mapped deposits (Figure 5.7C). These reflectors are interpreted to represent a blocky surface material of the deposits (cf. Deplus *et al.*, 2001; Masson *et al.*, 2002). In the available line, the hyperbolae are not densely packed and therefore may represent isolated blocks in the deposit. One of the identified deposits appears to be the toe of a subaerial RSF, identified in 5.4.1, which has runout below the water surface. Collected SBP lines over the toe only yield the bed surface with no subsurface penetration, preventing any seismic interpretation. As the deposit is likely to be part of the subaerial RSF deposit, estimates of the deposit area and volume are derived from collating the subaerial and subaqueous A_L. This indicates that approximately 36% of the total deposit area sits beneath the water surface.

Near the Matukituki delta, another deposit is identifiable (Figure 5.7D). It is the largest deposit by area identified in the lake at 5.66×10^5 m^2. The deposit exhibits a largely smooth surface with similar backscatter values to the adjacent non-affected lakebed. The bathymetric expression is largely subdued, extending only up to 2 m above the adjacent lakebed. However, the SBP data suggest that the deposit may be much thicker. A prominent reflector is detected up to 27 m below the lakebed (Figure 5.7F). Between the prominent reflector and the bed, the facies are largely acoustically transparent, and is interpreted to be a landslide deposit (cf.

Schnellmann *et al.,* 2002; Praet *et al.*, 2017; Sammartini *et al.,* 2019). This suggests that the deposit thickness is greater than the bathymetric expression. The SBP is over the proximal reaches of the deposit however, and therefore thicknesses derived are likely a maximum, and may not be representative across the whole deposit. Assuming a maximum thickness of 27 m yields an estimated volume of 1.02×10^7 m^3, following Equation 5.3. However, there are slightly deformed lateral reflectors at various depths between the basal contact and the top of the surface (Figure 5.7F). These reflectors are not continuous in the subsurface, suggesting that the deposit may be formed of multiple closely spaced failures. There is no obvious subaqueous scar(s) along the lateral slope for this deposit, but the subaerial slope above is heavily gullied with evidence of past shallow regolith failure. This deposit is therefore interpreted to be a coalesced deposit, resulting from repeated shallow regolith failures, such as debris flows/debris avalanches, from the subaerial slopes. If the deposit is a subaqueous failure, the scar may have been overprinted by input from the subaerial environment. There are no additional SBP lines available over this slope to assess.

There are two clear deposits that appear to have occurred entirely subaqueously. At the south-western end of The Peninsula, a 1120 m long, 430 m wide feature is identified that protrudes above the adjacent bathymetric floor by approximately 6-10 m (Figure 5.8A). A possible source scar is identified upslope of the deposit. The scar is laterally extensive but occurs on a relatively shallow slope of c. 7°. The possible scar appears along the break of a shallower shelf that slopes down towards a deep area of the lake basin. Morphological features, such as blocks and ridges, are all lacking on the deposit. The deposit does not exhibit any higher or lower backscatter values than the surrounding bed, suggesting the surface is not composed of a coarse substrate like bedrock, or draped by sediment. Sub-bottom lines do not cross the full length of the deposit. Only a short segment of sub-bottom data are available over the feature (Figure 5.8C). Differencing between the marked horizons indicates 2-6 m of laterally continuous low- to medium-amplitude reflectors, partially overprinting a 5-8 m acoustically transparent facies. The total thicknesses calculated are similar to the bathymetric expression of the feature. The laterally continuous reflectors are considered to represent layers of natural lake sedimentation (cf. Hjelstuen *et al.*, 2009; Turner *et al.,* 2012; Strasser *et al.,* 2020), and most likely Holocene depositions (Fitzsimons and Howarth, 2018; Levy *et al.*, 2018). The backscatter and two identified facies rule out the possibility that the feature is a bedrock protuberance. Based on bathymetric investigation and analysis of the SBP data, this feature is suggested to be a subaqueous landslide deposit, resulting from failed lake sediments on the shallow shelf. The

deposit is the second largest identified, with an estimated volume of 1.09×10^6 m^3, based on Equation 5.3. The deposit has a maximum run out of 1487 m. A small-scale (5.3×10^4 m^2) cone of material is identified at the base of a steep rock slope (Figure 5.9A). No surficial features or individual blocks can be identified on the deposit. The deposit appears to have originated from a small subaqueous scar. The scar is cut back into the steep rock slope. Therefore, it is likely that this deposit is a talus accumulation, most likely from a small collapse of the subaqueous rock slope.

Two adjacent deposits are also identified west of Mou Waho Island. The deposits are conical in geometry, and fan radially at the slope-lakebed boundary (Figure 5.9C). No surficial features are identifiable on the deposit, but backscatter reveals streaks of higher amplitude data extending down both deposits (Figure 5.9D). This suggests that coarser sediments are being routed over the deposit surfaces to the lake floor. The lakebed exhibits a high-amplitude reflector and limited to no sub-bottom penetration is achieved (Figure 5.9E). The sub-bottom data of the deposit shows stacked, overlapping high amplitude reflectors. This may indicate that the deposit is composed of multiple stacked failures rather than a single failure, but it is difficult to ascertain with the available data. Both deposits are conservatively assumed to be single failures.

At several locations around the lake, onshore morphological evidence of possible source scars has been identified, but no associated deposit is identified on the lakebed (e.g. Figure 5.6B and C). Scars were identified by steep breaks in the hillslope, similar to the RSFs identified with associated deposits (Figure 5.7A, Figure 5.9C, Figure 5.10A), and/or qualitative assessments in the differences in vegetation cover, where possible. Limited to non-existent sub-bottom penetration and/or preservation at these locations precludes identifying any deposits within the subsurface. The scars were mapped to derive first-order approximate areas and volumes, which may correspond to the volume and material possibly within the lake (Table 5.1). Similarly, in two instances, subaqueous scars are identified with no clear deposit on the bed (Figure 5.8D). Sub-bottom data over the likely runout path of the largest scar does provide subsurface penetration up to 34 m (Figure 5.8F). However, no seismic facies analogous to a landslide deposit (cf. Figure 5.8C) is evident. The sub-bottom data show regularly laminated seismic reflectors that most likely represent ongoing lake sedimentation. The lakebed is relatively flat and shows a smooth surface. Subaerial RSF deposits identified along the north-eastern lake edge do not appear to have extended below the water surface as no bathymetric expression can be detected (Figure 5.10A, and cf. Figure 5.7A and B).

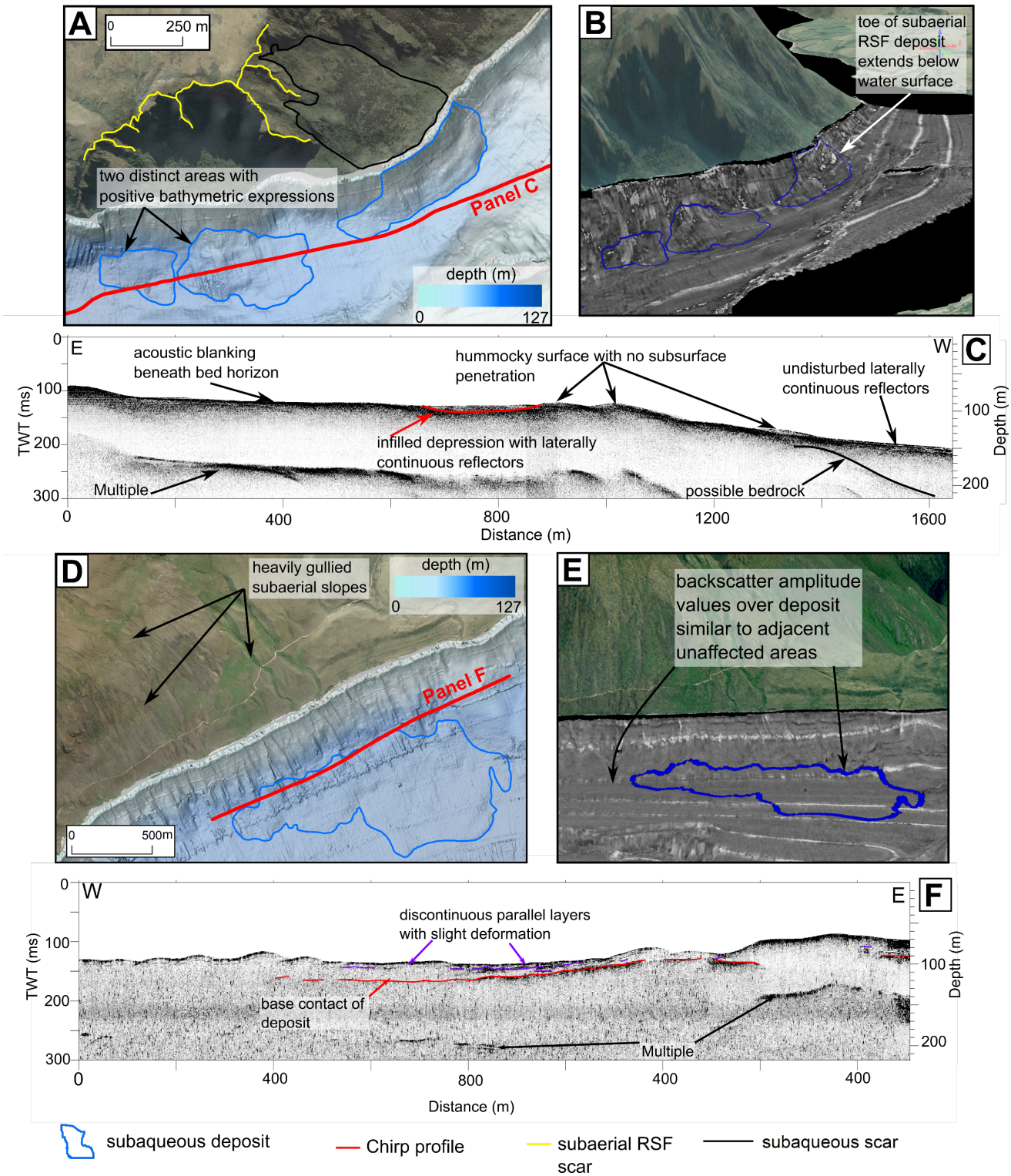

Figure 5.7. Bathymetric morphologies and sub-bottom profiles of STS landslide deposits at the southern end of the Peninsula (A-C), and near the Matukituki Delta (D-F). Panels A and D are orientated North. In vertically exaggerated 3D perspective panels (B, E), the backscatter data are overlain. See Figure 5.2 for location. Unprocessed versions of these and following SBP presented within the chapter are available in Appendix B.

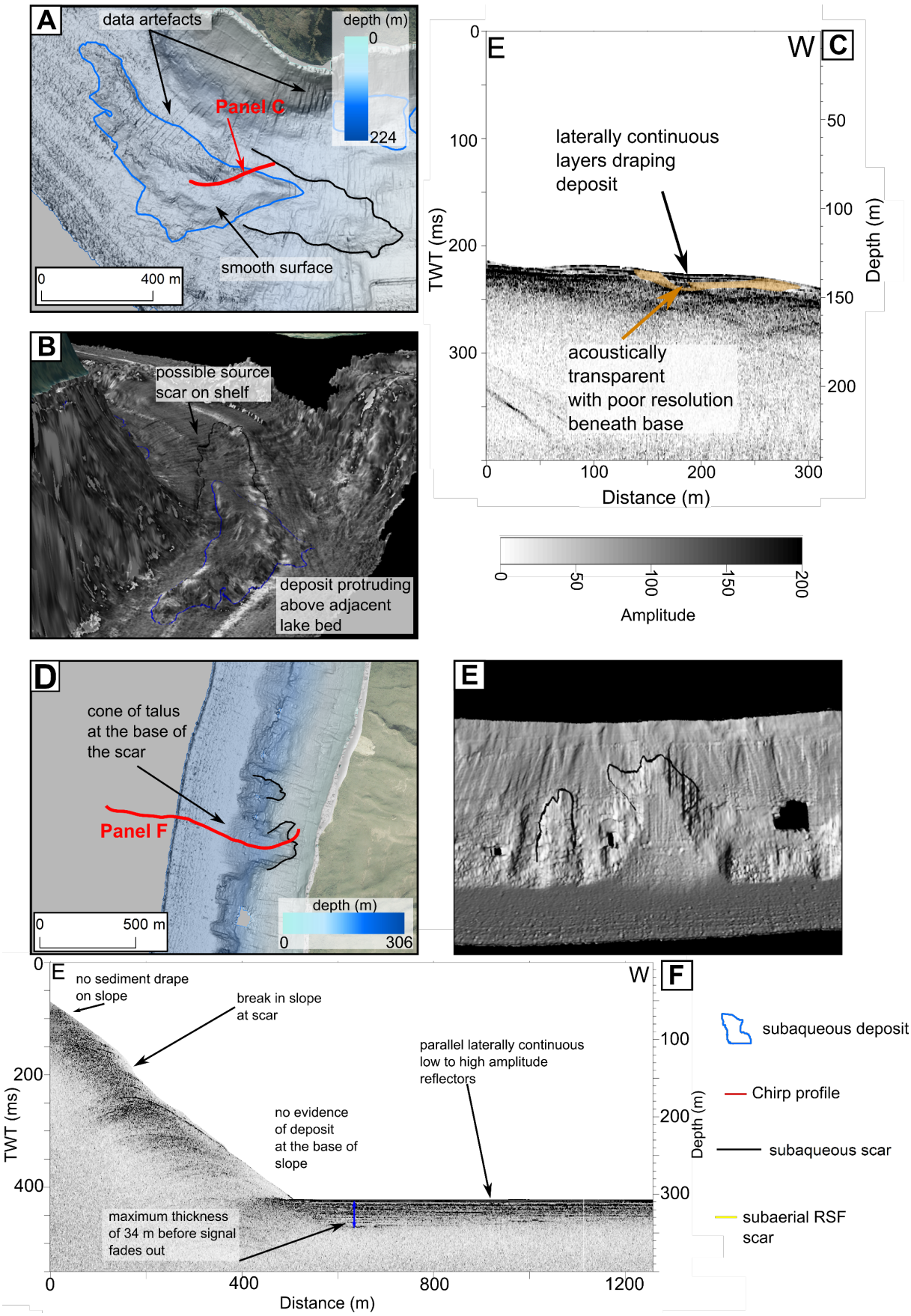

Figure 5.8. Bathymetric morphologies and sub-bottom profiles of wholly subaqueous deposits (A-C) and scars with no associated deposit (D-F). Perspective view in Panel B has backscatter data overlain on the deposit. See Figure 5.2 for location.

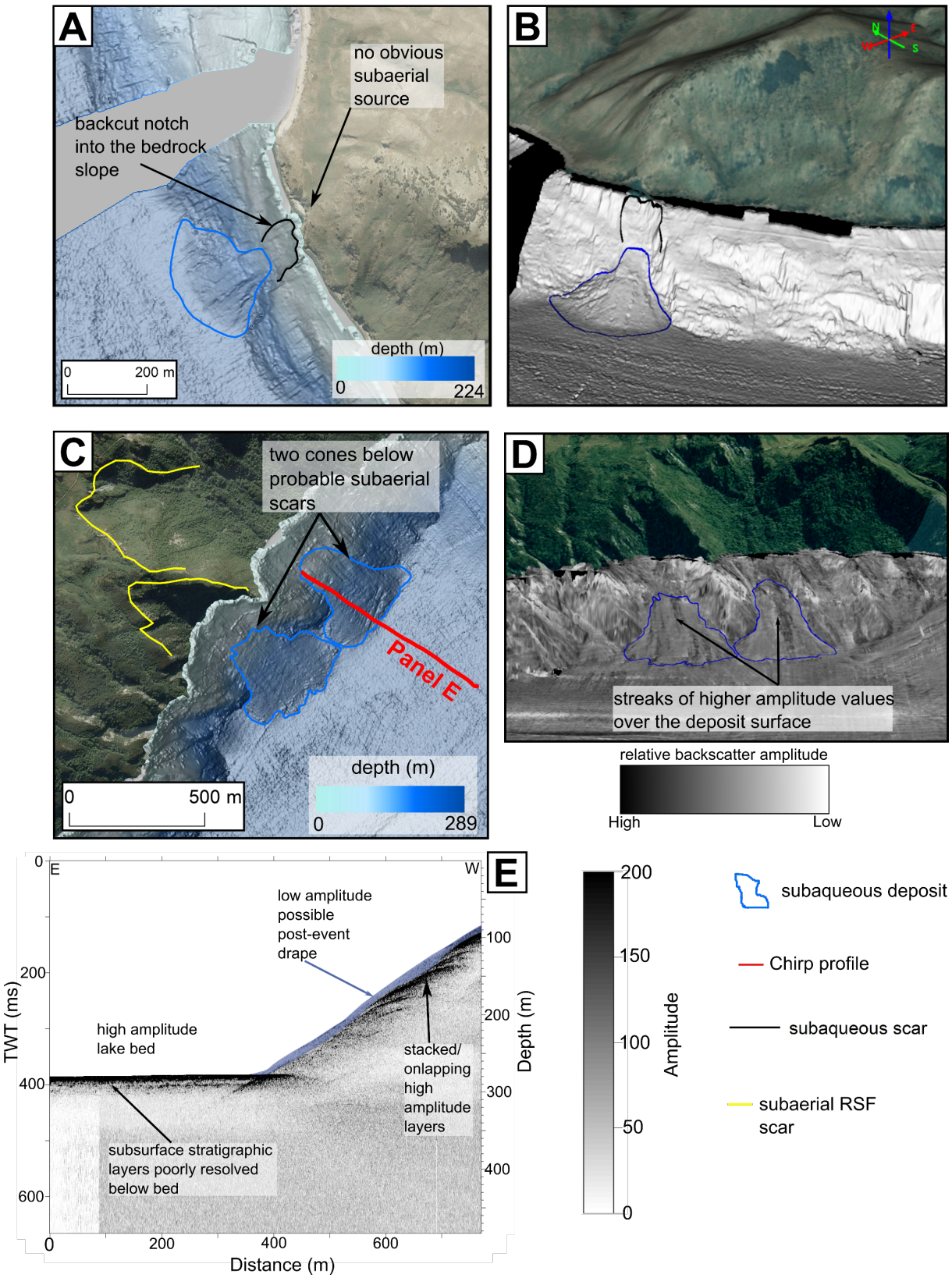

Figure 5.9. Bathymetric morphology of a subaqueous RSF deposit (A, B), and subaerial to subaqueous RSF deposits (C, D), both with conical morphologies. Also shown is sub-bottom profile collected over one STS deposit (E). See Figure 5.2 for location.

5.4.4. Fan deltas and deltaic failures

Several river and alluvial fan deltas are also visible in the BTM. The fan deltas have built up offshore from the tributary rivers and creek catchments. The onshore slopes of the fan deltas along the north-eastern margin of the lake are ≥10°, indicating that they could be colluvium fans (Figure 5.10A) (Blikra and Nemec, 1998; Hansen *et al.*, 2016). Along the western margin of the lake, the onshore fan deltas are <5°. The north-eastern subaqueous fan delta slopes are steep-fronted (20-30° in proximal reaches), whilst the north-western fan delta slopes exhibit a slightly shallower gradient (13-25°). However, the full slope gradients cannot be ascertained here due to missing bathymetry. The fan delta slopes on both sides of the lake are generally smooth but are intercalated with local shallow channels/scars (Figure 5.10). The channels/scars exhibit higher backscatter values to the surrounding smooth slopes, indicating routing of coarse material (cf. Postma, 1990), or recent shallow failures.

At the base of some of the fans in the north-eastern end of the lake, areas of positive bathymetric expression from the surrounding lakebed are identifiable. These are interpreted to be deposits from small-scale deltaic failures (Figure 5.10A, C). Due to the lack of bathymetric and sub-bottom data on the north-western side of the lake, deposits cannot be identified, despite the presence of scars. The scar areas are not used in any further analysis to maintain consistency in analysing deposits. These deposits are small, ranging from 8.28×10^3 to 7.24×10^4 m^2 in area. Not every identifiable scar has an associated deposit at its base, suggesting that they are more likely channels routing sediment to the lakebed, or failures are so small that they are indistinguishable within the BTM. Similarly, some deposits have no obvious scar associated on the delta, indicating that sediment has built up in the scar making it indistinguishable in the bathymetric data.

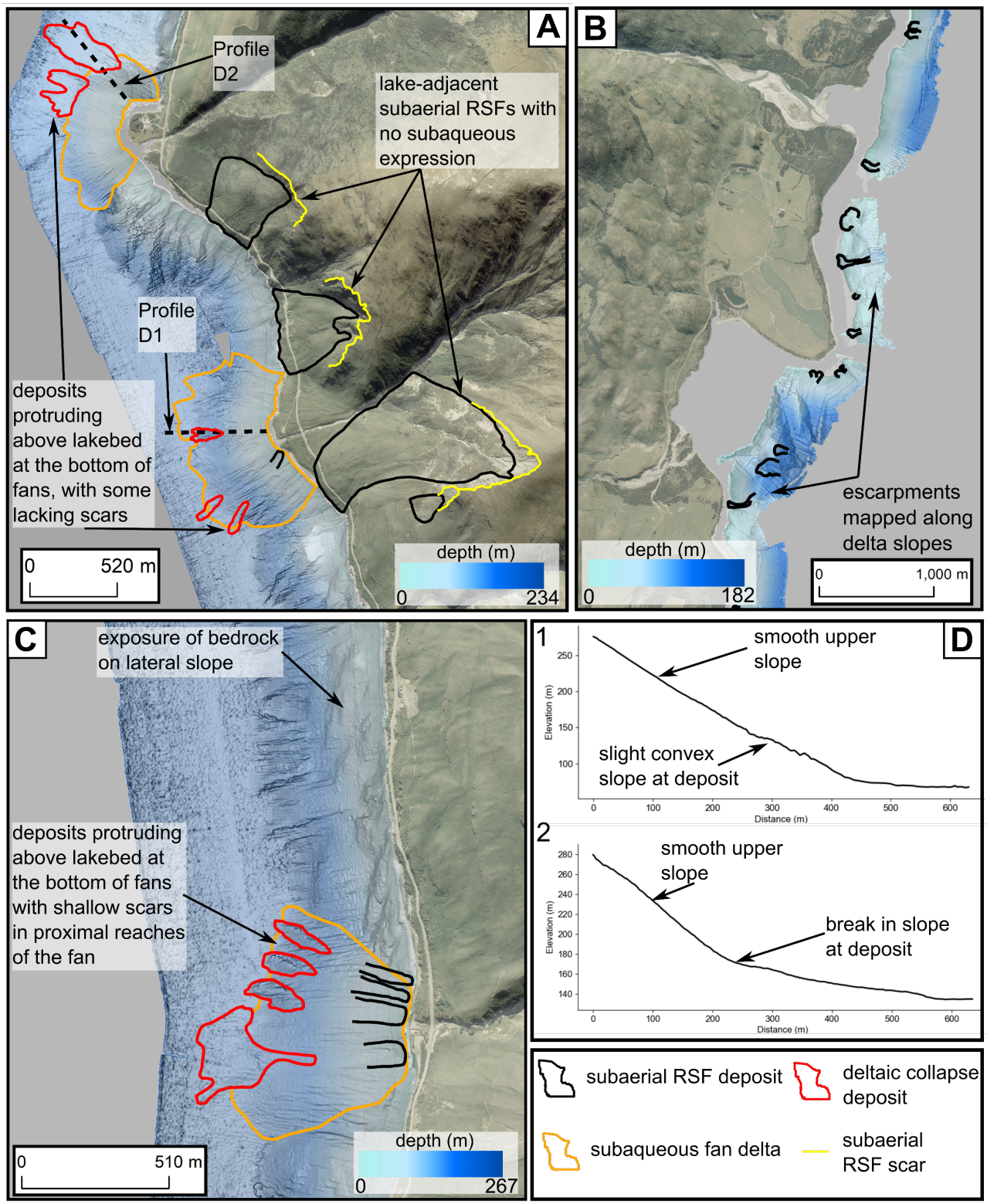

Figure 5.10. A-C - Examples of deltaic collapse deposits and scars on subaqueous fan delta slopes within the lake. D – Topographic profile over subaqueous fans with deposit, illustrating the break in slope at deposit boundaries. Locations of profiles are indicated in Panel A. Locations of Panels A-C are indicated on Figure 5.2.

Table 5.1. Summary of identified scars with no associated deposit in bathymetry, and estimated areas and volumes

Source scars with no associated deposit	ID	Source scar area (m^2)	Estimated scar volume (m^3)*
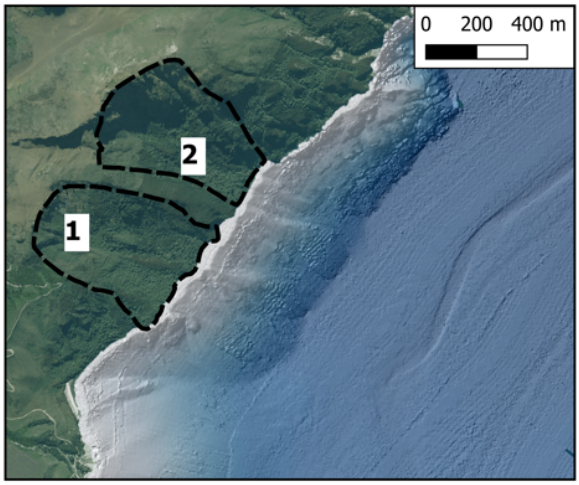	**1**	2.43 x10^5	2.65 x10^6
	2	2.25 x10^5	2.36 x10^6
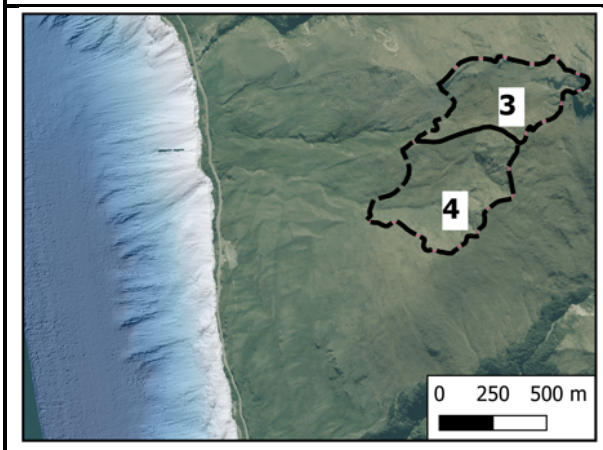	**3**	1.89 x10^5	1.82 x10^6
	4	2.47 x10^5	2.70 x10^6
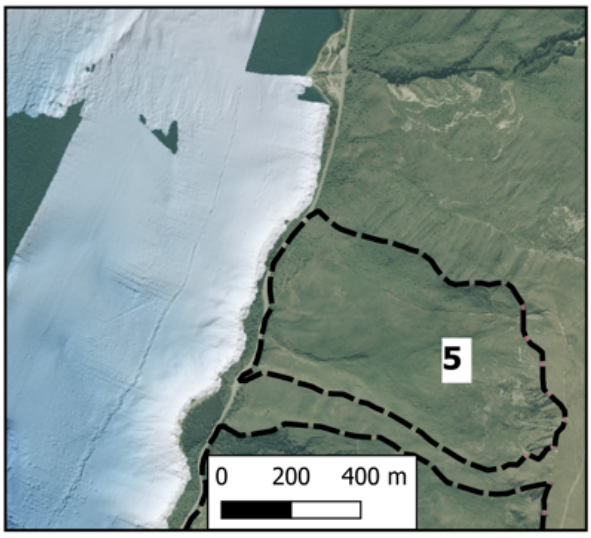	**5**	3.85 x10^5	5.25 x10^6

Table 5.1 continued

Source scars with no associated deposit	ID	Source scar area (m^2)	Estimated scar volume (m^3)*
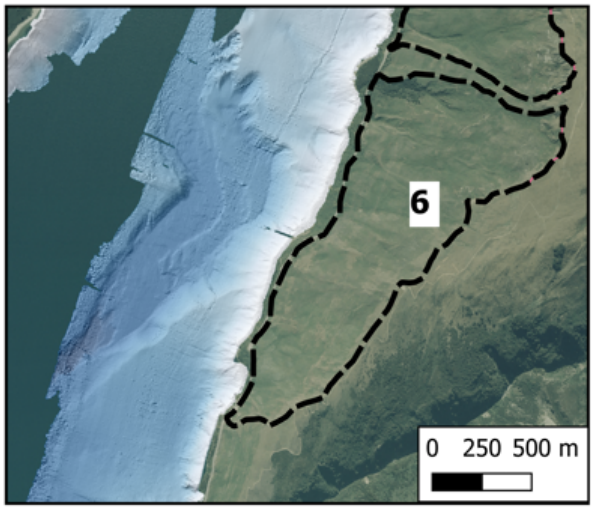	**6**	1.16 x10^6	2.73 x10^7
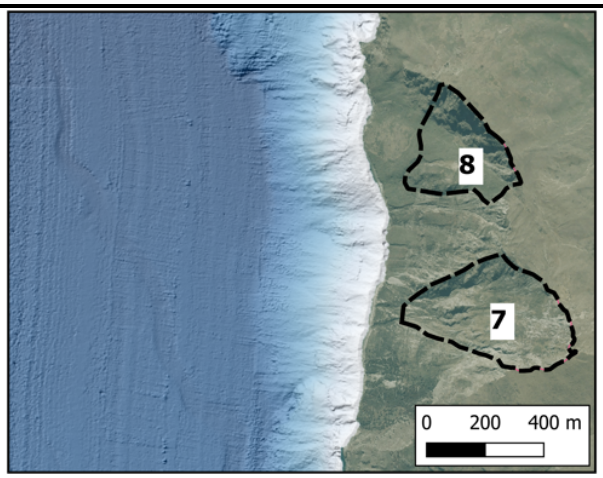	**7**	1.46 x10^5	1.24 x10^6
	8	9.11 x10^4	6.14 x10^5

*Volume derived using same volume-area scaling relationship as used on the subaerial and STS deposits (5.3.1)

5.4.5. The sedimentary infill of Lake Wānaka

In several of the collected survey lines, sub-bottom penetration was poor, often only recording the lake bottom with total signal blanking/attenuation of sub-bottom data below. This impedes subsurface interpretation and estimations of the sedimentary infill. The wide spacing between surveyed lines and limited intersection makes constructing isopach maps within the basin impossible to achieve. North of the island of Mou Waho, the penetration was greater. The seismic facies stratigraphy in some of the profiles (e.g. Figure 5.11A) show regular, continuous, low- to medium amplitude, horizontally laminated reflectors that are interpreted to represent layers of natural lake sedimentation. The horizontally laminated facies have a maximum thickness of 30 m before the signal fades out. Acoustic gain enhancement applied from the

lakebed was unable to resolve more facies layers below this depth. The maximum depth recorded in this horizon is 34 m (Figure 5.9E). Profiles run over the lateral slopes show no laterally continuous facies, suggesting that there is no sediment drape on the slopes, or that the sediment drape is too thin to be resolved in the profiles. East of the island of Mou Tapu (Figure 5.6, Figure 5.11B), a SBP across the lakebed appears to detect a downward-dipping, higher amplitude acoustic basement reflector in the profile. This feature is detectable c. 115 m below the lakebed surface before fading out, despite the rest of the profile being able to resolve much in the subsurface below the lakebed. This reflector is interpreted to be the continuation of the bedrock of the nearby island. This is the maximum sub-bottom depth achieved in any of the profiles, indicating that the sediment infill within the lake is at least 115 m.

The calculated average modern sedimentation rate in the lake from Equation 5.4 is 1.24 mm a^{-1}. Extrapolating this rate to the subaqueous landslide deposit (Figure 5.8A) where the maximum post-event drape of 6 m was detected in the SBP (Figure 5.8C) gives an age of 4838.7 ka. However, the sedimentation rate extrapolated over the assumed 18 ka age of the entire basin yields 22 m of postglacial sediment infill within the lake. This estimate is lower than values derived from the available SBP data. Further extrapolation of the sedimentation rate back to 29 ka, based on the dated ice-contact boundaries of Evans (2015), gives a conservative maximum infill of 36 m. This is similar to the maximum depth recorded in the laterally continuous facies (Figure 5.9E and Figure 5.11A). However, in those profiles an acoustic basement, that would indicate a possible bedrock structure or glacial till/diamicton, is not detected at the base. Instead, the signal seems to fade with depth. Further layers could not be resolved with signal gain enhancements. Furthermore, the extrapolation is still far less than the maximum thickness of 115 m derived in the SBP (Figure 5.11B). Therefore the calculated sedimentation rate appears too low, and thus is likely unsuitable to calculate estimated ages of the deposits where post-event drapes are detected in SBPs.

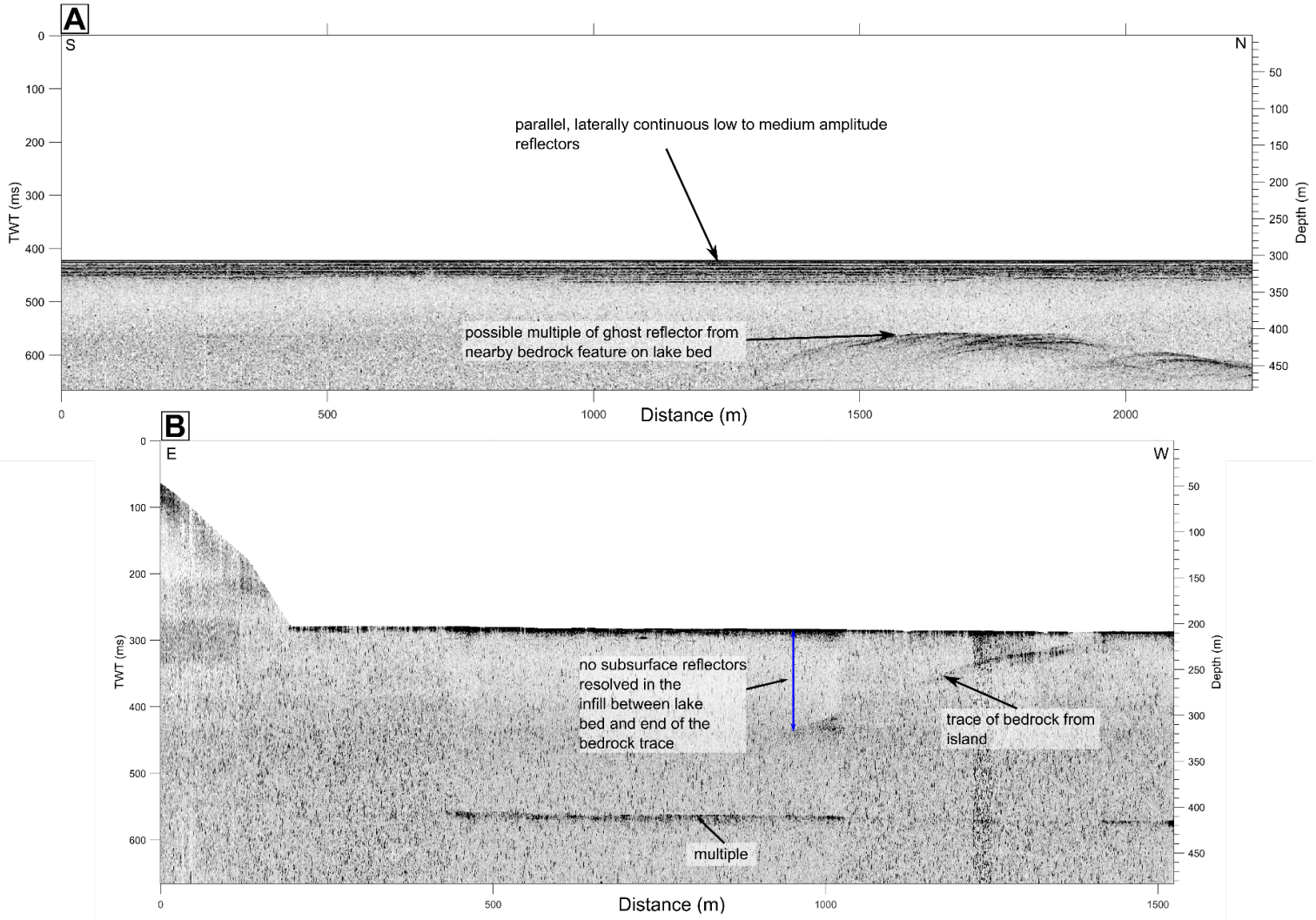

Figure 5.11. Sub-bottom profiles showing typical horizontal, laterally continuous facies interpreted as natural sediment infill in the lake (A) and the maximum subsurface depth achieved of 115 m below the bed, with bedrock trace of Mou Tapu island (B). See Figure 5.2 and Figure 5.6 for line locations of A and B respectively.

5.4.6. Landslide size-frequency distribution

The estimated power law distribution of the subaerial deposits A_L produced a power law exponent (β) of -1.863 and a cutoff point at 1.96x10^5 m^2 (Figure 5.12A, C). The small number of deltaic and non-deltaic subaqueous deposits ($n=17$) precludes deriving a robust subaqueous frequency distribution curve. Therefore, combined subaerial-subaqueous CDF and FAD curves were produced (Figure 5.12B, D). Inclusion of the subaqueous landslide deposit A_L has a very marginal increase on β to -1.860, and a marginal reduction in the parameter standard deviation, but no effect on the cutoff point (Table 5.2). Any indication of an exact rollover point is not entirely clear in either FAD plots, but tentatively may lie around deposits where $A_L \leq 10^5$ m^2 in both cases (Figure 5.12C, D).

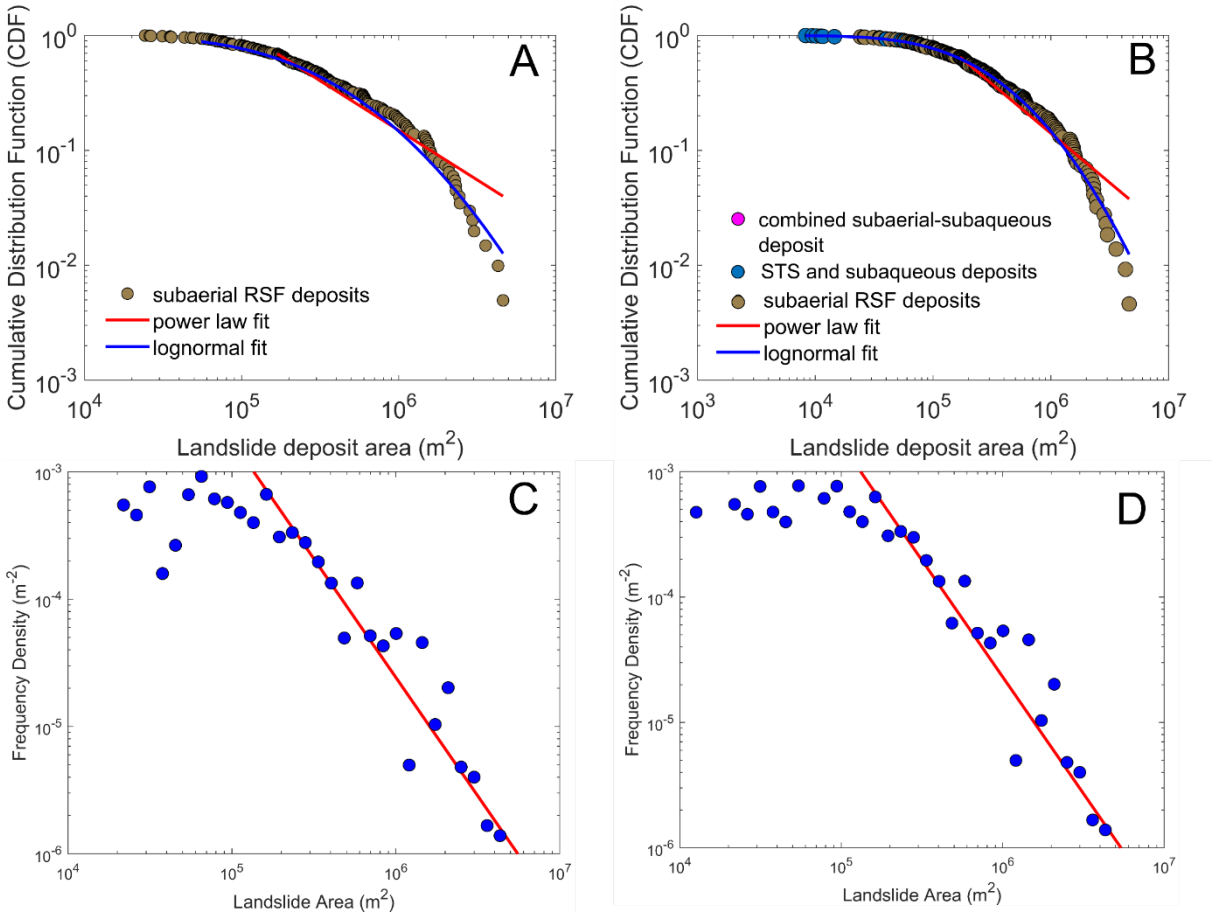

Figure 5.12. The cumulative and non-cumulative distribution of the subaerial (A, C) and combined subaerial-subaqueous (B, D) deposits in this study. A power law is fitted to both the cumulative and non-cumulative distributions, whilst a lognormal fit is only fitted to the cumulative distributions. The exponents and cutoff points are detailed in Table 5.2. The data in the non-cumulative distributions are logarithmically binned, therefore the areas cannot be plotted by deposit type.

In both set of analyses, a power law was found to be a poor fit. The p-values derived from the KS statistic are below the 0.1 threshold that would suggest a plausible fit (Table 5.2) (Clauset *et al.*, 2009). The power law was calculated on A_L above the cutoff (*n=140* and *n=141* in the subaerial and subaerial-subaqueous, respectively). Therefore, several deposits were excluded from the fit. For comparison, a lognormal distribution was also fit to both datasets (Figure 5.12A, B). In both lognormal distributions, the p-value exceeds 0.1 (Table 5.2) indicating that a lognormal distribution is a better fit to the data. The lognormal fit was stronger in the subaerial-subaqueous plot where the fit began on the smallest deposit in the dataset. In both the power law and lognormal distributions, a poor fit to the data is found on deposits $>10^6$ m^2. Statistical comparisons between the power law and lognormal fits were therefore tested following the approach of Vuong (1989). The comparison test yields a p-value of 0.988 and 0.991 for the subaerial and subaerial-subaqueous fits respectively. This suggests that the lognormal fit cannot be favoured over the power law fit (Vuong, 1989).

Table 5.2. The power-law and log normal exponents, cutoff values, mLS for the subaerial and combined subaerial-subaqueous deposits in this study

Power law	p-value[1]	β	Cutoff point (x10^5 m^2)	mLS (±1σ)
Subaerial	0	-1.863±0.75	1.96±4.28	4.95± 0.72
Subaerial-subaqueous	0.0002	-1.860±0.72	1.96±4.13	4.92± 0.70
Lognormal				
Subaerial	0.115	μ = 12.46 σ = 1.29	55318	-
Subaerial-subaqueous	0.252	μ = 12.47 σ = 1.28	8278	-
Vuong (1989) comparison between modelled fits:			Subaerial: p=0.988,	Subaerial-subaqueous: p=0.991

[1] p-value derived from Kolmogorov-Smirnov (KS) goodness of fit statistic.

5.5. Discussion

5.5.1. Distribution of subaerial and subaqueous landslides

Analysis of the 202 subaerial and 17 subaqueous deposits within the lake basin and in the catchment show the deposit area, A_L , spans four orders of magnitude (10^3 – 10^6 m^2). An inverse power law and lognormal distribution was fit to the data. However, the observed power law distribution for the deposits is poor. Whilst it is possible to fit several power law distributions

to an entire landslide inventory (e.g. Van Den Eeckhaut et al. 2007), this was not done here. A lognormal distribution fits the data better, particularly when the subaqueous deposits are included. Including the subaqueous deposits improves the goodness of fit (*p=0.252* for subaerial-subaqueous deposits, up from *p=0.115* for subaerial). Additionally, there is no truncation of the deposit area data i.e. the cutoff point (8278 m^2) is the smallest deposit surface area in the inventory, compared to the cutoff point for subaerial deposits alone (55 318 m^2) (Figure 5.12, Table 5.2). Lognormal distributions have been proposed to explain subaerial (Dunning *et al.*, 2007), submarine (Chaytor *et al.*, 2009; ten Brink *et al.*, 2009), and in one instance STS landslides (Böhme *et al.*, 2015). However, the significance of the lognormal fit compared to the power law fit is unknown here given that neither fitted distribution can be favoured. This study therefore highlights that in this instance, a lognormal distribution characterises the distribution of deposit A_L better. Both fits are considered when examining the factors that may control the distribution of both subaqueous and subaerial deposits.

Attempts to fit a power law distribution to the observed deposits show that the exponent β>1.5. This indicates that smaller-scale magnitude RSFs are the most common within the catchment (cf. Hovius *et al.*, 1997; Korup, 2005a, 2006a). Whilst all subaerial deposits produce shallower depositional surfaces to the modal hillslope angle in the catchment (Figure 5.3), the smallest deposits are only a few degrees below the mode. Furthermore, few small deposits extend the entirety of the hillslopes to cause sufficient hillslope lowering (Figure 5.4). As such, the hillslopes have adjusted to these more numerous small-scale landslide occurrences, assuming the landslides occur more frequently than the largest ($\geq 10^6$ m^2) landslides (Korup, 2005a). Furthermore, only the largest deposits affect the entire length of the hillslope, causing the pronounced hillslope angle lowering. Lowering of the hillslope angles may result in a slope being below a critical threshold angle necessary for failure to occur (Clarke and Burbank, 2010; Blöthe *et al.*, 2015).

The spatial distribution, and size frequency distribution of both subaerial and subaqueous deposits is biased due to the largely unknown observational period. The identification of a cutoff and rollover in the power law distribution indicates that this may be an incomplete inventory. The subaerial and subaqueous deposits within this study can be seen as an example of a historical landslide inventory (Malamud *et al.*, 2004). As such, the inventory is likely incomplete. Several explanations for the incomplete inventory include under sampling small deposits as an artefact of dataset resolution (Stark and Hovius, 2001). This seems unlikely here as a function of the resolution imagery used during API (0.3 m and 0.75 m). However under

sampling of such small-scale deposits on the DEM are possible as the highest resolution DEMs (8 m, 15 m, and 25 m), are all derived from contour interpolations, whilst the satellite-derived DEMs are two orders of magnitude lower resolution than the best imagery available. Conversely, the high resolution of the BTM (2 m) has allowed detection of smaller scale deposits (10^3 m^2). The apparent under sampling may also reflect the physical preservation potential of deposits in the subaerial environment. Smaller deposits can be eroded within years, whilst the largest deposits, typically >1 km^2, can exist in landscapes for $10^2 – 10^4$ years (Hancox & Perrin, 2009; Korup, 2005a; Korup, 2006a). The smallest subaerial deposit has an area of $2.43x10^4$ m^2, which is an order of magnitude larger than the smallest subaqueous deposit. Therefore, it is entirely possible that the smallest subaerial deposits have been eroded. The erosion may be by fluvial action as 50% of the mapped deposits are directly connected to streams (Figure 5.4). Furthermore, erosion of larger deposits can still occur, which reduces their areal extents without full removal of the deposit (Chevalier *et al.*, 2009). Therefore the surface areas of the largest deposits may have also been affected.

Additionally, due to the absence of a detailed temporal record, amalgamation of deposits by overprinting successive slope failures may have occurred. Amalgamation can cause divergence from the cutoff point, producing a disproportionately high number of large deposits, and underestimate the total number of deposits within an inventory (Tanyaş *et al.*, 2019). In both the power law and lognormal distributions of all deposits, a divergence of the fit appears to occur on deposits >10^6 m^2. This could therefore be a result of deposit amalgamation within the catchment, either by successive or closely spaced deposits in valleys. However, Korup (2005a) suggests that the occurrence of the largest landslides in the southwest of New Zealand (>1 km^2 in their study) may be more controlled by external triggering mechanisms, such as earthquakes.

The inclusion of the subaqueous deposits into the distribution produced a near identical lognormal distribution fit to the fit solely based on the subaerial dataset (Table 5.2). The only marked response was that the fit was not truncated when subaqueous deposits were included. Similar observations with the power law distribution occurred with little to no change in the β and cutoff values when including the subaqueous deposits. This might therefore relate to the limited number of deposits identified within the lake basin (*n=17*), which may represent the incompleteness of deposits within the lake basin. Factors that may represent the limited number of deposits include the physical characteristics of the lake basin controlling landslide distribution and occurrence. The steep lake basin slope angles (>20°) inhibit sufficient sediment accumulation to occur (e.g. Figure 5.8E). Subaqueous slope angles are above the 5-20° range

that is necessary for sediment to accumulate and generate noticeable landslide deposits (Praet *et al.*, 2017; Moernaut *et al.*, 2019). Therefore, landsliding and associated deposits from the subaqueous lateral slopes are unlikely to occur, or to have occurred, within the lake. The lack of lateral slope landslides is not uncommon in intramountainous glaciogenic lakes (Hansen *et al.*, 2016; Strasser *et al.*, 2020). In such lakes, the main deposits identified originate from deltaic failures, or RSFs from steep subaerial and/or subaqueous slopes (Hilbe *et al.*, 2011; Hilbe and Anselmetti, 2014; Hansen *et al.*, 2016). Such findings correlate to the deposits identified here, where landsliding is dominated by deltaic failures and RSFs from subaerial and subaqueous slopes. Assuming the scar angle is an indicator for pre-failure slope angle, the one probable landslide in sediments failed along a slope within the 5-20° range.

Erosion and reworking of subaqueous deposits by the sublacustrine channels may also be censoring depositional records. Analogous processes occur through submarine canyons in oceans (Smith *et al.*, 2007) and channels within fjords (Clare *et al.*, 2016). Reworking of deposits through the channels may possibly explain part of the lack of identified STS RSF deposits towards the head of the lake, despite prominent scarps along the hillslopes (Table 5.1). The channel from the Makarora River Delta appears to have eroded and cut down at least 65 m compared to the surrounding lakebed surface. Whilst unable to resolve with the SBP, this erosion is most likely to be removing and reworking sediment infill. Backscatter values around the channel are similar to areas of lakebed unaffected by the channels. Slumping along the channel sidewall at the Matukituki Delta channel is evident (Figure 5.6A) which have been identified in subaqueous channels eroding through sedimentary infill elsewhere (Conway *et al.*, 2012; Pope *et al.*, 2019). Additionally, a sufficient sediment build up has been identified as a key control on the formation and development of subaqueous channels (Pope *et al.*, 2019). However, the lack of RSF deposits in the areas of unaffected channels at both the Matukituki and Makarora Deltas suggests that erosion through channel formation and development is unlikely to have removed all the deposits. Furthermore, how active, and erosive, these channels are is largely unknown as the BTM data is the first of its kind from Lake Wānaka. Such channels have been observed as active conduits for hyperpycnal flows (Irwin, 1980). Repeat surveys and monitoring of the channels would aid investigation of the rates of geomorphic change within these channels (Heijnen *et al.*, 2020).

The large spacing of SBP profiles and incomplete BTM may result in missed deposits within the lake basin. The BTM data is missing in downslope locations where subaqueous scars are evident along deltaic slopes in the northwest region of the basin (Figure 5.10B). However, in

other locations across the lake basin where the lakebed is imaged, no deposits are identified on the bed or in available SBP data where probable evidence for subaerial and subaqueous scars exists (Table 5.1, Figure 5.6 and Figure 5.8E). Supraglacial deposition and transportation of the landslides is a possible explanation for this paucity of STS deposits (Shugar and Clague, 2011; Uhlmann *et al.*, 2013; Dunning *et al.*, 2015), leading to such an absence of deposits on the bed (Carter, 2015). However, for supraglacial deposition from the subaqueous scars to occur, >1 km of vertical downwasting would have been needed, based on the modelled LGM ice extents (James *et al.*, 2019).

A significant factor that may explain the limited identification of deposits within the lake basin is the absence of subsurface data resolved in many of the SBP profiles. The lack of subsurface data has precluded identifying deposits within the stratigraphic sequence, as opposed to those on the surface. Similarly, the sediment infill may be obscuring the number and areal extent of deposits in the stratigraphic/temporal record than is detectable in the BTM data alone. This is especially pertinent given that the bathymetric expression of some of the deposit(s) is far less than thicknesses derived from available SBP data (cf. Figure 5.7D and Figure 5.7F (2 m vs. 27 m thicknesses respectively). Therefore, it is not unreasonable to assume that more deposits may be sequestered within the subsurface stratigraphy, obscured from detection in the available BTM, and beyond the depths achieved in SBP where subsurface penetration occurred. In formerly glaciated regions it has been found that the size and/or frequency of landslides decreases over time since deglaciation (Ballantyne, 2002; Ballantyne *et al.*, 2014; Böhme *et al.*, 2015). However, this has not been proven in New Zealand due to deposit censoring, and lack of absolute dating of the subaerial RSF deposits (Bainbridge, 2017). The estimated areas and volumes of probable subaerial source scars around the lake, whilst approximate as pre-failure topography is unknown, indicate larger volumes compared to the deposits identified within the lake (Table 5.1). Therefore if these locations are indeed source scars of past landslides, the lack of bathymetric expression might mean that the RSFs occurred relatively soon after deglaciation/early into the lake infill, the subsequent deposits may be buried deep in the stratigraphy beyond the resolved data here. This might also explain the lack of any $>10^6$ m^2 deposits within the lake basin. The areas and volumes of the mapped probable scars (Table 5.1) suggest that larger deposits could have feasibly occurred previously. However, due to the uncertainty in the pre-event topography, and the derivation of volumes by a scaling relationship, these values should be treated with caution. Furthermore, supraglacial deposition of these possible RSFs could have also occurred, as previously mentioned.

Adams (1978) estimated the postglacial infill in Lake Wānaka to be between 200 - 400 m. Such infill estimates are much greater than the maximum thicknesses derived from the SBP data in this study. However, no SBPs in this study identified the full acoustic basement. The maximum sediment thickness derived in the SBP data range from 30 to 65 m, with a maximum thickness of c. 115 m (Figure 5.11B), therefore indicating that the sediment infill may be at least that. This SBP is located near where the sublacustrine channel from the Matukituki Delta becomes unconfined (Figure 5.6). Any possible hyperpycnal flows, turbidity currents and associated deposits through the channels may be depositing sediment more rapidly in this region compared to areas within the lake far from sublacustrine channels (Heijnen *et al.*, 2020). However, the estimates of the postglacial infill by Adams (1978) for the Mackenzie Lakes (Tekapo, Pukaki, Ōhau) are similar to the thicknesses derived from the SBP data in those locations (Krause, 2016; Mountjoy *et al.*, 2019). SBP-derived estimates of postglacial sediment infill in Milford Sound/Piopiotahi is at least 300 m (Dykstra, 2012). Similar sediment infills have been detected in other formerly-glaciated fjords elsewhere (Lysså *et al.*, 2010; Bellwald *et al.*, 2016). Such estimates may not be unreasonable for Lake Wānaka.

Estimations of a sedimentation rate based on the thicknesses suggested by Adams (1978) over 18 ka yields averages of 11-22 mm a^{-1}, which is an order of magnitude greater than the rate estimated in this study (1.24 mm a^{-1}) by Equation 5.4. The estimated sedimentation rates over 29 ka from Adams (1978) are lower (7-14 mm a^{-1}), but still greater than the calculated rates. However, such rates are similar to rates derived from cores in Lake Tekapo (10-22 mm a^{-1}) (Pickrill and Irwin, 1983; Mildenhall *et al.*, 2006). Furthermore, Mildenhall *et al.,* (2006) estimate the 22 mm a^{-1} rate occurring in Lake Tekapo as recently as the last 100 years. Extrapolation of the 11-22 mm a^{-1} rate gives a first order age assessment for the maximum derived thicknesses of the continuous, acoustically laminated reflectors (34 m) (Figure 5.8F) of 3090-1545 BP respectively. This suggests, as a first order estimate, that if the deposit originating from the subaqueous scar occurred postglacially (Figure 5.8D), it may be older than 3090 BP. For the subaqueous deposit where the 6 m post-event drape is resolved in SBP (Figure 5.8A), a tentative age may be 545-272 BP. Similarly, the age for the deposit whose total thickness is largely obscured by sediment infill near the Matukituki delta (Figure 5.7D) may be between 2454-1227 BP. Furthermore the maximum infill derived in this study (115 m) could be between 10,454-5227 BP. These possible ages suggest that, even at 115 m, such sedimentation thicknesses may only extend from the Holocene period. Deglaciation and Late-Glacial ages appear to be unresolved, even at the maximum ascertained thickness. However,

such ages are very approximate based on crude extrapolations, and remain highly uncertain. The infill estimates derived by Adams (1978) could not be verified with the limited SBP-derived thicknesses in this study. As such it cannot be known yet whether those initial estimates are accurate. Therefore those subsequently estimated sedimentation rate for Lake Wānaka may be wrong.

A significant uncertainty with sedimentation rate derived in this study is that the rate is derived from a constant SSY through time. The SSY data collected over a short temporal period (c. 20-30 years) during the late 20th Century (Hicks *et al.*, 2011). The sedimentation rate calculated in Equation 5.4 is approximate to the rate of vertical uplift over this region of the Southern Alps (~1 mm yr^{-1} (Tippett and Kamp, 1995)). This is in line with the findings across the South Island by Robinson *et al.,* (2016). New Zealand is in long-term dynamic tectonic equilibrium, extending back 270 kyr (Barth *et al.*, 2014), suggesting the denudation and sediment yields have been relatively constant over this period. However, assuming a constant SSY and sedimentation rate cannot explain the infill detected in SBPs. SSY and subsequent sedimentation rates are, therefore, unlikely to have been constant within the lake. Other, non-tectonic, factors such as the effects of repeated glaciations. Long-term erosion (and therefore sedimentation) rates have been established from an offshore core collected to the east of the South Island. These rates have shown that these rates east of the Main Divide in New Zealand's Southern Alps were 2 to 10 times higher in glacial periods than now (Cogez *et al.*, 2015). It is possible that erosion and subsequent sedimentation rates were higher into Lake Wānaka during glacial and early deglaciation, than at present.

The SSY data are also largely an indirect measurement of aseismic (i.e. rainfall-induced) erosion (Hicks *et al.*, 2011; Robinson *et al.*, 2016). Heightened sediment fluxes in fluvial catchments can occur because of strong earthquakes. Strong shaking can increase erosion in hillslopes which eventually move through the fluvial system and into the lake basin. Howarth *et al.,* (2012, 2014) have identified this heightened post-seismic sediment fluxes and sedimentation in lake cores from Alpine Fault-proximal lakes along the West Coast of the South Island (Mapourika, Paringa and Ellery). Additionally, this heightened sediment flux into the lakes occurs for up to 50 years post-earthquake (Howarth *et al.*, 2012, 2014). Therefore, past, and future strong earthquakes within the region could have caused a temporary increase in the erosion within the catchment, and subsequent sedimentation rates into the lake.

The uncertainty in the long-term sedimentation rate and sedimentary infill within the lake highlights the need for both lake cores and more extensive sub-bottom data. Additionally, greater SBP coverage is needed using systems that can resolve more subsurface penetration than achieved here. Cores would allow more accurate sedimentation rates to be ascertained, as well as dating of possible deposits. The greater expansion of sub-bottom data across the lake using lower frequency systems, such as boomer or sparker, may increase the sub-bottom penetration. This would allow quantification of the total sediment infill within the lake as well as identification of possible deposits older in the temporal record that may lack a bathymetric expression. Furthermore, identification of STS deposits visible on the bed may indicate a relatively recent failure. Therefore sites of potential future STS RSFs need to be identified and monitored either by remotely sensed techniques such as satellite-based phased-differencing interferometric synthetic aperture radar (InSAR), and/or ground-based monitoring and instrumentation (Harbitz *et al.*, 2014).

5.5.2. Potential triggering mechanisms

With the exception of the Young River RSF (Massey *et al.*, 2013; McSaveney and Massey, 2013), the absolute ages of the subaerial and subaqueous deposits within the catchment are unknown. This precludes assigning, and/or excluding, known external triggers. Expansion of absolute dating on deposits is thus needed in order to address this issue (Pánek, 2019). Several possible triggering mechanisms have been established for subaerial landslides in New Zealand. These include earthquakes (Hancox *et al.*, 2002), rainfall (Hovius *et al.*, 1997), degradation of permafrost as a result of climatic changes (Allen *et al.*, 2011; Allen and Huggel, 2013), and possible paraglacial processes (McColl and Davies, 2013). Due to the limited number of studies, few triggers other than earthquakes have been established for subaqueous landslides in New Zealand (Howarth *et al.*, 2014, 2016; Mountjoy *et al.*, 2019). The distribution of deposits across the catchment and within the lake basin does, however, provide some insight.

5.5.2.1. Rainfall

Some of the clusters of RSF deposits are located within the driest regions of the catchment, whilst fewer deposits are observed in the wettest part of the catchment (Figure 5.5B). Only 12 (6%) of the mapped subaerial RSFs originated in the lower quarter of the slope profile (Figure 5.4) and are each relatively small. Rainfall-induced landslides have been identified to also cluster in the lower portion of slopes and near streams (Meunier *et al.*, 2008). This would suggest that rainfall may not be the primary trigger across the catchment. The modelled rainfall is only derived from the 30-year annual average total rainfall, and likely does not account for

extreme rainfall events that may have occurred during that period. Nonetheless, no catastrophic RSFs have been observed during that time, except for the Young River RSF. Rainfall has also been eliminated as a trigger of the Young River RSF (McSaveney and Massey, 2013).

Over the longer record, modelled estimates of precipitation change since the LGM show a general increase across the South Island (Drost *et al.*, 2007). However, no high temporal resolution data across the catchment are available that would elucidate post-LGM and Holocene variations in precipitation to fully assess rainfall/extreme precipitation as a trigger through time. Across the South Island, the spatial distribution of catastrophic RSF deposits of known ages appears to occur independently of average annual total rainfall (Bainbridge, 2017), further suggesting rainfall is unlikely to trigger RSFs here. Rainfall cannot be discounted as a preparatory factor for slope failure however and may possibly cause the debris flows that could have deposited the STS deposit near the Matukituki delta (Figure 5.7D). Rainfall may have an effect on deltaic failures through increased terrestrial runoff from floods and rapid sediment loading of the delta fans (Strasser *et al.*, 2013; Van Daele *et al.*, 2015).

5.5.2.2. Permafrost degradation

There is insufficient evidence to fully assess permafrost degradation as a trigger of both subaerial and STS RSFs in the catchment. The permafrost distribution is poorly constrained in New Zealand (Sattler *et al.*, 2016). Only first-order modelled estimates by Gruber (2012) are available, indicating any likely permafrost is largely constrained to where the glaciers are currently distributed. How permafrost has changed through time since the LGM is currently unknown. The role of permafrost degradation for preparing, and/or triggering, recent (<70 years) RSFs in contemporary glaciated regions of New Zealand is still inconclusive as isolating permafrost degradation over other external factors, such as seismic strain accumulation (McSaveney *et al.*, 2015), remains difficult (Allen *et al.*, 2011; Cox, McSaveney, *et al.*, 2015).

5.5.2.3. Earthquakes

Earthquakes have been identified as a common triggering mechanism for large ($>10^6$ m^3) catastrophic RSFs across the South Island (Hancox *et al.*, 2003; Parker *et al.*, 2015; Bainbridge, 2017; Massey *et al.*, 2020). However, in the catchment and wider Otago region, few $M_w>5$ earthquakes have been recorded (Warren-Smith *et al.*, 2017). No $M_w\geq6$ earthquakes have been recorded in the region since records began. Stirling et al., (2012) estimate a probabilistic peak ground acceleration (PGA) of ≥ 0.4g over a 475 year return period, and ≥ 0.6g over a 2500 year period, across the catchment. The derived PGA/shaking intensity (MM) relationship for New

Zealand (Hancox *et al.*, 2002) indicates that the hillslopes in the catchment are likely to experience shaking intensities of MM8-9 in the 475 year period, and MM≥9 in the 2500 year cycle. As c. MM9 shaking intensities are generally needed for triggering large catastrophic RSFs in the subaerial environment (Hancox *et al.*, 2002; Howarth *et al.*, 2014), this indicates a high probability of coseismic failure in the catchment at least every 2500 years.

The distribution of the subaerial RSF deposits show that 48.5% (98) of the mapped deposits in the catchment originate in the upper quarter of hillslopes, and the largest deposits also originate here (Figure 5.4). Ridge clustering of the scars and deposits may point to a seismic origin (Meunier *et al.*, 2008) through topographic amplification of seismic waves at ridge crests (Wang *et al.*, 2020). This suggests that earthquakes have likely triggered at least some of the subaerial RSFs mapped within the catchment. An earthquake has been assumed as the trigger for other large ($>10^6$ m^3) RSFs in adjacent catchments of similar lithology where ages of the deposits are known (Sweeney *et al.*, 2013; McColl *et al.*, 2019). Therefore, expansion of absolute dating on the subaerial and subaqueous deposits is needed to establish a chronology. This would aid in identifying any possible temporal clusters. Dating of the RSFs may be able to aid with correlation of independently constrained earthquake ruptures. However, caution would be needed as error bounds on dates could show aseismic failures in the lead up to ruptures due to accumulated strain. This has been suggested as a possible trigger for recently documented RSFs in the Southern Alps (McSaveney *et al.*, 2015).

The MM threshold for subaqueous landslides in New Zealand is estimated as MM 6 (Howarth *et al.*, 2014). Therefore, the lake basin is likely to experience sufficient shaking to trigger failures within a 475-year return period. Given the lack of sediment drape on the subaqueous slopes, failures are most likely to occur from the fan delta slopes, or possibly where the entirely subaqueous sediment failure has been identified (Figure 5.8A). Other sites in the lake basin not surveyed may also be prone to failure. This could be more likely at the southern end of the lake where shallowing towards the township occurs (Irwin and Ridgeway, 1976), but warrant further high-resolution bathymetric sonar and SBP surveys and subsequent data to fill the missing data gaps.

Active faults near, or within the catchment on which earthquakes may occur include the NW Cardrona Fault, Highland Fault, and the Alpine Fault (Figure 5.1). Apart from the Alpine Fault, past rupture history is largely unknown on these faults. The NW Cardrona Fault is estimated to generate M_w 7 earthquakes, with an estimated recurrence of 5500 years (Barrell, 2019). It is

therefore likely to have ruptured at least 3 times during an assumed 18 ka age for the lake basin. Whilst no modelled isoseismals are available, the magnitude-shaking intensity (M_w - MM) relationship of Hancox et al. (2002) suggests that shaking intensities of MM9 are probable with a M_w 7 earthquake. Therefore, catastrophic RSF occurrence may be likely with earthquakes on this fault. The clusters of subaerial deposits at the southern end of the catchment, and the subaqueous deposits at the southern end of the Peninsula, are all within 10 km of the NW Cardrona Fault (Figure 5.5D and Figure 5.7A). This could suggest an earthquake from this fault as a triggering mechanism for these deposits. The only known dated rupture on the NW Cardrona Fault is along its southern section near Kawarau valley at 11.2±1.5 ka (Barrell, 2019). No expression of past fault ruptures is identifiable further towards the Wanaka township. However, rapid geomorphic change across the Southern Alps has attributed to eroding any evidence of past ruptures on faults with long recurrences (Cox *et al.*, 2012).

The Alpine Fault is one of the most geologically active faults in the South Island with an estimated recurrence of 291 ± 23 years (Cochran *et al.*, 2017; Howarth *et al.*, 2018), and capable of generating M_w 8.0 earthquakes (Sutherland *et al.*, 2007). Dates of past ruptures on this fault are well constrained compared to other faults in New Zealand, with records extending from the early Holocene to the most recent earthquake in 1717 AD (Berryman, Cochran, *et al.*, 2012; Howarth *et al.*, 2018). The magnitude and MM intensity of the last three ruptures on the fault over the central South Island have been reconstructed by Howarth et al., (2014) (Figure 5.13A-D). Reconstructions of past shaking intensities from the earlier earthquakes is currently unknown. The reconstructions show that of those ruptures, only the 1717 AD earthquake could have generated sufficient MM in a small part of the catchment to trigger catastrophic subaerial RSFs. In the other cases, the MM values appear too low across much of the catchment. This supports modelled estimates by Robinson et al., (2016) that shows a relatively low probability of coseismic subaerial RSFs being generated from a future M_w 8.0 Alpine Fault earthquake (Figure 5.13E).

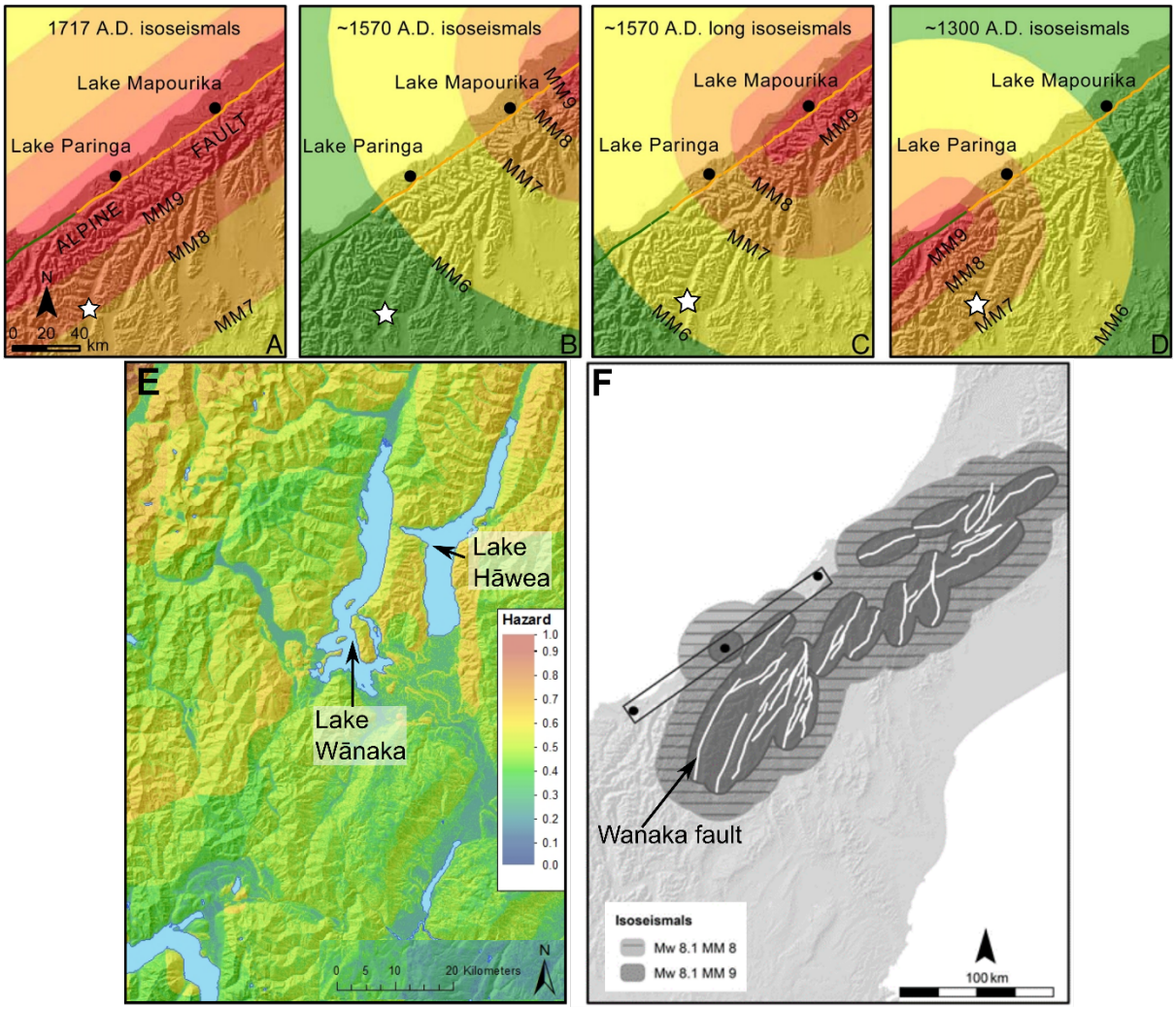

Figure 5.13. A-D: Modelled isoseismals of past Alpine Fault earthquakes. Star superimposed is location of Lake Wānaka in relation to the isoseismals; E – Robinson et al., (2016) modelled coseismic landslide hazard across Queenstown Lake District from a M_w 8.0 Alpine Fault earthquake scenario; F – modelled isoseismals of potentially active faults producing $M_w \geq 7$ earthquakes with Wanaka Fault highlighted. Figures A-D sourced and modified from Howarth et al., (2014); Figure E provided from Tom Robinson (pers. comm.); Figure F sourced and modified from Howarth et al., (2016). Note, Howarth et al., (2014) favour scenario B over C for the ~1570 AD earthquake.

The modelled isoseismals of the past Alpine Fault ruptures do however, suggest that shaking intensities of the past three ruptures were sufficient (MM≥6 (Howarth *et al.*, 2014)) to potentially trigger the deltaic landslides and some of the wholly subaqueous landslides in the lake. Two of the wholly subaqueous failures appear to have originated in bedrock (Figure 5.8D, Figure 5.9 A), and therefore may require higher shaking intensities. The only non-deltaic subaqueous landslide deposit (Figure 5.8A) could have been triggered from either seismic source, but other triggering factors such as lake level drawdowns (Anselmetti *et al.*, 2009; Moernaut *et al.*, 2010), possible weak layers (Locat *et al.*, 2016), excess pore pressures (Flemings *et al.*, 2008) cannot be ruled out. Similarly, the efficacy in using deltaic deposits to

establish a seismic trigger is difficult as deltas are highly susceptible to failure through non seismic processes (Strasser *et al.*, 2013). This can include rapid sedimentation leading to oversteepening (Strasser *et al.*, 2013) and excess pore pressure development. Similarly, deltas can fail due to gradual loading (Girardclos *et al.*, 2007). Van Daele et al., (2015) suggests deltaic deposits may only be useful to establish a seismic trigger in settings where seismic recurrence intervals are short enough to trigger failure before failure by continuous loading. Whether the c.300-year recurrence interval of Alpine Fault earthquakes, or indeed any of the other identified faults, is sufficiently short enough for seismic shaking to trigger deltaic failures over other processes currently remains uncertain. Identification of past deltaic failures across in all the distal fan regions from further SBP data collection might be able to identify coeval deposits. Lake coring campaigns would also provide chronology of possible events.

Other faults within the catchment such as the Moonlight Fault and Wanaka Fault have been inferred active (Turnbull, 2000). However, reassessment by Barrell (2019) suggests that many of these faults may be potentially active, but have no surface expression. This is likely as a result of a potentially long recurrence rate, possible subaqueous occlusion for a segment of the Wanaka Fault, and geomorphic processes rapidly eroding surface expression of the fault (Cox *et al.*, 2012). The recurrence of the Wanaka Fault is estimated at 85,000 years (Barrell, 2019), but can potentially generate $M_w \geq 7$ earthquakes (Cox *et al.*, 2012). Modelled shaking intensities from an earthquake on this fault by Howarth et al., (2016) derived values of MM8-9 across much of the catchment (Figure 5.13F). This suggests that coseismic failures would be likely across the catchment from an earthquake on this fault. No topographic offsets or expressions are evident in the available BTM that might suggest an active fault structure. However the long recurrence estimated by Barrell (2019) indicates that if any rupture has occurred within the lake since deglaciation, it could be obscured by the sediment infill. The lack of penetration in the SBP data collected near the proposed fault location (e.g. Figure 5.11B) limits the ability to assess offsets in the subsurface. Further SBP data that can resolve the subsurface reflectors might help in identifying any evidence of past fault ruptures.

5.5.2.4. Paraglacial processes

Paraglacial processes may include glacial debuttressing, glacio isostatic induced seismicity, whilst palaeo lake levels may have affected subaerial (Pánek *et al.*, 2018) and subaqueous slope stability (Anselmetti *et al.*, 2009; Moernaut *et al.*, 2010). Without reliable age constraints, there is insufficient evidence to fully evaluate debuttressing here. Only two deposits in New Zealand have ages that pre-date the Holocene (Hancox and Perrin, 2009; McColl, 2020). However, this

may reflect the preservation of such old deposits and lack of absolute ages (Bainbridge, 2017). Nevertheless, RSF deposits are identified in valleys within the catchment where ice was absent in modelled LGM reconstructions (Figure 5.14). Furthermore, catastrophic RSF activity in the catchment has occurred as recently as 2007 (Massey *et al.*, 2013; McSaveney and Massey, 2013). Similarly, dated catastrophic RSFs in adjacent schist-dominated catchments include the 4 ka Polnoon Burn rock avalanche (Korup, 2011), the 7.9 ka Hillocks rock avalanche (McColl *et al.*, 2019), and 6-9 ka Lochnagar rockslide dam (Sweeney *et al.*, 2013) that would question the efficacy of glacial debuttressing as a trigger here. However, it cannot be excluded that debuttressing together with other processes such as glacial erosion and undercutting did not prepare slopes for failure within the catchment.

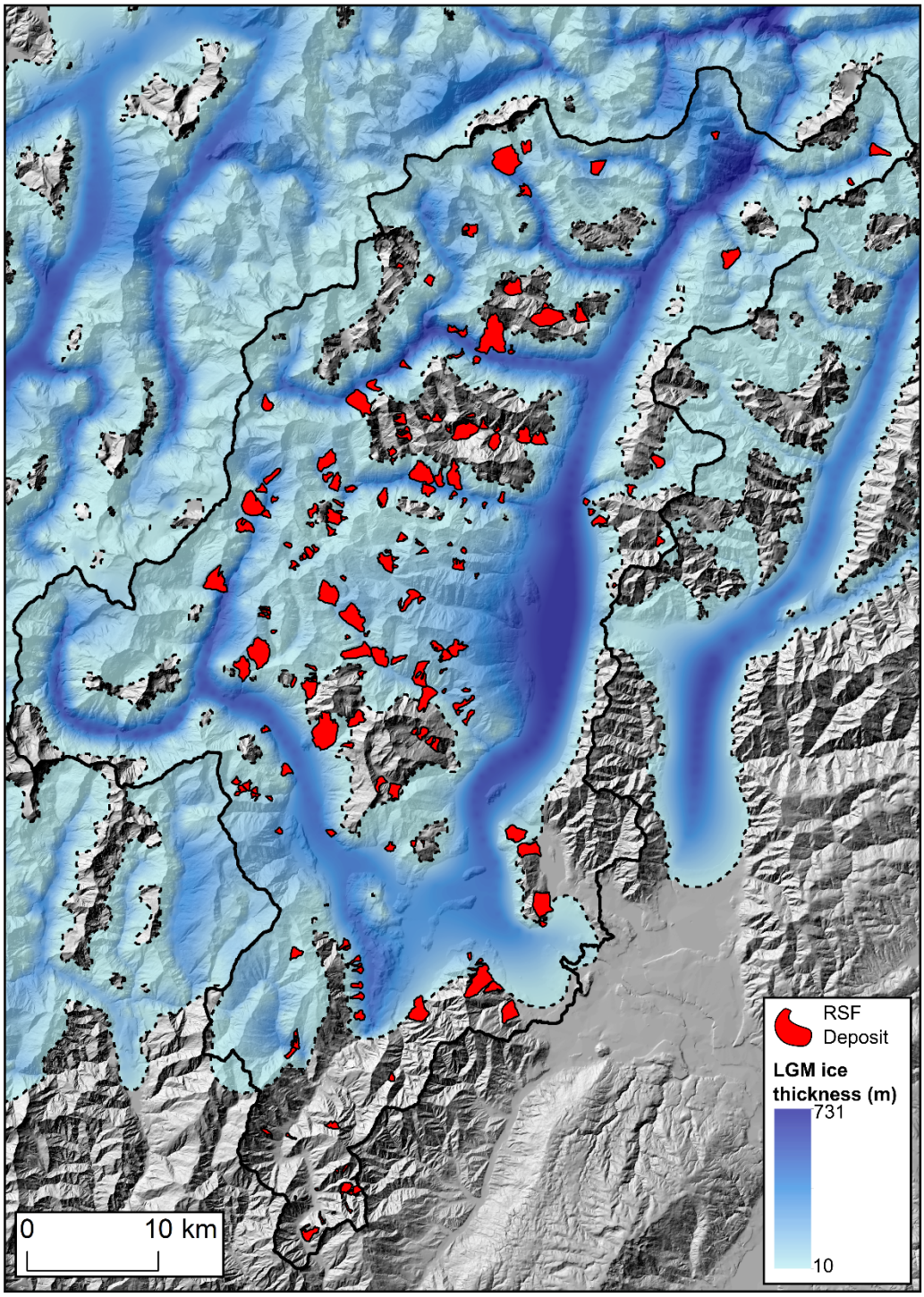

Figure 5.14. Distribution of subaerial RSF deposits compared to modelled LGM ice extents and thicknesses LGM ice model from James et al., (2019). Black line delineates the catchment boundary from the lake outlet.

Enhanced seismicity due to isostatic rebound has been suggested as the trigger of paraglacial RSFs in seismically quiescent regions elsewhere (Ballantyne *et al.*, 2014). However, isostatic adjustment is thought to be low across the South Island (Pickrill *et al.*, 1992), but is generally poorly constrained. Lack of tilting has been identified on paleo-lake level shorelines around nearby Lake Wakatipu (Cook, McColl, *et al.*, 2013). This suggests that either isostasy was

uniform across the whole 80 km long lake, or ice thicknesses during the LGM were insufficient to cause significant crustal deformation. No in-depth studies into possible tilting of the palaeoshorelines around Lake Wānaka have been done beyond their initial identification by Sutherland et al., (2019). However, the current model of LGM ice extent for New Zealand points to more valley-extensive glaciation rather than a localised ice sheet or ice cap (James *et al.*, 2019). Therefore, ice thicknesses may not have been extensive to induce sufficient isostasy, and subsequent isostatic-induced seismicity. Furthermore, the tectonically and seismically active nature of the South Island makes isolating isostatic-induced uplift and seismicity difficult.

The identification of palaeoshorelines around the lake (Sutherland, Carrivick, Shulmeister, *et al.*, 2019) indicate that the subaerial and subaqueous slopes have experienced fluctuating water levels since lake formation. The lack of identified intermediate shorelines between 309 m and the present-day lake level (277 m) could indicate a continued or rapid drainage event of the lake basin. The lack of age constraints of both deposits and palaeoshorelines make assessing timings of lake level drops in relation to slope failures difficult. Changes in water levels may have affected the overburden stresses experienced by subaqueous slopes to initiate failure (Urlaub *et al.*, 2013). Furthermore, the fluctuations may have led to the development of excess pore pressures (Moernaut *et al.*, 2010) that could have primed some subaqueous slope failures. The effects on the subaerial hillslopes could include changes in the groundwater and seepage pressures on lake adjacent hillslopes (Pánek *et al.*, 2018). This may have controlled the movement of the RSFs towards the head of the lake (Figure 5.10A), where slopes failed to re-establish stability and is perhaps why the deposits do not appear to have a subaqueous bathymetric expression. However, lake level fluctuations will only have had an effect on a small number of the lake-adjacent deposits, and therefore cannot explain most of the deposits in the subaerial environment. Furthermore, fluctuating reservoir levels has been found to have a negligible effect on other schist landslide movement rates nearby (Macfarlane, 2009).

5.6. Conclusion

This study has provided a new inventory of subaerial and subaqueous landslide deposits across an intramountainous lake in New Zealand, where data were previously sparse. The newly collected, high-resolution PDBS, and SBP data from Lake Wānaka provide the first evidence of landslide deposits (*n=17*) within the lake basin. Some deposits originated from previously unknown failures in the subaerial environment and runout into the lake. The PDBS data also

indicate that entirely deltaic, and non-deltaic subaqueous landsliding has occurred within the lake.

Both the subaerial and subaqueous inventories are considered incomplete, as indicated by a divergence from a power law fit to the area frequency distribution. Erosion and loss of deposits, and amalgamation of subaerial deposits may explain this divergence. Combining the subaqueous and subaerial inventories has limited effect or improvement on the overall fit of models to the cumulative and non-cumulative frequency-area distributions. It seems like this may be an undersampling of deposits in the subaqueous environment. Processes such as overprinting by background sedimentary infill within the lake is likely obscuring the extent and number of deposits through time. Limited penetration from the sub-bottom data collected here was unable to resolve the relative temporal distribution. Therefore, further sub-bottom investigations from lower frequency systems are needed to resolve subsurface data to depths beyond what is achieved here.

No definitive triggering mechanism(s) can be ascertained for either the subaerial or subaqueous deposits due to the comparatively small sample size, and absence of known ages of the deposits. Given the topographic position of the subaerial deposits, and clusters of subaerial and subaqueous deposits within relatively close proximity to known active (and potentially active) faults, a seismic trigger seems a likely candidate for many of the deposits, but the effects of paraglacial processes such as debuttressing and fluctuating lake levels cannot be dismissed. Expansion of absolute dating of subaerial deposits would aid in deciphering the timing, controls, and possible triggers of such events. Similarly, core extraction from the lake basin could aid in the establishing ages of the subaqueous deposits. The results here provide a good comparison of the other intramountainous lake catchments in New Zealand that have similar geology and relief, such as Lake Hāwea and Lake Wakatipu. Potential similarities and/or discrepancies in the spatial and temporal distribution of landslide deposits within these lakes may provide some insight into possible regional triggering mechanisms such as earthquakes. Furthermore, comparisons of deposit types i.e. STS RSFs or entirely subaqueous may provide more insight into the preconditioning and controlling factors that may be affecting the distribution in Lake Wānaka.

Finally, the identification of landslide deposits within the lake also highlights a potential tsunami hazard that needs to be assessed. With the identification of STS deposits, monitoring the subaerial rock slopes around the lake for signs of movement or deformation may provide

some indication of when a possible catastrophic collapse may occur. Similarly, dynamic analysis of landslide runout, and tsunami wave generation and runup is needed to quantify the risk to the southern shoreline on which the township is located.

Chapter 6. Discussion

The overarching aim of this thesis was to better understand the distribution and dynamics of landslides within lakes and fjords in New Zealand, to improve the understanding of the hazard. Three main research questions were outlined in Chapter 1 to address the aim:

> RQ1. Do lakes and fjords in New Zealand contain an archive of landslide deposits that help to resolve the landslide magnitude-frequency relationship?
>
> RQ2. What are the controls on the landslide distribution within lakes and fjords in New Zealand?
>
> RQ3. What is the dynamic behaviour of landslides in a lake or fjord environment?

This chapter summarises the key findings from this thesis in relation to the research questions outlined in Chapter 1 (sections 6.1, 6.2, 6.3). Section 6.4 discusses the geohazard implications of the findings of this thesis. This chapter concludes with a discussion of future research directions based on the findings from within this thesis (Section 6.5).

6.1. Do lakes and fjords in New Zealand contain an archive of landslide deposits that help to resolve the landslide magnitude-frequency relationship?

For landslide hazard assessments, and magnitude-frequency of past events, establishing an inventory of subaqueous deposits is necessary (Blikra *et al.*, 2006; Longva *et al.,* 2009; Mountjoy and Micallef, 2018; Mountjoy *et al.,* 2019). Such datasets also provide a baseline for magnitude of past landslides (Avdievitch et al., 2020; Stacey et al., 2020). The lake and fjord environments of New Zealand are posited in the literature as containing an archive of previously unidentified STS and subaqueous landslide deposits (Dykstra, 2012; Bainbridge, 2017).

Chapter 3 presented an inventory of 15 lakes and 5 fjords with known landslide deposits was presented (Table 3.2, Figure 3.7, Figure 3.8, and Figure 3.9). This new inventory highlights that, landslides into and within lakes and fjords have occurred across both the North and South Island of New Zealand (*n=20*). Many of the identified landslide cases are from observations (*n=9*), and are single, isolated events that preclude understanding the magnitude of the event, especially as bathymetric data are lacking for these cases. Additionally, the frequency of the landslides is temporally restricted to the historical and observational record, which in New Zealand is comparatively short (c.180 years). The lack of hydroacoustic data in many of the

lakes and fjords limit identification and assessment of the magnitude-frequency of deposits beyond the observed and historical record. SBP data from several of the lakes and fjords indicates past landslides have occurred within these basins (Table 3.2). The acquisition of high-resolution MBES data from Lake Tekapo and Milford Sound/Piopiotahi have revealed several more landslide deposits across the basin floors. However, the inventory does detail that landslide deposits are prevalent in many more lakes and fjords than previously thought.

In *Chapter 5*, a catchment-scale investigation of subaerial and subaqueous landslide deposits was conducted in intramountainous Lake Wānaka and its surrounding catchment. A total of 202 subaerial landslide deposits were mapped in this thesis (Figure 5.5), ranging in area of 10^4-10^6 m^2. Newly collected high-resolution bathymetric and sub-bottom data were also collected from Lake Wānaka to identify any subaqueous landslide deposits. In total, 17 new, previously unknown, deposits were discovered on the 40% total coverage of the lakebed from the bathymetric data. Several large (>10^5 m^2) possible subaerial source scars were identified around the lake (Table 5.1), and 2 subaqueous scars were identified in the BTM (Figure 5.8). However, no deposits were identified on the lakebed that could be associated to the scars. No deposits were also identified buried within the sedimentary infill in the available sub-bottom profile data. Limited to no sub-bottom penetration was achieved in many of the collected profiles, with typical sub-bottom penetration depths ranging between 20 - 35 m, and a localised isolated subsurface depth of 115 m identified in one profile (Figure 5.11A). The limited number of deposits within the lakebed relative to those in the subaerial catchment has limited effect on the overall magnitude-frequency distribution (Figure 5.12). The estimated areas of possible subaerial scars identified around the lake suggest that some large catastrophic RSF deposits may be missing in the Wanaka magnitude-frequency distribution. However, due to the uncertain nature of the pre-failure topography, the estimated areas should be treated with caution. The new investigation into Lake Wānaka emphasises the need to expand hydroacoustic surveys in New Zealand lakes and fjords.

The results in *Chapter 4* revise the total number of previously identified catastrophic RSF (rock avalanche) deposits to 16, down from the 22 initially identified by Dykstra (2012). Some deposits are still STS landslides, but more likely from shallow regolith failures. Despite the slight revisions, the deposits identified in Milford Sound/Piopiotahi are located across a comparatively small area (25 km^2). A similar number of deposits have been identified in the subaerial catchment (Dykstra, 2012; Bainbridge, 2017), despite the subaerial catchment covering a substantially larger area (542 km^2) (Table 6.1). Furthermore, previous CDF analysis

of the RSF deposits within Milford Sound/Piopiotahi indicates that most of the STS RSF deposits occupy the low-end (< $4x10^6$ m^3) of the size frequency distribution (Figure 6.1A) (Taig and McSaveney, 2015). These findings still hold true, even with the revisions in mapping and total number of deposits from the analysis in *Chapter 4* (Figure 6.1B). These results suggest that equivalent magnitude subaerial RSF deposits have since been lost from the catchment by various censoring processes, most likely overprinting by vegetation and fluvial erosion (Bainbridge, 2017). Therefore, the record in the fjord bottom of Milford Sound is a crucial archive that helps to resolve the catchment-wide magnitude-frequency distribution. No STS deposit in Milford Sound is of equivalent magnitude to the largest subaerial deposit. As well as the deposits visible in the MBES dataset, Dykstra (2012) also identified areas of hyperbolic facies, interpreted as STS RSF deposits in SBP data from the fjord bottom (Figure 6.2). Due to the limited SBP coverage the relative size magnitude of deposits cannot be ascertained in the profile.

In the wider context, it appears that subaqueous environments in New Zealand are effective in preserving landslide deposits. Only by having hydroacoustic datasets can the landslide magnitude-frequency distribution in a region be resolved. The deposits identified in Milford Sound/Piopiotahi (Figure 6.1) and Lake Wānaka (Figure 5.12) occupy the low end of the distributions. However, the rollover, cutoff, and divergence from the power law and lognormal fits in both datasets indicates the magnitude-frequency distributions at both locations are considered incomplete. The lack of equivalent magnitude landslide deposits in the subaqueous environments of both Milford Sound/Piopiotahi and Lake Wānaka, compared to the largest events in the subaerial environment suggests that such events may be missing from the current subaqueous datasets. The largest magnitude landslides may have occurred immediately after deglaciation or early Holocene, as has been reported in subaqueous and/or subaerial environments elsewhere (Blikra *et al.*, 2006; Ballantyne *et al.*, 2014; Böhme *et al.*, 2015; Stacey *et al.*, 2020). If that holds true for New Zealand lakes and fjords, such deposits may be deep within the infill. The buried deposits in Milford Sound/Piopiotahi may contain a spatial and temporal archive of STS RSFs that extend immediately after deglaciation (Blikra *et al.*, 2006; Ballantyne *et al.*, 2014; Böhme *et al.*, 2015; Stacey *et al.*, 2020). Therefore, it is unknown whether any of the buried deposits are of comparable magnitude to the deposits in the subaerial environment (Figure 6.1), or whether the buried material relates to any of the deposits with positive bathymetric expressions identified along the fjord bottom (Figure 4.3).

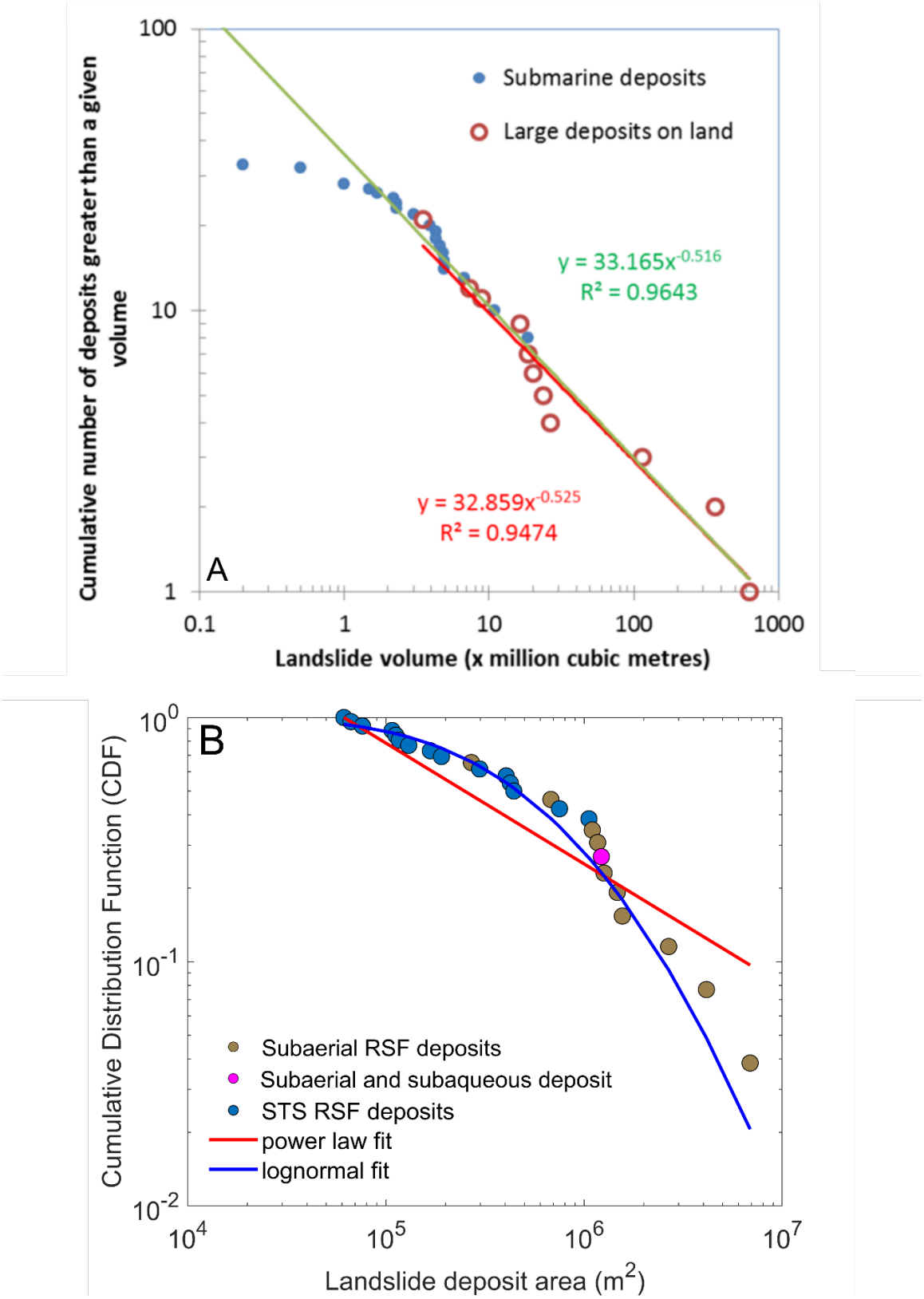

Figure 6.1. Size-frequency distribution of subaqueous and subaerial Milford Sound/Piopiotahi landslide deposits. Panel A figure from Taig and McSaveney (2015), based on original findings from Dykstra (2012). Panel B recalculated with the STS RSF A_L results from *Chapter 4* within this thesis. Panel B only focusses on the RSF (rock avalanche) deposits in Milford Sound/Piopiotahi, therefore excluding talus cones and deltaic collapse deposits. Subaerial RSF deposit surface areas from Dykstra (2012).

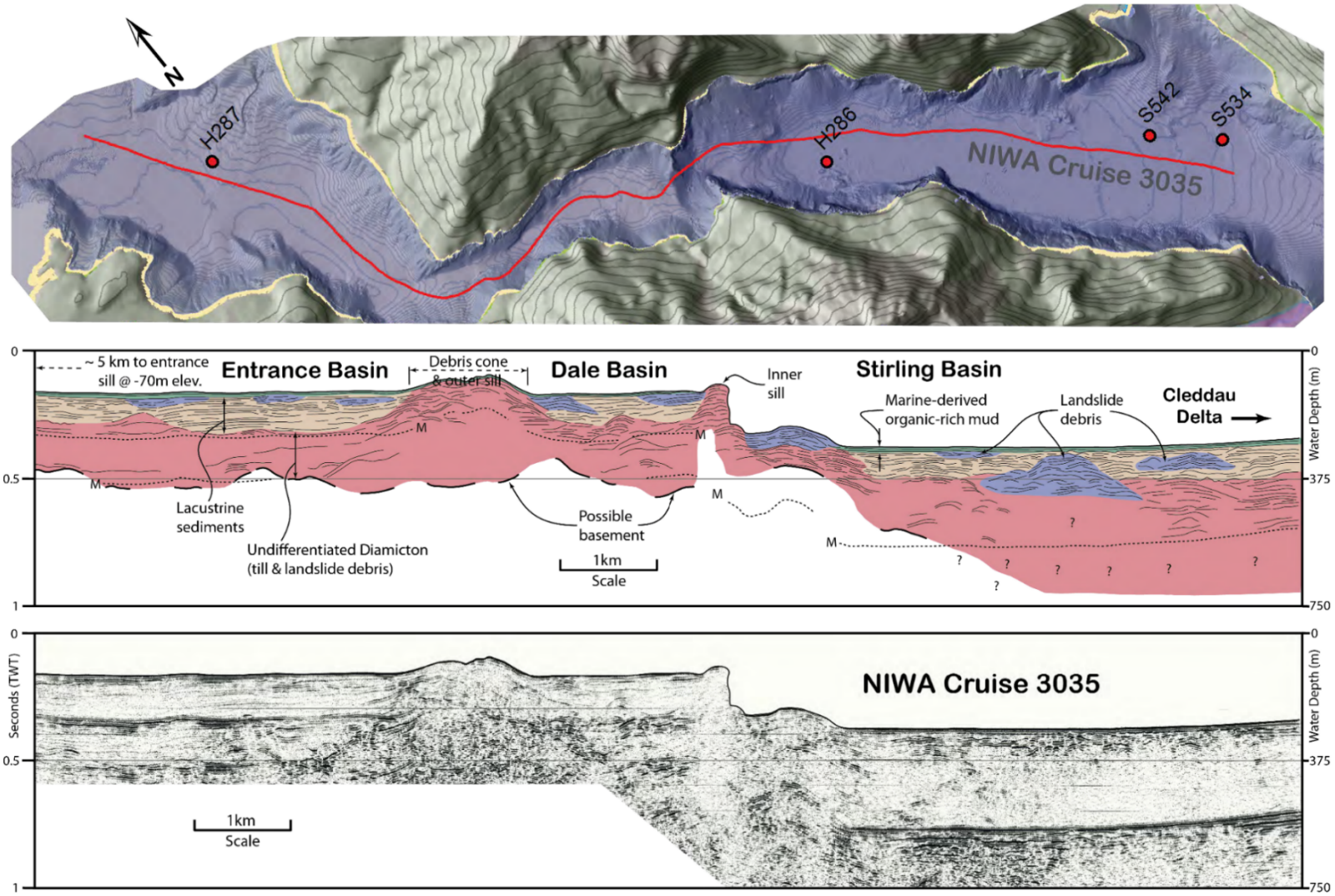

Figure 6.2. Airgun profile data and subsequent seismic interpretation. Profile location indicated in top panel. Middle panel is the seismic interpretation of the airgun profile (bottom panel). Note thick, discontinuous, parallel-bedded unit (lacustrine, light brown) overlying poorly reflective, chaotic diamicton fill (till and landslide debris, red). Figure source: Dykstra (2012).

6.1.1. Burial of deposits by sedimentation

As suggested for Lake Wānaka (*Chapter 5*), the sediment infill may be a factor that has limited identification of deposits within subaqueous basins, relative to the available methods applied. Comparatively fewer deposits were identified in the BTM of Lake Wānaka compared to probable subaerial and subaqueous scars identified (Table 5.1, Figure 5.8D). Furthermore, no deposits were identified in the subsurface data where penetration was achieved with the sub-bottom profiler. The exceptions are the deposits identified that exhibited positive bathymetric expression (Figure 5.7, Figure 5.8). The available SBP data from Lake Ōhau (Krause, 2016; Fitzsimons and Howarth, 2018), Lake Pukaki (Clark *et al.*, 2015), and Lake Tekapo (Upton and Osterberg, 2007; Mountjoy *et al.*, 2019), reveal buried lateral slope and deltaic collapse deposits within their respective infills suggesting burial of deposits is likely (Figure 3.10). Additionally, SBP data from Milford Sound/Piopiotahi show buried STS deposit material within the subsurface (Figure 6.2) (Dykstra, 2012).

Sedimentation rates in these lakes appears to be an order of magnitude greater than even the highest rates from the fjords (Table 6.1). However, there are few established sedimentation rates for many of the other lakes compared to many of the fjords. It is currently unknown whether the other lakes, such as Lake Wānaka, experience similar sedimentation rates. The rate derived by Equation 5.4 for Lake Wānaka is comparatively low (1.24 mm a^{-1}) comparted to many of the lakes, and some fjords (Table 6.1). The rate derived based on estimated fill of Lake Wānaka (11-22 mm a^{-1}) is similar to many of the other lakes. Many of the large lakes are situated across the eastern and western Central Southern Alps, where long-term uplift rates are high (Tippett and Kamp, 1995). Denudation rates are equivalent to the uplift rates as New Zealand is in long term dynamic equilibrium (Adams, 1980). Therefore catchments across the Southern Alps are experiencing comparatively high denudation rates to those in Fiordland, where uplift and denudation rates are lower (Tippett and Kamp, 1995; House *et al.*, 2005), and subsequent relief is also lower (Hancox and Perrin, 2009). The geology of the eastern and western central Southern Alps are composed of schistose and sandstone bedrock (Turnbull, 2000). The sandstones and schists that comprise the catchments are easily erodible (Pickrill, 1987). It is not improbable that comparatively high sedimentation rates may also occur in many of the other lakes, despite the lack of absolute rates.

Whilst the full sedimentary infill within Lake Wānaka was unresolved in *Chapter 5*, the thickness is estimated at 200 - 400 m (Adams, 1978). The estimated thickness is not too dissimilar to the Tekapo, Pukaki, and Ōhau, whose infills are typically between 150 – 300 m

(section 3.4). Therefore, if any relatively older STS and subaqueous landslides occurred in Lake Wānaka since deglaciation, it is possible that the deposits were rapidly buried. However, more SBP data that resolve deeper penetration is needed to establish whether older landslides did occur and to establish their relative stratigraphic position to gain insight into relative timing since basin formation, whilst cores are needed to establish more accurate sedimentation rates.

Cores from many of the fjords in Fiordland indicate that modern sedimentation rates are low (<1 mm yr^{-1}) (Table 6.1, and references therein) largely due to the resistant geology and thick vegetation cover precluding erosion (Pickrill, 1993; Augustinus, 1995). No longer term estimates on sedimentation rates are available due to the short core lengths (Stanton and Pickard, 1981; Ramirez *et al.*, 2016). The comparatively thin postglacial sediment thicknesses (16 m, and 15 – 25 m) in Te Awaroa/Long Sound, Rakituma/Preservation Inlet; and Te Awa -o- Tū/Thompson Sound Kaikiekie/Bradshaw Sound, respectively (Pickrill, 1993), suggest sedimentation rates have not varied significantly since deglaciation of these fjord basins. Furthermore, glacial geomorphological features are visible in MBES data from Te Awa -o- Tū/Thompson Sound Kaikiekie/Bradshaw Sound, further suggesting a comparatively thin sediment infill within this fjord (Barnes *et al.*, 2016). Measured suspended sediment yields (SSYs) from the main inflow rivers to the fjords are low (Table 6.1) (Pickrill, 1993; Hicks *et al.*, 2011), further suggesting low sediment influxes into the fjord basins.

However, sedimentation rates derived from a 4 m core from Milford Sound/Piopiotahi in are comparatively high (2-3 mm yr^{-1}) over the last 1340 years, compared to the other fjords (Table 6.1) (Knudson *et al.*, 2011). This is despite similar SSY from the Cleddau River (Table 6.1). The comparatively high sedimentation rate may be due to the size of Milford Sound/Piopiotahi compared to its tributary catchment. The catchment area/fjord area ratio is the greatest of all the fjords (Table 6.1). Furthermore, the core from Milford Sound/Piopiotahi exhibits pulses of granular sediment interspersed between the marine gyttja (Knudson *et al.*, 2011; Dykstra, 2012). These pulses have been attributed a post-seismic increase in the terrestrial sediment flux as a result of catchment scale erosion (Dykstra, 2012). Given the proximity of Milford Sound/Piopiotahi to the Alpine Fault, shaking from these ruptures are likely sufficient to (re)mobilise terrestrial sediment in the catchment, as well as possibly trigger further catastrophic RSFs. Similar sediment layers have been identified in cores from Alpine Fault-adjacent Lakes Paringa, Ellery, and Mapourika (Howarth *et al.*, 2014, 2016).

The sedimentation rates from Milford Sound/Piopiotahi are temporally short due to the limited core depth, relative to the total sediment infill within the fjord bottom (Figure 6.2). Furthermore, such sedimentation rates are too low to explain the sediment infill within the fjord bottom given the constrained deglacial chronology (Dykstra, 2012). Therefore sedimentation rates must have been higher during earlier periods. High sedimentation rates have been observed in other mid-latitude fjords during deglaciation, such as in Norway (Lyså *et al.*, 2010; Bellwald *et al.*, 2016, 2019). Due to the uncertainties in sedimentation rates, no absolute ages can be established for the buried deposits (Figure 6.2).

Table 6.1. Catchment areas, sedimentation rates, and suspended sediment yields (SSYs) from lakes and fjords in New Zealand from literature.

Fjord/Lake		Catchment area (km^2)	Fjord/Lake area (km^2)	Catchment area/fjord/lake area (ratio)	Sedimentation rates ($mm\ yr^{-1}$)	Age ranges	SSY ($t/km^2/yr$)	Reference
Fjord	Milford Sound/Piopiotahi	542	25.3	21.4	2.22 – 3.13	700 – 1340 cal. yr. BP	78[a] (Cleddau River)	(Stanton and Pickard, 1981; Knudson *et al.*, 2011)
	Te Houhou/George Sound	305	32.9	9.3	0.63 – 1.04	0 – 2180 cal. yr. BP	-	(Stanton and Pickard, 1981; Knudson *et al.*, 2011)
	Te Awa -o-Tū/Thompson Sound	152	28.4	5.4	0.62 – 1.73	1220 – 4300 cal. yr. BP	70[b]	(Stanton and Pickard, 1981; Knudson *et al.*, 2011)
					0.24 – 0.71	2610-5360 ±130 ^{14}C yr. BP		(Pickrill, 1993)
	Kaikiekie/Bradshaw Sound	290	20.9	13.9	1.27	400 – 1780 cal. yr. BP	70[b]	(Stanton and Pickard, 1981; Knudson *et al.*, 2011)
					0.77 – 0.85	1230-2040 ±130 ^{14}C yr. BP		(Pickrill, 1993)
	Hinenui/Nancy Sound	91.9	13.9	6.6	0.84 – 1.02	1135 – 1260±75 ^{14}C yr. BP	118[b]	(Pickrill, 1993)
	Te Awaroa/Long Sound, Rakituma/Preservation Inlet	562	93	6.0	0.54 – 1.15	1090 – 7430 ±140 ^{14}C yr. BP		(Pickrill, 1993)
					1.50±0.10	c. 100-150 cal. yr. BP	43[b]	(Stanton and Pickard, 1981; Ramirez *et al.*, 2016)

Fjord/Lake		Catchment area (km^2)	Fjord/Lake area (km^2)	Catchment area/fjord/Lake area (ratio)	Sedimentation rates ($mm\ yr^{-1}$)	Age ranges	SSY ($t/km^2/yr$)	Reference
	Tamatea/Dusky Sound	861	181	4.8	1.60±0.20	c. 100-150 cal. yr. BP	-	(Stanton and Pickard, 1981; Ramirez *et al.*, 2016)
	Doubtful Sound/Patea	627	83.7	7.5	2.50±0.30	c. 100-150 cal. yr. BP	-	(Stanton and Pickard, 1981; Ramirez *et al.*, 2016)
Lake	Lake Tekapo	1463	87	16.8	6.2	unknown	628[a] (Tekapo Spillway)	(Quinn, 2004)
					8	unknown		(Quinn and Wilson, 2004)
					10	unknown		(Pickrill and Irwin, 1983)
					22	1891 AD – 1991 AD[c]		(Mildenhall *et al.*, 2006)
	Lake Ōhau	1198	54	22.2	5-6	1900 AD – 2010 AD[d]	-	(Roop *et al.*, 2016)
					unknown	573-787 AD – 2010 AD		(Vandergoes *et al.*, 2018)
	Lake Pukaki	1413	178.7	7.9	10-15	unknown	-	(Pickrill, 1993)
					27	0-12000 yr. BP		(Adams, 1980)
	Lake Wānaka	2578	192	13.4	1.24	29-18 ka BP to present day	900[a] (Matukituki river)	This thesis
					11-22			

[a] data from Hicks et al., (2011); [b] data from Pickrill (1993); [c] age approximated based on assumed annual deposition of pollen; [d] rate calculated only on the top 60 cm of a 5.5 m long core. Subsequent ages from the core are from independently dated samples and age modelling; bracketed names under SSY values are where SSY was measured. Values without brackets are where measurement locations are not reported.

6.2. What are the controls on landslide distribution within lakes and fjords in New Zealand?

In the inventory of known landslides into and within lakes and fjords presented in *Chapter 3*, the type(s) of deposits and triggering mechanism (where known) were surmised. STS RSFs appear to be the predominant failure type in the fjords and intramountainous lakes (Figure 3.9). This includes Milford Sound/Piopiotahi, where STS RSF deposits were identified on the fjord bottom (Dykstra 2012; this thesis). The new bathymetric data from Lake Wānaka also show similar results, where STS landslides (*n=6*) are the predominant non-deltaic landslide deposits identified (*Chapter 5*, Figure 5.7). Deltaic collapses are also identified within Milford Sound/Piopiotahi and Lake Wānaka at the river inflows.

In both Milford Sound/Piopiotahi (*Chapter 4,* Figure 4.3) and Lake Wānaka (*Chapter 5,* Figure 5.7, 5.8, 5.9, 5.10), no apparent landslides from failures in lateral slope sediments are identified in the bathymetric data. No sediment drape is identified in the available SBP data from Lake Wānaka, where lateral slope gradients are >20° (Figure 5.8F). Whilst no SBP data from Milford Sound/Piopiotahi were investigated in this thesis, the available SBP data for the fjord only extend centrally across the fjord bottom (Figure 6.2). The deposits identified in Milford Sound/Piopiotahi are the result of STS landslides and deltaic collapses (Figure 4.3). The subaqueous slopes are well in excess of >20°. SBP from Te Houhou/George Sound, Rakituma/Preservation Inlet, and Te Awa -o- Tū/Thompson Sound and Kaikiekie/Bradshaw Sound all show a lack of laterally continuous reflectors on the subaqueous slopes that would indicate a sediment drape (Pickrill, 1987, 1993; Pickrill *et al.*, 1992; Barnes *et al.*, 2016). Therefore sedimentation along the slopes seems limited or unlikely.

In subaqueous basins globally, the threshold slope angles that necessitate sufficient sediment accumulations, and discernible landslide deposits, is typically between 5-20° (Strasser *et al.*, 2011; Praet *et al.*, 2017; Moernaut *et al.*, 2019). Slopes steeper than >20° are likely to have small-scale, frequent spontaneous failures that leave no noticeable deposit on the basin floor (Hilbe and Anselmetti, 2014; Praet *et al.*, 2017). Therefore, in the fjords and intramountainous lakes of New Zealand, the steep slope topography is unlikely to facilitate necessary conditions for lateral slope failures to occur, or that the sediment cover may be too thin for noticeable lateral slope failures to be identified on the basin floor. An apparent lack of lateral slope failures has been observed in intramountainous lakes elsewhere (Hansen *et al.*, 2016; Strasser *et al.*, 2020).

In contrast, the available SBP data from Lake Ōhau (Krause, 2016; Fitzsimons and Howarth, 2018), and MBES and SBP data from Lake Tekapo (Upton and Osterberg, 2007; Mountjoy *et al.*, 2019) show multiple, and stacked locations of lateral slope landslide deposits (Figure 3.10). Both lakes are piedmont-style lakes, less bound by steep subaerial topography, despite being carved by repeated glaciations. Non-deltaic, lateral slope angles in Lake Tekapo are 10-20° (Mountjoy *et al.*, 2019), within the threshold ranges for sufficient sediment to accumulate, and landsliding to occur. Lateral slope landsliding may only occur in the piedmont lakes in New Zealand, where subaqueous slope angles may be shallower than the steep subaerial and subaqueous hillslopes that bound the intramountainous lakes. Furthermore, STS RSFs appear to be less likely in the piedmont lakes due to the lack of steep subaerial topography. No apparent STS RSFs have been identified on the bed of Lake Tekapo (Mountjoy *et al.*, 2019). However, acoustic signal attenuation by free gas in the sedimentary infill within the lake precluded identification of any possibly buried STS RSFs at the base of the subaerial hillslopes (Mountjoy *et al.*, 2019). Therefore it is unknown whether there are any buried STS RSF deposits within the lake. Many of the other lakes are also lacking bathymetric data, so it is still unknown whether some STS deposits may be visible on the lakebed.

In the inventory compiled in *Chapter 3,* earthquakes are, or are assumed to be, the predominant triggering mechanism for landslide occurrences in 14 of the lakes and fjords in New Zealand (Table 3.2). Furthermore, earthquakes are the most prevalent trigger of subaerial catastrophic RSFs with known ages and/or triggering mechanism across the South Island (Bainbridge, 2017). Earthquake(s) have also been suggested as a likely trigger for the deposits, in particular the STS RSF deposits, within Lake Wānaka (*Chapter 5*), due to their close proximity to the NW Cardrona Fault, a known active fault (Figure 5.1). Furthermore, the topographic position of c. 50% of the RSF deposits in the subaerial catchment extend towards the upper 25% of the hillslopes and ridge crests (Figure 5.4). The topographic position suggests possible earthquakes as a trigger as seismic waves are focussed at ridge crests by topographic amplification, resulting in more severe shaking (Meunier *et al.*, 2008; McColl *et al.*, 2012). Therefore landslide failures from ridge crests may indicate a past earthquake as a trigger. However, due to the apparent long recurrence of earthquakes within this region (Litchfield *et al.*, 2014; Langridge *et al.*, 2016; Barrell, 2019), earthquake-triggered landslides occur much more infrequently compared to lakes and fjords close to active faults with more frequent recurrence intervals. In Milford Sound/Piopiotahi, earthquakes are also assumed as the triggering mechanism of the STS RSFs due to the close proximity to the Alpine Fault, and correlation of ages between dated subaerial

RSFs in the catchment (Dykstra, 2012; Hancox *et al.*, 2013) and known past rupture ages along the Alpine Fault (Berryman, Cooper, *et al.*, 2012; Cochran *et al.*, 2017; Howarth *et al.*, 2018). However, as no ages are available for the deposits within both Lake Wānaka and Milford Sound/Piopiotahi, it remains unknown whether such events were triggered by earthquakes, or by other mechanisms such as rainfall and/or paraglacial processes.

6.2.1. Conceptual model of landslide distribution in New Zealand lake and fjords

The results of this thesis and the synthesis presented above to research questions 1 and 2 reveal that the distribution of landslide deposits is highly variable between fjords and lakes, and even between lakes in intramountainous catchments to more piedmont-style lakes. The following sections outline and detail three possible end-member conceptual scenarios that could explain the distribution of landslide deposits within subaqueous environments. For simplicity, all the conceptual models begin with the respective subaqueous basins fully occupied with a glacier, and ice scouring down to the bedrock, removing all pre-LGM sediments (Panel A on Figure 6.3 Figure 6.4, Figure 6.5).

6.2.1.1. Fjords

In the scenario, the fjord basins are infilled with glaciers during the LGM. The mountainous valley topography is steepened through glacial erosion. The termini of the glaciers extend out of the fjords and reach the continental shelves (Figure 6.3A).

During deglaciation, large thicknesses of diamictic sediment are deposited within the basin floor that forms much of the basement. Whilst eustatic sea levels are low, the fjords exist as a proglacial lake system, where rapid sedimentation deposits a lacustrine unit. The smaller fjords relative to their subaerial catchment (Table 6.1) exhibit a comparatively thicker lacustrine unit. The steep subaqueous fjord slopes inhibit sediment accumulation on the lateral slopes, but subaqueous fan deltas begin to form at the tributary catchment interface with fjord. During deglaciation, subaerial catastrophic RSFs occur from the fjord walls. The RSFs may be the result of paraglacial processes, such as enhanced seismicity from isostatic rebound, permafrost degradation, or debuttressing. The RSFs may also be the result of increasing precipitation since the LGM (Drost *et al.*, 2007), or from large (M_w >7) and frequent earthquakes, either on the Alpine Fault, or the Fiordland/Puysegur Subduction Zones. The RSFs runout into the fjord bottom and are quickly buried over during the period of rapid sedimentation. The RSFs may have been of larger magnitude and frequency, as has been reported elsewhere (Blikra *et al.*,

2006; Ballantyne *et al.*, 2014; Böhme *et al.*, 2015; Stacey *et al.*, 2020). However, the current evidence in this thesis and elsewhere precludes making such assumptions here (Figure 6.3B).

Rapid sedimentation rates continue until the complete retreat of the valley glaciers, and until marine transgression occurs towards the end of the LGIT period. Once transgression occurs, sedimentation is dominated by marine processes. From the transgression, and throughout the Holocene to present, sedimentation rates within the fjords are lower due to the erosion resistant geology of Fiordland. The rivers therefore have low suspended sediment yields (SSYs) as a result. However, large, and relatively frequent earthquakes from either the Alpine Fault, or the Fiordland/Puysegur Subduction Zones continue to occur. These earthquakes possibly trigger one, or several, RSFs in both the subaerial catchment, and from the subaerial fjord walls that could propagate into the fjord. The earthquakes may also trigger the failure of subaqueous fan deltas, leading to deltaic collapses. Increasing precipitation patterns through the Holocene may also trigger RSFs, given the location of the fjords to the prevailing weather systems. The low background rates of sedimentation mean that the deposits are visible on the fjord bottom by conventional MBES data, and depending on their age, there is little to no obscuration of the deposit surface morphology. Depending on the magnitude of the earthquake and its effects on the subaerial catchment, a period of heightened terrestrial sediment fluxes within the catchment may occur for several decades after the earthquake. The heightened sediment flux is a result of erosion and reworking of material through the catchment by fluvial systems, depositing in the fjord (Figure 6.3C).

Figure 6.3. Overleaf. Conceptual model of landslide occurrence in fjords since the LGM to present day. Relative earthquake magnitude is denoted by size of the symbol. The '?' are where such information are currently unknown but suggested within the model. (1) illustrates that no sediment is draping the steep lateral slopes; (2) – marine transgression during eustatic sea level rise; (3) – precipitation variations depending on site, with comparatively lower precipitation to the fjords in the south; (4) – the vertical arrow represents fluctuations in palaeolake level and then sea level with marine transgression; (5) – limited apparent post-event sedimentation covering the deposits, so surface morphology is still visible. Curved black lines adjacent to subaerial and subaqueous slopes symbolise shaking intensity. More lines represent stronger shaking intensities. The figures have been designed to be consistent with Moernaut (2020) model (Figure 2.2).

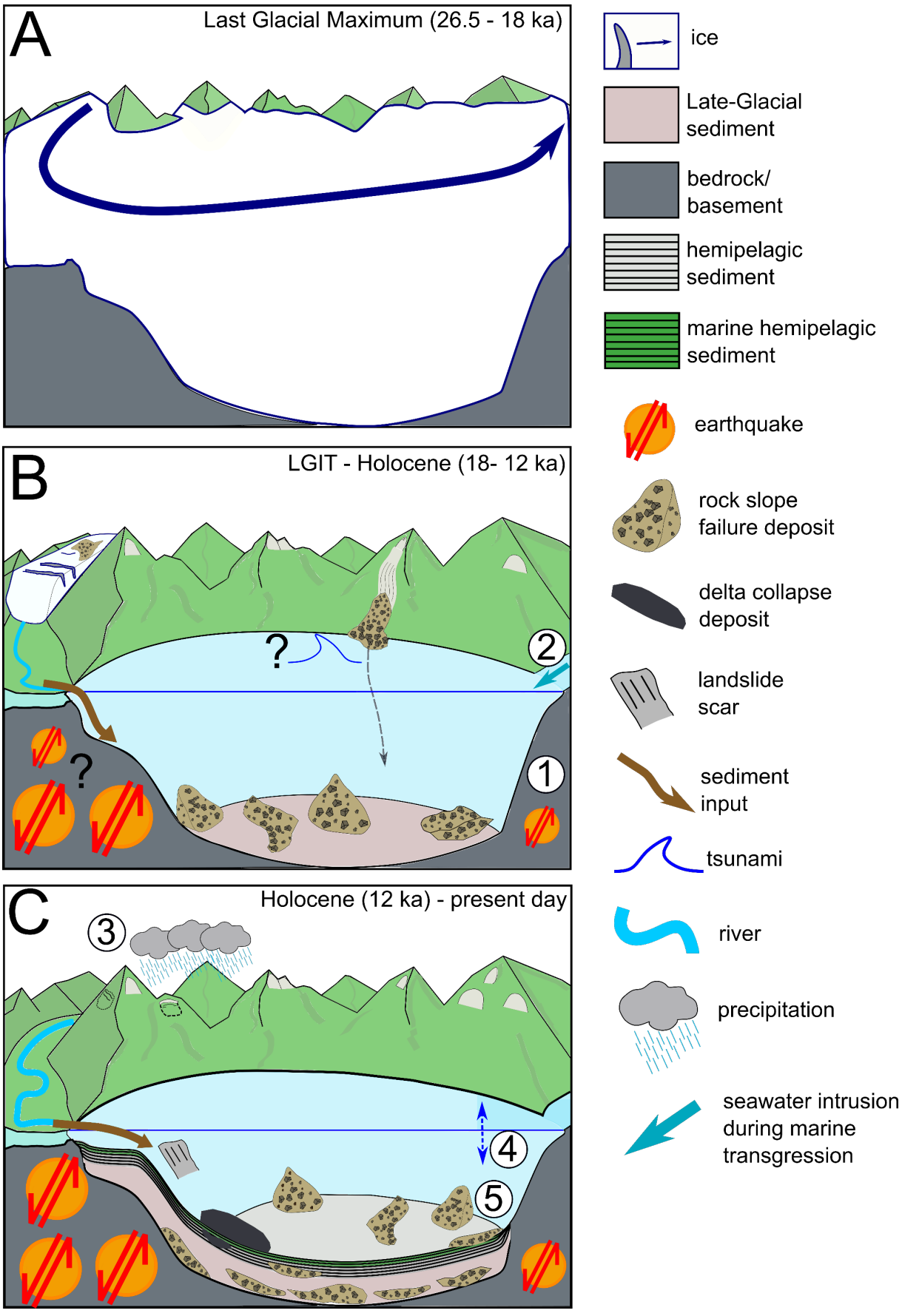
A
Last Glacial Maximum (26.5 - 18 ka)
B
LGIT - Holocene (18- 12 ka)
?
?
1
2
C
Holocene (12 ka) - present day
3
4
5
ice
Late-Glacial sediment
bedrock/ basement
hemipelagic sediment
marine hemipelagic sediment
earthquake
rock slope failure deposit
delta collapse deposit
landslide scar
sediment input
tsunami
river
precipitation
seawater intrusion during marine transgression

This model applies to the fjords of Fiordland in a general sense. Milford Sound/Piopiotahi may represent the extreme endmember of the fjords model. Annual precipitation (Macara, 2014), and relief decrease trending southwards from Milford Sound/Piopiotahi, though the topography is no less steep (Hancox and Perrin, 2009). Furthermore, Milford Sound/Piopiotahi has the greatest catchment area/fjord area ratio of all the fjords (Table 6.1. and references therein) and therefore may have a comparatively greater sedimentary infill than the other fjords (Pickrill, 1987, 1993; Pickrill *et al.*, 1992; Dykstra, 2012). In fjords with smaller catchment area/fjord area ratios, sediment infill may be comparatively less, which may mean any older (pre-Holocene) deposits may be visible on the fjord bottoms, as glacial geomorphological features are still evident in Te Awa -o- Tū/Thompson Sound and Kaikiekie/Bradshaw Sound (Barnes *et al.*, 2016).

Earthquakes from the Alpine Fault may have the most significant effects on Milford Sound/Piopiotahi, given the proximity of the fjord to the fault. The fjords to the south may be more affected by earthquakes generated in the Fiordland and Puysegur Subduction Zone. Earthquakes in this region appear more frequent than Alpine Fault earthquakes (Barnes *et al.*, 2013) and therefore the fjords to the south may experience more frequent and intense shaking. However, subduction zone earthquakes may have a reduced efficacy of generating significant catastrophic RSFs, as observed in the 2003 M_w 7.2 earthquake (Hancox *et al.*, 2003), and 2009 Dusky Sound M_w 7.6 earthquake (Fry *et al.*, 2010). This may explain the apparent lack of deposits identified in the MBES data collected from some of the other fjords including Taiari/Chalky Inlet, Moana-whenua-pōuri/Edwardson Sound, Te Korowhakaunu/Cunaris Sound, Rakituma/Preservation Inlet, and Te Awaroa/Long Sound, and the partial MBES data from Tamatea/Dusky Sound and Te Pauitaha/Breaksea Sound (LINZ, 2020)

6.2.1.2. Intramountainous Lakes

The intramountainous lakes scenario is comparatively similar to the model proposed for the fjords. Both locations are bound by steep subaerial and subaqueous topography. This model may apply to several lakes including Lake Wānaka, Hāwea, Wakatipu, Te Anau, and Manapouri. However, several differences are highlighted between the fjords and the lakes here. In the intramountainous lake scenario, the fjord basins are infilled with glaciers during the LGM, as in the previous scenario. Similarly to the fjords, the mountainous valley topography is steepened through glacial erosion. The termini of the glaciers extend to the ends of the lakes (Figure 6.4A).

During deglaciation, a proglacial lake system develops. Sediment is deposited rapidly as the glaciers retreat up-valley, where rapid sedimentation deposits a likely Late-Glacial (glacio-) lacustrine unit. The steep subaqueous slopes inhibit sediment accumulation on the lateral slopes, but subaqueous fan deltas begin to form at the tributary catchment interface with the lake. During deglaciation, subaerial RSFs may have occurred within the ice-free catchment. STS RSFs may have also occurred from the subaerial hillslopes above the lake. The RSFs may be the result of paraglacial processes, such as enhanced seismicity from isostatic rebound, permafrost degradation, or debuttressing. The RSFs may also be the result of increasing precipitation since the LGM (Drost *et al.*, 2007). However this may only affect west coast intramountainous lakes, as annual precipitation decreases with increasing distance from the Southern Alps Main Divide (Macara, 2015). Large (M_w >7) earthquakes from fault ruptures may have also occurred that could have triggered RSFs. However, this is largely dependent on the recurrence interval of the faults, which can vary from $>10^3 – 10^4$ years (Litchfield *et al.*, 2014; Langridge *et al.*, 2016). Nevertheless, if RSFs occurred during this period, and runout into the lake, the deposits are quickly buried over during the period of rapid sedimentation. As in the fjords, the RSFs may have been of higher magnitude and frequency. However, as within the fjords the current evidence in this thesis and elsewhere precludes making such assumptions here (Figure 6.4B).

Figure 6.4. Overleaf. Conceptual model of landslide occurrence in intramountainous lakes since the LGM to present day. Relative earthquake magnitude is denoted by size of the symbol. The '?' are where such information are currently unknown but suggested within the model. (1) illustrates that no sediment is draping the steep lateral slopes; (2) – precipitation variations depending on site, with comparatively lower precipitation east of the Southern Alps Main Divide; (3) – the vertical arrow represents fluctuations in lake level since LGM; (4) – high sedimentation (dark grey) rapidly burying STS RSF deposit. The figures have been designed to be consistent with Moernaut (2020) model (Figure 2.2).

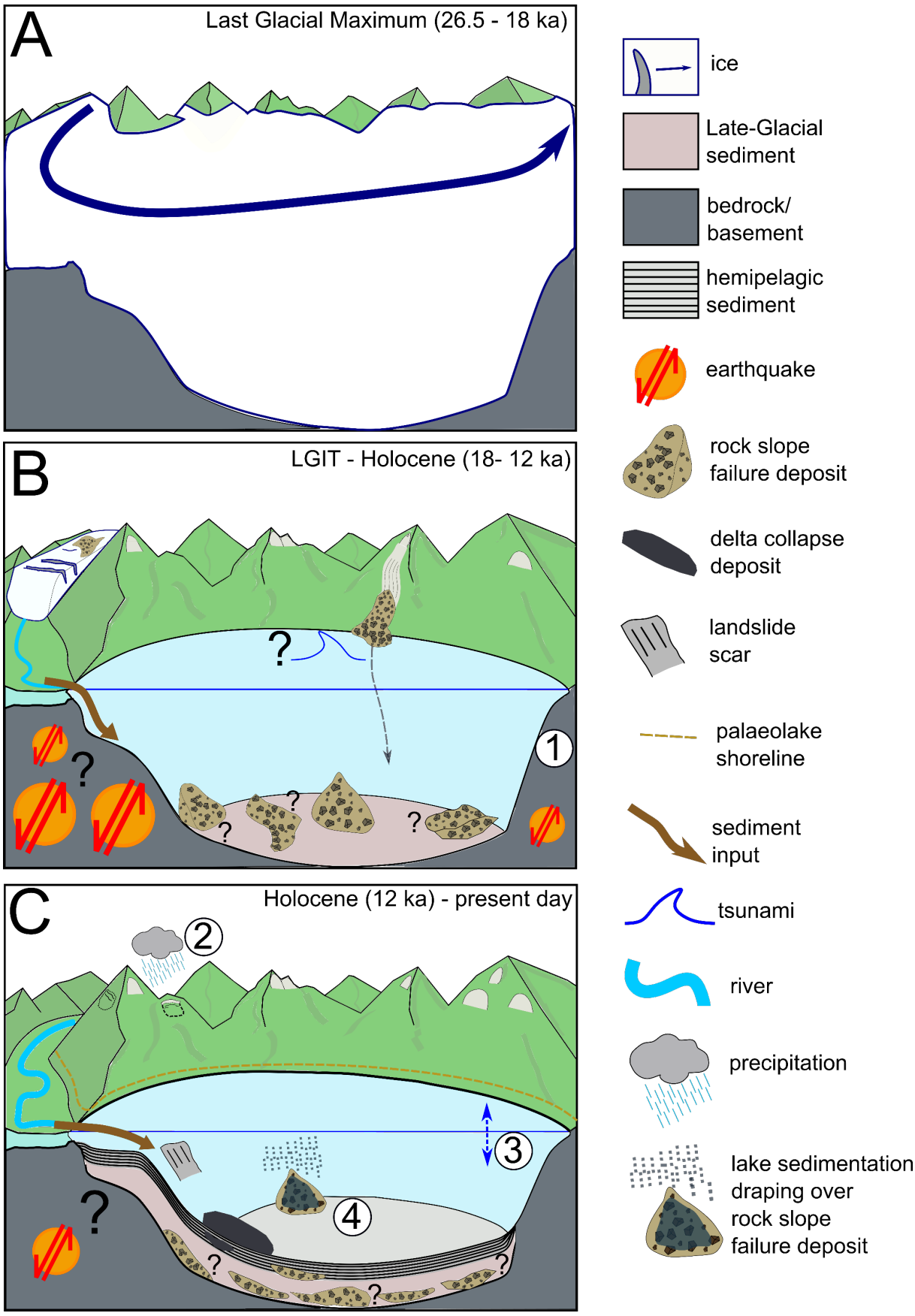
A
Last Glacial Maximum (26.5 - 18 ka)
B
LGIT - Holocene (18- 12 ka)
1
C
Holocene (12 ka) - present day
2
3
4
ice
Late-Glacial sediment
bedrock/ basement
hemipelagic sediment
earthquake
rock slope failure deposit
delta collapse deposit
landslide scar
palaeolake shoreline
sediment input
tsunami
river
precipitation
lake sedimentation draping over rock slope failure deposit

The comparatively long recurrence intervals on many more local faults may control the number and frequency of RSFs being triggered into the lakes throughout the Holocene. The long recurrence intervals result in fewer earthquakes with sufficient shaking intensities (MM≥9) to trigger catastrophic RSFs. Furthermore, many of the lakes may be too far from the Alpine Fault. Earthquakes generated on the Alpine Fault may result in insufficient shaking intensities (MM<9) to trigger catastrophic RSFs at many of the lakes in the eastern Southern Alps (Figure 3.2). However west coast lakes such as Lake Kaniere and Lake McKerrow are in close proximity to the Alpine Fault. Therefore earthquake triggered landsliding is most likely dependent on proximity to the Alpine Fault (or other active faults). The lack of sufficient shaking from the Alpine Fault may only apply to the lakes of the eastern Southern Alps, where modelled shaking intensities are too low (MM<9) (Figure 3.2). Events that do occur may be a result of long-term strength degradation of a hillslope, or another trigger such as rainfall. Alpine Fault shaking intensities would however be sufficient to trigger subaqueous landsliding (MM≥6) (Figure 3.2), such as the failure of subaqueous fan deltas, leading to deltaic collapses. The steep non-deltaic subaqueous slopes inhibit sediment accumulation that is necessary to generate sufficient subaqueous landsliding.

One of the main differences between the fjords and intramountainous lakes is the variations in sedimentation rates. Unlike the fjords, high sedimentation rates continue within the lakes throughout the Holocene (Table 6.1). High sedimentation rates are likely the result of high rates of denudation in catchments matching high rates of uplift for dynamic tectonic equilibrium to occur (Tippett and Kamp, 1995). Additionally the schistose and sandstone geology that dominates the eastern and western Southern Alps is more erodible than the gneissic and granitic geology of Fiordland (Augustinus, 1995). As such, the river systems that input into the lakes have a comparatively higher SSYs than the Fiordland counterparts (Hicks *et al.*, 2011). The comparatively high background rates of sedimentation mean that any deposits on the lake basin floor may become rapidly buried within the subsurface. Therefore, any deposits that are detected within MBES datasets may be comparatively young (Figure 6.4C).

6.2.1.3. Piedmont Lakes

In this scenario, the lake basins are infilled with glaciers during the LGM, as in the previous scenarios. However, the glaciers are less confined by topography, allowing the ice to spread laterally beyond the present-day lake boundaries. Reconstructions of the Tekapo glacier suggest a piedmont-style (Sutherland, Carrivick, Evans, *et al.*, 2019). The lake basin may be less steeply incised in comparison to the fjords and intramountainous lake basins (Figure 6.5A).

During the LGIT towards the Holocene, glacial ice retreats up-valley, and is accompanied by high rates of sedimentation within the lake basins due to outwash from the retreating ice. Little to no subaqueous failures occur during this phase, as the slopes are not charged with sediment. However, high sedimentation rates mean sediment starts rapidly accumulating along the subaqueous slopes (e.g. Strasser et al. 2007). Shallower gradient subaqueous slope (≤20°) facilitate sufficient sediment to accumulate (Praet *et al.*, 2017). Furthermore, deltas may begin to prograde into the lake, forming subaqueous fan deltas from the sediment charged rivers. STS RSFs may have occurred due to possible high-magnitude (and possibly increased) tectonic activity, and/or paraglacial processes. The limited steep subaerial hillslopes around the piedmont lakes mean that if such RSFs occurred, they are restricted to small portions on the lake perimeter (Figure 6.5B).

Throughout the Holocene to present day (Figure 6.5C), rapid sedimentation rates continue within the lakes due high background rates of hillslope denudation within the catchments. Subsequently, the rivers contain high suspended sediment yields that is deposited within the lakes. Sedimentation is dominated by hemipelagic sedimentation. Possible local, and/or distal, large earthquakes may generate sufficient shaking intensities (MM≥6) that trigger coeval subaqueous landslides within the lake basins (Howarth *et al.*, 2016). Recurrence intervals of earthquakes is site dependent, with some lake basins, such as Lakes Mapourika, Paringa, and Ellery (Howarth *et al.*, 2016), experiencing more regular, periodic, high shaking intensities than others due to the proximity to the Alpine Fault. Furthermore, deltaic slopes may also fail, either as a result of seismic shaking, or by independent processes such as gradual loading (Girardclos *et al.*, 2007). STS RSFs are only likely to occur during this period by a local seismic source that can generate sufficient shaking intensities (MM≥9). Such shaking intensities will be variable between lakes, with Alpine Fault-proximal lakes likely to experience such shaking intensities more regularly than other lakes, particularly in the eastern Southern Alps, where the apparent seismic recurrence is less frequent. This model may apply to, but not exclusively, Lakes Pukaki, Tekapo, Ōhau, Brunner, Mapourika, Ellery, and Paringa.

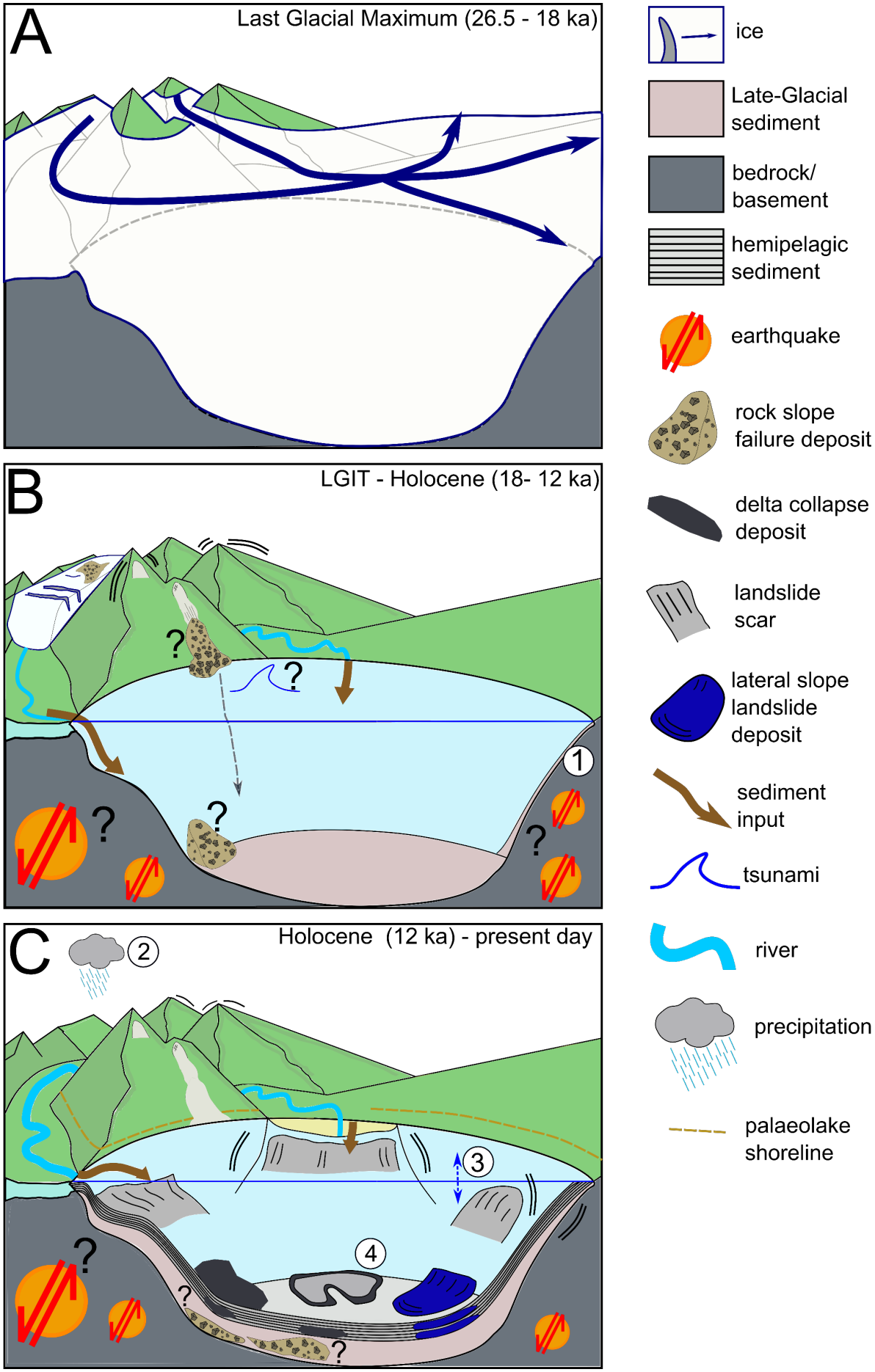
A
Last Glacial Maximum (26.5 - 18 ka)
B
LGIT - Holocene (18- 12 ka)
1
C
Holocene (12 ka) - present day
2
3
4
ice
Late-Glacial sediment
bedrock/ basement
hemipelagic sediment
earthquake
rock slope failure deposit
delta collapse deposit
landslide scar
lateral slope landslide deposit
sediment input
tsunami
river
precipitation
palaeolake shoreline

Figure 6.5. Overleaf. Conceptual model of landslide occurrence in piedmont lakes since the LGM to present day. Relative earthquake magnitude is denoted by size of the symbol. The '?' are where such information are currently unknown but suggested within the model. (1) illustrates the beginning of sediment draping lateral slopes; (2) – precipitation variations depending on site, with comparatively lower precipitation east of the Main Divide; (3) – the vertical arrow represents fluctuations in lake level since LGM; (4) – sedimentation (light grey) burying the subaqueous delta collapse deposit (dark grey). Curved black lines adjacent to subaerial and subaqueous slopes symbolise shaking intensity. More lines represent stronger shaking intensities. The figures have been designed to be consistent with Moernaut (2020) model (Figure 2.2).

6.3. What is the dynamic behaviour of landslides in a lake or fjord environment?

Landslides that runout into, or within, subaqueous environments are rarely observed. Therefore the dynamic behaviour of these events are poorly known (Piper *et al.*, 2012; De Blasio, 2013). Identification, analysis, and characterisation of the deposit morphology can provide some insight into the kinematic behaviour of a landslide (Bull *et al.*, 2009). The morphological and morphometric analysis allows some understanding of what factors could affect the emplacement of the deposits. *Chapter 4* addressed this question by morphological and morphometric analysis of 16 subaqueous rock avalanche deposits that originated in the subaerial environment and runout into the fjord bottom of Milford Sound/Piopiotahi. These deposits are in a single arm fjord and exhibit a variety of morphologies and morphometries, despite occurring in a geologically similar location with similar physiographic setting. By investigating multiple deposits, the results presented in *Chapter 4* within this thesis allowed assessment of what factor(s) influence the emplacement of rock avalanches in fjord environments.

The study found that 13/16 deposits can be characterised as a blocky, conical geometry, with greater thickness in the proximal reaches, but thinning distally. The other 3 deposits (RA2, RA3, RA10), are characterised as elongated deposits with irregular thicknesses. The lack of topographic confinement is likely a factor as it allows the rock avalanche mass to freely spread during runout. The initiation and runout down steep fjord walls (>70°) onto flatter fjord bottoms (<10°) also affected emplacement of the deposits. The abrupt changes in the slope angles along the deposits' travel paths create obstructions to flow. This results in energy absorption from the flowing mass (Whittall et al., 2017), the compaction of the deposits' fronts (Strom, 2006) and reduction in the overall deposit length. This may also help to explain the transverse ridge features identified on 7 of the deposits (Figure 4.4). Equally, rock avalanches that runout over a shallower gradient subaerial path and/or onto steeper subaqueous slopes before the fjord

bottom appear to form more elongated deposits. The steep subaqueous slopes may have resulted in the moving rock avalanches to maintain their acceleration and momentum, thereby increasing their overall runout (Figure 4.6D), further elongating the deposits (Figure 4.6A). Morphological evidence of aligned blocks on RA2 indicates velocities in the direction of flow were greater than perpendicular flow velocities at the time of emplacement (Figure 4.4F) (Dufresne and Davies, 2009).

Additionally, STS rock avalanches moved from a subaerial to subaqueous environment. The change from surrounding medium of air to water had a control on emplacement, most likely a deceleration in the flowing mass. Reductions in the rock avalanche velocity upon entering the water is seen in the numerical modelling of RAs 2-5 (Figure 4.10). This is likely representative of the interaction of the rock avalanches with the water during subaqueous runout, which causes some landslide momentum transfer to the water (Mohammed and Fritz, 2012; Mulligan and Take, 2017). In addition, increased drag forces result from the increase in the surrounding medium density (due to moving through water compared to air) (Bregoli *et al.,* 2017). These factors result in greater resistance to landslide motion, prior to deposition. The deceleration likely also occurred in the runout and deposition of the other 11 rock avalanches.

Collectively, it appears many of these factors exhibit some control on the overall rock avalanche emplacement dynamics, which ultimately controls the final deposit geometries, runout distances, and subsequent mobility. The deposits in Milford Sound/Piopiotahi are geometrically similar to STS rock avalanche deposits identified in fjords across the globe (Blikra *et al.,* 2006; Bornhold *et al.,* 2007; Longva *et al.,* 2009). The Milford Sound/Piopiotahi deposits also exhibit low mobility (H/L_{max}) and comparatively short runout (L_{max}) for rock avalanches, but not too dissimilar for STS rock avalanches elsewhere (Figure 4.12). Therefore, many of the factors outlined affecting the rock avalanche emplacement and subsequent mobility in Milford Sound/Piopiotahi might also apply more generally for STS rock avalanches in fjords and is an area that requires further research.

One factor that may also exhibit a control on the rock avalanche runout is the substrate interaction between the flowing rock avalanche mass and fjord-bottom sediments. The evidence is too limited to make any conclusions on the substrate interaction, due to a lack of detailed SBP data across the deposits in the fjord. The only evidence of a possible concentric ridge is at the lateral margin of RA5 deposit (Figure 4.4A) which may indicate some basal substrate deformation and confinement was involved during the emplacement of RA5. basal deformation

features and processes have been identified in lakes and fjords impacted by rock avalanches and other granular landslides events elsewhere (Schnellmann *et al.,* 2005; Blikra *et al.,* 2006; Hilbe *et al.,* 2011; Van Daele *et al.,* 2013). This suggests that this may be a common feature of landslide impacts on basins. The lack of features may be a result of burial by post-event sedimentation (section 6.1.1), especially as rock avalanche material has been identified in the long-valley seismic profile that are not visible in the bathymetric data (Dykstra, 2012) (Figure 6.2). Therefore, more extensive SBP data are needed across the deposits in Milford Sound/Piopiotahi to fully investigate the role of substrate on STS rock avalanche emplacement here.

In addition to the morphometric and morphological analysis, 5 of the deposits (RAs 1 - 5) were back analysed with the numerical runout model DAN3D to provide first-order insights into their runout behaviours through time (Figure 4.8). Numerical modelling can also be used to understand the runout and emplacement behaviour of landslides, particularly in cases where direct observations are lacking (Pitman *et al.*, 2003; McDougall and Hungr, 2004; Kelfoun and Druitt, 2005; Kelfoun *et al.*, 2010; Sosio, Crosta and Hungr, 2012; Sosio, Crosta, Chen, *et al.*, 2012; Mergili *et al.*, 2017). The modelling produced reasonable simulations of the 5 STS rock avalanche runouts using two rheologies along the travel path, with a change at the present-day sea level (Figure 4.8, Table 4.8), and using parameter values within the range of those already published (Figure 4.13). This change in rheology could possibly be representative of simulating the phase change from subaerial to subaqueous runout environments. None of the best fit parameters for each respective modelled case simulated the runout of the other cases, most likely due to the variations in deposit volumes, morphologies, and geometries. However, the Voellmy rheology appears to be the most effective rheology in simulating the rock avalanche events in Milford Sound/Piopiotahi. Voellmy was employed in the subaqueous portion of runout in all 5 cases (Table 4.7). The two adjustable parameters of basal friction coefficient and turbulence in the Voellmy rheology give more control in replicating runout. The turbulence coefficient likely represents resistance to flow in the same way that the water would resist the flowing of the rock avalanche through increased drag and momentum transfer to the water on impact.

In the wider context, comparisons of impact velocity of the best fit results of each modelled rock avalanche (RAs 1-5) with its respective velocity previously estimated by Dykstra (2012), who employed an empirical equation of a rigid block model. The best fit simulations within this thesis show a reduced impact velocity in all cases (Table 6.2). Furthermore, the modelled rock

avalanches in *Chapter 4* represent the range of most estimated deposit volumes geometries, and apparent mobilities (Table 4.3, Table 4.4). It may be probable that the impact velocities of other deposits not modelled could be within the range of the velocities in Table 6.2. The numerical runout model simulations in *Chapter 4* show freely spreading, flow-like, behaviour during the runout. Whilst DAN3D can implement a rigid body component to simulate *en masse* sliding after failure is initiated (Aaron and Hungr, 2016b), none of the best fit simulations in *Chapter 4* employed the rigid body component. These findings further question the suitability of assuming a rigid block landslide. Given the similarities in deposit morphologies, geometries, and mobilities in Milford Sound/Piopiotahi to other STS rock avalanches in fjords across the globe, a Voellmy rheology could also be applied in numerical simulations whether it is a universal rheology for such landslides.

Table 6.2. Comparisons of velocity data derived from the runout modelling in *Chapter 4*, with initial analytical estimates from Dykstra (2012).

Rock avalanche				Velocity at sea level from best fit runout model (m s^{-1})	Dykstra (2012) estimated impact velocity at sea level (m s^{-1})
This thesis ID	Dykstra (2012) ID	Volume (x10^6 m^3)	Dykstra (2012) Volume (x10^6 m^3)		
RA1	SM17	3.1	3.0	24	49
RA2	SM3	8.1[1] (2.1)[2] (2.67)[3]	2.2	46	85
RA3	SM11	2.4	2.3	70	120
RA4	SM7	1.7	1.5	46	74
RA5	SM9	13.5	11	46	81

[1] model results support that the subaerial deposit in the Sinbad Gully, and subaqueous deposit from valley mouth most likely originated from the same event; [2] the volume of deposit material calculated from pre-and post-DEM analysis; [3] the volume of deposit that propagated into the fjord in the best fit model.

6.4. Geohazard implications

6.4.1. Landslide tsunami hazard and risk assessments

Potentially the biggest implication for the findings presented within this thesis is the potential for landslide-generated tsunamis (landslide-tsunamis) within the lakes and fjords of New Zealand. Landslide-tsunamis have been observed in 4 of the 15 lakes, and 2 of the 5 fjords across the North and South Island in *Chapter 3*, where known STS or subaqueous landsliding occurred. The lake and fjord tsunami record in New Zealand is limited due to the temporally short historical record (c. 180 years). Tsunamis may have occurred in the other lakes and fjords

where pre-historic landslides have been identified. Numerical models suggest that tsunamis were likely generated by the landslides identified in Lake Tekapo (Mountjoy *et al.*, 2019) (Figure 6.6).

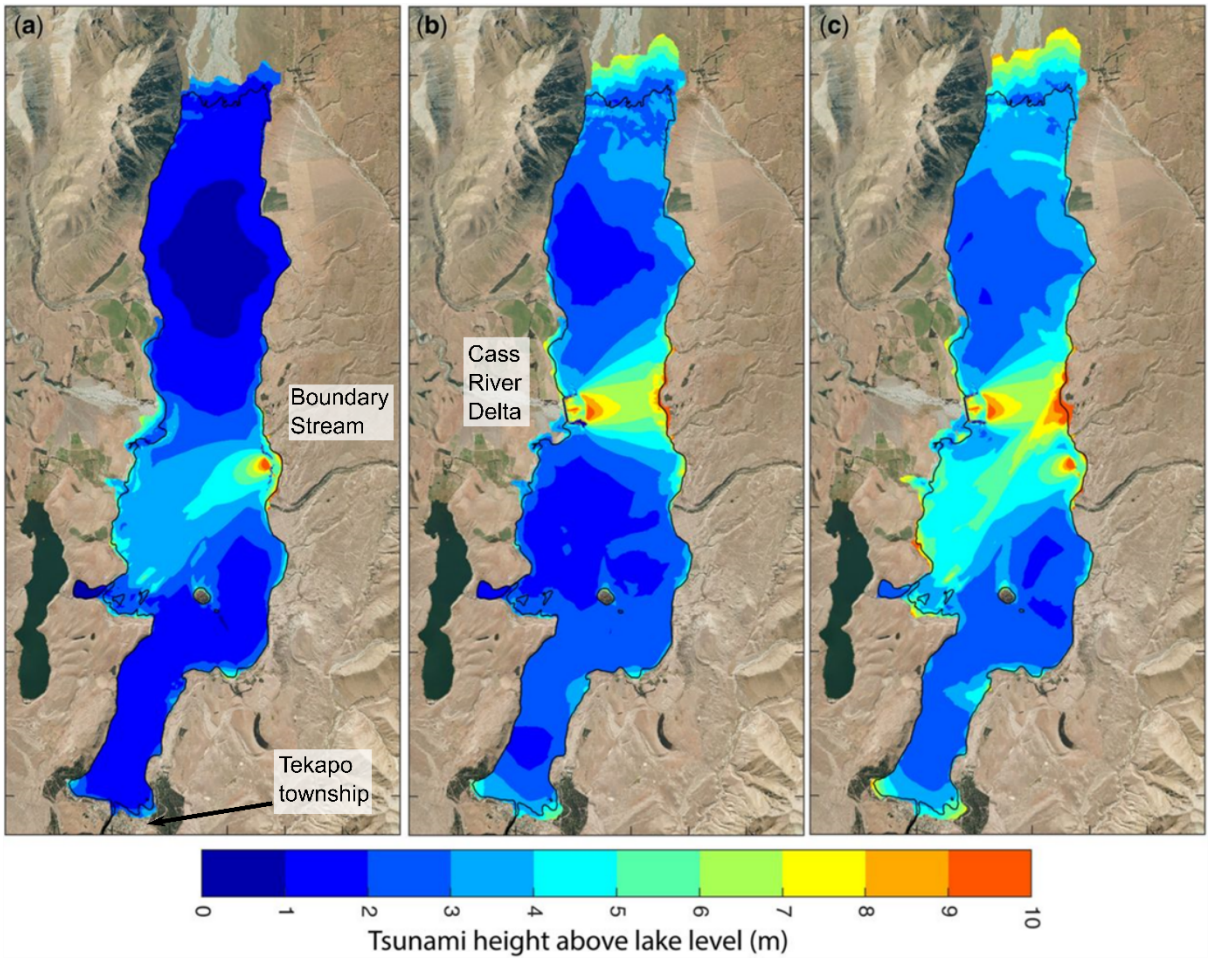

Figure 6.6. Probable tsunami wave heights on Lake Tekapo from a landslide at Boundary Stream (a); deltaic collapse of the Cass River Delta (b); and both landslides occurring concurrently (c). Township highlighted on (a) for context. Figure modified from Mountjoy et al., (2019).

The landslide-tsunami hazard within Milford Sound/Piopiotahi has initially been assessed by Dykstra (2012), and revised by Taig and McSaveney (2015). Both approaches used a series of analytical and empirical relationships to derive the dynamics of the rock avalanche deposits, and subsequent tsunami waves generated. However, the morphological and morphometric analysis and runout modelling results of *Chapter 4* highlights some critical disparities in the rock avalanche behaviour that may have significant implications for the tsunamis generated. Dykstra (2012) derived estimations of the impact velocity of each rock avalanche at the water level using the empirical equations established by Slingerland and Voight (1979). The equation is based on treating the landslide as an incompressible rigid block throughout runout and

deposition. However, the morphologies and geometries of deposits in Milford Sound/Piopiotahi are more representative of RSF (rock avalanche) deposits. Rigid block studies have been criticised for failing to replicate the morphology of deposits found in subaqueous environments elsewhere (Mohammed and Fritz, 2012).

Rock avalanche runout is analogous to granular flows (Legros, 2002; Davies and McSaveney, 2009). Physical modelling experiments of granular landslides indicate that landslides with a long subaerial travel distance develop into a long and thin deposit before impact with the water (Miller *et al.*, 2017). In those granular landslides, only a fraction of the landslide mass (the "effective mass") generates the tsunami (Miller *et al.*, 2017). Most of the STS deposits in Milford Sound/Piopiotahi occurred on slopes above 500 m (Dykstra, 2012), though some of the source areas extend to sea level (e.g. RA1, RA5). Therefore, some deposits may not have formed long, and thin deposits during runout before impacting the water. Physical modelling experiments indicate that the mobility of landslides affect the wave generation, with lower mobility landslides producing smaller waves in near field (Bullard *et al.*, 2019; Mulligan *et al.*, 2019).

The numerical modelling results provide velocity data throughout the rock avalanche emplacement. The numerically-modelled rock avalanches have similar volumes to those calculated by Dykstra (2012). The velocity of the landslide is a critical parameter in the generation of tsunamis (Panizzo *et al.*, 2005; Harbitz *et al.*, 2006; Bornhold and Thomson, 2012; Yavari-Ramshe and Ataie-Ashtiani, 2019). Given the velocities at sea level in the numerical runout models of *Chapter 4* are lower than those derived empirically by Dykstra (2012) (Table 6.2), the initial near-field wave amplitudes estimated by Dykstra (2012) may have been overestimated. Similar findings from other studies also found the use of rigid blocks have been found to overestimate the wave amplitudes generated (Fritz, 2002; Mohammed and Fritz, 2012; Yavari-Ramshe and Ataie-Ashtiani, 2016, 2019).

The new insights into the dynamics of the STS rock avalanches *Chapter 4* therefore indicates that a reassessment of tsunami wave amplitudes and subsequent runup at critical shorelines, such as Milford Sound Village, are needed. Such reassessments are beyond the scope of this thesis as tsunami generation and propagation is highly complex. As well as the velocity of the rock avalanche, the initial wave amplitude is also contingent on deposit volume, frontal geometry, and rock mass permeability (Harbitz *et al.*, 2006; Bornhold and Thomson, 2012; Løvholt *et al.*, 2015; Bregoli *et al.*, 2017; Evers *et al.*, 2019). The wavelength of leading wave

of a tsunami is also strongly dependent on the runout of the subaqueous portion of the landslide event (Fritz *et al.*, 2004). Whilst the numerical model results in *Chapter 4* have provided quantifiable information on many of these landslide parameters, estimating potential wave amplitudes is difficult with empirical relationships that are often based on laboratory experiments. As well as the landslide dynamics, the propagation, reflection, and attenuation of tsunami waves is also contingent on the subaerial topography, and bathymetry (Harbitz *et al.*, 2006, 2014; Løvholt *et al.*, 2015; Yavari-Ramshe and Ataie-Ashtiani, 2016). Therefore, numerical modelling of both landslides and tsunamis appear to be the way to define the characteristics and behaviour of the potential tsunami waves spatially (Tinti *et al.*, 2006; Giachetti *et al.*, 2011; Harbitz *et al.*, 2014; Yavari-Ramshe and Ataie-Ashtiani, 2016).

Numerical tsunami models could account for the complexity of the fjord topography and shallowing in the bathymetric data towards the Cleddau Delta. Numerical models may provide better estimations of wave heights and subsequent runup at Milford Sound Village, or indeed the lakeshore communities if applied in Lake Wānaka, which would aid tsunami hazard assessments. Furthermore, the landslide runout modelling of deposits within Milford Sound/Piopiotahi has provided quantifiable, time-step information of the rock avalanches. The modelling results provide initial boundary conditions, such as velocity, frontal thickness and deposit width, on which to numerically model tsunami wave generation and propagation (Heller and Hager, 2010; Mohammed and Fritz, 2012; Yavari-Ramshe and Ataie-Ashtiani, 2016, 2019; Mulligan *et al.*, 2019). A similar coupling approach has been done on two subaqueous landslide deposits in Lake Tekapo (Mountjoy *et al.*, 2019).

The newly identified STS RSF, and subaqueous landslide deposits within Lake Wānaka (*Chapter 5*) also emphasise the need for tsunami hazard assessment as the 5 deposits at the southern end of the Peninsula are in close proximity (< 2 km) from the populated lake shoreline. The larger deposits towards the southern end of Lake Wānaka may also facilitate detailed coupled numerical landslide, and tsunami modelling. Infilling the missing MBES BTM could further aid in more detailed modelling of tsunami wave propagation across the lake, as well as identify any (as yet) unknown deposits. The deltaic deposits identified in the northern region of the lake may have limited hazardous tsunami capabilities due to their relatively small sizes ($<10^4$ m^2), and further distance from the Wanaka township. However, with the available data, it cannot be ascertained whether larger-scale failures have occurred previously. Sub-bottom data over the fan deltas is limited as profiles were prioritised and collected at sites where onshore geomorphic evidence suggested that past landsliding had occurred (i.e. probable scars).

Future sub-bottom data collection should prioritise collection of detailed grids at the base of the mapped fan deltas.

One aspect that warrants consideration with the tsunami hazard assessment in the lakes and fjords is the effect on tsunami wave heights from concurrent landslides into, and/or within, the subaqueous basins. Coeval landslide deposits have been identified within lake basins globally, and are often indicators of a regional trigger such as an earthquake (Schnellmann *et al.*, 2002; Moernaut *et al.*, 2007; Upton and Osterberg, 2007; Strasser *et al.*, 2013; Van Daele *et al.*, 2015; Praet *et al.*, 2017). Furthermore, up to 40 coeval subaqueous lateral slope and deltaic landslide deposits, with combined volumes of $15\pm5 \times 10^7$ m^3, have been identified within SBP data from Lake Tekapo (Upton and Osterberg, 2007; Mountjoy *et al.*, 2019). These coeval failures have been attributed to coseismically generated by an earthquake on the Irishman Creek Fault (Upton and Osterberg, 2007). Numerical tsunami modelling in Lake Tekapo by Mountjoy et al. (2019) suggests an increased wave height in the far field can occur from concurrent landslides compared to isolated, single landslide occurrences (Figure 6.6).

The results from *Chapter 5* suggests earthquakes may be a likely trigger for some of the STS RSF as ~50% of the mapped subaerial RSF deposits in the Wanaka catchment extend to the upper 25% of ridge crests on the hillslopes (Figure 5.4), However, further work is needed to constrain the deposit ages within the lake, and to eliminate other possible triggers. There are insufficient data presented within this thesis to identify whether the few subaqueous landslide deposits identified within Lake Wānaka are coeval.

Estimated wave runup heights in the current tsunami hazard assessment for Milford Sound/Piopiotahi are also based on each past landslide propagating into the fjord occurring as an isolated event (Dykstra, 2012; Taig and McSaveney, 2015). However, absolute, and relative dating of subaerial rock avalanche deposits within the catchment by Dykstra (2012) appear to show age clustering of some of the deposits. The ages appear to correspond to independently dated palaeo-earthquakes on the Alpine Fault (Berryman, Cochran, *et al.*, 2012; Berryman, Cooper, *et al.*, 2012; Howarth *et al.*, 2018). Historical, large ($M_w \geq 7$) earthquakes in New Zealand have triggered multiple catastrophic RSFs such as rock avalanches (Parker *et al.*, 2015; Bainbridge, 2017). Due to the absence of dating of the deposits on the basin floor their ages remain unknown at present. It is perhaps not unreasonable however, to assume that at least some of the deposits visible in the MBES data of Milford Sound/Piopiotahi may have occurred concurrently. Therefore, any future revisions of the tsunami hazard should consider concurrent

landslides a possibility, though this may be difficult to resolve with analytical, and empirical relationships. This further emphasises the need to use numerical models to simulate possible tsunamis.

Much of the current work on landslide tsunami hazards in New Zealand has been contingent on identification and analysis of landslide deposits in MBES, and SBP datasets. Whilst such detailed studies are greatly beneficial in improving our understanding of both landslides, and possible tsunamis; acquisition surveys are both time intensive and expensive. Additionally, there are many lakes and fjords across the whole of New Zealand (Table 3.1), with some in hard to access locations. Therefore it may present a logistical challenge to collect high-resolution MBES and SBP data from all the subaqueous environments. A desk-based, probabilistic landslide tsunami hazard assessment may provide a first-order estimation, such as the workflow established by Strupler et al. (Strupler, Anselmetti, *et al.*, 2020; Strupler, Evers, *et al.*, 2020). The workflow methods can be readily applied using pre-existing datasets, including terrestrial and subaqueous DEMs, seismic hazard models, and with simple assumptions of subaqueous slope gradients and sediment thicknesses (Strupler, Anselmetti, *et al.*, 2020; Strupler, Evers, *et al.*, 2020).

Many of these datasets already exist for New Zealand, including the New Zealand Seismic Hazard Model (Stirling *et al.*, 2012), and low-resolution bathymetric DEMs from digitised bathymetric charts (James *et al.*, 2019; Sutherland, Carrivick, Shulmeister, *et al.*, 2019). Furthermore, subaqueous lateral slope gradients controlling the occurrence of non-deltaic subaqueous landslides in Lakes Wānaka and Tekapo appear in keeping with values derived globally (Praet *et al.*, 2017). A qualitative validation of such methods could be against the documented landslides within 15 lakes, and 5 fjords (inclusive of Lake Tekapo and Milford Sound/Piopiotahi), summarised in *Chapter 3* (Table 3.2, Figure 3.7), as well as the newly identified deposits in Lake Wānaka. Such assessments could identify further lakes to prioritise for future hydroacoustic and sedimentological studies. A similar, GIS-based approach has already been implemented in the Aoraki Mt. Cook region (Allen *et al.*, 2009), where apparently frequent, aseismic RSFs are occurring (McSaveney, 2002; Allen *et al.*, 2011; McSaveney *et al.*, 2015). Additionally, the region contains rapidly growing proglacial lakes (Robertson *et al.*, 2012; Purdie *et al.*, 2016), and where lake tsunamis have occurred more recently (McSaveney, 2002; Downes *et al.*, 2017).

6.4.2. Future landslides in the subaqueous environments

Landslide occurrence is the result of changing intrinsic and extrinsic, time-dependent and time-independent properties that eventually reduce slope stability to a point where it may lead to failure (McColl, 2015). Therefore, assessments of subaerial and subaqueous slope stability often require detailed, geotechnical information which is beyond the scope of this thesis. However, one of the initial motivations of this thesis was the potential for landslides into, and within, the lakes and fjords within the context of the next Alpine Fault earthquake. The Alpine Fault represents the greatest seismic hazard to the South Island due to its geologically short, and regular recurrence period (c. 300 years) (Cochran *et al.*, 2017; Howarth *et al.*, 2018), and potential to generate great ($M_w \geq 8$) earthquakes (Sutherland *et al.*, 2007; Berryman, Cochran, *et al.*, 2012; Howarth *et al.*, 2018).

The results from analysis of the landslide deposits within Lake Wānaka and its surrounding catchment in *Chapter 5*, suggest that whilst earthquakes may have been a trigger for some of the landslide events (Figure 5.4). However, based on reconstructed isoseismals from the most recent past ruptures along the Alpine Fault, it appears that the MMI experienced across the catchment is too low to have triggered subaerial and STS landslides (MM<9) (Figure 5.13). Such findings are in line with the existing coseismic subaerial landslide probability model, developed by Robinson *et al.,* (2016). The model provides a first-order estimation for landsliding into the lakes and fjords. The model suggests a low probability for subaerial landslides, and therefore landslides into the lakes, for most of the lakes in the eastern Southern Alps (including Lake Wānaka), and fjords (apart from Milford Sound/Piopiotahi) (Figure 6.7). However, without dating of the deposits, coseismic landsliding in the Wanaka catchment from an Alpine Fault earthquake cannot be ruled out. Subaerial earthquake-triggered landsliding appears more probable in lakes proximal to the Alpine Fault, such as Paringa, Ellery, Mapourika, Kaniere (Figure 3.7F) and Brunner. Dated subaqueous landslide deposits within lakes Ellery, Mapourika, Paringa and Kaniere correspond to known Alpine Fault ruptures extending back 2000 years (Howarth *et al.*, 2014, 2016, 2018, 2021).

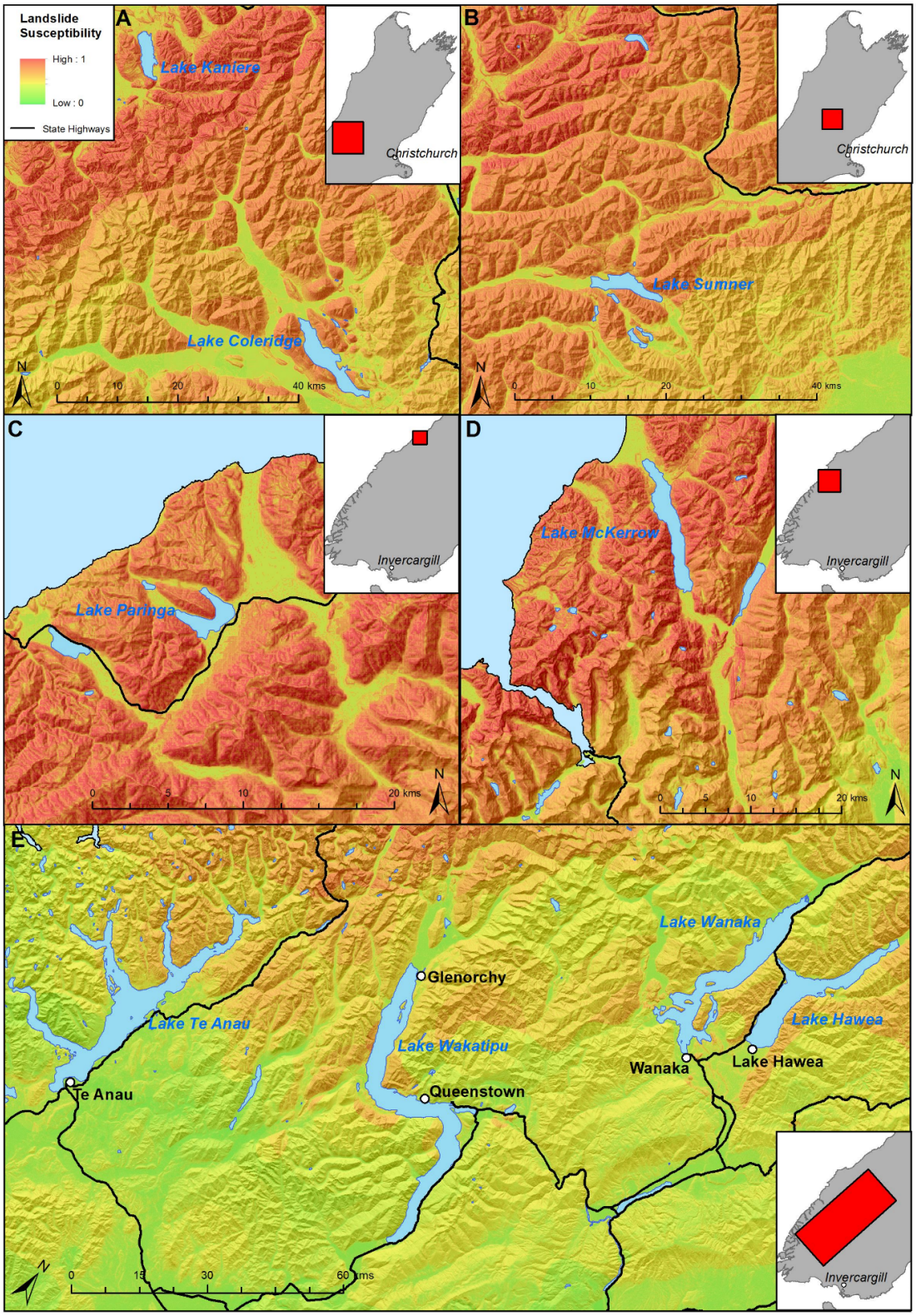

Figure 6.7. Coseismic landslide susceptibility from an M_w 8.0 Alpine Fault earthquake for A) Lake Coleridge and Lake Kaniere; B) Lake Sumner; C) Lake Paringa; D) Lake McKerrow and Milford Sound/Piopiotahi; and E) Lake Te Anau, Lake Wakatipu, Lake Wānaka, and Lake Hāwea. Figure modified from Robinson (2014).

The model by Robinson *et al.,* (2016) currently only assesses the subaerial landslide probability.

Assessment of the probability of subaqueous landslides is based on the shaking intensity

thresholds of MM≥6 (Howarth *et al.*, 2016). Modelled shaking intensities indicate shaking intensities may be sufficient to trigger subaqueous landslides at many of the lake basins (Figure 3.2). However, as identified in the hydroacoustic data of Lake Wānaka (*Chapter 5*) and suggested in the conceptual models above (6.2.2), the steep (>20°), non-deltaic, subaqueous lateral slopes may lack a sufficient drape of sediments, limiting the efficacy for lateral slope subaqueous landslides. Subaqueous landslide(s) may only occur on subaqueous fan deltas. In piedmont lakes, however, lateral slopes may facilitate sufficient sediment accumulation where noticeable landsliding could occur, as is noted in Lake Tekapo (Mountjoy *et al.*, 2019). Furthermore, initial dating of the most recent deposit within Lake Ōhau appears to correspond to the 1717 AD Alpine Fault earthquake (Fitzsimons and Howarth, 2018).

Many of the documented landslides into, and within, the lakes and fjords, where earthquake was the trigger (Table 3.2), occurred from earthquakes along more locally generated faults. No reported ages of subaqueous deposits in Lake Tekapo appear to correspond to known rupture events along the Alpine Fault (Upton and Osterberg, 2007; Mountjoy *et al.*, 2019). New age assessments of the deposits are currently under revision with newly collected cores (Mountjoy *et al.*, 2019). Current dated coeval deposits in Lake Tekapo have an age of 1720 ± 344 yr. BP, corresponding to inferred rupture ages on the local Irishman Creek Fault (Upton and Osterberg, 2007). However, many of these faults have a much longer recurrence interval (>10^3 years) than the Alpine Fault (Litchfield *et al.*, 2014; Langridge *et al.*, 2016). Additionally, the model of Robinson *et al.* (2016) is based on an assumed M_w 8.0 earthquake, with a southwest hypocentre, and north-east trending rupture directivity. Differences in hypocentres, earthquake magnitude will all affect shaking intensities across the South Island (Figure 3.2) (Bradley *et al.*, 2017). This, in turn, may affect where subaqueous, and subaerial, landslides are triggered. Therefore, the Alpine Fault still represents a significant seismic hazard to the Southern Alps, but an earthquake may not trigger many catastrophic landslides around many of the lakes farther from the fault. The earthquake could trigger subaqueous landslides but may be dependent on whether lake basins have sufficient conditions for subaqueous landsliding to occur.

6.5. Limitations and future research directions

Whilst this thesis has provided new insights into the distribution and dynamics of landslides within the lakes and fjords of New Zealand, there are several limitations and therefore key areas for future research that could build on the findings presented here. The recommendations are outlined below.

1. **Expansion of sub-bottom/seismic reflection data in the subaqueous environments**. The limited subsurface data resolved in Lake Wānaka due to the limited sub-bottom penetration is a limiting factor in assessing the magnitude and frequency of the deposits visible in the bathymetric data. It currently remains unknown whether there may be more deposits buried by post-event sedimentation. Similarly, whilst the available sub-bottom data in Milford Sound/Piopiotahi do indicate buried deposits, the limited spatial extent means that the size and spatial distribution of the buried deposits cannot be characterised. Therefore, it is currently unknown what the magnitude of deposits identified within MBES data relative to what may be buried within the subsurface. An expansion of both very high frequency (VHF (e.g. boomer)), and high-resolution deep penetrating (HRDP (e.g. sparker, airgun)) sub-bottom data could resolve the full postglacial sediment infill within these subaqueous environments. Additionally, these data could allow for a full magnitude-frequency assessment of landslide occurrences and associated deposits within the subaqueous environments since their formation after the LGM. Furthermore, dense grids could better resolve deposit thicknesses and volume. This would provide more quantifiable, independent data with which to assess the landslide runout models, as well as reduce the uncertainty in volumes derived from volume-area scaling relationships. Sub-bottom data could also serve useful in identifying locations with notable horizons or facies, such as buried landslides and/or turbidites, to prioritise for future core extractions.
2. **Lake and fjord coring to constrain subaqueous deposit ages.** The lack of age constraints on the subaqueous deposits in both Milford Sound/Piopiotahi and Lake Wānaka is a large limitation. Accurately dated deposits allows comparisons against other records of independently dated processes (e.g. tectonic, climatic, or glacial (McColl, 2020)). Cores could aid in establishing an absolute chronology using radiometric dating methods (^{137}Cs ^{210}Pb ^{14}C), and/or independent stratigraphic horizons such as tephra layers (Vandergoes *et al.*, 2018). Furthermore, the cores could be used to derive sedimentation rates from the basins. Sedimentation rates and independently dated samples could aid in establishing the ages of the subaqueous deposits. Core extraction may provide some insight into the sedimentology of stratigraphic layers and horizons which could subsequently aid sub-bottom facies interpretations, within the scope of the vertical error of the sub-bottom data. Cores may reveal impact of extrinsic forces, such as rainstorms and earthquakes, on the sedimentation and depositional processes into and within the subaqueous basin (Moernaut, 2020).

3. **Landslide-tsunami hazard assessments.** The numerical modelling within the thesis only analysed the landslide runout and did not account for the probable tsunami(s) that likely occurred during the propagation into the fjord. The numerical landslide modelling did however use a constant rheology of Voellmy to simulate the subaqueous portion of the landslide runout in Milford Sound/Piopiotahi. The landslide runout modelling results should be coupled with a landslide-tsunami model to Milford Sound/Piopiotahi and Lake Wānaka, where landslide deposits are identified within the bathymetry. Numerical models could establish possible runup heights and inundation zones at townships to aid with hazard planning of possible tsunami evacuation zones. Furthermore, establishing past inundation zones could suggest sites where possible tsunami deposits may be preserved onshore, which in turn, could aid in validating the tsunami models. For the lakes and fjords which lack detailed bathymetric data or evidence of past landsliding, a rapid, desk-based tsunami hazard assessment could be applied, as mentioned above (section 6.4.1). The results could serve to prioritise future field investigations.
4. **Acquisition of high-resolution MBES/bathymetric data from lakes and fjords.** The largest limitation in the inventory of lakes and fjords with landslides occurring into, and within is that 9 of the known lakes and fjords are compiled from observations of such events. This limits detection of older, pre-historic deposits, and the relative magnitude of these landslide events. MBES and high-resolution bathymetric datasets have been hugely beneficial in this thesis to identify previously unknown deposits in subaqueous environments, such as those identified in Lake Wānaka. However, the bathymetric data are incomplete, and therefore completing the BTM could address uncertainty over any potential deposits purely missed from lack of data acquisition. The high-resolution MBES data from Milford Sound/Piopiotahi has allowed detailed analysis of the well-preserved surface morphology of the deposits on the basin floor. This has provided insights into the emplacement dynamics of STS rock avalanches, of which there are limited studies globally. Other MBES surveys within other lakes and fjords could aid in identifying other unknown deposits and allow for comparisons between basins. For example, the recent acquisition of bathymetric data from Lake Wakatipu by NIWA in 2019 (NIWA, 2019) could serve as a complimentary dataset on which to compare the results from Lake Wānaka in *Chapter 5*. Lake Wakatipu and its surrounding catchment is similar in relief to Lake Wānaka; both catchments have a similar catchment geology (Turnbull, 2000), both lake basins were extensively glaciated during the LGM, and there

are known postglacial, catastrophic RSF deposits within the terrestrial catchment (McColl and Davies, 2011; McColl *et al.*, 2019). Recent MBES data have also been collected in several of the fjords by LINZ in 2019-2020 (LINZ, 2020). These datasets could also compliment the results of Milford Sound/Piopiotahi. Furthermore, comparisons with existing MBES datasets previously collected by NIWA and LINZ could provide a regional comparison of any landslides within the fjords. This could aid in assessing the conceptual model posited for the distribution of deposits within the fjords (6.2.2).

5. **Active and passive hillslope monitoring for potential future failures around lakes and fjords.** As part of future site risk assessments around lakes and fjords, identifying, and monitoring possible hillslope displacement could aid in assessing any potential future landslides into the subaqueous environments. Such methods for monitoring could be by in-situ instrumentation that could provide near real-time data on slope movement. Other methods could include analysis of archives of freely available, satellite-based interferometric synthetic aperture radar (InSAR) datasets. InSAR datasets could show slope movements over a longer-timeframe, and particularly where rates of slope movement are smaller than is detectable in aerial, and satellite imagery. Satellite-based InSAR data could provide a New Zealand-wide analysis like the approach adopted in Norway (https://insar.ngu.no/). Such approaches could be particularly useful for the steep fjord walls, where in-situ monitoring and instrumentation may be more difficult to install.

Chapter 7. Conclusions

This chapter returns to the aim and objectives outlined in *Chapter 1*. The overarching aim of this thesis is to better understand the distribution and dynamics of landslides within lakes and fjords in New Zealand, to improve the understanding of the hazard. Investigating the landslide distribution in lakes and fjords was to establish whether subaqueous environments may contain an archive of deposits that would be otherwise lost in a subaerial environment, thereby obscuring the overall magnitude-frequency distribution of such events. This, in conjunction with investigating the dynamic behaviour of the landslides are to better understand the hazard. A series of objectives were set out in *Chapter 1* to address the overall thesis aim. The conclusions are presented in the context of those objectives below.

Objective 1. To establish an inventory of known occurrences where landslides into, and within, lakes and fjords have been documented in New Zealand, to understand potential controls and triggers.

Based on a systematic review of the existing literature, this thesis has presented the first New Zealand-wide inventory of lakes and fjords with occurrences of landslide occurrences into, and within, the basins. In total, and prior to the results of *Chapter 5*, 15 lakes and 5 fjords have recorded evidence of past landsliding. The inventory has highlighted the type(s) of deposits within these basins including STS landslides ($n=7$), deltaic collapses ($n=4$), and undefined MTDs, most likely from subaqueous lateral slope failures ($n=7$). In Milford Sound/Piopiotahi and Lake Tekapo, multiple deposit types are identifiable (STS and deltaic landslides in Milford Sound/Piopiotahi; lateral slope and deltaic landslides in Lake Tekapo). From the known landslide occurrences, earthquakes are the primary trigger ($n=9$), or inferred trigger ($n=5$), with storms the trigger in possibly 2 cases. However, there are currently no known triggers or controls for 7 of the lakes and fjords. Many of these identified landslide cases are single, isolated events that preclude understanding any controls on the occurrence. Observations of landslide and/or resultant landslide-tsunami is the predominant identification method ($n=9$) in the inventory. This record is temporally restricted to the historical and observational record, which in New Zealand is comparatively short (c. 180 years). Hydroacoustic data (MBES and/or SBP) identified deposits in 6 of the basins, whilst coring campaigns identified a further 5 lakes with deposits. The hydroacoustic and core data also aided in established triggers, highlighting the value of conducting these investigations within New Zealand lakes and fjords.

Objective 2. To characterise the morphology and morphometry of previously identified landslide deposits in a subaqueous environment to gain insight into their emplacement dynamics.

Morphological and morphometric analyses as conducted on previously identified STS rock avalanche deposits in Milford Sound/Piopiotahi (*Chapter 4*). Remapping of the deposits in this thesis revised the total number of rock avalanche deposits to 16, down from 22 that were previously identified. The revision in this thesis suggests some deposits are more likely subaqueous fans, or non-rock avalanche STS failures. The morphological and morphometric analyses indicates that, despite a relatively uniform geology, tectonic, and glacial history, the rock avalanche deposits vary in volume ($2.9x10^5$ – $1.7x10^7$ m^3), runout (315 m (RA9) – 3495 m (RA2)), geometries (conically-shaped, proximally thick, and thinning distally vs irregular, elongated deposits with variable thicknesses independent from distance from the source), and mobilities (H/L_{max} = 0.46 – 0.89). Diagnostic morphological features such as transverse ridges, concentric rings, aligned blocks, outrunner blocks, and a blocky carapace are also identifiable on some deposits. The morphologies and morphometries provide insight into the emplacement dynamics of the deposits. The factors that have been suggested in this thesis as affecting the rock avalanche emplacement dynamics are related to the lack of topographic confinement, together with runout down the steeper subaerial fjord walls onto the flatter fjord bottom. This sudden change in angle likely dissipates energy at the front of the rock avalanche, slowing the leading edge of the deposit faster than the rest of the flow. This results in proximally thick, more lobate deposits that spread both laterally as well as forward. Conversely, rock avalanches that runout over a shallower gradient subaerial path onto steeper fjord bottom appear to form more elongated deposits.

Additionally, rock avalanches moving from a subaerial to subaqueous environment exhibit deceleration as momentum is transferred to the water body, which also causes a drag on the flowing landslide mass. These factors control the overall runout length and the mobility of the deposits, which are towards the low end of traditional metric to assess apparent rock avalanche mobility (H/L_{max}). However, such values are not too dissimilar to other studied STS rock avalanches globally, suggesting that similar factors may have occurred in those cases. Interaction of the rock avalanches with fjord-bottom sediments may also contribute to their overall runout and mobility through basal deformation and confinement. However, the evidence is too limited to investigate this fully.

Objective 3. To numerically model the runout of landslide deposits in subaqueous environments to investigate whether the modelling can also provide information on the landslide emplacement dynamics.

Using the numerical model DAN3D, the work in this thesis was able to produce reasonable simulations of all 5 of the modelled rock avalanches (RA1-5) from Milford Sound/Piopiotahi (*Chapter 4*). No model produced entirely perfect simulations of the modelled rock avalanches, but due to the uncertainty in both the mapped deposits, and assumptions in the pre-event topography, the simulated rock avalanches can be considered reasonable first-order results. The best fit modelled results were achieved with only a single rheology change at the present-day sea level. No single rheological parameters could replicate the runout and emplacement of all 5 deposits, but that is more likely due to the morphological and geometrical variability of the modelled cases. The modelled results do, however, show consistency with the basal rheology, especially in the subaqueous component of runout. All 5 of the best fit scenarios employed a Voellmy rheology (μ = 0.1-0.57, ξ = 50-100 m s^{-2} for RA1-RA5 in the subaqueous portion of the runout). Voellmy appears to be effective as the turbulence parameter is a velocity-limiting term that provides resistance to flow beyond the basal friction. The turbulence parameter limits the velocity of the rock avalanche motion in a manner that could be considered analogous to water increasing drag and buoyancy during subaqueous runout. A reduction in the turbulence value was found between the models that used Voellmy for the subaerial runout portion (RA1-3, 5), whilst the subaqueous Voellmy parameters of RA4 are consistent with the other modelled cases. The consistency in Voellmy rheologies and calibrated parameters established here could provide first-order predictions in future modelling/forecasting the runout of potential future failures into Milford Sound/Piopiotahi if sites of instability are identified. A Voellmy rheology could also be applied to other STS rock avalanches in fjords across the globe to establish whether it is a universal rheology for such landslides.

The modelling results presented in this thesis provide evolving time step simulations of flow-like landslide runout. Such information is lacking with traditional landslide empirical equations that do not reflect the observed landslide behaviour/deposit. The models also provide information on key landslide dynamics such as velocity and flow depths. These parameters could be coupled with numerical tsunami models to estimate initial wave heights with landslide impact, as tsunami inundation may be a more significant hazard to the shoreline infrastructures at Milford Sound Village. Numerically modelling the landslides is therefore a better approach

to establish key landslide dynamics, and to provide input data that can be coupled with landslide-tsunami models.

Objective 5. To collect high-resolution bathymetric data of a lake to generate a high-resolution bathymetric terrain model (BTM) to assist identification of landslide deposits on the lakebed.

PDBS data were collected in Lake Wānaka as part of the work in *Chapter 5*. The PDBS data were used to produce a high-resolution 2 m BTM of parts of the lakebed. A full bathymetric survey over the lake was not undertaken due to limited time constraints and inclement weather conditions. 17 new, previously unknown landslide deposits were identified in the available bathymetric data of the lakebed. The deposits are identifiable by a positive bathymetric expression. The deposits include STS landslides (*n=6*, both catastrophic RSFs and possible large debris flows), and deltaic (*n=9*) and non-deltaic (*n=2*) subaqueous landslides. The total number of deposits within the lake is relatively few compared to the subaerial catchment, where *n=202* subaerial RSF deposits were mapped in this thesis. Divergence from the power law in the frequency distribution of deposits suggests the landslide inventory is incomplete. Eight probable subaerial scars were identified around the lake, and 2 subaqueous scars were identified. The BTM data over the lake floor are available in the likely runout zones of these events, but no deposits are identified, suggesting that deposits are either buried deep within the subsurface, or have possibly been eroded by other processes such as supraglacial deposition and transportation, or glacial erosion. Additionally, scars were located along subaqueous fan deltas, but due to the incomplete BTM, no deposits could be identified as the runout and depositional zones were not captured.

Objective 6. To collect sub-bottom profiler data to detect potential landslide deposits buried within the sedimentary infill.

In the study of Lake Wānaka (*Chapter 5*), high-frequency sub-bottom profile (chirp) data were collected in conjunction with the bathymetric data. Many of the chirp lines extended beyond the BTM extent to identify any deposits that may have just been missed because of the incomplete PDBS coverage. However, limited subsurface penetration in most of the collected lines limited the ability to identify (m)any deposits. The only deposits identified in the sub-bottom data are linked to those with positive bathymetric expressions. In lines where sub-bottom penetration was achieved no deposits could be identified. This included at sites where probable subaerial and subaqueous scars are visible. However, the typical sub-bottom penetration, where possible, was between 20 – 35 m, but a maximum isolated subsurface

reflector was detected at 115 m below the lakebed. Therefore it remains unknown whether there are landslides buried within the sedimentary infill but buried at depths beyond the capabilities of the chirp system used in this thesis.

Overall, the findings within this thesis suggest that landslides are likely within lakes and fjords, but that their occurrence may be dependent on external triggers, particularly earthquakes. Furthermore, more landslides may be contained within Milford Sound/Piopiotahi, Lake Wānaka, and indeed many of the other lakes across the Southern Alps, but their identification in hydroacoustic data is contingent on resolving the subsurface. High sedimentation rates in the Southern Alps lakes may result in rapid burial of deposits on the lakebed, meaning that the deposits may not be visible in MBES data, but should be detectable in SBP data, particularly HRDP systems, where a subsurface penetration should be greater than VHF systems. In contrast, the fjords experience comparatively lower modern rates of sedimentation, meaning that deposits are buried more slowly. Therefore deposits may exhibit a bathymetric expression for comparatively longer. Deposits may still be buried in these systems but would require either phases of more rapid sedimentation rates, or a longer time.

The hydroacoustic data can also reveal insights into the dynamic behaviour of landslides, particularly STS rock avalanches in these settings. Where deposits are visible, however, detailed insights into their emplacement can be conducted, and numerical modelling with existing models rheologies can provide first-order information on STS landslides, which until now, had been largely neglected in landslide modelling. The models also provide critical information on flow velocities and flow depths. This work, in conjunction with the relative magnitude-frequency distribution of deposits, is critical in the assessment both of future landslides into and within these environments, but also for possible tsunamis.

Appendix A. Morphology of Milford Sound/Piopiotahi STS rock avalanche deposits

The following figures are the STS deposits from Milford Sound/Piopiotahi. The figures show each deposit with the mapped source area, an uninterpreted and/or morphologically interpreted deposit, and 3D perspective views of each deposit (with 1.5 x vertical exaggeration).

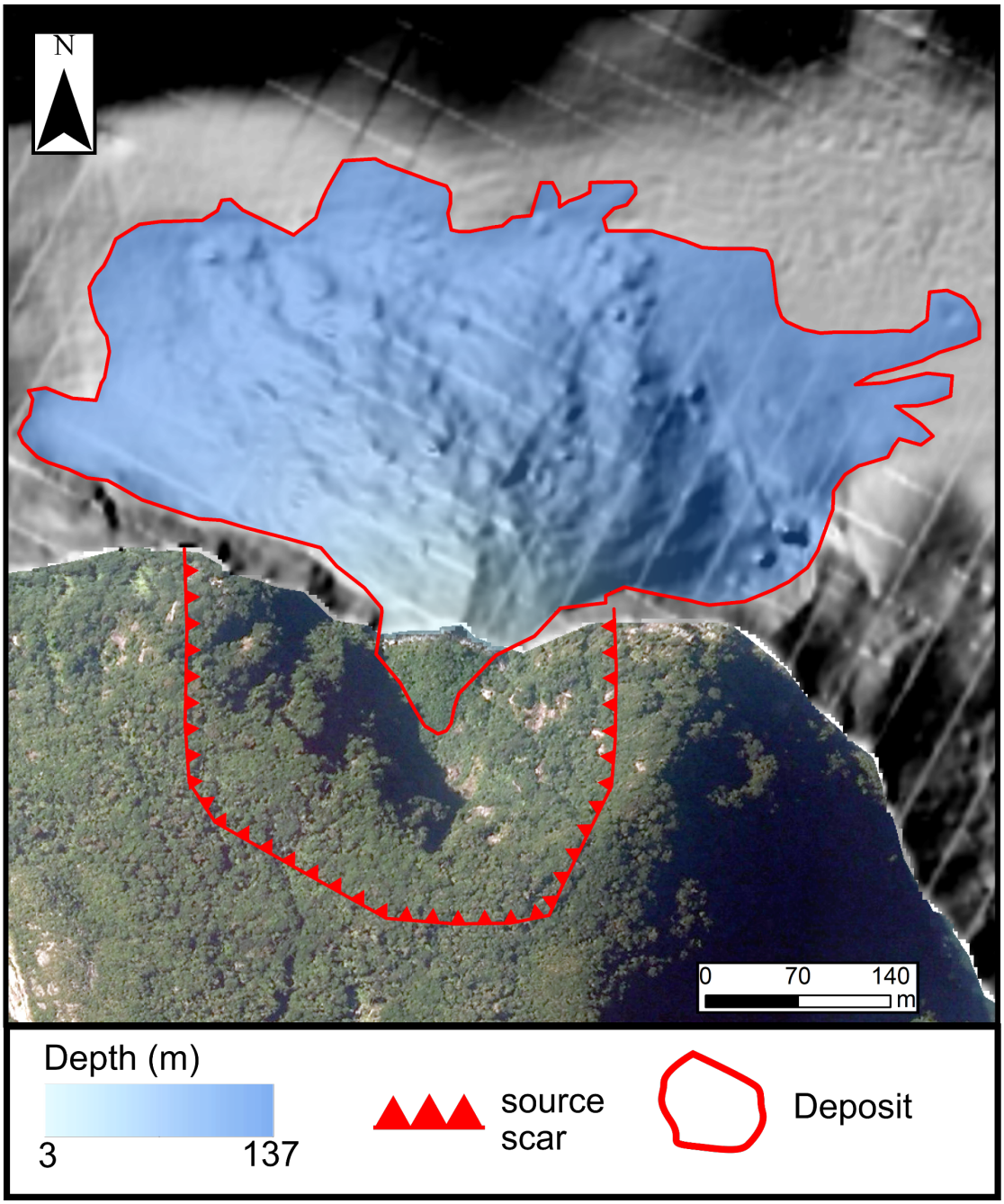

Figure A.1. RA1 subaqueous deposit and source scar area. Imagery available under Creative Commons 4.0. Copyright is owned by The Southland Consortium (Southland District Council, Gore District Council, Environment Southland, and Department of Conservation).

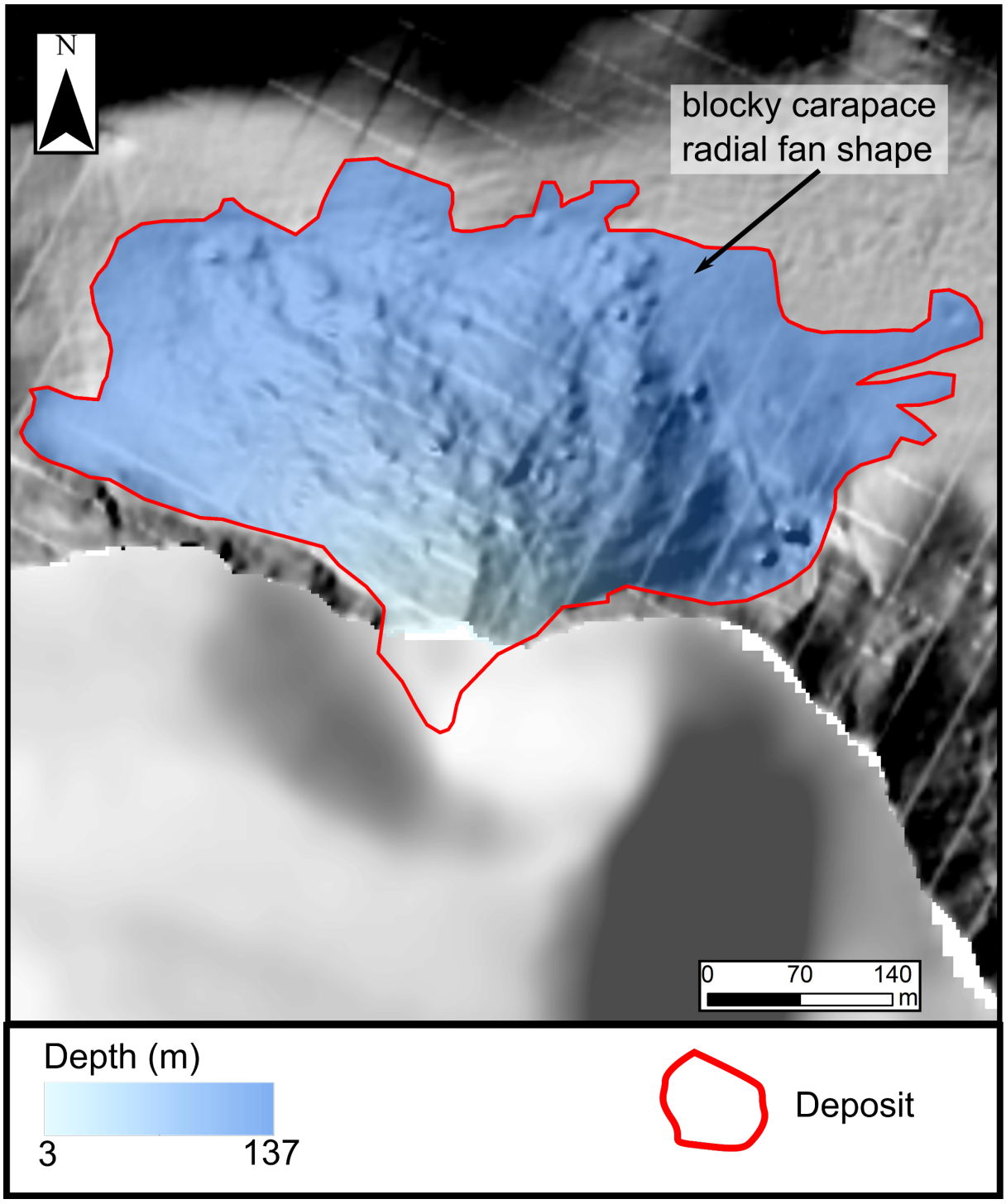

Figure A.2. Morphology of RA1 deposit, showing the radial fan shape, and lack of features beyond the blocky carapace.

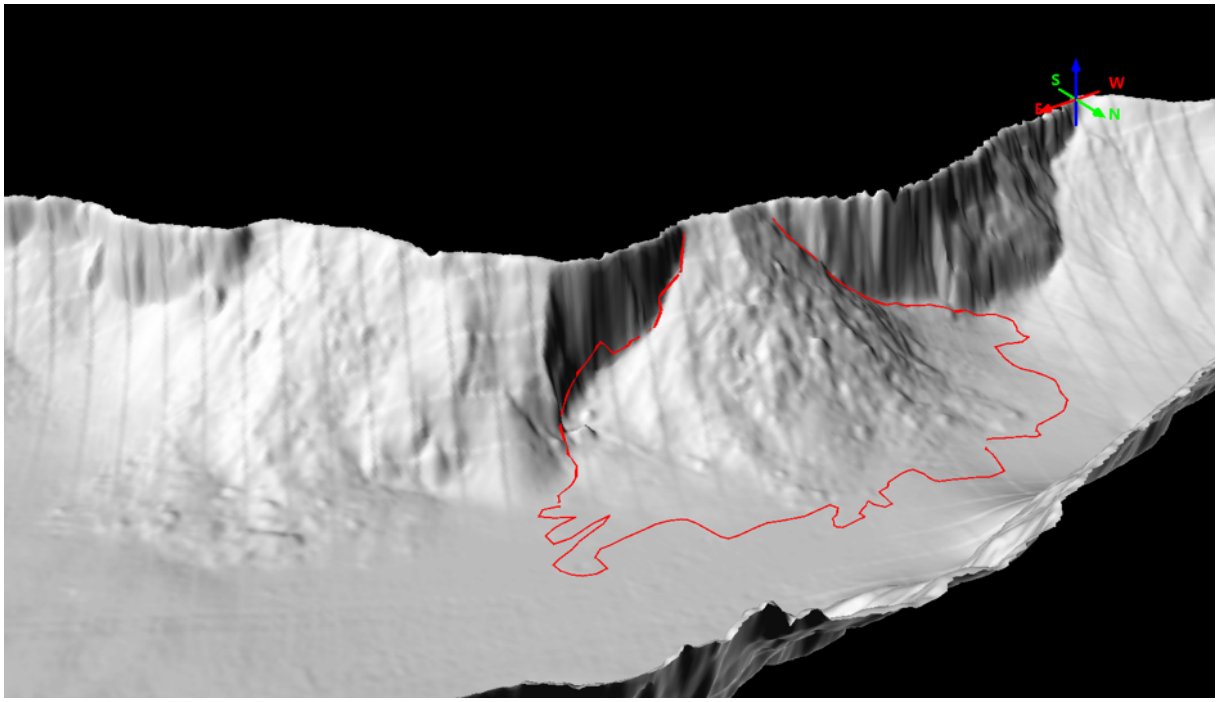

Figure A.3. 3D perspective view of RA1 subaqueous deposit with 1.5x vertical exaggeration.

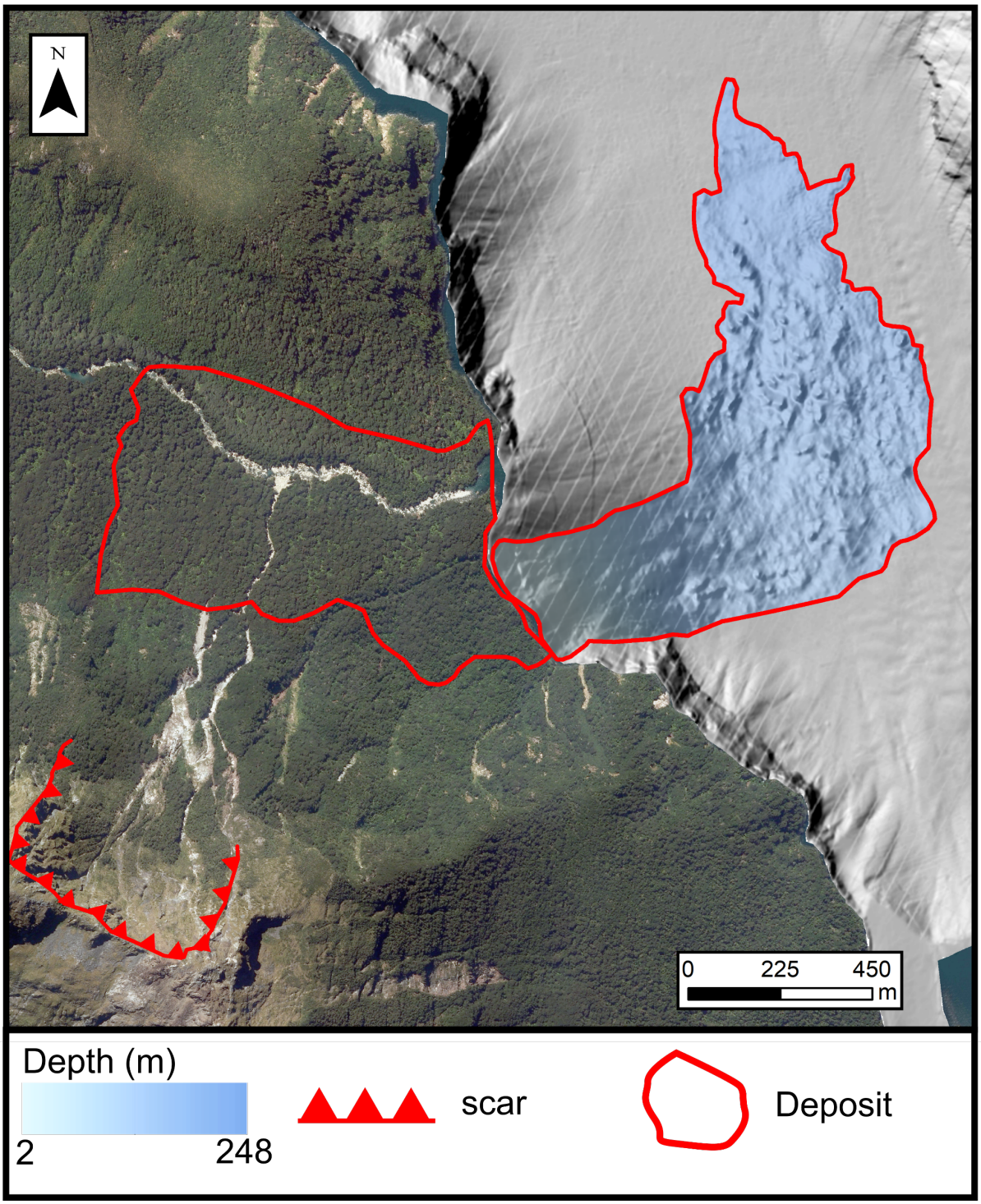

Figure A.4. RA2 subaerial and subaqueous deposit and source scar area. Imagery available under Creative Commons 4.0. Copyright is owned by The Southland Consortium (Southland District Council, Gore District Council, Environment Southland, and Department of Conservation).

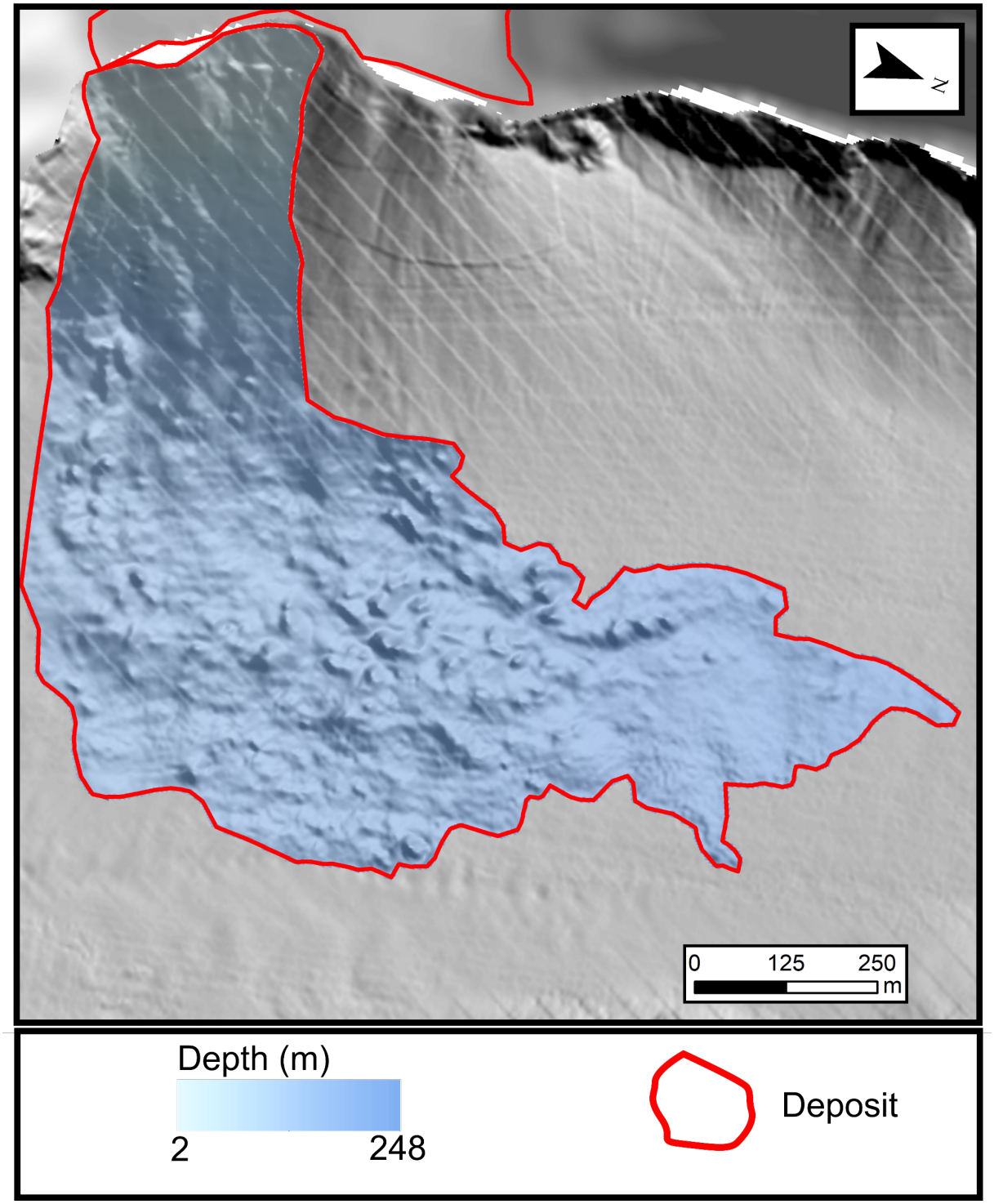

Figure A.5. Detailed, uninterpreted morphology of RA2 subaqueous deposit.

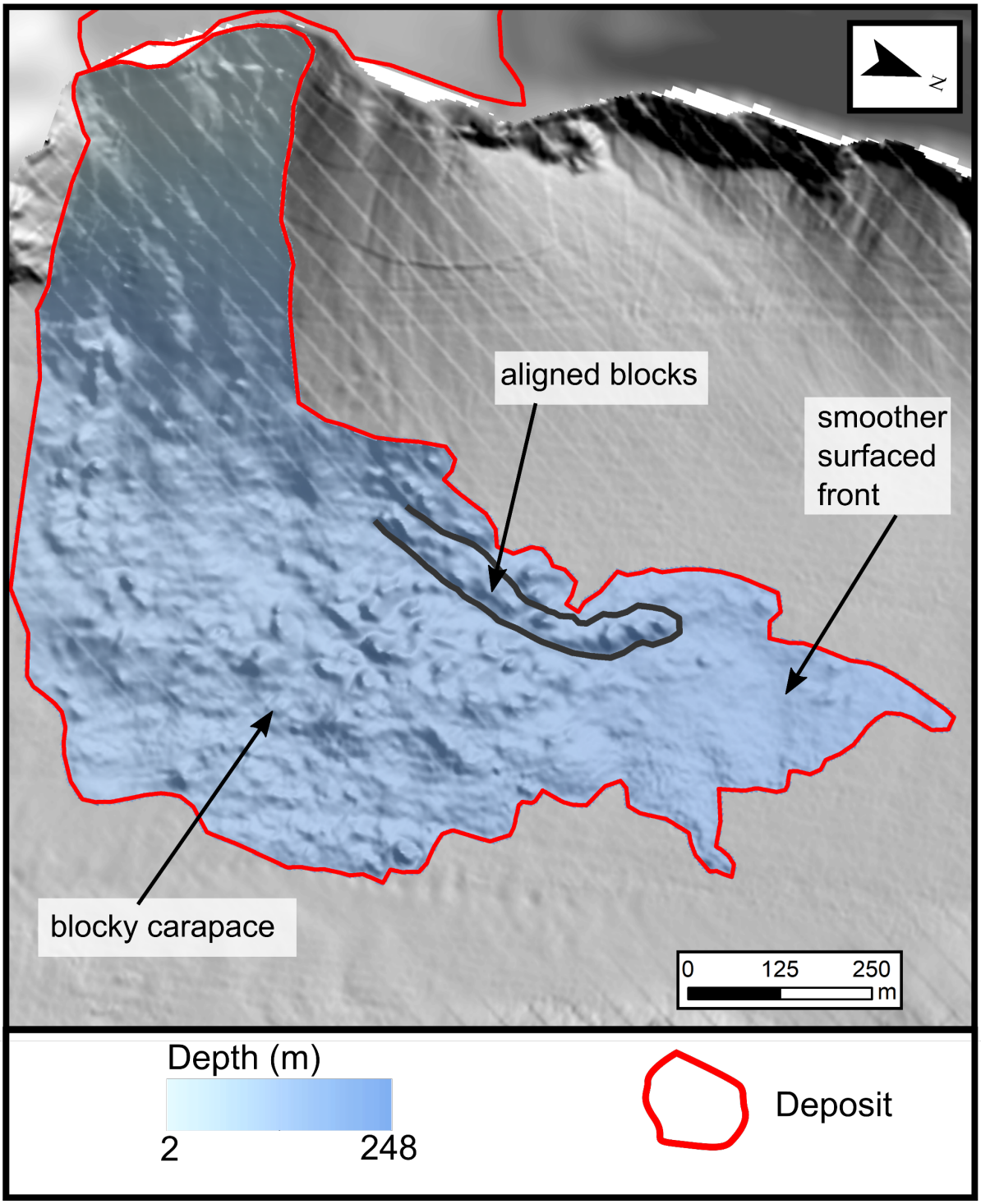

Figure A.6. Interpreted morphology of RA2 subaqueous deposit.

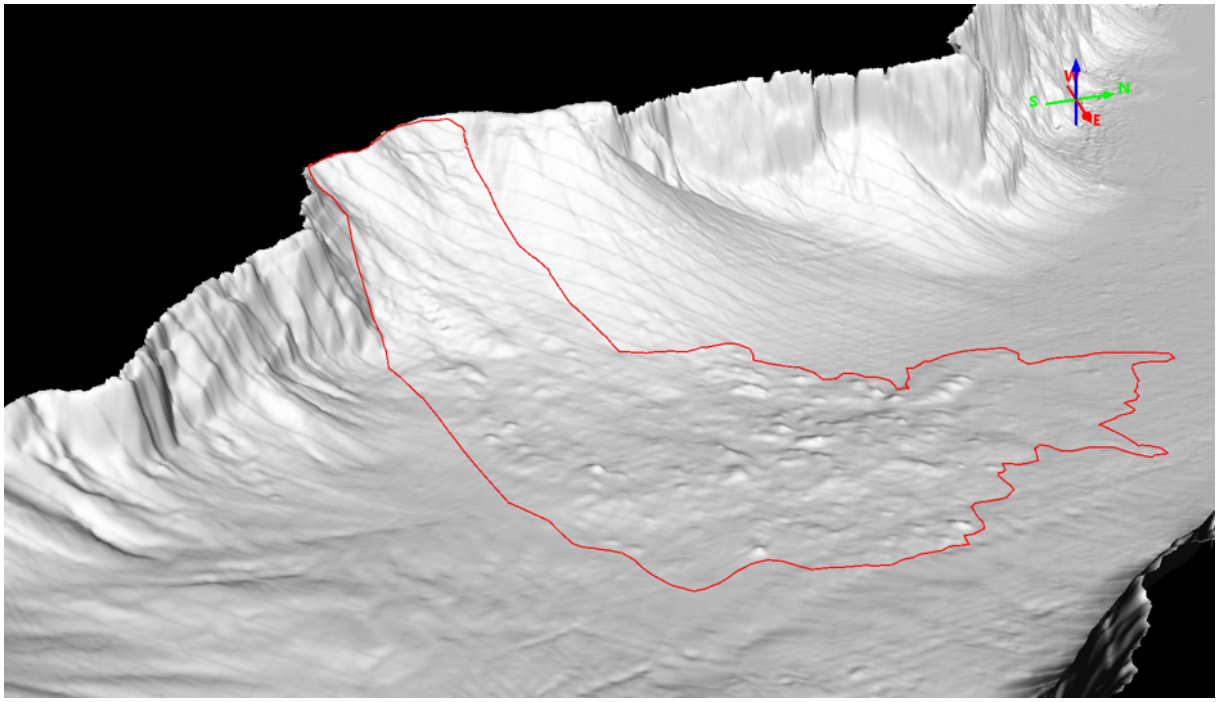

Figure A.7. 3D perspective view of RA2 subaqueous deposit with 1.5x vertical exaggeration.

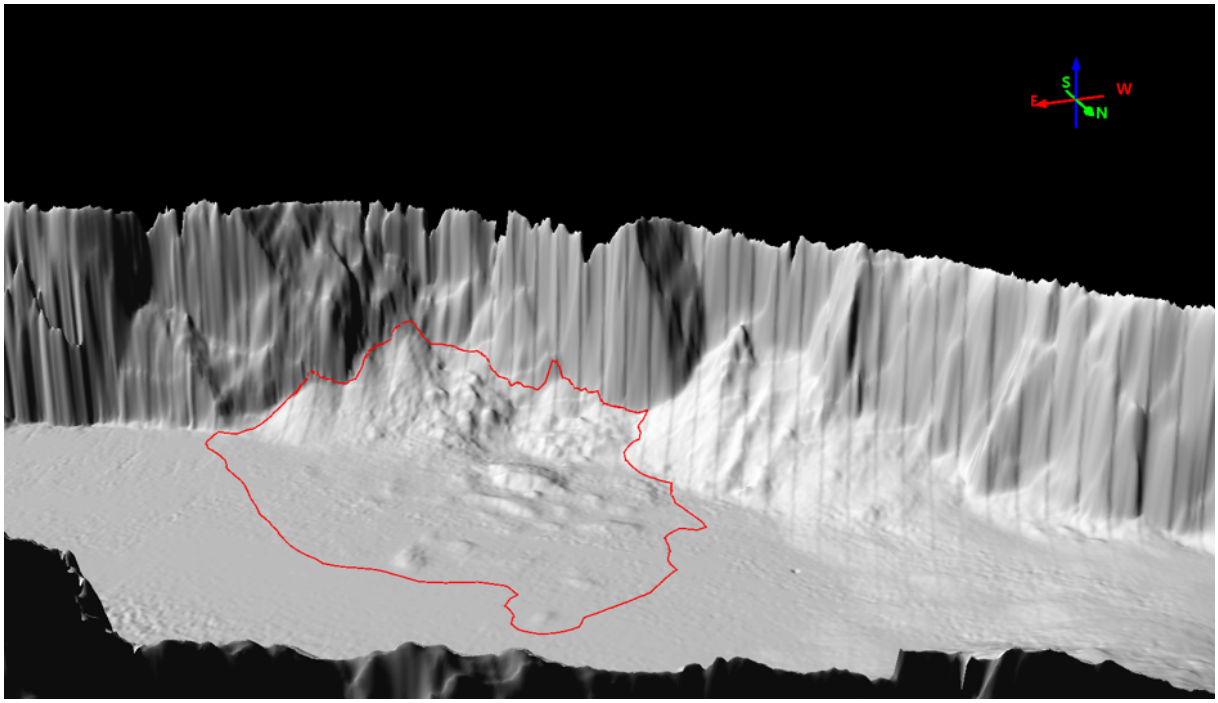

Figure A.8. 3D perspective view of RA3 subaqueous deposit with 1.5x vertical exaggeration.

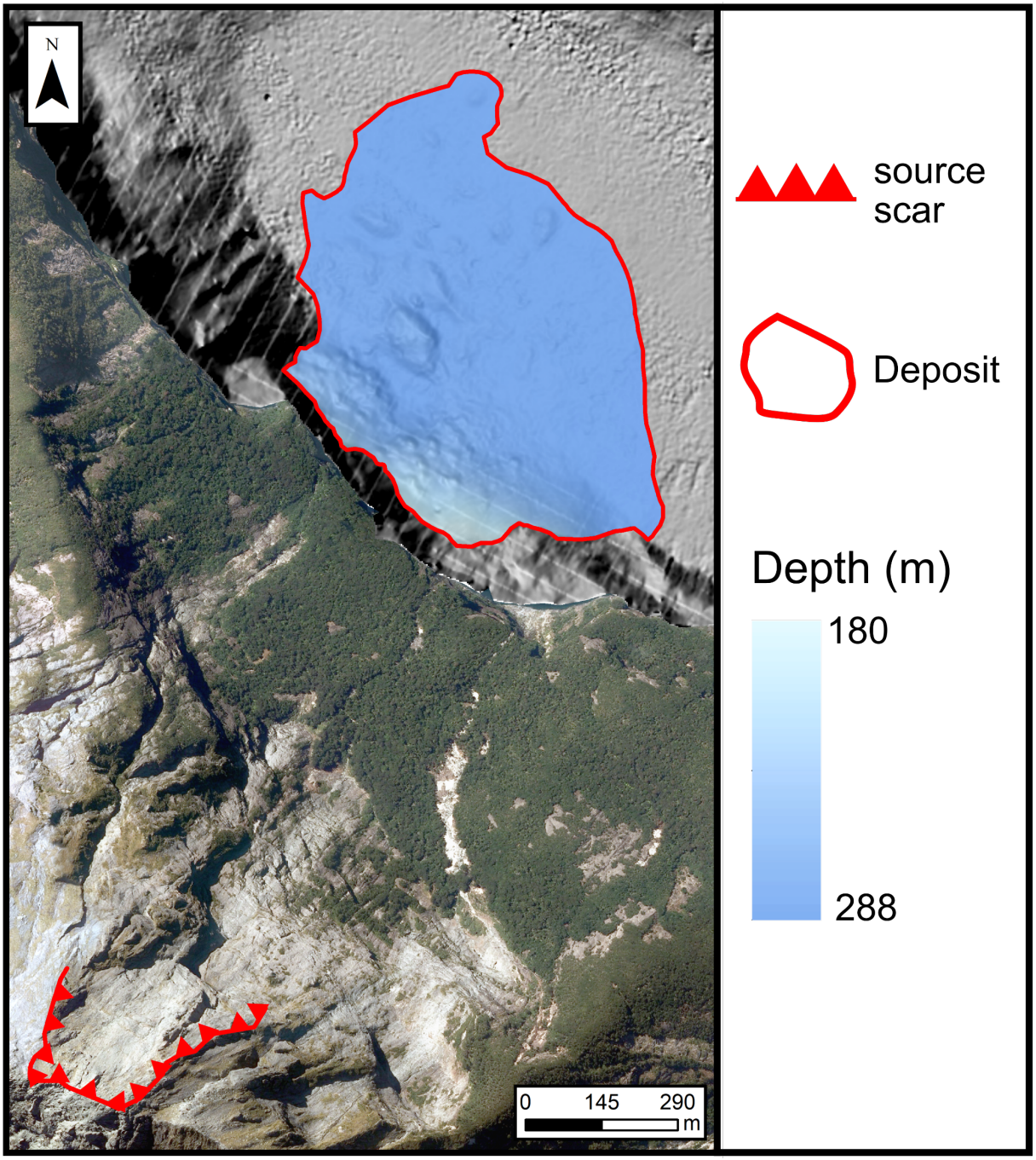

Figure A.9. RA3 subaqueous deposit and source scar area. Imagery available under Creative Commons 4.0. Copyright is owned by The Southland Consortium (Southland District Council, Gore District Council, Environment Southland, and Department of Conservation).

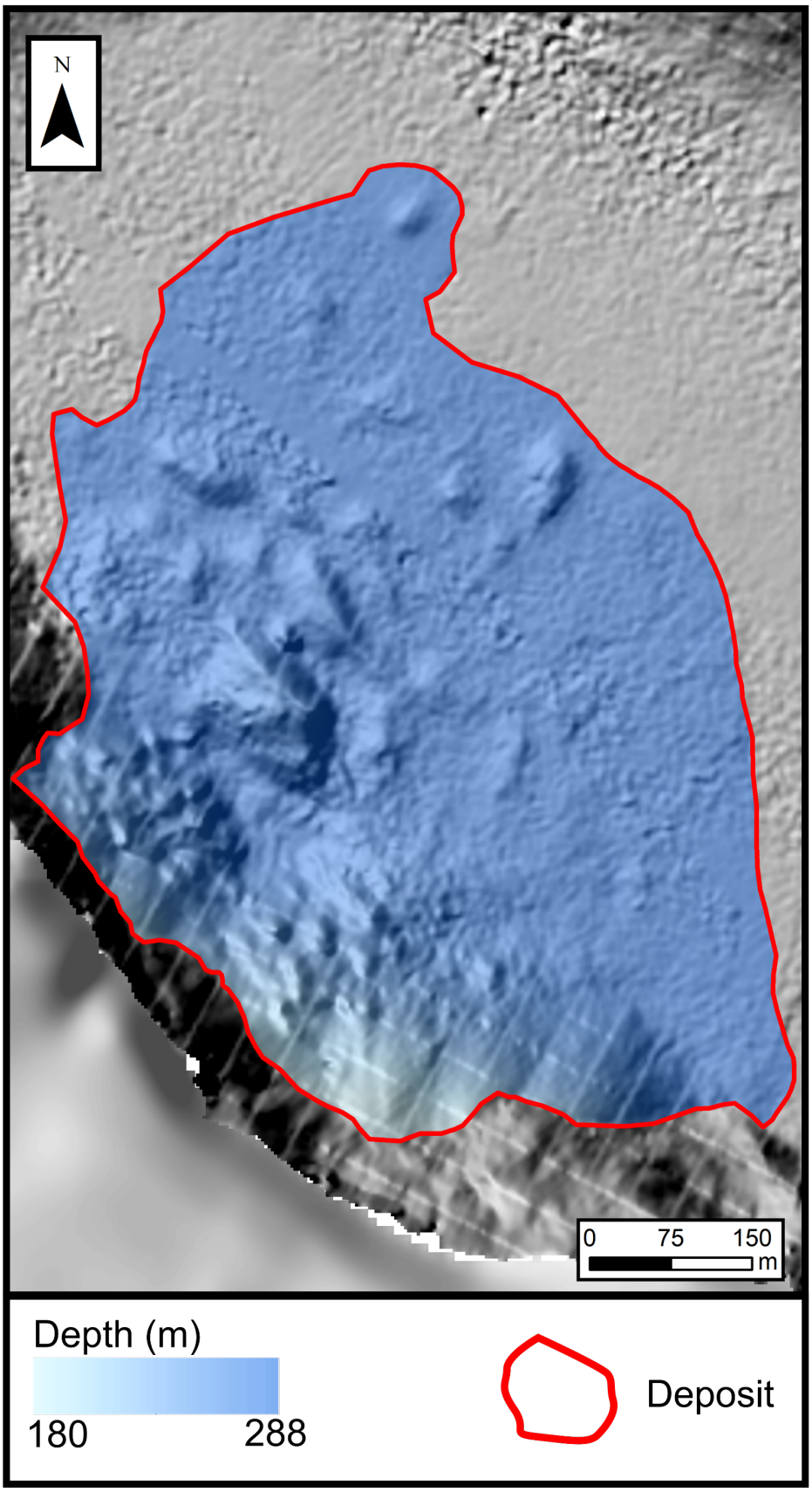

Figure A.10. Detailed, uninterpreted morphology of RA3 subaqueous deposit.

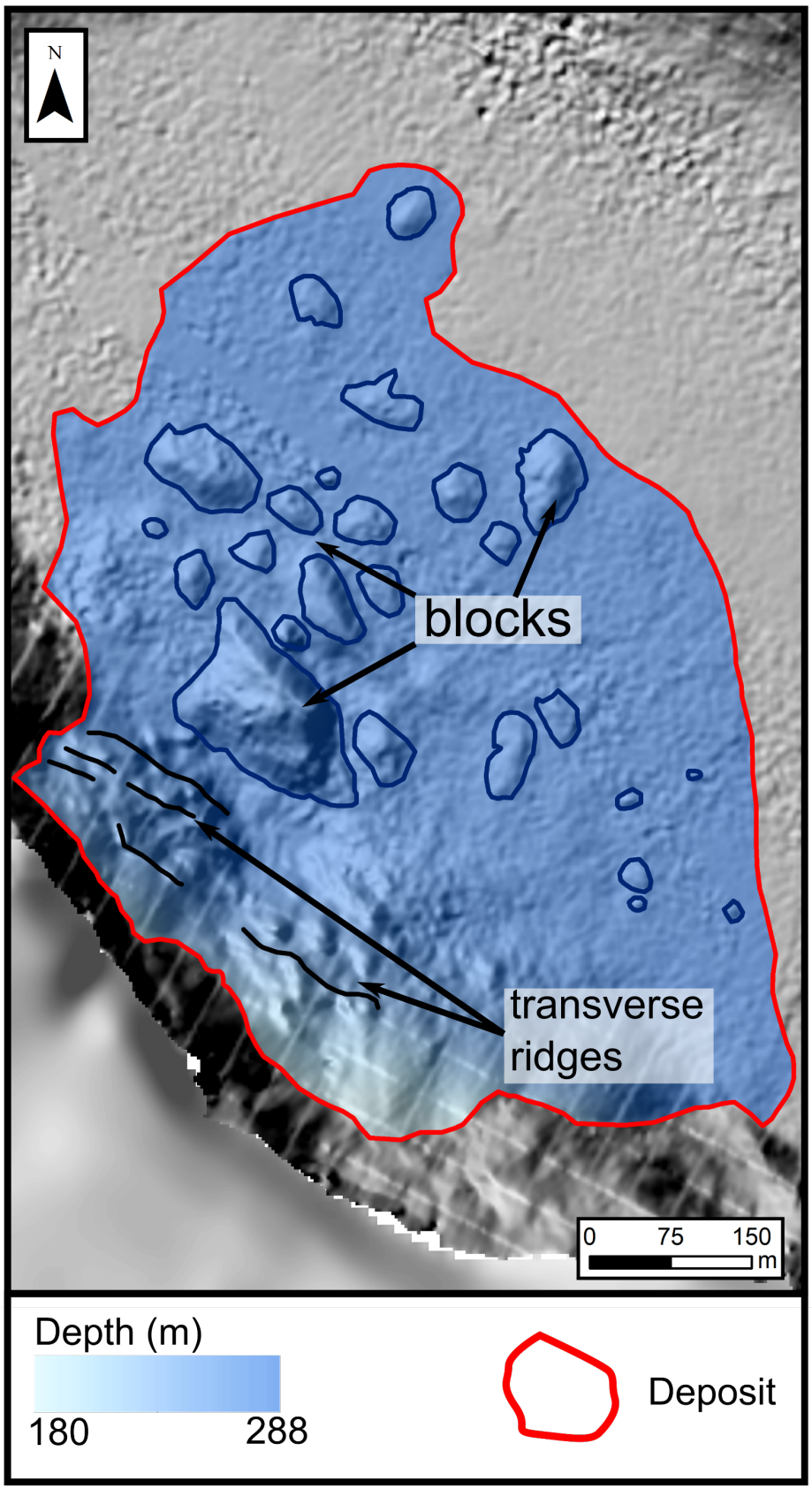

Figure A.11. Interpreted morphology of RA3 subaqueous deposit

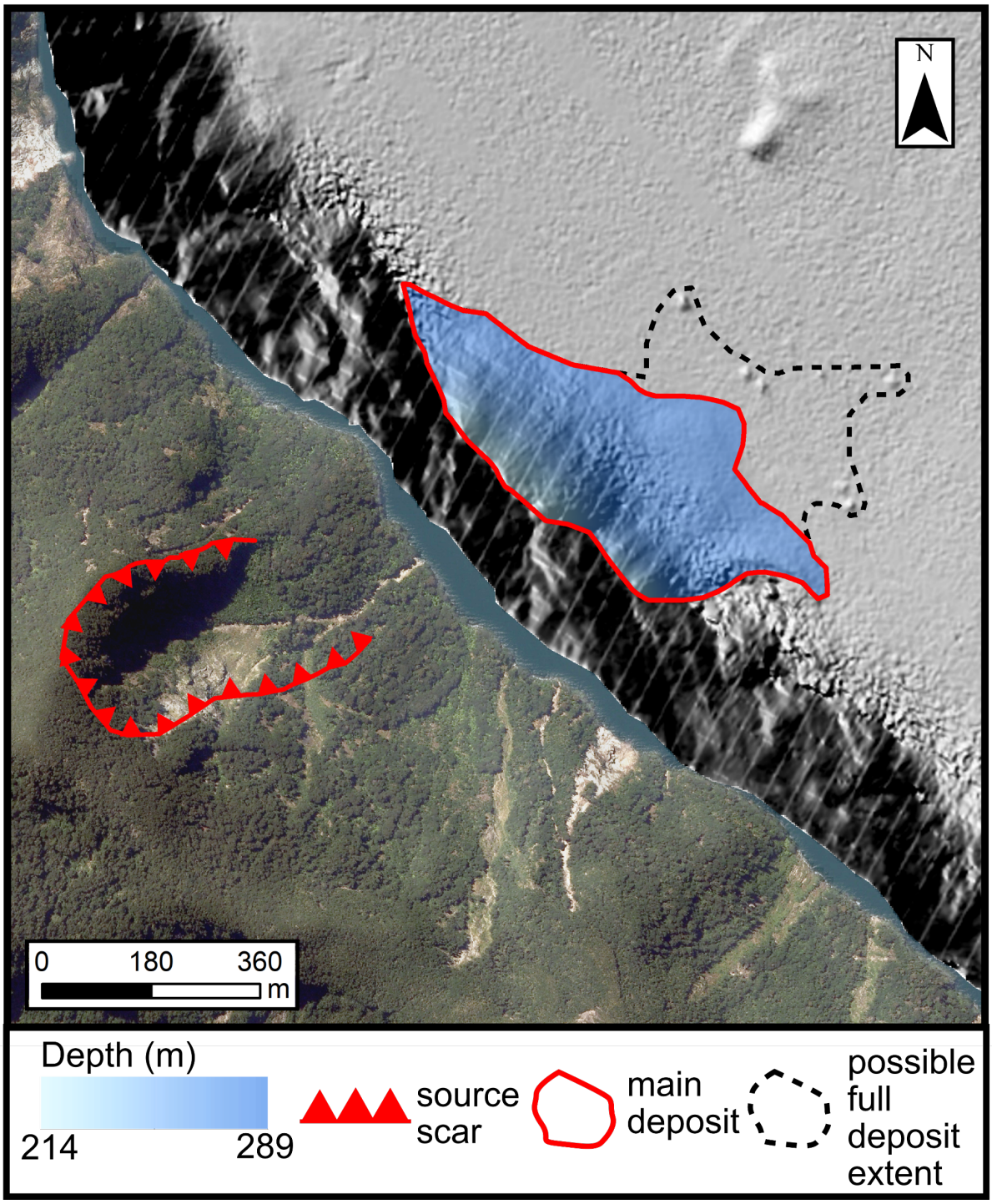

Figure A.12. RA4 subaerial and subaqueous deposit and source scar area. Imagery available under Creative Commons 4.0. Copyright is owned by The Southland Consortium (Southland District Council, Gore District Council, Environment Southland, and Department of Conservation).

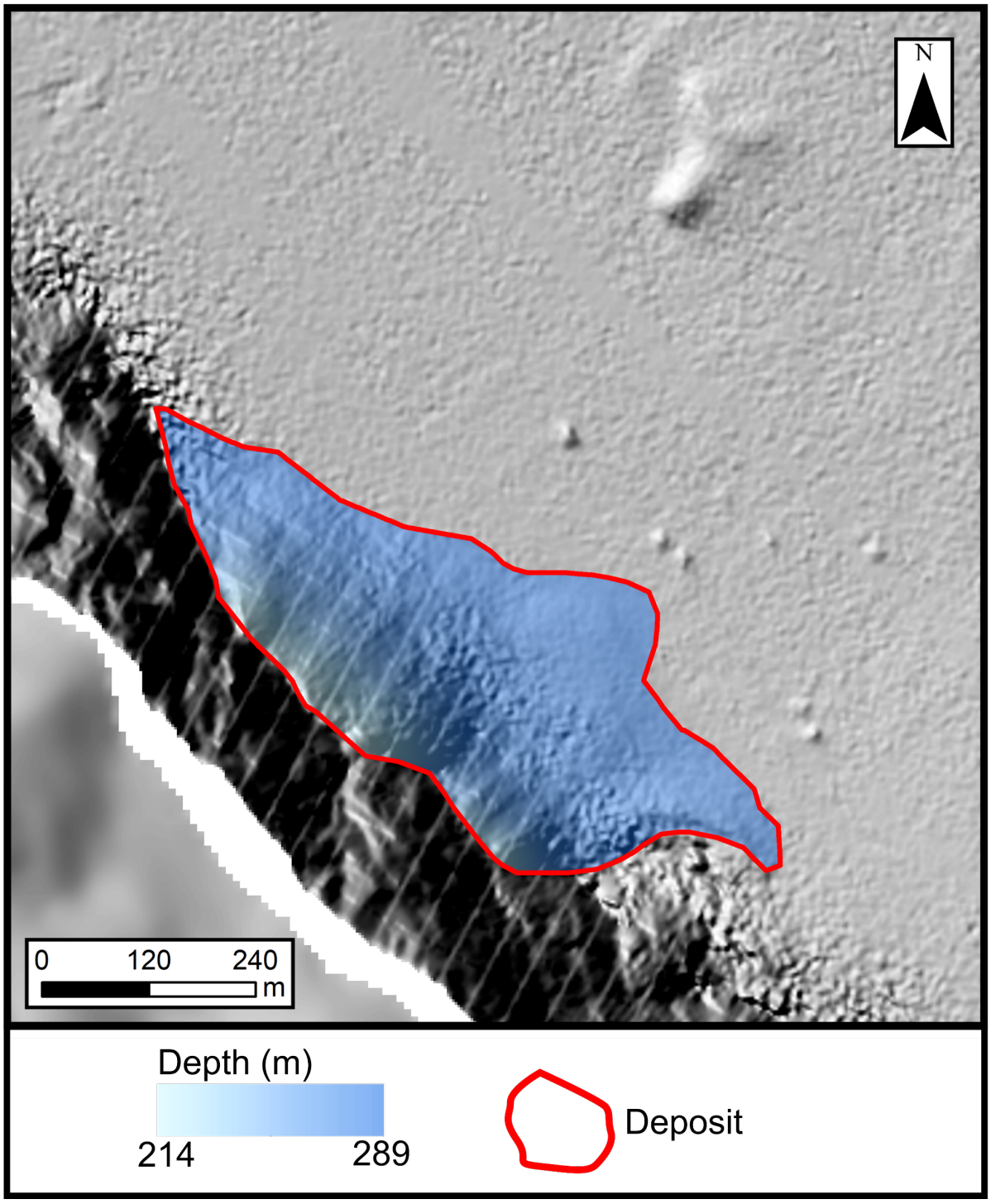

Figure A.13. Detailed, uninterpreted morphology of RA4 subaqueous deposit.

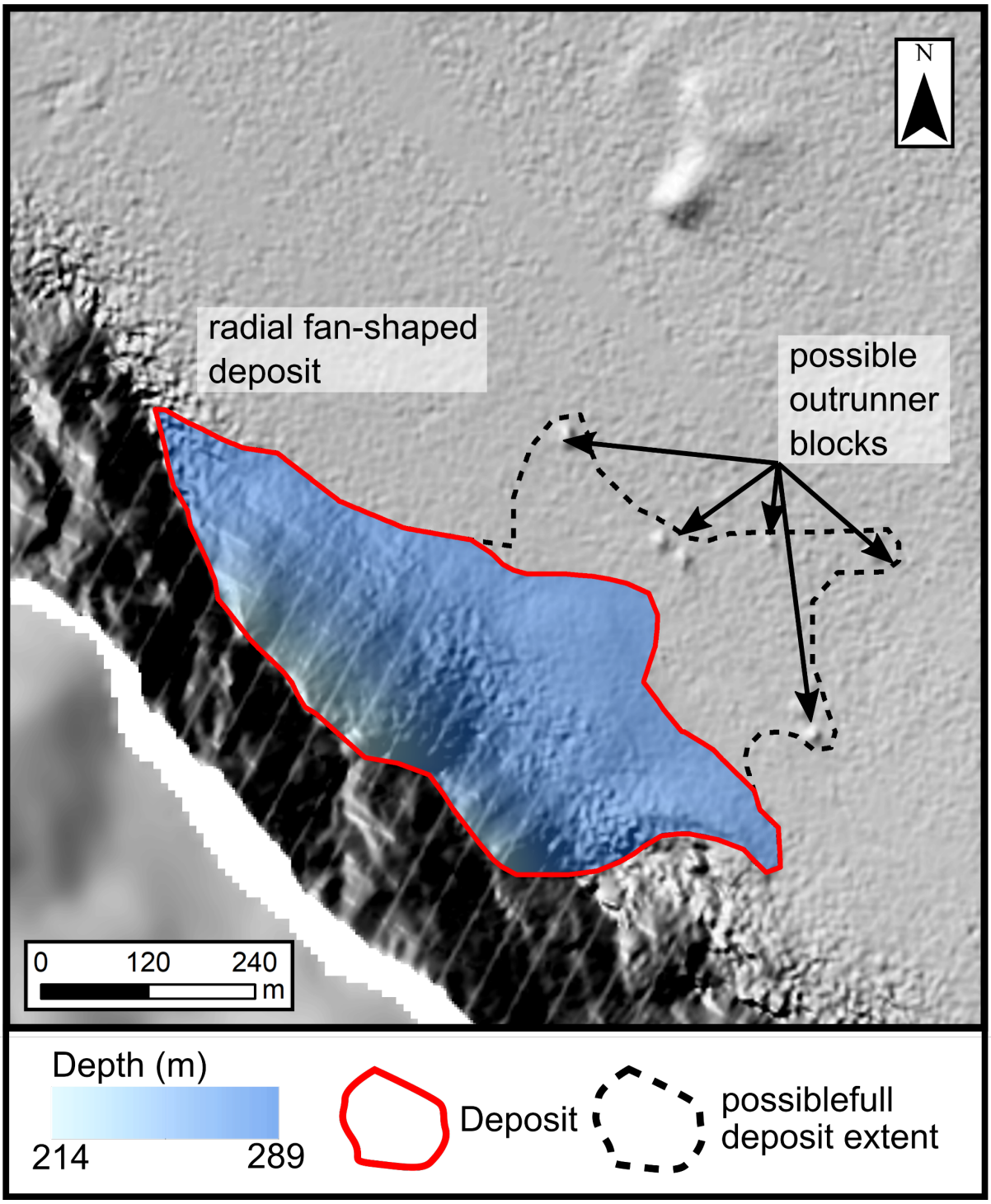

Figure A.14. Interpreted morphology of RA4 subaqueous deposit.

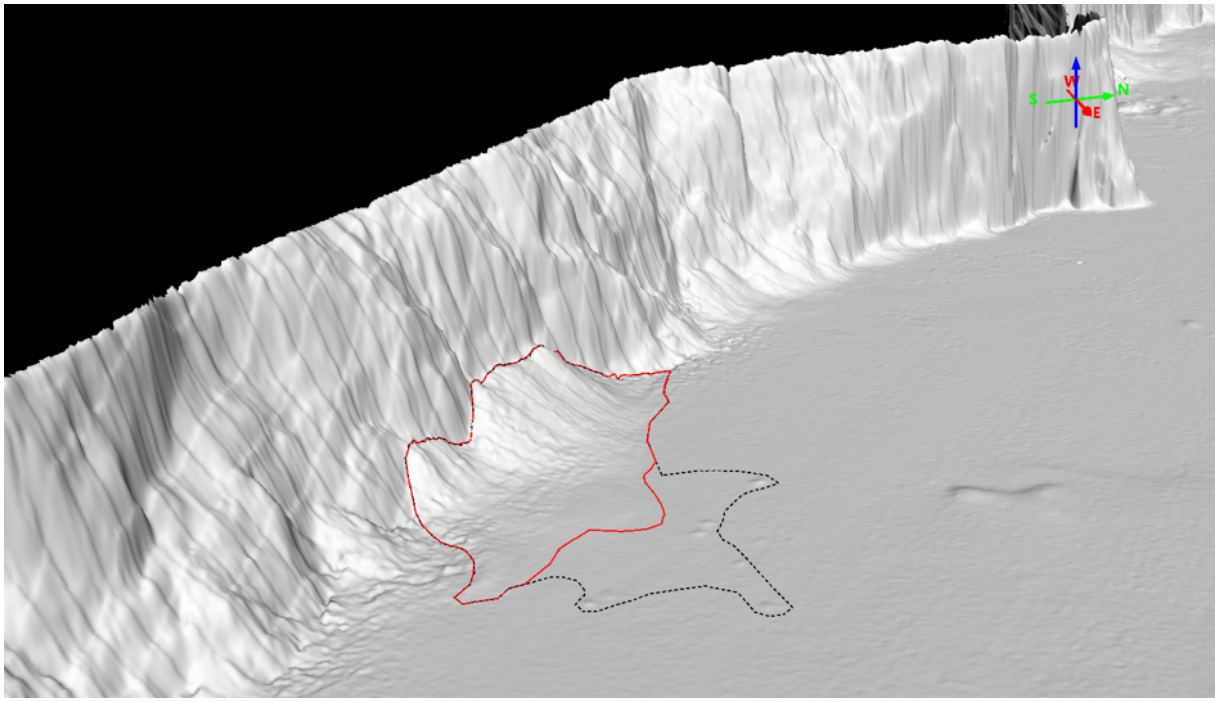

Figure A.15. 3D perspective view of RA4 subaqueous deposit with 1.5x vertical exaggeration.

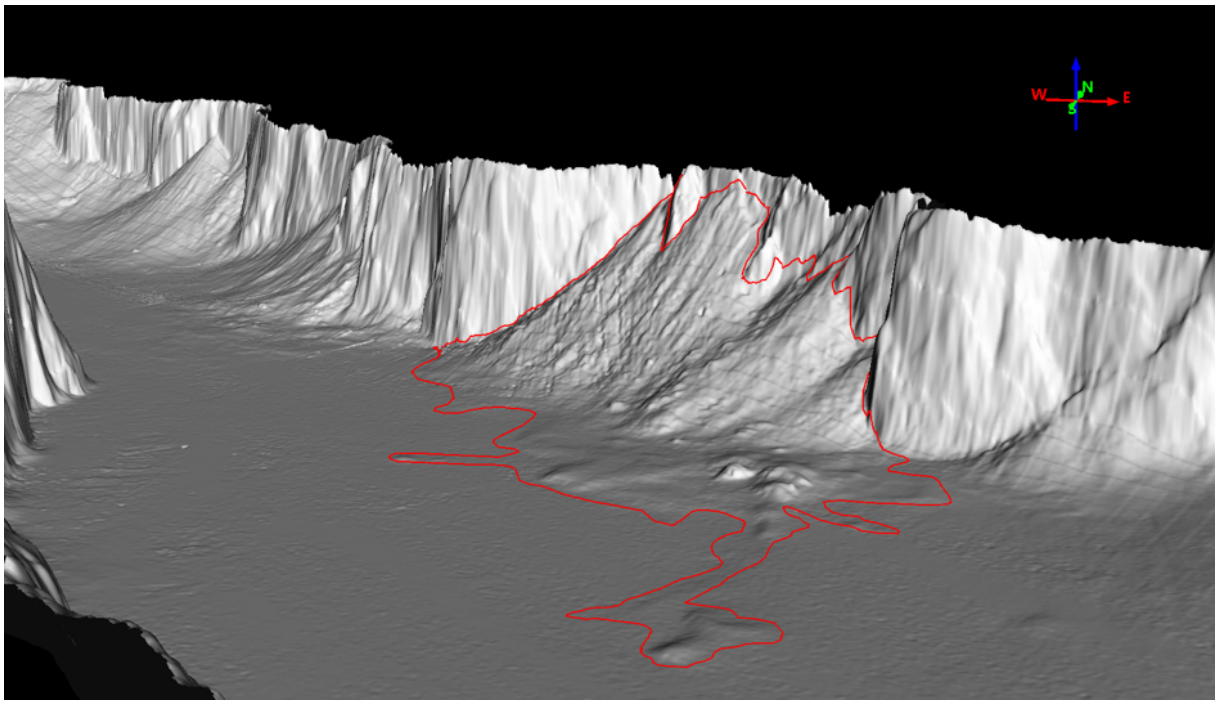

Figure A.16 3D perspective view of RA5 subaqueous deposit with 1.5x vertical exaggeration.

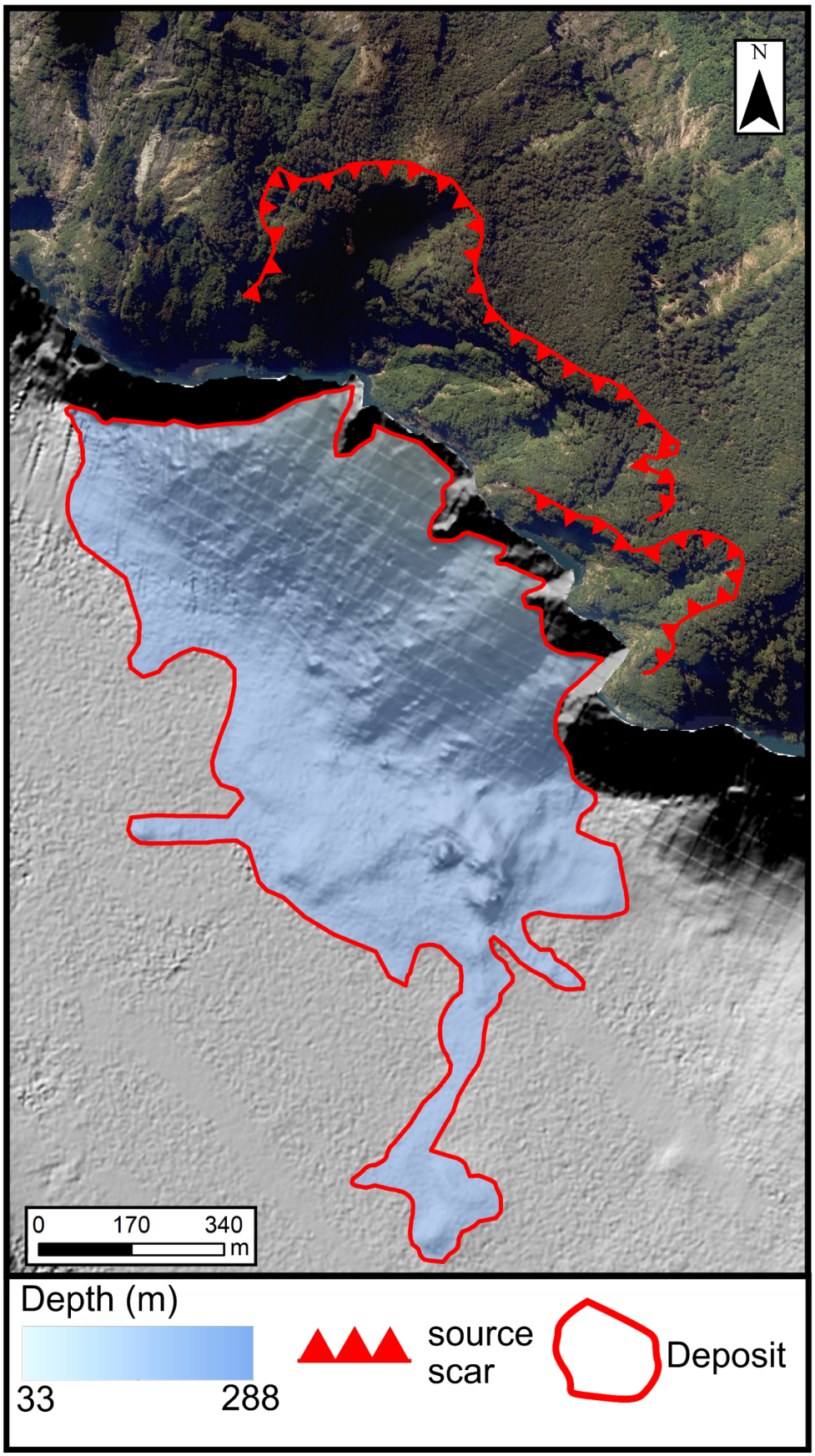

Figure A.17. RA5 subaqueous deposit and source scar area. Imagery available under Creative Commons 4.0. Copyright is owned by The Southland Consortium (Southland District Council, Gore District Council, Environment Southland, and Department of Conservation).

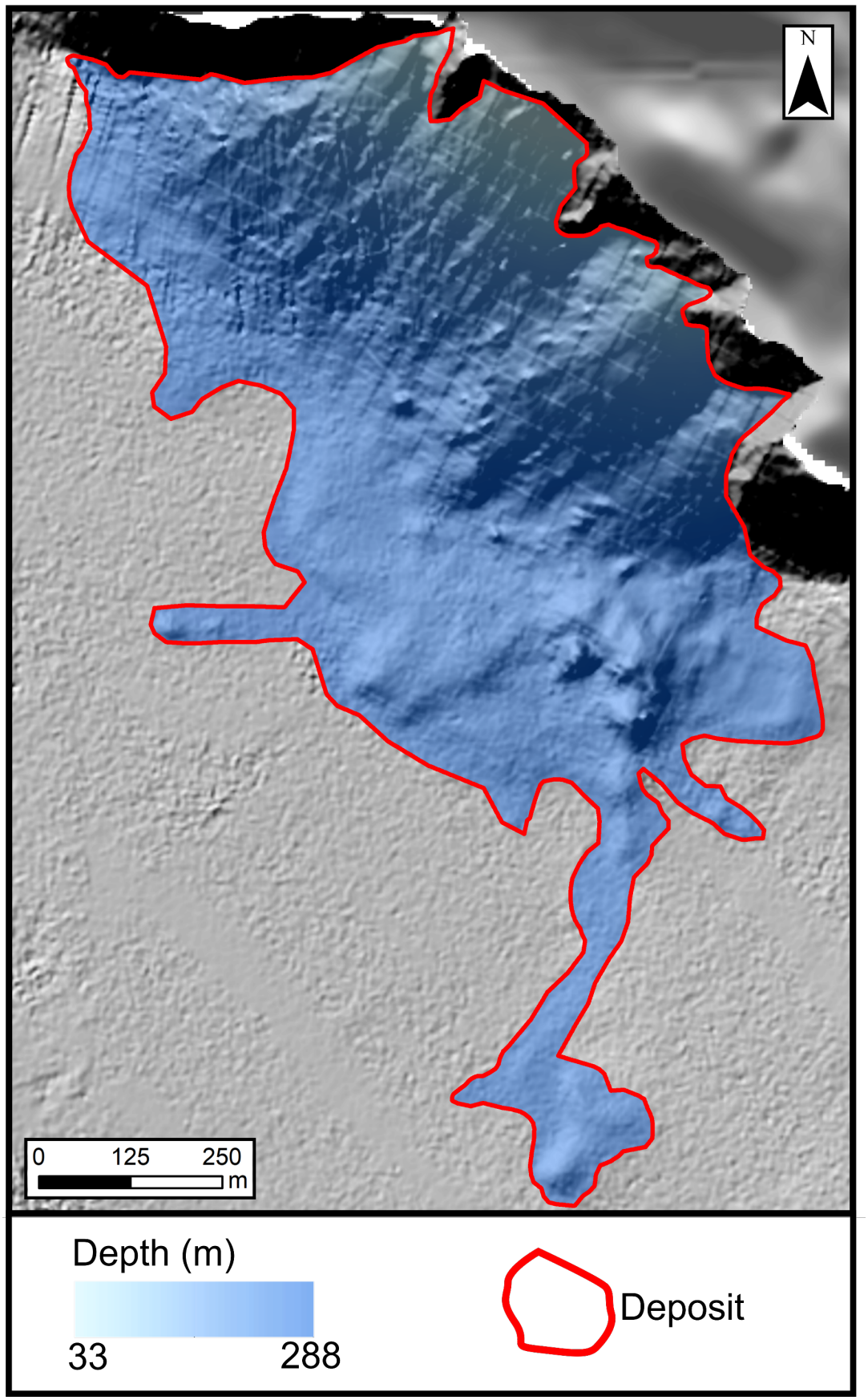

Figure A.18. Detailed, uninterpreted morphology of RA5 subaqueous deposit.

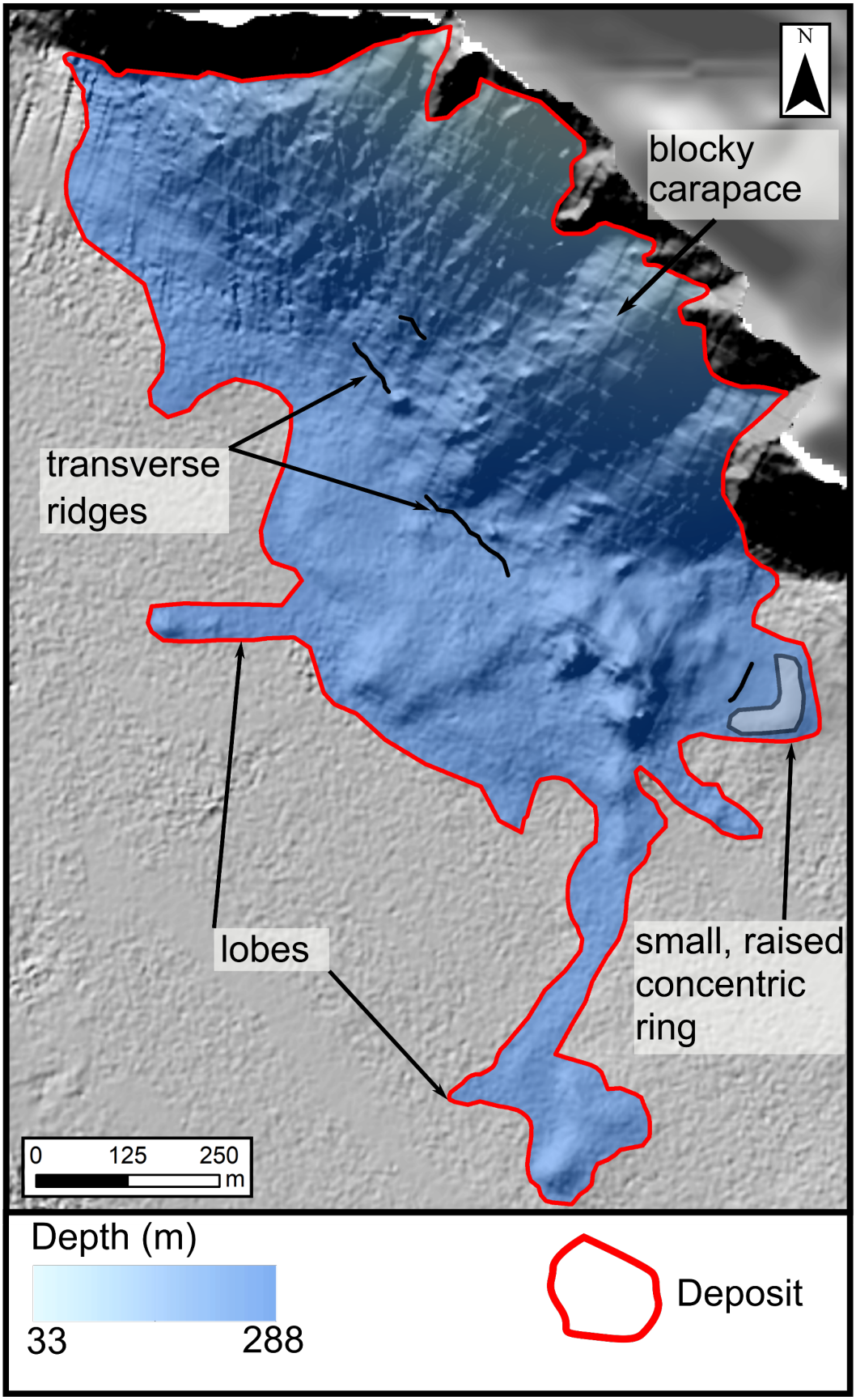

Figure A.19. Interpreted morphology of RA5 subaqueous deposit.



Figure A.20. RA6 subaqueous deposit. No source scar area mapped as it could not be confidently identified. Imagery available under Creative Commons 4.0. Copyright is owned by The Southland Consortium (Southland District Council, Gore District Council, Environment Southland, and Department of Conservation).

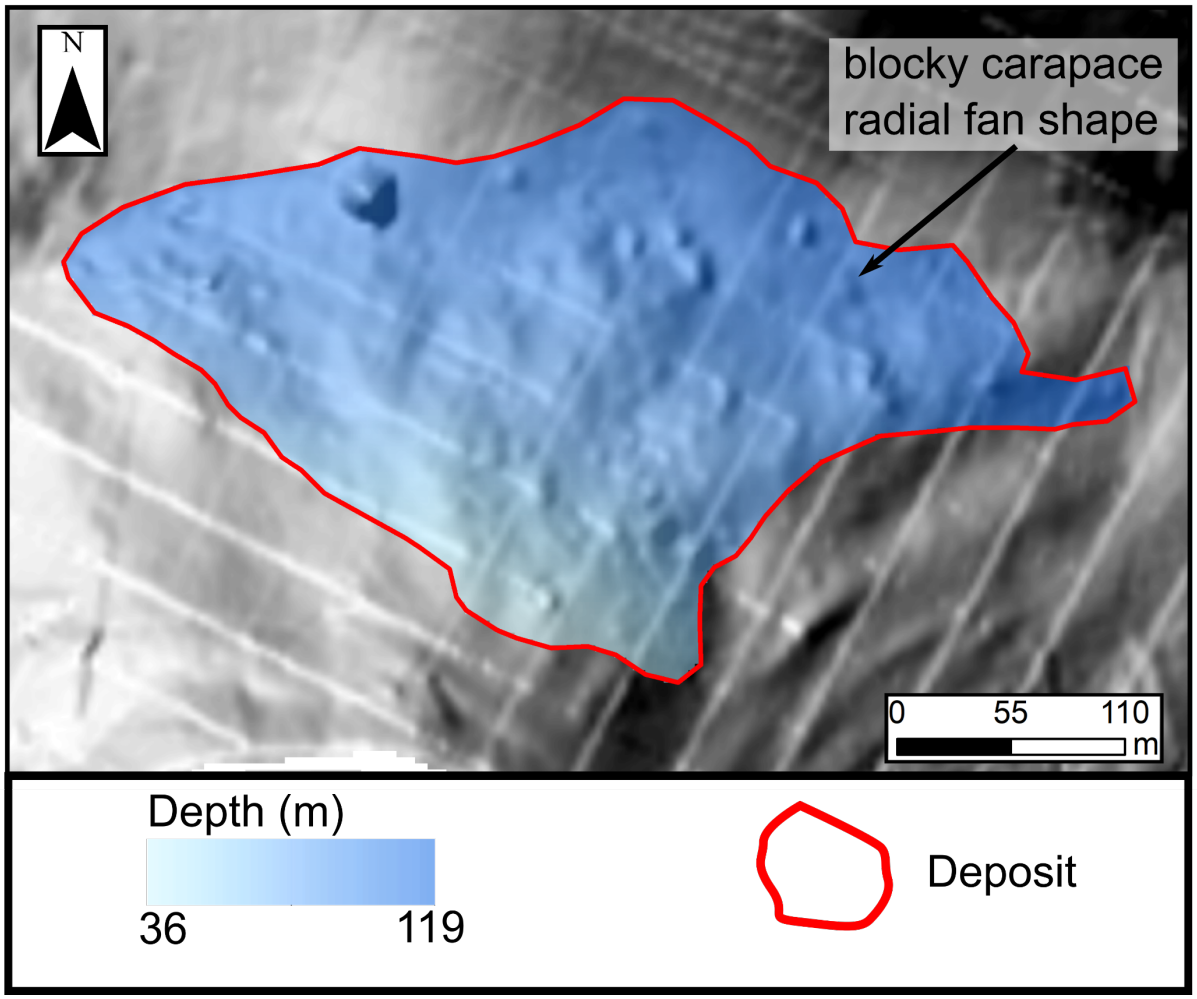

Figure A.21. Morphology of RA6 deposit, showing the radial fan shape, and lack of features beyond the blocky carapace, possibly due to overprinting by fan development.

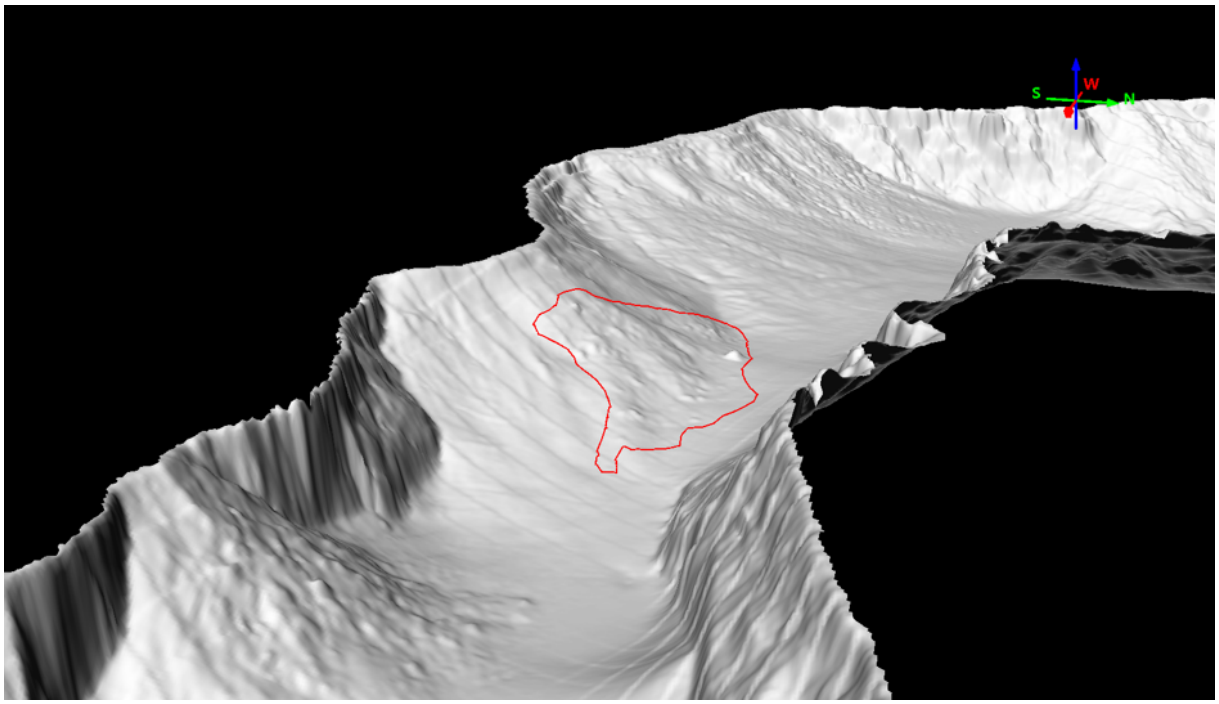

Figure A.22. 3D perspective view of RA6 subaqueous deposit with 1.5x vertical exaggeration.

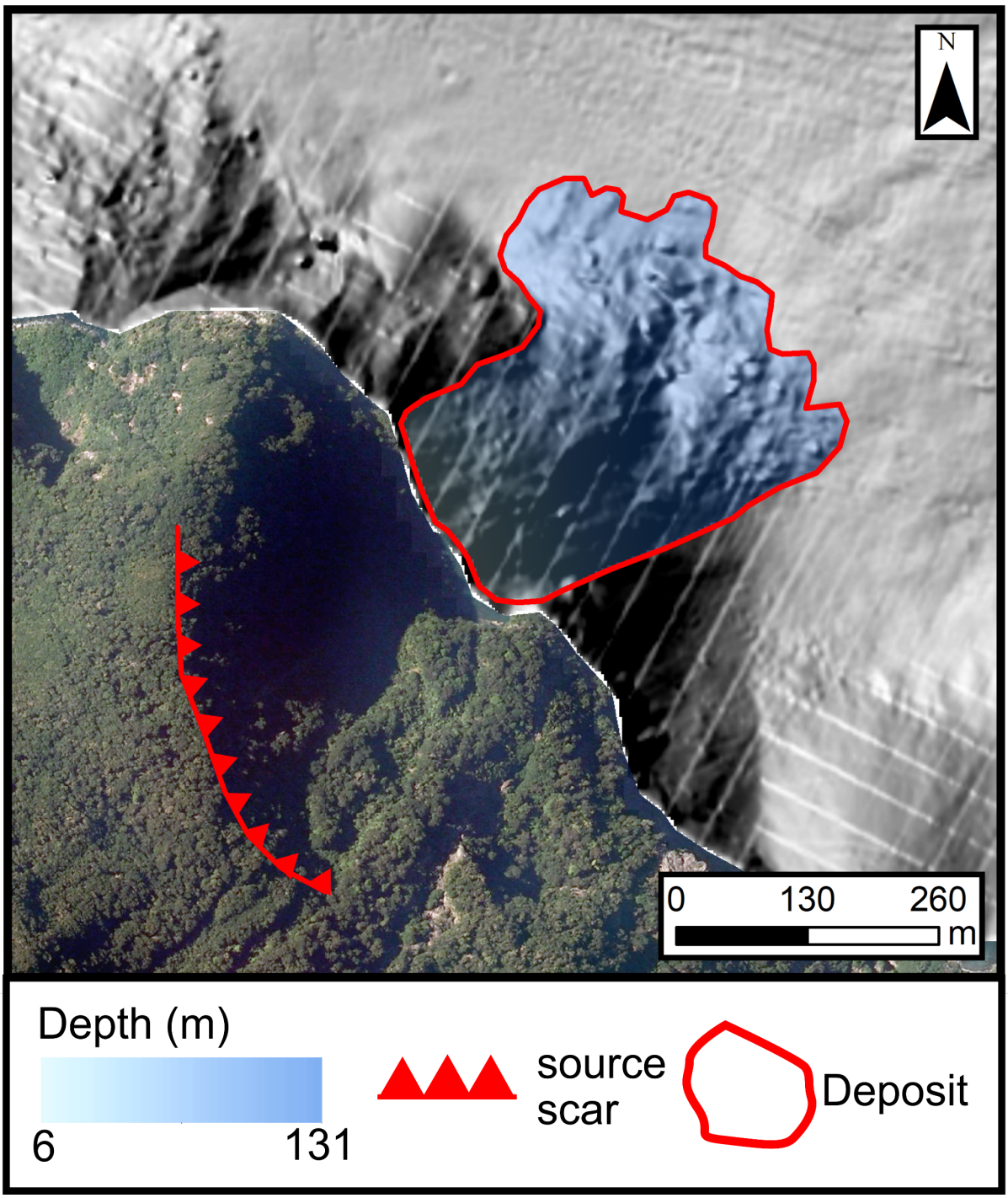

Figure A.23. RA7 subaqueous deposit and source scar area. Imagery available under Creative Commons 4.0. Copyright is owned by The Southland Consortium (Southland District Council, Gore District Council, Environment Southland, and Department of Conservation).

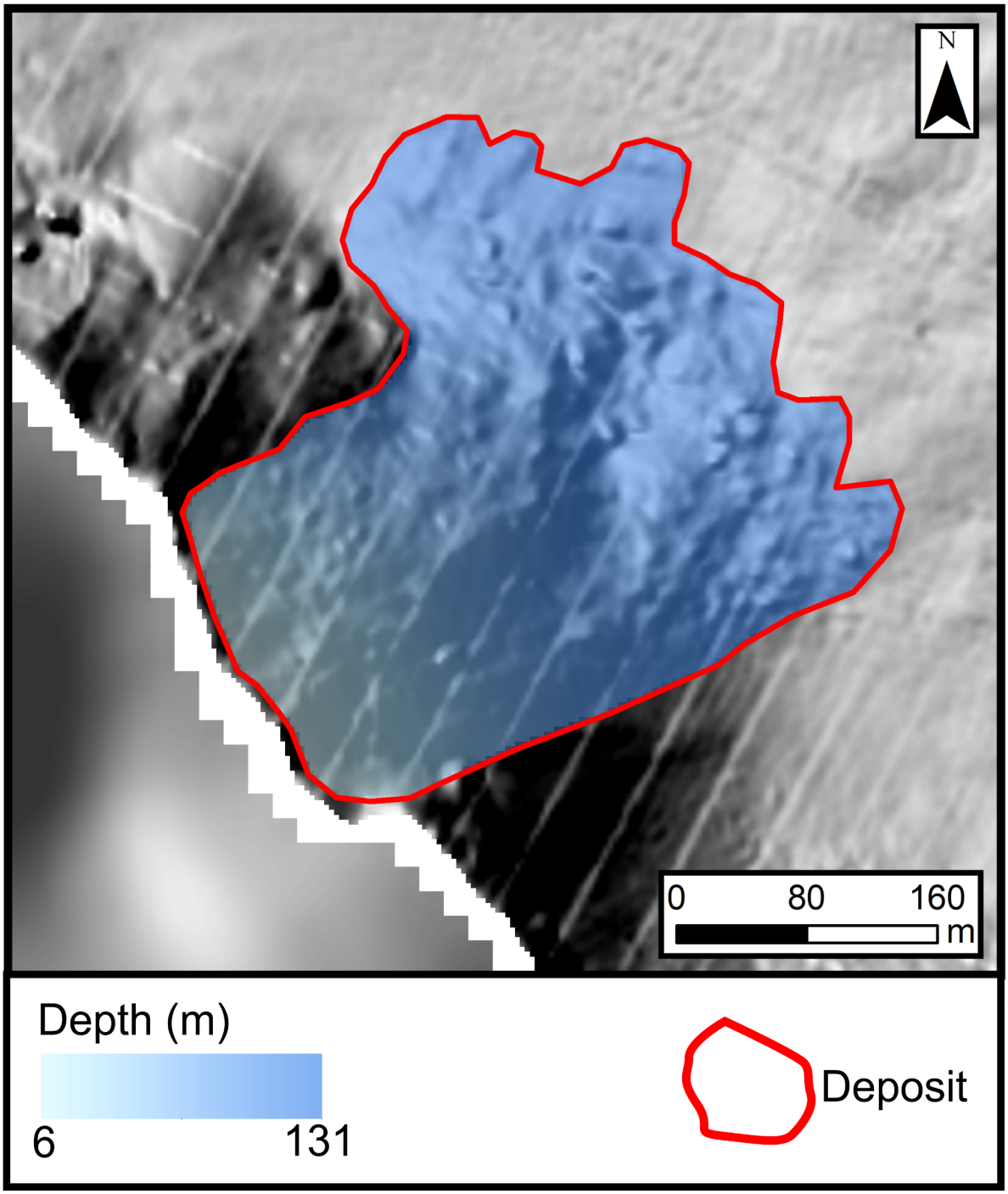

Figure A.24. Detailed, uninterpreted morphology of RA7 subaqueous deposit.

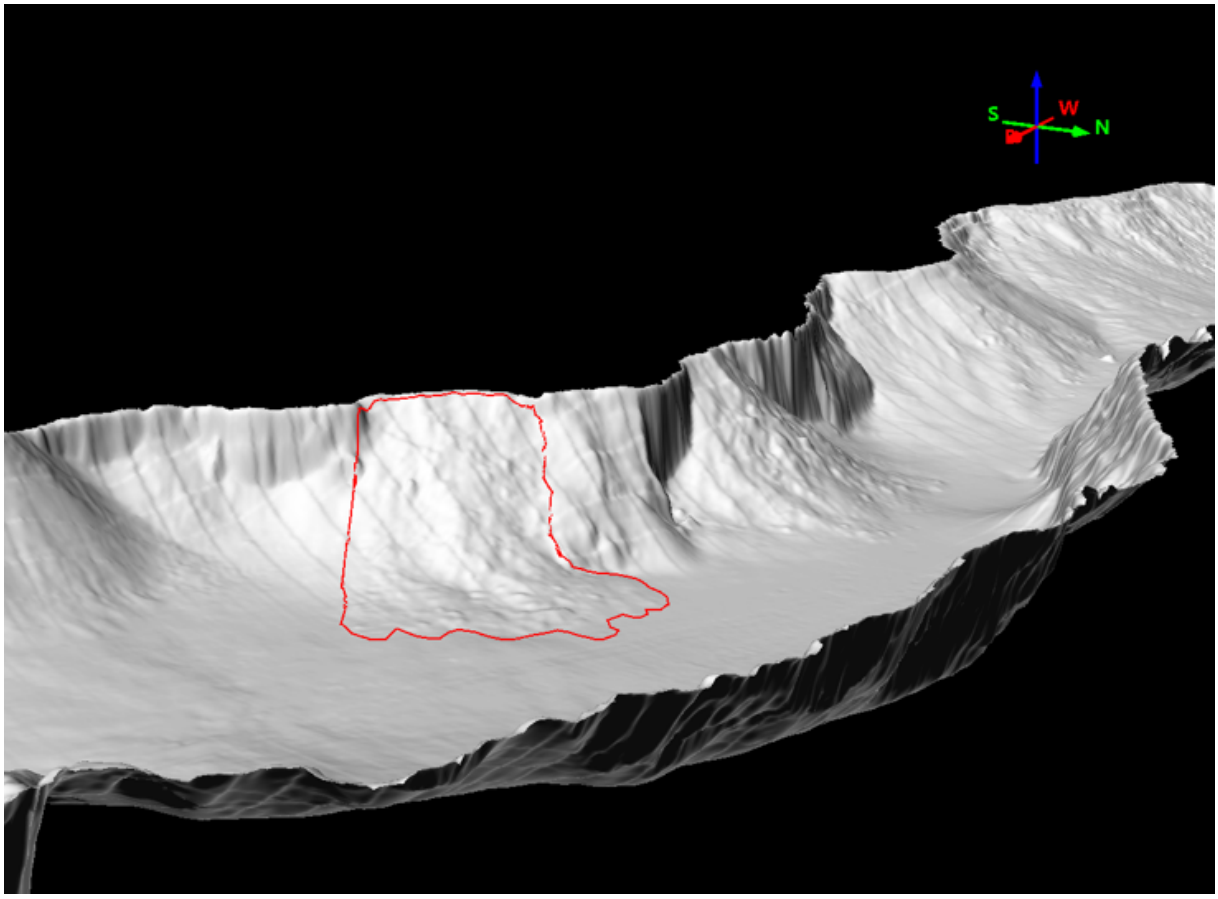

Figure A.25. 3D perspective view of RA7 subaqueous deposit with 1.5x vertical exaggeration.

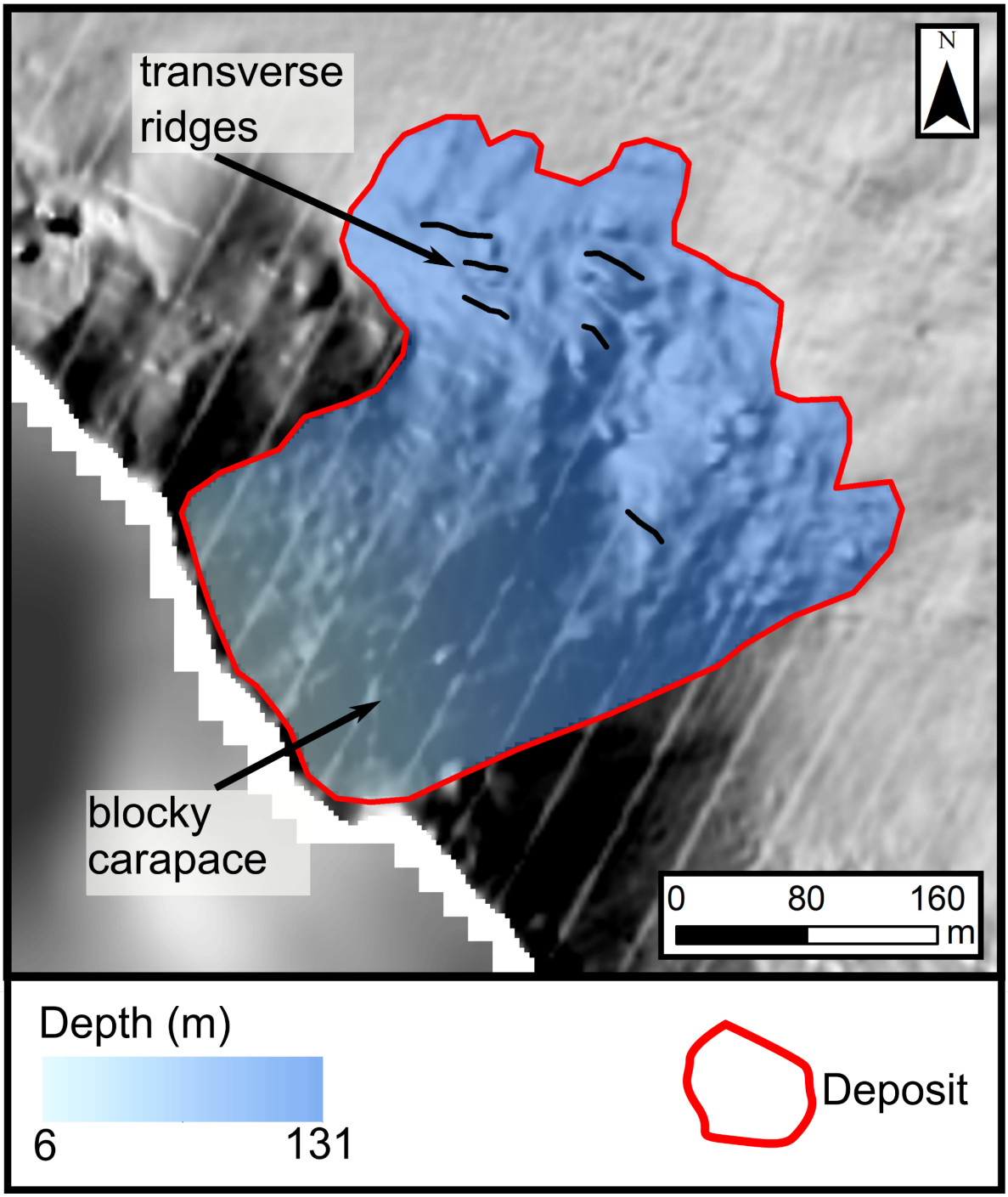

Figure A.26. Interpreted morphology of RA7 subaqueous deposit.

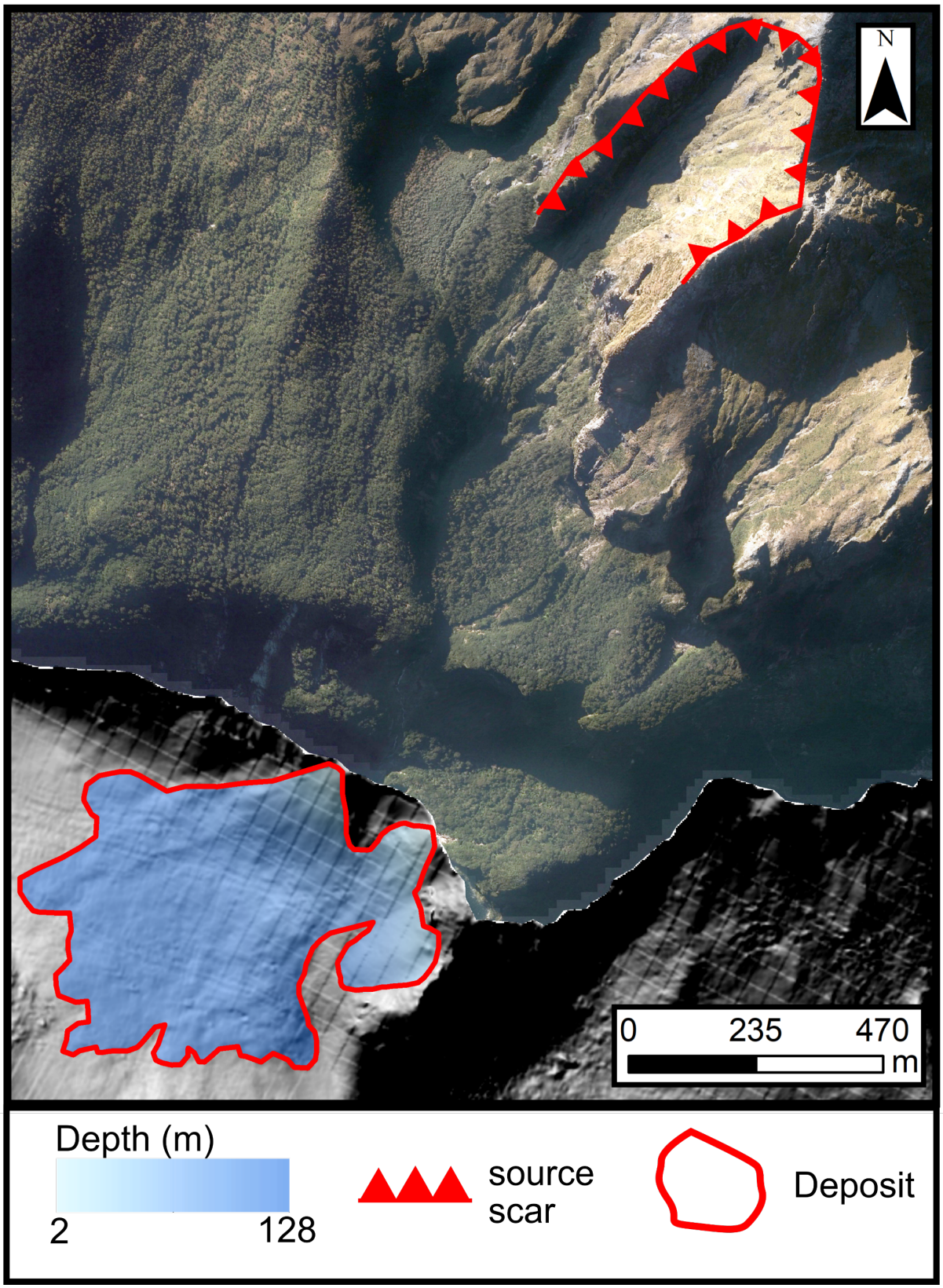

Figure A.27. RA8 subaqueous deposit and source scar area. Imagery available under Creative Commons 4.0. Copyright is owned by The Southland Consortium (Southland District Council, Gore District Council, Environment Southland, and Department of Conservation).

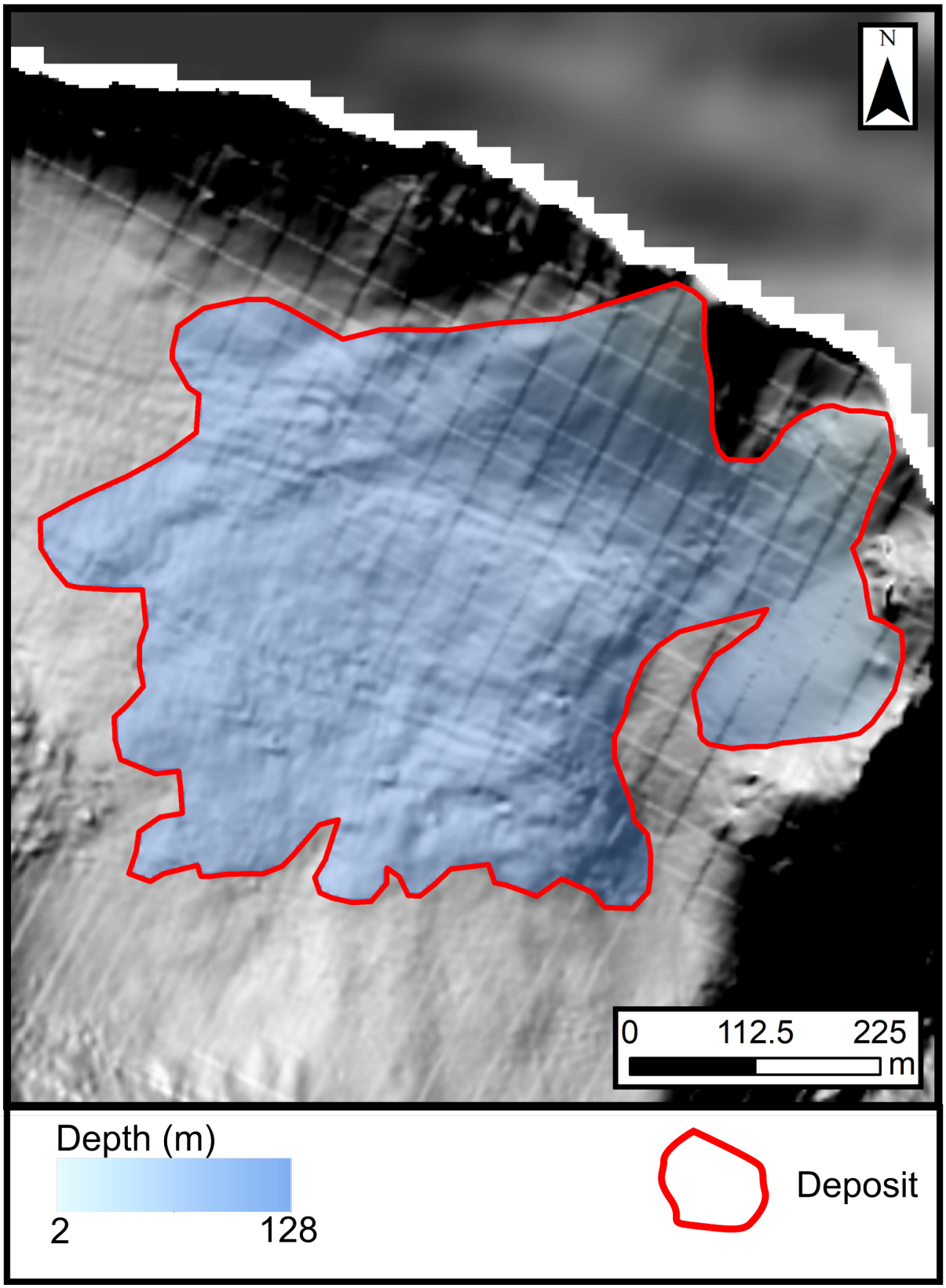

Figure A.28. Detailed, uninterpreted morphology of RA8 subaqueous deposit.

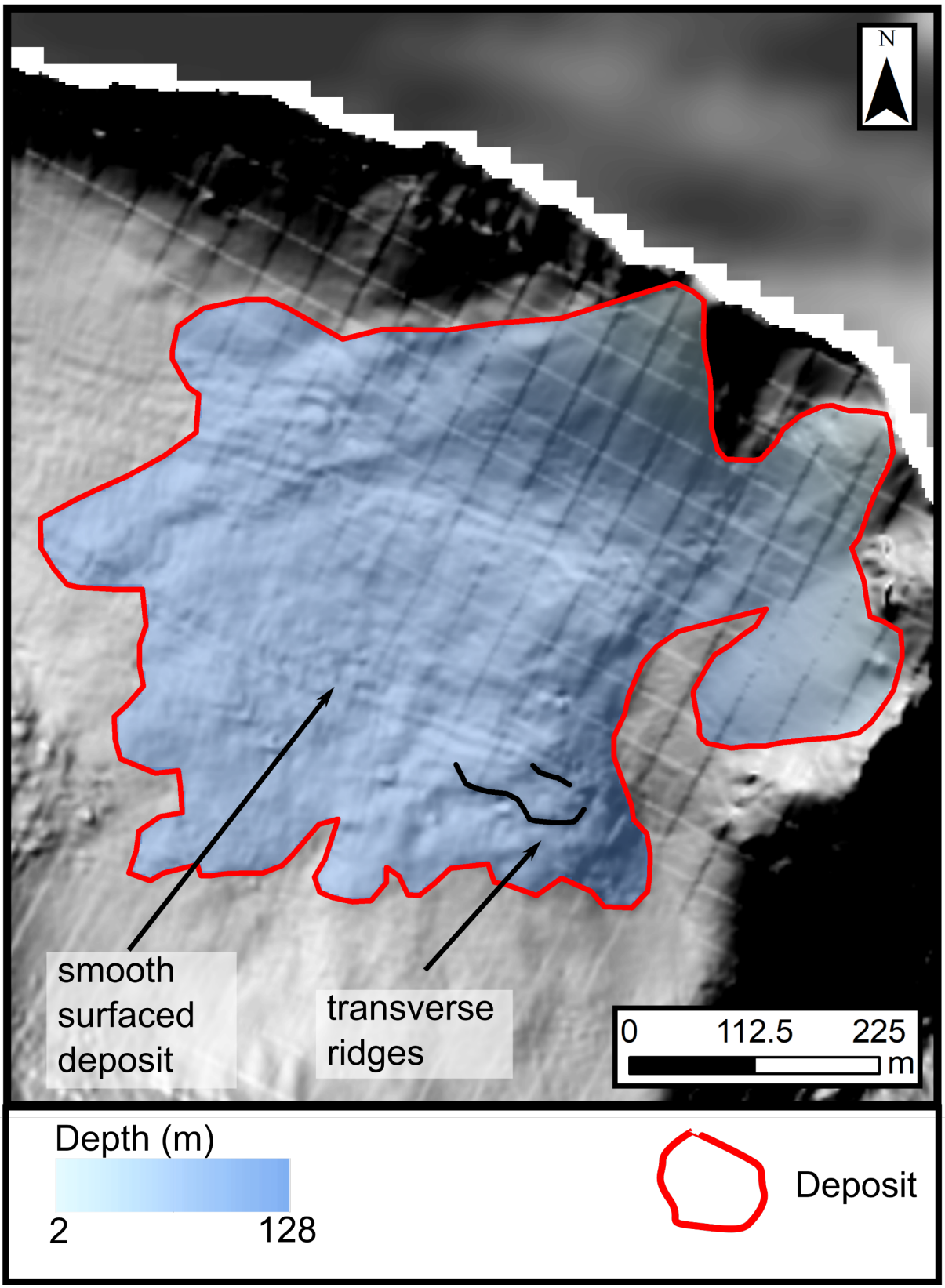

Figure A.29. Interpreted morphology of RA8 subaqueous deposit.

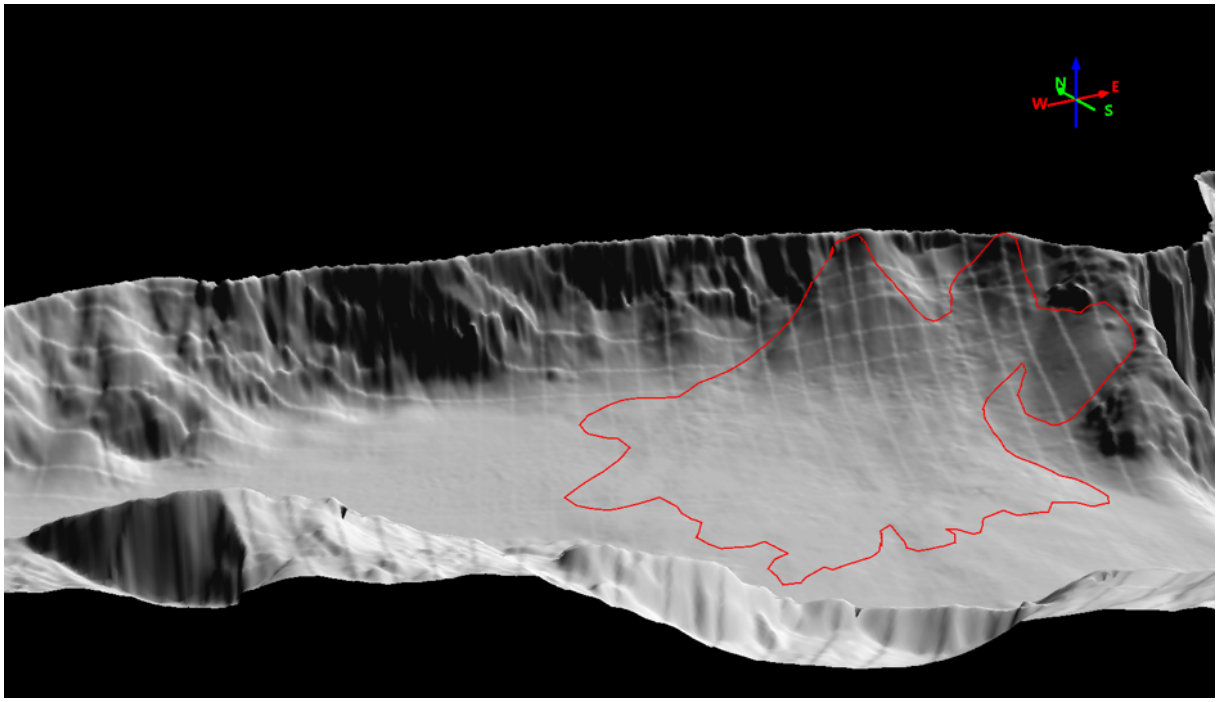

Figure A.30. 3D perspective view of RA8 subaqueous deposit with 1.5x vertical exaggeration.

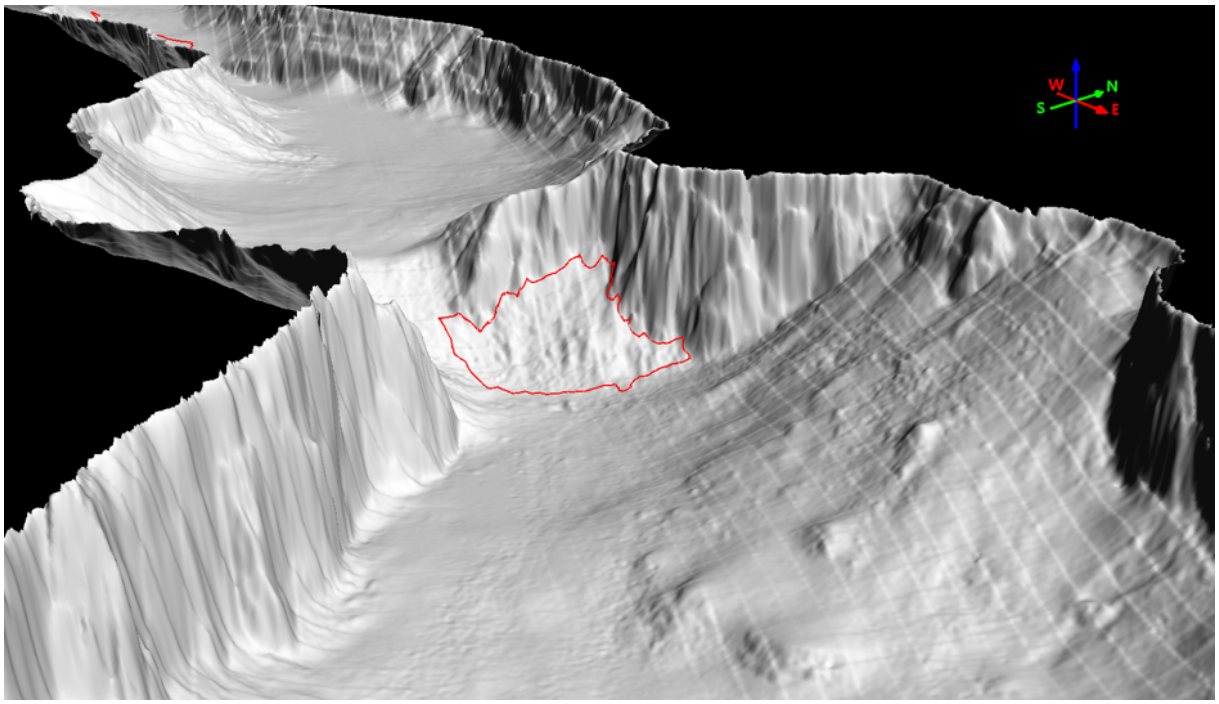

Figure A.31. 3D perspective view of RA9 subaqueous deposit (in red) with 1.5x vertical exaggeration.

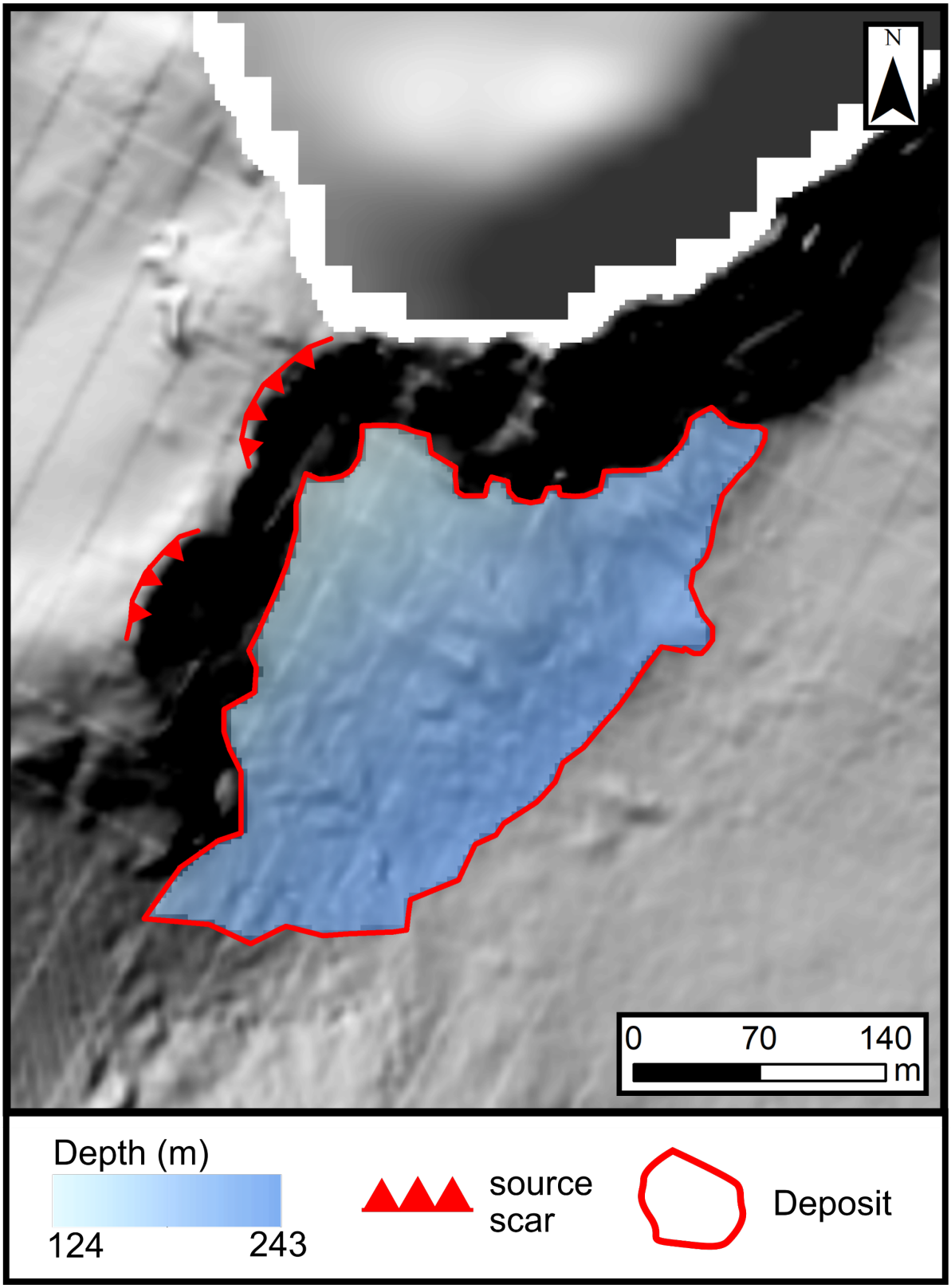

Figure A.32. Detailed, uninterpreted morphology of RA9 subaqueous source and deposit.

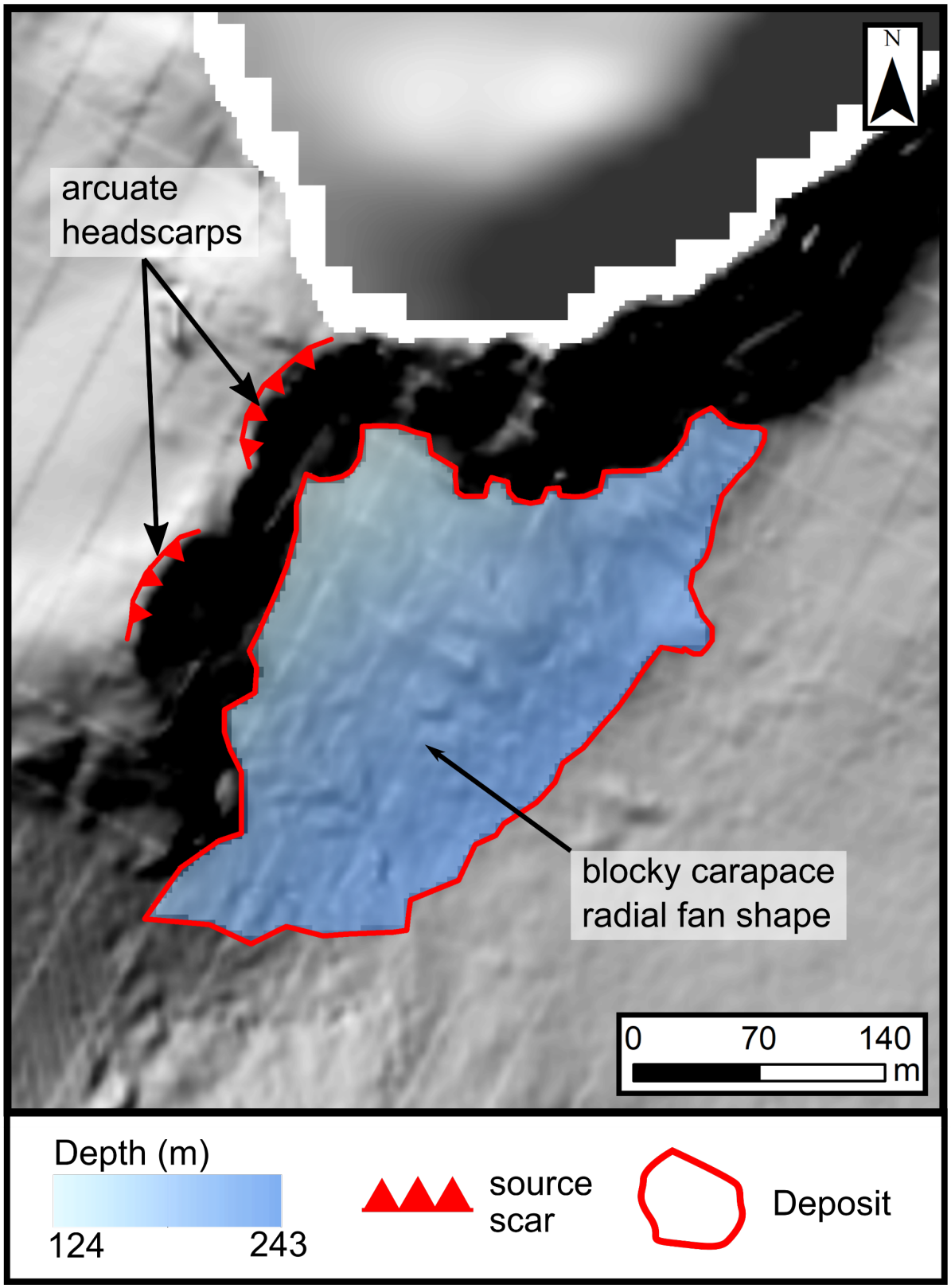

Figure A.33. Interpreted morphology of RA9 subaqueous deposit.

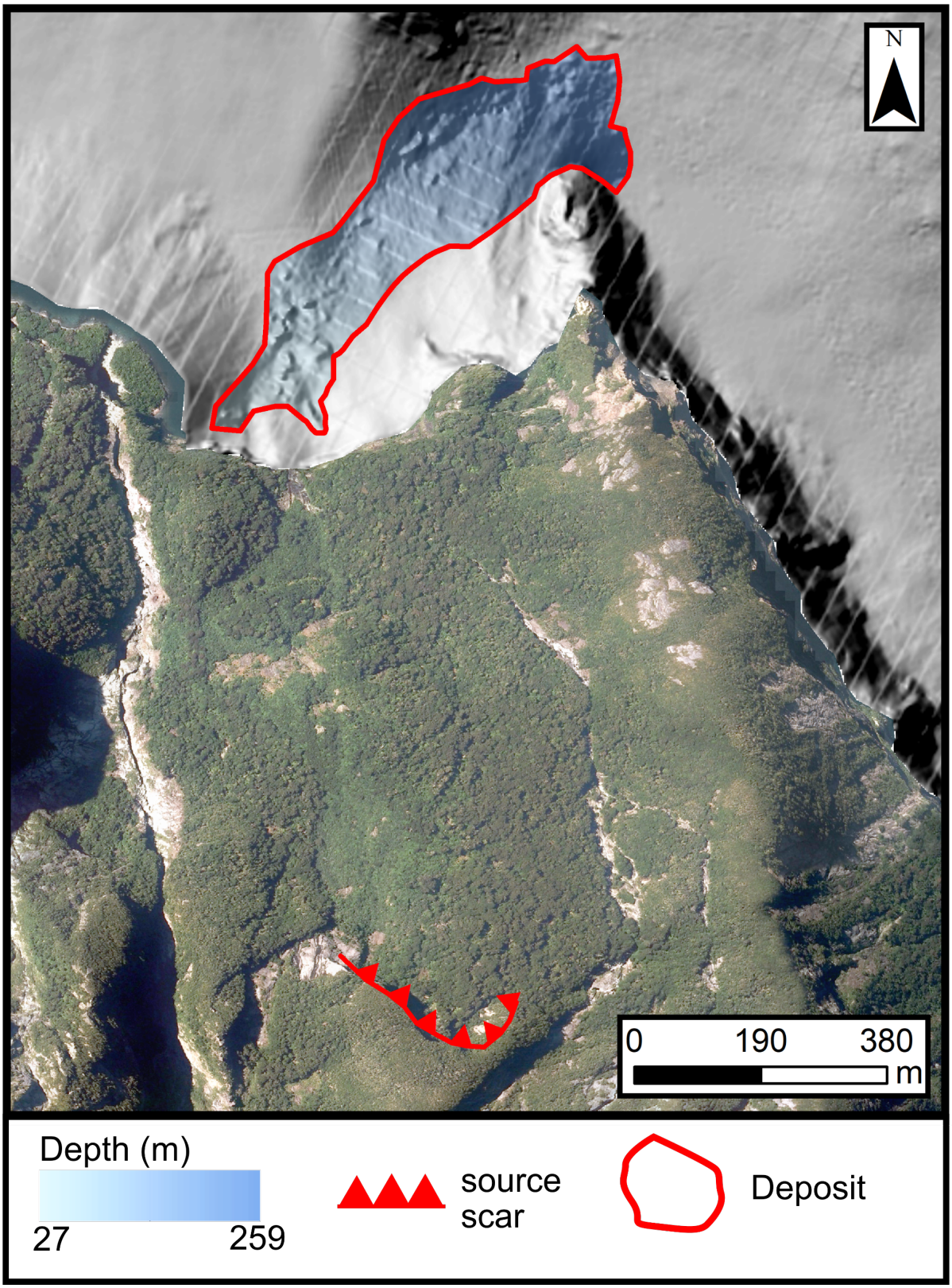

Figure A.34. RA10 subaqueous deposit and source scar area. Imagery available under Creative Commons 4.0. Copyright is owned by The Southland Consortium (Southland District Council, Gore District Council, Environment Southland, and Department of Conservation).

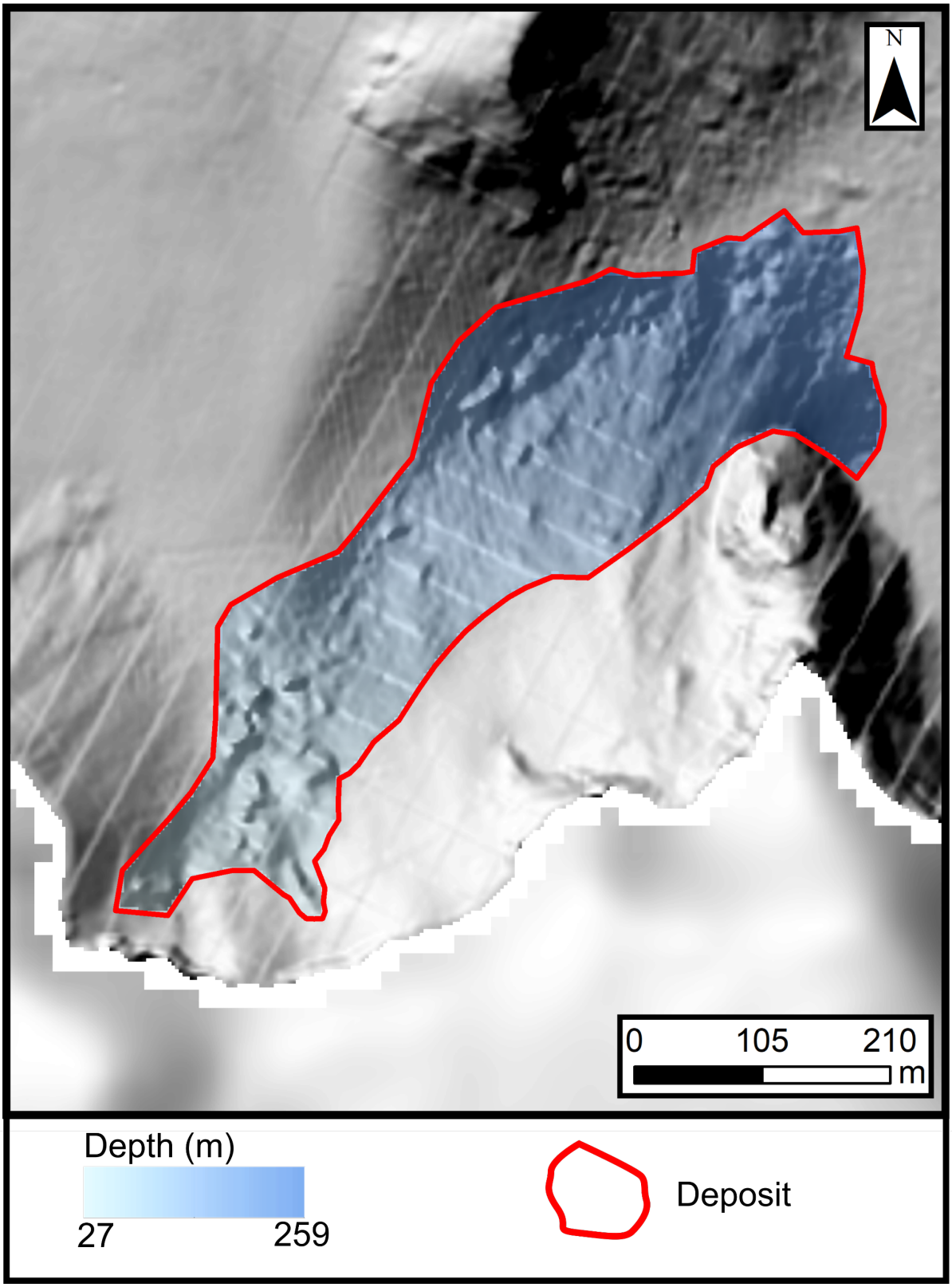

Figure A.35. Detailed, uninterpreted morphology of RA10 subaqueous deposit.

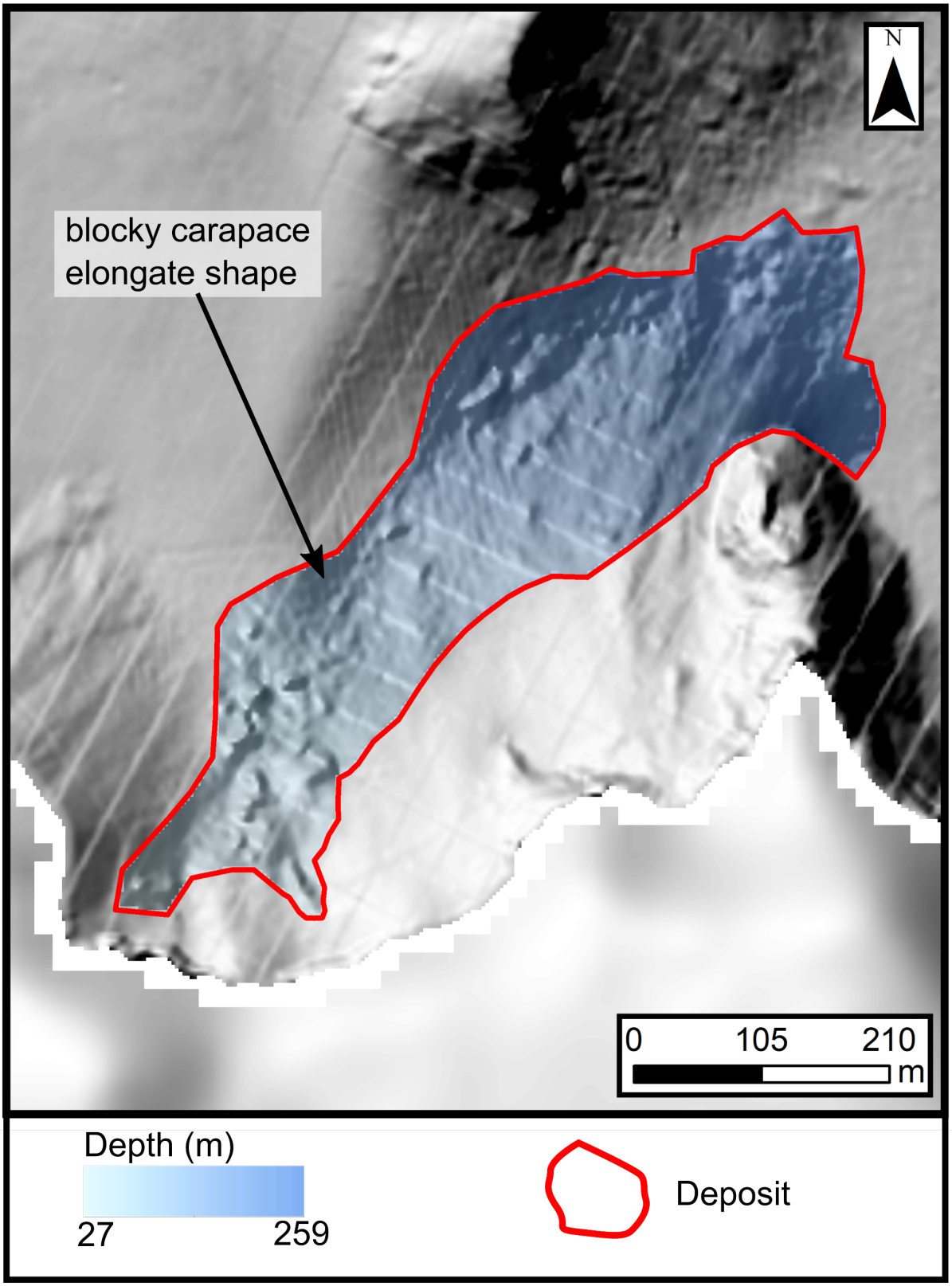

Figure A.36. Interpreted morphology of RA10 subaqueous deposit.

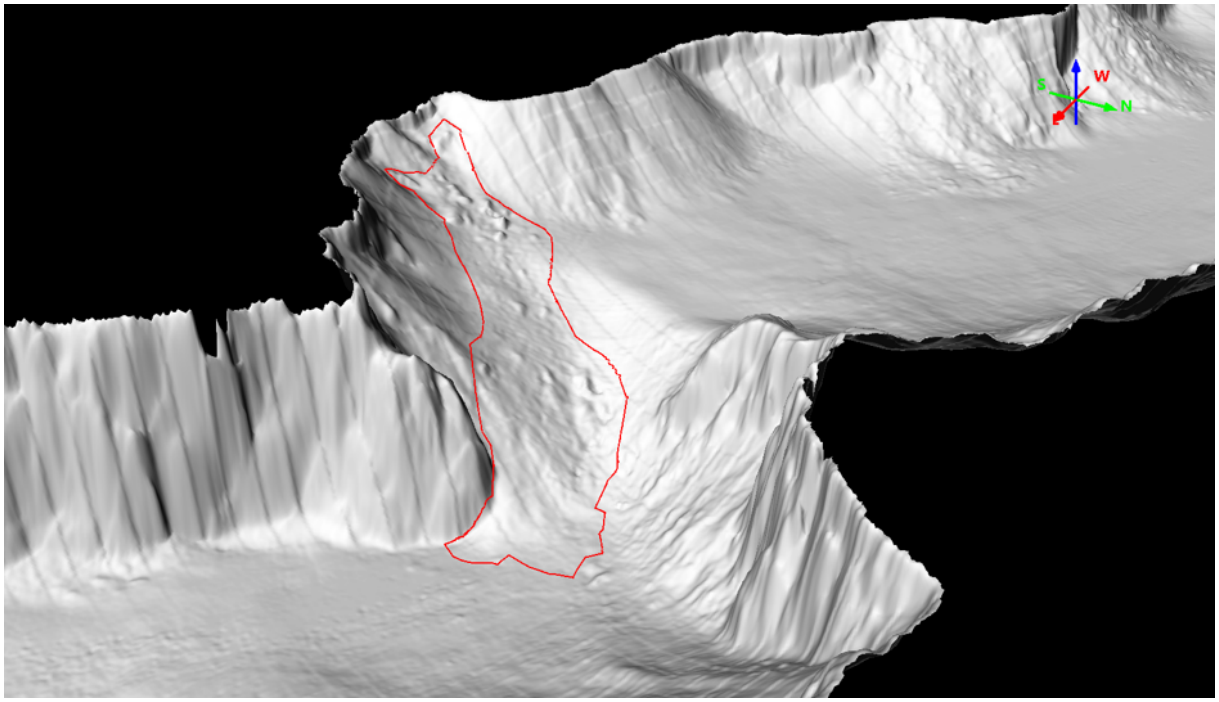

Figure A.37. 3D perspective view of RA10 subaqueous deposit with 1.5x vertical exaggeration.

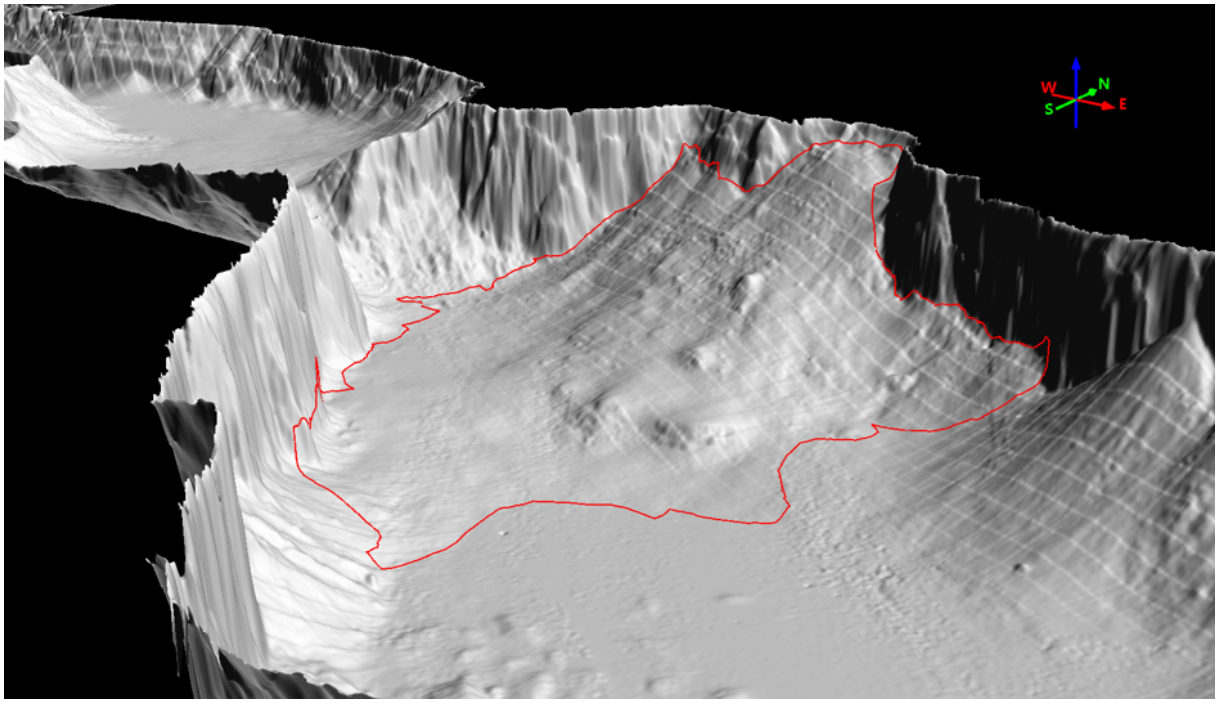

Figure A.38. 3D perspective view of RA11 subaqueous deposit with 1.5x vertical exaggeration.

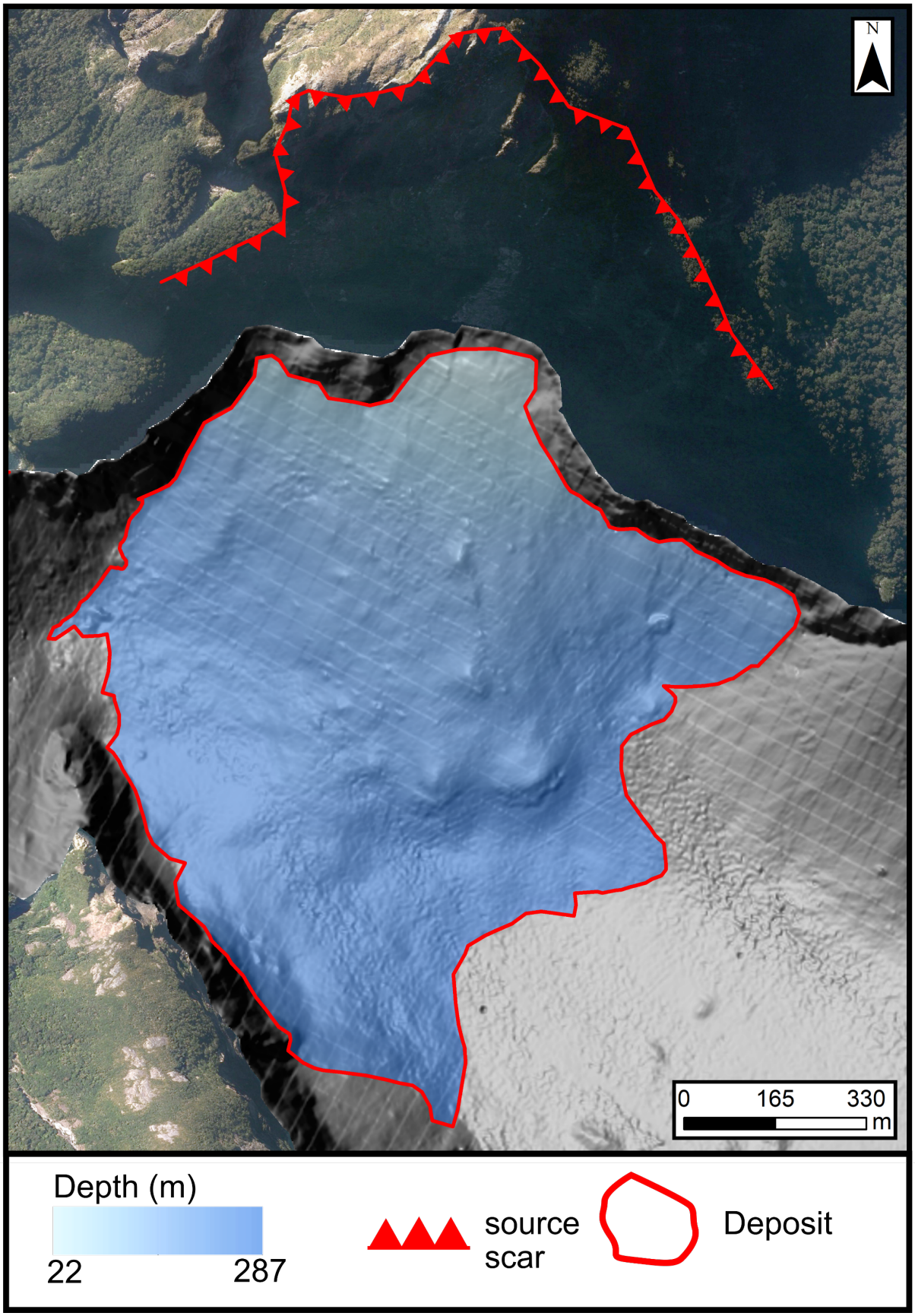

Figure A.39. RA11 subaqueous deposit and source scar area. Imagery available under Creative Commons 4.0. Copyright is owned by The Southland Consortium (Southland District Council, Gore District Council, Environment Southland, and Department of Conservation).

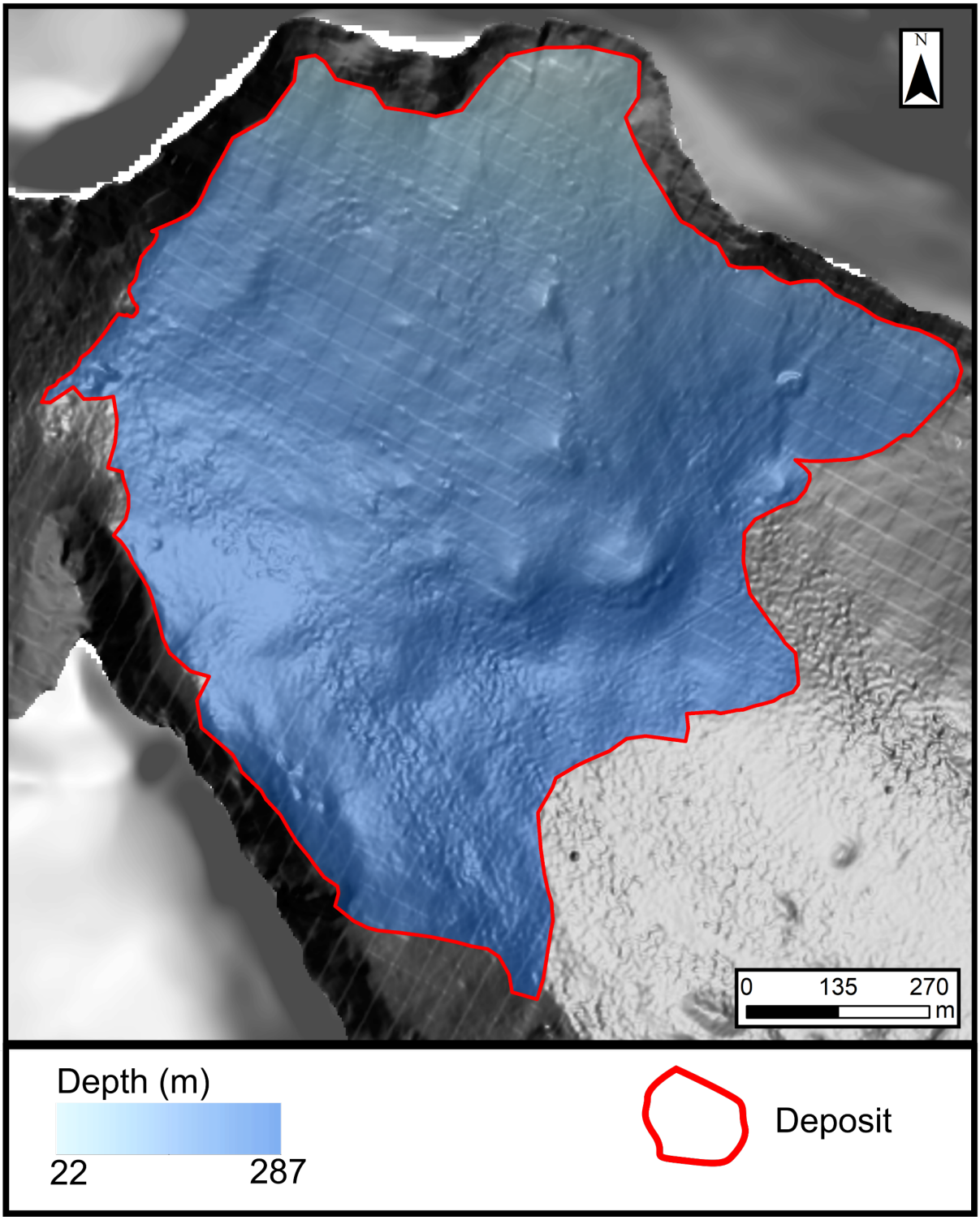

Figure A.40. Detailed, uninterpreted morphology of RA11 subaqueous deposit.

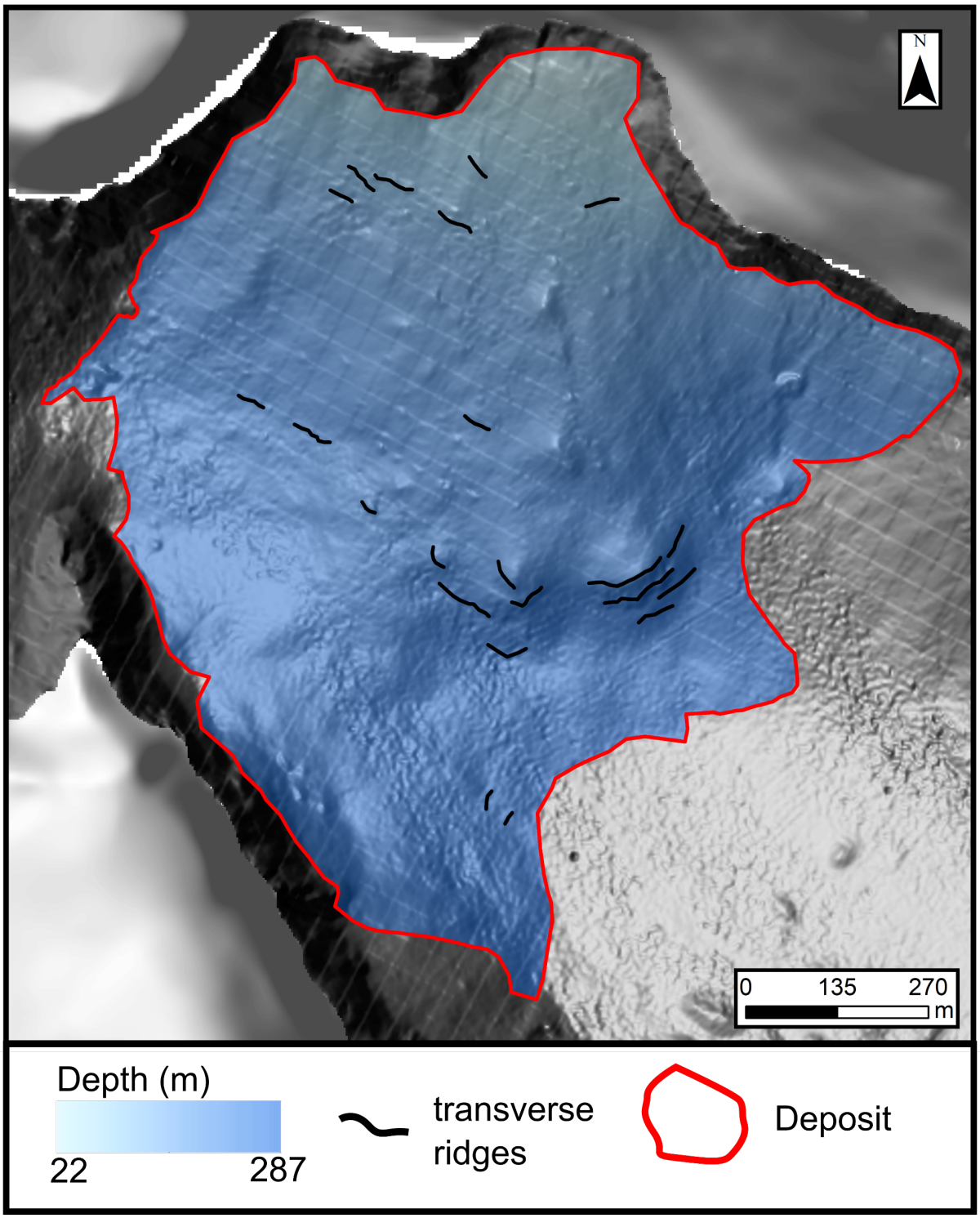

Figure A.41. Interpreted morphology of RA11 subaqueous deposit.

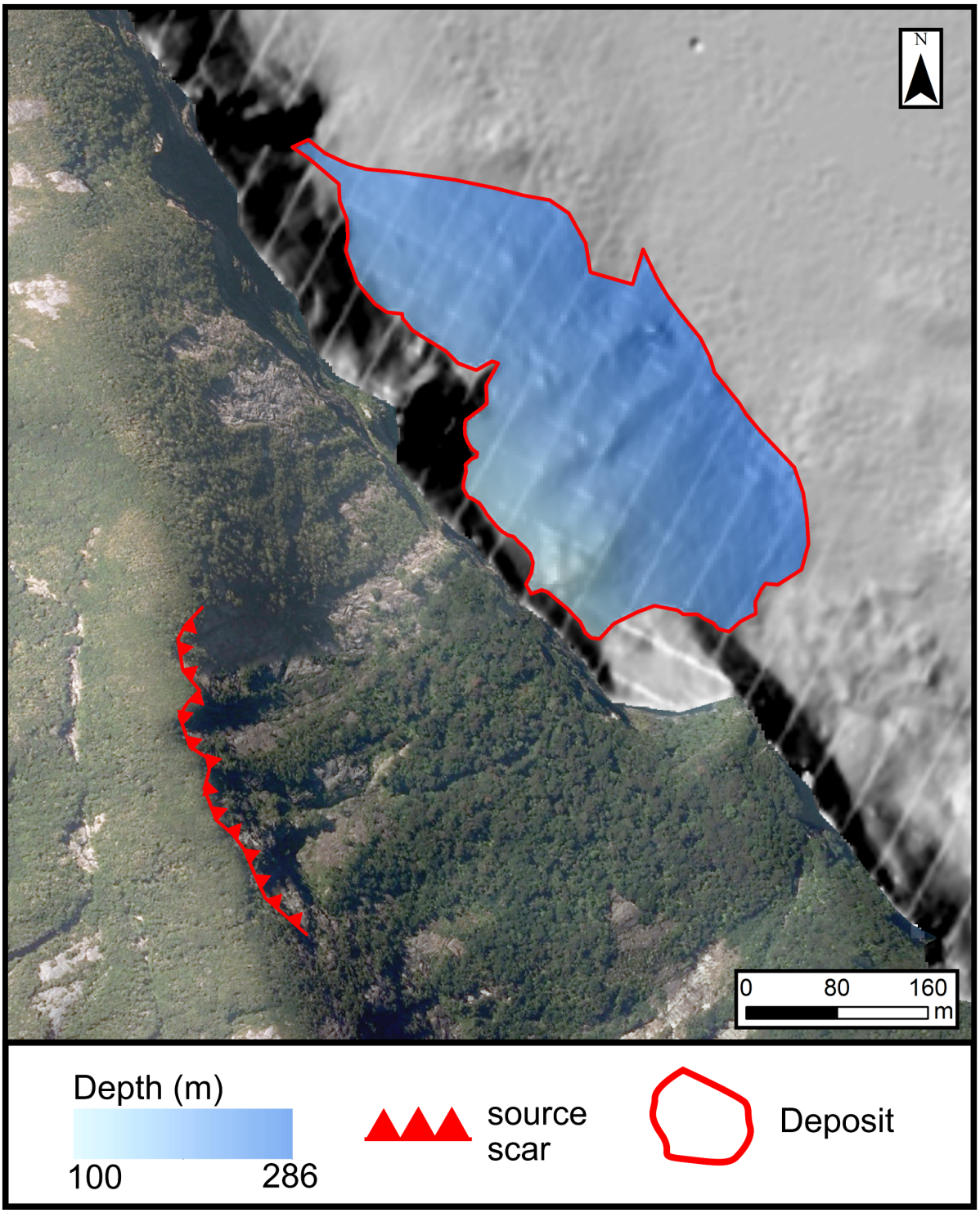

Figure A.42. RA12 subaerial and subaqueous deposit and source scar area. Imagery available under Creative Commons 4.0. Copyright is owned by The Southland Consortium (Southland District Council, Gore District Council, Environment Southland, and Department of Conservation).

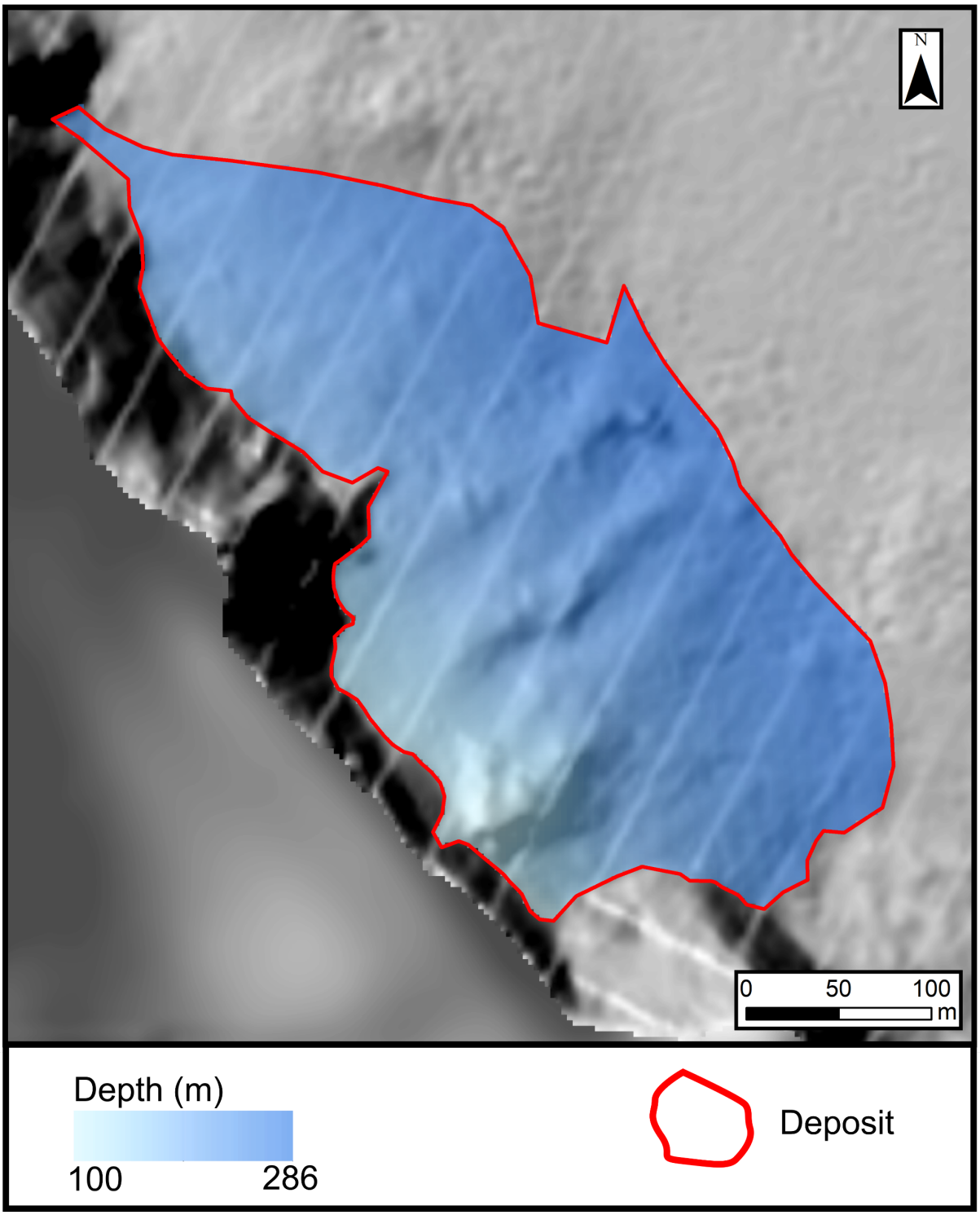

Figure A.43. Detailed, uninterpreted morphology of RA12 subaqueous deposit.

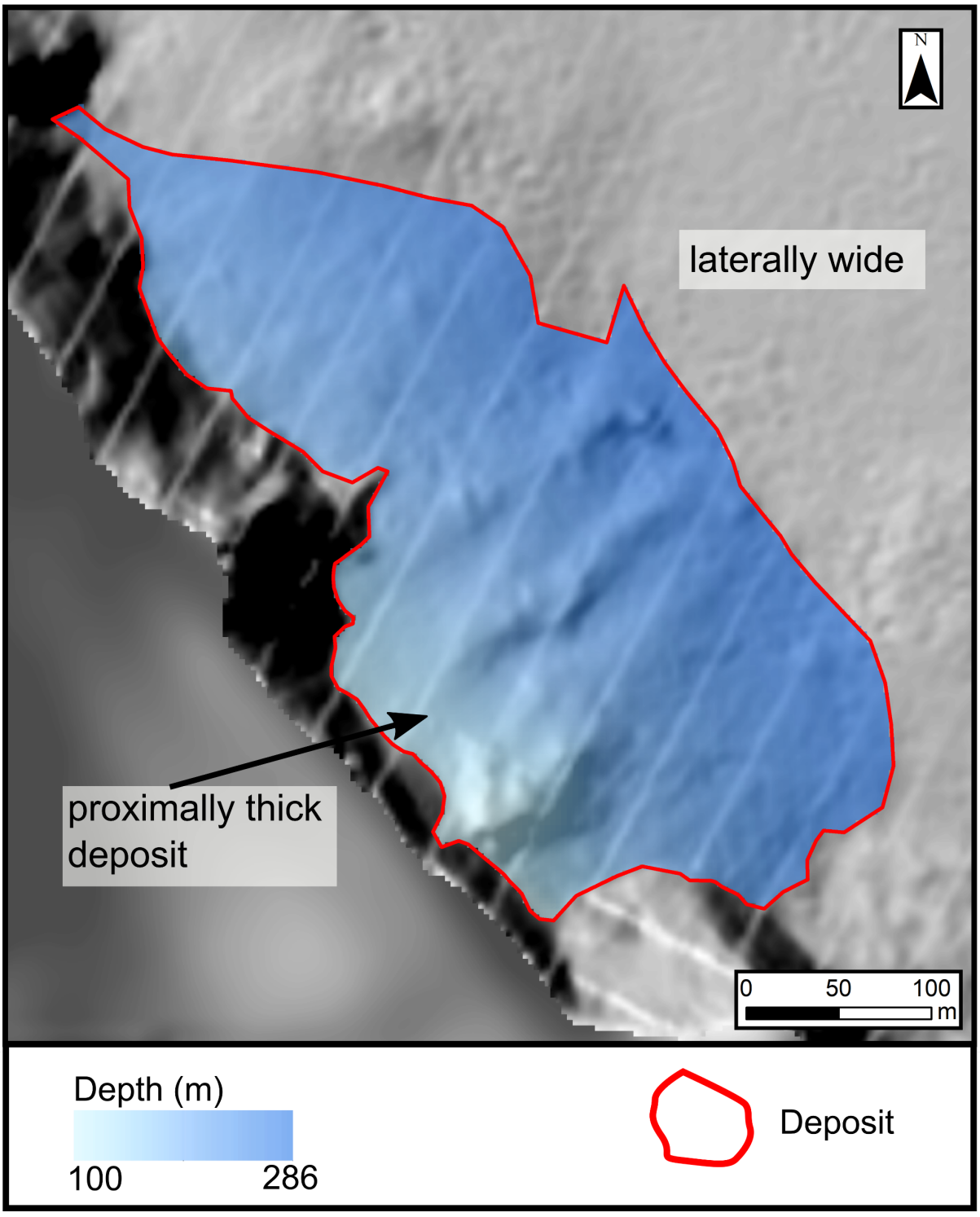

Figure A.44. Interpreted morphology of RA12 subaqueous deposit.

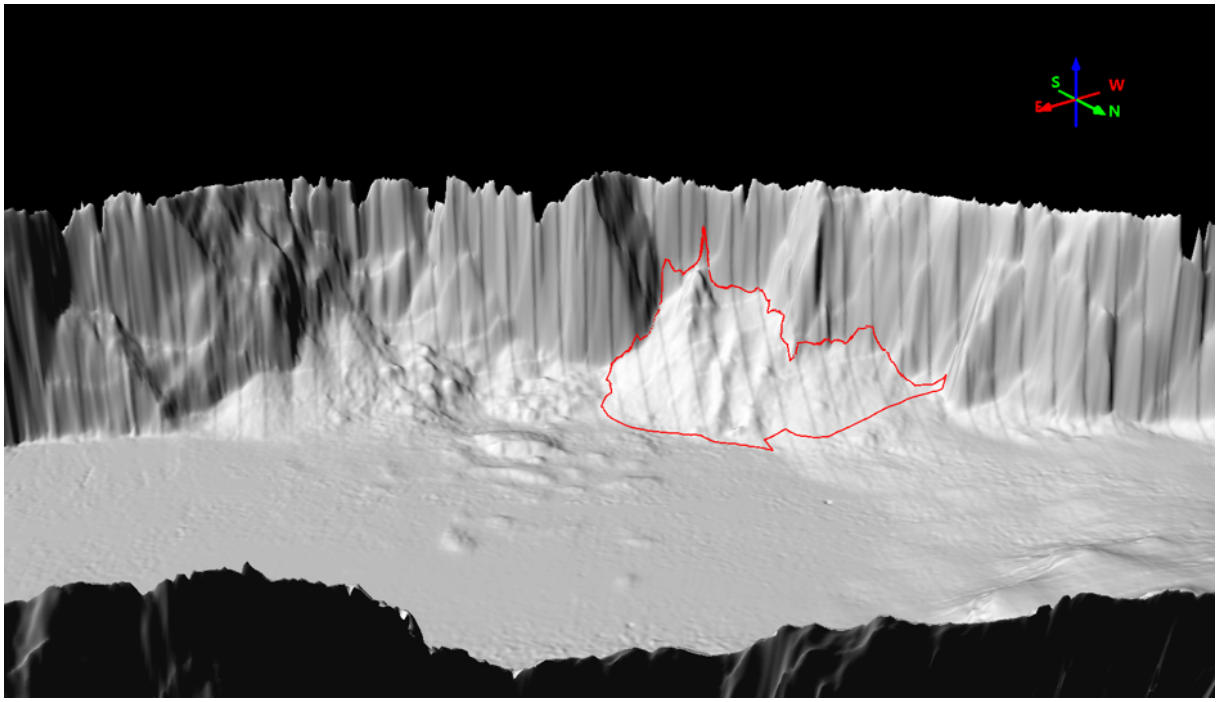

Figure A.45. 3D perspective view of RA12 subaqueous deposit with 1.5x vertical exaggeration.

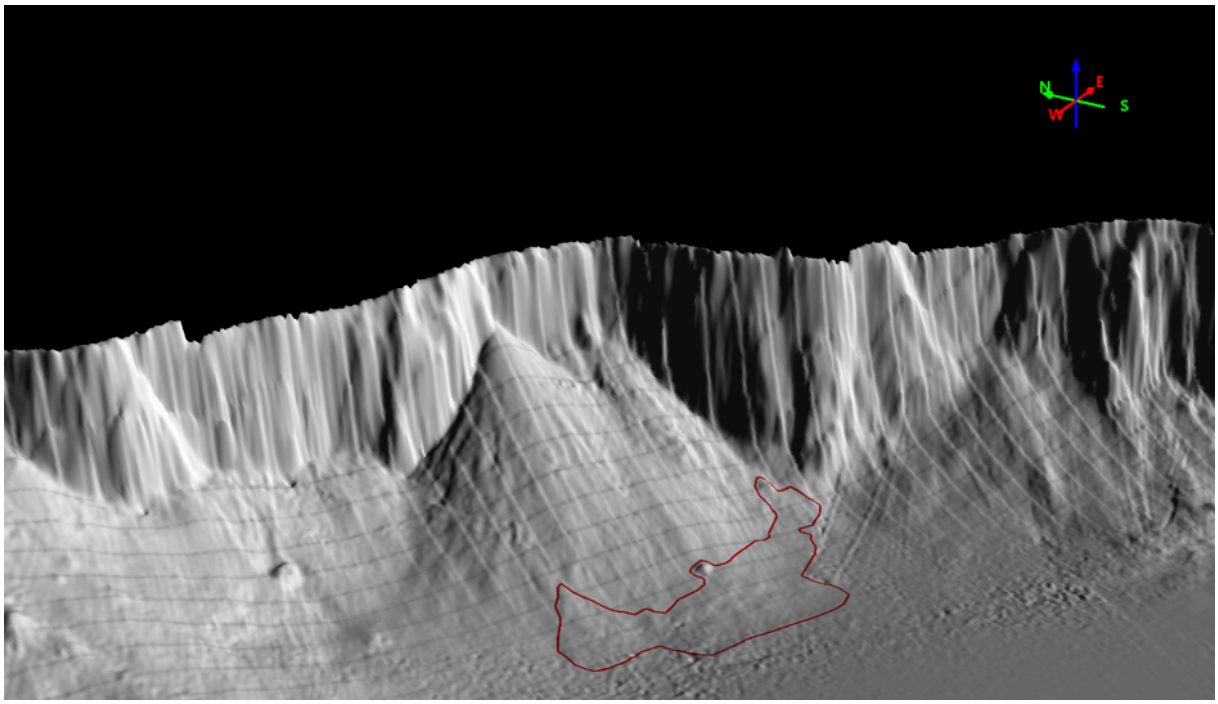

Figure A.46. 3D perspective view of RA13 subaqueous deposit with 1.5x vertical exaggeration.

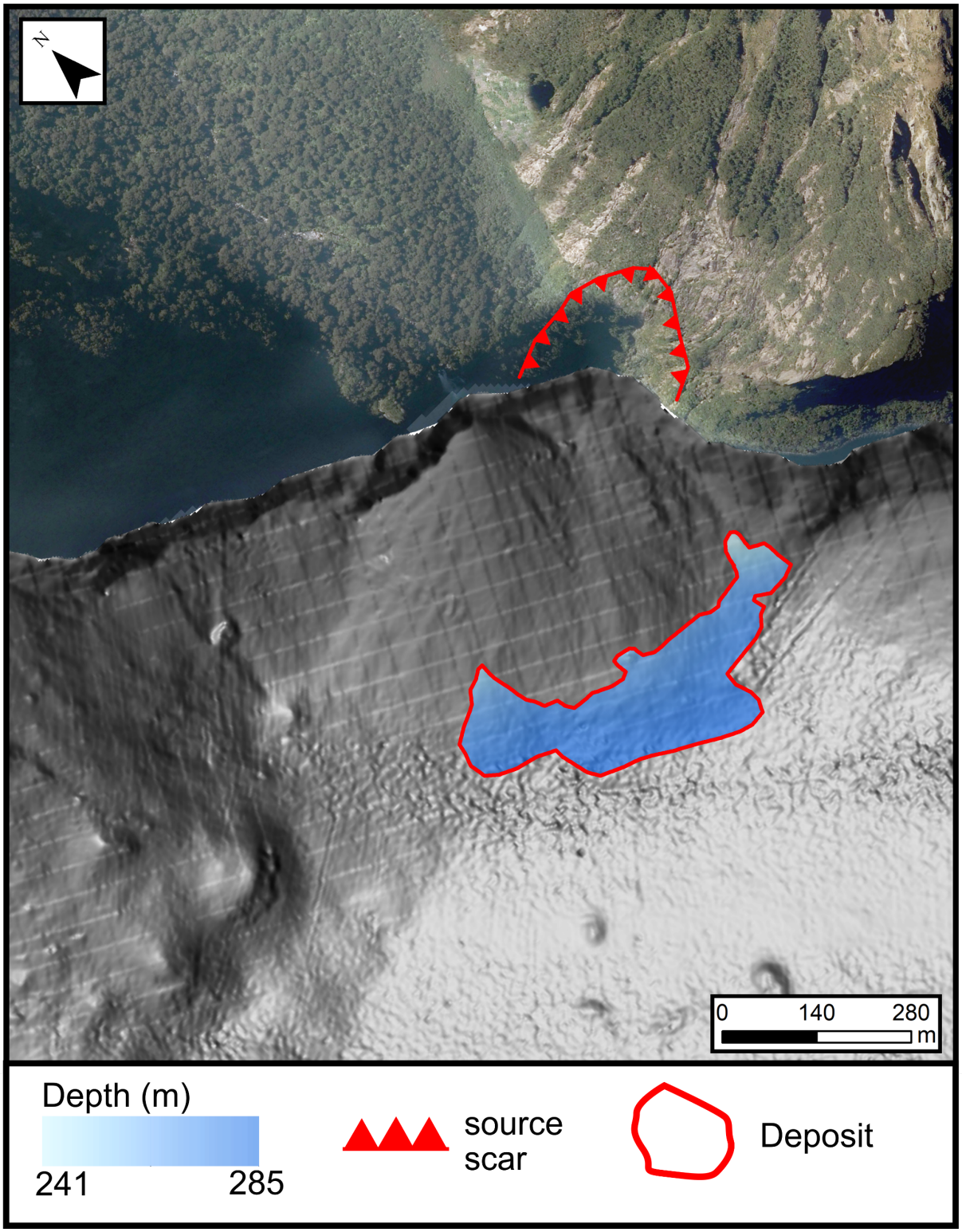

Figure A.47. RA13 subaerial and subaqueous deposit and source scar area. Imagery available under Creative Commons 4.0. Copyright is owned by The Southland Consortium (Southland District Council, Gore District Council, Environment Southland, and Department of Conservation).

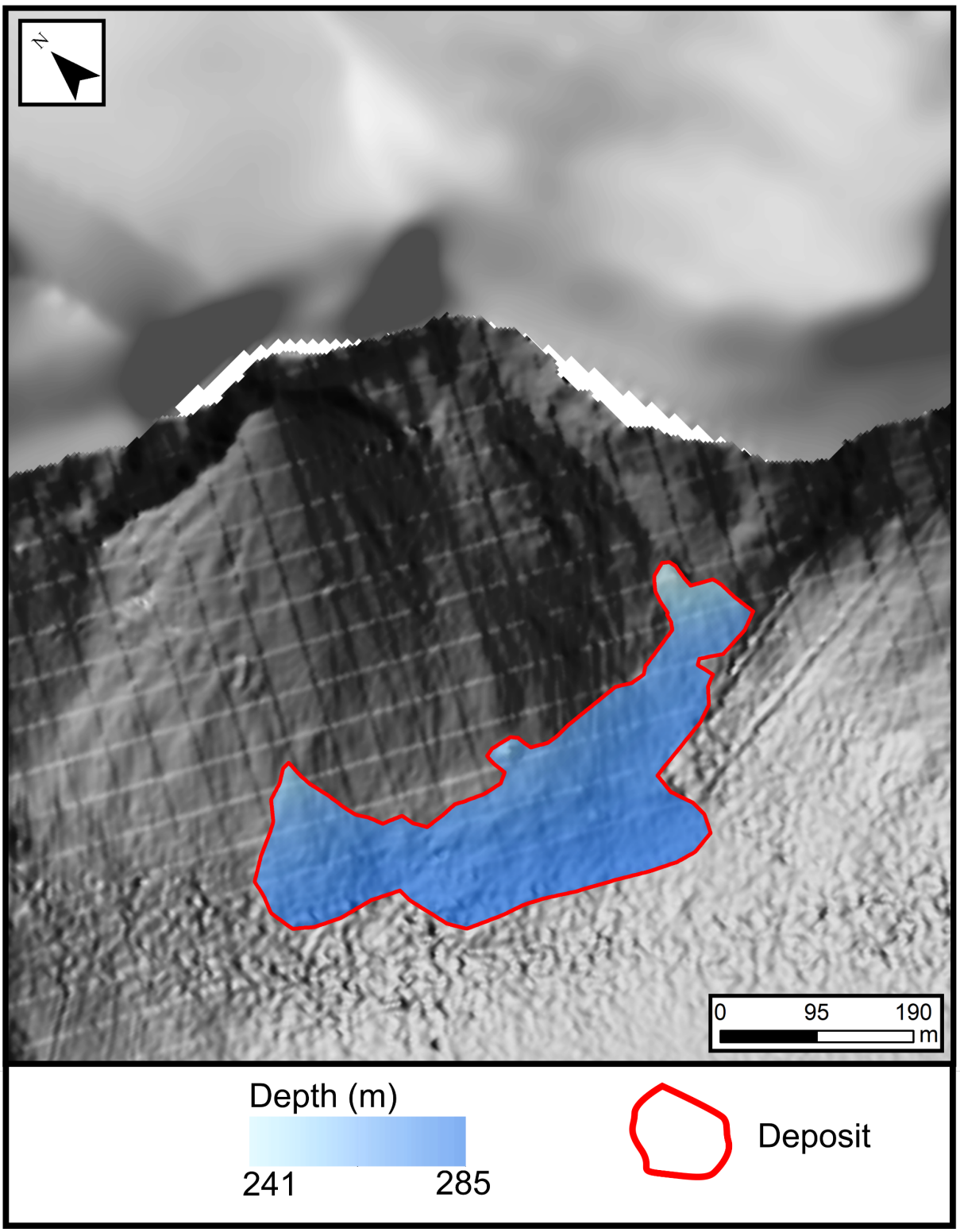

Figure A.48. Detailed, uninterpreted morphology of RA13 subaqueous deposit.

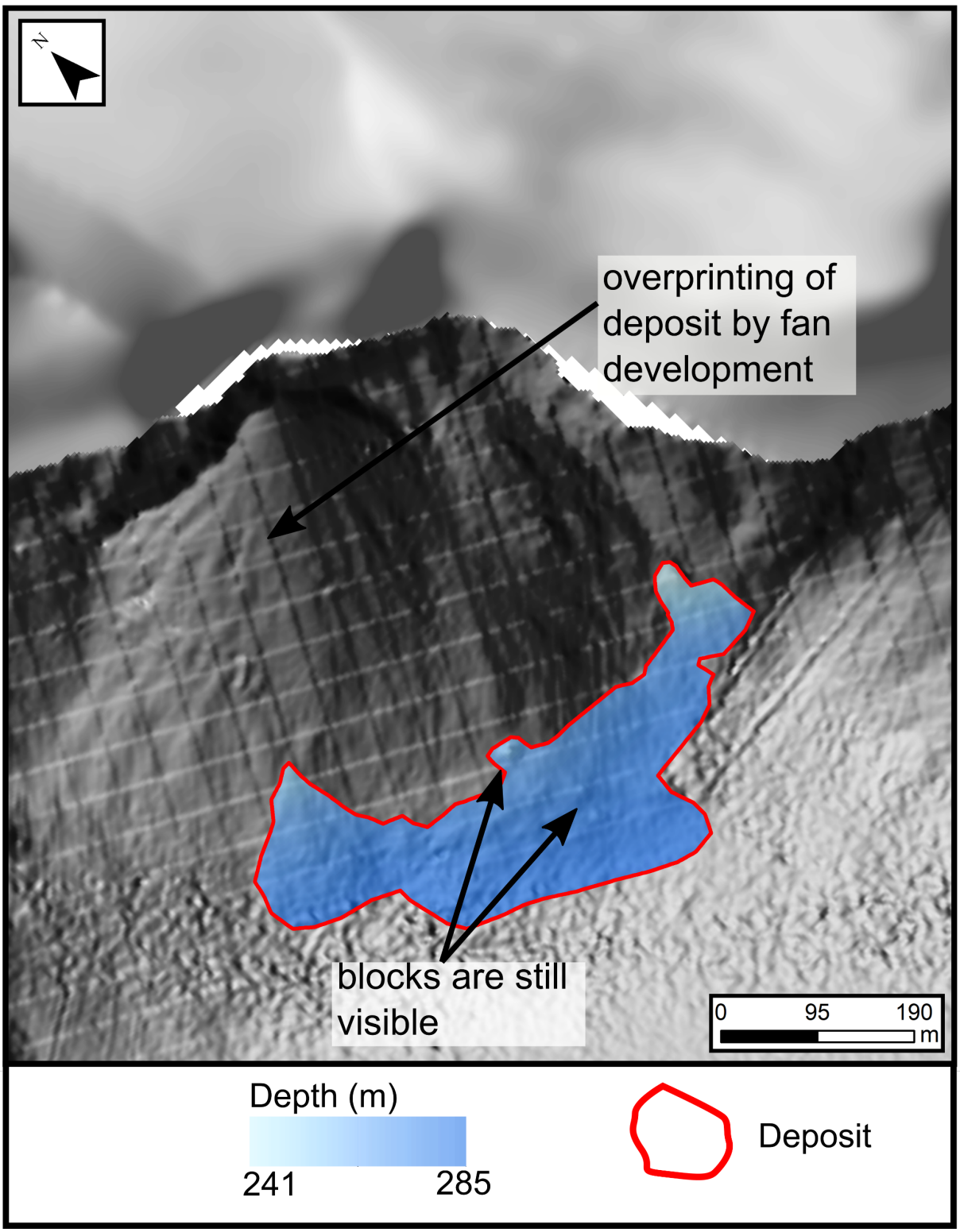

Figure A.49. Interpreted morphology of RA13 subaqueous deposit.

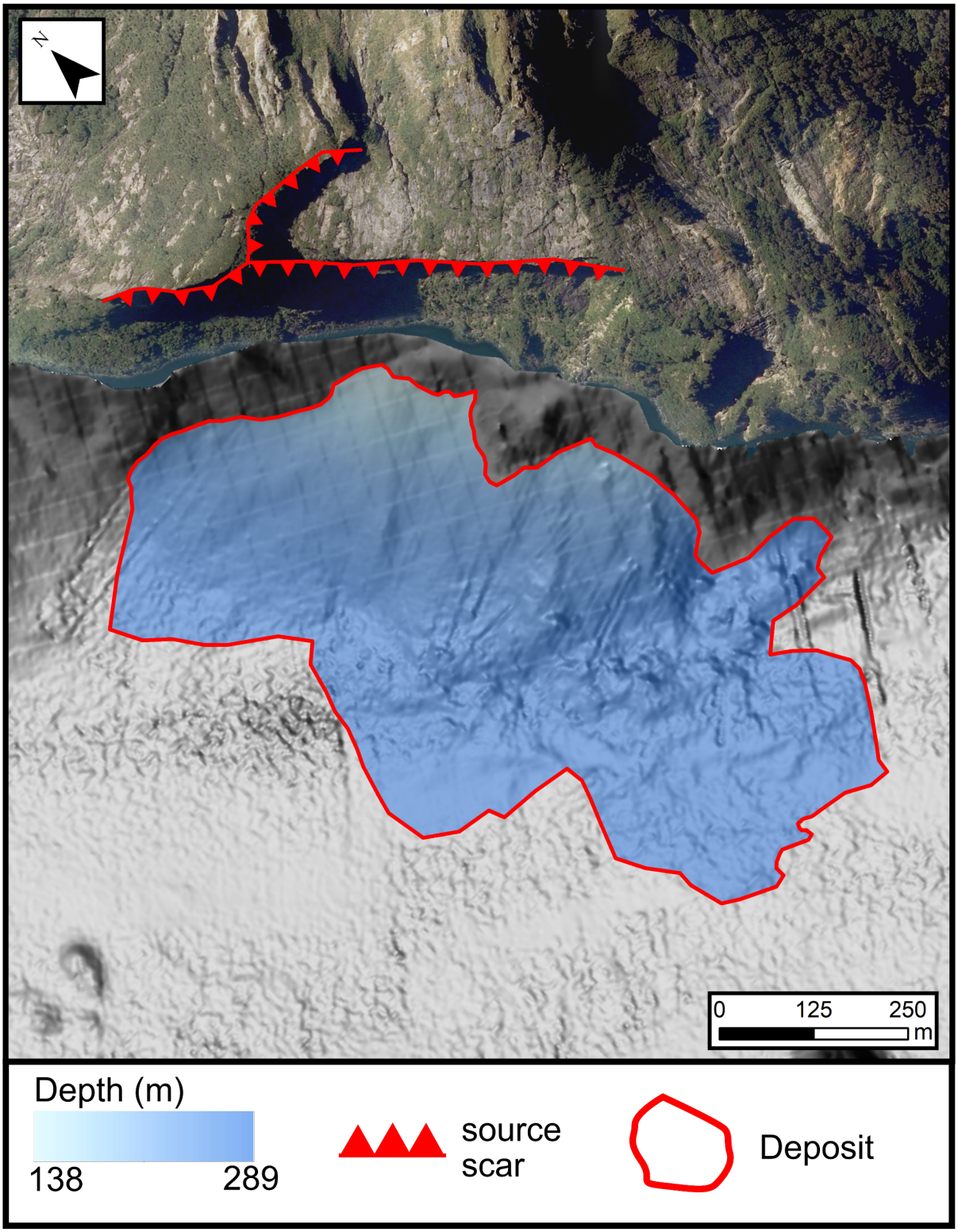

Figure A.50. RA14 subaerial and subaqueous deposit and source scar area. Imagery available under Creative Commons 4.0. Copyright is owned by The Southland Consortium (Southland District Council, Gore District Council, Environment Southland, and Department of Conservation).

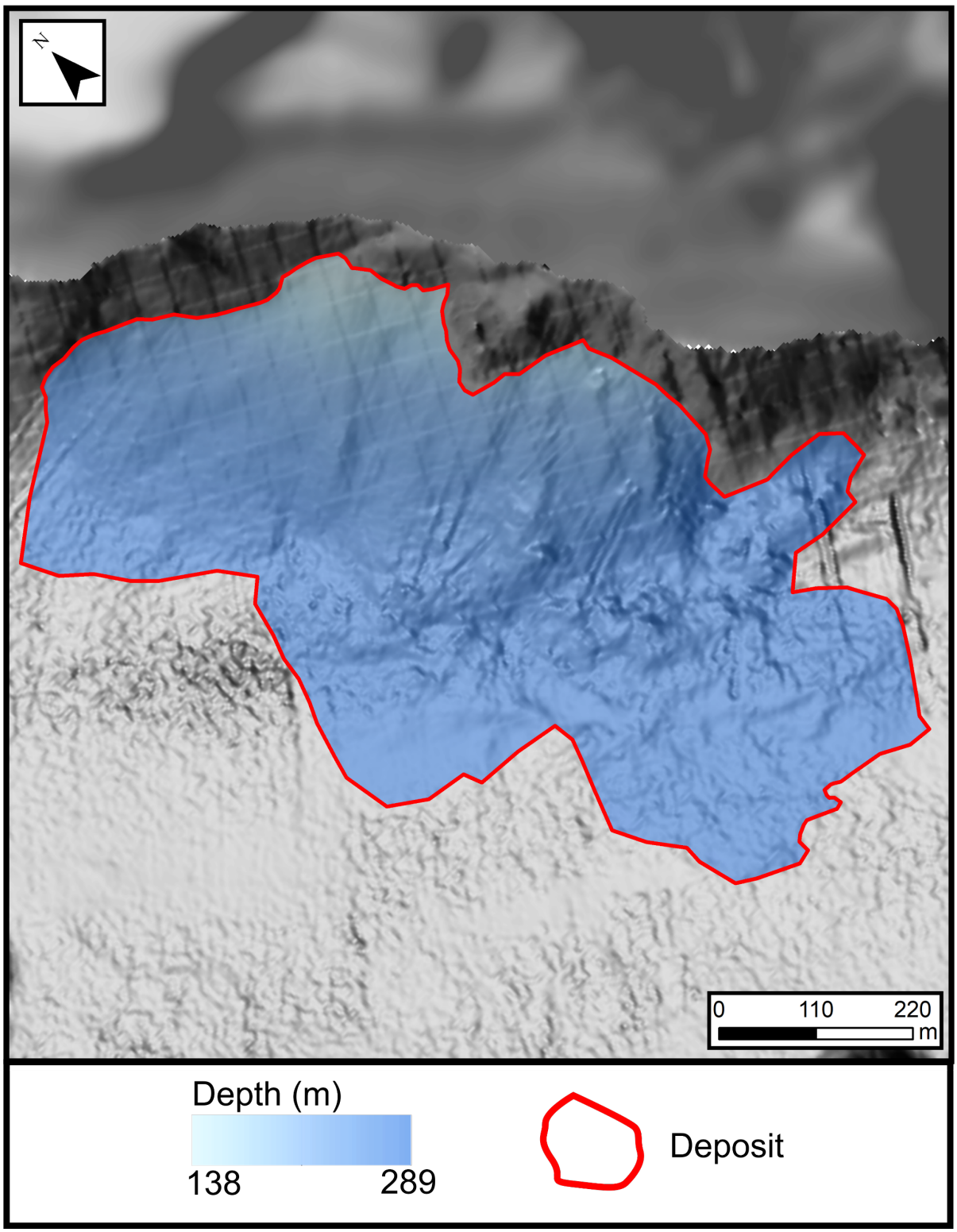

Figure A.51. Detailed, uninterpreted morphology of RA14 subaqueous deposit.

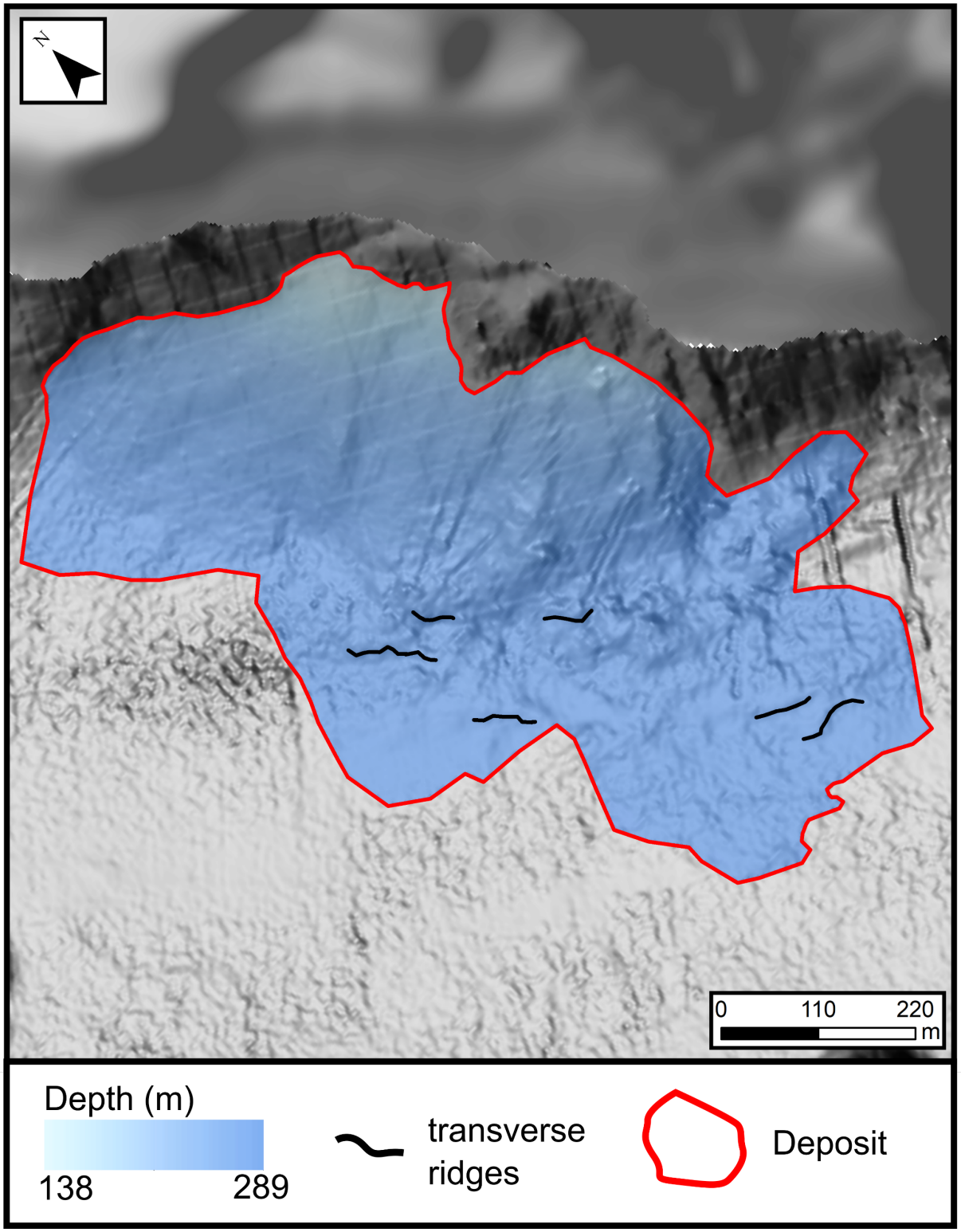

Figure A.52. Interpreted morphology of RA14 subaqueous deposit.

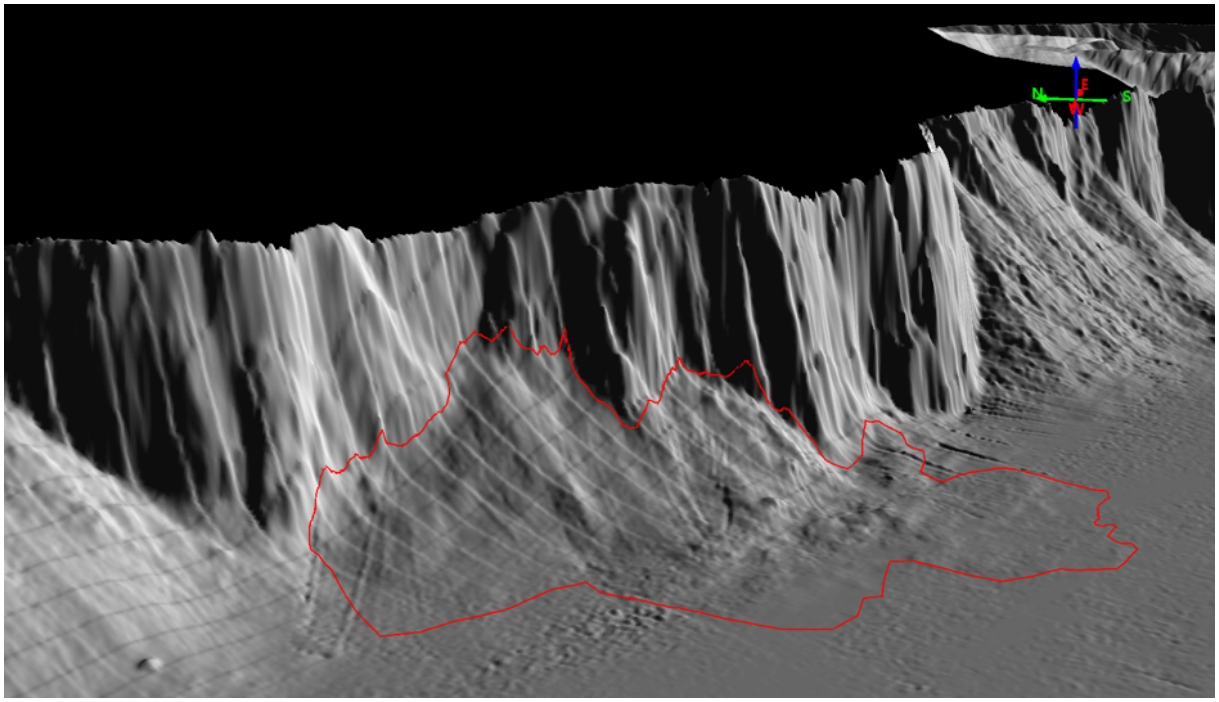

Figure A.53. 3D perspective view of RA14 subaqueous deposit with 1.5x vertical exaggeration.

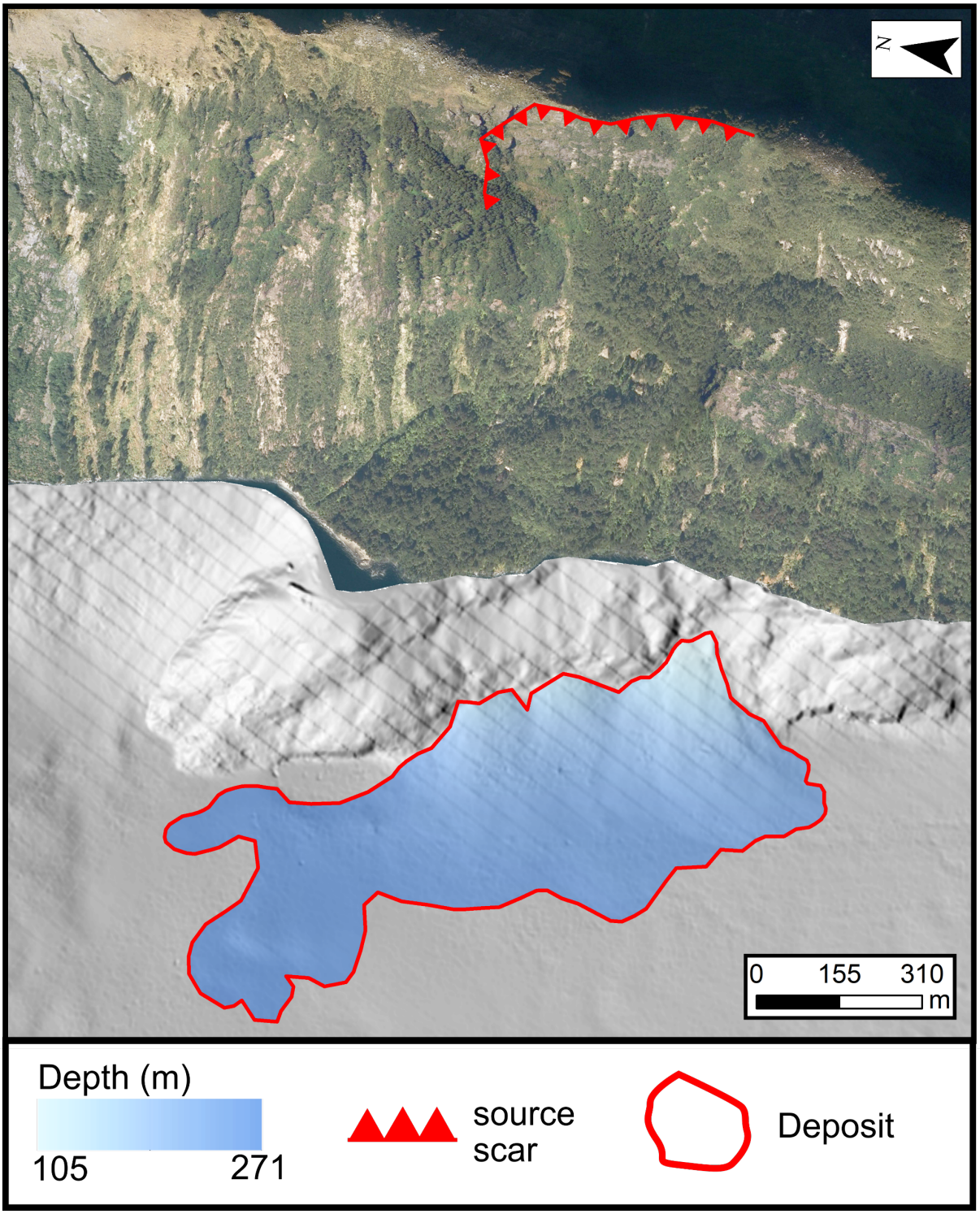

Figure A.54. RA15 subaqueous deposit and source scar area. Imagery available under Creative Commons 4.0. Copyright is owned by The Southland Consortium (Southland District Council, Gore District Council, Environment Southland, and Department of Conservation).

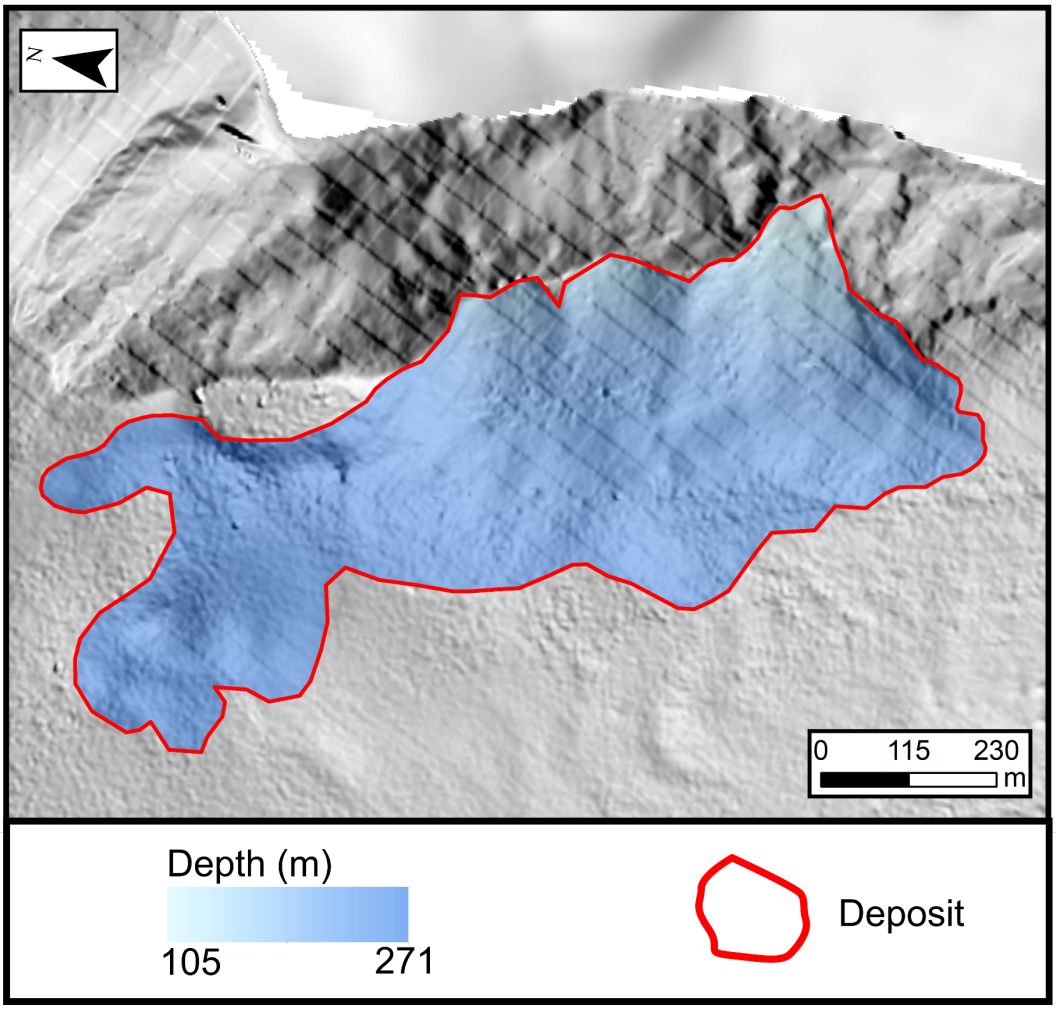

Figure A.55. Detailed, uninterpreted morphology of RA15 subaqueous deposit.

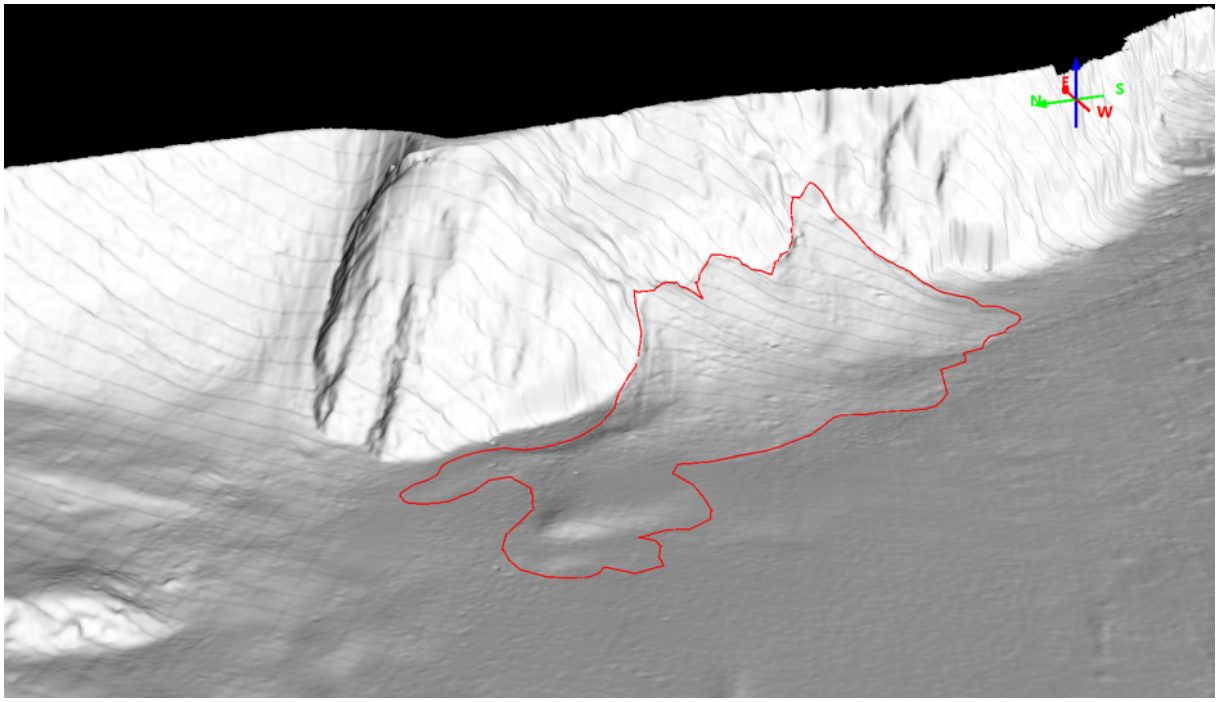

Figure A.56. 3D perspective view of RA15 subaqueous deposit with 1.5x vertical exaggeration.

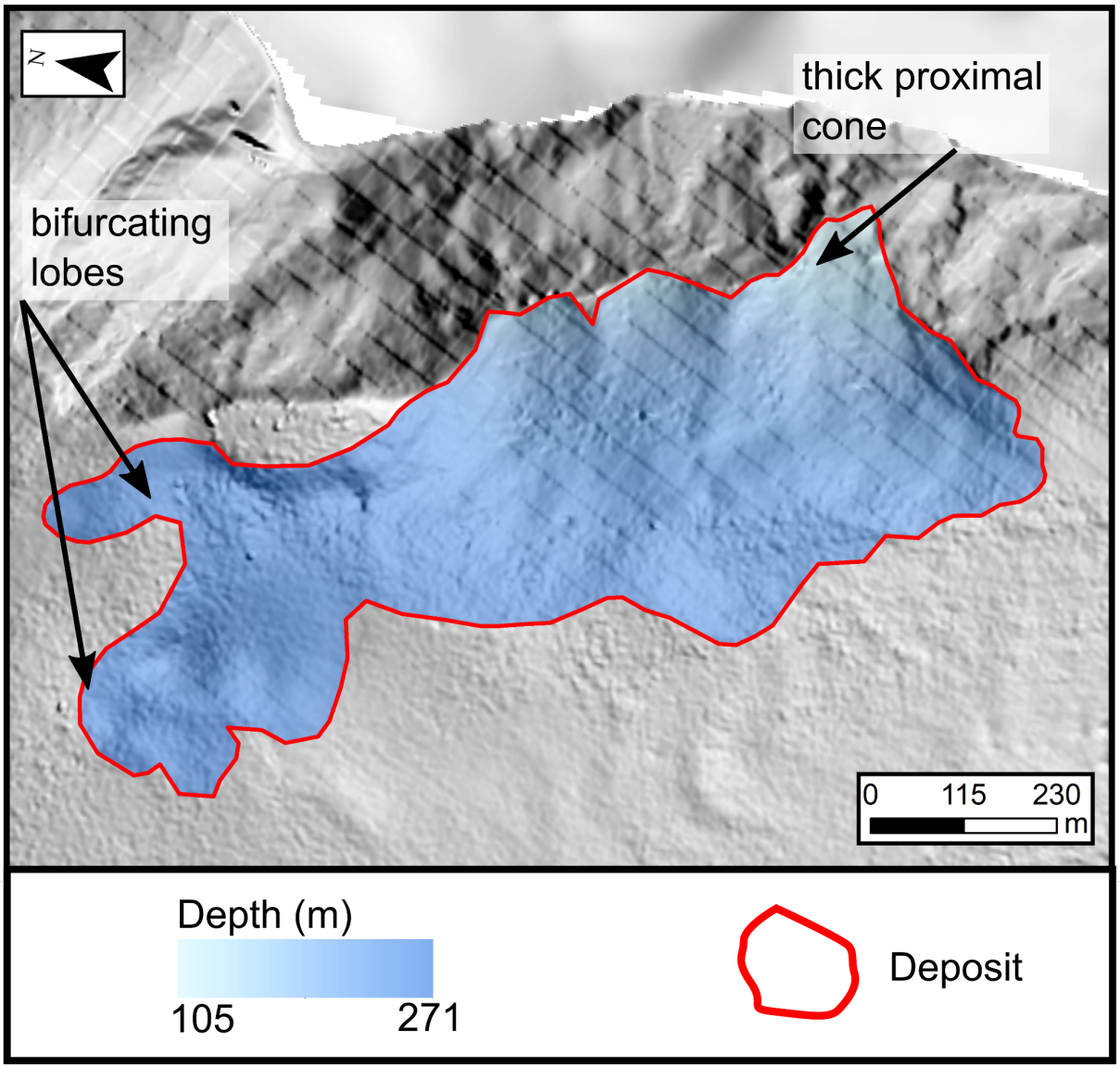

Figure A.57. Interpreted morphology of RA15 subaqueous deposit.

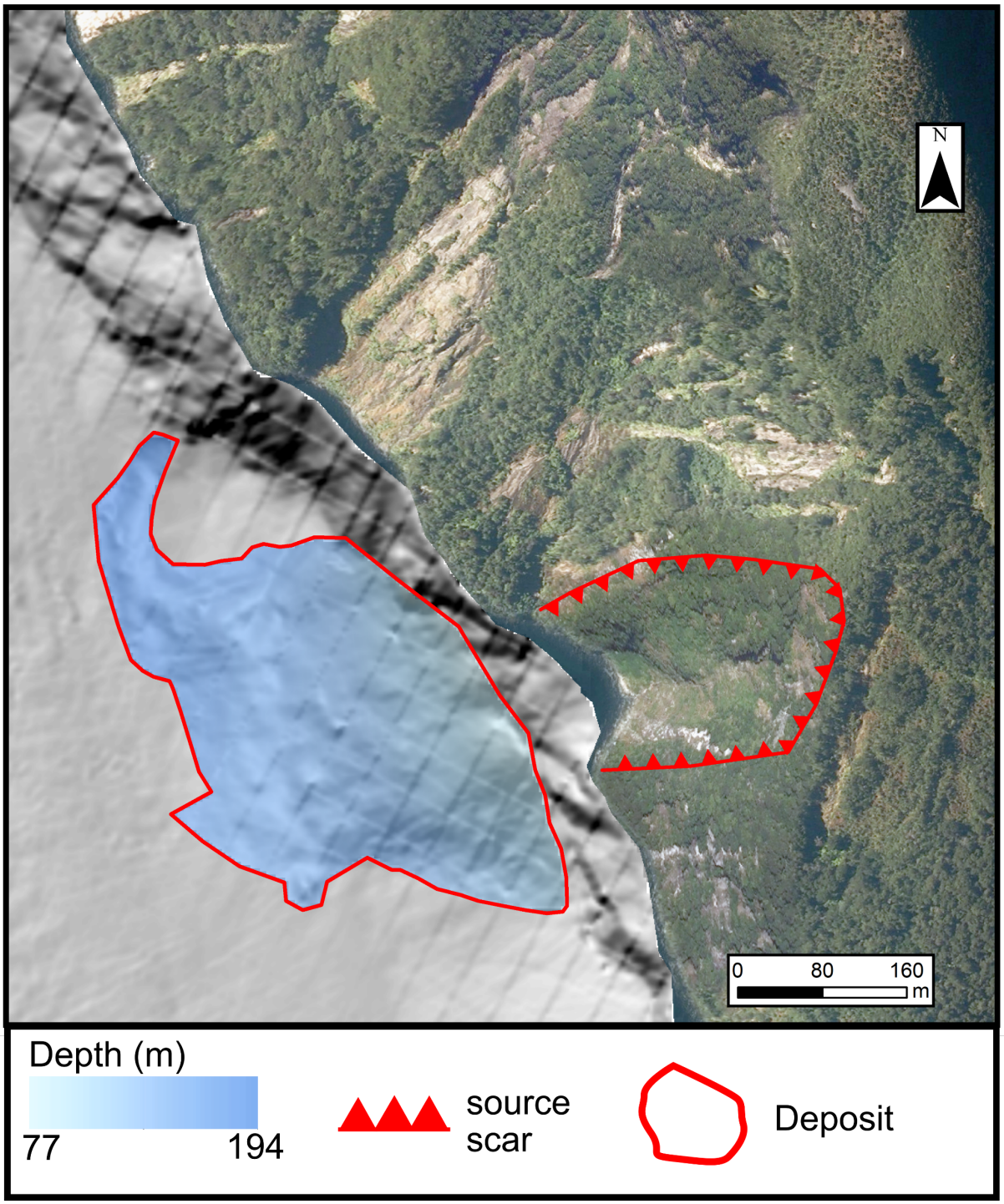

Figure A.58. RA16 subaqueous deposit and source scar area. Imagery available under Creative Commons 4.0. Copyright is owned by The Southland Consortium (Southland District Council, Gore District Council, Environment Southland, and Department of Conservation).

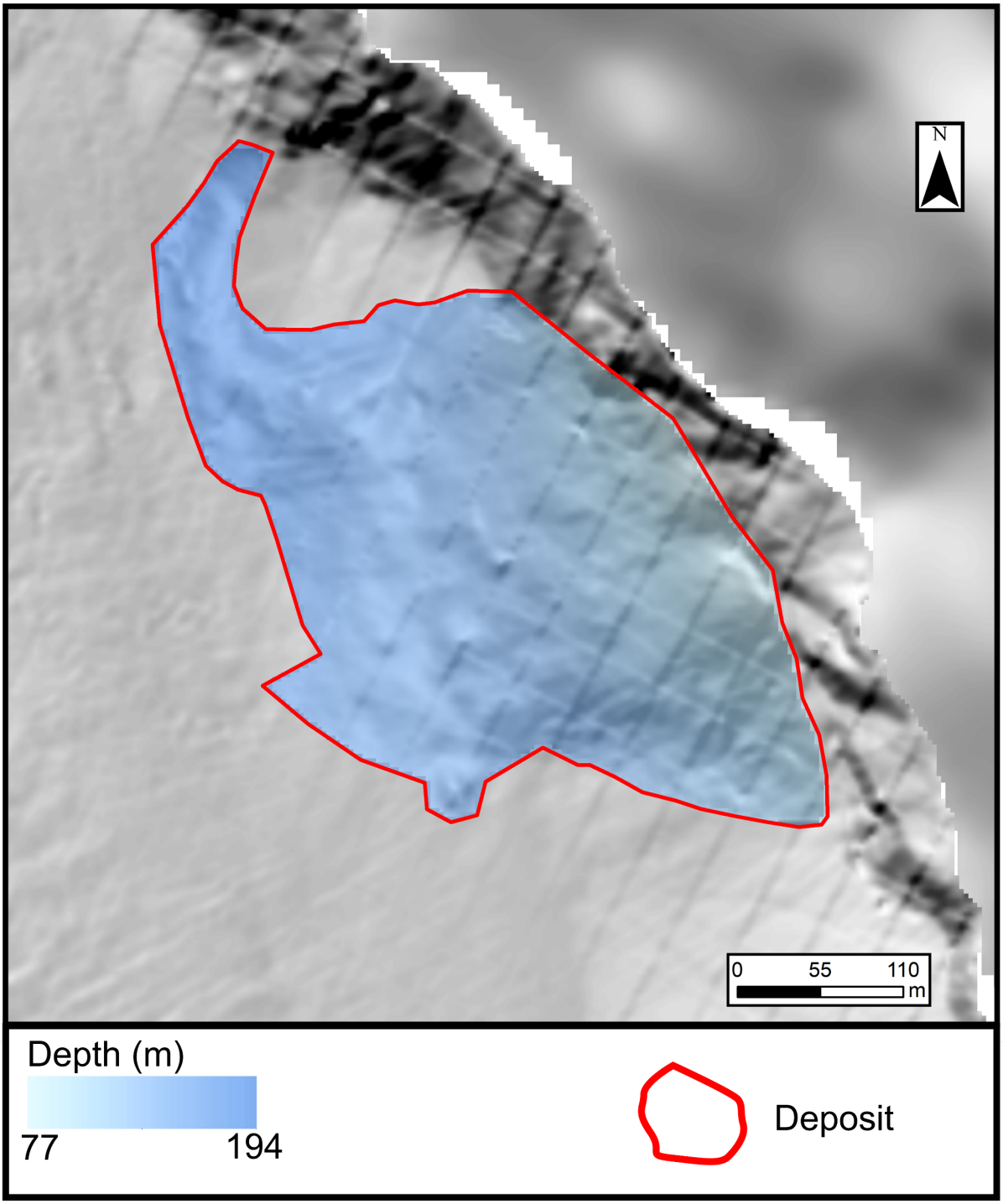

Figure A.59. Detailed, uninterpreted morphology of RA16 subaqueous deposit.

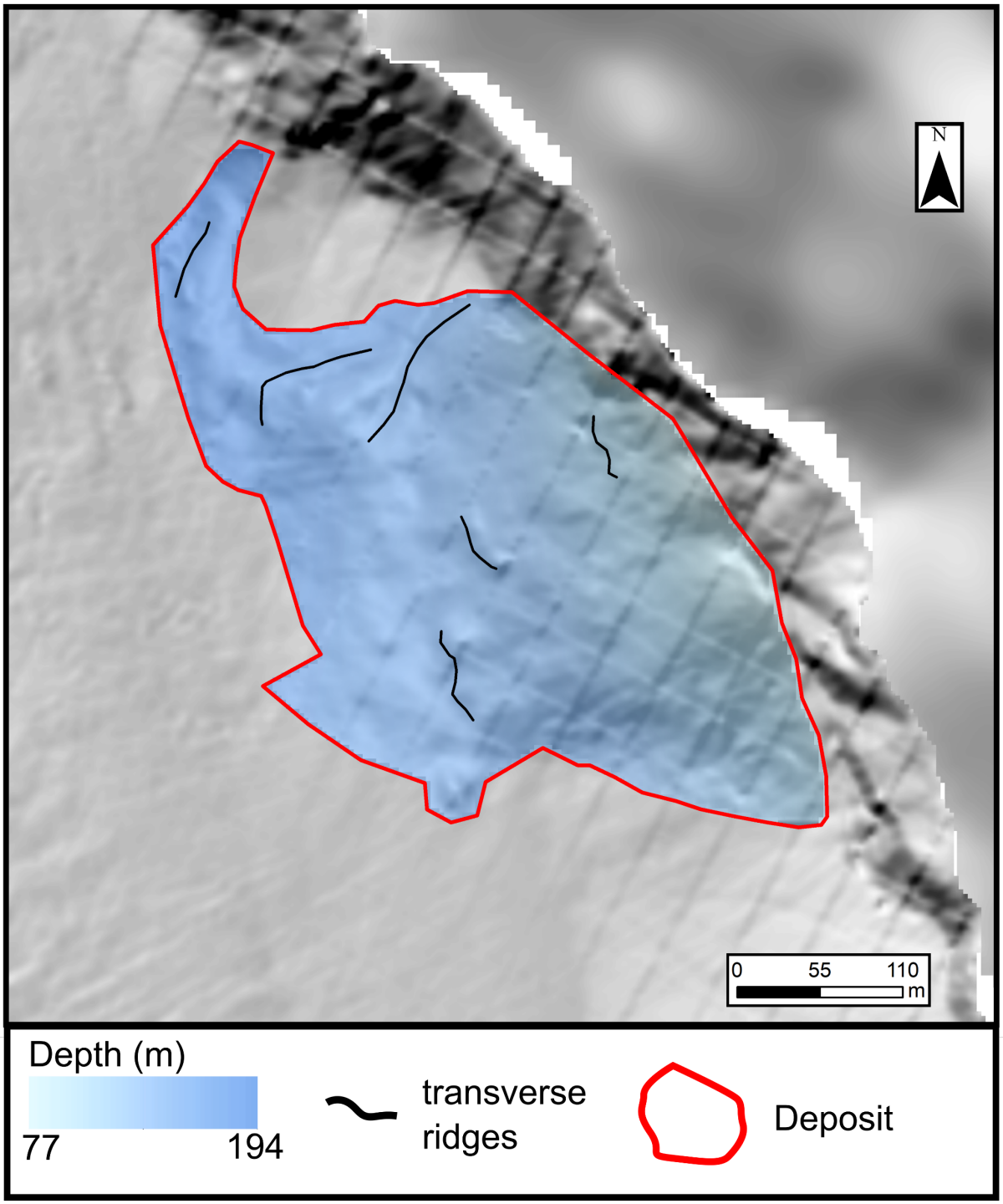

Figure A.60. Interpreted morphology of RA16 subaqueous deposit.

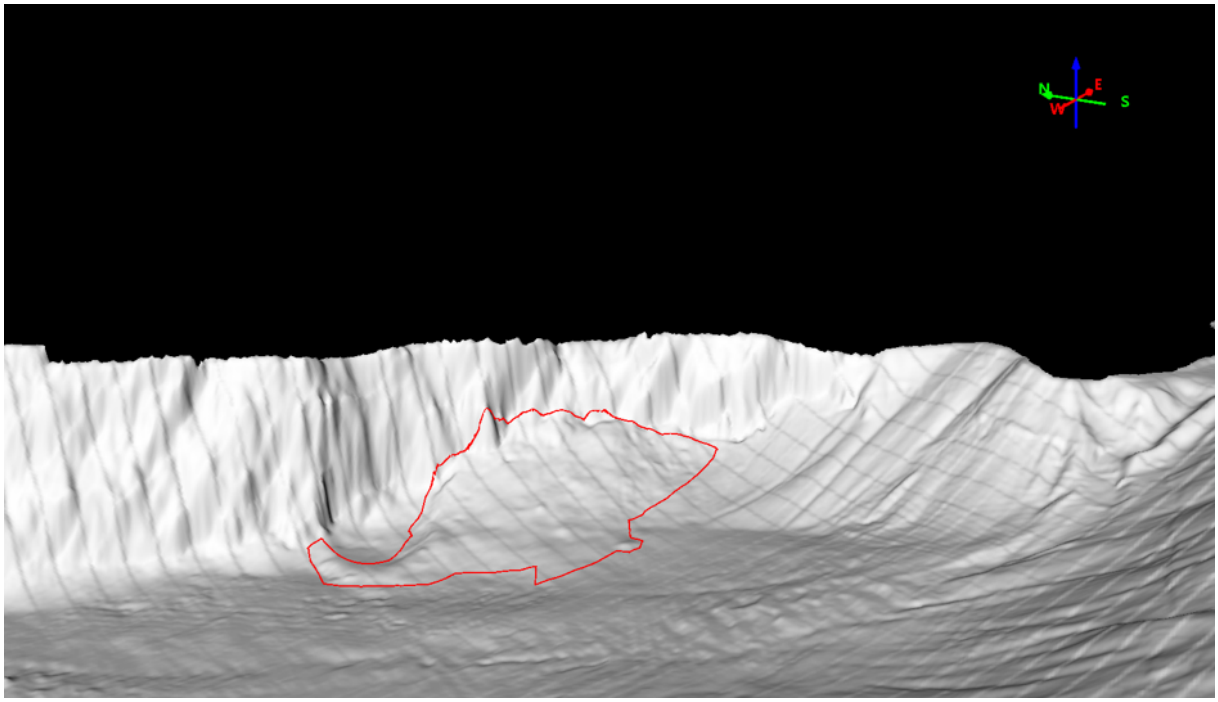

Figure A.61. 3D perspective view of RA16 subaqueous deposit with 1.5x vertical exaggeration.

Appendix B. DAN3D best fit model parameters from cases in literature

Table B.0.1. Summary of DAN3D case parameters. FID 1-44 taken from Aaron and McDougall (2019), and references therein; 45-51 from Sosio *et al.* (2012a,b), 52-56 from this study; 57 from Mazzanti and Bozzano (2009); 58 from Schleier *et al.,* (2017); and 59 from Mazzanti and Bozzano (2011).

ID	Name	RA type	Path material	Frictional rheology	Voellmy rheology		References
				Friction angle (°)	Friction coefficient	turbulence	
1	Zymoetz	RA	saturated sediments	-	0.11	1600	(Schwab *et al.*, 2003; Boultbee *et al.*, 2006; McDougall *et al.*, 2006)
2	Crammont	RA	snow	-	0.17	300	(Deline *et al.*, 2011)
3	Six des Faux Froides	RA	saturated sediments	-	0.13	200	(CREALP, 2001; McDougall and Hungr, 2006)
4	Huascaran	GRA	glacier ice	-	0.05	1700	(Plafker and Ericksen, 1978; Chalindar, 2005; Evans, Bishop, *et al.*, 2009)
5	Kolka	GRA	glacier ice	-	0.05	1000	(Huggel *et al.*, 2005; McDougall, 2006; Evans, Tutubalina, *et al.*, 2009)
6	Mt Meager	RA	saturated sediments	-	0.05	500	(Guthrie *et al.*, 2012; Moretti *et al.*, 2015; McDougall, 2017)
7	Mt Steele	GRA	glacier ice	-	0.14	2100	(Lipovsky *et al.*, 2008)
8	Nomash	RA	saturated sediments	-	0.06	400	(McDougall and Hungr, 2005; McDougall, 2006)
9	Sherman	GRA	glacier ice	-	0.03	2000	(McSaveney, 1978; Sosio, Crosta, Chen, *et al.*, 2012)
10	Thurweisser	GRA	glacier ice	-	0.05	1000	(Poisel *et al.*, 2008; Sosio *et al.*, 2008; Favreau *et al.*, 2010)
11	McAuley	RA	saturated sediments	-	0.1	500	(McDougall, 2006; Brideau *et al.*, 2012)
12	Val Pola	RA	saturated sediments	-	0.27	300	(Crosta *et al.*, 2004; McDougall, 2006; Pirulli and Mangeney, 2008)
13	Avalanche Lake	RA	saturated sediments	-	0.1	1000	(Evans *et al.*, 1994; Aaron and Hungr, 2016a)
14	Goldau	RA	saturated sediments	-	0.07	500	(Berner, 2004; Thuro *et al.*, 2006; Fitze, 2010; Aaron and Hungr, 2016b)

ID	Name	RA type	Path material	Frictional rheology	Voellmy rheology		References
				Friction angle (°)	Friction coefficient	Turbulence	
15	Mystery Creek	RA	saturated sediments	-	0.16	500	(Eisbacher, 1983; Evans and Savigny, 1994; Nichol *et al.*, 2002)
16	Turnoff Creek	RA	saturated sediments	-	0.15	600	(Beguería, van Hess, *et al.*, 2009)
17	Madison Canyon	RA	unsaturated sediment	-	0.23	900	(Hadley, 1978; Wolter *et al.*, 2016)
18	Chisca	RA	saturated sediments	-	0.16	750	(Geertsema *et al.*, 2006)
19	Hope	RA	saturated sediments	-	0.24	750	(Mathews and McTaggart, 1978; Hungr and Evans, 1996)
20	West Salt Creek	RA	saturated sediments	Bingham rheology used for runout			(White *et al.*, 2015; Coe *et al.*, 2016; Aaron *et al.*, 2017)
21	Frank	RA	Saturated sediments	-	0.17	500	(Cruden and Krahn, 1978; Cruden and Hungr, 1986; McDougall, 2006)
22	Guinsaugon	RA	saturated sediments	-	0.1	500	(Evans *et al.*, 2007; Catane *et al.*, 2008; Guthrie *et al.*, 2009)
			flooded field		0.04	700	
23	Bingham Canyon 1	RA	bedrock	26	-	-	(Aaron *et al.*, 2017; Moore *et al.*, 2017)
23	Bingham Canyon 2	RA	bedrock	26	-	-	(Aaron *et al.*, 2017; Moore *et al.*, 2017)
24	Sentinel	RA	unsaturated sediment	-	0.27	200	(Castleton *et al.*, 2016)
25	Daubensee	RA	bedrock	22	-	-	(Grämiger *et al.*, 2016)
26	Rinderhorn	RA	saturated sediments	-	0.12	700	(Grämiger *et al.*, 2016)
27	Rautispitz	RA	saturated sediments	-	0.17	300	(Nagelisen *et al.*, 2015; Aaron *et al.*, 2017)
28	Platten	RA	saturated sediments	-	0.15	200	(Nagelisen *et al.*, 2015)

ID	Name	RA type	Path material	Frictional rheology	Voellmy rheology		References
				Friction angle (°)	Friction coefficient	turbulence	
29	Chehalis	STS RA (SA+SQ)	bedrock	-	0.32	900	(Si *et al.*, 2018)
30	Martin River 2	GRA	glacier ice	-	0.05	1500	(Sosio, Crosta, Chen, *et al.*, 2012)
31	Martin River unnamed 1	GRA	glacier ice	-	0.04	1000	(Sosio, Crosta, Chen, *et al.*, 2012)
32	Martin River unnamed 2	GRA	glacier ice	-	0.05	1000	(Sosio, Crosta, Chen, *et al.*, 2012)
33	Steller	GRA	glacier ice	-	0.05	1500	(Sosio, Crosta, Chen, *et al.*, 2012)
34	Beccas di Luseney	GRA	glacier ice	-	0.04	1250	(Sosio, Crosta, Chen, *et al.*, 2012)
35	Eperon de la Brenva	GRA	glacier ice	-	0.06	1000	(Sosio, Crosta, Chen, *et al.*, 2012)
36	Bering 3 - Steller	GRA	glacier ice	-	0.05	1000	(Sosio, Crosta, Chen, *et al.*, 2012)
37	Black rapids-west	GRA	glacier ice	-	0.08	1000	(Sosio, Crosta, Chen, *et al.*, 2012)
38	Martin River 3	GRA	glacier ice	-	0.1	1000	(Sosio, Crosta, Chen, *et al.*, 2012)
39	Black rapids-east	GRA	glacier ice	-	0.03	1000	(Sosio, Crosta, Chen, *et al.*, 2012)
40	Bering 2 - Steller	GRA	glacier ice	-	0.03	1000	(Sosio, Crosta, Chen, *et al.*, 2012)
41	Martin River 4	GRA	glacier ice	-	0.03	1000	(Sosio, Crosta, Chen, *et al.*, 2012)
42	Martin River 5	GRA	glacier ice	-	0.06	1000	(Sosio, Crosta, Chen, *et al.*, 2012)
43	Illamna – Red Glacier	GRA	glacier ice	-	0.04	1500	(Sosio, Crosta, Chen, *et al.*, 2012)
44	Mt. Munday	GRA	glacier ice	-	0.07	1000	(Sosio, Crosta, Chen, *et al.*, 2012)
45	Iriga	VDA	Unknown	4.8	-	-	(Sosio, Crosta and Hungr, 2012)
46	Llullaillaco SRTM	VDA	Unknown	4.2	-	-	(Sosio, Crosta and Hungr, 2012)
46	Llullaillaco ASTER	VDA	Unknown	5.3	-	-	(Sosio, Crosta and Hungr, 2012)

ID	Name	RA type	Path material	Frictional rheology	Voellmy rheology		References
				Friction angle (°)	Friction coefficient	turbulence	
47	Mombacho-El crater SRTM	VDA	Unknown	4.5	-	-	(Sosio, Crosta and Hungr, 2012)
47	Mombacho-El crater ASTER	VDA	Unknown	5.8	-	-	(Sosio, Crosta and Hungr, 2012)
48	Pacaya SRTM	VDA	Unknown	4.5	-	-	(Sosio, Crosta and Hungr, 2012)
48	Pacaya ASTER	VDA	Unknown	5	-	-	(Sosio, Crosta and Hungr, 2012)
49	St Helens SRTM	VDA	Unknown	7.5	-	-	(Sosio, Crosta and Hungr, 2012)
49	St Helens ASTER	VDA	Unknown	5	-	-	(Sosio, Crosta and Hungr, 2012)
50	Socompa	VDA	Unknown	3	-	-	(Sosio, Crosta and Hungr, 2012)
51	Shiveluch	VDA	Unknown	7.5	-	-	(Sosio, Crosta and Hungr, 2012)
52	Milford RA1	STS RA (SA)	bedrock	-	0.57	500	this thesis
		STS RA (SQ)	bedrock + fjord-bottom sediments	-	0.57	50	
53	Milford RA2	STS RA (SA)	bedrock	-	0.25	300	this thesis
		STS RA (SQ)	bedrock + fjord-bottom sediments	-	0.1	100	
54	Milford RA3	STS RA (SA)	bedrock	-	0.1	500	this thesis
		STS RA (SQ)	bedrock + fjord-bottom sediments	-	0.1	100	

ID	Name	RA type	Path material	Frictional rheology	Voellmy rheology		References
				Friction angle (°)	Friction coefficient	turbulence	
55	Milford RA4	STS RA (SA)	bedrock	28	0	0	this thesis
		STS RA (SQ)	bedrock + fjord-bottom sediments	-	0.25	100	
56	Milford RA5	STS RA (SA)	bedrock	-	0.1	500	this thesis
		STS RA (SQ)	bedrock + fjord-bottom sediments	-	0.32	100	
57	Lake Albano rockslide	STS RS (SA)	bedrock	28	-	-	(Mazzanti and Bozzano, 2009)
		STS RS (SQ)	not defined	-	0.4	40	
58	Innfjorden rock avalanche 1	STS RA (SA)	unsaturated sediment	-	0.13	600	(Schleier *et al.*, 2017)
		STS RA (SQ)	valley-fill sediments	-	0.09	700	
		STS RA (SQ)	saturated sediments	-	0.03	1000	
59	Scilla Rock avalanche	STS RA (SA)	bedrock	16	-	-	(Mazzanti and Bozzano, 2011)
		STS RA (SQ)	not defined	2.86	0.05	220	

Key

RA	Subaerial rock avalanche
VDA	Volcanic debris avalanche
GRA	Rock avalanche on a glacier
STS RA (SA)	Subaerial to subaqueous rock avalanche (subaerial portion)
STS RA (SQ)	Subaerial to subaqueous rock avalanche (subaqueous portion)
STS RS (SA)	Subaerial to subaqueous rockslide (subaerial portion)
STS RS (SQ)	Subaerial to subaqueous rockslide (subaqueous portion)

Appendix C. Unprocessed sub-bottom profiles from Lake Wānaka

The following figures are the unprocessed versions of the SBP presented within *Chapter 5*.

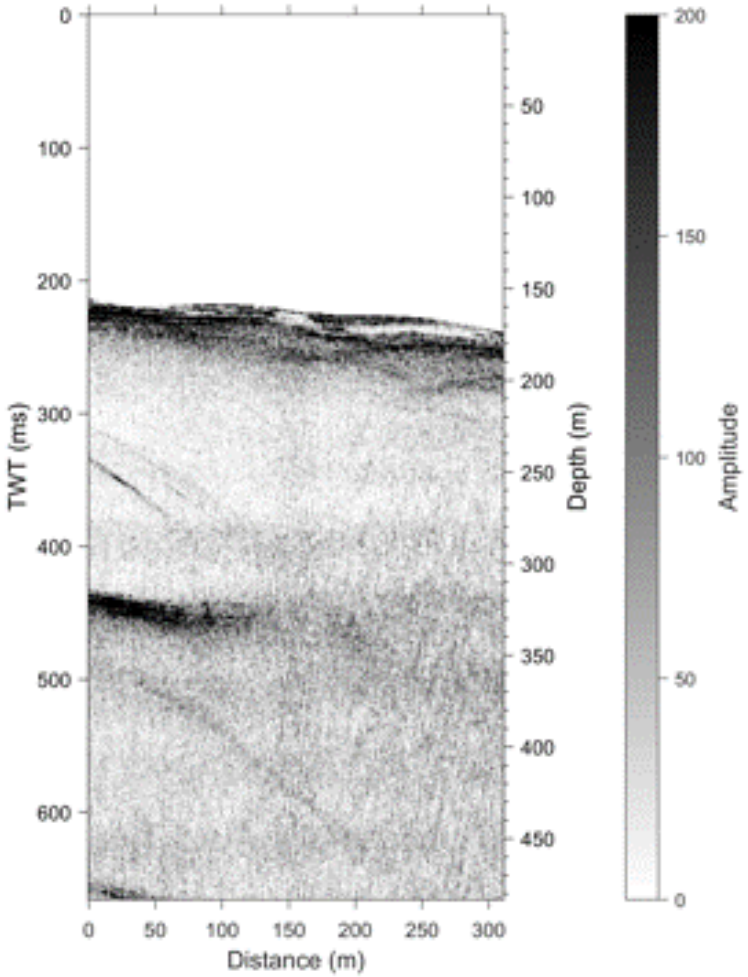

Figure C.1. Unprocessed SBP line of Figure 5.8C

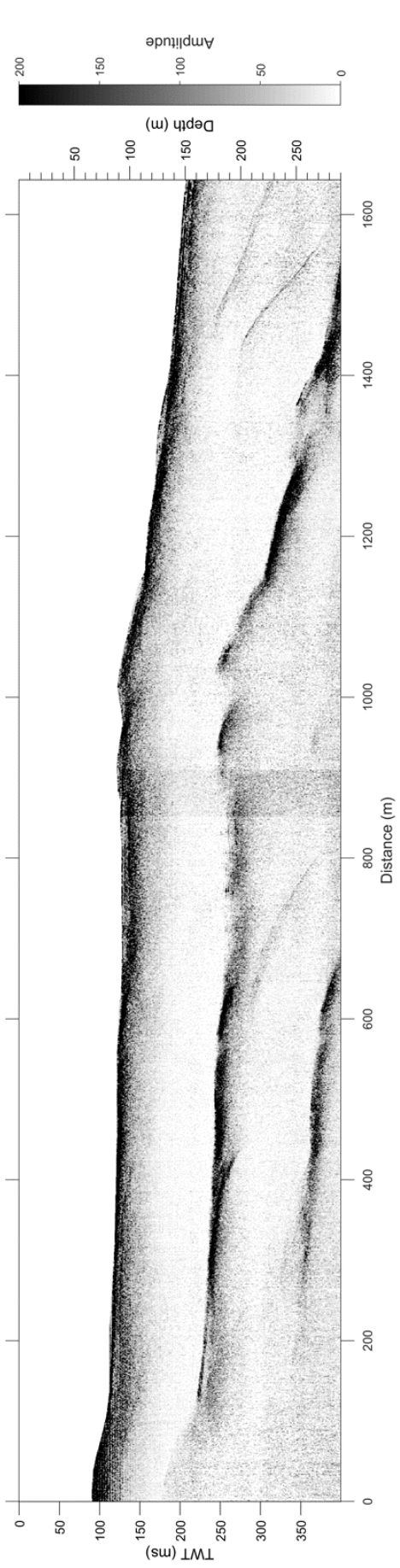

Figure C.2 Unprocessed SBP line of Figure 5.7C

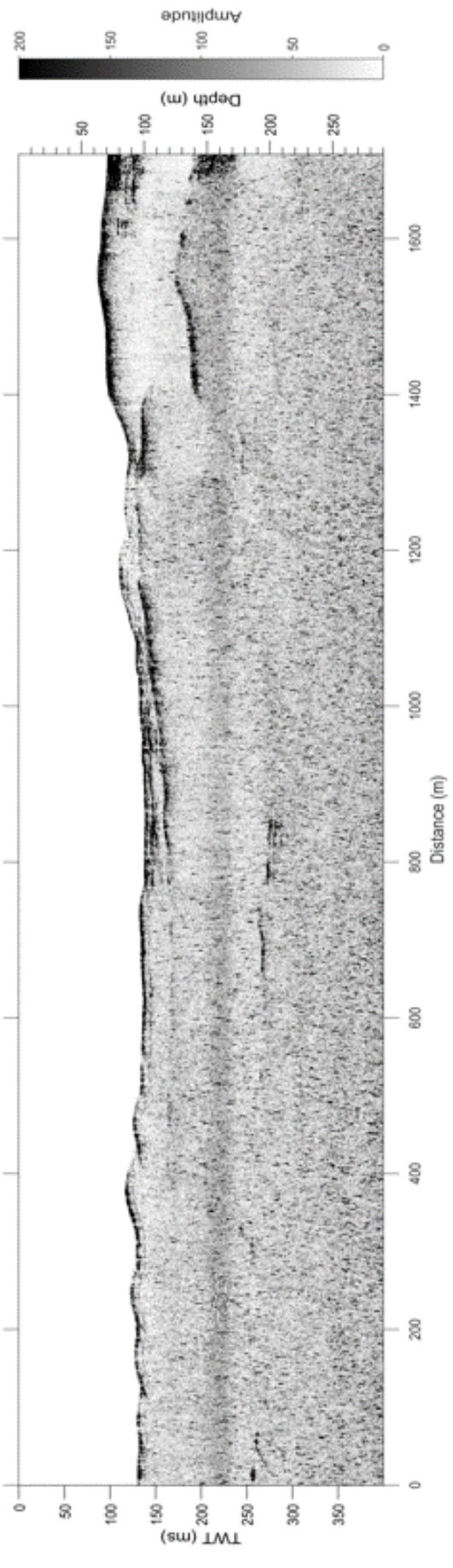

Figure C.3. Unprocessed SBP line of Figure 5.7F

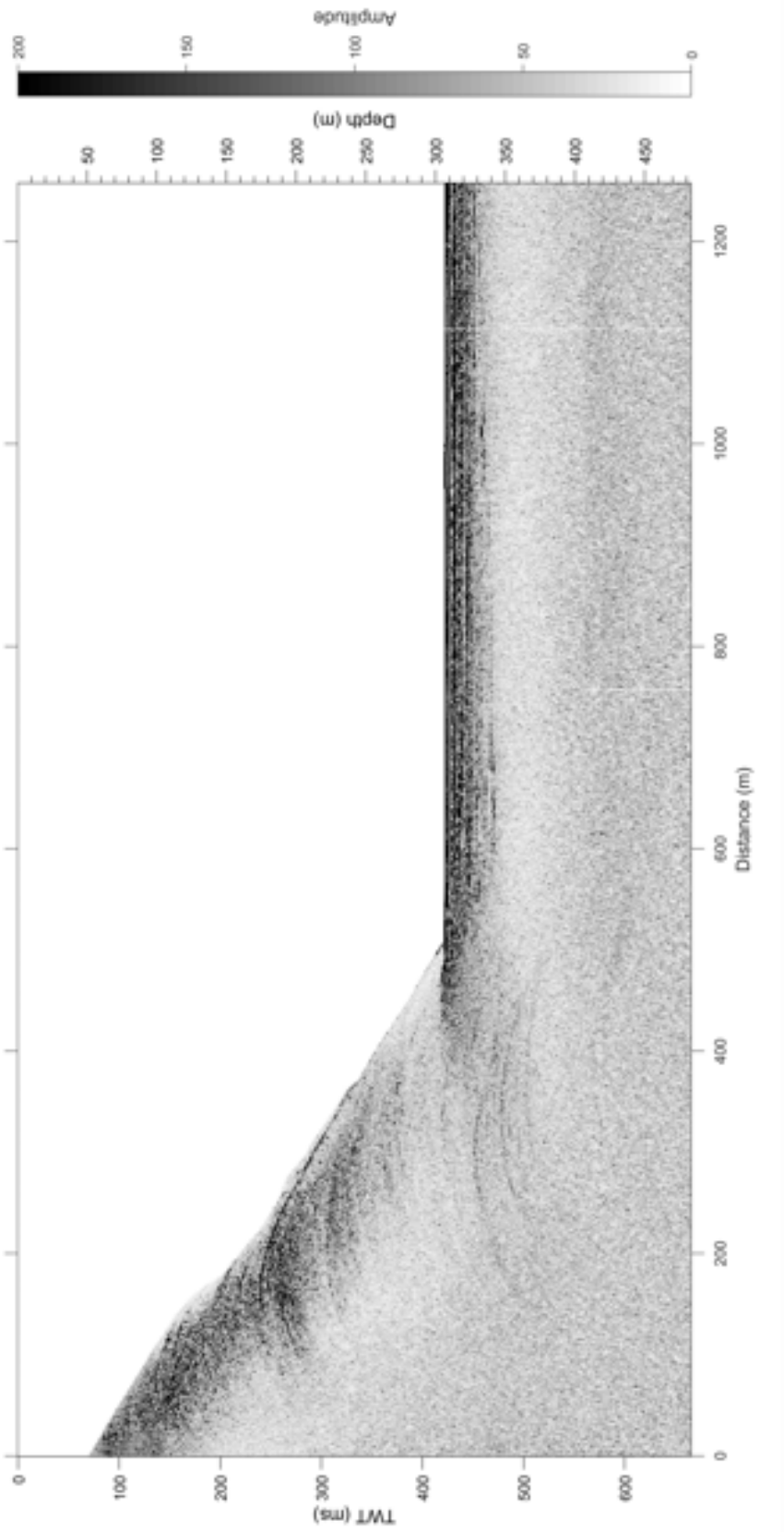

Figure C.4. Unprocessed SBP line of Figure 5.8F

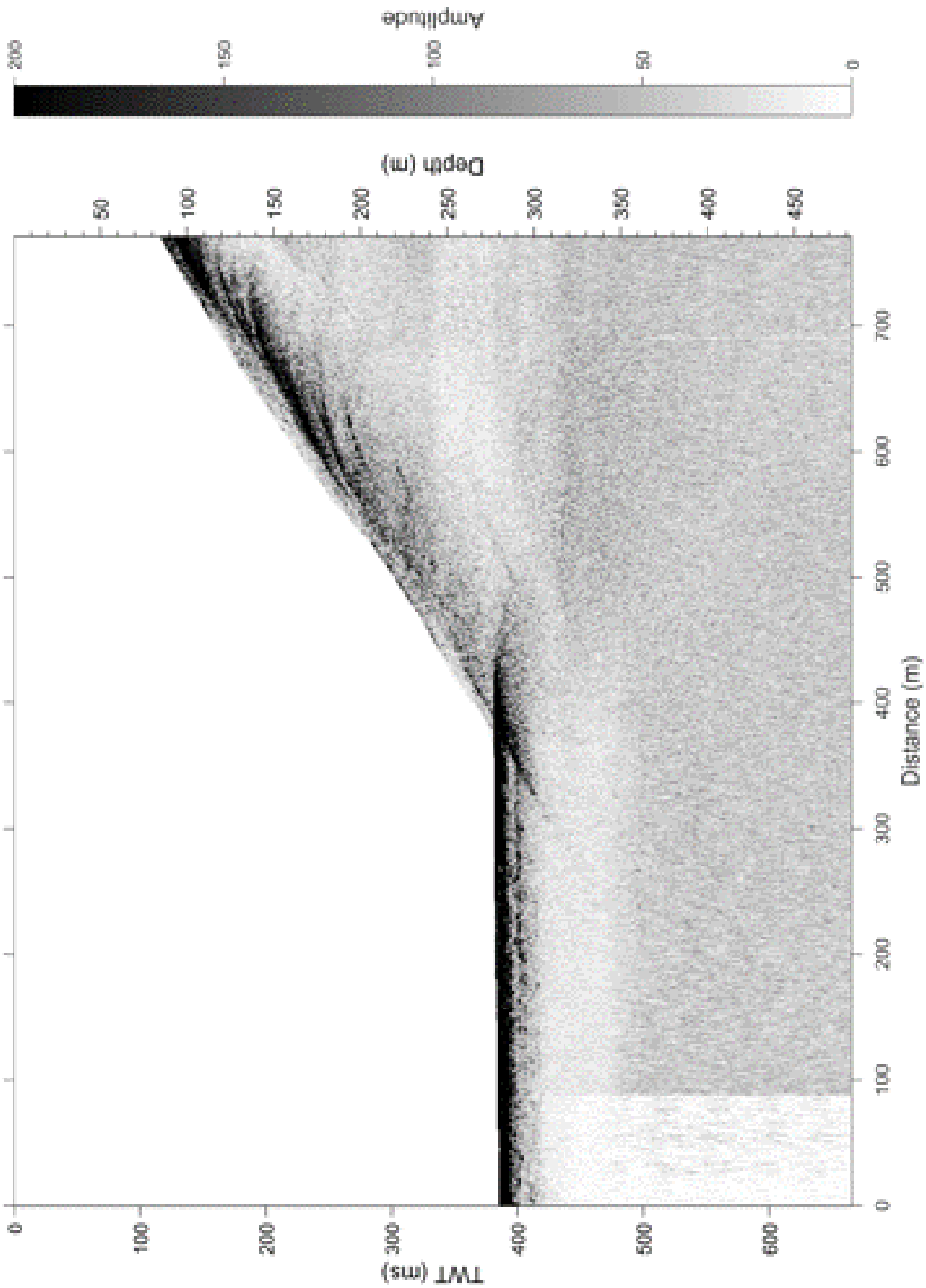

Figure C.5. Unprocessed SBP line of Figure 5.9E

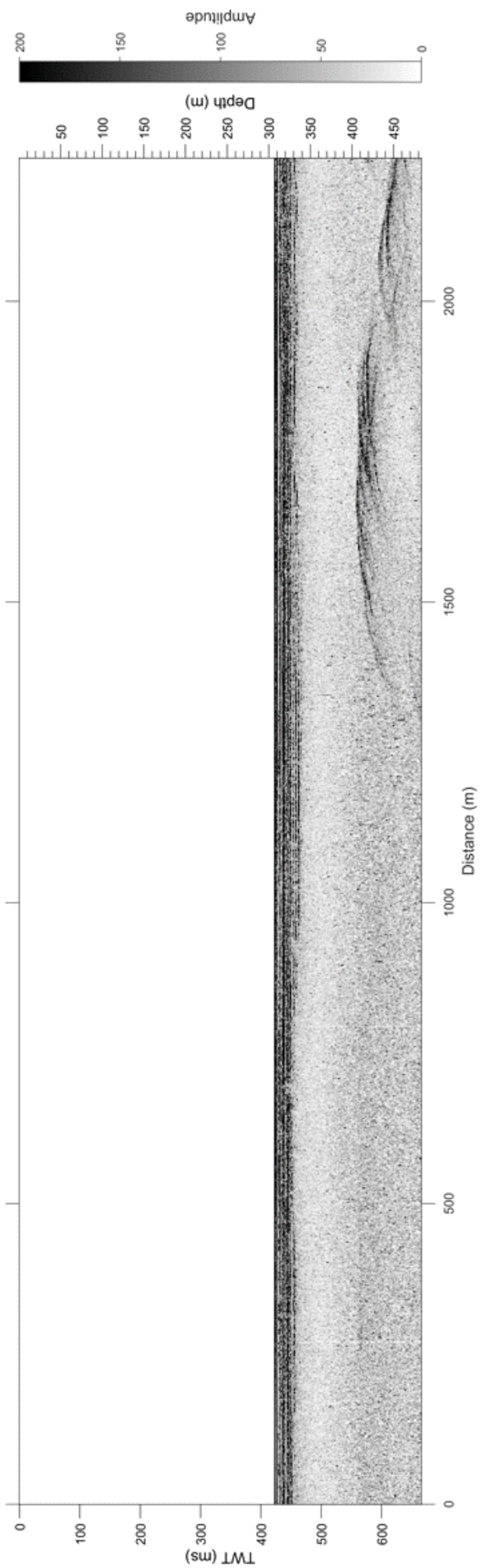

Figure C.6. Unprocessed SBP line of Figure 5.11A

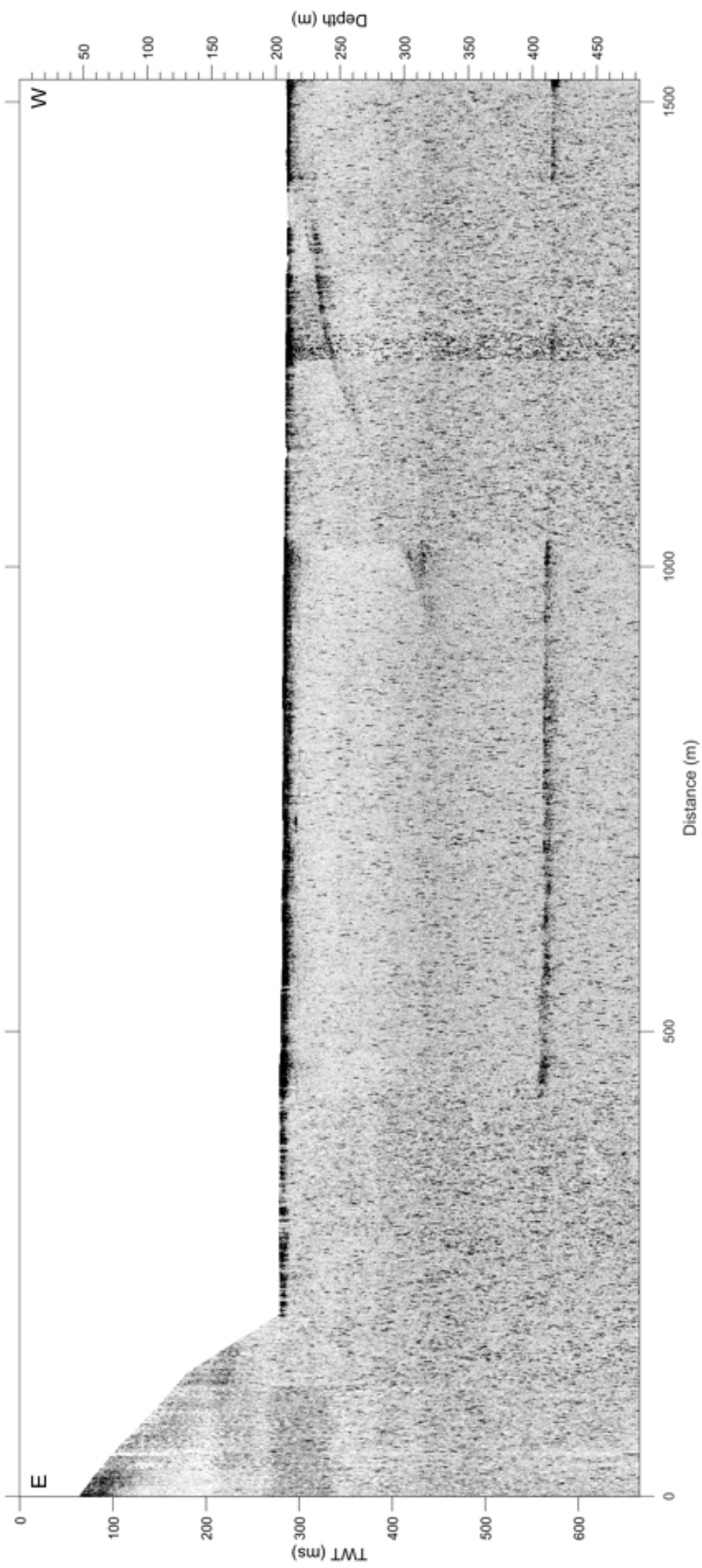

Figure C.7. Unprocessed SBP line of Figure 5.11B

References

Aaron, J. and Hungr, O. (2016a) 'Dynamic analysis of an extraordinarily mobile rock avalanche in the Northwest Territories, Canada', *Canadian Geotechnical Journal*, 53(6), pp. 899–908. doi: 10.1139/cgj-2015-0371.

Aaron, J. and Hungr, O. (2016b) 'Dynamic simulation of the motion of partially-coherent landslides', *Engineering Geology*, 205, pp. 1–11. doi: 10.1016/j.enggeo.2016.02.006.

Aaron, J. and McDougall, S. (2019) 'Rock avalanche mobility: The role of path material', *Engineering Geology*, 257. doi: 10.1016/j.enggeo.2019.05.003.

Aaron, J., McDougall, S., Moore, J. R., Coe, J. A. and Hungr, O. (2017) 'The role of initial coherence and path materials in the dynamics of three rock avalanche case histories', *Geoenvironmental Disasters*, 4(1), p. 5. doi: 10.1186/s40677-017-0070-4.

Aaron, J., McDougall, S. and Nolde, N. (2019) 'Two methodologies to calibrate landslide runout models', *Landslides*, 16(5), pp. 907–920. doi: 10.1007/s10346-018-1116-8.

Adams, J. (1978) *Late Cenozoic erosion in New Zealand*. Victoria University Wellington, PhD Thesis, pp 109.

Adams, J. (1980) 'Contemporary uplift and erosion of the Southern Alps, New Zealand', *Bulletin of the Geological Society of America*, 91(1 PART2), pp. 1–114. doi: 10.1130/GSAB-P2-91-1.

Agliardi, F., Crosta, G. and Zanchi, A. (2001) 'Structural constraints on deep-seated slope deformation kinematics', *Engineering Geology*, 59(1–2), pp. 83–102. doi: 10.1016/S0013-7952(00)00066-1.

Allen, S. and Huggel, C. (2013) 'Extremely warm temperatures as a potential cause of recent high mountain rockfall', *Global and Planetary Change*. doi: 10.1016/j.gloplacha.2013.04.007.

Allen, S. K., Cox, S. C. and Owens, I. F. (2011) 'Rock avalanches and other landslides in the central Southern Alps of New Zealand: A regional study considering possible climate change impacts', *Landslides*, 8(1), pp. 33–48. doi: 10.1007/s10346-010-0222-z.

Allen, S. K., Schneider, D. and Owens, I. F. (2009) 'First approaches towards modelling glacial hazards in the Mount Cook region of New Zealand's Southern Alps', *Natural Hazards and Earth System Sciences*, 9(2), pp. 481–499. doi: 10.5194/nhess-9-481-2009.

Alloway, B. V., Lowe, D. J., Barrell, D. J. A., Newnham, R. M., Almond, P. C., Augustinus, P. C., Bertler, N. A. N., Carter, L., Litchfield, N. J., McGlone, M. S., Shulmeister, J., Vandergoes, M. J., Williams, P. W., Anderson, B., Brackley, H., Burge, P., Carter, J., Cochran, U., Cooke, P., Crampton, J., Crouch, E., Crundwell, M., Deng, Y., Drost, F., Graham, I., Harper, M., Hayward, B., Hendy, C., Hollis, C., Hughes, M., Kennedy, D., Kennedy, L., King, D., Mackintosh, A., Manighetti, B., Marra, M., Mildenhall, D., Morgenstern, U., Naish, T., Neil, H., Nobes, D., Page, M., Palmer, A., Prior, C., Rieser, U., Rother, H., Shane, P., Strong, P., Suggate, P., Thomson, J., Tonkin, P., Trustrum, N., Van Dissen, R., Vucetich, C., Wilmshurst, J., Woodward, C. and Zondervan, A. (2007) 'Towards a climate event stratigraphy for New Zealand over the past 30 000 years (NZ-INTIMATE project)', *Journal of Quaternary Science*, 22(1), pp. 9–35. doi: 10.1002/jqs.1079.

Anselmetti, F. S., Ariztegui, D., De Batist, M., Catalina Gebhardt, A., Haberzettl, T., Niessen, F., Ohlendorf, C. and Zolitschka, B. (2009) 'Environmental history of southern Patagonia unravelled by the seismic stratigraphy of Laguna Potrok Aike', *Sedimentology*, 56(4), pp. 873–892. doi: 10.1111/j.1365-3091.2008.01002.x.

Augustinus, P. C. (1995) 'Glacial valley cross-profile development: the influence of in situ rock stress and rock mass strength, with examples from the Southern Alps, New Zealand', *Geomorphology*. doi: 10.1016/0169-555X(95)00050-X.

Avdievitch, N. N., Schmitt, R. G. and Coe, J. A. (2020) 'Inventory map of submarine and subaerial-to-submarine landslides in Glacier Bay, Glacier Bay National Park and Preserve, Alaska'. U.S. Geological Survey. doi: 10.5066/P9GCDYT2.

Azpiroz-Zabala, M., Cartigny, M. J. B., Talling, P. J., Parsons, D. R., Sumner, E. J., Clare, M. A., Simmons, S. M., Cooper, C. and Pope, E. L. (2017) 'Newly recognized turbidity current structure can explain prolonged flushing of submarine canyons', *Science Advances*, 3(10), p. e1700200. doi: 10.1126/sciadv.1700200.

Bainbridge, R. (2017) *Lost landslides: Rock-avalanche occurrence and fluvial censoring processes on South Island, New Zealand*. Northumbria University, PhD Thesis, pp. 262. Available at: http://nrl.northumbria.ac.uk/32621/1/Rupert Bainbridge - thesis - Lost landslides%2C Rock-avalanche occurrence and fluvial censoring processes on South Island%2C New Zealand.pdf (Accessed: 25 October 2018).

Ballantyne, C. K. (2002) 'Paraglacial geomorphology', *Quaternary Science Reviews*, 21(18–

19), pp. 1935–2017. doi: 10.1016/S0277-3791(02)00005-7.

Ballantyne, C. K. (2018) 'Glacially moulded landslide runout debris in the Scottish Highlands', *Scottish Geographical Journal*, 134(3–4), pp. 224–236. doi: 10.1080/14702541.2018.1501085.

Ballantyne, C. K., Sandeman, G. F., Stone, J. O. and Wilson, P. (2014) 'Rock-slope failure following Late Pleistocene deglaciation on tectonically stable mountainous terrain', *Quaternary Science Reviews*, 86, pp. 144–157. doi: 10.1016/j.quascirev.2013.12.021.

Barnard, P. L., Owen, L. A., Sharma, M. C. and Finkel, R. C. (2001) 'Natural and human-induced landsliding in the Garhwal Himalaya of northern India', *Geomorphology*, 40(1–2), pp. 21–35. doi: 10.1016/S0169-555X(01)00035-6.

Barnes, P. M. (2009) 'Postglacial (after 20 ka) dextral slip rate of the offshore Alpine fault, New Zealand', *Geology*, 37(1), pp. 3–6. doi: 10.1130/G24764A.1.

Barnes, P. M., Bostock, H. C., Neil, H. L., Strachan, L. J. and Gosling, M. (2013) 'A 2300-Year Paleoearthquake Record of the Southern Alpine Fault and Fiordland Subduction Zone, New Zealand, Based on Stacked Turbidites', *Bulletin of the Seismological Society of America*, 103(4), pp. 2424–2446. doi: 10.1785/0120120314.

Barnes, P. M., Pickrill, R. A. and Bostock, H. C. (2016) 'Thompson and Bradshaw sounds, Fiordland, New Zealand: A relict, mid-latitude, temperate glacier system', *Geological Society Memoir*, 46(1), pp. 45–46. doi: 10.1144/M46.45.

Barrell, D. J. A. (2011) 'Quaternary Glaciers of New Zealand', in *Developments in Quaternary Science*, pp. 1047–1064. doi: 10.1016/B978-0-444-53447-7.00075-1.

Barrell, D. J. A. (2019) *General Distribution and Characteristics of Active Faults and Folds in the Queenstown Lakes and Central Otago districts, Otago*, *GNS Science Consultancy Report 2018/207*. Lower Hutt, New Zealand.

Barth, N. C. (2014) 'The Cascade rock avalanche: Implications of a very large Alpine Fault-triggered failure, New Zealand', *Landslides*, 11(3), pp. 327–341. doi: 10.1007/s10346-013-0389-1.

Barth, N. C., Kulhanek, D. K., Beu, A. G., Murray-Wallace, C. V., Hayward, B. W., Mildenhall, D. C. and Lee, D. E. (2014) 'New c. 270kyr strike-slip and uplift rates for the southern Alpine Fault and implications for the New Zealand plate boundary', *Journal of Structural Geology*, 64, pp. 39–52. doi: 10.1016/j.jsg.2013.08.009.

Beguería, S., Van Asch, T. W. J., Malet, J. P. and Gröndahl, S. (2009) 'A GIS-based numerical model for simulating the kinematics of mud and debris flows over complex terrain', *Natural Hazards and Earth System Science*, 9(6), pp. 1897–1909. doi: 10.5194/nhess-9-1897-2009.

Beguería, S., van Hess, M. J. and Geertsema, M. (2009) 'Comparison of three landslide runout models on the Turnoff Creek rock avalanche, British Columbia', in *Landslide Processes Conference: A tirbute to Theo von Asch*. Strasbourg, pp. 243–247.

Bellwald, B., Hjelstuen, B. O., Sejrup, H. P. and Haflidason, H. (2016) 'Postglacial mass movements and depositional environments in a high-latitude fjord system – Hardangerfjorden, Western Norway', *Marine Geology*, 379, pp. 157–175. doi: 10.1016/j.margeo.2016.06.002.

Bellwald, B., Hjelstuen, B. O., Sejrup, H. P., Stokowy, T. and Kuvås, J. (2019) 'Holocene mass movements in west and mid-Norwegian fjords and lakes', *Marine Geology*, 407, pp. 192–212. doi: 10.1016/J.MARGEO.2018.11.007.

Benjamin, J., Rosser, N. J., Dunning, S. A., Hardy, R. J., Kelfoun, K. and Szczuciński, W. (2018) 'Transferability of a calibrated numerical model of rock avalanche run-out: Application to 20 rock avalanches on the Nuussuaq Peninsula, West Greenland', *Earth Surface Processes and Landforms*, 43(15), pp. 3057–3073. doi: 10.1002/esp.4469.

Berner, C. (2004) *Der Bergsturz von Goldau. Geologie, Ausbreitung und Dynamik des grossten historischen Bersturzes der Schweiz*. ETH Zurich.

Berryman, K., Cochran, U. A., Clark, K. J., Biasi, G. P., Langridge, R. M. and Villamor, P. (2012) 'Major earthquakes occur regularly on an isolated plate boundary fault', *Science*, 336(6089), pp. 1690–1693. doi: 10.1126/science.1218959.

Berryman, K., Cooper, A., Norris, R., Villamor, P., Sutherland, R., Wright, T., Schermer, E., Langridge, R. and Biasi, G. (2012) 'Late Holocene Rupture History of the Alpine Fault in South Westland, New Zealand', *Bulletin of the Seismological Society of America*, 102(2), pp. 620–638. doi: 10.1785/0120110177.

Biasi, G. P., Langridge, R. M., Berryman, K. R., Clark, K. J. and Cochran, U. A. (2015) 'Maximum-likelihood recurrence parameters and conditional probability of a ground-rupturing earthquake on the southern Alpine fault, South Island, New Zealand', *Bulletin of the Seismological Society of America*, 105(1), pp. 94–106. doi: 10.1785/0120130259.

Bichler, M. G., Reindl, M., Reitner, J. M., Drescher-Schneider, R., Wirsig, C., Christl, M.,

Hajdas, I. and Ivy-Ochs, S. (2016) 'Landslide deposits as stratigraphical markers for a sequence-based glacial stratigraphy: a case study of a Younger Dryas system in the Eastern Alps', *Boreas*, 45(3), pp. 537–551. doi: 10.1111/bor.12173.

De Blasio, F. V. (2011) 'Subaqueous Landslides', in *Introduction to the Physics of Landslides*. Springer, Dordrecht, pp. 295–351. doi: 10.1007/978-94-007-1122-8_9.

De Blasio, F. V. (2013) 'Dynamics, Velocity, and Run-Out of Subaqueous Rock Avalanches', in *Landslide Science and Practice: Volume 5: Complex Environment*, pp. 57–63. doi: 10.1007/978-3-642-31445-2.

De Blasio, F. V., Elverhøi, A., Engvik, L., Issler, D., Gauer, P. and Harbitz, C. B. (2006) 'Understanding the high mobility of subaqueous debris flows', *Norwegian Journal of Geology*, 86, pp. 275–284.

De Blasio, F. V, Engvik, L., Harbitz, C. B. and Elverhøi, A. (2004) 'Hydroplaning and submarine debris flows', *Journal of Geophysical Research: Oceans*, 109(C1), p. n/a-n/a. doi: 10.1029/2002JC001714.

Blikra, L. H., Braathen, A. and Skurtveit, E. (2002) *Hazard evaluation of rock avalanches; the Baraldsnes–Oterøya area*, *NGU report*. Trondheim. Available at: http://www.ngu.no/upload/Publikasjoner/Rapporter/2001/2001_108.pdf (Accessed: 1 November 2018).

Blikra, L. H., Longva, O., Braathen, A., Anda, E., Dehls, J. F. and Stalsberg, K. (2006) 'Rock Slope Failures in Norwegian Fjord Areas: Examples, Spatial Distribution and Temporal Pattern', in *Landslides from Massive Rock Slope Failure*. Dordrecht: Springer Netherlands, pp. 475–496. doi: 10.1007/978-1-4020-4037-5_26.

Blikra, L. H. and Nemec, W. (1998) 'Postglacial colluvium in western Norway: depositional processes, facies and palaeoclimatic record', *Sedimentology*, 45(5), pp. 909–959. doi: 10.1046/j.1365-3091.1998.00200.x.

Blikra, L., Longva, O., Harbitz, C. and Lovholt, F. (2005) 'Quantification of rock-avalanche and tsunami hazard in Storfjorden , western Norway', *Landslides and Avalanches: ICFL 2005, Norway*, pp. 57–64.

Blöthe, J. H., Korup, O. and Schwanghart, W. (2015) 'Large landslides lie low: Excess topography in the Himalaya-Karakoram ranges', *Geology*. doi: 10.1130/g36527.1.

Bøe, R., Hovland, M., Instanes, A., Rise, L. and Vasshus, S. (2000) 'Submarine slide scars and mass movements in Karmsundet and Skudenesfjorden, southwestern Norway: Morphology and evolution', *Marine Geology*, 167(1–2), pp. 147–165. doi: 10.1016/S0025-3227(00)00017-7.

Bøe, R., Rise, L., Blikra, L. H., Longva, O. and Eide, A. (2003) 'Holocene mass-movement processes in Trondheimsfjorden , Central Norway', *Norwegian Journal of Geology*, 83, pp. 3–22. Available at: http://www.mendeley.com/research/holocene-massmovement-processes-trondheims-fjorden-central-norway/?utm_source=desktop&utm_medium=1.10.1&utm_campaign=open_catalog&userDocumentId=%7B2fd2b3e4-d963-40ab-9f10-7051af011001%7D.

Bohannon, R. G. and Gardner, J. V (2004) 'Submarine landslides of San Pedro Escarpment, southwest of Long Beach, California', *Marine Geology*, 203(3–4), pp. 261–268. doi: 10.1016/S0025-3227(03)00309-8.

Böhme, M., Oppikofer, T., Longva, O., Jaboyedoff, M., Hermanns, R. L. and Derron, M. H. (2015) 'Analyses of past and present rock slope instabilities in a fjord valley: Implications for hazard estimations', *Geomorphology*, 248, pp. 464–474. doi: 10.1016/j.geomorph.2015.06.045.

Bornhold, B. D., Harper, J. R., McLaren, D. and Thomson, R. E. (2007) 'Destruction of the First Nations village of Kwalate by a rock avalanche-generated tsunami', *Atmosphere - Ocean*, 45(2), pp. 123–128. doi: 10.3137/ao.450205.

Bornhold, B. D. and Thomson, R. E. (2012) 'Tsunami hazard assessment related to slope failures in coastal waters', *Landslides: Types, Mechanisms and Modeling*. Edited by J. J. Clague and D. Stead, pp. 108–120. doi: 10.1017/CBO9780511740367.011.

Boultbee, N., Stead, D., Schwab, J. and Geertsema, M. (2006) 'The Zymoetz River rock avalanche, June 2002, British Columbia, Canada', *Engineering Geology*. doi: 10.1016/j.enggeo.2005.06.038.

Bovis, M. J. (1982) 'Uphill-facing (antislope) scarps in the Coast Mountains, southwest British Columbia.', *Geological Society of America Bulletin*, 93(8), pp. 804–812. doi: 10.1130/0016-7606(1982)93<804:UASITC>2.0.CO;2.

Bowman, E. T., Take, W. A., Rait, K. L. and Hann, C. (2012) 'Physical models of rock avalanche spreading behaviour with dynamic fragmentation', *Canadian Geotechnical Journal*, 49(4), pp. 460–476. doi: 10.1139/T2012-007.

Bozzano, F., Mazzanti, P., Anzidei, M., Esposito, C., Floris, M., Fasani, G. B. and Esposito, A. (2009) 'Slope dynamics of Lake Albano (Rome, Italy): insights from high resolution bathymetry', *Earth Surface Processes and Landforms*, 34(11), pp. 1469–1486. doi: 10.1002/esp.1832.

Bradley, B. A., Bae, S. E., Polak, V., Lee, R. L., Thomson, E. M. and Tarbali, K. (2017) 'Ground motion simulations of great earthquakes on the Alpine Fault: effect of hypocentre location and comparison with empirical modelling', *New Zealand Journal of Geology and Geophysics*, 60(3), pp. 188–198. doi: 10.1080/00288306.2017.1297313.

Brain, M. J., Rosser, N. J. and Tunstall, N. (2017) 'The control of earthquake sequences on hillslope stability', *Geophysical Research Letters*, 44(2), pp. 865–872. doi: 10.1002/2016GL071879.

Bregoli, F., Bateman, A. and Medina, V. (2017) 'Tsunamis generated by fast granular landslides: 3D experiments and empirical predictors', *Journal of Hydraulic Research*, 55(6), pp. 743–758. doi: 10.1080/00221686.2017.1289259.

Brideau, M. A., McDougall, S., Stead, D., Evans, S. G., Couture, R. and Turner, K. (2012) 'Three-dimensional distinct element modelling and dynamic runout analysis of a landslide in gneissic rock, British Columbia, Canada', *Bulletin of Engineering Geology and the Environment*. doi: 10.1007/s10064-012-0417-8.

ten Brink, U. S., Andrews, B. D. and Miller, N. C. (2016) 'Seismicity and sedimentation rate effects on submarine slope stability', *Geology*, 44(7), pp. 563–566. doi: 10.1130/G37866.1.

ten Brink, U. S., Barkan, R., Andrews, B. D. and Chaytor, J. D. (2009) 'Size distributions and failure initiation of submarine and subaerial landslides', *Earth and Planetary Science Letters*, 287(1–2), pp. 31–42. doi: 10.1016/j.epsl.2009.07.031.

Brodie, J. W. and Irwin, J. (1970) 'Morphology and sedimentation in lake Wakatipu, New Zealand', *New Zealand Journal of Marine and Freshwater Research*, 4(4), pp. 479–496. doi: 10.1080/00288330.1970.9515362.

Bull, S., Cartwright, J. and Huuse, M. (2009) 'A review of kinematic indicators from mass-transport complexes using 3D seismic data', *Marine and Petroleum Geology*, 26(7), pp. 1132–1151. doi: 10.1016/J.MARPETGEO.2008.09.011.

Bullard, G. K., Mulligan, R. P., Carreira, A. and Take, W. A. (2019) 'Experimental analysis of

tsunamis generated by the impact of landslides with high mobility', *Coastal Engineering*, 152, p. 103538. doi: 10.1016/j.coastaleng.2019.103538.

Canals, M., Lastras, G., Urgeles, R., Casamor, J. L., Mienert, J., Cattaneo, A., De Batist, M., Haflidason, H., Imbo, Y., Laberg, J. S., Locat, J., Long, D., Longva, O., Masson, D. G., Sultan, N., Trincardi, F. and Bryn, P. (2004) 'Slope failure dynamics and impacts from seafloor and shallow sub-seafloor geophysical data: Case studies from the COSTA project', *Marine Geology*, 213(1–4), pp. 9–72. doi: 10.1016/j.margeo.2004.10.001.

Carrivick, J. L., James, W. H. M., Grimes, M., Sutherland, J. L. and Lorrey, A. M. (2020) 'Ice thickness and volume changes across the Southern Alps, New Zealand, from the little ice age to present', *Scientific Reports*, 10(1), pp. 1–10. doi: 10.1038/s41598-020-70276-8.

Carson, M. A. and Griffiths, G. A. (1989) 'Gravel transport in the braided Waimakiriri River: mechanisms, measurements and predictions', *Journal of Hydrology*, 109, pp. 201–220.

Carter, G. (2015) 'Rock avalanche scars in the geological record: an example from Little Loch Broom, NW Scotland', *Proceedings of the Geologists' Association*, 126(6), pp. 698–711. doi: http://dx.doi.org/10.1016/j.pgeola.2015.09.003.

Carter, G. D. O., Cooper, R., Gafeira, J., Howe, J. A. and Long, D. (2020) 'Morphology of small-scale submarine mass movement events across the northwest United Kingdom', *Geomorphology*, 365, p. 107282. doi: 10.1016/j.geomorph.2020.107282.

Carter, L. (2001) 'A large submarine debris flow in the path of the Pacific deep western boundary current off New Zealand', *Geo-Marine Letters*, 21(1), pp. 42–50. doi: 10.1007/s003670100066.

Carter, L. and Carter, R. M. (1990) 'Lacustrine sediment traps and their effect on continental shelf sedimentation-South Island, New Zealand', *Geo-Marine Letters*, 10(2), pp. 93–100. doi: 10.1007/BF02431026.

Castleton, J. J., Moore, J. R., Aaron, J., Christl, M. and Ivy-Ochs, S. (2016) 'Dynamics and legacy of 4.8 ka rock avalanche that dammed Zion Canyon, Utah, USA', *GSA Today*, 26(6), pp. 4–9. doi: 10.1130/GSATG269A.1.

Catane, S. G., Cabria, H. B., Zarco, M. A. H., Saturay, R. M. and Mirasol-Robert, A. A. (2008) 'The 17 February 2006 Guinsaugon rock slide-debris avalanche, Southern Leyte, Philippines: Deposit characteristics and failure mechanism', *Bulletin of Engineering Geology and the*

Environment. doi: 10.1007/s10064-008-0120-y.

Chalindar, S. (2005) 'Modélisation d ' avalanches rocheuses', in *Internship Report. Civil and Environmental Engineering (ENAC) - Laboratory for Rock Mechanics (LMR)*.

Chaytor, J. D., ten Brink, U. S., Solow, A. R. and Andrews, B. D. (2009) 'Size distribution of submarine landslides along the U.S. Atlantic margin', *Marine Geology*, 264(1–2), pp. 16–27. doi: 10.1016/j.margeo.2008.08.007.

Chen, H. and Lee, C. F. (2003) 'A dynamic model for rainfall-induced landslides on natural slopes', *Geomorphology*, 51(4), pp. 269–288. doi: 10.1016/S0169-555X(02)00224-6.

Chevalier, G., Davies, T. and McSaveney, M. (2009) 'The prehistoric Mt Wilberg rock avalanche, Westland, New Zealand', *Landslides*, 6(3), pp. 253–262. doi: 10.1007/s10346-009-0156-5.

Chinn, T., Fitzharris, B. B., Willsman, A. and Salinger, M. J. (2012) 'Annual ice volume changes 1976-2008 for the New Zealand Southern Alps', *Global and Planetary Change*, 92–93, pp. 105–118. doi: 10.1016/j.gloplacha.2012.04.002.

Chinn, T. J. (2001) 'Distribution of the glacial water resources of New Zealand', *Journal of Hydrology New Zealand*.

Chinn, T. J., Kargel, J. S., Leonard, G. J., Haritashya, U. K. and Pleasants, M. (2014) 'New Zealand's Glaciers', in Kargel, J. S., Leonard, G. J., Bishop, M. P., Kääb, A., and Raup, B. H. (eds) *Global Land Ice Measurements from Space*. Berlin, Heidelberg: Springer Berlin Heidelberg, pp. 675–715. doi: 10.1007/978-3-540-79818-7_29.

Christen, M., Kowalski, J. and Bartelt, P. (2010) 'RAMMS: Numerical simulation of dense snow avalanches in three-dimensional terrain', *Cold Regions Science and Technology*, 63(1–2), pp. 1–14. doi: 10.1016/j.coldregions.2010.04.005.

Clague, J. J. (2015) 'Paleolandslides', in *Landslide Hazards, Risks, and Disasters*. Elsevier Inc., pp. 321–344. doi: 10.1016/B978-0-12-396452-6.00010-0.

Clare, M. A., Hughes Clarke, J. E., Talling, P. J., Cartigny, M. J. B. and Pratomo, D. G. (2016) 'Preconditioning and triggering of offshore slope failures and turbidity currents revealed by most detailed monitoring yet at a fjord-head delta', *Earth and Planetary Science Letters*, 450, pp. 208–220. doi: 10.1016/j.epsl.2016.06.021.

Clare, M., Chaytor, J., Dabson, O., Gamboa, D., Georgiopoulou, A., Eady, H., Hunt, J., Jackson, C., Katz, O., Krastel, S., León, R., Micallef, A., Moernaut, J., Moriconi, R., Moscardelli, L., Mueller, C., Normandeau, A., Patacci, M., Steventon, M., Urlaub, M., Völker, D., Wood, L. and Jobe, Z. (2018) 'A consistent global approach for the morphometric characterization of subaqueous landslides', *Geological Society, London, Special Publications*, 477, p. SP477.15. doi: 10.1144/SP477.15.

Clark, K., Upton, P., Carey, J., Rosser, B. and Strong, D. (2015) *Tsunami and Seiche Hazard Scoping Study for Lakes Tekapo, Pukaki, Ohau, Alexandrina and Ruataniwha*, *GNS Science Consultancy Report 2014/227*.

Clark, P. U., Dyke, A. S., Shakun, J. D., Carlson, A. E., Clark, J., Wohlfarth, B., Mitrovica, J. X., Hostetler, S. W. and McCabe, A. M. (2009) 'The Last Glacial Maximum', *Science*, 325(5941), pp. 710–714. doi: 10.1126/science.1172873.

Clarke, B. A. and Burbank, D. W. (2010) 'Bedrock fracturing, threshold hillslopes, and limits to the magnitude of bedrock landslides', *Earth and Planetary Science Letters*, 297(3–4), pp. 577–586. doi: 10.1016/j.epsl.2010.07.011.

Clauset, A., Shalizi, C. R. and Newman, M. E. J. (2009) 'Power-law distributions in empirical data', *SIAM Review*, 51(4), pp. 661–703. Available at: http://www.santafe.edu/~aaronc/powerlaws/. (Accessed: 11 February 2020).

Cochran, U. A., Clark, K. J., Howarth, J. D., Biasi, G. P., Langridge, R. M., Villamor, P., Berryman, K. R. and Vandergoes, M. J. (2017) 'A plate boundary earthquake record from a wetland adjacent to the Alpine fault in New Zealand refines hazard estimates', *Earth and Planetary Science Letters*, 464, pp. 175–188. doi: 10.1016/j.epsl.2017.02.026.

Cody, E., Draebing, D., McColl, S., Cook, S. and Brideau, M.-A. (2020) 'Geomorphology and geological controls of an active paraglacial rockslide in the New Zealand Southern Alps', *Landslides*, 17(4), pp. 755–776. doi: 10.1007/s10346-019-01316-2.

Coe, J. A. (2020) 'Bellwether sites for evaluating changes in landslide frequency and magnitude in cryospheric mountainous terrain: a call for systematic, long-term observations to decipher the impact of climate change', *Landslides*, pp. 1–19. doi: 10.1007/s10346-020-01462-y.

Coe, J. A., Baum, R. L., Allstadt, K. E., Kochevar, B. F., Schmitt, R. G., Morgan, M. L., White, J. L., Stratton, B. T., Hayashi, T. A. and Kean, J. W. (2016) 'Rock-avalanche dynamics revealed

by large-scale field mapping and seismic signals at a highly mobile avalanche in the West Salt Creek valley, western Colorado', *Geosphere*, 12(2), pp. 607–631. doi: 10.1130/GES01265.1.

Cogez, A., Meynadier, L., Allègre, C., Limmois, D., Herman, F. and Gaillardet, J. (2015) 'Constraints on the role of tectonic and climate on erosion revealed by two time series analysis of marine cores around New Zealand', *Earth and Planetary Science Letters*, 410, pp. 174–185. doi: 10.1016/j.epsl.2014.11.029.

Collins, G. S. and Melosh, H. J. (2003) 'Acoustic fluidization and the extraordinary mobility of sturzstroms', *Journal of Geophysical Research: Solid Earth*. doi: 10.1029/2003jb002465.

Collot, J.-Y., Lewis, K., Lamarche, G. and Lallemand, S. (2001) 'The giant Ruatoria debris avalanche on the northern Hikurangi margin, New Zealand: Result of oblique seamount subduction', *Journal of Geophysical Research: Solid Earth*, 106(B9), pp. 19271–19297. doi: 10.1029/2001jb900004.

Columbus, J., Sirguey, P. and Tenzer, R. (2011) 'A free fully assessed 15 metre digital elevation model for New Zealand', *Survey Quarterly*, 66, pp. 16–19.

Conway, K. W. and Barrie, J. V. (2018) 'Large bedrock slope failures in a British Columbia, Canada fjord: first documented submarine sackungen', *Geo-Marine Letters*, 38(3), pp. 195–209. doi: 10.1007/s00367-018-0533-y.

Conway, K. W., Barrie, J. V., Picard, K. and Bornhold, B. D. (2012) 'Submarine channel evolution: Active channels in fjords, British Columbia, Canada', *Geo-Marine Letters*, 32(4), pp. 301–312. doi: 10.1007/s00367-012-0280-4.

Conway, K. W. and Barrie, J. V (2015) *Large submarine slope failures and associated Quaternary faults in Douglas Channel , British Columbia*, *Geological Survey of Canada. Current Research 2015*.

Conway, S. J. and Balme, M. R. (2014) 'Decameter thick remnant glacial ice deposits on Mars', *Geophysical Research Letters*, 41(15), pp. 5402–5409. doi: 10.1002/2014GL060314.

Cook, S. J., McColl, S. and Stahl, T. (2013) *Surveying and dating post glacial lake shorelines in New Zealand*. London. doi: 10.13140/RG.2.1.1551.0564.

Cook, S. J., Porter, P. R. and Bendall, C. A. (2013) 'Geomorphological consequences of a glacier advance across a paraglacial rock avalanche deposit', *Geomorphology*, 189, pp. 109–120. doi: 10.1016/j.geomorph.2013.01.022.

Coombs, M. L., White, S. M. and Scholl, D. W. (2007) 'Massive edifice failure at Aleutian arc volcanoes', *Earth and Planetary Science Letters*, 256(3), pp. 403–418. doi: http://dx.doi.org/10.1016/j.epsl.2007.01.030.

Corominas, J. (1996) 'The angle of reach as a mobility index for small and large landslides', *Canadian Geotechnical Journal*, 33. doi: 10.1139/t96-005.

Costa, J. E. and Schuster, R. L. (1988) 'The formation and failure of natural dams', *Geological Society of America Bulletin*, 100(7), pp. 1054–1068. doi: 10.1130/0016-7606(1988)100<1054:TFAFON>2.3.CO;2.

Cox, S. C., Barrell, D. J. A., Dellow, G. D., McColl, S. T. and Horspool, N. A. (2015) *Landslides and ground damage during the Mw 5.8 Matukituki earthquake, 4 May 2015, Central Otago, New Zealand*, *GNS Science Report 2015/17*.

Cox, S. C., McSaveney, M. J., Spencer, J., Allen, S. K., Ashraf, S., Hancox, G. T., Sirguey, P., Salichon, J. and Ferris, B. G. (2015) 'Rock avalanche on 14 July 2014 from Hillary Ridge, Aoraki/Mount Cook, New Zealand', *Landslides*, 12(2), pp. 395–402. doi: 10.1007/s10346-015-0556-7.

Cox, S. C., Stirling, M. W., Herman, F., Gerstenberger, M. and Ristau, J. (2012) 'Potentially active faults in the rapidly eroding landscape adjacent to the Alpine Fault, central Southern Alps, New Zealand', *Tectonics*, 31(2). doi: 10.1029/2011TC003038.

CREALP (2001) 'Eboulement du 30 Mai 1946 du Six des Eaux Froides pres du Rawyl (Valais), Sion, Switzerland.'

Crosta, G. B., Chen, H. and Lee, C. F. (2004) 'Replay of the 1987 Val Pola Landslide, Italian Alps', *Geomorphology*. doi: 10.1016/j.geomorph.2003.07.015.

Crosta, G. B., Frattini, P., Valbuzzi, E. and De Blasio, F. V. (2018) 'Introducing a New Inventory of Large Martian Landslides', *Earth and Space Science*, 5(4), pp. 89–119. doi: 10.1002/2017EA000324.

Crosta, G. B., Imposimato, S. and Roddeman, D. (2009) 'Numerical modelling of entrainment/deposition in rock and debris-avalanches', *Engineering Geology*, 109(1–2), pp. 135–145. doi: 10.1016/J.ENGGEO.2008.10.004.

Crosta, G. B., Imposimato, S. and Roddeman, D. G. (2003) *Numerical modelling of large landslides stability and runout*, *Natural Hazards and Earth System Sciences*. Available at:

http://www.feat.nl. (Accessed: 15 February 2021).

Crosta, G. B., Imposimato, S. and Roddeman, D. G. (2006) 'Continuum numerical modelling of flow-like landslides', in Evans, S. G., Scarascia Mugnozza, G., Strom, A. L., and Hermanns, R. L. (eds) *Landslides from Massive Rock Slope Failure*. Dordrecht: Springer Netherlands, pp. 211–232.

Cruden, D. and Krahn, J. (1978) 'Frank Rockslide, Alberta, Canada', in Voight, B. (ed.) *Rockslides and Avalanches, Vol 1 Natural Phenomena*. Amsterdam: Elsevier Scientific Publishing. doi: 10.1016/B978-0-444-41507-3.50010-6.

Cruden, D. M. and Hungr, O. (1986) 'The debris of the Frank Slide and theories of rockslide-avalanche mobility.', *Canadian Journal of Earth Sciences*. doi: 10.1139/e86-044.

Cruden, D. M. and Varnes, D. J. (1996) 'Landslides: investigation and mitigation. Chapter 3-Landslide types and processes', *Transportation research board special report*, 247(247), p. 76. Available at: https://www.researchgate.net/publication/269710355_CrudenDM_Varnes_DJ_1996_Landslide_Types_and_Processes_Special_Report_Transportation_Research_Board_National_Academy_of_Sciences_24736-75.

Crutchley, G. J., Karstens, J., Berndt, C., Talling, P. J., Watt, S. F. L., Vardy, M. E., Hühnerbach, V., Urlaub, M., Sarkar, S., Klaeschen, D., Paulatto, M., Le Friant, A., Lebas, E. and Maeno, F. (2013) 'Insights into the emplacement dynamics of volcanic landslides from high-resolution 3D seismic data acquired offshore Montserrat, Lesser Antilles', *Marine Geology*, 335, pp. 1–15. doi: 10.1016/j.margeo.2012.10.004.

Crutchley, G. J. and Kopp, H. (2018) 'Reflection and Refraction Seismic Methods', in *Springer Geology*. Springer, pp. 43–62. doi: 10.1007/978-3-319-57852-1_4.

Van Daele, M., Moernaut, J., Doom, L., Boes, E., Fontijn, K., Heirman, K., Vandoorne, W., Hebbeln, D., Pino, M., Urrutia, R., Brümmer, R. and De Batist, M. (2015) 'A comparison of the sedimentary records of the 1960 and 2010 great Chilean earthquakes in 17 lakes: Implications for quantitative lacustrine palaeoseismology', *Sedimentology*. Edited by J. Trofimovs, 62(5), pp. 1466–1496. doi: 10.1111/sed.12193.

Van Daele, M., Versteeg, W., Pino, M., Urrutia, R. and De Batist, M. (2013) 'Widespread deformation of basin-plain sediments in aysén fjord (chile) due to impact by earthquake-

triggered, onshore-generated mass movements', *Marine Geology*, 337, pp. 67–79. doi: 10.1016/j.margeo.2013.01.006.

Dahl-Jensen, T., Larsen, L. M., Pedersen, S. A. S., Pedersen, J., Jepsen, H. F., Pedersen, G., Nielsen, T., Pedersen, A. K., Von Platen-Hallermund, F. and Weng, W. (2004) 'Landslide and Tsunami 21 November 2000 in Paatuut, West Greenland', *Natural Hazards*, 31(1), pp. 277–287. doi: 10.1023/B:NHAZ.0000020264.70048.95.

Dahl, M. P. J., Gauer, P., Kalsnes, B. G., Mortensen, L. E., Jensen, N. H. and Veihe, A. (2013) 'Numerical runout simulation of debris avalanches in the Faroe Islands, North Atlantic Ocean', *Landslides*, 10(5), pp. 623–631. doi: 10.1007/s10346-012-0355-3.

Dai, C., Higman, B., Lynett, P. J., Jacquemart, M., Howat, I. M., Liljedahl, A. K., Dufresne, A., Freymueller, J. T., Geertsema, M., Ward Jones, M. and Haeussler, P. J. (2020) 'Detection and assessment of a large and potentially-tsunamigenic periglacial landslide in Barry Arm, Alaska', *Geophysical Research Letters*, 47(22). doi: 10.1029/2020gl089800.

Dan, G., Sultan, N. and Savoye, B. (2007) 'The 1979 Nice harbour catastrophe revisited: Trigger mechanism inferred from geotechnical measurements and numerical modelling', *Marine Geology*. doi: 10.1016/j.margeo.2007.06.011.

Davies, T. and McSaveney, M. (2012) 'Mobility of long-runout rock avalanches', in Clague, J. J. and Stead, D. (eds) *Landslides: Types, Mechanisms and Modeling*. Cambridge: Cambridge University Press, pp. 50–58. doi: 10.1017/CBO9780511740367.006.

Davies, T. R. H. (1982) 'Spreading of rock avalanche debris by mechanical fluidization', *Rock Mechanics Felsmechanik Mécanique des Roches*, 15(1), pp. 9–24. doi: 10.1007/BF01239474.

Davies, T. R. and McSaveney, M. J. (1999) 'Runout of dry granular avalanches', *Canadian Geotechnical Journal*, 36(2), pp. 313–320. doi: 10.1139/t98-108.

Davies, T. R. and McSaveney, M. J. (2006) 'Geomorphic constraints on the management of bedload-dominated rivers', *Journal of Hydrology (New Zealand)*, 45(2), pp. 111–130. Available at: http://www.jstor.org/stable/43944945.

Davies, T. R. and McSaveney, M. J. (2009) 'The role of rock fragmentation in the motion of large landslides', *Engineering Geology*, 109(1), pp. 67–79. doi: https://doi.org/10.1016/j.enggeo.2008.11.004.

Davies, T. R., McSaveney, M. J. and Hodgson, K. A. (1999) 'A fragmentation-spreading model

for long-runout rock avalanches', *Canadian Geotechnical Journal*, 36(6), pp. 1096–1110. doi: 10.1139/t99-067.

Daxer, C., Moernaut, J., Taylor, T., Haas, J. N. and Strasser, M. (2018) 'Late Glacial and Holocene sedimentary infill of Lake Mondsee (Eastern Alps, Austria) and historical rockfall activity revealed by reflection seismics and sediment core analysis', *Austrian Journal of Earth Sciences*, 111(1), pp. 111–134. doi: 10.17738/ajes.2018.0008.

Daxer, C., Sammartini, M., Molenaar, A., Piechl, T., Strasser, M. and Moernaut, J. (2020) 'Morphology and spatio-temporal distribution of lacustrine mass-transport deposits in Wörthersee, Eastern Alps, Austria', *Geological Society, London, Special Publications*, 500(1), pp. 235–254. doi: 10.1144/sp500-2019-179.

Deering, R., Bell, T., Forbes, D. L., Campbell, C. and Edinger, E. (2018) 'Morphological characterization of submarine slope failures in a semi-enclosed fjord, Frobisher Bay, eastern Canadian Arctic', *Geological Society, London, Special Publications*, p. SP477.35. doi: 10.1144/sp477.35.

Delaney, K. B. and Evans, S. G. (2014) 'The 1997 Mount Munday landslide (British Columbia) and the behaviour of rock avalanches on glacier surfaces', *Landslides*, 11(6), pp. 1019–1036. doi: 10.1007/s10346-013-0456-7.

Delaney, K. B. and Evans, S. G. (2015) 'The 2000 Yigong landslide (Tibetan Plateau), rockslide-dammed lake and outburst flood: Review, remote sensing analysis, and process modelling', *Geomorphology*, 246, pp. 377–393. doi: 10.1016/j.geomorph.2015.06.020.

Deline, P., Alberto, W., Broccolato, M., Hungr, O., Noetzli, J., Ravanel, L. and Tamburini, A. (2011) 'The December 2008 Crammont rock avalanche, Mont Blanc massif area, Italy', *Natural Hazards and Earth System Science*, 11(12), pp. 3307–3318. doi: 10.5194/nhess-11-3307-2011.

Deplus, C., Le Friant, A., Boudon, G., Komorowski, J.-C., Villemant, B., Harford, C., Ségoufin, J. and Cheminée, J.-L. (2001) 'Submarine evidence for large-scale debris avalanches in the Lesser Antilles Arc', *Earth and Planetary Science Letters*, 192(2), pp. 145–157. doi: 10.1016/S0012-821X(01)00444-7.

Dlabola, E. K., Wilson, G. S., Gorman, A. R., Riesselman, C. R. and Moy, C. M. (2015) 'A post-glacial relative sea-level curve from Fiordland, New Zealand', *Global and Planetary Change*, 131, pp. 104–114. doi: 10.1016/j.gloplacha.2015.05.010.

Dortch, J. M., Owen, L. A., Haneberg, W. C., Caffee, M. W., Dietsch, C. and Kamp, U. (2009) 'Nature and timing of large landslides in the Himalaya and Transhimalaya of northern India', *Quaternary Science Reviews*, 28(11–12), pp. 1037–1054. doi: 10.1016/j.quascirev.2008.05.002.

Downes, G., Barberopoulou, A., Cochran, U., Clark, K. and Scheele, F. (2017) 'The New Zealand Tsunami database: Historical and modern records', *Seismological Research Letters*, 88(2), pp. 342–353. doi: 10.1785/0220160135.

Downes, G., Cochran, U., Wallace, L., Reyners, M., Berryman, K., Walters, R., Callaghan, F., Barnes, P. and Bell, R. (2005) *Understanding local source tsunami : 1820s Southland tsunami*, *EQC Project 03/490*. Available at: https://www.eqc.govt.nz/sites/public_files/3723-Understanding-local-source-tsunami-1820s-Southland-tsunami.pdf (Accessed: 28 February 2019).

Drost, F., Renwick, J., Bhaskaran, B., Oliver, H. and McGregor, J. (2007) 'A simulation of New Zealand's climate during the Last Glacial Maximum', *Quaternary Science Reviews*, 26(19–21), pp. 2505–2525. doi: 10.1016/j.quascirev.2007.06.005.

Dufresne, A., Bösmeier, A. and Prager, C. (2016) 'Sedimentology of rock avalanche deposits – Case study and review', *Earth-Science Reviews*, 163, pp. 234–259. doi: 10.1016/j.earscirev.2016.10.002.

Dufresne, A. and Davies, T. R. (2009) 'Longitudinal ridges in mass movement deposits', *Geomorphology*, 105(3–4), pp. 171–181. doi: 10.1016/j.geomorph.2008.09.009.

Dufresne, A., Davies, T. R. and McSaveney, M. J. (2009) 'Influence of runout-path material on emplacement of the Round Top rock avalanche, New Zealand', *Earth Surface Processes and Landforms*, 35(2), p. n/a-n/a. doi: 10.1002/esp.1900.

Dufresne, A. and Dunning, S. A. (2017) 'Process dependence of grain size distributions in rock avalanche deposits', *Landslides*, 14(5), pp. 1555–1563. doi: 10.1007/s10346-017-0806-y.

Dufresne, A., Geertsema, M., Shugar, D. H., Koppes, M., Higman, B., Haeussler, P. J., Stark, C., Venditti, J. G., Bonno, D., Larsen, C., Gulick, S. P. S., McCall, N., Walton, M., Loso, M. G. and Willis, M. J. (2018) 'Sedimentology and geomorphology of a large tsunamigenic landslide, Taan Fiord, Alaska', *Sedimentary Geology*, 364, pp. 302–318. doi: 10.1016/j.sedgeo.2017.10.004.

Dugan, B. and Sheahan, T. C. (2012) 'Offshore sediment overpressures of passive margins: Mechanisms, measurement, and models', *Reviews of Geophysics*, 50(3). doi: 10.1029/2011rg000379.

Dunning, S. A., Mitchell, W. A., Rosser, N. J. and Petley, D. N. (2007) 'The Hattian Bala rock avalanche and associated landslides triggered by the Kashmir Earthquake of 8 October 2005', *Engineering Geology*, 93(3–4), pp. 130–144. doi: 10.1016/J.ENGGEO.2007.07.003.

Dunning, S. A., Rosser, N. J., McColl, S. T. and Reznichenko, N. V. (2015) 'Rapid sequestration of rock avalanche deposits within glaciers', *Nature Communications*, 6, p. 7964. doi: 10.1038/ncomms8964.

Dykstra, J. L. (2012) *The Post-Lgm Evolution of Milford Sound, Fiordland, New Zealand Timing of Ice Retreat, The role of Mass wasting & Implications for Hazards*. University of Canterbury.

Van Den Eeckhaut, M. and Hervás, J. (2012) 'State of the art of national landslide databases in Europe and their potential for assessing landslide susceptibility, hazard and risk', *Geomorphology*, 139–140, pp. 545–558. doi: 10.1016/j.geomorph.2011.12.006.

Van Den Eeckhaut, M., Poesen, J., Govers, G., Verstraeten, G. and Demoulin, A. (2007) 'Characteristics of the size distribution of recent and historical landslides in a populated hilly region', *Earth and Planetary Science Letters*. doi: 10.1016/j.epsl.2007.01.040.

Eisbacher, G. (1983) *Field Trip Guidebook - Slope Stability and Mountain Torrents Fraser Lowlands and Southern Coast Mountains, British Columbia*. Geological Society of Canada.

Ekström, G. and Stark, C. P. (2013) 'Simple scaling of catastrophic landslide dynamics', *Science*, 339(6126), pp. 1416–1419. doi: 10.1126/science.1232887.

Elverhøi, A., de Blasio, F. V., Butt, F. A., Issler, D., Harbitz, C., Engvik, L., Solheim, A. and Marr, J. (2002) 'Submarine mass-wasting on glacially-influenced continental slopes: processes and dynamics', *Geological Society, London, Special Publications*, 203(1), pp. 73–87. doi: 10.1144/GSL.SP.2002.203.01.05.

Evans, s. G., Mugnozza, g. S., strom, a. L., Hermanns, r. L., Ischuk, a. and Vinnichenko, s. (2006) 'Landslides from massive rock slope failure and associated phenomena', in Evans, S. G., Mugnozza, G. S., Strom, A., and Hermanns, R. L. (eds) *Landslides from Massive Rock Slope Failure*. Dordrecht: Springer Netherlands, pp. 3–52. doi: 10.1007/978-1-4020-4037-5_1.

Evans, L. P. (2015) *Sedimentological Investigation of Late Glacial (Otiran) Exposures Along the Southern Margins of Lake Wanaka, South Island, New Zealand*. University of Queensland. Available at: https://espace.library.uq.edu.au/view/UQ:374172 (Accessed: 10 July 2017).

Evans, S. G., Bishop, N. F., Fidel Smoll, L., Valderrama Murillo, P., Delaney, K. B. and Oliver-Smith, A. (2009) 'A re-examination of the mechanism and human impact of catastrophic mass flows originating on Nevado Huascarán, Cordillera Blanca, Peru in 1962 and 1970', *Engineering Geology*, 108(1–2), pp. 96–118. doi: 10.1016/j.enggeo.2009.06.020.

Evans, S. G., Guthrie, R. H., Roberts, N. J. and Bishop, N. F. (2007) 'The disastrous 17 February 2006 rockslide-debris avalanche on Leyte Island, Philippines: A catastrophic landslide in tropical mountain terrain', *Natural Hazards and Earth System Science*. doi: 10.5194/nhess-7-89-2007.

Evans, S. G., Hungr, O. and Enegren, E. G. (1994) 'The Avalanche Lake rock avalanche, Mackenzie Mountains, Northwest Territories, Canada: description, dating, and dynamics', *Canadian Geotechnical Journal*, 31(5), pp. 749–768. doi: 10.1139/t94-086.

Evans, S. G. and Savigny, K. W. (1994) 'Landslides in the Vancouver-Fraser Valley-Whistler region', *Bulletin - Geological Survey of Canada*. doi: 10.1016/0148-9062(95)99020-x.

Evans, S. G., Tutubalina, O. V., Drobyshev, V. N., Chernomorets, S. S., McDougall, S., Petrakov, D. A. and Hungr, O. (2009) 'Catastrophic detachment and high-velocity long-runout flow of Kolka Glacier, Caucasus Mountains, Russia in 2002', *Geomorphology*, 105(3–4), pp. 314–321. doi: 10.1016/j.geomorph.2008.10.008.

Evers, F. M., Hager, W. H. and Boes, R. M. (2019) 'Spatial Impulse Wave Generation and Propagation', *Journal of Waterway, Port, Coastal, and Ocean Engineering*. doi: 10.1061/(asce)ww.1943-5460.0000514.

Expedition Scientists, 340 (2012) *Lesser Antilles volcanism and landslides: implications for hazard assessment and long-term magmatic evolution of the arc*, *IODP Preliminary Report*. doi: 10.2204/iodp.pr.340.2012.

Fan, X., Dufresne, A., Siva Subramanian, S., Strom, A., Hermanns, R., Tacconi Stefanelli, C., Hewitt, K., Yunus, A. P., Dunning, S., Capra, L., Geertsema, M., Miller, B., Casagli, N., Jansen, J. D. and Xu, Q. (2020) 'The formation and impact of landslide dams – State of the art', *Earth-Science Reviews*. Elsevier B.V., p. 103116. doi: 10.1016/j.earscirev.2020.103116.

Favreau, P., Mangeney, A., Lucas, A., Crosta, G. and Bouchut, F. (2010) 'Numerical modeling of landquakes', *Geophysical Research Letters*. doi: 10.1029/2010GL043512.

Fischer, J. T., Kowalski, J. and Pudasaini, S. P. (2012) 'Topographic curvature effects in applied avalanche modeling', *Cold Regions Science and Technology*, 74–75, pp. 21–30. doi: 10.1016/j.coldregions.2012.01.005.

Fitze, P. (2010) *Runout analysis of rapid, flow-like landslides*. Hochschule für Technik Rapperswil, Rapperswil-Jona, St. Gallen.

Fitzharris, B. B., Clare, G. R. and Renwick, J. (2007) 'Teleconnections between Andean and New Zealand glaciers', *Global and Planetary Change*, 59(1–4), pp. 159–174. doi: 10.1016/j.gloplacha.2006.11.022.

Fitzsimons, S. and Howarth, J. (2018) 'Glaciolacustrine Processes', in *Past Glacial Environments: Second Edition*. Elsevier, pp. 309–334. doi: 10.1016/B978-0-08-100524-8.00009-9.

Flemings, P., Long, H., Dugan, B., Germaine, J., John, C., Behrmann, J., Sawyer, D. and Jackson, K. G. (2008) 'Pore pressure penetrometers document high overpressure near the seafloor where multiple submarine landslides have occurred on the continental slope, offshore Louisiana, Gulf of Mexico'. doi: 10.1016/j.epsl.2007.12.005.

Forsyth, P. J., Turnbull, I. M., Beanland, S. and Thomson, R. (2006) *Surface effects and geological observations following the 1988 Te Anau and 1989 Doubtful Sound earthquakes, Fiordland, New Zealand*. Available at: internal-pdf://213.77.50.64/Forsyth et al. 2006 surface_effects_and_geolog.pdf.

Frey-Martínez, J., Cartwright, J. and James, D. (2006) 'Frontally confined versus frontally emergent submarine landslides: A 3D seismic characterisation', *Marine and Petroleum Geology*, 23(5), pp. 585–604. doi: 10.1016/j.marpetgeo.2006.04.002.

Le Friant, A., Ishizuka, O., Boudon, G., Palmer, M. R., Talling, P. J., Villemant, B., Adachi, T., Aljahdali, M., Breitkreuz, C., Brunet, M., Caron, B., Coussens, M., Deplus, C., Endo, D., Feuillet, N., Fraas, A. J., Fujinawa, A., Hart, M. B., Hatfield, R. G., Hornbach, M., Jutzeler, M., Kataoka, K. S., Komorowski, J.-C., Lebas, E., Lafuerza, S., Maeno, F., Manga, M., Martínez-Colón, M., McCanta, M., Morgan, S., Saito, T., Slagle, A., Sparks, S., Stinton, A., Stroncik, N., Subramanyam, K. S. V., Tamura, Y., Trofimovs, J., Voight, B., Wall-Palmer, D., Wang, F. and

Watt, S. F. L. (2015) 'Submarine record of volcanic island construction and collapse in the Lesser Antilles arc: First scientific drilling of submarine volcanic island landslides by IODPExpedition 340', *Geochemistry, Geophysics, Geosystems*, 16(2), pp. 420–442. doi: 10.1002/2014GC005652.

Fritz, H. M. (2002) 'Initial phase of landslide generated impulse waves', *Mitteilungen der Versuchsanstalt fur Wasserbau, Hydrologie und Glaziologie an der Eidgenossischen Technischen Hochschule Zurich*, (178), pp. 1–253. doi: 10.3929/ethz-a-004443906.

Fritz, H. M., Hager, W. H. and Minor, H.-E. (2004) 'Near Field Characteristics of Landslide Generated Impulse Waves', *Journal of Waterway, Port, Coastal, Ocean Enginnering*, 130(6), pp. 287–302. doi: 10.1061/(ASCE)0733-950X(2004)130:6(287).

Fritz, H. M., Mohammed, F. and Yoo, J. (2009) 'Lituya bay landslide impact generated mega-tsunami 50th anniversary', in *Pure and Applied Geophysics*, pp. 153–175. doi: 10.1007/s00024-008-0435-4.

Froude, M. J. and Petley, D. N. (2018) 'Global fatal landslide occurrence from 2004 to 2016', *Natural Hazards and Earth System Sciences*, 18(8), pp. 2161–2181. doi: 10.5194/nhess-18-2161-2018.

Fry, B., Bannister, S., Beavan, J., Bland, L., Bradley, B., Cox, S., Cousins, J., Gale, N., Hancox, G., Holden, C., Jongens, R., Power, W., Prasetya, G., Reyners, M., Ristau, J., Robinson, R., Samsonov, S. and Wilson, K. (2010) 'The mw 7.6 dusky sound earthquake of 2009: Preliminary report', *Bulletin of the New Zealand Society for Earthquake Engineering*, 43(1), pp. 24–40. doi: 10.5459/bnzsee.43.1.24-40.

Gage, M. (1975) 'Glacial Lakes', in Jolly, V. H. and Brown, J. M. A. (eds) *New Zealand Lakes*. 1st edn. Auckland University Press, pp. 57–69.

Gales, J. A., Talling, P. J., Cartigny, M. J. B., Hughes Clarke, J., Lintern, G., Stacey, C. and Clare, M. A. (2019) 'What controls submarine channel development and the morphology of deltas entering deep-water fjords?', *Earth Surface Processes and Landforms*, 44(2), pp. 535–551. doi: 10.1002/esp.4515.

Gao, Y., Yin, Y., Li, B., Feng, Z., Wang, W., Zhang, N. and Xing, A. (2017) 'Characteristics and numerical runout modeling of the heavy rainfall-induced catastrophic landslide–debris flow at Sanxicun, Dujiangyan, China, following the Wenchuan Ms 8.0 earthquake', *Landslides*,

14(4), pp. 1361–1374. doi: 10.1007/s10346-016-0793-4.

Gardner, J. V., Mayer, L. A. and Hughs Clarke, J. E. (2000) 'Morphology and processes in Lake Tahoe (California-Nevada)', *Bulletin of the Geological Society of America*, 112(5), pp. 736–746. doi: 10.1130/0016-7606(2000)112<736:MAPILT>2.0.CO;2.

Gauthier, D., Anderson, S. A., Fritz, H. M. and Giachetti, T. (2018) 'Karrat Fjord (Greenland) tsunamigenic landslide of 17 June 2017: initial 3D observations', *Landslides*, 15(2), pp. 327–332. doi: 10.1007/s10346-017-0926-4.

Gee, M. J. R., Uy, H. S., Warren, J., Morley, C. K. and Lambiase, J. J. (2007) 'The Brunei slide: A giant submarine landslide on the North West Borneo Margin revealed by 3D seismic data', *Marine Geology*, 246(1), pp. 9–23. doi: 10.1016/j.margeo.2007.07.009.

Gee, M. J. R., Watts, A. B., Masson, D. G. and Mitchell, N. C. (2001) 'Landslides and the evolution of El Hierro in the Canary Islands', *Marine Geology*, 177(3), pp. 271–293. doi: http://dx.doi.org/10.1016/S0025-3227(01)00153-0.

Geertsema, M., Clague, J. J., Schwab, J. W. and Evans, S. G. (2006) 'An overview of recent large catastrophic landslides in northern British Columbia, Canada', *Engineering Geology*. doi: 10.1016/j.enggeo.2005.06.028.

George, D. L. and Iverson, R. M. (2014) 'A depth-averaged debris-flow model that includes the effects of evolving dilatancy. II. Numerical predictions and experimental tests', *Proceedings of the Royal Society A: Mathematical, Physical and Engineering Sciences*, 470(2170). doi: 10.1098/rspa.2013.0820.

George, D. L., Iverson, R. M. and Cannon, C. M. (2017) 'New methodology for computing tsunami generation by subaerial landslides: Application to the 2015 Tyndall Glacier landslide, Alaska', *Geophysical Research Letters*, 44(14), pp. 7276–7284. doi: 10.1002/2017GL074341.

Ghirotti, M. (2012) 'The 1963 Vaiont landslide, Italy', in Clague, J. J. and Stead, D. (eds) *Landslides: Types, Mechanisms and Modeling*. Cambridge: Cambridge University Press, pp. 359–372. doi: 10.1017/cbo9780511740367.030.

Giachetti, T., Paris, R., Kelfoun, K. and Pérez-Torrado, F. J. (2011) 'Numerical modelling of the tsunami triggered by the Güìmar debris avalanche, Tenerife (Canary Islands): Comparison with field-based data', *Marine Geology*. doi: 10.1016/j.margeo.2011.03.018.

Gillespie, C. S. (2015) 'Fitting heavy tailed distributions: The poweRlaw Package', *Journal of*

Statistical Software, 64(2), pp. 1–16. doi: 10.18637/jss.v064.i02.

Girardclos, S., Schmidt, O. T., Sturm, M., Ariztegui, D., Pugin, A. and Anselmetti, F. S. (2007) 'The 1996 AD delta collapse and large turbidite in Lake Brienz', *Marine Geology*, 241(1–4), pp. 137–154. doi: 10.1016/j.margeo.2007.03.011.

Glade, T. and Crozier, M. J. (2005) 'The Nature of Landslide Hazard Impact', in *Landslide Hazard and Risk*. John Wiley & Sons, Ltd, pp. 41–74. doi: 10.1002/9780470012659.ch2.

Glimsdal, S., L'Heureux, J. S., Harbitz, C. B. and Løvholt, F. (2016) 'The 29th January 2014 submarine landslide at Statland, Norway—landslide dynamics, tsunami generation, and run-up', *Landslides*, 13(6), pp. 1435–1444. doi: 10.1007/s10346-016-0758-7.

Golledge, N. R., Mackintosh, A. N., Anderson, B. M., Buckley, K. M., Doughty, A. M., Barrell, D. J. A., Denton, G. H., Vandergoes, M. J., Andersen, B. G. and Schaefer, J. M. (2012) 'Last Glacial Maximum climate in New Zealand inferred from a modelled Southern Alps icefield', *Quaternary Science Reviews*, 46, pp. 30–45. doi: 10.1016/j.quascirev.2012.05.004.

Goren, L. and Aharonov, E. (2007) 'Long runout landslides: The role of frictional heating and hydraulic diffusivity', *Geophysical Research Letters*. doi: 10.1029/2006GL028895.

Grämiger, L. M., Moore, J. R., Gischig, V. S., Ivy-Ochs, S. and Loew, S. (2017) 'Beyond debuttressing: Mechanics of paraglacial rock slope damage during repeat glacial cycles', *Journal of Geophysical Research: Earth Surface*, 122(4), pp. 1004–1036. doi: 10.1002/2016JF003967.

Grämiger, L. M., Moore, J., Vockenhuber, C., Aaron, J., Hajdas, I. and Ivy-Ochs, S. (2016) 'Two early Holocene rock avalanches in the Bernese Alps (Rinderhorn, Switzerland)', *Geomorphology*, 268. doi: 10.1016/j.geomorph.2016.06.008.

Gruber, S. (2012) 'Derivation and analysis of a high-resolution estimate of global permafrost zonation', *The Cryosphere*, 6(1), pp. 221–233. doi: 10.5194/tc-6-221-2012.

Guthrie, R. H., Evans, S. G., Catane, S. G., Zarco, M. A. H. and Saturay, R. M. (2009) 'The 17 February 2006 rock slide-debris avalanche at Guinsaugon Philippines: A synthesis', *Bulletin of Engineering Geology and the Environment*, 68(2), pp. 201–213. doi: 10.1007/s10064-009-0205-2.

Guthrie, R. H., Friele, P., Allstadt, K., Roberts, N., Evans, S. G., Delaney, K. B., Roche, D., Clague, J. J. and Jakob, M. (2012) 'The 6 August 2010 Mount Meager rock slide-debris flow,

Coast Mountains, British Columbia: Characteristics, dynamics, and implications for hazard and risk assessment', *Natural Hazards and Earth System Science*. doi: 10.5194/nhess-12-1277-2012.

Guzzetti, F., Ardizzone, F., Cardinali, M., Rossi, M. and Valigi, D. (2009) 'Landslide volumes and landslide mobilization rates in Umbria, central Italy', *Earth and Planetary Science Letters*, 279(3–4), pp. 222–229. doi: 10.1016/j.epsl.2009.01.005.

Hadley, J. B. (1978) 'Madison canyon rockslide, montana, U.S.A.', in *Developments in Geotechnical Engineering*. doi: 10.1016/B978-0-444-41507-3.50012-X.

Haeberli, W., Schaub, Y. and Huggel, C. (2017) 'Increasing risks related to landslides from degrading permafrost into new lakes in de-glaciating mountain ranges', *Geomorphology*, 293, pp. 405–417. doi: 10.1016/j.geomorph.2016.02.009.

Haeussler, P. J., Gulick, S. P. S., McCall, N., Walton, M., Reece, R., Larsen, C., Shugar, D. H., Geertsema, M., Venditti, J. G. and Labay, K. (2018) 'Submarine Deposition of a Subaerial Landslide in Taan Fiord, Alaska', *Journal of Geophysical Research: Earth Surface*, 123(10), pp. 2443–2463. doi: 10.1029/2018JF004608.

Hage, S., Cartigny, M. J. B., Clare, M. A., Sumner, E. J., Vendettuoli, D., Clarke, J. E. H., Hubbard, S. M., Talling, P. J., Gwyn Lintern, D., Stacey, C. D., Englert, R. G., Vardy, M. E., Hunt, J. E., Yokokawa, M., Parsons, D. R., Hizzett, J. L., Azpiroz-Zabala, M. and Vellinga, A. J. (2018) 'How to recognize crescentic bedforms formed by supercritical turbidity currents in the geologic record: Insights from active submarine channels', *Geology*, 46(6), pp. 563–566. doi: 10.1130/G40095.1.

Haines, A. J. and Wallace, L. M. (2020) 'New Zealand-Wide Geodetic Strain Rates Using a Physics-Based Approach', *Geophysical Research Letters*, 47(1). doi: 10.1029/2019GL084606.

Halliday, G. S. (2010) 'Large-scale toppling of schist in North-West Otago, Southern Alps, NZ; a precursor to rockslides and rock avalanches', *Geologically Active*. Edited by W. et al. Taylor and Francis, p. 10.

Hamilton, D. P., McBride, C., Özkundakci, D., Schallenberg, M., Verburg, P., de Winton, M., Kelly, D., Hendy, C. and Ye, W. (2012) 'Effects of Climate Change on New Zealand Lakes', in *Climatic Change and Global Warming of Inland Waters: Impacts and Mitigation for Ecosystems and Societies*. Chichester, UK: John Wiley & Sons, Ltd, pp. 337–366. doi:

10.1002/9781118470596.ch19.

Hampton, M. A., Lee, H. J. and Locat, J. (1996) 'Submarine landslides', *Reviews of Geophysics*, 34(1), pp. 33–59. doi: 10.1029/95RG03287.

Hancox, G. T. (2012) *Environment Southland Tsunami and Seiche Study – Stage 2 : Evaluation of potential earthquake-induced landslide sites where tsunami waves could be generated on Lake Manapouri and Lake Te Anau*, *GNS Science Consultancy Report 2012/146*.

Hancox, G. T., Cox, S., Turnbull, I. M. and Crozier, M. J. (2003) *Reconnaissance studies of landslides and other ground damage caused by the Mw 7.2 Fiordland earthquake of 22 August 2003*, *Institute of Geological & Nuclear Sciences science report 2003/30*.

Hancox, G. T. and Perrin, N. D. (2009) 'Green Lake Landslide and other giant and very large postglacial landslides in Fiordland, New Zealand', *Quaternary Science Reviews*, 28(11–12), pp. 1020–1036. doi: 10.1016/j.quascirev.2008.08.017.

Hancox, G. T., Perrin, N. D. and Dellow, G. D. (2002) 'Recent studies of historical earthquake-induced landsliding, ground damage, and MM intensity in New Zealand', *Bulletin of the New Zealand Society for Earthquake Engineering*, 35(2), pp. 59–95. doi: 10.5459/bnzsee.35.2.59-95.

Hancox, G. T., Vandergoes, M., Langridge, R. M., Archibald, G. and Perrin, N. D. (2013) *Recent mapping and radiocarbon dating of three giant landslides in northern Fiordland, New Zealand*, *GNS Sciene Report 2012/45*.

Hancox, G. and Thomson, R. (2013) *The January 2013 Mt Haast Rock Avalanche The January 2013 Mt Haast Rock Avalanche and Ball Ridge Rock Fall in Aoraki / Mt Cook National Park , New Zealand*, *GNS Science Report*.

Hansen, L., Waldmann, N., Storms, J. E. A., Eilertsen, R. S., Ariztegui, D., Chapron, E. and Nesje, A. (2016) 'Morphological signatures of mass wasting and delta processes in a fjord-lake system: Insights from Lovatnet, western Norway', *Norsk Geologisk Tidsskrift*, 96(3). doi: 10.17850/njg96-3-02.

Harbitz, C. B., Glimsdal, S., Løvholt, F., Kveldsvik, V., Pedersen, G. K. and Jensen, A. (2014) 'Rockslide tsunamis in complex fjords: From an unstable rock slope at Åkerneset to tsunami risk in western Norway', *Coastal Engineering*, 88, pp. 101–122. doi: 10.1016/j.coastaleng.2014.02.003.

Harbitz, C. B., Løvholt, F., Pedersen, G. and Masson, D. G. (2006) 'Mechanisms of tsunami generation by submarine landslides: A short review', *Norsk Geologisk Tidsskrift*, 86(3), pp. 255–264. Available at: https://foreninger.uio.no/ngf/ngt/pdfs/NJG_86_255-264.pdf.

Harrison, L. M., Dunning, S. A., Woodward, J. and Davies, T. R. H. (2015) 'Post-rock-avalanche dam outburst flood sedimentation in Ram Creek, Southern Alps, New Zealand', *Geomorphology*, 241, pp. 135–144. doi: 10.1016/j.geomorph.2015.03.038.

Heijnen, M. S., Clare, M. A., Cartigny, M. J. B., Talling, P. J., Hage, S., Lintern, D. G., Stacey, C., Parsons, D. R., Simmons, S. M., Chen, Y., Sumner, E. J., Dix, J. K. and Hughes Clarke, J. E. (2020) 'Rapidly-migrating and internally-generated knickpoints can control submarine channel evolution', *Nature Communications*, 11(1), pp. 1–15. doi: 10.1038/s41467-020-16861-x.

Heller, V. and Hager, W. H. (2010) 'Impulse Product Parameter in Landslide Generated Impulse Waves', *Journal of Waterway, Port, Coastal, and Ocean Engineering*, 136(3), pp. 145–155. doi: 10.1061/(ASCE)WW.1943-5460.0000037.

Hermanns, R. L., Blikra, L. H., Naumann, M., Nilsen, B., Panthi, K. K., Stromeyer, D. and Longva, O. (2006) 'Examples of multiple rock-slope collapses from Köfels (Ötz valley, Austria) and western Norway', *Engineering Geology*, 83(1–3), pp. 94–108. doi: 10.1016/j.enggeo.2005.06.026.

Hermanns, R. L., L'Heureux, J.-S. and Blikra, L. H. (2013) 'Landslide Triggered Tsunami, Displacement Wave', in Bobrowsky, P. T. (ed.) *Encyclopedia of Natural Hazards*. Dordrecht: Springer Netherlands, pp. 611–615. doi: 10.1007/978-1-4020-4399-4_95.

Heron, D. W. (custodian) (2014) 'Geological map of New Zealand 1:250,000', *GNS Science Geological Map*. Lower Hutt, New Zealand: GNS Science.

Hewitt, K. (2009a) 'Glacially conditioned rock-slope failures and disturbance-regime landscapes, Upper Indus Basin, northern Pakistan', *Geological Society, London, Special Publications*, 320(1), pp. 235–255. doi: 10.1144/SP320.15.

Hewitt, K. (2009b) 'Rock avalanches that travel onto glaciers and related developments, Karakoram Himalaya, Inner Asia', *Geomorphology*, 103(1), pp. 66–79. doi: 10.1016/j.geomorph.2007.10.017.

Hewitt, K., Clague, J. J. and Orwin, J. F. (2008) 'Legacies of catastrophic rock slope failures in

mountain landscapes', *Earth-Science Reviews*, 87(1–2), pp. 1–38. doi: 10.1016/j.earscirev.2007.10.002.

Hewitt, K., Gosse, J. and Clague, J. J. (2011) 'Rock avalanches and the pace of late Quaternary development of river valleys in the Karakoram Himalaya', *Geological Society of America Bulletin*, 123(9–10), pp. 1836–1850. doi: 10.1130/B30341.1.

Hicks, D. M., Hill, J. and Shankar, U. (1996) 'Variation of suspended sediment yields around New Zealand: the relative importance of rainfall and geology', *IAHS*, 236, p. 156.

Hicks, D. M., Shankar, U., Mckerchar, A. I., Basher, L., Lynn, I., Page, M. and Jessen, M. (2011) 'Suspended sediment yields from New zealand rivers', *Journal of Hydrology New Zealand*, 50(1), pp. 81–142.

Hicks, M., Shankar, U. and Mckerchar, A. (2003) 'Sediment yield estimates: a GIS tool', *Water & Atmosphere*, 11(4), pp. 26–27.

Higman, B., Shugar, D. H., Stark, C. P., Ekström, G., Koppes, M. N., Lynett, P., Dufresne, A., Haeussler, P. J., Geertsema, M., Gulick, S., Mattox, A., Venditti, J. G., Walton, M. A. L., McCall, N., Mckittrick, E., MacInnes, B., Bilderback, E. L., Tang, H., Willis, M. J., Richmond, B., Reece, R. S., Larsen, C., Olson, B., Capra, J., Ayca, A., Bloom, C., Williams, H., Bonno, D., Weiss, R., Keen, A., Skanavis, V. and Loso, M. (2018) 'The 2015 landslide and tsunami in Taan Fiord, Alaska', *Scientific Reports*, 8(1). doi: 10.1038/s41598-018-30475-w.

Hilbe, M. and Anselmetti, F. S. (2014) 'Signatures of slope failures and river-delta collapses in a perialpine lake (Lake Lucerne, Switzerland)', *Sedimentology*, 61(7), pp. 1883–1907. doi: 10.1111/sed.12120.

Hilbe, M., Anselmetti, F. S., Eilertsen, R. S., Hansen, L. and Wildi, W. (2011) 'Subaqueous morphology of Lake Lucerne (Central Switzerland): implications for mass movements and glacial history', *Swiss Journal of Geosciences*, 104(3), pp. 425–443. doi: 10.1007/s00015-011-0083-z.

Hilton, R. G., Galy, A. and Hovius, N. (2008) 'Riverine particulate organic carbon from an active mountain belt: Importance of landslides', *Global Biogeochemical Cycles*, 22(1), p. n/a-n/a. doi: 10.1029/2006GB002905.

Hjelstuen, B. O., Haflidason, H., Sejrup, H. P. and Lysså, A. (2009) 'Sedimentary processes and depositional environments in glaciated fjord systems - Evidence from Nordfjord, Norway',

Marine Geology, 258(1–4), pp. 88–99. doi: 10.1016/j.margeo.2008.11.010.

House, M. A., Gurnis, M., Sutherland, R. and Kamp, P. J. J. (2005) 'Patterns of Late Cenozoic exhumation deduced from apatite and zircon U-He ages from Fiordland, New Zealand', *Geochemistry, Geophysics, Geosystems*, 6(9), p. n/a-n/a. doi: 10.1029/2005GC000968.

Hovius, N., Meunier, P., Lin, C.-W., Chen, H., Chen, Y.-G., Dadson, S., Horng, M.-J. and Lines, M. (2011) 'Prolonged seismically induced erosion and the mass balance of a large earthquake', *Earth and Planetary Science Letters*, 304(3–4), pp. 347–355. doi: 10.1016/J.EPSL.2011.02.005.

Hovius, N., Stark, C. P. and Allen, P. A. (1997) 'Sediment flux from a mountain belt derived by landslide mapping', *Geology*, 25(3), pp. 231–234. doi: 10.1130/0091-7613(1997)025<0231:SFFAMB>2.3.CO;2.

Howarth, J. D., Barth, N. C., Fitzsimons, S. J., Richards-Dinger, K., Clark, K. J., Biasi, G. P., Cochran, U. A., Langridge, R. M., Berryman, K. R. and Sutherland, R. (2021) 'Spatiotemporal clustering of great earthquakes on a transform fault controlled by geometry', *Nature Geoscience*, 14(5), pp. 314–320. doi: 10.1038/s41561-021-00721-4.

Howarth, J. D., Cochran, U. A., Langridge, R. M., Clark, K., Fitzsimons, S. J., Berryman, K., Villamor, P. and Strong, D. T. (2018) 'Past large earthquakes on the Alpine Fault: paleoseismological progress and future directions', *New Zealand Journal of Geology and Geophysics*, 61(3), pp. 309–328. doi: 10.1080/00288306.2018.1464658.

Howarth, J. D., Fitzsimons, S. J., Norris, R. J. and Jacobsen, G. E. (2012) 'Lake sediments record cycles of sediment flux driven by large earthquakes on the Alpine fault, New Zealand', *Geology*, 40(12), pp. 1091–1094. doi: 10.1130/G33486.1.

Howarth, J. D., Fitzsimons, S. J., Norris, R. J. and Jacobsen, G. E. (2014) 'Lake sediments record high intensity shaking that provides insight into the location and rupture length of large earthquakes on the Alpine Fault, New Zealand', *Earth and Planetary Science Letters*, 403, pp. 340–351. doi: 10.1016/j.epsl.2014.07.008.

Howarth, J. D., Fitzsimons, S. J., Norris, R. J., Langridge, R. and Vandergoes, M. J. (2016) 'A 2000 yr rupture history for the Alpine fault derived from Lake Ellery, South Island, New Zealand', *Bulletin of the Geological Society of America*, 128(3–4), pp. 627–643. doi: 10.1130/B31300.1.

Hu, W., Huang, R. Q., McSaveney, M., Yao, L., Xu, Q., Feng, M. S. and Zhang, X. H. (2019) 'Superheated steam, hot CO 2 and dynamic recrystallization from frictional heat jointly lubricated a giant landslide: Field and experimental evidence', *Earth and Planetary Science Letters*, 510, pp. 85–93. doi: 10.1016/j.epsl.2019.01.005.

Huggel, C., Zgraggen-Oswald, S., Haeberli, W., Kääb, A., Polkvoj, A., Galushkin, I. and Evans, S. G. (2005) 'The 2002 rock/ice avalanche at Kolka/Karmadon, Russian Caucasus: Assessment of extraordinary avalanche formation and mobility, and application of QuickBird satellite imagery', *Natural Hazards and Earth System Science*. doi: 10.5194/nhess-5-173-2005.

Hughes Clarke, J. E. (2018) 'Multibeam Echosounders', in *Springer Geology*. Springer, pp. 25–41. doi: 10.1007/978-3-319-57852-1_3.

Hughes, K. E., Geertsema, I. M., Kwoll, I. E., Koppes, I. M. N., Roberts, I. N. J., Clague, I. J. J., Rohland, I. S., Lake, B. and Columbia, C. (2020) 'Previously undiscovered landslide deposits in Harrison Lake, British Columbia, Canada', *Landslides*, pp. 1–10. doi: 10.1007/s10346-020-01514-3.

Hungr, O. (1981) *Dynamics of rock avalanches and slope movements*. University of Alberta, Edmonton.

Hungr, O. (1995) 'A model for the runout analysis of rapid flow slides, debris flows, and avalanches', *Canadian Geotechnical Journal*, 32(4), pp. 610–623. doi: 10.1139/t95-063.

Hungr, O. and Evans, S. G. (1996) 'Rock avalanche runout prediction using a dynamic model', in Senneset, K. and Balkema, A. A. (eds) *Proceedings of the 7th International Symposium on Landslides, Trondheim, Norway*. Rotterdam, pp. 233–238.

Hungr, O. and Evans, S. G. (2004) 'Entrainment of debris in rock avalanches: an analysis of a long run-out mechanism', *Geological Society of America Bulletin*, 116. doi: 10.1130/B25362.1.

Hungr, O., Leroueil, S. and Picarelli, L. (2014) 'The Varnes classification of landslide types, an update', *Landslides*, 11(2), pp. 167–194. doi: 10.1007/s10346-013-0436-y.

Hungr, O. and McDougall, S. (2009) 'Two numerical models for landslide dynamic analysis', *Computers and Geosciences*, 35(5), pp. 978–992. doi: 10.1016/j.cageo.2007.12.003.

Hungr, O., Morgenstern, N. and Wong, H. N. (2007) 'Review of benchmarking exercises on landslide debris runout and mobility modelling', in Ho and Li (eds) *Proceedings of the 2007 International Forum on Landslide Disaster Management*, pp. 755–812.

Imre, Bernd, Laue, Jan, Sarah, ·, Springman, M., Imre, B, Laue, J and Springman, · S M (2010) 'Fractal fragmentation of rocks within sturzstroms: insight derived from physical experiments within the ETH geotechnical drum centrifuge', *Granular Matter 2010 12:3*, 12(3), pp. 267–285. doi: 10.1007/S10035-009-0163-1.

Irwin, J. (1980) 'Sublacustrine channels in Lake Wanaka', *New Zealand Journal of Marine and Freshwater Research*, 14(1), pp. 87–92. doi: 10.1080/00288330.1979.9515848.

Irwin, J. and Ridgeway, N. M. (1976) 'Lake Wanaka, Bathymetry 1:55 440', *New Zealand Oceanographic Institute Chart, Lake Series*. Available at: internal-pdf://123.15.206.202/Irwin-1976-Lake Wanaka, Bathymetry 1_55 440.pdf.

Iverson, R. M. (1997) 'The physics of debris flows', *Reviews of Geophysics*, 35(3), pp. 245–296. doi: 10.1029/97RG00426.

Iverson, R. M. (2003) 'How should mathematical models of geomorphic processes be judged?', in *Geophysical Monograph Series*. Blackwell Publishing Ltd, pp. 83–94. doi: 10.1029/135GM07.

Iverson, R. M. and George, D. L. (2014) 'A depth-averaged debris-flow model that includes the effects of evolving dilatancy. I. Physical basis', *Proceedings of the Royal Society A: Mathematical, Physical and Engineering Sciences*, 470(2170). doi: 10.1098/rspa.2013.0819.

James, W. H. M., Carrivick, J. L., Quincey, D. J. and Glasser, N. F. (2019) 'A geomorphology based reconstruction of ice volume distribution at the Last Glacial Maximum across the Southern Alps of New Zealand', *Quaternary Science Reviews*, 219, pp. 20–35. doi: 10.1016/j.quascirev.2019.06.035.

Jibson, R. W. (1996) 'Use of landslides for paleoseismic analysis', *Engineering Geology*, 43(4), pp. 291–323. doi: 10.1016/S0013-7952(96)00039-7.

Jibson, R. W., Harp, E. L., Schulz, W. and Keefer, D. K. (2006) 'Large rock avalanches triggered by the M 7.9 Denali Fault, Alaska, earthquake of 3 November 2002', *Engineering Geology*, 83(1–3), pp. 144–160. doi: 10.1016/J.ENGGEO.2005.06.029.

Joanne, C., Collot, J. Y., Lamarche, G. and Migeon, S. (2010) 'Continental slope reconstruction after a giant mass failure, the example of the Matakaoa Margin, New Zealand', *Marine Geology*, 268(1–4), pp. 67–84. doi: 10.1016/j.margeo.2009.10.013.

Joanne, C., Lamarche, G. and Collot, J.-Y. (2013) 'Dynamics of giant mass transport in deep

submarine environments: the Matakaoa Debris Flow, New Zealand', *Basin Research*, 25(4), pp. 471–488. doi: 10.1111/bre.12006.

Johnson, B. C., Campbell, C. S. and Melosh, H. J. (2016) 'The reduction of friction in long runout landslides as an emergent phenomenon', *Journal of Geophysical Research, Earth Surface*, 121. doi: 10.1002/2015JF003751.

Keefer, D. K. (1984) 'Landslides caused by earthquakes', *Bulletin of the Geological Society of America*, 95(4), pp. 406–421. doi: 10.1130/0016-7606(1984)95<406:lcbe>2.0.co;2.

Keefer, D. K. (2000) 'Statiscal analysis of an earthquake-induced landslide distribution - The 1989 Loma Prieta, California event', *Engineering Geology*. doi: 10.1016/S0013-7952(00)00037-5.

Keefer, D. K. (2002) 'Investigating landslides caused by earthquakes - A historical review', *Surveys in Geophysics*, 23(6), pp. 473–510. doi: 10.1023/A:1021274710840.

Kelfoun, K. (2011) 'Suitability of simple rheological laws for the numerical simulation of dense pyroclastic flows and long-runout volcanic avalanches', *Journal of Geophysical Research: Solid Earth*, 116(8), p. 8209. doi: 10.1029/2010JB007622.

Kelfoun, K. and Druitt, T. H. (2005) 'Numerical modeling of the emplacement of Socompa rock avalanche, Chile', *Journal of Geophysical Research*, 110(B12), p. B12202. doi: 10.1029/2005JB003758.

Kelfoun, K., Giachetti, T. and Labazuy, P. (2010) 'Landslide-generated tsunamis at Réunion Island', *Journal of Geophysical Research: Earth Surface*, 115(4), pp. 1–17. doi: 10.1029/2009JF001381.

King, D. N. and Goff, J. R. (2010) 'Benefitting from differences in knowledge, practice and belief: Māori oral traditions and natural hazards science', *Nat. Hazards Earth Syst. Sci.*, 10(9), pp. 1927–1940. doi: 10.5194/nhess-10-1927-2010.

King, D. N., Shaw, W. S., Meihana, P. N. and Goff, J. R. (2018) 'Māori oral histories and the impact of tsunamis in Aotearoa-New Zealand', *Natural Hazards and Earth System Sciences*, 18(3), pp. 907–919. doi: 10.5194/nhess-18-907-2018.

King, D. N. T., Goff, J. and Skipper, A. (2007) 'Māori environmental knowledge and natural hazards in aotearoa-new zealand', *Journal of the Royal Society of New Zealand*, 37(2), pp. 59–73. doi: 10.1080/03014220709510536.

Klaucke, I. (2018) 'Sidescan Sonar', in *Springer Geology*. Springer, pp. 13–24. doi: 10.1007/978-3-319-57852-1_2.

Knudson, K. P., Hendy, I. L. and Neil, H. L. (2011) 'Re-examining Southern Hemisphere westerly wind behavior: Insights from a late Holocene precipitation reconstruction using New Zealand fjord sediments', *Quaternary Science Reviews*, 30(21–22), pp. 3124–3138. doi: 10.1016/j.quascirev.2011.07.017.

Korup, O. (2002) 'Recent research on landslide dams - A literature review with special attention to New Zealand', *Progress in Physical Geography*, 26(2), pp. 206–235. doi: 10.1191/0309133302pp333ra.

Korup, O. (2005a) 'Distribution of landslides in southwest New Zealand', *Landslides*, 2(1), pp. 43–51. doi: 10.1007/s10346-004-0042-0.

Korup, O. (2005b) 'Geomorphic hazard assessment of landslide dams in South Westland, New Zealand: Fundamental problems and approaches', *Geomorphology*, 66(1-4 SPEC. ISS.), pp. 167–188. doi: 10.1016/j.geomorph.2004.09.013.

Korup, O. (2005c) 'Geomorphic imprint of landslides on alpine river systems, southwest New Zealand', *Earth Surface Processes and Landforms*, 30(7), pp. 783–800. doi: 10.1002/esp.1171.

Korup, O. (2005d) 'Large landslides and their effect on sediment flux in South Westland, New Zealand', *Earth Surface Processes and Landforms*, 30(3), pp. 305–323. doi: 10.1002/esp.1143.

Korup, O. (2006a) 'Effects of large deep-seated landslides on hillslope morphology, western Southern Alps, New Zealand', *Journal of Geophysical Research: Earth Surface*, 111(1). doi: 10.1029/2004JF000242.

Korup, O. (2006b) 'Rock-slope failure and the river long profile', *Geology*, 34(1), pp. 45–48. doi: 10.1130/G21959.1.

Korup, O. (2008) 'Rock type leaves topographic signature in landslide-dominated mountain ranges', *Geophysical Research Letters*, 35(11). doi: 10.1029/2008GL034157.

Korup, O. (2011) 'Rockslide and Rock Avalanche Dams in the Southern Alps, New Zealand', in Evans, S. G., Hermanns, R. L., Strom, A., and Scarascia-Mugnozza, G. (eds) *Natural and Artificial Rockslide Dams*. Springer, Berlin, Heidelberg, pp. 123–146. doi: 10.1007/978-3-642-04764-0_4.

Korup, O. (2012) 'Earth's portfolio of extreme sediment transport events', *Earth-Science Reviews*, 112(3–4), pp. 115–125. doi: 10.1016/j.earscirev.2012.02.006.

Korup, O. and Clague, J. J. (2009) 'Natural hazards, extreme events, and mountain topography', *Quaternary Science Reviews*, 28(11–12), pp. 977–990. doi: 10.1016/j.quascirev.2009.02.021.

Korup, O., Clague, J. J., Hermanns, R. L., Hewitt, K., Strom, A. L. and Weidinger, J. T. (2007) 'Giant landslides, topography, and erosion', *Earth and Planetary Science Letters*, 261(3–4), pp. 578–589. doi: 10.1016/j.epsl.2007.07.025.

Korup, O., Densmore, A. L. and Schlunegger, F. (2010) 'The role of landslides in mountain range evolution', *Geomorphology*, 120(1–2), pp. 77–90. doi: 10.1016/j.geomorph.2009.09.017.

Korup, O. and Dunning, S. (2015) 'Catastrophic mass wasting in high mountains', *The High-Mountain Cryosphere*, pp. 127–146. doi: 10.1017/CBO9781107588653.008.

Korup, O. and Tweed, F. (2007) 'Ice, moraine, and landslide dams in mountainous terrain', *Quaternary Science Reviews*, 26(25–28), pp. 3406–3422. doi: 10.1016/J.QUASCIREV.2007.10.012.

Krause, M. (2016) *Characterise change in post-glacial climate using seismic imaging of Lake Ohau sediments*. University of Otago, Dunedin.

Kremer, K., Hilbe, M., Simpson, G., Decrouy, L., Wildi, W. and Girardclos, S. (2015) 'Reconstructing 4000 years of mass movement and tsunami history in a deep peri-Alpine lake (Lake Geneva, France-Switzerland)', *Sedimentology*, 62(5), pp. 1305–1327. doi: 10.1111/sed.12190.

Kremer, K., Wirth, S. B., Reusch, A., Fäh, D., Bellwald, B., Anselmetti, F. S., Girardclos, S. and Strasser, M. (2017) 'Lake-sediment based paleoseismology: Limitations and perspectives from the Swiss Alps', *Quaternary Science Reviews*. Elsevier Ltd, pp. 1–18. doi: 10.1016/j.quascirev.2017.04.026.

Kwan, J. and Sun, H. W. (2007) 'Benchmarking exercise on landslide mobility modelling – runout analyses using 3dDMM', in Ho and Li (eds) *Proceedings of the 2007 International Forum on Landslide Disaster Management*, pp. 945–966.

L'Heureux, J.-S., Hansen, L., Longva, O. and Eilertsen, R. S. (2013) 'Landslides Along Norwegian Fjords: Causes and Hazard Assessment', in *Landslide Science and Practice*. Springer Berlin Heidelberg, pp. 81–87. doi: 10.1007/978-3-642-31427-8_10.

Lajeunesse, P., Sinkunas, B., Morissette, A., Normandeau, A., Joyal, G., St-Onge, G. and Locat, J. (2017) 'Large-scale seismically-induced mass-movements in a former glacial lake basin: Lake Témiscouata, northeastern Appalachians (eastern Canada)', *Marine Geology*, 384, pp. 120–130. doi: 10.1016/j.margeo.2016.04.007.

Lamarche, G., Joanne, C. and Collot, J. Y. (2008) 'Successive, large mass-transport deposits in the south Kermadec fore-arc basin, New Zealand: The Matakaoa Submarine Instability Complex', *Geochemistry, Geophysics, Geosystems*, 9(4), p. n/a-n/a. doi: 10.1029/2007GC001843.

Langridge, R. M., Ries, W. F., Litchfield, N. J., Villamor, P., Van Dissen, R. J., Barrell, D. J. A., Rattenbury, M. S., Heron, D. W., Haubrock, S., Townsend, D. B., Lee, J. M., Berryman, K. R., Nicol, A., Cox, S. C. and Stirling, M. W. (2016) 'The New Zealand Active Faults Database', *New Zealand Journal of Geology and Geophysics*, 59(1), pp. 86–96. doi: 10.1080/00288306.2015.1112818.

Larsen, I. J., Montgomery, D. R. and Korup, O. (2010) 'Landslide erosion controlled by hillslope material', *Nature Geoscience*, 3(4), pp. 247–251. doi: 10.1038/ngeo776.

Lastras, G., Amblas, D., Calafat, A. M., Canals, M., Frigola, J., Hermanns, R. L., Lafuerza, S., Longva, O., Micallef, A., Sepúlveda, S. A., Vargas, G., Batist, M. De, Daele, M. Van, Azpiroz, M., Bascuñán, I., Duhart, P., Iglesias, O., Kempf, P. and Rayo, X. (2013) 'Landslides Cause Tsunami Waves: Insights From Aysén Fjord, Chile', *Eos, Transactions American Geophysical Union*, 94(34), pp. 297–298. doi: 10.1002/2013EO340002.

Lastras, G., Amblas, D., Canals, M., Azpiroz, M., Bascuñán, I., Calafat, A. M., Duhart, P., Frigola, J., Hermanns, R. L., Iglesias, O., Kempf, P., Lafuerza, S., Longva, O., Micallef, A., Rayo, X., Sepúlveda, S. A. and Vargas, G. (2016) 'Fjord-flank collapse and associated deformation in Aysén Fjord, Chile', *Geological Society Memoir*, 46(1), pp. 107–108. doi: 10.1144/M46.15.

Lee, H., Ryan, H., Kayen, R. E., Haeussler, P. J., Dartnell, P. and Hampton, M. A. (2006) 'Varieties of submarine failure morphologies of seismically-induced landslides in Alaskan fjords', *Norwegian Journal of Geology*, 86(3), pp. 221–230. Available at: http://pubs.er.usgs.gov/publication/70028701.

Lee, J., Davies, T. and Bell, D. (2009) 'Successive Holocene rock avalanches at Lake Coleridge, Canterbury, New Zealand', *Landslides*, 6(4), pp. 287–297. doi: 10.1007/s10346-009-0163-6.

Legros, F. (2002) 'The mobility of long-runout landslides', *Engineering Geology*, 63(3–4), pp. 301–331. doi: 10.1016/S0013-7952(01)00090-4.

Levy, R. H., Dunbar, G. B., Vandergoes, M. J., Howarth, J. D., Kingan, T., Pyne, A. R., Brotherston, G., Clarke, M., Dagg, B., Hill, M., Kenton, E., Little, S., Mandeno, D., Moy, C., Muldoon, P., Doyle, P., Raines, C., Rutland, P., Strong, D., Terezow, M., Cochrane, L., Cossu, R., Fitzsimons, S., Florindo, F., Forrest, A. L., Gorman, A. R., Kaufman, D. S., Lee, M. K., Li, X., Lurcock, P., McKay, N., Nelson, F., Purdie, J., Roop, H. A., Geoffrey Schladow, S., Sood, A., Upton, P., Walker, S. L. and Wilson, G. S. (2018) 'A high-resolution climate record spanning the past 17 000 years recovered from Lake Ohau, South Island, New Zealand', *Scientific Drilling*, 24, pp. 41–50. doi: 10.5194/sd-24-41-2018.

Lintern, D. G., Mosher, D. C. and Scherwath, M. (2019) 'Advancing from subaqueous mass movement case studies to providing advice and mitigation', *Geological Society Special Publication*, 477(1), pp. 1–14. doi: 10.1144/SP477-2018-190.

LINZ (2020) *New Zealand Long-Term Prioritised Hydrographic Survey Plan (HYPLAN)*.

Lipovsky, P. S., Evans, S. G., Clague, J. J., Hopkinson, C., Couture, R., Bobrowsky, P., Ekström, G., Demuth, M. N., Delaney, K. B., Roberts, N. J., Clarke, G. and Schaeffer, A. (2008) 'The July 2007 rock and ice avalanches at Mount Steele, St. Elias Mountains, Yukon, Canada', *Landslides*. doi: 10.1007/s10346-008-0133-4.

Litchfield, N. J., Van Dissen, R., Sutherland, R., Barnes, P. M., Cox, S. C., Norris, R., Beavan, R. J., Langridge, R., Villamor, P., Berryman, K., Stirling, M., Nicol, A., Nodder, S., Lamarche, G., Barrell, D. J. A., Pettinga, J. R., Little, T., Pondard, N., Mountjoy, J. J. and Clark, K. (2014) 'A model of active faulting in New Zealand', *New Zealand Journal of Geology and Geophysics*, 57(1), pp. 32–56. doi: 10.1080/00288306.2013.854256.

Livanos, I., Nomikou, P., Papanikolaou, D. and Rousakis, G. (2013) 'The volcanic debris avalanche on the SE submarine slope of Nisyros volcano, Greece: Geophysical exploration and implications for subaerial eruption history', *Geo-Marine Letters*, 33(6), pp. 419–431. doi: 10.1007/s00367-013-0338-y.

Locat, J. and Lee, H. J. (2002) 'Submarine landslides: advances and challenges', *Can. Geotech. J.*, 39(1), pp. 193–212. doi: 10.1139/t01-089.

Locat, J., Leroueil, S., Locat, A. and Lee, H. (2016) 'Weak layers: Their definition and

classification from a geotechnical perspective', in *Submarine Mass Movements and Their Consequences, 6th International Symposium*. Kluwer Academic Publishers, pp. 3–12. doi: 10.1007/978-3-319-00972-8_1.

Longva, O., Blikra, L. H. and Dehls, J. (2009) 'Rock avalanches - distribution and frequencies in the inner part of Storfjorden, Møre og Romsdal County, Norway', *NGU report*, 2009.002, p. 32.

Løvholt, F., Pedersen, G., Harbitz, C. B., Glimsdal, S. and Kim, J. (2015) 'On the characteristics of landslide tsunamis', *Philosophical Transactions of the Royal Society*, 373(1), pp. 1–18. doi: 10.1109/TR.1979.5220496.

Lowe, D. J. and Green, J. D. (1987) 'Origins and development of the lakes', in Viner, A. B. (ed.) *Inland Waters of New Zealand*. Wellington: New Zealand Department of Scientific and Industrial Research, pp. 1–64. Available at: https://hdl.handle.net/10289/10555.

Lowe, D. J. and Green, J. D. (1992) 'Lakes', in Soons, J. M. and Selby, M. J. (eds) *Landforms of New Zealand*. 2nd Editio. Auckland: Longman Paul, pp. 107–143.

Lucas, A., Mangeney, A. and Ampuero, J. P. (2014) 'Frictional velocity-weakening in landslides on Earth and on other planetary bodies', *Nature Communications*, 5.

Lyså, A., Hjelstuen, B. O. and Larsen, E. (2010) 'Fjord infill in a high-relief area: Rapid deposition influenced by deglaciation dynamics, glacio-isostatic rebound and gravitational activity', *Boreas*, 39(1), pp. 39–55. doi: 10.1111/j.1502-3885.2009.00117.x.

Macara, G. R. (2014) *The Climate and Weather of Southland*, *NIWA Science and Technology Series*. Available at: http://www.nrc.govt.nz/Resource-Library-Summary/Research-and-reports/Climate-and-weather/The-Climate-and-Weather-of-Northland/.

Macara, G. R. (2015) *The Climate and Weather of Otago*. 2nd Editio, *NIWA SCIENCE AND TECHNOLOGY SERIES NUMBER 67*. 2nd Editio. doi: 10.31826/9781463208868-002.

Macfarlane, D. F. (2009) 'Observations and predictions of the behaviour of large, slow-moving landslides in schist, Clyde Dam reservoir, New Zealand', *Engineering Geology*, 109(1–2), pp. 5–15. doi: 10.1016/j.enggeo.2009.02.005.

Mackey, B. (2015) *Seismic Hazard in Queenstown Lakes District*. Dunedin, New Zealand. Available at: internal-pdf://104.130.199.122/Seismic Hazard in Queenstown Lakes District.pdf.

Malamud, B. D., Turcotte, D. L., Guzzetti, F. and Reichenbach, P. (2004) 'Landslide inventories and their statistical properties', *Earth Surface Processes and Landforms*, 29(6), pp. 687–711. doi: 10.1002/esp.1064.

Manzella, I., Penna, I., Kelfoun, K. and Jaboyedoff, M. (2016) 'High-mobility of unconstrained rock avalanches: Numerical simulations of a laboratory experiment and an Argentinian event', in *Landslides and Engineered Slopes. Experience, Theory and Practice*.

Marc, O., Hovius, N., Meunier, P., Uchida, T. and Hayashi, S. (2015) 'Transient changes of landslide rates after earthquakes', *Geology*, 43(10), pp. 883–886. doi: 10.1130/G36961.1.

Massey, C. I., Townsend, D. T., Lukovic, B., Morgenstern, R., Jones, K., Rosser, B. and de Vilder, S. (2020) 'Landslides triggered by the MW7.8 14 November 2016 Kaikōura earthquake: an update', *Landslides*, pp. 1–8. doi: 10.1007/s10346-020-01439-x.

Massey, C., McSaveney, M. and Davies, T. (2013) 'Evolution of an Overflow Channel Across the Young River Landslide Dam, New Zealand', in *Landslide Science and Practice*. Springer Berlin Heidelberg, pp. 43–49. doi: 10.1007/978-3-642-31319-6_7.

Masson, D. G., Harbitz, C. B., Wynn, R. B., Pedersen, G. and Løvholt, F. (2006) 'Submarine landslides: Processes, triggers and hazard prediction', *Philosophical Transactions of the Royal Society A: Mathematical, Physical and Engineering Sciences*, 364(1845), pp. 2009–2039. doi: 10.1098/rsta.2006.1810.

Masson, D. G., Watts, A. B., Gee, M. J. R., Urgeles, R., Mitchell, N. C., Le Bas, T. P. and Canals, M. (2002) 'Slope failures on the flanks of the western Canary Islands', *Earth-Science Reviews*, 57(1–2), pp. 1–35. doi: 10.1016/S0012-8252(01)00069-1.

Mathews, W. H. and McTaggart, K. C. (1978) 'Hope Rockslides, British Columbia, Canada', in Voight, B. (ed.) *Rockslides and Avalanches, 1 Natural Phenomena*. Elsevier Scientific Publishing, pp. 259–275. doi: 10.1016/B978-0-444-41507-3.50015-5.

Mazzanti, P. and De Blasio, F. V. (2010) 'Peculiar Morphologies of Subaqueous Landslide Deposits and Their Relationship to Flow Dynamics', in *Submarine Mass Movements and Their Consequences*. Dordrecht: Springer Netherlands, pp. 141–151. doi: 10.1007/978-90-481-3071-9_12.

Mazzanti, P. and De Blasio, F. V. (2013) 'The Dynamics of Subaqueous Rock Avalanches: The Role of Dynamic Fragmentation', in Margottini, C., Canuti, P., and Sassa, K. (eds) *Landslide*

Science and Practice. Berlin, Heidelberg: Springer Berlin Heidelberg, pp. 35–40. doi: 10.1007/978-3-642-31427-8_4.

Mazzanti, P. and Bozzano, F. (2009) 'An equivalent fluid/equivalent medium approach for the numerical simulation of coastal landslides propagation: Theory and case studies', *Natural Hazards and Earth System Science*, 9(6), pp. 1941–1952. doi: 10.5194/nhess-9-1941-2009.

Mazzanti, P. and Bozzano, F. (2011) 'Revisiting the February 6th 1783 Scilla (Calabria, Italy) landslide and tsunami by numerical simulation', *Marine Geophysical Research*, 32(1), pp. 273–286. doi: 10.1007/s11001-011-9117-1.

McArdell, B. W., Bartelt, P. and Kowalski, J. (2007) 'Field observations of basal forces and fluid pore pressure in a debris flow', *Geophysical Research Letters*, 34(7). doi: 10.1029/2006GL029183.

McColl, S. T. (2012) 'Paraglacial rock-slope stability', *Geomorphology*, 153–154, pp. 1–16. doi: 10.1016/J.GEOMORPH.2012.02.015.

McColl, S. T. (2015) 'Landslide Causes and Triggers', in *Landslide Hazards, Risks and Disasters*. Elsevier, pp. 17–42. doi: 10.1016/B978-0-12-396452-6.00002-1.

McColl, S. T. (2020) 'The Anomalously Old Bush Stream Rock Avalanche and Its Implications for Landslide Inventories in Dynamic Landscapes', *Frontiers in Earth Science*, 8, p. 103. doi: 10.3389/feart.2020.00103.

McColl, S. T., Cook, S. J., Stahl, T. and Davies, T. R. H. (2019) 'Origin and age of The Hillocks and implications for post-glacial landscape development in the upper Lake Wakatipu catchment, New Zealand', *Journal of Quaternary Science*, 34(8), pp. 685–696. doi: 10.1002/jqs.3168.

McColl, S. T. and Davies, T. R. (2011) 'Evidence for a rock-avalanche origin for "The Hillocks" "moraine", Otago, New Zealand', *Geomorphology*, 127(3–4), pp. 216–224. doi: http://dx.doi.org/10.1016/j.geomorph.2010.12.017.

McColl, S. T. and Davies, T. R. H. (2013) 'Large ice-contact slope movements: glacial buttressing, deformation and erosion', *Earth Surface Processes and Landforms*, 38(10), pp. 1102–1115. doi: 10.1002/esp.3346.

McColl, S. T., Davies, T. R. H. and Mcsaveney, M. J. (2012) 'The effect of glaciation on the intensity of seismic ground motion', *Earth Surface Processes and Landforms*, 37(12), pp.

1290–1301. doi: 10.1002/esp.3251.

McColl, S. T., Davies, T. R. H. and McSaveney, M. J. (2010) 'Glacier retreat and rock-slope stability : debunking debuttressing', in *Geologically active : delegate papers 11th Congress of the International Association for Engineering Geology and the Environmen*. Auckland, pp. 467–474.

McDougall, S. (2006) *A New continuum dynamic model for the analysis of extremely rapid landslide motion across complex 3D terrain*. University of British Columbia. doi: 10.14288/1.0052928.

McDougall, S. (2017) '2014 Canadian Geotechnical Colloquium: Landslide runout analysis — current practice and challenges', *Canadian Geotechnical Journal*, 54(5), pp. 605–620. doi: 10.1139/cgj-2016-0104.

McDougall, S., Boultbee, N., Hungr, O., Stead, D. and Schwab, J. W. (2006) 'The Zymoetz River landslide, British Columbia, Canada: Description and dynamic analysis of a rock slide-debris flow', *Landslides*. doi: 10.1007/s10346-006-0042-3.

McDougall, S. and Hungr, O. (2004) 'A model for the analysis of rapid landslide motion across three-dimensional terrain', *Canadian Geotechnical Journal*, 41(6), pp. 1084–1097. doi: 10.1139/t04-052.

McDougall, S. and Hungr, O. (2005) 'Dynamic modelling of entrainment in rapid landslides', *Canadian Geotechnical Journal*, 42. doi: 10.1139/t05-064.

McDougall, S. and Hungr, O. (2006) 'Landslide Dynamic Analysis in 2D and 3D', in *Sea to Sky Geotechnique, the 59th Canadian Geotechnical Conference*.

McDougall, S., McKinnon, M. and Hungr, O. (2012) 'Developments in landslide runout prediction', in Clague, J. J. and Stead, D. (eds) *Landslides: Types, Mechanisms and Modeling*. Cambridge: Cambridge University Press, pp. 187–195. doi: 10.1017/CBO9780511740367.017.

Mckinnon, M. (2010) 'Landslide Runout: Statistical Analysis of Physical Characteristics and Model Parameters', (June).

McSaveney, M., Cox, S. and Hancox, G. (2015) *Increasing rock-avalanche frequency correlates with increasing seismic moment release in New Zealand's Southern Alps*, *Geophysical Research Abstracts*.

McSaveney, M. J. (1978) 'Sherman glacier rock avalanche, alaska, U.S.A.', in *Developments in Geotechnical Engineering*. Elsevier, pp. 197–258. doi: 10.1016/B978-0-444-41507-3.50014-3.

McSaveney, M. J. (1995) *Debris flows and bridge losses at Waterfall Creek, SH6 at Lake Wanaka, New Zealand*, *Institute of Geological and Nuclear Sciences science report 95/21*.

McSaveney, M. J. (2002) 'Recent rockfalls and rock avalanches in Mount Cook National Park, New Zealand', in Evans, S. G. and Degraff, J. V (eds) *Catastrophic Landslides*. Geological Society of America. Available at: http://dx.doi.org/10.1130/REG15-p35.

McSaveney, M. and Massey, C. (2013) 'Did Radiative Cooling Trigger New Zealand's 2007 Young River Landslide?', in *Landslide Science and Practice*. Springer Berlin Heidelberg, pp. 347–353. doi: 10.1007/978-3-642-31337-0_44.

Medina, V., Hürlimann, M. and Bateman, A. (2008) 'Application of FLATModel, a 2D finite volume code, to debris flows in the northeastern part of the Iberian Peninsula', *Landslides*, 5(1), pp. 127–142. doi: 10.1007/s10346-007-0102-3.

Melosh, H. J. (1979) 'Acoustic fluidization: a new geologic process?', *Journal of Geophysical Research*, 84. doi: 10.1029/JB084iB13p07513.

Mergili, M., Fischer, J. T., Krenn, J. and Pudasaini, S. P. (2017) 'R.avaflow v1, an advanced open-source computational framework for the propagation and interaction of two-phase mass flows', *Geoscientific Model Development*, 10(2), pp. 553–569. doi: 10.5194/gmd-10-553-2017.

Meunier, P., Hovius, N. and Haines, A. J. (2007) 'Regional patterns of earthquake-triggered landslides and their relation to ground motion', *Geophysical Research Letters*, 34(20), pp. 1–5. doi: 10.1029/2007GL031337.

Meunier, P., Hovius, N. and Haines, J. A. (2008) 'Topographic site effects and the location of earthquake induced landslides', *Earth and Planetary Science Letters*, 275(3–4), pp. 221–232. doi: 10.1016/j.epsl.2008.07.020.

Meyer, N. K., Schwanghart, W., Korup, O. and Nadim, F. (2015) 'Roads at risk: Traffic detours from debris flows in southern Norway', *Natural Hazards and Earth System Sciences*, 15(5), pp. 985–995. doi: 10.5194/nhess-15-985-2015.

Micallef, A. (2011) 'Chapter Thirteen - Marine Geomorphology: Geomorphological Mapping and the Study of Submarine Landslides', in Mike J. Smith, P. P. and James, S. G. (eds)

Developments in Earth Surface Processes. Elsevier, pp. 377–395. doi: http://doi.org/10.1016/B978-0-444-53446-0.00013-6.

Mildenhall, D. C., Cochran, U. A. and Cook, R. A. (2006) 'Reconnaissance sediment and microfossil analyses of a laminated short piston core from lake tekapo, South Island, New Zealand', *New Zealand Journal of Geology and Geophysics*, 49(4), pp. 463–476. doi: 10.1080/00288306.2006.9515181.

Miller, D. J. (1960) *Giant waves in Lituya Bay, Alaska*, *Geological Survey Professional Paper*. Available at: http://pubs.er.usgs.gov/publication/pp354C.

Miller, G. S., Andy Take, W., Mulligan, R. P. and McDougall, S. (2017) 'Tsunamis generated by long and thin granular landslides in a large flume', *Journal of Geophysical Research: Oceans*, 122(1), pp. 653–668. doi: 10.1002/2016JC012177.

Moernaut, J. (2020) 'Time-dependent recurrence of strong earthquake shaking near plate boundaries: A lake sediment perspective', *Earth-Science Reviews*, 210, p. 103344. doi: 10.1016/j.earscirev.2020.103344.

Moernaut, J. and De Batist, M. (2011) 'Frontal emplacement and mobility of sublacustrine landslides: Results from morphometric and seismostratigraphic analysis', *Marine Geology*, 285(1–4), pp. 29–45. doi: 10.1016/j.margeo.2011.05.001.

Moernaut, J., De Batist, M., Charlet, F., Heirman, K., Chapron, E., Pino, M., Brümmer, R. and Urrutia, R. (2007) 'Giant earthquakes in South-Central Chile revealed by Holocene mass-wasting events in Lake Puyehue', *Sedimentary Geology*, 195(3–4), pp. 239–256. doi: 10.1016/j.sedgeo.2006.08.005.

Moernaut, J., De Batist, M., Heirman, K., Van Daele, M., Pino, M., Brümmer, R. and Urrutia, R. (2009) 'Fluidization of buried mass-wasting deposits in lake sediments and its relevance for paleoseismology: Results from a reflection seismic study of lakes Villarrica and Calafquén (South-Central Chile)', *Sedimentary Geology*, 213(3–4), pp. 121–135. doi: 10.1016/j.sedgeo.2008.12.002.

Moernaut, J., Van Daele, M., Heirman, K., Fontijn, K., Strasser, M., Pino, M., Urrutia, R. and De Batist, M. (2014) 'Lacustrine turbidites as a tool for quantitative earthquake reconstruction: New evidence for a variable rupture mode in south central Chile', *Journal of Geophysical Research: Solid Earth*, 119(3), pp. 1607–1633. doi: 10.1002/2013JB010738.

Moernaut, J., Van Daele, M., Heirman, K., Wiemer, G., Molenaar, A., Vandorpe, T., Melnick, D., Hajdas, I., Pino, M., Urrutia, R. and De Batist, M. (2019) 'The subaqueous landslide cycle in south-central Chilean lakes: The role of tephra, slope gradient and repeated seismic shaking', *Sedimentary Geology*, 381, pp. 84–105. doi: 10.1016/j.sedgeo.2019.01.002.

Moernaut, J., Verschuren, D., Charlet, F., Kristen, I., Fagot, M. and De Batist, M. (2010) 'The seismic-stratigraphic record of lake-level fluctuations in Lake Challa: Hydrological stability and change in equatorial East Africa over the last 140 kyr', *Earth and Planetary Science Letters*. doi: 10.1016/j.epsl.2009.12.023.

Mohammed, F. and Fritz, H. M. (2012) 'Physical modeling of tsunamis generated by three-dimensional deformable granular landslides', *Journal of Geophysical Research: Oceans*, 117(C11015), pp. 1–20. doi: 10.1029/2011JC007850.

Mohrig, D., Ellis, C., Parker, G., Whipple, K. X. and Hondzo, M. (1998) 'Hydroplaning of subaqueous debris flows', *GSA Bulletin*, 110(3), pp. 387–394. Available at: http://dx.doi.org/10.1130/0016-7606(1998)110%3C0387:HOSDF%3E2.3.CO.

Monecke, K., Anselmetti, F. S., Becker, A., Sturm, M. and Giardini, D. (2004) 'The record of historic earthquakes in lake sediments of Central Switzerland', *Tectonophysics*, 394(1–2), pp. 21–40. doi: 10.1016/j.tecto.2004.07.053.

Montgomery, D. R. (2001) 'Slope distributions, threshold hillslopes, and steady-state topography', *American Journal of Science*, 301(4–5), pp. 432–454. Available at: https://www.scopus.com/inward/record.uri?eid=2-s2.0-0035535911&partnerID=40&md5=137fa50a9fa1487b431a98dc08af9b71.

Moore, J. R., Pankow, K. L., Ford, S. R., Koper, K. D., Hale, J. M., Aaron, J. and Larsen, C. F. (2017) 'Dynamics of the Bingham Canyon rock avalanches (Utah, USA) resolved from topographic, seismic, and infrasound data', *Journal of Geophysical Research: Earth Surface*, 122(3), pp. 615–640. doi: 10.1002/2016JF004036.

Moretti, L., Allstadt, K., Mangeney, A., Capdeville, Y., Stutzmann, E. and Bouchut, F. (2015) 'Numerical modeling of the Mount Meager landslide constrained by its force history derived from seismic data', *Journal of Geophysical Research: Solid Earth*. doi: 10.1002/2014JB011426.

Moscardelli, L. and Wood, L. (2016) 'Morphometry of mass-transport deposits as a predictive

tool', *Bulletin of the Geological Society of America*, 128(1–2), pp. 47–80. doi: 10.1130/B31221.1.

Mountjoy, J. J., Georgiopoulou, A., Chaytor, J., Clare, M. A., Gamboa, D. and Moernaut, J. (2020) 'Subaqueous mass movements in the context of observations of contemporary slope failure', *Geological Society, London, Special Publications*, 500(1), pp. 1–12. doi: 10.1144/SP500-2019-237.

Mountjoy, J. J., Howarth, J. D., Orpin, A. R., Barnes, P. M., Bowden, D. A., Rowden, A. A., Schimel, A. C. G., Holden, C., Horgan, H. J., Nodder, S. D., Patton, J. R., Lamarche, G., Gerstenberger, M., Micallef, A., Pallentin, A. and Kane, T. (2018) 'Earthquakes drive large-scale submarine canyon development and sediment supply to deep-ocean basins', *Science Advances*, 4(3), p. eaar3748. doi: 10.1126/sciadv.aar3748.

Mountjoy, J. J., Wang, X., Woelz, S., Fitzsimons, S., Howarth, J. D., Orpin, A. R. and Power, W. (2019) 'Tsunami hazard from lacustrine mass wasting in Lake Tekapo, New Zealand', *Geological Society, London, Special Publications*, 477(1), pp. 413–426. doi: 10.1144/SP477.21.

Mountjoy, J. and Micallef, A. (2018) 'Submarine Landslides', in *Submarine Geomorphology*. Springer, pp. 235–250. doi: 10.1007/978-3-319-57852-1_13.

Muir-Wood, R. (2000) 'Deglaciation Seismotectonics: a principal influence on intraplate seismogenesis at high latitudes', *Quaternary Science Reviews*, 19(14–15), pp. 1399–1411. doi: 10.1016/S0277-3791(00)00069-X.

Mulder, T. and Cochonant, H. P. (1996) *Classification of offshore mass movement*, *Journal of Sedimentary Research*. doi: 10.1306/D42682AC-2B26-11D7-8648000102C1865D.

Mulligan, R. P. and Take, W. A. (2017) 'On the transfer of momentum from a granular landslide to a water wave', *Coastal Engineering*, 125, pp. 16–22. doi: 10.1016/J.COASTALENG.2017.04.001.

Mulligan, R. P., Take, W. A. and Bullard, G. K. (2019) 'Non-Hydrostatic Modeling of Waves Generated by Landslides with Different Mobility', *Journal of Marine Science and Engineering*, 7(8), p. 266. doi: 10.3390/jmse7080266.

Nagelisen, J., Moore, J. R., Vockenhuber, C. and Ivy-Ochs, S. (2015) 'Post-glacial rock avalanches in the Obersee Valley, Glarner Alps, Switzerland', *Geomorphology*, 238, pp. 94–

111. doi: 10.1016/j.geomorph.2015.02.031.

Nichol, S. L., Hungr, O. and Evans, S. G. (2002) 'Large-scale brittle and ductile toppling of rock slopes', *Canadian Geotechnical Journal*. doi: 10.1139/t02-027.

Nicoletti, P. G. and Sorriso-Valvo, M. (1991) 'Geomorphic controls of the shape and mobility of rock avalanches', *Geological Society of America Bulletin*, 103(10), pp. 1365–1373. doi: 10.1130/0016-7606(1991)103<1365:GCOTSA>2.3.CO;2.

NIWA (2019) *NIWA mapping Whakatipu lake floor*. Available at: https://niwa.co.nz/news/niwa-mapping-whakatipu-lake-floor.

NIWA (2020) *Suspended-sediment yield estimator*. Available at: https://niwa.co.nz/freshwater/management-tools/sediment-tools/suspended-sediment-yield-estimator.

Normandeau, A., Lajeunesse, P. and Philibert, G. (2013) 'Late-Quaternary morphostratigraphy of Lake St-Joseph (southeastern Canadian Shield): Evolution from a semi-enclosed glacimarine basin to a postglacial lake', *Sedimentary Geology*, 295, pp. 38–52. doi: 10.1016/j.sedgeo.2013.07.005.

Norris, R. J. and Cooper, A. F. (2001) 'Late Quaternary slip rates and slip partitioning on the Alpine Fault, New Zealand', *Journal of Structural Geology*, 23(2–3), pp. 507–520. doi: 10.1016/S0191-8141(00)00122-X.

Norris, R. J. and Cooper, A. F. (2007) 'The Alpine Fault, New Zealand: Surface geology and field relationships', in *Geophysical Monograph Series*. Blackwell Publishing Ltd, pp. 157–175. doi: 10.1029/175GM09.

Orchiston, C., Mitchell, J., Wilson, T., Langridge, R., Davies, T., Bradley, B., Johnston, D., Davies, A., Becker, J. and McKay, A. (2018) 'Project AF8: developing a coordinated, multi-agency response plan for a future great Alpine Fault earthquake', *New Zealand Journal of Geology and Geophysics*, 61(3), pp. 389–402. doi: 10.1080/00288306.2018.1455716.

Orpin, A. R., Carter, L., Page, M. J., Cochran, U. A., Trustrum, N. A., Gomez, B., Palmer, A. S., Mildenhall, D. C., Rogers, K. M., Brackley, H. L. and Northcote, L. (2010) 'Holocene sedimentary record from Lake Tutira: A template for upland watershed erosion proximal to the Waipaoa Sedimentary System, northeastern New Zealand', *Marine Geology*, 270(1–4), pp. 11–29. doi: 10.1016/j.margeo.2009.10.022.

Pánek, T. (2019) 'Landslides and Quaternary climate changes—The state of the art', *Earth-Science Reviews*, 196, p. 22. doi: 10.1016/j.earscirev.2019.05.015.

Pánek, T. and Klimeš, J. (2016) 'Temporal behavior of deep-seated gravitational slope deformations: A review', *Earth-Science Reviews*, 156, pp. 14–38. doi: 10.1016/j.earscirev.2016.02.007.

Pánek, T., Korup, O., Lenart, J., Hradecký, J. and Březný, M. (2018) 'Giant landslides in the foreland of the Patagonian Ice Sheet', *Quaternary Science Reviews*, 194, pp. 39–54. doi: 10.1016/j.quascirev.2018.06.028.

Panizzo, A., De Girolamo, P. and Petaccia, A. (2005) 'Forecasting impulse waves generated by subaerial landslides', *Journal of Geophysical Research*, 110(C12). doi: 10.1029/2004jc002778.

Paris, A., Okal, E. A., Guérin, C., Heinrich, P., Schindelé, F. and Hébert, H. (2019) 'Numerical Modeling of the June 17, 2017 Landslide and Tsunami Events in Karrat Fjord, West Greenland', *Pure and Applied Geophysics*, 176(7), pp. 3035–3057. doi: 10.1007/s00024-019-02123-5.

Paris, R., Giachetti, T., Chevalier, J., Guillou, H. and Frank, N. (2011) 'Tsunami deposits in Santiago Island (Cape Verde archipelago) as possible evidence of a massive flank failure of Fogos volcano', *Sedimentary Geology*, 239(3–4), pp. 129–145. doi: 10.1016/j.sedgeo.2011.06.006.

Parker, R. N., Hancox, G. T., Petley, D. N., Massey, C. I., Densmore, A. L. and Rosser, N. J. (2015) 'Spatial distributions of earthquake-induced landslides and hillslope preconditioning in the northwest South Island, New Zealand', *Earth Surface Dynamics*, 3(4), pp. 501–525. doi: 10.5194/esurf-3-501-2015.

Parsons, T., Geist, E. L., Ryan, H. F., Lee, H. J., Haeussler, P. J., Lynett, P., Hart, P. E., Sliter, R. and Roland, E. (2014) 'Source and progression of a submarine landslide and tsunami: The 1964 Great Alaska earthquake at Valdez', *Journal of Geophysical Research: Solid Earth*, 119(11), pp. 8502–8516. doi: 10.1002/2014JB011514.

De Pascale, G. P. and Langridge, R. M. (2012) 'New on-fault evidence for a great earthquake in A.D. 1717, central alpine fault, New Zealand', *Geology*, 40(9), pp. 791–794. doi: 10.1130/G33363.1.

Pedersen, S. A. S., Larsen, L. M., Dahl-jensen, T., Jepsen, H. F., Krarup, G., Nielsen, T.,

Pedersen, A. K., Platen-Hallermund, F. Von and Weng, W. (2002) 'Tsunami-generating rock fall and landslide on the south coast of Nuussuaq , central West Greenland', *Geology of Greenland Survey Bulletin*, 191(November 2000), pp. 73–83.

Pedley, K. L., Barnes, P. M., Pettinga, J. R. and Lewis, K. B. (2010) 'Seafloor structural geomorphic evolution of the accretionary frontal wedge in response to seamount subduction, Poverty Indentation, New Zealand', *Marine Geology*, 270(1–4), pp. 119–138. doi: 10.1016/j.margeo.2009.11.006.

Pickrill, R. . (1987) 'Circulation and sedimentation of suspended particulate matter in New Zealand fjords', *Marine Geology*, 74(1–2), pp. 21–39. doi: 10.1016/0025-3227(87)90003-X.

Pickrill, R. . and Irwin, J. (1983) 'Sedimentation in a deep glacier-fed lake-Lake Tekapo, New Zealand', *Sedimentology*, 30(1), pp. 63–75. doi: 10.1111/j.1365-3091.1983.tb00650.x.

Pickrill, R. A. (1993) 'Sediment Yields in Fiordland', *Journal of Hydrology (New Zealand)*, 31(1), pp. 39–55. Available at: https://www.jstor.org/stable/43944697?seq=1 (Accessed: 7 March 2021).

Pickrill, R. A., Fenner, J. M. and McGlone, M. S. (1992) 'Late Quaternary Evolution of a Fjord Environment in Preservation Inlet, New Zealand', *Quaternary Research*, 38(3), pp. 331–346. doi: 10.1016/0033-5894(92)90042-H.

Pinet, N., Brake, V., Campbell, C. and Duchesne, M. J. (2015) 'Geomorphological characteristics and variability of holocene mass-transport complexes, st. lawrence river estuary, canada', *Geomorphology*, 228, pp. 286–302. doi: 10.1016/j.geomorph.2014.09.008.

Piper, D. J. W., Mosher, D. C. and Campbell, D. C. (2012) 'Controls on the distribution of major types of submarine landslides', in Clague, J. J. and Stead, D. (eds) *Landslides: Types, Mechanisms and Modeling*. Cambridge University Press, pp. 95–107. doi: 10.1017/cbo9780511740367.010.

Pirulli, M. (2005) *Numerical Modelling of Landslide Runout A continuum mechanics approach*. Politecnico Di Torino.

Pirulli, M. and Mangeney, A. (2008) 'Results of back-analysis of the propagation of rock avalanches as a function of the assumed rheology', *Rock Mechanics and Rock Engineering*, 41(1), pp. 59–84. doi: 10.1007/s00603-007-0143-x.

Pitman, E. B., Nichita, C., Patra, A., Bauer, A., Sheridan, M. and Bursik, M. (2003) 'Computing

granular avalanches and landslides', *Physics of Fluids*, 15. doi: 10.1063/1.1614253.

Plafker, G. and Ericksen, G. E. (1978) 'Nevados huascarán avalanches, peru', in *Developments in Geotechnical Engineering*. doi: 10.1016/B978-0-444-41507-3.50016-7.

Poiré, A. G., Lajeunesse, P., Normandeau, A., Francus, P., St-Onge, G. and Nzekwe, O. P. (2018) 'Late-Quaternary glacial to postglacial sedimentation in three adjacent fjord-lakes of the Québec North Shore (eastern Canadian Shield)', *Quaternary Science Reviews*, 186, pp. 91–110. doi: 10.1016/j.quascirev.2018.02.013.

Poisel, R., Preh, A. and Hungr, O. (2008) 'Run Out of Landslides - Continuum Mechanics versus Discontinuum Mechanics Models', *Geomechanik und Tunnelbau*. doi: 10.1002/geot.200800036.

Pope, E. L., Normandeau, A., Ó Cofaigh, C., Stokes, C. R. and Talling, P. J. (2019) 'Controls on the formation of turbidity current channels associated with marine-terminating glaciers and ice sheets', *Marine Geology*, 415, p. 105951. doi: 10.1016/j.margeo.2019.05.010.

Pope, E. L., Talling, P. J. and Carter, L. (2017) 'Which earthquakes trigger damaging submarine mass movements: Insights from a global record of submarine cable breaks?', *Marine Geology*, 384, pp. 131–146. doi: 10.1016/j.margeo.2016.01.009.

Postma, G. (1990) 'Depositional Architecture and Facies of River and Fan Deltas: A Synthesis', in Colella, A. and Prior, D. B. (eds) *Coarse-Grained Deltas*. Wiley Blackwell, pp. 13–27. doi: 10.1002/9781444303858.ch2.

Pouderoux, H., Proust, J. N., Lamarche, G., Orpin, A. and Neil, H. (2012) 'Postglacial (after 18ka) deep-sea sedimentation along the Hikurangi subduction margin (New Zealand): Characterisation, timing and origin of turbidites', *Marine Geology*, 295–298, pp. 51–76. doi: 10.1016/j.margeo.2011.11.002.

Power, W., Downes, G., Mcsaveney, M., Beavan, J. and Hancox, G. (2005) 'The Fiordland Earthquake and Tsunami, New Zealand, 21 August 2003', in Satake, K. (ed.) *Tsunamis: Case Studies and Recent Developments*. Dordrecht: Springer Netherlands, pp. 31–42. doi: 10.1007/1-4020-3331-1_2.

Praet, N., Moernaut, J., Van Daele, M., Boes, E., Haeussler, P. J., Strupler, M., Schmidt, S., Loso, M. G. and De Batist, M. (2017) 'Paleoseismic potential of sublacustrine landslide records in a high-seismicity setting (south-central Alaska)', *Marine Geology*, 384, pp. 103–119. doi:

10.1016/j.margeo.2016.05.004.

Prager, C., Zangerl, C., Patzelt, G. and Brandner, R. (2008) 'Age distribution of fossil landslides in the Tyrol (Austria) and its surrounding areas', *Natural Hazards and Earth System Sciences*, 8(2), pp. 377–407. doi: 10.5194/nhess-8-377-2008.

Prior, D. B., Bornhold, B. D., Coleman, J. M. and Bryant, W. R. (1982) 'Morphology of a submarine slide, Kitimat Arm, British Columbia.', *Geology*, 10(11), pp. 588–592. doi: 10.1130/0091-7613(1982)10<588:MOASSK>2.0.CO;2.

Pudasaini, S. P. (2012) 'A general two-phase debris flow model', *Journal of Geophysical Research: Earth Surface*, 117(F3), p. n/a-n/a. doi: 10.1029/2011JF002186.

Pudasaini, S. P. (2014) 'Dynamics of submarine debris flow and tsunami', *Acta Mech*, 225, pp. 2423–2434. doi: 10.1007/s00707-014-1126-0.

Pudasaini, S. P. and Krautblatter, M. (2014) 'A two-phasemechanical model for rock-ice avalanches', *Journal of Geophysical Research F: Earth Surface*, 119(10), pp. 2272–2290. doi: 10.1002/2014JF003183.

Pudasaini, S. P. and Mergili, M. (2019) 'A Multi-Phase Mass Flow Model', *Journal of Geophysical Research: Earth Surface*, 124(12), pp. 2920–2942. doi: 10.1029/2019JF005204.

Purdie, H., Bealing, P., Tidey, E., Gomez, C. and Harrison, J. (2016) 'Bathymetric evolution of Tasman Glacier terminal lake, New Zealand, as determined by remote surveying techniques', *Global and Planetary Change*, 147, pp. 1–11. doi: 10.1016/j.gloplacha.2016.10.010.

Putnam, A. E., Schaefer, J. M., Denton, G. H., Barrell, D. J. A., Birkel, S. D., Andersen, B. G., Kaplan, M. R., Finkel, R. C., Schwartz, R. and Doughty, A. M. (2013) 'The Last Glacial Maximum at 44°S documented by a 10Be moraine chronology at Lake Ohau, Southern Alps of New Zealand', *Quaternary Science Reviews*, 62, pp. 114–141. doi: 10.1016/j.quascirev.2012.10.034.

Quinn, A. N. (2004) *High resolution environmental magnetism of short sediment cores from Lake Tekapo, New Zealand*. University of Otago. Available at: http://theses.otagogeology.org.nz/items/show/435 (Accessed: 4 March 2021).

Quinn, A. N. and Wilson, G. S. (2004) 'High resolution environmental magnetism of short sediment cores from Lake Tekapo, New Zealand', in *Geological Society of New Zealand Miscellaneous Publication 117a*.

R Core Team (2019) 'R: A language and environment for statistical computing'. Vienna, Austria: R Foundation for Statistical Computing. Available at: https://www.r-project.org/.

Rait, K. L., Bowman, E. T. and Lambert, C. (2012) 'Dynamic fragmentation of rock clasts under normal compression in sturzstrom', *Geotechnique Letters*, 2(7–9), pp. 167–172. doi: 10.1680/geolett.12.00038.

Ramirez, M. T., Allison, M. A., Bianchi, T. S., Cui, X., Savage, C., Schüller, S. E., Smith, R. W. and Vetter, L. (2016) 'Modern deposition rates and patterns of organic carbon burial in Fiordland, New Zealand', *Geophysical Research Letters*, 43(22), pp. 11,768-11,776. doi: 10.1002/2016GL070021.

Rattenbury, M. S. and Isaac, M. J. (2012) 'The QMAP 1:250 000 Geological Map of New Zealand project', *New Zealand Journal of Geology and Geophysics*, 55(4), pp. 393–405. doi: 10.1080/00288306.2012.725417.

Rattenbury, M. S., Jongens, R. and Cox, S. C. (2010) *Geology of the Haast area*, *Institute of Geological and Nuclear Sciences 1:250,000 Geological Map*.

Reznichenko, N. V., Davies, T. R. H. and Alexander, D. J. (2011) 'Effects of rock avalanches on glacier behaviour and moraine formation', *Geomorphology*, 132(3–4), pp. 327–338. doi: 10.1016/j.geomorph.2011.05.019.

RGI Consortium (2017) 'Randolph Glacier Inventory – A Dataset of Global Glacier Outlines: Version 6.0: Technical Report'. Colorado,USA. doi: https://doi.org/10.7265/N5-RGI-60.

Roberts, N. J., McKillop, R., Hermanns, R. L., Clague, J. J. and Oppikofer, T. (2014) 'Preliminary Global Catalogue of Displacement Waves from Subaerial Landslides', in *Landslide Science for a Safer Geoenvironment*. Cham: Springer International Publishing, pp. 687–692. doi: 10.1007/978-3-319-04996-0_104.

Roberts, N. J., McKillop, R. J., Lawrence, M. S., Psutka, J. F., Clague, J. J., Brideau, M.-A. and Ward, B. C. (2013) 'Impacts of the 2007 Landslide-Generated Tsunami in Chehalis Lake, Canada', in Margottini, C., Canuti, P., and Sassa, K. (eds) *Landslide Science and Practice: Volume 6: Risk Assessment, Management and Mitigation*. Berlin, Heidelberg: Springer Berlin Heidelberg, pp. 133–140. doi: 10.1007/978-3-642-31319-6_19.

Robertson, C. M., Benn, D. I., Brook, M. S., Fuller, I. C. and Holt, K. A. (2012) 'Subaqueous calving margin morphology at Mueller, Hooker and Tasman glaciers in Aoraki/Mount Cook

National Park, New Zealand', *Journal of Glaciology*, 58(212), pp. 1037–1046. doi: 10.3189/2012JoG12J048.

Robinson, T. R. (2014) *Assessment of Coseismic Landsliding From an Alpine Fault Earthquake Scenario, New Zealand*. University of Canterbury.

Robinson, T. R. (2018) 'Road impacts from the 2016 Kaikōura earthquake: an analogue for a future Alpine Fault earthquake?', *New Zealand Journal of Geology and Geophysics*, 61(3), pp. 403–411. doi: 10.1080/00288306.2018.1470539.

Robinson, T. R. and Davies, T. R. H. (2013) 'Review Article: Potential geomorphic consequences of a future great (Mw = 8.0+) Alpine Fault earthquake, South Island, New Zealand', *Natural Hazards and Earth System Sciences*, 13(9), pp. 2279–2299. doi: 10.5194/nhess-13-2279-2013.

Robinson, T. R., Davies, T. R. H., Wilson, T. M. and Orchiston, C. (2016) 'Coseismic landsliding estimates for an Alpine Fault earthquake and the consequences for erosion of the Southern Alps, New Zealand', *Geomorphology*, 263, pp. 71–86. doi: http://dx.doi.org/10.1016/j.geomorph.2016.03.033.

Roop, H. A., Levy, R., Dunbar, G. B., Vandergoes, M. J., Howarth, J., Fitzsimons, S., Moon, H. S., Zammit, C., Ditchburn, R., Baisden, T. and Yoon, H. Il (2016) 'A hydroclimate-proxy model based on sedimentary facies in an annually laminated sequence from Lake Ohau, South Island, New Zealand', *Journal of Paleolimnology*, 55(1). doi: 10.1007/s10933-015-9853-3.

Rosser, B., Dellow, S., Haubrock, S. and Glassey, P. (2017) 'New Zealand's National Landslide Database', *Landslides*, 14(6), pp. 1949–1959. doi: 10.1007/s10346-017-0843-6.

Salinger, M. J., Fitzharris, B. B. and Chinn, T. (2019) 'Atmospheric circulation and ice volume changes for the small and medium glaciers of New Zealand's Southern Alps mountain range 1977–2018', *International Journal of Climatology*, 39(11), pp. 4274–4287. doi: 10.1002/joc.6072.

Sammartini, M., Moernaut, J., Anselmetti, F. S., Hilbe, M., Lindhorst, K., Praet, N. and Strasser, M. (2019) 'An Atlas of Mass-Transport Deposits in Lakes', in Ogata, K., Festa, A., and Pini, G. A. (eds) *Submarine landslides: Subaqueous Mass Transport Deposits from Outcrops to Seismic Profiles. Geophysical Monograph Series 247*. American Geophysical Union, p. 384.

Sassa, K. and Wang, G. hui (2005) 'Mechanism of landslide-triggered debris flows: Liquefaction phenomena due to the undrained loading of torrent deposits', in *Debris-flow Hazards and Related Phenomena*. Springer Berlin Heidelberg, pp. 81–104. doi: 10.1007/3-540-27129-5_5.

Sattler, K., Anderson, B., Mackintosh, A., Norton, K. and de Róiste, M. (2016) 'Estimating Permafrost Distribution in the Maritime Southern Alps, New Zealand, Based on Climatic Conditions at Rock Glacier Sites', *Frontiers in Earth Science*, 4, p. 4. doi: 10.3389/feart.2016.00004.

Savage, S. B. and Hutter, K. (1989) 'The motion of a finite mass of granular material down a rough incline', *Journal of Fluid Mechanics*, 199(2697), pp. 177–215. doi: 10.1017/S0022112089000340.

Sawyer, D. E. and Devore, J. R. (2015) 'Elevated shear strength of sediments on active Margins: Evidence for seismic strengthening', *Geophysical Research Letters*, 44(23), pp. 216–221. doi: 10.1002/2015GL066603.Received.

Scheidegger, A. E. (1973) 'On the prediction of the reach and velocity of catastrophic landslides', *Rock Mechanics Felsmechanik Mécanique des Roches*, 5(4), pp. 231–236. doi: 10.1007/BF01301796.

Scherler, D. and Schwanghart, W. (2020) 'Drainage divide networks - Part 1: Identification and ordering in digital elevation models', *Earth Surface Dynamics*, 8(2), pp. 245–259. doi: 10.5194/esurf-8-245-2020.

Schleier, M., Hermanns, R. L., Gosse, J. C., Oppikofer, T., Rohn, J. and Tønnesen, J. F. (2017) 'Subaqueous rock-avalanche deposits exposed by post-glacial isostatic rebound, Innfjorddalen, Western Norway', *Geomorphology*, 289, pp. 117–133. doi: 10.1016/j.geomorph.2016.08.024.

Schneider, D., Bartelt, P., Caplan-Auerbach, J., Christen, M., Huggel, C. and McArdell, B. W. (2010) 'Insights into rock-ice avalanche dynamics by combined analysis of seismic recordings and a numerical avalanche model', *Journal of Geophysical Research*, 115(F4), p. F04026. doi: 10.1029/2010JF001734.

Schneider, D., Huggel, C., Haeberli, W. and Kaitna, R. (2011) 'Unraveling driving factors for large rock-ice avalanche mobility', *Earth Surface Processes and Landforms*, 36(14), pp. 1948–1966. doi: 10.1002/esp.2218.

Schnellmann, M., Anselmetti, F. S., Giardini, D. and McKenzie, J. A. (2005) 'Mass movement-induced fold-and-thrust belt structures in unconsolidated sediments in Lake Lucerne (Switzerland)', *Sedimentology*, 52(2), pp. 271–289. doi: 10.1111/j.1365-3091.2004.00694.x.

Schnellmann, M., Anselmetti, F. S., Giardini, D. and McKenzie, J. A. (2006) '15,000 Years of mass-movement history in Lake Lucerne: Implications for seismic and tsunami hazards', *Eclogae Geologicae Helvetiae*, 99(3), pp. 409–428. doi: 10.1007/s00015-006-1196-7.

Schnellmann, M., Anselmetti, F. S., Giardini, D., McKenzie, J. A. and Ward, S. N. (2002) 'Prehistoric earthquake history revealed by lacustrine slump deposits', *Geology*, 30(12), pp. 1131–1134. doi: 10.1130/0091-7613(2002)030<1131:PEHRBL>2.0.CO;2.

Schraml, K., Thomschitz, B., Mcardell, B. W., Graf, C. and Kaitna, R. (2015) 'Modeling debris-flow runout patterns on two alpine fans with different dynamic simulation models', *Hazards Earth Syst. Sci*, 15, pp. 1483–1492. doi: 10.5194/nhess-15-1483-2015.

Schwab, J., Geertsema, M. and Evans, S. G. (2003) 'Catastrophic rock avalanches, west-central British Columbia', *Proceedings 3rd Canadian Conference on Geotechnique and Natural Hazards*.

Schwanghart, W. and Scherler, D. (2014) 'Short Communication: TopoToolbox 2 – MATLAB-based software for topographic analysis and modeling in Earth surface sciences', *Earth Surf. Dynam*, 2, pp. 1–7. doi: 10.5194/esurf-2-1-2014.

Schwanghart, W. and Scherler, D. (2017) 'Bumps in river profiles: uncertainty assessment and smoothing using quantile regression techniques', *Earth Surf. Dynam*, 55194, pp. 821–839. doi: 10.5194/esurf-5-821-2017.

Shaw, J., Stacey, C. D., Wu, Y. and Lintern, D. G. (2017) 'Anatomy of the Kitimat fiord system, British Columbia', *Geomorphology*, 293, pp. 108–129. doi: 10.1016/J.GEOMORPH.2017.04.043.

Shea, T. and van Wyk de Vries, B. (2008) 'Structural analysis and analogue modeling of the kinematics and dynamics of rockslide avalanches', *Geosphere*, 4(4), pp. 657–686. doi: 10.1130/GES00131.1.

Shea, T., van Wyk de Vries, B. and Pilato, M. (2008) 'Emplacement mechanisms of contrasting debris avalanches at Volcán Mombacho (Nicaragua), provided by structural and facies analysis', *Bulletin of Volcanology*, 70(8), pp. 899–921. doi: 10.1007/s00445-007-0177-7.

Shreve, R. L. (1968) 'Leakage and fluidization in air-layer lubricated avalanches', *Bulletin of the Geological Society of America*. doi: 10.1130/0016-7606(1968)79[653:LAFIAL]2.0.CO;2.

Shugar, D. H. and Clague, J. J. (2011) 'The sedimentology and geomorphology of rock avalanche deposits on glaciers', *Sedimentology*, 58(7), pp. 1762–1783. doi: 10.1111/j.1365-3091.2011.01238.x.

Shulmeister, J., Thackray, G. D., Rittenour, T. M., Fink, D. and Patton, N. R. (2019) 'The timing and nature of the last glacial cycle in New Zealand', *Quaternary Science Reviews*, 206, pp. 1–20. doi: 10.1016/J.QUASCIREV.2018.12.020.

Si, P., Aaron, J., McDougall, S., Lu, J., Yu, X., Roberts, N. J. and Clague, J. J. (2018) 'A non-hydrostatic model for the numerical study of landslide-generated waves', *Landslides*, 15(4), pp. 711–726. doi: 10.1007/s10346-017-0891-y.

Siebert, L. (2002) 'Landslides resulting from structural failure of volcanoes', in Evans, S. G. and Degraff, J. V. (eds) *Catastrophic Landslides: Effects, Occurrence, and Mechanisms*. Boulder, Colorado: Geological Society of America, pp. 209–235. doi: 10.1130/REG15-p209.

Slingerland, R. L. and Voight, B. (1979) 'Occurrences, properties, and predictive models of landslide-generated water waves', in *Developments in Geotechnical Engineering*. Elsevier, pp. 317–394. doi: 10.1016/B978-0-444-41508-0.50017-X.

Smith, D. P., Kvitek, R., Iampietro, P. J. and Wong, K. (2007) 'Twenty-nine months of geomorphic change in upper Monterey Canyon (2002-2005)', *Marine Geology*, 236(1–2), pp. 79–94. doi: 10.1016/j.margeo.2006.09.024.

Smith, G. M., Davies, T. R., McSaveney, M. J. and Bell, D. H. (2006) 'The Acheron rock avalanche, Canterbury, New Zealand- Morphology and dynamics', *Landslides*, 3(1), pp. 62–72. doi: 10.1007/s10346-005-0012-1.

Smith, W. D., Dunning, S. A., Brough, S., Ross, N. and Telling, J. (2020) 'GERALDINE (Google Earth Engine supRaglAciaL Debris INput dEtector): A new tool for identifying and monitoring supraglacial landslide inputs', *Earth Surface Dynamics*, 8(4), pp. 1053–1065. doi: 10.5194/esurf-8-1053-2020.

Sosio, R., Crosta, G. B., Chen, J. H. and Hungr, O. (2012) 'Modelling rock avalanche propagation onto glaciers', *Quaternary Science Reviews*, 47, pp. 23–40. doi: 10.1016/j.quascirev.2012.05.010.

Sosio, R., Crosta, G. B. and Hungr, O. (2008) 'Complete dynamic modeling calibration for the Thurwieser rock avalanche (Italian Central Alps)', *Engineering Geology*, 100(1–2), pp. 11–26. doi: 10.1016/j.enggeo.2008.02.012.

Sosio, R., Crosta, G. B. and Hungr, O. (2012) 'Numerical modeling of debris avalanche propagation from collapse of volcanic edifices', *Landslides*, 9(3), pp. 315–334. doi: 10.1007/s10346-011-0302-8.

Stacey, C. D., Lintern, D. G., Shaw, J. and Conway, K. W. (2020) 'Slope stability hazard in a fjord environment: Douglas channel, Canada', in *Geological Society Special Publication*. Geological Society of London, pp. 427–451. doi: 10.1144/SP500-2019-191.

Stanton, B. R. and Pickard, G. L. (1981) *Physical Oceonography of the New Zealand Fiords*, *New Zealand Oceanographic Institure Memoir*.

Stark, C. P. and Hovius, N. (2001) 'The characterization of landslide size distributions', *Geophysical Research Letters*, 28(6), pp. 1091–1094. doi: 10.1029/2000GL008527.

Stirling, M., McVerry, G., Gerstenberger, M., Litchfield, N., Van Dissen, R., Berryman, K., Barnes, P., Wallace, L., Villamor, P., Langridge, R., Lamarche, G., Nodder, S., Reyners, M., Bradley, B., Rhoades, D., Smith, W., Nicol, A., Pettinga, J., Clark, K. and Jacobs, K. (2012) 'National Seismic Hazard Model for New Zealand: 2010 Update', *Bulletin of the Seismological Society of America*, 102(4), pp. 1514–1542. doi: 10.1785/0120110170.

Stoker, M. S., Wilson, C. R., Howe, J. A., Bradwell, T. and Long, D. (2010) 'Paraglacial slope instability in Scottish fjords: Examples from Little Loch Broom, NW Scotland', *Geological Society Special Publication*, 344(1), pp. 225–242. doi: 10.1144/SP344.16.

Strasser, M., Anselmetti, F. S., Fäh, D., Giardini, D. and Schnellmann, M. (2006) 'Magnitudes and source areas of large prehistoric norhern Alpine earthquakes revealed by slope failures in lakes', *Geology*, 34(12), pp. 1005–1008. doi: 10.1130/G22784A.1.

Strasser, M., Berberich, T., Fabbri, S., Hilbe, M., Huang, J.-J. S., Lauterbach, S., Ortler, M., Rechschreiter, H., Brauer, A., Anselmetti, F. and Kowarik, K. (2020) 'Geomorphology and event-stratigraphy of recent mass-movement processes in Lake Hallstatt (UNESCO World Heritage Cultural Landscape, Austria)', *Geological Society, London, Special Publications*, 500(1), pp. SP500-2019–178. doi: 10.1144/sp500-2019-178.

Strasser, M., Hilbe, M. and Anselmetti, F. S. (2011) 'Mapping basin-wide subaquatic slope

failure susceptibility as a tool to assess regional seismic and tsunami hazards', *Marine Geophysical Research*, 32(1), pp. 331–347. doi: 10.1007/s11001-010-9100-2.

Strasser, M., Monecke, K., Schnellmann, M. and Anselmetti, F. S. (2013) 'Lake sediments as natural seismographs: A compiled record of Late Quaternary earthquakes in Central Switzerland and its implication for Alpine deformation', *Sedimentology*, 60(1), pp. 319–341. doi: 10.1111/sed.12003.

Strasser, M., Stegmann, S., Bussmann, F., Anselmetti, F. S., Rick, B. and Kopf, A. (2007) 'Quantifying subaqueous slope stability during seismic shaking: Lake Lucerne as model for ocean margins', *Marine Geology*, 240(1–4), pp. 77–97. doi: 10.1016/j.margeo.2007.02.016.

Strom, A. L. (2006) 'Morphology and internal structure of rockslides and rock avalanches: grounds and constraints for their modelling', in *Landslides from Massive Rock Slope Failure*. Dordrecht: Springer Netherlands, pp. 305–326. doi: 10.1007/978-1-4020-4037-5_17.

Strom, A., Li, L. and Lan, H. (2019) 'Rock avalanche mobility: optimal characterization and the effects of confinement', *Landslides*, pp. 1–16. doi: 10.1007/s10346-019-01181-z.

Strong, D., Turnbull, R., Haubrock, S. and Mortimer, N. (2016) 'Petlab: New Zealand's national rock catalogue and geoanalytical database', *New Zealand Journal of Geology and Geophysics*, 59(3), pp. 475–481. Available at: https://www.tandfonline.com/doi/full/10.1080/00288306.2016.1157086 (Accessed: 21 September 2018).

Strupler, M., Anselmetti, F. S., Hilbe, M., Kremer, K. and Wiemer, S. (2020) 'A workflow for the rapid assessment of the landslide-tsunami hazard in peri-alpine lakes', in *Geological Society Special Publication*. Geological Society of London, pp. 81–95. doi: 10.1144/SP500-2019-166.

Strupler, M., Anselmetti, F. S., Hilbe, M. and Strasser, M. (2019) 'Quantitative characterization of subaqueous landslides in Lake Zurich (Switzerland) based on a high-resolution bathymetric dataset', *Geological Society, London, Special Publications*, 477(1), pp. 399–412. doi: 10.1144/SP477.7.

Strupler, M., Evers, F. M., Kremer, K., Cauzzi, C., Bacigaluppi, P., Vetsch, D. F., Boes, R. M., Fäh, D., Anselmetti, F. S. and Wiemer, S. (2020) 'A Simplified Classification of the Relative Tsunami Potential in Swiss Perialpine Lakes Caused by Subaqueous and Subaerial Mass-Movements', *Frontiers in Earth Science*, 8, p. 400. doi: 10.3389/feart.2020.564783.

Strupler, M., Hilbe, M., Anselmetti, F. S., Kopf, A. J., Fleischmann, T. and Strasser, M. (2017) 'Probabilistic stability evaluation and seismic triggering scenarios of submerged slopes in Lake Zurich (Switzerland)', *Geo-Marine Letters*, 37(3), pp. 241–258. doi: 10.1007/s00367-017-0492-8.

Sultan, N., Cochonat, P., Canals, M., Cattaneo, A., Dennielou, B., Haflidason, H., Laberg, J. S., Long, D., Mienert, J., Trincardi, F., Urgeles, R., Vorren, T. O. and Wilson, C. (2004) 'Triggering mechanisms of slope instability processes and sediment failures on continental margins: A geotechnical approach', *Marine Geology*, 213(1–4), pp. 291–321. doi: 10.1016/j.margeo.2004.10.011.

Sumner, E. J., Siti, M. I., McNeill, L. C., Talling, P. J., Henstock, T. J., Wynn, R. B., Djajadihardja, Y. S. and Permana, H. (2013) 'Can turbidites be used to reconstruct a paleoearthquake record for the central Sumatran margin?', *Geology*, 41(7), pp. 763–766. doi: 10.1130/G34298.1.

Sutherland, J. L., Carrivick, J. L., Evans, D. J. A., Shulmeister, J. and Quincey, D. J. (2019) 'The Tekapo Glacier, New Zealand, during the Last Glacial Maximum: An active temperate glacier influenced by intermittent surge activity', *Geomorphology*, 343(1), pp. 183–210. doi: 10.1016/j.geomorph.2019.07.008.

Sutherland, J. L., Carrivick, J. L., Shulmeister, J., Quincey, D. J. and James, W. H. M. (2019) 'Ice-contact proglacial lakes associated with the Last Glacial Maximum across the Southern Alps, New Zealand', *Quaternary Science Reviews*, 213, pp. 67–92. doi: 10.1016/j.quascirev.2019.03.035.

Sutherland, R., Berryman, K. and Norris, R. (2006) 'Quaternary slip rate and geomorphology of the Alpine fault: Implications for kinematics and seismic hazard in southwest New Zealand', *Geological Society of America Bulletin*, 118(3–4), pp. 464–474. doi: 10.1130/B25627.1.

Sutherland, R., Eberhart-Phillips, D., Harris, R. A., Stern, T., Beavan, J., Ellis, S., Henrys, S., Cox, S., Norris, R. J., Berryman, K. R., Townend, J., Bannister, S., Pettinga, J., Leitner, B., Wallace, L., Little, T. A., Cooper, A. F., Yetton, M. and Stirling, M. (2007) 'Do great earthquakes occur on the alpine fault in central South Island, New Zealand?', in *Geophysical Monograph Series*. Blackwell Publishing Ltd, pp. 235–251. doi: 10.1029/175GM12.

Sweeney, C. G., Brideau, M. A., Augustinus, P. C. and Fink, D. (2013) 'Lochnagar landslide-dam, Central Otago, New Zealand: geomechanics and timing of the event', in Chin, C. (ed.)

19th NZGS Geotechnical Symposium. Queenstown.

Taig, T. and McSaveney, M. J. (2015) *Milford Sound risk from landslide-generated tsunami*.

Talling, P. J., Clare, M., Urlaub, M., Pope, E., Hunt, J. E. and Watt, S. F. L. (2014) 'Large submarine landslides on continental slopes: Geohazards, methane release, and climate change', *Oceanography*. doi: 10.5670/oceanog.2014.38.

Tanyaş, H., Allstadt, K. E. and van Westen, C. J. (2018) 'An updated method for estimating landslide-event magnitude', *Earth Surface Processes and Landforms*, 43(9), pp. 1836–1847. doi: 10.1002/esp.4359.

Tanyaş, H., van Westen, C. J., Allstadt, K. E. and Jibson, R. W. (2019) 'Factors controlling landslide frequency–area distributions', *Earth Surface Processes and Landforms*, 44(4), pp. 900–917. doi: 10.1002/esp.4543.

Tappin, D. R. (2010) 'Digital elevation models in the marine domain: investigating the offshore tsunami hazard from submarine landslides', *Geological Society, London, Special Publications*, 345(1), pp. 81–101. doi: 10.1144/SP345.10.

Tappin, D. R., McNeil, L. C., Henstock, T. and Mosher, D. (2007) 'Mass wasting processes - Offshore Sumatra', *Submarine Mass Movements and Their Consequences, 3rd International Symposium*, pp. 327–336. doi: 10.1007/978-1-4020-6512-5_34.

Tebbens, S. F. (2020) 'Landslide Scaling: A Review', *Earth and Space Science*. Wiley-Blackwell Publishing Ltd. doi: 10.1029/2019EA000662.

Tenzer, R., Sirguey, P., Rattenbury, M. and Nicolson, J. (2011) 'A digital rock density map of New Zealand', *Computers & Geosciences*, 37(8), pp. 1181–1191. doi: 10.1016/J.CAGEO.2010.07.010.

Thuro, K., Berner, C. and Eberhard, E. (2006) 'Der Bergsturz von Goldau 1806 - Was Wissen wir 200 Jahre nach der Katastrophe?', *Bulletin fuer Angewandte Geologie*.

Tinti, S., Pagnoni, G. and Zaniboni, F. (2006) 'The landslides and tsunamis of the 30th of December 2002 in Stromboli analysed through numerical simulations', *Bulletin of Volcanology*, 68(5), pp. 462–479. doi: 10.1007/s00445-005-0022-9.

Tippett, J. M. and Kamp, P. J. J. (1995) 'Geomorphic evolution of the Southern Alps, New Zealand', *Earth Surface Processes and Landforms*, 20(2), pp. 177–192. doi:

10.1002/esp.3290200207.

Tripsanas, E. K., Piper, D. J. W., Jenner, K. A. and Bryant, W. R. (2008) 'Submarine mass-transport facies: New perspectives on flow processes from cores on the eastern North American margin', *Sedimentology*, 55(1), pp. 97–136. doi: 10.1111/j.1365-3091.2007.00894.x.

Turnbull, I. M. (2000) 'Geology of the Wakatipu area', *Institute of Geological and Nuclear Sciences 1:250,000 Geological Map*, pp. 1–72. Available at: https://www.scopus.com/inward/record.uri?eid=2-s2.0-85016361041&partnerID=40&md5=2ab44d59330c6d88df58c4a3e1eff819.

Turnbull, I. M., Allibone, A. H. and Jongens, R. (2010) *Geology of the Fiordland area*, *Institute of Geological and Nuclear Sciences 1:250,000 Geological Map*.

Turnbull, J. M. and Davies, T. R. H. (2006) 'A mass movement origin for cirques', *Earth Surface Processes and Landforms*, 31(9), pp. 1129–1148. doi: 10.1002/esp.1324.

Turner, A. J., Woodward, J., Dunning, S. A., Shine, A. J., Stokes, C. R. and Cofaigh, C. Ó. (2012) 'Geophysical surveys of the sediments of Loch Ness, Scotland: implications for the deglaciation of the Moray Firth Ice Stream, British-Irish Ice Sheet', *Journal of Quaternary Science*, 27(2), pp. 221–232. doi: 10.1002/jqs.1538.

Uhlmann, M., Korup, O., Huggel, C., Fischer, L. and Kargel, J. S. (2013) 'Supra-glacial deposition and flux of catastrophic rock-slope failure debris, south-central Alaska', *Earth Surface Processes and Landforms*, 38(7), pp. 675–682. doi: 10.1002/esp.3311.

Upton, P. and Osterberg, E. C. (2007) 'Paleoseismicity and mass movements interpreted from seismic-reflection data, Lake Tekapo, South Canterbury, New Zealand', *New Zealand Journal of Geology and Geophysics*, 50(4), pp. 343–356. doi: 10.1080/00288300709509841.

Urlaub, M., Talling, P. J. and Masson, D. G. (2013) 'Timing and frequency of large submarine landslides: Implications for understanding triggers and future geohazard', *Quaternary Science Reviews*, 72, pp. 63–82. doi: 10.1016/j.quascirev.2013.04.020.

Vandergoes, M. J., Howarth, J. D., Dunbar, G. B., Turnbull, J. C., Roop, H. A., Levy, R. H., Li, X., Prior, C., Norris, M., Keller, L. D., Baisden, W. T., Ditchburn, R., Fitzsimons, S. J. and Bronk Ramsey, C. (2018) 'Integrating chronological uncertainties for annually laminated lake sediments using layer counting, independent chronologies and Bayesian age modelling (Lake Ohau, South Island, New Zealand)', *Quaternary Science Reviews*, 188, pp. 104–120. doi:

10.1016/j.quascirev.2018.03.015.

Varnes, D. J. (1958) *Landslides Types and Processes*, *Landslides and Engineering Practice. Special Report 29, NAS-NRC Publication 544*. Edited by E. B. Eckel. Washington DC: Highway Research Board.

Venture Southland (2017) *Southland Tourism Key Indicators. MBIE Report*.

Voight, B., Le Friant, A., Boudon, G., Deplus, C., Komorowski, J. C., Lebas, E., Sparks, R. S. J., Talling, P. and Trofimovs, J. (2012) 'Undrained sediment loading key to long-runout submarine mass movements: Evidence from the caribbean volcanic arc', in *Submarine Mass Movements and Their Consequences - 5th International Symposium*. Kluwer Academic Publishers, pp. 417–428. doi: 10.1007/978-94-007-2162-3_37.

Völker, D., Scholz, F. and Geersen, J. (2011) 'Analysis of submarine landsliding in the rupture area of the 27 February 2010 Maule earthquake, Central Chile', *Marine Geology*, 288(1–4), pp. 79–89. doi: 10.1016/j.margeo.2011.08.003.

Vuong, Q. H. (1989) 'Likelihood Ratio Tests for Model Selection and Non-Nested Hypotheses', *Econometrica*, 57(2), p. 307. doi: 10.2307/1912557.

Wallace, L. M., Barnes, P., Beavan, J., Dissen, R. Van, Litchfield, N., Mountjoy, J., Langridge, R., Lamarche, G. and Pondard, N. (2012) 'The kinematics of a transition from subduction to strike-slip: An example from the central New Zealand plate boundary', *Journal of Geophysical Research: Solid Earth*, 117(B2), p. 2405. doi: 10.1029/2011JB008640.

Wallace, L. M., Beavan, J., McCaffrey, R., Berryman, K. and Denys, P. (2007) 'Balancing the plate motion budget in the South Island, New Zealand using GPS, geological and seismological data', *Geophysical Journal International*, 168(1), pp. 332–352. doi: 10.1111/j.1365-246X.2006.03183.x.

Wang, J., Howarth, J. D., McClymont, E. L., Densmore, A. L., Fitzsimons, S. J., Croissant, T., Gröcke, D. R., West, M. D., Harvey, E. L., Frith, N. V., Garnett, M. H. and Hilton, R. G. (2020) 'Long-term patterns of hillslope erosion by earthquake-induced landslides shape mountain landscapes', *Science Advances*, 6(23), pp. 1–9. doi: 10.1126/sciadv.aaz6446.

Warren-Smith, E., Chamberlain, C. J., Lamb, S. and Townend, J. (2017) 'High-Precision Analysis of an Aftershock Sequence Using Matched-Filter Detection: The 4 May 2015 M L 6 Wanaka Earthquake, Southern Alps, New Zealand', *Seismological Research Letters*, 88(4), pp.

1065–1077. doi: 10.1785/0220170016.

Watson, S. J., Mountjoy, J. J. and Crutchley, G. J. (2020) 'Tectonic and geomorphic controls on the distribution of submarine landslides across active and passive margins, eastern New Zealand', *Geological Society, London, Special Publications*, 500(1), pp. 477–494. doi: 10.1144/SP500-2019-165.

Watt, S. F. L., Talling, P. J. and Hunt, J. E. (2014) 'New insights into the emplacement dynamics of volcanic island landslides', *Oceanography*, 27(2), pp. 46–57. doi: 10.5670/oceanog.2014.39.

Watt, S. F. L., Talling, P. J., Vardy, M. E., Heller, V., Hühnerbach, V., Urlaub, M., Sarkar, S., Masson, D. G., Henstock, T. J., Minshull, T. A., Paulatto, M., Le Friant, A., Lebas, E., Berndt, C., Crutchley, G. J., Karstens, J., Stinton, A. J. and Maeno, F. (2012) 'Combinations of volcanic-flank and seafloor-sediment failure offshore Montserrat, and their implications for tsunami generation', *Earth and Planetary Science Letters*, 319, pp. 228–240. doi: http://dx.doi.org/10.1016/j.epsl.2011.11.032.

Watt, S. F. L., Talling, P. J., Vardy, M. E., Masson, D. G., Henstock, T. J., Hühnerbach, V., Minshull, T. A., Urlaub, M., Lebas, E., Le Friant, A., Berndt, C., Crutchley, G. J. and Karstens, J. (2012) 'Widespread and progressive seafloor-sediment failure following volcanic debris avalanche emplacement: Landslide dynamics and timing offshore Montserrat, Lesser Antilles', *Marine Geology*, 323, pp. 69–94. doi: http://dx.doi.org/10.1016/j.margeo.2012.08.002.

Watts, A. B. and Masson, D. G. (2001) 'New sonar evidence for recent catastrophic collapses of the north flank of Tenerife, Canary Islands', *Bulletin of Volcanology*, pp. 8–19. doi: 10.1007/s004450000119.

Weidinger, J. T., Korup, O., Munack, H., Altenberger, U., Dunning, S. A., Tippelt, G. and Lottermoser, W. (2014) 'Giant rockslides from the inside', *Earth and Planetary Science Letters*, 389, pp. 62–73. doi: 10.1016/j.epsl.2013.12.017.

White, J. L., Morgan, M. L. and Berry, K. A. (2015) *Bulletin 55 - The West Salt Creek Landslide: A Catastrophic Rockslide and Rock/Debris Avalanche in Mesa County*. Golden, Colorado: Colorado Geological Survey.

Whitehouse, I. E. (1983) 'Distribution of large rock avalanche deposits in the central Southern Alps, New Zealand', *New Zealand Journal of Geology and Geophysics*, 26(3), pp. 271–279.

doi: 10.1080/00288306.1983.10422240.

Whitehouse, I. E. and Griffiths, G. A. (1983) 'Frequency and hazard of large rock avalanches in the central Southern Alps, New Zealand.', *Geology*, 11(6), pp. 331–334. doi: 10.1130/0091-7613(1983)11<331:FAHOLR>2.0.CO;2.

Whittall, J., Eberhardt, E. and McDougall, S. (2017) 'Runout analysis and mobility observations for large open pit slope failures', *Canadian Geotechnical Journal*, 54(3), pp. 373–391. doi: 10.1139/cgj-2016-0255.

Wiemer, G., Moernaut, J., Stark, N., Kempf, P., De Batist, M., Pino, M., Urrutia, R., de Guevara, B. L., Strasser, M. and Kopf, A. (2015) 'The role of sediment composition and behavior under dynamic loading conditions on slope failure initiation: a study of a subaqueous landslide in earthquake-prone South-Central Chile', *International Journal of Earth Sciences*, 104(5), pp. 1439–1457. doi: 10.1007/s00531-015-1144-8.

Wilkinson, C., Hikuroa, D. C. H., MacFarlane, A. H. and Hughes, M. W. (2020) 'Mātauranga Māori in geomorphology: Existing frameworks, case studies, and recommendations for incorporating Indigenous knowledge in Earth science', *Earth Surface Dynamics*, 8(3), pp. 595–618. doi: 10.5194/esurf-8-595-2020.

Wolter, A., Gischig, V., Stead, D. and Clague, J. J. (2016) 'Investigation of geomorphic and seismic effects on the 1959 Madison Canyon, Montana, landslide using an integrated field, engineering geomorphology mapping, and numerical modelling approach', *Rock Mechanics and Rock Engineering*, 49(6), pp. 2479–2501. doi: 10.1007/s00603-015-0889-5.

Yavari-Ramshe, S. and Ataie-Ashtiani, B. (2016) 'Numerical modeling of subaerial and submarine landslide-generated tsunami waves—recent advances and future challenges', *Landslides*, 13(6), pp. 1325–1368. doi: 10.1007/s10346-016-0734-2.

Yavari-Ramshe, S. and Ataie-Ashtiani, B. (2019) 'On the effects of landslide deformability and initial submergence on landslide-generated waves', *Landslides*, 16(1), pp. 37–53. doi: 10.1007/s10346-018-1061-6.

Yetton, M. D. and McCahon, I. F. (2008) *Earthquake Hazard Assessment for Waimate, and part Waitaki dictrict*, *Environment Canterbury Report*.

Yoshida, H. (2014) 'Hummock alignment in Japanese volcanic debris avalanches controlled by pre-avalanche slope of depositional area', *Geomorphology*, 223(1), pp. 67–80. doi:

10.1016/j.geomorph.2014.06.024.

Yoshida, H., Sugai, T. and Ohmori, H. (2012) ‘Size-distance relationships for hummocks on volcanic rockslide-debris avalanche deposits in Japan’, *Geomorphology*, 136(1), pp. 76–87. doi: 10.1016/j.geomorph.2011.04.044.